Circulation in Port Valdez, Alaska measured by Lagrangian Drifter Experiments, towed acoustic Doppler current profiler and hydrographic profiles in June and September 2016, and March 2017

Final Report

Prepared for:

Prince William Sound Regional Citizens' Advisory Council

by

Shelton M. Gay III, Ph.D.[1]

[1]Prince William Sound Science Center, Cordova Alaska

March 22, 2018

TABLE OF CONTENTS

LIST OF FIGURES……..……..……... iv

LIST OF TABLES ……..……..…….…….. xi

LIST OF DEFINITIONS ……..……..…….…… xii

1.0 EXECUTIVE SUMMARY……..…..…….…… 1

2.0 INTRODUCTION……..……..…….. 6

2.1 Study Area……..……..…….. 6

2.2.1 Regional Climatic and Oceanographic Conditions ……..……... 7

2.1.2 Oceanographic and Climatic Conditions within Port Valdez …..…….. 7

3.0 METHODS AND MATERIALS…….…….. 8

3.1 ADCP Transects and Hydrographic Profiles ....…….……..... 8

3.2 Drifter Deployments ....……..…….… 9

3.3 Data Processing and Analysis ....……..…. 9

3.3.1 Ekman Layer Calculations ....……..…. 10

3.3.2 Dynamic Topography and Geostrophic Velocities ....…….... 10

3.3.4 Drifter Speeds and Dispersion Calculations …….…..….. 11

4.0 RESULTS……..……..…….....…..... 12

4.1 Meteorological Data and Freshwater Input: June 2016 ....……..….... 12

4.2 Hydrography .....……...…….……..……..... 13

4.2.1 Temperature and Salinity (T/S) Profile …….……..…….... 13

4.2.2 Vertical T/S Sections ……...…….……..……..... 14

4.3 ADCP Currents ……...…….……..…….…..... 14

4.4 Drifter Trajectories ……...…….……..…….…..... 15

4.4.1 Ispheres (0-0.3*m*) ……...…….……..…….…..... 15

4.4.2 Microstars (1*m*) ……...…….……..……..... 16

4.4.3 SVP Drifters (10*m* and 40*m*) ……...…….……..……..... 17

4.4.4 Dispersion Experiments ……...…….……..……..... 18

4.4.4.1 Ispheres ……...…….……..……..... 19

4.4.4.2 Microstars ……...…….……..……..... 19

4.4.4.3 SVP Drifters (10*m*) ……...…….……..…….…..... 19

4.5 Meteorological Data and Freshwater Input: September 2016 .....……..... 20

4.6 Hydrography .....……...…….……..……..... 21

4.6.1 Temperature and Salinity (T/S) Profiles 21

4.6.2 Vertical T/S Sections 21

4.7 ADCP Currents 22

4.8 Drifter Trajectories 22

4.8.1 Ispheres (0-0.3*m*) 23

4.8.2 Microstars (1*m*) 24

4.8.3 SVP Drifters (10*m*) 26

4.8.4 SVP Drifters (40*m*) 27

4.9 Meteorological Data and Freshwater Input: March 2017..... 28

4.10 Hydrography 29

4.10.1 Temperature and Salinity (T/S) Profiles 29

4.10.2 Vertical T/S Sections 28

4.11 ADCP Currents 29

4.12 Drifter Trajectories 31

4.12.1 Ispheres (0-0.3*m*) 31

4.12.2 Microstars (1*m*) 32

4.12.3 SVP Drifters (10*m* and 40*m*) 33

4.13 Dynamic Topography and Geostrophic Velocities 34

4.13.1 June 2016 34

4.13.2 September 2016 35

4.13.3 March 2017 36

4.14 Drifter Speeds and Dispersion Rates 37

4.14.1 June 2016 37

4.14.2 September 2016 38

4.14.3 March 2017 40

4.15 Principal Axes of Variance and Times of Retention or Flushing 42

4.15.1 June 2016 43

4.15.2 September 2016 44

4.15.3 March 2017 45

4.16 Average Speeds and Along-Channel (*u*) Velocities, and Time Series of Flushing vs. Retention 46

4.16.1 June 2016 46

4.16.2 September 2016 48

4.16.3 March 2017 49

5.0 DISCUSSION……..……..……..…….... 50

5.1 Estuarine Circulation in Relation to Small PWS Fjords and Port Valdez; adapted from Gay (2013b) ……..……..……..…….... 50

5.2 Wind and Wave Effects on Fjord Circulation …….……..……..……..... 51

5.3 Factors Affecting Horizontal Circulation ……..... 53

5.3.1 Winds, Coriolis and Tides ……...……..……..…. 53

5.3.2 Estuarine Conditions and Baroclinic-Geostrophic flow……..….. 54

5.3.3 Large and Small Scale Turbulence .....……..….. 55

5.4 Lagrangian Flow Patterns ……...……..……..….... 56

5.4.1 Early Summer ……...……..……..…..... 56

5.4.2 Early Fall ……...……..……..…..... 58

5.4.3 Late Winter ……...……..……..…..... 59

5.5 Drifter Dispersion ……...……..……..……..….... 60

5.6 Circulation Patterns Affecting Flushing and Retention ……..……..….... 64

5.6.1 Early Summer ……...……..……..……... 64

5.6.2 Early Fall ……...……..……..…..... 65

5.6.3 Late Winter ……...……..……..…..... 67

5.7 Changes in Circulation Modes due to Winds …….……..…..... 69

5.8 Locations at Risk from Contaminants …...……..……..…..... 69

5.9 Dispersant Effectiveness with regards to Temperature and Salinity ……..... 71

6.0 SUMMARY AND CONCLUSIONS…….……..…..…. 73

7.0 ACKNOWLEDGMENTS…….……..……... 77

8.0 REFERENCES…….……..…..... 78

Appendix A: Lists of CTD casts, plots of station locations and profiles of temperature and salinity.

Appendix B: Lists of ADCP transect parameters and plots of along-channel (u) velocities and horizontal vectors not shown in the text.

Appendix C: Drifter deployments, including dates, times and start and end coordinates.

Appendix D: T Tests for means of drifter speeds & u velocities.

Appendix E: Detailed description of a possible future RCAC program to model Port Valdez circulation (provided by J. Robiba of PWSRCAC).

LIST OF FIGURES

Fig. 1. Locations and bathymetry of Prince William Sound and Port Valdez in south central Alaska.

Fig. 2. General schematics of repeated towed ADCP transects and CTD stations.

Fig. 3. Examples of oceanographic instruments to be used in the Port Valdez circulation experiments.

Fig. 4. Semi-diurnal tides occurring during each experiment and periods of tides during oceanographic surveys and the number of ADCP transect runs and CTD sets for each period.

Fig. 5. Meteorological data collected in June 2016 at the Valdez, Alaska NOAA-COOPS station 9454240.

Fig. 5 (cont.). Wind vectors for the month of June 2016 measured at the Valdez, Alaska NOAA-COOPS station 9454240.

Fig. 6. Mean across-channel temperature and salinity profiles for transects 1, 3, 5, 7 and 9 for Run A on June 22 and Run F on June 26.

Fig. 6 (cont). Mean across-channel temperature versus salinity for transects 1, 3, 5, 7 and 9 for Run A on June 22 and Run F on June 26.

Fig. 7A. Vertical sections of along-channel temperature, salinity and density for transects 1 and 3, Run A on June 22, 2016.

Fig. 7B. Vertical sections of along-channel temperature, salinity and density for transects 1 and 3, Run F on June 26, 2016.

Fig. 7C. Vertical sections of across-channel density for transects 1, 5 and 9, Runs A and F on June 22 and 26, 2016.

Fig. 8A. ADCP currents measured on June 22, 2016 over the first flood tide during the 36 hr survey.

Fig. 8B. ADCP currents measured on June 22, 2016 over the last half of ebb tide 1 and the first 47 min of flood tide 2 during the 36 hr survey.

Fig. 8C. ADCP currents measured on June 23, 2016 over the last 2.3 hr of flood tide 2 and the first 2.0 hr of ebb tide 2 during the 36 hr survey.

Fig. 8D. ADCP currents measured on June 23, 2016 over the second ebb tide during the 36 hr survey.

Fig. 8E. ADCP currents measured on June 23, 2016 over the last 2.0 hr of ebb tide 2 and the first 2.5 hr of flood tide 3 during the 36 hr survey.

Fig. 9. ADCP current vectors at 7 to 15 m measured on June 24 to 25, 2016 following the 36 hr survey.

Fig. 10. Trajectories of ispheres showing combined wind and surface flows for deployments #1 and #4 of i0460 on June 22nd and 24th and deployment #2 of i5480 on June 22.

Fig. 10 (cont). Trajectories of ispheres showing combined wind and surface flows for deployments #3 and #5 of i9460 and i6350 on the 23rd and 25th respectively, and deployments #10 and #11 of i9460 and i0460 on the 29th.

Fig. 10 (cont). Microstar trajectories showing flows at 1m depth for deployments #1 and #2 of m007 and m001 on June 22, and deployments #3 to #5 of m007, m001 and m003 on June 23rd, 24th and 25th respectively.

Fig. 10 (cont.). Trajectories of SVP drifters showing flows at 10m depths for deployments #2 to #5 of s004, s008, s007 and s002 respectively from June 22 to 27, and deployments #8 and #9 of s005 and s006 and s004 respectively on June 28.

Fig. 10 (cont). Trajectory of SVP #001 showing flows at 40m depth from June 25 to July 01.

Fig. 11. The first dispersion experiment (deployments #6 and #7) consisting of three sets of drifters released together in the central fjord on June 27 and three microstars redeployed on June 28.

Fig. 11 (cont.). The second dispersion experiment (deployments #10 and #11) consisting of two ispheres and three sets of microstars and 10m SVPs released nearly simultaneously in the central fjord on June 29.

Fig. 11 (cont). Microstar trajectories showing flows at 1m depth during the final two dispersion experiments consisting of deployments #12a and #13 of microstars m004, m005 and m006 on the June 29th and 30th respectively, and deployments #12b of microstars m003, m007and m008 on the 29th.

Fig. 12. Meteorological data collected in September 2016 at the Valdez, Alaska NOAA-COOPS station 9454240.

Fig. 13. Wind vectors for the month of September 2016 measured at the Valdez, Alaska NOAA-COOPS station 9454240.

Fig. 14. Mean across-channel temperature and salinity for transects 1, 3, 5, 7 and 9, Run A on September 21, 2016.

Fig. 14 (cont). Mean across-channel temperature and salinity for transects 1, 3, 5, 7 and 9, Run H on September 25, 2016.

Fig. 15A. Vertical sections of along-channel temperature, salinity and density for transect 1 Run A and H on September 21 and 25, 2016.

Fig. 15B. Vertical sections of along-channel temperature, salinity and density for transect 3, Run A and H on September 21 and 25, 2016.

Fig. 15C. Vertical sections of across-channel density for transects 1, 5 and 9, Runs A and H on September 21 and 25, 2016.

Fig. 16A. ADCP currents measured during the second ebb tide of the 36 hr survey on September 21, 2016.

Fig. 16B. ADCP currents measured over the last 2.25 hr of ebb tide 2 and the first 2.6 hr of flood tide 2 during the 36 hr survey from September 21 to 22, 2016.

Fig. 16C. ADCP currents measured over the second flood tide during the 36 hr survey from September 21 to 22, 2016.

Fig. 16D. ADCP currents measured over the last 2.75 hr of ebb tide 3 and the first 0.5 hr of flood tide 3 during the 36 hr survey from September 21 to 22, 2016.

Fig. 17A. ADCP currents measured on September 23, 2016 following the 36 hr survey.

Fig. 17B. ADCP currents measured on September 24, 2016 following the 36 hr survey.

Fig. 17C. ADCP currents measured on September 25, 2016 following the 36 hr survey.

Fig. 18. Trajectories of ispheres showing surface flows on September 21 to 23, 2016.

Fig. 18 (cont.). Trajectories of ispheres showing surface flows on September 24 to 26, 2016.

Fig. 18 (cont.). Trajectories of ispheres showing surface flows on September 26 to 28, 2016.

Fig. 18 (cont.). Trajectories of ispheres showing surface flows on September 28 to 29, 2016.

Fig. 19. Trajectories of microstars showing flows at 1*m* on September 21 to 23, 2016.

Fig. 19 (cont.). Trajectories of microstars showing flows at 1*m* on September 23 to 25, 2016.

Fig. 19 (cont.). Trajectories of microstars showing flows at 1*m* on September 25 to 27, 2016.

Fig. 19 (cont.). Trajectories of microstars showing flows at 1*m* on September 27 to 29, 2016.

Fig. 19 (cont.). Trajectories of microstars showing flows at 1*m* on September 29 to 30, 2016.

Fig. 20. Trajectories of svp10 drifters showing flows at 10*m* on September 21 to 25, 2016.

Fig. 20 (cont.). Trajectories of svp10 drifters showing flows at 10*m* on September 25 to 30, 2016.

Fig. 20 (cont.). Trajectories of SVP drifters showing flows at 10*m* and 40*m* in September 2016.

Fig. 21. Meteorological data collected in March 2017 at the Valdez, Alaska NOAA-COOPS station 9454240.

Fig. 21 (cont.). Hourly wind vectors for the month of March 2017 measured at the Valdez, Alaska NOAA-COOPS station 9454240.

Fig. 22. Mean across-channel temperature and salinity for transects 1, 5 and 9, Run A/B on March 21 and 23, 2017.

Fig. 23. Mean across-channel temperature and salinity for transects 1, 3, 5, 7 and 9, Run C on March 24, 2017.

Fig. 24A. Vertical sections of along-channel temperature, salinity and density for transect 1 on March 21-23 and 24, 2017.

Fig. 24B. Vertical sections of along-channel temperature, salinity and density for transect 3 on March 21-23 and 24, 2017.

Fig. 24C. Vertical sections of across-channel density for transects 1 and 9, Runs A/B and C on March 21-23 and 24, 2017.

Fig. 25A. ADCP currents measured during the second ebb tide on March 21, 2017.

Fig. 25B. ADCP currents measured during the end of ebb tide #2 and first half of flood tide #2 on March 21, 2017.

Fig. 25C. ADCP currents measured during the second ebb tide on March 24, 2017.

Fig. 26. Trajectories of ispheres showing surface flows from March 24 to 25, 2017.

Fig. 26 (cont.). Trajectories of ispheres showing surface flows from March 26 to 30, 2017.

Fig. 27. Trajectories of microstars showing flows at 1*m* on March 24 to 27, 2016.

Fig. 27 (cont.). Trajectories of microstars showing flows at 1*m* on March 26 to 30, 2017.

Fig. 28. Trajectories of svp10 drifters showing flows at 10*m* on March 24 to 29, 2017.

Fig. 28 (cont.). Trajectories of svp10 drifters showing flows at 10*m* on March 26 to 30, 2017.

Fig. 28 (cont.). Trajectories of svp40 drifters showing flows at 40*m* on March 24 to 30, 2017.

Fig. 29. Examples of dynamic topography (1/100db) in June 2016.

Fig. 30. Geostrophic velocities from along-fjord CTD transects on June 22 and 26, 2016.

Fig. 31. Geostrophic velocities from cross-channel CTD transects on June 22, 2016.

Fig. 32. Geostrophic velocities from cross-channel CTD transects on June 26, 2016.

Fig. 33. Examples of dynamic topography (1/100db) in September 2016.

Fig. 34. Geostrophic velocities from along-channel CTD transects on September 21 and 24, 2016.

Fig. 35. Geostrophic velocities from cross-channel CTD transects on September 21 and 25, 2016

Fig. 36. Examples of dynamic topography in March 2017.

Fig. 37. Geostrophic velocities from along-channel CTD transects on March 21 to 25, 2017.

Fig. 38. Geostrophic velocities from cross-channel CTD transects on March 21 to 25, 2017.

Fig. 39. Drifter speeds and dispersion during the first dispersion experiment conducted from June 27 to 29, 2016.

Fig. 41. Drifter speeds and dispersion during the third dispersion experiment conducted from June 29 to 30, 2016.

Fig. 42. Drifter speeds and dispersion during the first and second dispersion experiments conducted from September 21 to 23, 2016.

Fig. 43. Drifter speeds and dispersion over time during the third and fourth experiments conducted from September 22 to 23, 2016.

Fig. 44. Drifter speeds and dispersion during the fifth to seventh dispersion experiments conducted from September 23 to 25, 2016.

Fig. 45. Drifter speeds and dispersion during the fifth to seventh dispersion experiments conducted from Sept. 23 to 25, 2016.

Fig. 46. Drifter speeds and dispersion over time during experiment #10 conducted from September 26 to 27, 2016.

Fig. 47. Drifter speeds and dispersion over time during experiments #11 to #13 conducted from September 27 to 29, 2016.

Fig. 48. Drifter speeds and dispersion over time during experiments #14 and #16 conducted from September 27 to 29, 2016.

Fig. 49. Drifter speeds and dispersion over time during experiments #16 to #18 conducted from September 28 to 30, 2016.

Fig. 50. Drifter speeds and dispersion over time during experiments #1 and #2, conducted from March 24 to 25, 2017.

Fig. 51. Drifter speeds and dispersion over time during experiment #3, conducted from March 25 to 29, 2017.

Fig. 52. Drifter speeds and dispersion over time during experiment #4, conducted on March 26, 2017.

Fig. 53. Drifter speeds and dispersion over time during experiment #5, conducted on March 26 to 29, 2017.

Fig. 54. Drifter speeds and dispersion over time during experiment #6, conducted on March 27 to 30, 2017.

Fig. 55. Drifter speeds and dispersion over time during experiments #7 and #8, conducted on March 28 to 30, 2017.

Fig. 56A. Scatter plots of U’ and V’ and principal axes of variation for ispheres on June 22 to 27, 2016.

Fig. 56B. Scatter plots of U’ and V’ and principal axes of variation for microstars on June 22 to 27, 2016.

Fig. 56C. Scatter plots of U' and V' and principal axes of variation for 10*m* SVPs on June 22 to 29, 2016.

Fig. 57A. Scatter plots of U' and V' and principal axes of variation for ispheres, microstars and 10*m* SVPs for the first dispersion experiment on June 27th, 2016.

Fig. 57B. Scatter plots of U' and V' and principal axes of variation for ispheres, microstars and 10*m* SVPs (d,e) for the second dispersion experiment on June 29th, 2016.

Fig. 57C. Scatter plots of U' and V' and principal axes of variation for microstars during the third dispersion experiment on June 29th, 2016.

Fig. 58A. Scatter plots of U' and V' and principal axes of variation for ispheres, microstars and 10*m* SVPs (e,f) for drifters deployed on September 21, 2016.

Fig. 58B. Scatter plots of U' and V' and principal axes of variation for ispheres (b,e), microstars (a,c,f) and 10m SVPs (d,g) for drifters deployed on September 21, 2016.

Fig. 58C. Scatter plots of U' and V' and principal axes of variation for ispheres, microstars and 10*m* SVPs for drifters deployed on September 25, 2016.

Fig. 58D. Scatter plots of U' and V' and principal axes of variation for ispheres and microstars deployed on September 26, 2016.

Fig. 58E. Scatter plots of U' and V' and principal axes of variation for ispheres, microstars and 10*m* SVPs for drifters deployed on September 27, 2016.

Fig. 58E. Scatter plots of U' and V' and principal axes of variation for ispheres, microstars and 10*m* SVPs for drifters deployed on September 27, 2016.

Fig. 58F. Scatter plots of U' and V' and principal axes of variation for ispheres, microstars and 10*m* SVPs for drifters in deployments #14 and #16 on September 28, 2016.

Fig. 58G. Scatter plots of U' and V' and principal axes of variation for ispheres group B, microstars group A, microstars group B and 10*m* SVPs group A for drifters in deployments #16, #17 and #18 on September 28 and 29, 2016.

Fig. 58H. Scatter plots of U' and V' and principal axes of variation for 40*m* SVPs launched during deployments 4, 5 and 7 respectively on September 22, 23, and 24, 2016.

Fig. 59A. Scatter plots of U' and V' and principal axes of variation for ispheres, microstars and 10*m* SVPs for deployments #1 and #2 on March 24, 2017.

Fig. 59B. Scatter plots of U' and V' and principal axes of variation for ispheres, microstars and 10*m* SVPs for deployment #3 on March 25, 2017.

Fig. 59C. Scatter plots of U' and V' and principal axes of variation for ispheres, microstars and 10*m* SVPs for deployment #5 on March 26, 2017.

Fig. 59D. Scatter plots of U' and V' and principal axes of variation for ispheres, microstars and 10*m* SVPs for deployment #6 on March 27, 2017.

Fig. 59E. Scatter plots of U' and V' and principal axes of variation for ispheres and 10*m* SVPs for deployment #7 on March 28, 2017.

Fig. 60. Profiles of drifter speeds and along-channel (*u*) velocities, ADCP *u* and *v* velocities and barotropic tidal currents in June 2016.

Fig. 61. Duration and cumulative hours of retention versus flushing for surface (ispheres) and 1*m* (microstars) deployed in June 2016.

Fig. 61 (cont.). Duration and cumulative hours of retention versus flushing for 10*m* and 40*m* SVPs deployed in June 2016.

Fig. 62. Profiles of drifter speeds and along-channel (*u*) velocities and ADCP *u* and *v* velocities and barotropic tidal currents in September 2016.

Fig. 63. Duration and cumulative hours of retention versus flushing for surface (ispheres) and 1*m* (microstars) deployed in September 2016.

Fig. 63 (cont.). Duration and cumulative hours of retention versus flushing for 10*m* and 40*m* SVP drifters deployed in September 2016.

Fig. 64. Profiles of drifter speeds and along-channel (*u*) velocities and ADCP *u* and *v* velocities in March 2017.

Fig. 65. Duration and cumulative hours of retention versus flushing for surface (ispheres) and 1*m* (microstars) deployed in March 2017.

Fig. 65 (cont.). Duration and cumulative hours of retention versus flushing for 10*m* and 40*m* SVP drifters deployed in March 2017.

Fig. 66. Scatter plots of U' and V' and principal axes of variation for ispheres, microstars group-A (deployment #3) and microstars group-B (deployment #4) released on September 22, 2016.

Fig. 67. Locations at a higher risk of contamination from oil advected at various depths shown by drifter trajectories and groundings within Port Valdez in June and September 2016 (a and b) and March 2017 (c).

LIST OF TABLES

Table 1. Drifters deployed during experiments in June and September 2016 and March 2017.

Table 2a. Principal Axes of Variation of velocities, Average Speeds and *u* Velocities, Distances and Drift/Flush Times in June 2016.

Table 2b. Averages and Standard Deviations of Rotation Angles, Speeds, *u* Velocities and Flushing/Retention Times in June 2016.

Table 3a. Principal Axes of Variation of velocities, Average Speeds, Distances and Drift/Flush Times in September 2016.

Table 3b. Averages and Standard Deviations of Rotation Angles, Speeds *u* Velocities and Flushing/Retention Times in September 2016.

Table 4a. Principal Axes of Variation of velocities, Average Speeds, Distances and Drift/Flush Times in March 2017.

Table 4b. Averages and Standard Deviations of Rotation Angles, Speeds *u* Velocities and Flushing/Retention Times in March 2017.

Table 5. Statistics for along-channel (*u*) velocities with respect to retention and flushing.

LIST OF DEFINITIONS

Acoustic Doppler Current Profiler (ADCP) - An oceanographic instrument used to measure profiles of current velocities by determining the average Doppler shift of sound reflected from discrete depth cells (bins) and using a built-in compass and bottom depth tracking to remove the ship's motion and resolve the residual sound shift into three components of velocity (*u*,*v* and *w*) representing the east-west, north-south and vertical flows respectively.

Anticyclonic and Cyclonic Flow – Currents turning to the right (clockwise) or left (counterclockwise) respectively in the Northern Hemisphere. The causes of the turning (i.e. vorticity) may be either Coriolis or turbulence in the flows themselves.

Baroclinic – Occurs when density is a function of other variables in addition to pressure (i.e. the pressure varies over surfaces of constant density). Baroclinic fields of mass are associated with horizontal density variation over a given distance such that the inclination of the isopycnal surfaces gradually diminishes over depth and becomes parallel over a geopotential surface known as the level of no motion.

Barotropic – Occurs when water density is a function of pressure only, such that isobaric and isopycnal surfaces are parallel (i.e. pressure is constant over surfaces of equal density). Barotropic fields of mass are typically associated with body-forces such as tides or horizontal changes in sea surface elevation due to wind transport.

Conductivity, Temperature and Depth (CTD) – This instrument is lowered by a ship's winch to obtain profiles of temperature and salinity over depth at discrete oceanographic stations. The temperature is measured directly by a thermocouple, whereas salinity is calculated from combinations of conductivity, temperature and pressure (i.e. depth).

Continuity of volume – The continuity equation ($\partial u/\partial x + \partial v/\partial y + \partial w/\partial z = 0$) comes from fluid dynamics and is used in modeling oceanic flows. It is based on conservation of mass and relates the rate of density changes in a fluid element to volume fluctuations due to the field of motion (Gill, 1982). It simply states that since mass remains constant for a material element, fluctuations in density related to the flow in one dimension must be balanced in the other dimensions (i.e. volume must be conserved).

Density (ρ) – Defined as the weight of seawater per unit volume in $kg\ m^{-3}$, density is calculated by the equation of state, which is a function of salinity, temperature and pressure $\rho = \rho(s,t,p)$.

Densimetric Froude Number (Fr_f) - The ratio of the freshwater velocity to the speed of an internal wave ($Fr_f = u_f / \sqrt{g' h}$) based on the difference in density of the seawater to freshwater, which gives reduced gravity ($g' = g\Delta\rho/\rho$). The Fr_f value can be used to classify an estuary based on a circulation-stratification diagram by Hansen and Rattray (1966) in which circulation is defined by Fr_f along with a stratification parameter ($\delta S/[S]$) defined as the ratio of the difference in surface to bottom salinity (δS) relative to the average vertical or cross-sectional salinity ([S]).

Dynamic Height (ΔD) – A unit used to express geopotential anomalies (i.e. δ' integrated over *p*) in terms of dynamic meters, such that a ΔD of one dynamic meter = $10 J\ kg^{-1}$ or $10 m^2\ s^{-2}$.

Eddy Viscosities (A_x, A_y, A_z) – Turbulent dissipation coefficients used in the equations of motion that relate Reynolds stresses to mean velocity gradients: $-\overline{u'u'} = A_x\, \partial\bar{u}/\partial x$; $-\overline{u'v'} = A_y\, \partial\bar{u}/\partial y$; $-\overline{u'w'} = A_z\, \partial\bar{u}/\partial z$.

Measured in units of $m^2 s^{-1}$ these kinematic viscosities range as high as 10^5 $m^2 s^{-1}$ for the horizontal coefficients (A_x, A_y) and up to 10^{-1} $m^2 s^{-1}$ for the vertical coefficient (A_z) (Pond and Pickard, 1983).

Ekman Layer and Depth (D_E) – A vertical layer in the ocean affected by wind stress (i.e. friction), which decreases exponentially with depth and in open ocean conditions is turned by Coriolis anticyclonically (clockwise) to form what is known as an Ekman spiral. The Ekman equations are based on a balance of Coriolis acceleration with vertical eddy viscosity, and solutions take on the following forms (Pond and Pickard, 1983):

$$u_E = V_0 \cos\left(\frac{\pi}{4} + \frac{\pi}{D_E} z\right) e^{\pi/D_E z} \quad \text{and} \qquad v_E = V_0 \sin\left(\frac{\pi}{4} + \frac{\pi}{D_E} z\right) e^{\pi/D_E z} \quad ,$$

where V_0 is the surface current, D_E is the Ekman depth at the bottom of the wind-affected layer. The empirical equations used to calculate D_E, V_0 and V_i at depths z are shown on page 10 of the text.

Entrainment –A one-way turbulent process that transports salt vertically into a fresh surface layer by the breaking of internal waves created at the density interface (i.e. pycnocline) by strong down-fjord gravitational motion of freshwater from fluvial discharge.

Eulerian Flow– The time varying current vectors at discrete points in a flow field (i.e. $\partial \mathbf{u}/\partial \mathbf{x}$). An example of this type of measurement would be a moored ADCP or a towed ADCP providing profiles of currents at discrete points specified by averaging currents over a given time and space interval.

Flow Ratio (u_s/u_f) – The ratio of the net surface current to the mean cross-sectional velocity (Dyer, 1997).

Freshwater Velocity (u_f) - Velocity based on the ratio of freshwater discharge (R) in $m^3 s^{-1}$ divided by the cross-sectional area of the estuary or a constriction (A) in m^2 ($u_f = R/A$).

Friction Velocity (u_*) - Friction velocity is given by the square root of wind stress divided by water density: $(\tau_a/\rho_w)^{-1/2}$, where $\tau = W^2 C_D \rho_a$ and C_D and ρ_a are the drag coefficient and density for air respectively.

Geopotential (Φ) – The work done to raise a body vertically over a small distance, $\Phi = g\,z$ Joules (J) kg^{-1}, where g is the gravitational acceleration ($9.8 m\,s^{-2}$) and z is in meters.

Geopotential Anomaly (Φ) – The specific volume anomaly (δ') integrated over pressure, which is equivalent to 10 times the dynamic height.

Geostrophic Flow – Described by the shallow water equations (Gill, 1982), geostrophic flows occur along isobars due to the balance of horizontal pressure gradients with acceleration due to Coriolis. The shallow water momentum equations replace density and horizontal pressure ($1/\rho \partial p \partial \mathbf{x}$) with gravitational acceleration and perturbation pressure due to variation in sea surface elevation ($g \partial \eta' \partial \mathbf{x}$) (Benoit and Cushman, 2008; Gill, 1982). Note that calculation of geostrophic flow is based on horizontal differences in dynamic heights divided by the distance between stations (in meters) and the Coriolis parameter $f = 2\Omega \sin\phi$, where Ω is the rotation rate of the earth in radians s^{-1} and ϕ is the latitude. Note that the velocities are relative to a deep reference level, which is assumed to be static (i.e. a level of no motion).

Inertial Period (*IP*) – The time interval in seconds in which currents moving by inertia only would make a full cycle due solely to planetary vorticity (i.e. $d\boldsymbol{V}/dt = f \cdot \boldsymbol{V}$). The inertial period is defined by the inverse

of the Coriolis parameter (*f*): $2\pi(rad)/f$ ($rad\ s^{-1}$) and flows associated with it are known as inertial currents. At 61° latitude, $f = 1.275 \times 10^{-4}\ rad\ s^{-1}$ and the *IP* is 13.687*hr*.

Isobaric and Isopycnal Surfaces – Surfaces with equal pressure and density respectively.

Katabatic Winds – Drainage winds from higher elevations. In coastal Alaska this involves gravitational flow of cold, dense arctic air through mountain gaps due to high atmospheric pressure in the interior. Such events produce easterly winter winds over Port at speeds >30$m\ s^{-1}$ (~60*kts*) (Carlson *et al*., 1969).

Lagrangian Flow – The path (i.e. trajectory) that a fluid element follows when traversing through a flow field specified at discrete points over time by Eulerian vectors. If all the vectors are tangential to the Lagrangian path then the latter forms a true streamline of the Eulerian field. Lagrangian flow represents the field acceleration in the equations of motion: $\vec{V} \bullet \nabla \vec{V}$.

Sigma-t (σ_t)- A quantity used as a convenience, σ_t refers to density (independent of pressure) with the weight of freshwater removed: $\sigma_{t=} \rho(s,t,0) - 1000\ kg\ m^{-3}$. Note that the units are typically omitted.

Significant Wave Height (H_s) – The highest one-third of the waves in a wave field.

Specific Volume (α) – The inverse of density ($\alpha = 1/\rho$) measured in units of $m^3\ kg^{-1}$.

Specific Volume Anomaly (δ') – Defined as $\delta' = \alpha(s,t,p) - \alpha(35,0,p)$, the specific volume anomaly is used in calculations of dynamic topography and geostrophic flow, both of which require density variations expressed as variations in δ over depth (see dynamic heights).

Stokes Drift – The net forward transport of water due to slightly unequal motions at the top and bottom of wave orbitals. Typically Stokes drift is a small fraction of the wave phase speed.

Stratification Parameter (δS/[S]) – see above Densimetric Froude Number (Fr_f).

Surface Roughness Length (z_0) – A parameter important in the transfer of wind momentum to the sea surface affecting both surface currents and scaling of dynamics of in the wave-affected zone. It has been suggested that z_0 increases with wind speed and is O($1/6^{th}$) the dominant surface wave length. Stacey (1999) has shown empirically that for Knight Inlet, a large fjord in northern British Columbia, z_0 is on the order of the significant wave height (H_s).

Rossby Number (R_o) – Derived from scaling the nonlinear field acceleration terms of the equations of motion by Coriolis, $R_0 = U/\Omega L$, where U is the velocity scale, Ω refers to the Coriolis parameter (*f*) at 61° latitude = $1.275 \times 10^{-4}\ rad\ s^{-1}$ and L is the length scale in meters.

Principal Axes of Variance – Major and minor axes based on the first and second Empirical Orthogonal Functions (EOF) calculated from the velocity components with the means removed to create a covariance matrix, $u' = u - \overline{u};\ v' = v - \overline{v}$. The major axis (mode 1) is rotated to show the dimension over which the maximum variance in velocities occurs and the minor axis (mode 2) contains the least amount of variance and is oriented orthogonally to the former axis. The principal axes are used to show the dominant directions of along-channel or cross-shelf exchange processes (Emory and Thomson, 2004).

1.0 EXECUTIVE SUMMARY

The Prince William Sound Science Center (PWSSC) conducted a study of circulation for the Prince William Sound Regional Citizens' Advisory Council (PWSRCAC) to describe and quantify the currents within Port Valdez, Alaska, and to address concerns regarding the potential dispersal of contaminants, such as spilled oil, within the fjord basin. PWSRCAC felt this research would help the oil spill response community to understand the fate and transport effects of oil, gather specific decision making information related to chemical dispersant use, and assist with prioritization and tactics related to sensitive area protection strategies. The knowledge gained from this study would also aid in designing and validating any future models of oil movement and general circulation applied to Port Valdez, including the oil spill contingency and response (OSCAR) model, the general NOAA oil modeling environment (GNOME) and regional ocean modeling system (ROMS).

The study was conducted during three seasons including early summer (June), early fall (September) and late winter (March). Each season was selected to best characterize how the circulation was affected by differing levels of meteorological variables, such as solar heating and freshwater input, and forcing by winds, tides and spatial variations in water density (i.e. geostrophic flows). The data consisted of Lagrangian flows (i.e. water parcels moving through a flow field) measured by tracking drifter buoys with drogues set to four different depths: surface, 1*m*, 10*m* and 40*m*. Measurements of the flow field were made using a towed acoustic Doppler current (ADCP) profiler and vertical profiles of temperature and salinity were collected using a tethered conductivity, temperature and depth (CTD) instrument lowered by a ship's winch. Ancillary meteorological and tidal data were obtained from archives of local NOAA weather assets located in Valdez, Alaska and historical records[1].

The ADCP data were collected along nine transect lines extending from the inner basin to the central region of the fjord and ending ~ 2*km* (1.08*nm*) west of the Security Zone (SZ). The lines were set up to obtain as much information as possible within the timeframe of the semi-diurnal tides. The instrument was towed at a depth of 2 to 3*m* but since the instrument has a blanking distance of 4*m* the currents in the upper 6 to 7*m* could not be measured. The data were collected in 8*m* depth bins, starting at ~ 7*m* and ending at a maximum depth of ~ 207*m*. The hydrography (CTD) profiles were collected during each repeated run of ADCP transects.

The drifters used in the study consisted of surface oil spill response buoys (ispheres) and subsurface type drifters with drogues centered at 1*m*, 10*m* and 40*m*. In June drifters were deployed singly at first, then as groups of three during dispersion experiments. In September and March all deployments were conducted to measure dispersion in groups of either two or three. Units were released at various regions of the middle and inner basin at points along the ADCP transects. The surface and 1*m* drifters were typically retrieved in one day or less depending on whether grounding occurred or if they had exited the study area, which included the entire fjord up to a western boundary located just north of the Narrows.

All data were quality checked using both standard oceanographic data methods and techniques developed by the author and a prior colleague at the Prince William Sound Science Center (PWSSC). In addition to basic descriptive statistics, more advanced analyses were performed including estimates the forcing of currents by winds, measurements of flow patterns and the magnitudes of currents forced by horizontal variations in mass or water density and principal axes of variation, which describe the directions along which most of the variation in flow occurs.

[1] Archives were from the NOAA Center for Operational Oceanographic Products (CO-OPS) and the Global Historical Climatology Network (GHCN) published online by the NOAA National Environmental Information Center.

The results showed that the patterns of circulation differed significantly between seasons, with circulation modes in the upper meter driven in the summer and fall primarily by winds and horizontal variations in the density (mass) field created by spatial differences in solar heating, freshwater input from cold, glacial sources and limited vertical mixing. The currents were significantly moderated by up-fjord and down-fjord winds, which caused changes in circulation modes on the order of hours from open and closed counterclockwise (cyclonic) and clockwise (anticyclonic) modes to linear flows oriented primarily along the main channel (i.e. east-west in direction). In late winter, the entire upper 80*m* of the water column were driven primarily by strong down-fjord winds. However, when a period of quiescence ensued the circulation modes returned to the prominent eddy modes observed in the previous months.

In all seasons a westerly (outflow) current was observed along the northern side of the fjord, driven by varying seasonal forcing mechanisms. In the summer and fall, for example, the outflows were related to estuarine currents due to freshwater runoff that caused marked horizontal changes in density stratification (i.e. layering) in the upper few meters. These flows were either impeded by daily, westerly sea breezes or enhanced by down-fjord, northeast winds from the interior in June and September respectively. In late winter the water column had nearly uniform physical properties due to vertical mixing from winds and the sinking of dense, salty surface water known as thermohaline convection[2]. At this time, the westerly outflow was generated by strong southeasterly winds transporting water to the northern side of the fjord, thus setting up a basin-scale counterclockwise (cyclonic) circulation extending to at least 80*m* in depth.

In many cases the ADCP data verified the 10*m* and 40*m* subsurface drifter flow patterns. For example, in June the 10*m* currents exhibited counterclockwise (cyclonic) circulations in the mid to outer fjord and northern inner basin at average speeds of 6 to 10*cm* s^{-1} (0.12 to 0.19*kts*) and 5 to 7*cm* s^{-1} (0.1 to 0.14*kts*) respectively, and clockwise (anticyclonic) flows at slightly slower speeds (3 to 4*cm* s^{-1}) in the southeastern inner basin. In contrast, the water at 40*m* moved very slowly and exhibited mostly small east-west oscillations at along-channel velocities consistent with the tidal currents (~1 to 2 *cm* s^{-1}). At times, however, the 40*m* flows in June accelerated to speeds of ~ 10*cm* s^{-1}(0.19*kts*).

In September the ADCP currents increased in to speeds of 25 to 35*cm* s^{-1} (~ 0.5 to 0.7*kts*) and 25 to 30*m* in depth due to partial mixing and deepening of the seasonal vertical temperature and salinity gradients known as the thermocline and halocline[3]. The ADCP data also showed persistent counterclockwise (cyclonic) currents extending from 7 to 23*m* in depth that were traced by the 10*m* drifters, but only during the initial deployments on September 21st to the 23rd. In contrast, the currents at the surface and 1*m* were primarily driven by combinations of estuarine (geostrophic) flow and down-fjord winds. Geostrophic currents are caused by horizontal variation in the density field, and in September these gradients extended deeper into the subsurface water (upper 20*m*) causing nearsurface currents ranging from 45 to 100*cm* s^{-1}. Also, the highest velocities occurred for stations close to large sources of freshwater discharge, such as the Lowe River and Valdez Glacier Stream.

The first half of the March survey was conducted under the influence of strong winds ranging from 12 to 15*m* s^{-1} (23 to 29*kts*) coming from either the southeast (Lowe River Valley) or from the northeast (Valdez Glacier Valley). The surface drifters initially moved to the northwest at speeds ranging from 30 to 45*cm* s^{-1} (0.6 to 0.9*kts*) during the southeast wind events and to the southwest at speeds of 20 to 27*cm* s^{-1} (0.4 to 0.5*kts*) during northeast winds. Based on Ekman layer dynamics and given that the surface drifters were directly driven at 3% to 5% of the wind speed, the surface currents during the above wind events probably

[2] Thermohaline convection occurs in the winter when freshwater input is negligible and maximum surface cooling causes the formation of dense, salty surface water that sinks and mixes of the upper water column over time. In PWS this process can cause mixing to ~100*m* in depth by late March.

[3] The seasonal thermocline and halocline are vertical gradients caused respectively by solar heating and freshwater inputs from direct precipitation and runoff.

ranged from 10 to 14*cm* s^{-1} (0.2 to 0.27*kts*) and 6.5 to 8.5*cm* s^{-1} (0.13 to 0.17*kts*) respectively due to winds and tidal currents. The latter were negligible during the first segment and estimated at only 1.0 to 1.5*cm* s^{-1} (~0.03*kts*) based on the approximate changes in tidal volume and cross-sectional area near the mouth.

The nearly continuous winds in March also affected the deeper flows as well, and forced drifters at all depths to initially move northwest. However, due to the long-shore flow developed by wind transport all the subsurface drifters then moved steadily westward at maximum speeds ranging from 20 to 25*cm* s^{-1} (0.4 to 0.5kts) for the 1*m* drifters and 12 to 15*cm* s^{-1} (0.23 to 0.29*kts*) for the 10*m* drifters. During the second half of the survey, however, the winds diminished and eventually a one-day period of quiescence began. At this time the drifter speeds decreased significantly and their motions showed highly varied tracks including open and closed cyclonic and anticyclonic modes similar to previous months.

In all seasons the north-south (cross-channel) flows were also important and frequently resulted in drifter groundings along the shoreline. In June and September, for example, cross-channel flows were responsible for grounding 100% of the surface drifter that exhibited retention; with retention being inferred by a net eastward movement of these drifters. Drifters exhibiting a net westward movement were considered to be flushing, and in the same months 67% and 40% of flushing surface buoys also grounded inside the fjord and thus were considered to be retentions by default. The 1*m* drifters, by contrast, were driven ashore in only two deployments in June, and in September none of the 1*m* drifter deployments exhibiting flushing ended in grounding inside the fjord. However, four of the latter cases were considered questionable due to the drifters grounding on the western shoreline beyond Shoup Bay.

In June the average east-west (along-channel) drifter movement generally inferred that retention occurred for 93% of the surface water and 75% of the flows at 1*m*. The subsurface currents showed 66% retention at 10*m* and a net eastward motion at 40*m* indicated that the deep, subsurface water in the inner basin had 100% retention. Conditions in the fall and winter favored flushing, but in September retention of the surface drifters was still relatively high (62%) due to grounding, whereas 85% of the 1*m* flows showed complete flushing. In late winter 45% of the surface flows exhibited flushing, but in all cases the drifters grounded before exiting the fjord. In contrast, 72% of the flows at 1*m* exhibited complete flushing and in only three cases water at 1*m* moved back into the fjord. Retention of water at 10*m* in the fall decreased only slightly with respect to June (55% vs. 66%), but in late winter this layer exhibited 90% flushing. However, in two of the 10*m* deployments in late winter three of the drifters snagged the bottom along the northern shore. The water would have continued to flush westward but partial retention could be considered due to the currents striking the sub-tidal zone. The flows at 40*m* exhibited 100% flushing also along the northern shoreline in both the fall and late winter, but in September two of these drifters also made contact with the northern subsurface benthic zone in the outer fjord.

Port Valdez and PWS share some common oceanographic characteristics. However, they also differ significantly in certain properties that drive circulation. For example, eddy circulations in Port Valdez occur from mesoscale turbulence caused by local vorticity in the flow field, as opposed to closed geostrophically balanced eddies that occur in central PWS. As such, these features in Port Valdez are highly ephemeral and frequently occur as open counterclockwise (cyclonic) and clockwise (anticyclonic) turns. Lateral dispersion due to turbulence is also generally limited in both systems but also highly variable depending on the prevailing conditions of winds, estuarine (geostrophic) flows and lateral shear in the flow field. Although dispersion in Port Valdez typically increased when flows reached the shore as expected, during periods of low winds the large-scale turbulence in the system created mesoscale eddies that gradually dispersed material, but also caused longer retention in comparison to flushing by currents forced by wind and estuarine driven currents. The maximum flushing should therefore occur for the surface and 1*m* layers, as they exhibited the most rapid down-fjord motions that periodically entered Valdez Arm. In contrast, the deeper flows at 10 and 40*m* were typically much slower and dispersion at these depths occurred later in the deployments.

Conclusions

Early Summer:

1) Oil spilled within the fjord in early summer (June) could be held within the system for long periods depending on the prevailing meteorological and oceanographic conditions. For example, surface oil dispersing into the central fjord basin could either contaminate the southeast shoreline in as little as 9*hr* or flush from the fjord in less than half a day (7*hr*) depending on whether diurnal, westerly winds forced inward retention or if oil became entrained into an outflow along the northern side of the fjord that is enhanced by weak, down-fjord winds at night.

2) A caveat is that due to strong, reversing actions of westerly winds in combination with flood tides at the Narrows oil that flushed from the fjord at night could return the following day and contaminate the northern shoreline in about one day (25*hr*).

3) In other cases, retention of oil could occur for as long as 64 to 66*hr*, and result in contamination of multiple areas due to wide oscillatory motions within the fjord, or oil could move directly into the inner basin and contaminate the eastern to northeastern shorelines.

4) If dispersants were applied allowing the oil to vertically mix then flushing at 1*m* in depth in June could occur in 17 to 27*hr*. However, oil in this layer could also undergo oscillatory motions similar to the surface water and hence remain in the fjord indefinitely until prolonged flushing conditions returned.

5) Oil mixed to depths of 10*m* and 40*m* would very likely remain within the fjord for long periods (5 to 16 days). At 10*m* it would move in large counterclockwise (cyclonic) motions before possibly contaminating various subtidal zones around the fjord. In certain cases, however, the oil in this layer may also be caught in mesoscale counterclockwise (cyclonic) eddies in the outer fjord basin and either eventually flush from the system or gradually move eastward towards the inner basin over 4 to 5 days time due to action of diurnal, westerly winds.

6) Oil mixed to 40*m* that reached the inner basin would remain there indefinitely, whereas in the outer basin the average flows may cause it to gradually flush out of the fjord.

Early Fall:

1) In September strong northeast winds could flush surface oil from the central fjord in six to 21*hr*, but even under the influence of weak, variable winds the strong estuarine outflows during this season could assist in flushing oil out in about 10 to 14*hr*.

2) A caveat is that surface oil moving slowly outward (e.g. 18 to 22*hr*) can be affected by strong cross-channel flows, resulting in contamination of the outer fjord shorelines. Also, retention may ensue due to resumption of eastward along-channel velocities forced by periodic shifts to diurnal, westerly winds. Under such conditions shorelines in the eastern (inner) fjord could be affected by oil in 9 to 21*hr*.

3) At 1*m* the frequency of total flushing was the highest of all depths and all seasons (85%), and under the action of strong, northeast winds flushing could occur in as little as 12 to 16*hr*. Also, out of four of the cases exhibiting retention (15%), two initially showed flushing but drifters either turned back into the fjord in the outer basin or grounded along the southeastern shoreline when exiting the inner basin.

4) The subsurface water at 10*m* and 40*m* exhibited very long residence times in the fall, ranging from 5 to 10 days respectively, but whereas the upper layer at 10*m* exhibited more variability in flushing due to

effects of mesoscale turbulence (SD = 41*hr*), the 40*m* flows moved steadily outward at 5*cm* s^{-1} resulting in much lower variation in flushing times (SD = 16*hr*). Under indirect effects of strong, northeast winds, however, flows at 40*m* could also strike the deep benthic regions on the northern side of the fjord.

Late Winter:

1) Flushing in late winter (March) was very strong due to the action of easterly winds, but little effects of density driven flows occurred since the water column physical properties were relatively homogeneous.

2) Marked cross-channel flows from wind and wave action invariably led to grounding of surface drifters, and under the action of strong southeasterly winds from the Lowe River Valley, for example, the northwestern shoreline could be contaminated by surface oil in as little as 10 to 11*hr*.

3) The water at 1 to 40*m* would move in the same general direction as the surface flows, but any oil at these depths would flush outward due to a long-shore current developed by piling of water along the northern shore from wind driven transport.

4) In contrast, when winds shift to the northeast surface oil could contaminate the southwestern shoreline in 20 to 31*hr*, but oil at 1*m* could either flush from the fjord in 45*hr* or be retained for nearly 8 days due to extremely small negative along-channel velocities.

5) Under the conditions of very weak winds or quiescence, however, water at both the surface and 1*m* would exhibit moderate to long residence times ranging from 70*hr* before surface flows reached the inner basin to nearly 14 days prior to flushing for water at 1*m*.

6) Under both sets of easterly winds, the flows at 10*m* would flush outward over the course of 2 to 5 days, but when the winds weaken the flows at this depth would begin moving in cyclonic eddies due to mesoscale turbulence. Flushing times under the above conditions exhibited extreme variations ranging from 3 to 20 days, the latter being essentially indefinite.

7) In contrast, the flows at 40*m* would move steadily outward under all conditions at average speeds similar to September (~ 5 *cm* s^{-1}), and would flush from the fjord in 86 to 93*hr*.

8) A final conclusion of the study regards areas in the fjord especially at risk of contamination from oil, particularly if dispersants were applied allowing it to mix vertically in the water column. Although these sites varied somewhat with the season and depth of the flows, there was significant overlap in the upper meter, particularly for the early summer and fall periods. In June, for example, thirteen locations were identified and included various points along the northern shoreline extending from east of Shoup Bay to Gold Creek and Mineral Creek Deltas and along the peninsula one nautical mile to the east; the eastern shoreline from the Valdez Glacier Stream northwards to the 'Duck Flats' region; the southeast region from the Lowe River to Solomon Gulch; the southwest shoreline east of Anderson Bay and at Entrance Island; and the entire western shoreline south of Shoup Bay (see Fig. 67a).

In the fall, the sites included the southwest shorelines at Valdez Narrows, Entrance Island and points east of Anderson Bay; the western shoreline south of Shoup Bay; the northwest shoreline between Shoup Bay and Gold Creek delta; the northeast shoreline both west and east of the harbor entrance and potentially the 'Duck Flats' and nearby islands; the eastern shoreline north of the Valdez Glacier Stream; and southeast shoreline near Solomon Gulch (see Fig. 67b).

In late winter, potential 'sensitive sites' during high easterly wind events were distributed mainly along the entire northern shoreline extending from one nautical mile east of Mineral Creek all the way to Shoup

Bay. During the northeast wind events various points between the Security Zone and Anderson Bay were at risk from surface oil, but during periods of calm or weak westerly winds flows at 1*m* also turned southwards, and potentially could contaminate the southern side of the fjord (see Fig. 67c).

2.0 INTRODUCTION

Port Valdez is a moderately large fjord located in north-central Prince William Sound (PWS), Alaska (Fig. 1a), and gained great importance in 1977 as the marine terminal for the Trans-Alaska Pipeline. Since the *T/V Exxon Valdez* disaster in 1989, diligence in preventing another oil spill has been improved dramatically by the addition of dual escort vessels and the requirement that tankers are double hulled, among other added prevention measures. However, there will always remain some danger of a future spill, particularly at the loading facility and terminal located in Port Valdez. The underlying rationale of the study was therefore to obtain more information on the circulation to predict how oil would move within the fjord should there be a spill, determine the potential residency times within the port, and provide a better understanding of the effects of transport on chemically dispersed oil within the upper water column. In addition, the information should aid in the planning of prioritization and tactics related to sensitive area protection strategies.

This report presents the final results of three Lagrangian drifter experiments and oceanographic surveys conducted in Port Valdez, Alaska in 2016 from June 22 to July 1 and September 21 to 30, and in 2017 from March 21 to 30. The objectives were to measure water circulation over space and time within the Port over three separate seasons representing water column conditions that are well mixed (winter), moderately stratified from initial heat and freshwater input (spring-early summer), and deeply stratified from maximum runoff and heat that are vertically mixed in the upper water column (early fall). In each season, distinct wind patterns affecting diurnal and spatial patterns of surface and subsurface currents and the degree of vertical mixing are also addressed.

The study included deployments of drifting buoys tracking flows at the surface and depths of 1, 10 and 40*m*. The surface and near-surface drifters were comprised respectively of oil-spill response buoys (ispheres), which measure currents driven by a combination of wind stress and water currents at the atmosphere-ocean interface, and Pacific Gyre (PG) microstars, which have an orthogonal (90^o) diamond shaped 1*m* drogue. The 10*m* and 40*m* drifters were PG Surface Velocity Program (SVP) drifters patterned after the holey sock drifters developed for the World Ocean Circulation Experiment (WOCE). Oceanographic surveys were also carried out over the first five days of each experiment. These surveys measured currents using a towed acoustic Doppler current profiler (ADCP) and hydrography from profiles of temperature and salinity over depth collected with a conductivity, temperature and depth profiler (CTD). Ancillary data included meteorological measurements of air temperature and winds from the NOAA-COOPS weather station in Port Valdez and at Potato Point in Valdez Narrows.

The report focuses on the drifter trajectories but also presents examples of the temperature and salinity (T/S) properties averaged across transects within the main inner basin, and ADCP currents measured over the same transects during successive tidal cycles and for ebb and flood tides respectively. Background circulation driven by horizontal density variation is determined by performing geostrophic calculations from CTD stations and surface currents are derived directly from the 1 m drifters and where applicable from the ispheres when wind driven speeds could be subtracted from the velocity vectors.

2.1 Study Area

The study area for the experiment included the entire Port (Fig. 1b), bounded to the west by the Narrows separating the fjord from Valdez Arm. However, only the smaller sub-region shown in Fig. 2a was surveyed for the oceanographic conditions (i.e. CTD and ADCP data). This sub-region is 7.4km (4.0*nm*)

in length and bounded by 1.9*km* (1.0*nm*) to the east and west of the Security Zone (SZ) respectively. The size of the sub-region was selected in order to achieve a sufficient number of repeated ADCP transects over semidiurnal tide cycles. The SZ around the terminal facility is outlined in purple in Fig. 2a. With the exception of two ispheres, all drifters were recovered prior to any entering the SZ.

2.1.1 Regional Climatic and Oceanographic Conditions

Prince William Sound is a large estuarine system with fjord-like physical properties. This is due to its deep basins that are restricted relative to the northern Gulf of Alaska (NGOA) continental shelf and high annual freshwater input. It also has a broad, deep (400*m*) central basin (Fig. 1a) exhibiting circulation similar to a small marginal sea (Niebauer *et al.*, 1994; Vaughan *et al*., 2001). The regional climate is mostly influenced by the Aleutian Low (Wilson and Overland, 1986; Stabeno et al., 2004), which generates strong cyclonic winds over the NGOA coast from early fall to late spring. During the winter, Ekman transport from these winds frequently causes surface layer inflow into PWS through Hinchinbrook Entrance with a corresponding outflow through Montague Strait (HE and MS in Fig. 1a) (Niebauer, et al., 1994; Vaughan et al., 2001; Halverson et al., 2013b). In the summer, however, relaxation of wind stress and horizontal changes in coastal water density (i.e. dynamic topography) result in inflow (Royer et al., 1979), outflow (Vaughan et al., 2001) or retroflection (Halverson et al., 2013a) at HE. Some common annual features of circulation, include deep water exchange (Schmidt, 1977) and the formation of a cyclonic gyre in the central basin (Niebauer, et al., 1994; Vaughan et al., 2001). In the fall, extreme runoff along the NGOA coast (Royer *et al*., 1979, 1982) is reflected in the seasonal increases in both local dynamic heights (0/100*m*) and the strength of the Alaska Coastal Current (ACC) (Johnson *et al*., 1988) (Fig. 1a). Under certain conditions portions of the ACC may become entrained in the general circulation within the Sound (Muench and Schmidt, 1975; Niebauer et al., 1994).

2.1.2 Oceanographic and Climatic Conditions within Port Valdez

Port Valdez (Fig1b) is classified as a fjord (Pritchard, 1967) due to its steep sides and U-shaped basin, which extends about 21*km* in an east-west orientation and has a width of about 5*km*. The bottom is relatively flat with maximum depths of 240*m* and a total average depth of 180*m* (Colonell, 1981). The western side of the fjord basin is bounded by a pair of sills at mid-depth (160*m*) located in Valdez Narrows (Fig. 2), which forms a hydraulic control point for water exchange between the fjord and PWS. Tides in Port Valdez are similar to PWS, consisting of mixed, semidiurnal types (see Fig. 5) with an average amplitude of 3.0*m* and maximum spring tides exceeding 5*m* (Colonell, 1981).

Sources of freshwater input occur from small streams scattered around the basin periphery (Fig. 1b), but the primary discharge points are from the Lowe and Robe Rivers located in the southeast and the Valdez Glacier stream located in the east-central area close to the original Valdez town site (Fig. 2a). Additional sources include Allison Creek and Solomon Gulch located in the south and east and Mineral Creek, Gold Creek and the Shoup Glacier Basin drainage, all of which are progressively distributed westward along the northern shoreline (Fig. 2). Periods of maximum and minimum freshwater input occur in July-August and March periods respectively (Carlson et al., 1969).

In the summer, the hydrography of the upper 100*m* of Port Valdez is very similar to that of PWS, with marked vertical stratification from both heat and freshwater input, but in winter vertical mixing from winds and thermohaline convection produces nearly uniform T/S conditions throughout the water column (Muench and Nebert, 1973; Colonell, 1981). Density intrusions are also evident in the deep water in the summer reflecting the effects of deep water exchange from PWS (Muench and Heggie, 1978; Colonell, 1981). Classical estuarine circulation driven by vertical entrainment has not been observed in Port Valdez. However, horizontal salinity gradients conducive to a general outflow within the upper 20*m* were

observed in the fall of 1971 by Muench and Nebert (1973) when freshwater input at the head of the fjord was maximal. This is discussed in more detail in the following section.

Winds within the Port vary seasonally between diurnal sea breeze type westerly winds in the summer to strong down-fjord katabatic (density driven) winds in winter caused by high atmospheric pressure from arctic air masses in the interior. The up-fjord winds in the summer are caused primarily by local heating of mountainous topography surrounding the Port, but when cooling occurs during the night, light winds can also reverse and blow outward. From fall through spring, low atmospheric pressure offshore of PWS either causes light winds to emanate from Port Valdez, even while strong winds occur within PWS, or it enhances the katabatic flow of arctic air seaward (Liu et al., 2008), similar to the dynamics of low-level jets from the Copper River basin and gap-winds within Port Wells (Olsson et al., 2003). The wind patterns observed during each of the experiments are described in detail in the Results section below.

3.0 METHODS AND MATERIALS

3.1 ADCP Transects and Hydrographic Profiles

The oceanographic surveys were conducted along transects shown in Fig. 2a-c. These lines were set up to obtain as much information as possible within the timeframe of the semidiurnal tides. Current profiles were collected using a towed 150*kHz* ADCP housed in an Endaco V-fin (Fig. 3d). It should be noted that since the instrument was towed at 2-3*m* depth the surface currents could not be measured. It also has a blanking distance of ~ 4*m*, so that with 8*m* depth bins the first bin covers 7 to 15*m*.

The ADCP data were collected over a series of semidiurnal tides showing instantaneous flows over space and time. The tide cycles occurring during each experiment are shown in Fig. 4. There were a total of nine cycles with an average period of 12.34*hrs* at a frequency of 0.081*cycles* hr^{-1}. The schedule of the surveys allowed for successively surveying the first three tidal cycles (36*hr*), followed by three individual cycles thereafter. A total of 16 and 14 ADCP runs were made in June and September, representing 12 and 10 repeated sets respectively. The number of transects was less than originally planned. However, there was enough consistency in the flow patterns that the totals were more than sufficient to quantify the currents.

The data in September had the least amounts of noise due to wave action, and thus they required minimal post-processing. In March, however, high waves caused by strong, easterly winds at times prohibited work, and the number of transects was reduced to five full sets and one partial, representing 2.5 repeated sets over three tide cycles. The data quality was also compromised by periodic interruptions to the stability of the ADCP V-fin caused by an inability of the tow cable damping system to respond quickly enough to the lifting action of high amplitude, short period waves. This created a yawing motion in the V-fin, which induced accelerations affecting the Doppler shift measured by the transducers and resulted in very noisy data (described below). The severity of the V-fin ‘kiting’ depended on the transect directions relative to the path of the oncoming wave trains. Quartering, for example, produced the least amount of interference while running parallel to the troughs resulted in the greatest loss of data quality.

Hydrography profiles of conductivity, temperature and depth (CTD) were also collected with a SeaBird Electronics (SBE) 19*plus* CTD to determine horizontal variations in density, which drive baroclinic (buoyancy induced) currents. The instrument was calibrated by SBE prior to the first experiment and casts were performed during each repeated set of ADCP transects. In June a total of 17 stations were initially designated (Fig. 2a). The additional time to make the casts increased the transit times by nearly 3 hrs during return ADCP runs. Therefore, to provide more time for the ADCP transects, the number of stations was reduced to 15 (Fig. 2b). After collecting data in June, it was determined that the number of stations could be reduced to 12 without sacrificing spatial resolution in September and March. Also, the across-channel spacing was increased to four stations occupied respectively at transects 1, 5 and 9 (Fig. 2c).

3.2 Drifter Deployments

Examples of the drifters used in this study are shown in Fig. 3a-c, and the numbers of each type deployed are given in Table 1. The drifters are designed to measure currents at specific depths based on midpoints of 10*m* and 40*m* for the SVP drogues (Fig. 3c) and a 1*m* center of area for the triangular microstar drogues (Fig. 3b). The ispheres (Fig. 3a) lack drogues and have nearly equal amounts of submerged and exposed surface area. They are affected directly by wind, but being very smooth this accounts for only about 30% of the wind-induced leeway (Röhrs et al., 2012). Both the ispheres and microstars are also affected by Stokes drift (due to wave action) as well as the wind induced surface currents, hence the trajectories can only be interpreted in the Lagrangian sense.

In June, a total of 19 drifters were deployed 56 times (Table 1); the release points for each group are shown in Fig. 2d. Initial deployments consisted of small groups of single drifters of each type. This was done for two reasons: 1) to assuage concerns of local stakeholders regarding possible interference of drifter drogues with shipping and 2) to observe the relative velocities prior to releasing larger groups for obtaining statistics on the Lagrangian speeds and trajectories. Only one of the 40*m* buoys was released in June and it wasn't recovered until July 1st.

In September, the number of drifters was increased to 24 used in 93 deployments. The release points for all deployment groups are shown in Fig. 2e. The number of replicates per deployment in September was reduced to two since previous results showed that lateral dispersion was minimal within each layer. This also allowed increasing the number of deployments in order to cover more area (Fig. 2e). In March, however, the numbers were decreased to 22 and 53 respectively due to severe weather that limited data collection during the first week. The release points in March are shown in Fig. 2f. Strong easterly wind conditions required deployments to initially be made from the inner basin, but after five days, when wind speeds abated, drifters were also released in the central basin.

In each experiment, the progress of the drifter buoys was monitored via a website operated by Pacific Gyre, which showed the positions at half hour intervals for all buoys except some of the surface ispheres, which transmitted hourly (Table 1). Buoys that ran aground or entered the SZ were retrieved and held for additional releases in groups of two to three. During the oceanographic surveys retrievals were accomplished using both the research vessel (M/V Auklet) and a skiff towed behind it. After the surveys were completed, retrievals and redeployments were done with a small motor vessel, the M/V Vixen.

3.3 Data Processing and Analysis

The hydrography (CTD) data consisting of conductivity, temperature and pressure measurements were post-processed using standard SBE algorithms to convert, filter, align and average the data into 1*m* depth bins. These data were used to derive additional parameters for subsequent calculations, such as depth, density, and specific volume anomaly.

The raw ADCP profiles were collected in 8*m* depth bins as binary data, and were converted into ascii files using the manufacturer's software. These files were further post-processed using techniques developed by the author and a prior colleague at the Prince William Sound Science Center by first horizontally averaging every two consecutive profiles into segments and then removing depth bins according to the following thresholds: 1) percentage of valid water echoes < 80%, 2) error velocities > 5 $cm\ s^{-1}$ and 3) vertical velocities > 10 $cm\ s^{-1}$. In certain cases, the deletion criteria were relaxed in order to compare segments in question with adjacent profiles to determine if the data within certain bins were actually good. In general profiles with > 20% of bins missing were removed entirely, however, and gaps in the remaining segments were filled in with linear interpolation. Additional screening included flagging bins in which the absolute value of the difference in either the *u* or *v* components between successive depth

bins exceeded 20$cm\ s^{-1}$. In such cases the bins were only deleted after segments were examined from plots of vertical sections containing the questionable data. Bins exhibiting unusually high accelerations typically occur at the very bottom of profiles, and these were always removed. Special processing of excessively noisy data was required for the ADCP data collected in March 2017, and these procedures are described in greater detail below under the results section.

The drifter data required very little post-processing other than to check for spurious GPS coordinates and subsample data sets collected at the default frequency of 10min^{-1} into hourly or half hourly data.

3.3.1 Ekman Layer Calculations

The effects of winds on the surface and subsurface currents were examined using equations from Pond and Pickard (1983, pp. 108-109) we can first approximate the Ekman depth (i.e. wind influence) (D_E) by the following empirical relationship:

$$D_E = 4.3W/(\sin\phi)^{1/2} \tag{1}$$

where W is the wind speed in $m\ s^{-1}$ and ϕ is the latitude. The surface velocity due to wind can then be determined using W and D_E in the following equation:

$$V_0 = 0.78 \times 10^{-5} W^2 / D_E |f| \tag{2}$$

where f is the Coriolis parameter = $2\Omega\sin\phi = 1.276 \times 10^{-4}\ rad\ s^{-1}$. The wind driven velocities over depth can then be calculated by the following relationship between V_0 and D_E :

$$V_i = V_0\, exp(\pi z/D_E). \tag{3}$$

A caveat to the above approach is that it assumes that the water density is homogeneous, the lateral boundary friction is negligible and that the wind blows long enough to set up the currents. As an example, to set up a fully developed wind wave field with vertical turbulence requires a 5$m\ s^{-1}$ wind blowing for at least 2hrs (Pond and Pickard, 1983). Away from the sides of the fjord and given the time scale of the winds the second two assumptions were reasonable. However, since the first assumption was not valid in both June and September, the depth of the Ekman layer was probably overstated and thus the surface currents were underestimated. The drifter motions at 1m and 10m and the geostrophic currents (described below) were therefore useful in estimating the true wind forcing in the upper layer.

3.3.2 Dynamic Topography and Geostrophic Velocities

To assess the effects of the density (mass) field on circulation, the dynamic heights and geostrophic velocities were calculated for all CTD stations. This was done using the geostrophic method, which is based on differences in geopotential anomaly over an isobaric surface between two stations. The geopotential anomaly (Φ') is equivalent to the dynamic height, ΔD = Φ'/10$J\ kg^{-1}$ and is determined by integrating the specific volume anomaly (δ') over depth (i.e. pressure) (Gill 1982):

$$\Delta D = -\Phi' = \int_{p1}^{p2} \delta' dp \tag{4}$$

where δ' is the specific volume anomaly [= δ(S,T,p) - δ(35,0,p)], S and T being the observed salinity and temperature, and dp being the pressure differential. Essentially, the method uses the hydrostatic relation: $gdz = d\Phi = -dp/\rho$ to substitute the gradient in geopotential anomaly in lieu of the pressure term:

$$\partial\Phi/\partial(x,y) = -\rho^{-1}\partial p/\partial(x,y)$$

which results in the following forms of the geostrophic equations (Gill, 1982):

$$-f\left(v_g(p_1)-v_g(p_2)\right)=-\frac{\partial}{\partial x}\{\partial\Phi'(p_1)-\partial\Phi'(p_2)\}\qquad f\left(u_g(p_1)-u_g(p_2)\right)=-\frac{\partial}{\partial y}\{\partial\Phi'(p_1)-\partial\Phi'(p_2)\} \tag{5}$$

where f is the Coriolis parameter (= $2\Omega\sin\varphi$), v_g and u_g are the geostrophic (relative) velocity components. Once the geopotential anomalies have been calculated over depth for a pair of stations, the solution to the above equations is found by numerical integration. The relative velocities are then found by dividing the difference in Φ' (i.e. δ'integrated over p) by the length scale L (distance in meters) and f as follows:

$$V_r=\frac{1}{fL}\Sigma\left[\Phi'(p_i)-\Phi'(p_2)\right]=\frac{1}{fL}\Sigma\left[\overline{\delta'}_i\Delta p\right] \tag{6}$$

The dynamic heights and geostrophic velocities were calculated for the 0 to 100*db* pressure levels, or essentially over the upper 100*m* of the water column. The exceptions occurred whenever the maximum depth of any station was less than 100*m*. In such cases, the lower level for p_2 was based on the shallowest cast depth. Failing to do this resulted in biased velocities that were typically much too high to be realistic.

Another caveat to the method is that in order to obtain absolute velocities the flow at p_2 is assumed to be static (i.e. no motion). This could not be totally assumed at all times, therefore, the velocities based on the density (mass) field are at best relative and under certain conditions (explained below) the magnitudes were far too large in comparison to the ADCP data and drifter speeds.

3.3.4 Drifter Speeds and Dispersion Calculations

The speed of drifters was calculated from the changes in position over time, whereas dispersion was quantified by two methods: 1) determining the average distance to the center of mass; and 2) calculating the changes in area demarked by the drifter positions at each time step. The first method could be applied to a minimum of two drifters released as pairs, but the second method required combinations of at least three drifters, so that the changes in triangular area over time could be computed from their positions.

The first method involved first finding the center of mass for any object, defined as the mass weighted position (x_{cm}, y_{cm}) of all particles in the object (Sears and Zemansky, 2006). This was done using the following equations:

$$x_{cm}=\sum m_i x_i/\sum m_i \qquad y_{cm}=\sum m_i y_i/\sum m_i \quad . \tag{7}$$

where x_i = longitude and y_i = latitude and m = mass. Since the mass of each type of drifter could be treated as identical, the above equations reduced to finding the average coordinates at each time step:

$$CM_x=m\sum x_i/3m=\sum x_i/3 \qquad CM_y=m\sum y_i/3m=\sum y_i/3 \tag{8}$$

The deviations of the positions from the mean ($CM_{x,y}$) were then used to find the distances in degrees to the center of mass. These were converted to meters and in the x axis adjusted by the cosine of the latitude:

$$\Delta x=\left|x_i-CM_x\right|\left(\cos(\overline{y_i}\right) \qquad \Delta y=\left|y_i-CM_y\right| \tag{9}$$

$$d_i=\sqrt{\left(\Delta x_i\right)^2+\left(\Delta y_i\right)^2} \tag{10}$$

The averages for each set of coordinates at all times were then calculated and plotted.

For the second method based on the changes in area, the dispersion rates were calculated by using Heron's formula for determining the areas of triangles as follows:

$$A_i = \sqrt{s(s-d_1)(s-d_2)(s-d_3)} \quad (11)$$

where d_1, d_2 and d_3 are the *i*th distances between three drifters at time (t_i), and $s = (d_1 + d_2 + d_3)/2$. The areas were shown in km^2 and the differences in area at times t_{i+1} and t_i were then used to calculate the dispersion rate in $m^2\ s^{-1}$.

4.0 RESULTS

The results of the three drifter experiments are described individually below. The ancillary weather data are discussed first, followed by the oceanographic data and drifter trajectories for each type of buoy. The weather data include winds, air temperatures and (where applicable) precipitation. The wind vectors are discussed in more detail below for each experiment. The experiments were conducted over the last 10 days of each month (21st to the 30th) except for early summer, which was conducted from June 22nd to July 1st. In all cases, the oceanographic surveys occupied the first five days of the experiments, followed by 5 days of drifter releases.

4.1 Meteorological Data and Freshwater Input: June 2016

The meteorological conditions during the month of June 2016 are shown in Fig. 5. The wind and air temperatures were collected every 6*min* at the NOAA-COOPS (Fig. 1b) located just west of the small boat harbor shown in Fig. 2a, and daily precipitation was listed in the GHCN-VDZ data archive. The wind magnitudes (Fig. 5a) are based on raw (0.1*hr*) measurements, whereas the velocities (Fig. 5e) were vector averaged into hourly observations prior to plotting.

In June, the winds are characterized mainly by diurnal (i.e. daily) increases in magnitude (Fig. 5a), with maximum speeds frequently exceeding 8$m\ s^{-1}$ (~16*kts*). The principal directions are westerly (Fig 5b) blowing into Port Valdez during the day. At night, however, the winds typically diminish in magnitude to $\leq 2\ m\ s^{-1}$ (~4*kts*) and blow down-fjord from the northeast. The strongest periods of winds occur in conjunction with clear skies and are likely enhanced by sea-breeze effects due to daily heating of the surrounding mountainous topography. These diurnal winds played a marked role in forcing all surface and 1*m* drifter trajectories. However, in either the absence of wind or weak velocities, tidal and estuarine forcing were also evident in the drifter trajectories.

Air temperatures in June 2016 also exhibit large diurnal fluctuations ranging from ~11 to 23^o *C* during the day and > 6 to 10^o *C* at night. During the experiment, the air temperature ranges were 12 to >15^o *C* and 8 to >10^o *C* respectively. The trend in air temperatures over June is weakly positive (R = 0.095) indicating that nearly equal amounts of surface water heat gained during the day are lost at night. However, the water column indeed showed a response to solar heating with surface temperatures reaching as high as 13^o *C*. These thermal effects certainly contributed to low nearsurface water density. However, the main driver of density stratification within the Port was freshwater input from cold alpine runoff. The latter also created surface temperature inversions, and this is discussed in greater detail below under hydrography.

Precipitation during the month of June was quite low (Fig. 5d), with only one day (20th) exhibiting ~ 2.5*cm* of rainfall. Other periods of rain occurred at the beginning and end of the month, but the amounts of precipitation were < 0.5*cm* on any day. As such, the primary source of runoff was from the release of stored precipitation in alpine snowfields and glaciers (Carleson et al., 1969). A number of streams and small rivers deliver this runoff around the periphery of Port Valdez (Fig. 1c), but the main drainages include Allison Creek, Solomon Gulch and the Lowe and Robe Rivers in the southeast, the Valdez River in the eastern region and Mineral and Gold Creeks located along the northern shoreline. The Shoup

Glacier Stream, located northeast of the Narrows, is also another significant source of freshwater input along the outer northern shoreline.

It should be noted, however, that during the beginning of this study an outburst from a glacial lake, which was part of the Valdez Glacier, created an unprecedented discharge of cold runoff into the eastern fjord, and this had a marked affect on the hydrography during the initial portions of the experiment. For example, on June 22nd fronts of this water appeared to be enhanced by diurnal winds from the southwest that transported surface water eastward, thus causing the estuarine region to pile up along the shore.

4.2 Hydrography

Examples of the physical properties in June are shown in three formats: 1) cross-channel average T/S profiles for transects 1, 3, 5, 7 and 9 on June 21 and 26 (Fig. 6a,c); 2) TS diagrams of the latter (Fig. 6b,d) and 3) vertical sections of along-channel T, S and Sigma_t [2] (density) on both days (Fig. 7).

4.2.1 Temperature and Salinity (T/S) Profiles

All the CTD casts indicate that by late June there is significant solar heating extending below 40m and freshwater discharge from the sources described above caused marked density stratification in the upper 10m throughout the fjord. The first set of data collected on June 21st (Fig. 6a) shows that the warmest upper water column occurs in the outer fjord (trans. 1 and 3), whereas stations in the inner basin (trans. 5 to 9) exhibit surface inversions caused by cold alpine discharge. Some of this probably resulted from an outburst flood from the Valdez Glacier (described above). For example, during the first day of the study a prominent front between fresh surface water and saltier water in the middle of the fjord was observed along the northern shoreline. This front was the result of surface convergence caused by the strong diurnal westerly winds. Relatively fresh surface water occurred at this time from transects 5 to 9, but when the winds relaxed during the night the front dissipated and was not observed the following morning.

The second set of data collected on June 26th (Fig. 6b) indicates that heat is mixed much deeper in the water column at all stations and that freshwater is dispersed over most of the fjord. Surface mixing by the strong diurnal winds (Fig. 5a) may have played a role in forming nearly uniform haloclines over the entire basin. For example, mixing of the cold glacial water is evident on June 21st as small, near-surface temperature minima and maxima in transects 3 to 7 (Fig. 6a), but by June 26th these properties have eroded considerably (Fig. 6b). Although the individual profiles (Appendix A) show that cross-channel variation in T/S properties is significant, it is still much weaker in comparison to the along-channel gradient shown by the average profiles (Fig. 6a,b).

The TS diagrams (Fig. 6c,d) show that the average cross-channel conditions changed dramatically over the first five days of the survey. The affects of freshwater on density relative to that of temperature are also quite obvious. For example, both plots show contours of density as sigma-t [4] based upon different combinations of temperature and salinity. Note that the isopycnals (contours of equal density) are nearly perpendicular to the x-axis, thus showing predominant effect of the salinity gradient on water density in comparison to the minor effect of temperature. The along-channel gradient in salinity may influence a general dispersal of water within the fjord, particularly during ebb tides. However, the flow would be relatively weak in comparison to the transport induced by winds.

[2] Sigma-t is the density of seawater (ρ) less the density of freshwater (i.e. $\rho - 1000$ kg/m^3).

4.2.2 Vertical T/S Sections

Marked spatial variation in physical properties on June 21st within the central and inner basins of the fjord is shown in Fig. 7A and C. For example, in the region near Mineral and Gold Creeks at PV1 there is strong evidence of pooling of freshwater (Fig. 7A, panel-a). This water is also relatively warm, with surface temperatures exceeding 13^{o} *C* (Fig. 7A, panel-a), and both physical properties create a marked local decrease in water density in the upper 10*m* (Fig. 7A, panel-c and 7C, panel-a). These conditions also appear to extend southward to PV4. In contrast, the conditions in the inner basin at PV14 and PV17 show freshwater only occurs close to the surface and heating there is also limited due to cold runoff. In both along-channel transects, however, progressive westward gradients in heat and subsurface freshwater content can be seen, but in the southern section (Fig. 7A, panels d,e) cool surface water overlays warm nearsurface water from PV13 to PV7 and the subsurface water at PV4 is relatively brackish in comparison to the northern transect.

By June 26th, the spatial variation of the physical properties within the central and inner fjord basins is much reduced (Fig. 7B), and subsurface freshwater at PV1 to PV4 is now mixed so that it now plays a lesser role in creating spatial variation in density (Fig. 7C, panels d-f). The subsurface heat increases over the entire basin, however, with cool, surface water dispersed westward (Fig. 7B, panel a,d). Taken as a whole, the changing physical conditions over time would certainly affect the spatial density distribution that drives subsurface baroclinic flows, distributing heat and salt under an outward dispersing fresh surface layer. These flows are described further under the next section on ADCP currents.

4.3 ADCP Currents

Examples of ADCP data collected over five sequential tide phases (flood 1 to flood 3) during the first 36*hr* of the oceanographic survey are shown in Fig. 8. In general, the currents in June were relatively weak over most of the water column (5-10*cm* s^{-1}) except in the upper 15 to 40*m*, where maximum speeds reached 15 to 20*cm* s^{-1} (~ 0.3 to 0.4*kts*)[5]. The magnitudes are mostly typical of open oceanic flows (Pond and Pickard, 1983; Gill 1982), whereas peak tidal flows for PWS locations exhibiting hydraulic effects of constrictions, such as Hinchinbrook Entrance (HE) and Valdez Narrows (VN) can range from 50 to > 100*cm* s^{-1} (~ 0.97 to >1.94*kts*) (Colonell, 1981; Vaughan et al., 2001). Subtidal flows at HE reach speeds as high as 30*cm* s^{-1} (Halverson et al., 2103a). The deep currents in Port Valdez below 30 to 50*m* are relatively benign, with flows typically ranging from 5 to 7*cm* s^{-1} (~ 0.10 to 0.13*kts*). However, reversals in direction do occur over the water column creating multiple baroclinic modes (i.e. layered flow).

One of the best examples of strong baroclinic currents in the Port is after the transition from flood 2 to ebb 2 early on the morning of the 23rd (Fig. 8C). Note that during this ebb tide the 10 to 40*m* layer still flows into the fjord at 10 to 15*cm* s^{-1}, and to balance the tidal prism the deep outflows occur at ~10 *cm* s^{-1}. The surface flows above the top ADCP depth bin (7-15*m*) may be surmised from effects of the horizontal density gradient created by surface heat and freshwater content, the winds and the tide phase. For example, during the night the winds weaken but reverse in direction (Fig. 5e), and a surface estuarine flow caused by low density along the outer northern shore (Fig. 7A and C) possibly disperses southwards but is constrained by Coriolis so that it flows out along the north side of the fjord. Both of these factors are synergistic with the large ebb tide (> 3.5*m*) and thus possibly resulted in enhanced surface outflow that is balanced in part by the 10-40*m* inflow described above.

[5] The conversion factor for m/s and cm/s to *kts* is 1.9438 and 0.019438 respectively. However, a simple rule of thumb is that 0.5 m/s or 50cm/s are equal to ~ 1.0kt.

Indeed, one of the 1*m* drifters (m001) released at 18:30*hrs* on the 22nd exhibited exactly this type of flow pattern over the night of the 23rd (see Fig. 10e). It should be pointed out here, that the ADCP data represent the combined effects of all forcing factors at discrete points only and are thus essentially Eulerian measurements ($\partial u/\partial t$) at different points of time and space. In contrast, the drifters follow a water parcel's reaction to field accelerations ($u \cdot \nabla u$) and are thus Lagrangian in character, with trajectories representing true streamlines only if the net flows are steady state (Pond and Pickard, 1983).

Another example of strong baroclinic flows occurred during the first ebb tide on June 22nd (Fig. 8B). At this time, currents in the outer basin exhibit marked westerly outflows in the upper water column (7-30*m*), but throughout the deep water column the flows were weak and mainly easterly in direction, reaching magnitudes of 5 to 10$cm\ s^{-1}$. The winds during this tide were still westerly at speeds of 3 to 4$m\ s^{-1}$ (6 to 8*kts*) and the reversed surface inflow due these winds may be a factor responsible for enhancing the subsurface outflow in the central basin (Fig. 8B). In fact, the trajectory of i5480, released at 18:00 on June 22nd exhibited the reversed pattern of inflow due to the westerly winds up until 21:00 (see Fig. 10b), after which, it exhibits a outward track over night along the north shore very similar to m001.

A particularly robust feature of the current field is a cyclonic (counterclockwise) flow observed in the outer transects (1-3), that separated flows in the central fjord from those within the inner basin. This pattern occurred primarily in the upper 7 to 20*m* during both tide phases (Figs. 8A, D and E) but in certain cases it was observed as deep as 30*m*. Further examples of this pattern are shown for 7 to 15*m* in Fig. 9 for flood and ebb tide 5, and ebb tide 6, and in Appendix B during the first hour of ebb 7 and the second half of both ebb 8 and flood 9. The *u* and *v* velocities (Fig. 8) depict this feature as westerly outflow in the north and easterly inflow in the south, but the vector plots show a horizontal shear associated with these flows and the separation it creates between circulation at mid-fjord and the inner basin. Frequently, the outflow occurred along the entire northern shore (Fig. 8A and 9), but the inflow in the south appeared to converge with flows in the inner basin. It either was being entrained northwards into the out-flowing currents or part of a large eddy that was unresolved due to the limited extent of the ADCP transects.

It should be noted that the cyclonic circulation in the central fjord was observed in the ADCP data as closed core eddies during ebb 8 and flood9 (Appendix B) and in the SVP 10m trajectories on June 27th (Fig. 11c). These eddies were observed again in September 2016 (see sections 4.7 and 4.8).

4.4 Drifter Trajectories

The drifter releases in June were done initially in small groups consisting of varied combinations of drifter types. This was done to observe drifter behavior prior to releasing larger groups due to concerns of various stakeholders expressed during the pre-deployment meeting held on June 21. These deployments are described first for each drifter type, followed by dispersion experiments performed later in the study. The entire record of all deployments, including dates, times and coordinates is given in Appendix C.

4.4.1 Ispheres (0-0.3m)

The trajectories of ispheres deployed from the 22nd to the 29th of June are shown in Figs. 10a to d. In all cases, these drifters exhibited highly varied trajectories due to combinations of wind, tidal and estuarine forcing. The rapid response of these drifters to afternoon sea-breeze events is shown by frequent periods of acceleration to speeds exceeding 50$cm\ s^{-1}$ (~1*kt*), and both tidal and wind driven currents worked together to create broad, sweeping oscillations in their tracks. For example, i0460 (Fig. 10a) released during deployment #1 on June 22nd was rapidly driven southeastward by both the west wind and the flood tide. It eventually grounded during the night near the Lowe River. However, when this drifter was redeployed on the 24th (deployment #4) it followed a much different path, and moved southwestward

during ebb tide (***a-b*** in Fig. 10a), but was then constrained along the south shore by NE winds blowing against the flood tide (***b-c***). It next moved eastward on the ebb tide (***c-d***) to become trapped briefly off Anderson Bay. Over the next four tide cycles and two shifts in winds from the SW to NE, this drifter made a series of broad anticyclonic (clockwise) and cyclonic (counterclockwise) turns and then it moved northwest directly to Gold Creek, where it grounded at 08:00 on the 27th.

The winds during deployment #4 (Fig. 5e) were weak but still exhibited periods of easterly and westerly directions during the day and night respectively. The clockwise turning of the isphere was indeed partly due to tide when the winds were weak, but the rapid inward track on the 26th occurred after 15:00 when easterly winds increase to ~ 4*m* s^{-1} (8*kts*) along with a flood tide (***h-i***). The motion to the NW towards Gold Creek the following night was possibly due to both down-fjord winds and freshwater dispersing along the north shoreline moving against a flood tide (***j-k***).

In contrast to i0460, isphere i5480, released in deployment #2 (Fig. 10b), traveled in the course of two days westward from the center of Port Valdez into Valdez Arm and back. It ultimately became trapped in the estuarine region between Mineral and Gold Creek and grounded at Gold Creek at 00:00 on the 26th. The initial up-fjord motion of deployment #2 was driven by strong up-fjord (westerly) winds with magnitudes reaching 4 to 5*m* s^{-1} (8-10*kts*). However, overnight on the 23rd this drifter moves rapidly down-fjord along the north shore at ~75*cm* s^{-1} (~1.5*kt*). Since this happened during a flood tide (***a'-b'***) and was accompanied by weak NE winds (Fig. 5e), the rapid down-fjord motion would suggest that surface freshwater is a significant driver of outflows on northern side of the fjord. The winds remained weak during the ensuing ebb tide, which had a large prism (~ 4*m*), and thus the drifter continued rapidly southward through the 'Narrows' and into Valdez Arm (Fig. 10b). The rapid northward return of 5480 back into Port Valdez was certainly caused by the flood tide (***c'-d'***) being accompanied by strong westerly winds on the afternoon of the 23rd (Fig. 5e).

Fig. 10c shows deployments #3 and #5 of ispheres on June 23rd and 25th respectively. Isphere 9460 drifted for 5.5 tide cycles and six wind shifts. It made large up and down-fjord excursions between the 23rd and 26th similar to i0460 and nearly grounded in the same spots close to the Lowe River and Gold Creek. However, after tracking southeast due to strong westerly winds and a flood tide (***a-b***) it turned back to the northwest on the ebb tide (***d-e***) and during a wind shift to the NE (Fig. 5B). It next moved inward due to the combined action of a flood tide (***e-f***) and westerly (diurnal) winds and then makes a sharp reversal at 16:00 followed by a long excursion down-fjord on an ebb tide (***f-g***) accompanied by another wind shift to the NE. Afterwards, it continued westward and made a broad anticyclonic turn during a flood tide and westerly winds, then turned back to the northwest to become nearly grounded off Gold Creek (Fig. 10c).

Isphere 6350 initially takes a southeast course on the 25th, and after making an anticyclonic reversal similar to i9460 (Fig. 10c) it too travels back to the northwest. The clockwise turning could have been due to a combination of tidal and wind effects, the latter becoming southwesterly by 1200*hr* (Fig. 5e). However, when this drifter reached the north-central region of the fjord it was then directly affected by the strong diurnal westerly winds, and occasionally the speeds exceed 50 *cm* s^{-1} (> 1.0*kt*). It moved parallel to shore over another tide cycle (***o'- q'***) and ultimately grounded in the eastern fjord (Fig. 10c).

4.4.2 Microstars (1m)

Examples of the trajectories of microstars deployed from the 22nd to the 27th of June are shown in Fig. 10e and f. Like the ispheres, the microstars showed periods of acceleration due to wind forcing, and the trajectories exhibited extensive tracks and large oscillations due to a combination of wind, tidal and estuarine forcing. Unlike the ispheres, however, the microstars were not affected by wind drag but there is evidence of small-scale turbulence in their tracks. In most cases the velocities are considerably less than

the ispheres but two exceptions occurred during deployments #1 and #3 on the 22nd and 23rd (Fig. 10e and f) in which m007 accelerated to ~ 50*cm* s^{-1} (1.0*kt*).

The two drifters deployed on the 22nd also exhibit varied paths due to differences in timing and location of the releases. For example, m007 was launched at the same time and location as i0460 in deployment #1, and due to the same wind and tidal forcing it followed a path similar to i0460. However, instead of grounding near the Lowe River it rapidly turned anticylonically (clockwise) back to the west, where it was retrieved at ~ 21:30 (Fig. 11a). The second drifter (m001) was released later on the 22nd at 18:30, and for two hours westerly winds initially forced it eastward, into the fjord, but then it abruptly made a tight cyclonic orbit and turned northwestward. Traveling along the north shoreline overnight it reversed direction at 12:00 on the 23rd as the tide started to flood and westerly winds began to accelerate (Fig. 10e).

The reason for the initial northward turning of m001 is uncertain, as the wind was variable at ≤ 0.5*m* s^{-1} (1.0*kt*) and the tide was nearing slack ebb (Fig. 10e), but a possible clue comes from the ADCP data at 7-15*m* at the end of ebb tide 1 (Fig. 8B). The latter show a relatively strong outflow of 15 to 20*cm* s^{-1} (0.3 - 0.4*kt*) within central basin that coincided with the initial period of this drifter. It is possible that once the wind slacked these currents were reinstated at the surface, and thus what started out as inertial turning was interrupted by a reversal of the surface currents. The tight cyclonic turn back to the north was therefore due to small-scale turbulence and not some major forcing mechanism such as wind or tidal turning. The flow along the north shore occurred over night when winds were light, however, and the relatively rapid westward motion (30-40 *cm* s^{-1}) may have been forced by unimpeded estuarine flow as described above for isph5480 (Fig. 10b).

The microstars released on the 23rd to the 24th of June (Fig. 10f) also exhibited highly varied and oscillatory trajectories. One of these drifters (m001) was released at 17:30 on the 24th when winds were relatively weak. This buoy traveled outward over night during an ebb tide (***a-b***) enhanced by northeast winds, then moved northwest during the flood (***b-c***) with winds blowing northward from the 'Narrows'. Afterwards, it paralleled the western shoreline during the ebb and flood tides (***c-e***) under weak winds, making it all the way through the 'Narrows' from the central basin in 1.5 days. The other two microstars remained entirely within the central and inner basins respectively. Their tracks were highly oscillatory (m007) or convoluted (m003), as shown by the small arrows in Fig. 10f.

The first drifter (m007) was released at 11:00 on June 23rd (deployment #3) and initially moved rapidly to the southeast towards the Lowe River, driven by a flood tide (***a'-b'***) and strong diurnal westerly winds at 4.5-5*m* s^{-1} (9-10*kt*). It then moved northwest apparently due to interaction of the westerly winds and the ebb tide (***b'-c'***) that possibly caused flow reversing and shear at 1*m* (see also section 4.4.4). After the next flood tide (***c'-d'***) the winds shifted to the northeast, however, and during the following ebb tide (***d'-e'***) it moved further down-fjord to begin a series of diagonal north-south oscillations within the central basin over nearly 6 more tide cycles and 6 to 7 wind shifts (Fig. 10f).

The last drifter (m003) was released at 15:00 on the 25th (deployment #5). It was forced southeastward initially by a flood tide that was synergistic with the west winds, but then moved back to the northwest at night when the ebb tide is accompanied by a wind shift to the northeast (Fig. 10f). However, unlike 007, this drifter remained in the north where it first meanders around south of Mineral Creek, and then during a flood tide and west wind it made a long excursion eastward into the inner fjord, then back to the west where it turned south from Mineral Creek and made a tight cyclonic loop to be retrieved on the 27th.

4.4.3 SVP Drifters (10m and 40m)

Examples of trajectories of the 10*m* SVP 'holey sock' drifters are shown in Fig. 10g and h. Like the surface and 1*m* drifters, highly varied trajectories occurred at 10*m* when buoys were released at different

points and times over the course of four days. The currents were relatively weak in comparison to the surface flows, however, with maximum speeds of only 18 to 20*cm* s^{-1}. The latter magnitudes are very close to the maximum velocities recorded by the ADCP at 7 to15*m* (Fig. 8), but the average drifter speeds were very slow (~5 to 7*cm* s^{-1}), which is similar to the background flows recorded by the ADCP. Due to the slow average velocities, the drift periods of the SVPs were significantly longer than the ispheres and microstars (Fig. 10a to f) and, consequently, they cover a greater number of tides.

The effects of tides are evident in some of the drift patterns but direct effects of winds are barely evident. For example, drifter s004 was released at the 18:30 on the 22nd when the diurnal westerly winds were ~4.5*m* s^{-1} (~9*kts*). This drifter moved at the maximum velocity stated above, but in the opposite direction indicating it was below the Ekman layer (D_E) (Pond and Pickard, 1983) if D_E were at10*m*. At the start of the drift the tide is at half ebb (***a***) and thus the currents should be maximal if they are synchronous with the tidal prism (Dyer, 1997). This is a reasonable assumption given the wide, deep morphometry of the fjord, and strong flows that moved this drifter westward are indeed shown in the ADCP currents at 7*m* to 15*m* (Fig. 8B,c). Drifter s004 continued to move westward on the flood (***b-c***), but once the wind relaxed at around 23:00 (Fig. 5B) it moved back in the opposite direction. It is held back and barely moved over the next ebb (***c-d***), however, then at the start of the following flood (***d-e***) it moved inward again at maximum speed until the next ebb. The influence of tides on this drifter are not very evident again until it turned outward, and moved westward at high speeds during a large ebb (***g-h***). It is possible these flows along the north shore were enhanced by subsurface baroclinic currents caused by low density from freshwater input on this side of the fjord. However, once the tide turned and began to flood (***h-i***), the drifter turned sharply to the southwest (Fig. 10g) and continued this drift pattern over the next three consecutive tide phases (***h-k***) until it grounded near Entrance Island.

The other SVP 10*m* drifters followed varied tracks over multiple tide cycles, but the two released in the central basin on the 23rd and 24th (deployments #3 and #4) took completely different directions (Fig. 10g). Drifter s008, for example, initially moved eastward over two tide cycles, then over six successive tides it moved to the northeast before making a relatively tight anticyclonic turn southward at the head of the basin. It then moved outward, west of the Lowe River. In contrast, drifter s007 initially moved northwest, but over the course of five tide cycles it made a wide cyclonic track and moved back into the fjord on the southern side. The last drifter, s002, took a course similar to s008 and also moved northwards within the inner basin. However, unlike s008, this drifter made a moderate cyclonic turn and moved outward along the northern shore (Fig 10g).

The trajectories of the deep 40m SVP drifter are shown in Fig. 10i. As expected (based on the ADCP data at 40*m*) the motions of this drifter were highly subdued, and it generally moved back and forth over ~11.5 tide cycles. It did exhibit a gradual southerly motion followed by movement back to the north, but when a prolonged period of westerly winds began on the 30th of June (Fig. 5e) this drifter also moved inward, albeit at very slow speeds (Fig. 10i). It also exhibited an anticyclonic turn on July 1st and is possibly in the process of turning back to the west, similar to the northerly 10*m* SVPs (Fig. 11d).

4.4.4 Dispersion Experiments

Starting on June 28th, a series of dispersion experiments was conducted by releasing in tandem three sets of three drifters of each type (i.e. depth) except the 40*m* SVPs (Fig 11). During these releases, all drifters exhibited a remarkable similarity in flow patterns, with very limited lateral dispersion except among the depth layers and whenever drifters reached the shoreline.

4.4.4.1 Ispheres

For example, the trajectories of first three ispheres relased on the 27th exhibited marked homogeneity, drifting eastward at ~50*cm* s^{-1} (1*kt*) until turning northward and dispersing within the shallow mudflat in the northeastern fjord (Fig. 11a). These ispheres either came close to shore prior to turning or they became permanently grounded. All but i2460 were retrieved and redeployed on June 29th. Although the two drifters redeployed were ~1*km* apart from each other, they follow a similar track to the southeast, driven inward by the flood tide along with westerly winds. A marked leeway to the winds is very obvious in both experiments, but on the 30th the winds shift to the NE near midnight and then slack in the early morning of July 1st, and on the ebb tide the two drifters ground in the Alyeska Oil Terminal.

4.4.4.2 Microstars

The groups of 1*m* drifters released on June 27th to the 30th (Fig. 11b,e,g) also exhibited relative homogeneity in trajectories during all experiments, albeit with greater lateral dispersion in comparison to the other drifters. Like the ispheres, the greatest dispersal of these drifters occurred whenever they approached shore, however. For example, in first experiment (deployment #6) the drifters initially moved southeast during the flood tide along with moderate westerly winds (Fig. 5e), but overnight they turn sharply to the west and then dispersed along the southern shore. The winds did shift to the northeast along with the ebb tide early in the morning, which possibly induced the cyclonic turning. However, the tide was also flooding during the main westward dispersal suggesting there was additional forcing by flows parallel to the shoreline. This group of drifters was redeployed shortly after retrieval on the 28th (deployment #7), and again they moved rapidly eastward at speeds of ~45*cm* s^{-1} (< 1*kt*) in response to moderate west winds (Fig. 5e). The trajectories then exhibited wide cyclonic (counter-clockwise) turns. Since the winds were relatively weak (< 0.5*m* s^{-1}) and from the NE at this time the motion was possibly due to combined forcing by the ebb tide and estuarine flow from the Valdez and Lowe Rivers turning northwest across the fjord due to Coriolis. This feature of estuarine conditions was observed in greater strength in September and is discussed in more detail below.

On June 29th a second dispersion experiment was performed (Fig. 11e) involving two groups of microstars (#10 and #11). In all cases the drifters traveled to the southeast forced inward by the diurnal winds, and group #10 dispersed eastward close to shore within the Alyeska Oil Terminal. These drifters were redeployed the next day again in the mid-central region of the fjord (Fig. 11g,h). The two groups (#12a and b) initially had similar trajectories and made broad cyclonic turns to the north and west, similar to buoys redeployed on the 28th (Fig. 11b). However, the two groups then dispersed in much different patterns. They both became entrained within the northern estuarine region between Mineral and Gold Creeks, but whereas the northern group either grounded (m003) or followed the shoreline westward (m007) or travelled southeastward (m008), the second group travelled together westward along the northern shoreline all the way to the 'Narrows'. The southeasterly motion of m008 was likely due to westerly diurnal winds. However, the pattern of outflow along the northern shoreline was common whenever 1*m* drifters entered the estuarine zone along the Mineral and Gold Creek discharges.

The drifters from deployment #12a were redeployed one final time in the central basin on the 30th (Fig. 11g). These drifters were driven southeastward by the diurnal west wind (> 5*m* s^{-1}, 10*kts*) moving water against the ebb tide, but as during deployment #10 on the 29th, when the winds became in sync with the flood tide the drifters dispersed eastward along the shore (Fig. 11g).

4.4.4.3 SVP Drifters (10m)

The three SVP 10*m* drifters released during the dispersion experiments are shown in Fig. 11c,f. In the first experiment (deployment #6) these drifters all exhibited very homogeneous tracks but with widening

cyclonic orbits, as suggested by the ADCP currents in Figs. 8A, D and E. The ADCP data indicate that these flows occur during both the flood and ebb tides (Figs. 8 and 9) but are ephemeral features that at certain times disappear entirely (Fig. 8B,C). The second dispersion experiment from June 29th to early on the 30th (Fig. 11f) shows similar cyclonic turning in the SVP 10*m* trajectories. However, the westerly winds on the 30th begin early in the day (1000*hr*) and persisted past midnight, with only a brief period of relaxation (Fig. 5e). These winds commenced in earnest again early on July 1st, and this lengthy period of up-fjord winds appears to cause an inward flow at 10*m* depth, shown in the trajectories of both sets of drifters (Fig. 11f). Group #10 (s005, s002 and s008) continued eastward on an anticyclonic trajectory, whereas after turning eastward group #11 (s004, s006 and s007) remained in the north-central basin close to the shore.

The cyclonic orbits and turning exhibited by drifters in groups #6, #10 and #11 and the ADCP data were not associated with any closed, geostrophic eddies. This was also indicated by the dynamic topography shown below in section 4.13. As such, these flows were likely induced by local, relative vorticity and thus are part of the large-scale turbulence in the flow field. The eastward motions of groups #10 and #11, however, may have been affected by wind-generated transport in the nearsurface layer. Wind speeds of 5$m\ s^{-1}$ (10*kts*) occurred during the last two days of the study, and given a uniform water density these winds would create a $D_E > 20m$ with surface velocities > 7$cm\ s^{-1}$. However, the persistence of this feature within the mid-central region of the fjord suggests the main forcing of these flows is not wind but mostly subsurface baroclinic flow. The latter may be induced by variations in the mass field (i.e. horizontal variations in subsurface water density), and this type of forcing is discussed in more detail below. However, it is certainly also moderated by strong inward transport in the nearsurface layer by winds.

4.5 Meteorological Data and Freshwater Input: September 2016

The meteorological conditions during the month of September 2016 are shown in Figs. 12 and 13. The winds in early September (Fig. 12a) exhibited periods of diurnal accelerations similar June, but this summer pattern was ephemeral and by September 9th winds blow from the northeast (Fig. 13), with gusts that exceeded 17$m\ s^{-1}$ (34*kts*). On the 10th the winds shifted to the southeast, blowing out of the Lowe River at sustained speeds of 4-5$m\ s^{-1}$ (8-10*kts*). This prolonged period of winds is important since it may have created a mixed layer that was observed deeper in the subsurface water during the drifter experiment (see Figs. 14 and 15). Four more diurnal westerly wind events occurred between the 14th and 19th, but at the start of the experiment the wind shifted on the 22nd to the NE for about a 36*hr* period, blowing steadily down-fjord at 4 to 5$m\ s^{-1}$ (8-10*kts*). Two more diurnal west wind events occurred on the 27th and 28th followed by a 24*hr* period of winds from the NE again from the 29th to the 30th (Fig. 12a and 13). The principal wind directions from the west and northeast are also shown in the wind rose plot (Fig. 12b).

Air temperatures in September 2016 still exhibited large diurnal fluctuations early in the month (1st to the 4th), with temperatures ranging from ~15 to 19$^o C$ during the day and >5 to 7$^o C$ at night. Following this the air temperatures steadily dropped as expected during the transition to fall weather patterns, and the trend in air temperatures was moderately negative through the month (R = -0.46) indicating that surface cooling was well under way. However, during the two periods when winds blew continuously from the NE (9th and 10th and 29th and 30th) the air was relatively warm, with diurnal temperatures ranging from 14-19$^o C$ and ~12-17$^o C$ respectively. These events may represent adiabatic warming of air from higher elevations in the interior, but the event at mid month preceded a period of low air temperatures (8-10$^o C$) with daily precipitation ranging from 5.5 to 6.5*cm*, (Fig. 12d). The next NE wind event on the 22nd followed after a period of moderate diurnal west winds and 6 to 7$^o C$ swings in daily air temperatures over the 17th to the 19th. The air remained cool during the NE wind event (8 to 10$^o C$) and is accompanied by another peak in rainfall on the 22nd (5*cm*) followed by a lengthy period of low precipitation (Fig. 12d).

Although by the end of the month freezing should have begun at high elevations (Carlson et el., 1969), alpine glacial melting and periodic precipitation was observed to feed high discharge from streams and rivers, particularly the Lowe River. This is consistent with changes observed over the past decade to a warmer and rainy fall climate at sea level in Port Valdez (J. Robida, pers. comm.).

4.6 Hydrography

4.6.1 Temperature and Salinity (T/S) Profiles

Examples of the physical properties in September are shown in (Figs. 14 and 15). By late September there was significant surface cooling shown by marked temperature inversions in the upper 5 to 7*m*. Near-surface haloclines from recent, cold freshwater input also occurred at these depths, and during the first CTD Run A, the near-surface temperature inversion continued down to 30 to 40*m* (Fig. 14a). There was also a minor halocline over the same depth range, and these features appear to be quasi thermostads and halostads (i.e. vertical regions of homogeneous physical properties) created either by mixing or interleaving of water masses via advection. In this case, these properties were most likely due to prior mixing that occurred during the strong winds on the 9th and 10th (Figs. 12a and 13). Beneath the semi-mixed areas of the water column the seasonal thermoclines extended from 35 to 60*m*, whereas the vertical salinity gradients showed very gradual changes over the same depths.

The average cross-channel T/S properties from first set of CTD casts collected on the 21st indicated that progressively warmer and saltier surface conditions extended from the inner basin to the central fjord (Fig. 14b). The seasonal thermoclines deepened down-fjord as well, as did the horizontal gradient in salinity over similar depths. The second set of casts on the 25th, however, (Fig. 14c,d) indicated there was a progressive erosion of the subsurface thermostads and halostads, as well as the seasonal thermoclines and haloclines, so that the T/S properties gradually became more uniform over time as expected. The horizontal gradients in physical properties from the inner basin to the central fjord remained in place within the upper 15*m* to 20*m*, however (Fig. 14c), and other than changes in the surface properties and a slight erosion of the subsurface temperature maxima, the average cross-channel T/S signatures (Fig. 14d) were very similar to those of the first set of data (Fig. 14b).

4.6.2 Vertical T/S Sections

Vertical sections of the physical properties (T/S/D) for along-channel transects 1 and 3 are shown in Fig. 15A and B for CTD sets A and H collected on September 21st and 25th respectively. The down-fjord spatial variation in physical properties is similar for the two transects on both dates, but a narrowing of the subsurface thermostad due to vertical diffusion of heat within the seasonal thermocline and deeper mixing of freshwater within the haloclines over time are quite evident. On September 21st an inward tilting of the isotherms and isohalines (and hence density) can also be seen in both sets of transects (Fig. 15A,B), which is removed by the 25th due to mixing. The nearsurface properties also have shallower gradients over time as well, presumably due to wind mixing over the fjord during the first two days (Fig. 13). This causes any new freshwater input or heat loss to occur over more homogeneous nearsurface water, and thus a narrowing of the vertical gradients at the surface. There are horizontal surface T/S/D gradients extending from the inner to outer basin along transect 3, however, that arose from mixing at PV9b to PV3 (Fig. 15B).

The cross-channel density variations are shown in vertical sections in Fig. 15C. These sections indicate that the same changes in physical properties over time observed in the along-channel transects also occur across the fjord channel. There are subsurface horizontal gradients in density along each transect on the 21st that are reduced by mixing over time by the 25th. However, the surface densities exhibit horizontal gradients showing slightly deeper nearsurface pycnoclines (i.e. vertical density gradients) from the north

to the south. Both the deep along-channel gradients early in the experiment and the lateral, cross-channel surface gradients later in the study had varied effects on the density driven circulation of these layers over the course of the study, and, as observed in past studies (Muench and Niebert, 1973; Colonell, 1981), estuarine surface flow and deeper density-driven baroclinic flows are both evident in the hydrography. This is addressed in greater detail under dynamic topography and geostrophic velocities in section 4.13.2.

4.7 ADCP Currents

Fig. 16A to D gives examples of ADCP data collected over four sequential tide phases[6] during the first 36*hr* of the oceanographic survey in September. As in June, the currents were typically strongest within the upper 20 to 30*m*, but the magnitudes were generally much higher by comparison (25 - 45$cm\ s^{-1}$ vs. 15 - 20$cm\ s^{-1}$). The remainder of the water column exhibited relatively weak flows with magnitudes of 5 to 10$cm\ s^{-1}$. The strongest subsurface currents again occur during ebb tides (Fig. 16A and B), and reversals in direction again created multiple baroclinic modes (i.e. layered flow). In contrast, the flows during flood tides (Fig. 16B, C and D) were concentrated above 20*m*, and at most times the deep subsurface currents beneath the active upper layer were relatively benign.

The cyclonic flow observed within the central basin in June occurred again in September during ebb tides and also during the transition into the flood tides (Fig. 16A to D). The pattern was also frequently present down to 31*m* in depth. During the second portion of the oceanographic survey, however, the cyclonic pattern disappeared and an inversion occurred, in which the strongest inflows were in the subsurface layer between 40 and 60*m* and the main outflows switched to the top 20 to 30*m* (Fig. 17A and B). This pattern created four baroclinic modes to the flows and it continued through two sequential tide phases (ebb 5 and flood 5). During next tide cycle (Fig. 17C and D) the nearsurface (7-15*m*) currents weakened, however, and the subsurface structure shifted back to moderate outflows ranging from 15 to 25$cm\ s^{-1}$. At this time, the cyclonic flow pattern resumed but was only observed below 15*m*. It occurred from the very end of flood 8 through the first 1.4*hr* of flood 9 (Figs. 17C and D), and this would indicate that the cyclonic pattern was principally an ebb tide phenomenon. However, it did not always occur during the ebb phases and it extended into the early portions of the flood tides as well.

The reasons for the marked discrepancies in the flow patterns over time in September are uncertain, but the tides switched in the middle of the oceanographic work from semi-diurnal-even tides to strongly uneven tides. The winds also shifted from the strong northeast winds over the 22nd and 23rd to a pattern alternating between weak westerly and northeasterly winds (Fig. 13). The vertical T/S/D gradients also began to mix over time as well, and perhaps the combination of factors played a role in affecting the changes observed in the ADCP data. This is discussed in more detail below.

4.8 Drifter Trajectories

In September, pairs of drifters were released from the very start of the study. These deployments were essentially the same as the dispersion experiments performed in June, and are described below for each drifter type. The entire record of deployments, including dates, times and coordinates is given in Appendix C.

[6] Sequential tide phases: ebb 2, flood 2, ebb 3 and flood 3

4.8.1 Ispheres (0-0.3m)

As in June, the isphere trajectories in September exhibited marked effects of shifting wind speeds and directions (Figs. 12a and 13). Tides and surface estuarine conditions also played a role in forcing the drifter motions. However, the spatial distribution of surface salinity was likely influenced by the winds, and thus the effects of estuarine surface flow on the drifters were highly varied during the study.

The effects of northeast winds on the ispheres over the 22nd and 23rd are indicated by the tracks shown in Fig. 18a,b. Initially, winds were westerly but then shifted to the northeast and back prior to blowing continuously from the northeast for nearly 1.5 days (Fig. 13). The first pair of ispheres in deployment #1 showed a varied response to both the wind shifts and tide change, making broad, anticyclonic turns during the start of a large flood tide. At this point, however, they began to disperse widely with i0600 moving northward and i8180 doubling back to the NE. The two drifters eventually moved westward under the actions of the NE winds, a large ebb tide and possibly estuarine outflow. In contrast, the ispheres released 4.5*hr* later (deployment #2) made wide cyclonic turns before joining the first two ispheres (Fig. 18a). Afterwards, all drifters moved in similar westerly tracks and eventually made large, gradual turns to the southwest where the first pair of drifters grounded near Entrance Island (Fig. 18a).

The same combined effects of northeast winds, an ebb tide and possibly estuarine outflow can be seen in the tracks of two pairs of ispheres in deployments #3 and #4 on the 22nd (Fig. 18b). In both cases, the drifters moved rapidly westward at average speeds of ~35 to 40*cm* s^{-1} (~0.7 to 0.8*kts*). The first pair of drifters was quickly recovered, with i8180 failing to transmit but located nearby i0460 (Fig. 18b). The second pair, however, quickly accelerated to speeds exceeding 65*cm* s^{-1} (~1.3*kts*) in the outer fjord, and then increased in speed through the 'Narrows' to an average of ~75*cm* s^{-1} (1.5*kts*). These two drifters then proceeded southwards into PWS and then moved WSW towards Perry Island (Fig. 18b). One of the ispheres (i2460) grounded on the island on the 26th and was recovered by the M/V Auklet. The other drifter (i0600) grounded but later refloated and moved southwest down Knight I. Pass (KIP). It eventually turned northward and grounded on the 30th at Green I. (Fig. 18b) and was recovered in early October by the PWSC research vessel, the R/V New Wave.

Drifters deployed on the 24th (Fig. 18c) showed responses to tide changes and apparently also to weak winds that shifted back and forth from the west to the north (Fig. 13). For example, the first group (deployment #6) moved southwestward during the end of the ebb and the first 1.5*hrs* of the flood tide due to mild westerly winds of 1.5 to 1.75*m* s^{-1} (3-3.5*kts*). Upon nearing shore, however, the ispheres abruptly turned eastward, and over the course of 3 to 4*hrs* they grounded within the Alyeska Oil Terminal, but then later refloated and were picked up inside the security zone (SZ). The westerly winds appear to have also balanced the outward motion of drifters in deployment #7, which remained nearly stationary during last 1.2*hrs* of the ebb. During the following flood tide they moved eastward and made tight anticyclonic (clockwise) loops before being driven onshore by winds from the west and northwest (Fig. 13).

Deployments #8 and #9 on the 25th are shown in Fig. 18d. This is an interesting case since there were no strong winds to force these drifters, as at the beginning of the study. In fact, the winds were initially from the southwest at speeds of 1.0 to 1.5*m* s^{-1} (2-3*kts*) and then became very light (<< 0.5*m* s^{-1}, or <1*kt*) and variable, but mainly northerly in direction (Fig. 13). Both sets of drifters moved to the west, but group #9 is initially forced to the NNW at an average speed of ~30*cm* s^{-1}. It is uncertain what the surface current vectors were at this time, but if the ADCP data in the top depth bin (7-15*m*) are any indication (Fig. 17C), then the flow would have been weak (<10*cm* s^{-1}) and northwestward in the vicinity of the drifter release. Thus the light (slightly rotated) wind driven surface currents and the weak, westerly ebb tidal currents could not have caused the rapid, northerly motions of the two drifters (Fig. 18d). The same could be argued for group #8, which moved initially close to the northern shore at similar speeds. Therefore an additional force must have aided in moving these drifters, and this force was likely estuarine flow. When

all the drifters reached the 'Narrows' they accelerated to average speeds of 80 to 90*cm* s^{-1} (1.6-1.8*kts*), except for 5600, which averaged 34*cm* s^{-1} (~0.7*kts*), before grounding on the western shore (Fig. 18d).

The remaining isphere deployments (#10 to #16) are shown in Fig. 18e to g. The tracks of these drifters were highly varied, showing effects of weak to moderate winds that shifted regularly from westerly to northeasterly (Fig. 13) combined with various tide phases and estuarine (geostrophic) outflow. Many of the drifter trajectories from the 26th to the 29th appeared chaotic and unpredictable, but for deployments #10 to #13 the drifters tended to move to the SE under westerly winds and back to the north under northeast winds (Fig. 18e,f). Also, the drifters released at mid-basin on the 28th (Fig. 18g) exhibited westward motion in the outer basin under very light winds (Fig. 13) and a large ebb tide, that was probably aided by estuarine (geostrophic) outflow, unimpeded by strong westerly winds as in June.

Most drifter pairs remained close together and exhibited limited dispersion, except for group #10b deployed in the inner basin on the 26th. These two ispheres remained static until the end of the ebb tide, after which a west wind and flood tide moved them to the southeast (Fig. 18e). During the next ebb tide and wind shifted to the northeast but they departed on much different tracks, with i5600 moving northward along the eastern side of the fjord and i6350 angling to the NW into the central basin. The other pair of drifters (group #10a) briefly moved westward on the ebb tide, but as the west wind accelerated to speeds > 3*m* s^{-1} the two drifters turned southeast. During the next flood tide, however, they made moderate anticyclonic loops before moving back to the northeast until the winds weakened to << 1*m* s^{-1} and started blowing from the north (Fig. 13). They then made an abrupt reversal and moved westward along the northern shore similar to i6350 (Fig. 18e).

The tracks of i6350 and group #10a on the 27th are of interest, since the low wind speeds that night may have allowed the Lowe River plume to move northwestward in a manner shown by i6350. The latter drifter and those of group #10a may have been caught in this outflow along the northern side, and microstars that exhibited this same type of pattern are described next.

4.8.2 Microstars (1m)

Fig. 19 shows the flows at 1*m* tracked by the microstars from September 21 to 30. In almost every case, varied amounts of wind, tidal and estuarine forcing moved the drifters outward. A few notable exceptions included group #6 on the 24th (Fig. 19d), drifter m003 of group #10b on the 26th (Fig. 19f) and group #17 on the 29th (Fig. 19i). In these three deployments the first two cases showed drifters initially moving down-fjord but then they reversed direction and either moved to the north (group #6) or ran aground (m003). In the third case, the drifters were moving eastward from the north-central basin until strong east winds out of the Lowe River drove them ashore.

The first two pairs of drifters were deployed 2*hr* apart on the 21st (Fig. 19a), but they both were initially affected by westerly winds and a flood tide that held back their outward motion. After the ebb tide commenced, however, the winds speeds increased (4.0*m* s^{-1}, ~8*kt*) and shifted to the east and northeast. All drifters then began to accelerate down-fjord at maximum speeds exceeding 40*cm* s^{-1} for the northern drifters and 26*cm* s^{-1} for the drifters at mid-fjord (Fig. 19a). The two groups dispersed, however, once they approached the 'Narrows', and the northern group ran aground just west of Shoup Bay, whereas the southern group continued southwards and were retrieved within the 'Narrows'.

The two groups of drifters released on the 22nd (Fig. 19b) initially moved to the WNW during the flood tide and northeast winds but then followed very similar tracks down-fjord close to the northern shoreline. Once they approached the western side of the fjord, however, the drifters began to move parallel to the shoreline, dispersing and grounding over a distance of ~5*km* (2.7*nm*). Drifter m004 was exceptional and moved northwards into Shoup Bay, whereas all the other drifters dispersed southward (Fig. 19b).

On the 23rd, four microstars (group #5) were deployed in the central basin (Fig. 19c) under weakening northeast winds and small ebb and flood tide amplitudes. All drifters moved westward at an average maximum group speed of 40*cm* s^{-1} (~0.8*kt*). Other than a gradual cyclonic turning, the effects of the above factors were minimal and all four drifters must be responding to unimpeded estuarine (geostrophic) currents. However, near the end of the flood tide and under mild westerly winds (< 0.5*m* s^{-1}, 1*kt*) they all turned abruptly to the east.

The two deployments on the 24th (Fig. 19d) exhibited highly divergent tracks under conditions of weak, but shifting winds from the west to the north (Fig. 13), a small ebb and flood tide, followed by a relatively large ebb (Fig. 19d). The two sets of drifters responded much differently to these forces, and whereas group #7 moved initially outward on the ebb and then to the north during the flood, group #6 initially moved down-fjord to the southwest during the two small tides and light westerly winds (Fig. 13). Afterwards, group #7 moved continually westward along the northern shoreline, but group #6 moved in the opposite direction, first heading ESE and then reversing course over the same track prior to turning to the NNE (Fig. 19d). It is suspected that the down-fjord motion of group #7 was driven by an estuarine (geostrophic) outflow. However, the response of group #6 to both the wind and tidal forcing is less certain. The initial southwest motion occurred over both the small ebb and flood tides and under light westerly winds that turned briefly from the north. During the ensuing ebb tide the winds shifted again to the west and NW and the drifters responded by moving inward against the tide. This was followed by the reversed (westward) and northward motions, both of which occurred during the flood tide (Fig. 19d).

During the next three deployments the net motion all the microstars was down-fjord to the west (Figs. 19e,f). What is interesting, however, are the divergent tracks of deployments #8 and #9 on the 25th and 26th. The two groups were deployed in the north-central and mid-central basin respectively, but whereas the outer group moved to the NW the inner group moved diagonally across the fjord to the southwest and out into the 'Narrows'. The winds were relatively weak and the tidal amplitudes small, except for the one ebb tide during the middle of the deployment. The average velocities are relatively low (20*cm* s^{-1}), but none-the-less the drifters all moved steadily down-fjord, possibly due to widening of the estuarine current due to dispersal. The latter is uncertain but is addressed in section 4.14 below.

The drifters deployed on the 26th (Fig. 19f) showed initial responses to the ebb tide and winds from the west that increase in magnitude. However, the currents in the outer basin appear to be dominated by (widened estuarine?) outflow, moderated by the wind and tides, whereas the tidal currents along with the effects of the westerly winds appear to be stronger in the inner basin. The latter may be why group #10b exhibited such sharp inflections to the southeast. On the change to the ebb tide the winds weakened and blew briefly from the northeast, followed by very weak crosswinds (Fig. 13). The two drifters in group #10b turned westward on the ebb tide, but m003 was forced onshore, whereas m004 continued westward along the southern shoreline. In contrast, the outer group (#10a) continued on a southwesterly trajectory, making broad anticyclonic turns close to shore, followed by dispersing laterally down-fjord but then drastically diverging at the mouth to the southwest and northwest respectively (Fig. 19f).

All the drifters deployed on the 27th exhibited net outflows along the southern side of the fjord, except m008, which drastically deviated from the general pattern. For example, groups #11 and #12 initially moved southwestward apparently due to westerly winds working against the ebb tide (Fig. 19g). When the flood tide began the winds exhibited a clockwise (negative) rotation from the southwest to the northeast with brief maximum speeds of 4*m* s^{-1} or ~8*kt* (Fig. 13). At this time all the drifters moved southward, and then under the NE winds and an ebb tide three of them moved down-fjord close to the southern shoreline. Drifter m008 took a vastly different path, however, and moved diagonally across the fjord to the northwest. The reason for this drifter's strange track turned out to be the loss of its drogue,

and this is discussed further below. The fourth drifter (m003) showed little effect of the wind shifts and mostly moved back and forth with the tides until finally moving outward along the shore (Fig. 19g).

The deployments on the 28th (Fig. 19h) occurred under light winds (1.25 to 1.5*m s*$^{-1}$, 1.5-2*kt*) that shifted abruptly from southwest to northeast with little rotary effects (Fig. 13). Initially, all the drifters moved either southward (m003 and m007) or southeastward (m004 and m006) during the transition to the ebb tide, followed abruptly by westward motion on the ebb after the winds shifted to NE (Fig. 19h). As the flood tide phase began, however, the winds slackened and during the last third of the drift period they remained very light and from the west. This caused clockwise (anticyclonic) motions in two of the drifters, and stalled the westward drifts of m003 and m007 (Fig. 19h). Once the tide changed, all drifters moved westward on the large ebb tide (-3.8*m*), particularly the two reaching the mouth of the fjord.

The last two deployments of microstars (Fig. 19i) occurred just prior to an acceleration in winds to speeds ranging from 3.5 to 4*m s*$^{-1}$ (7-8*kts*). All drifters initially moved eastward briefly during the latter portion of the flood tide and slack winds, but then responded rapidly to the increase in wind forcing. Interestingly, the strong winds initially came out of the Lowe River and registered briefly as east winds at the NOAA weather station, but quickly shifted to the NE (Fig. 13). Both sets of drifters rapidly responded to the easterly winds combined with a large ebb tide by moving either northwest (group #18) or NNW (group #17). However, in the course of 4 to 5*hrs* the winds shifted to the northeast and drifters in group #17 were driven westward, where m004 made an anticyclonic loop east of Mineral Creek prior to the drifters dispersing to the northwest and southwest respectively (Fig. 19i). The other two microstars were driven rapidly northward by the easterly winds, where the author photographed them gradually approaching the City Dock (Fig. 19j,k). Drifter m007 was retrieved using a boat hook as it drifted past a ladder attached to the dock, but m006 became trapped near shore and required retrieval by boat the following morning.

4.8.3 SVP Drifters (10m)

The trajectories of the 10*m* SVP drifters in September are shown in Fig. 20a to e. The deployments were done mainly in pairs and a listing of all groups including start and end dates, times and coordinates are given in Appendix C. These drifters generally showed higher maximum speeds (16-43*cm s*$^{-1}$) relative to June (18-20*cm s*$^{-1}$), but the ranges of average speed per deployment were similar in both months (5 to 7*cm s*$^{-1}$, 0.1 to 0.14*kts* in June vs. 4 to 10 *cm s*$^{-1}$, 0.08 to 0.2*kts* in Sept.). As in June, this resulted in relatively long drift periods. The trajectories appear to be mostly influenced by subsurface baroclinic currents due to interactions of the mass field (i.e. horizontal variation in water density), tides and wind driven transport, but the two periods of strong northeasterly winds (Fig. 13) may have affected the flows directly at 10*m* and indirectly at 40*m* depth.

In the first two sets of deployments (Fig. 20a) pairs of drifters were released in the central basin within 2.5*hrs* and 3.7*km* of each other. However, with exception of initially moving eastward on the first flood tide, they exhibited much different tracks. For example, group #1 remained within the inner basin over 2 to 3 tide cycles making either a small cyclonic orbit (s006) or a wide cyclonic arc to the north (s005) before moving westward along the northern side of the fjord. As described above, the winds (Fig. 13) were initially westerly (but variable) and shifted to the northeast on the 22nd, reaching speeds ranging from ~4 to 4.5*m s*$^{-1}$ (8-9*kts*) for more than 24*hr*. The two drifters in the inner basin may possibly have been affected by the northeast winds, particularly s005, which accelerated to maximum speeds of 30 to 37*cm s*$^{-1}$ and quickly reached the outer basin early on the 23rd. Drifter s006 also accelerated briefly along the north shore, but it lagged behind s005 and did not reach the same area in the outer basin until ~1900 on the 24th (Fig. 20a). At about midday on the 23rd the winds weakened to ≤ 1.5*m s*$^{-1}$ (~3*kts*) and during this period s006 slowly advanced westward over 11.1*km* from the northern shore at an average speed of 8*cm s*$^{-1}$.

The second set of drifters (group #2) initially moved westward, but then made broad cyclonic orbits before moving eastward along the southern side of the fjord at speeds exceeding 40*cm* s^{-1} (Fig. 20a). Drifter s004 also made one small cyclonic orbit to the north before both drifters proceeded eastward into the southern side of the inner basin, where they then retroflected back to the west. The ADCP data show similar cyclonic circulations in the central basin during the latter part of ebb tide 2 on the 21st and the beginning of flood tide 2 on the 22nd (Fig. 16A and B). During the second flood tide (Fig. 16C) the cyclonic flow at 7 to 15*m* disappeared but was observed deeper in the water column. The ADCP data also showed reversing flows between the northern and southern sides of the fjord over both tides, and this explains in part the different motions of the two sets of drifters. Although there is an apparent tidal component to the orbital patterns, they are not entirely synchronized with the tide phases. It should also be noted that cyclonic orbital motions were not observed further in the drifter data. The ADCP data, however, showed this type of flow occurred later on the 25th but only at depths of 20*m* to 40*m* (Fig. 17C).

The next set of deployments (#5 to #7) showed much different drift patterns on the 23rd and 24th in comparison to the first two sets. After the initial deployment (#5), the winds shifted back to a pattern of westerly, northerly and northeasterly directions, but at much lower speeds (Fig. 13). Drifter s005 was possibly affected by the northeast winds at first, but once the winds subsided and turned from the west the velocities slow to mere background speeds of < 5 *cm* s^{-1}. The second set of drifters (#6) exhibited markedly differing patterns of drift, and considering the negligible dispersion within the inner basin of group #7 the motion of s004 is an anomaly that can not be easily explained. It does appear to follow the same current along the northern shore that moved both drifters of group #1 (Fig. 20a).

In deployments #8 to #12 (Figs. 20c to d) pairs of drifters were released in the western and eastern sides of the central basin. Initially the groups moved in separate directions, and the drifters in the inner basin moved slowly eastward and then turned back anticyclonically, whereas the pair at mid-fjord moved slowly down-fjord to the west. In both cases small oscillations occur in the tracks that are not totally synchronized with the tides. The speeds of the drifters were also relatively low, with average magnitudes of only ~5 to 10*cm* s^{-1}. This was similar to the background flow shown by the ADCP data at 7 to 15*m* over the interim period on the 24th and 25th when winds were light (Figs. 13 and 17A,B). Occasionally, some of the drifters attained relatively high speeds of 18*cm* s^{-1} (~0.35*kts*). This occurred in the outer fjord on the 25th and 27th for deployments #9 and #11 respectively (Fig. 20c,d).

The final deployments (#16 and #18) took place on the 28th and 29th respectively (Fig. 20e). These drifters showed relatively little motion over course of one to two days, and group #16 appeared to oscillate back and forth with the tidal motions. The drifters in the inner basin (#18) also moved very slowly, but showed minimal tidal responses and gradually moved outward along the south side of the fjord similar to groups #8 and #12. Although neither set of drifters appeared to respond significantly to the marked increase in northeast winds (Fig. 13), some limited effects may be shown by the outward motions of s008 in the north and s006 and s003 in the southern group. There were possibly also some affects of winds on group #11, as shown by their outward drift on the 29th to the 30th (Fig. 20d).

4.8.4 SVP Drifters (40m)

Fig. 20f shows the trajectories of the SVP drifters with 40*m* drogues (deployments #2, #5 and #7) released individually on a daily basis from the 22nd to the 24th. The trajectories cover 11 to 15 tide cycles over roughly 6 to 8 days and numerous changes in wind velocities (Fig. 13). Drifter #002 had the longest deployment and was released during the marked northeast wind event on the 22nd, whereas the other two drifters were released during interim period (described above) of light winds that frequently shifted in direction from the west to northeast. All of the drifters were in place during the final east-northeast wind event on the 29th and 30th (Fig. 13).

From Fig. 20f it is obvious that in September the 40*m* drifters exhibited more complex drift patterns and attained much higher velocities in comparison to June (Fig. 10i). This is shown by the small to large cyclonic and anticyclonic orbits of all the drifters and the relatively rapid down-fjord westward motions of #001 and #003 along the northern shoreline on the 29th and 30th. The other drifter (#002) also exhibited accelerations in the central and outer basin, but it moved between basins before finally ending up in the same location as the former two drifters on September 30th.

The maximum speeds of the 40*m* drifters were close, ranging from 12 to 13*cm* s^{-1}, However, the periods of highest velocities were not limited to the major northeast wind events, indicating that some other forcing besides wind was responsible for moving the 40*m* SVPs at speeds of 5 to 13*cm* s^{-1}. For example, given a wind speed of 8*m* s^{-1} at 61^{o} latitude the D_E would be 37*m*. This gives a surface flow (V_0) of 10.6*cm* s^{-1} and at 37*m* the flow would be negligible at 0.5*cm* s^{-1} or 1/10th the background flows of 5*cm* s^{-1}. The ADCP velocities at 40*m* show maximum speeds of 15 to 20*cm* s^{-1} and minimum speeds of 5 to 10*cm* s^{-1} for both ebb and flood tides (Figs. 16 and 17). This is consistent with the motions of the 40*m* drifters and would indicate tidal and subsurface baroclinic flows, driven by either the mass (density) field or a response to wind transport in the Ekman layer, may be responsible for the relatively high velocities at 40*m* observed in September.

4.9 Meteorological Data and Freshwater Input: March 2017

The meteorological conditions during the month of March 2017 are shown in Fig. 21. The winds during this month (Fig. 21a,e) exhibited continuous periods of high speeds often sustained at 10*m* s^{-1} (20*kts*) with maxima frequently exceeding 15*m* s^{-1} (30*kts*). The predominant direction (i.e. principal axis) was from the northeast (Fig. 21b), which is similar to winds blowing from the interior in September (Fig. 13), but there were also frequent periods of winds from the east and southeast, blowing out of the Lowe River Valley at speeds of 8 to 10*m* s^{-1} (~16 to 20*kts*) (Fig. 21e). The continuous winds in March are important since they undoubtedly resulted in deep mixing observed in hydrography (see Figs. 22 and 23 below). The strong easterly winds also influenced the northwesterly trajectories observed for all drifters. Late on the 28th, however, a period of calm occurred followed by light, variable winds to the end of the project (Fig. 21e).

Air temperatures in March 2017 (Fig. 21c) exhibited small diurnal fluctuations and remained below freezing (0 ^{o} *C*) up until the 21st. Large fluctuations ranging from 5 to 10^{o} *C* occurred on the order of days, and between the 19th and the 21st air temperatures rose by more than 11 ^{o} *C*. The general trend was positive for the month (R = 0.68), but if the high temperatures after the 20th were excluded it would likely be nearly flat up to that date (i.e. slope of the regression ~ 0). The surface warming indicated by air temperatures after the 21st was negligible and absent from the water temperature profiles (Fig. 22).

The periodic rise in air temperatures may at times represent adiabatic increases in heat during katabatic wind events blowing from interior, but this relationship was not consistent throughout the month, and there were periods when rising temperatures occurred during low winds (Figs. 21c,e). The magnitude of the changes would also depend on the types of continental air masses in place at the time. For instance, if the air were from the arctic, and thus very cold (<< 0 C), the adiabatic warming would have been less in comparison to the negative changes caused by the cold air mass displacing warmer air at sea level.

Precipitation throughout March was negligible until the end of the month, when snowfall began on the 27th. Some of the snow initially melted, however, due to above freezing air temperatures. Any freshwater input to the fjord would have been negligible but minor decreases in the surface salinities were observed, and this is described in the next section. The conditions in March were consistent with descriptions for late winter in past studies (Carlson et el., 1969; Muench and Niebert, 1973; Colonell, 1981).

4.10 Hydrography

4.10.1 Temperature and Salinity (T/S) profiles

Fig. 22 shows the mean cross-channel T/S profiles from the combined set of casts on the 21st and 23rd. These data indicated that by late winter 2017 the water column was very cold and salty, as expected, and there was significant mixing that varied spatially, however. For example, transect 1 showed mixed conditions all the way to depth, whereas transects 5 and 9 had minor vertical temperature reversals (ΔT = -0.2 to -0.35 ^{o} C) and slight vertical salinity gradients ($\Delta S < 0.2$) within the upper 20 to 30m (Fig. 22a). The T/S profiles also showed that shallow mixed layers existed in the upper 5m at both transects 5 and 9. The T/S diagram, however, revealed that the subsurface T/S minima at 10 to 20m for transect 5 was stable since the sigma-t values remained constant over those depths (Fig. 22b).

Although the air temperatures exhibited a rising trend during the days of the experiment (Fig. 21c), the cooling in the subsurface water may have resulted from minor amounts of very cold runoff, which were also evident from decreases in salinity. These conditions were confined to the inner basin, however, since transect 1 showed such deep mixing.

Fig. 23 shows the third set of casts on the 24th. These data showed an erosion of the upper layer vertical T/S gradients occurred over time due to the constant winds encountered during the first five days of the survey (Fig. 21e). Very slight vertical T/S gradients occurred in the upper 20m for both transects 5 and 9, whereas transect 1 remained well mixed to depth. The vertical gradients showed that the former two transects had very gradual increases in T/S properties that now extended to 80m (Fig. 23a). The T/S diagrams also reflected the more uniform physical properties with a water column density (sigma-t) of 25.4, but two inconsistencies that occurred in the surface water are shown by marked inflections in salinity. Since by the 24th there was still no precipitation to speak of, these gradients may still reflect very minor inputs of cold freshwater.

4.10.2 Vertical T/S Sections

Vertical sections of the physical properties (T/S/D) in March 2017 are shown for along-channel transects I and III from CTD sets A/B and C collected on the 21st/23rd and 24th respectively (Fig. 24A,B), and for cross-channel transects 1 and 9 on the same dates (Fig. 24C). The along-channel transects indicated that slight amounts of cold, freshwater occurred within the upper 15 to 20m along northern side on the initial cast dates, but over time these minor vertical gradients eroded significantly due to mixing. In contrast, the physical properties for the southern transect (III) remained nearly spatially uniform over time (Fig. 24B), and only minor vertical gradients occurred in the upper 20m at station PV16 located in the southeast inner basin (Fig. 24B). The vertical sections of density for cross-channel transect 1 (Fig. 24C) showed that the outer-central basin also remained homogenous over time (shown also by the mean profiles in Figs. 22 and 23), whereas transect 9 initially exhibited a cross-channel density gradient within the inner basin due to the small input of cold, freshwater on the northeast side (Fig. 24C). By the 24th, however, mixing by the continuous, easterly winds (Fig. 21e) rendered the latter gradient barely visible (Fig. 24C(d)).

The changes in physical properties over time in Port Valdez illustrate the effectiveness of katabatic winds from the interior in removing heat and uniformly mixing salt through the water column by late winter, thus setting the stage for stratified conditions that occur in the early summer from solar heating and initial freshwater input, all of which were shown in the previous sections. The highly uniform density of the water also allowed uninhibited vertical exchange between depth layers, and deep effects of winds were observed in both the drifter trajectories shown in section 4.12 and the ADCP data presented next.

4.11 ADCP Currents

Examples of ADCP data collected in March are shown in Fig. 25. The severity of the winds during the five days of the oceanographic survey (Fig. 21e) prohibited work on certain days and the resultant wave action caused noise in the data for portions of the transects where waves affected the stability of the depressor fin (described above). The data therefore required extra processing beyond the normal quality checks (see Gay, 2013). The secondary processing was done by first removing spurious *u* and *v* components for an ensemble by filtering bins and keeping only components in which *u* or $v \leq 2$ *standard deviations* of the mean values for an ensemble, then interpolating horizontally to fill in the missing data.

A caveat here is that these data have high amounts of uncertainty in the interpolated portions of transects, and thus they should be used for descriptive purposes only. Having said this, the data still proved to be very useful in interpreting the drifter patterns during periods of strong easterly winds.

The first set of repeated transects made on March 21 (Fig. 25A,B) represented the best data quality for the entire five day survey. The transects were made during the second ebb and flood tides for that day, and the flow patterns remained very similar in both cases illustrating the extreme effects of the winds on the homogenous water column. The main features of these flows are that they were highly barotropic (i.e. uniform with depth) but also exhibited substantial horizontal shear, which certainly aided in mixing the water column.

On the morning of the 21st, the winds initially blew from the northeast at ~2$m\ s^{-1}$ (~4*kts*) thus allowing the ADCP survey to commence. By noon, however, the winds begin to accelerate from the east out of the Lowe River Valley. Eventually, the winds blew northwestward in a plume across the fjord at speeds ranging 6 to 7$m\ s^{-1}$ (~12 to 14*kts*), with gusts frequently exceeding 10$m\ s^{-1}$ (>20*kts*) (Figs. 21a,e). The currents within the inner fjord basin are relatively light and moving westward, but in the central basin the winds along with the ebb tide formed a wide jet moving to the northwest, almost exactly in the direction of the winds measured at the City Dock (Fig. 21e). To the north of the jet the flows appeared to turn northwards. During the flood tide (Fig. 25B) the jet in the central basin persisted, but currents to the north continued to turn, possibly forming an anticyclonic eddy, particularly in the subsurface water below 15*m*.

The second data set were collected during the second ebb tide on March 24th (Fig. 25C). The winds were again blowing from the Lowe River Valley but with sustained velocities of 8$m\ s^{-1}$ (16*kts*) and gusts > 13$m\ s^{-1}$ (26*kts*). The general flow to the northwest was again evident in the flow pattern, but there was also greater spatial homogeneity to these flows along the north side of the fjord in comparison to the 21st (Fig. 25A,B). How much of this is realistic is uncertain, since the relatively poor data quality resulted in the removal of many of the original vectors and interpolation was performed. However, the general NW flow over the inner fjord was also evident in data contaminated with noise prior to secondary processing. In the southeastern region of the fjord the northerly wind driven currents also appear to create a cyclonic circulation that was evident at all depths (Fig. 25C).

The maximum depths of the wind driven currents are inferred by the sustained speeds in March (Fig. 21). These winds frequently ranged from 10 to 15$m\ s^{-1}$ (20-30*kts*) and the D_E from eq. 1 would be 46*m* to 70*m*. On March 3rd, however, winds reached speeds of 20$m\ s^{-1}$ (~40*kts*), which would result in a D_E of ~90*m*. The above values are consistent with the depths of mixing and the quasi barotropic flows observed from the oceanographic work, as these properties were the products of sustained high winds during the survey.

4.12 Drifter Trajectories

In order to minimize potential losses or strandings that would have prolonged retrieval due to rough sea conditions, drifters in March were not released until the middle of the oceanographic survey on the 24th. Three deployments were performed over the last two days of high winds, and five more were performed over the second half of the experiment, when the winds slackened somewhat on the 26th, but still blew over more than two days from the northeast at speeds of 3 to 5*m s*$^{-1}$ (6-10*kts*). Following this, the wind ceased on the 29th and a period of quiescence occurred until the 30th when the winds of relatively low magnitude began blowing from the west (Fig. 21e). The drifters in March were released in groups of two to three, and the record of all deployments is given in Appendix C.

4.12.1 Ispheres (0-0.3m)

The initial deployments of ispheres on March 24th (Fig. 26a) were done in two groups (#1 and #2) located along the northern and southern portions of transect 7 (Fig. 2c). The winds at this time were blowing to the WNW at speeds of 6 to 7*m s*$^{-1}$ (12-14*kts*) and all drifters moved rapidly to the northwest and slightly to the right of the wind, at an average speed of 39*cm s*$^{-1}$. The two ispheres released in group #3 on the 25th (Fig. 26b) also moved WNW at a similar average speed (35*cm s*$^{-1}$). The winds were essentially the same as on the 24th, except for being slightly more southeasterly (Fig. 21e), but in both cases it was quite obvious that the easterly winds were the dominant force affecting all drifter trajectories.

The trajectories of ispheres deployed from the 26th to the 27th are shown in Fig. 26c. The drifters in groups #4 and #5 were released in the morning and afternoon at the start of the prolonged period of northeasterly winds (Fig. 21e). In both deployments the average speeds were ~27*cm s*$^{-1}$ and the general directions were to the southwest. Group #4 quickly grounded on the southern side of the fjord, whereas group #5 traveled westward prior to making a broad turn southward, and then moved southwest to ultimately ground in Anderson Bay (Fig. 26c). The tide during the two drift periods was flooding for #4 and ebbing for #5, and this probably caused the first group to move closer to the direction of the winds. Group #5, however, first moved WSW during the ebb, but the drifters began turning southward at slack tide and continued turning as the flood increased. The reason for the westward swing is uncertain, but it may be due to boundary friction that caused the flows to weaken and thus allowed Coriolis and Stokes-Coriolis force due to wave action (Röhrs and Christensen, 2015) to steer the ispheres to the right. The effects of waves on drifters are discussed further below in section 5.3.

The deployments on the 27th and 28th (Fig. 26d) differ markedly from each other, but it was obvious that group #6 was again forced in a southwest direction by the northeast winds, and all drifters moved at close to the average speed (26*cm s*$^{-1}$). The drifters reached shore at the end of the second ebb tide on the 27th and then two of them refloated during the flood tide and moved westward along shore similar to group #5. It is uncertain where drifter i6350 went on the flood tide because it quit transmitting and was never found. The other two, however, remained relatively motionless during the flood tide, and then on the ebb tide on the 28th they moved westward again towards Anderson Bay (Fig. 26d).

In the final deployment (#7), the ispheres were released during the period of becalmed winds (Fig. 26d). The two drifters remained together for the entire period, which covered 43*hrs* over 3.5 tide cycles. During this time the drift exhibited a pattern similar to prior months when slackened winds and negligible estuarine flow allowed tides to become the dominant forcing mechanism, albeit at speeds < 5 *cm s*$^{-1}$. However, in the present case the drifter motions did not always correlate with the tidal phases and a marked eastward acceleration to 50*cm s*$^{-1}$occurred at the start of a large ebb tide on the morning of the 30th. The drifters then continued moving to the southeast at average speed of 32*cm s*$^{-1}$. The accelerations actually began during the start of two anticyclonic orbits over the final three tide phases (Fig. 26d), and this illustrates the vagaries in circulation that occur when weak winds permit the nonlinear effects of eddy

viscosity, tides and rotational effects of relative and planetary vorticity time to act upon the flows. However, considering the lack of wind forcing what exactly drove group #6 to such high speeds is highly uncertain.

4.12.2 Microstars (1m)

Fig. 27 shows the flows at 1*m* tracked by the microstars deployed from March 24 to 30. Note that some of the positions of m004 over the 25th to the 27th (Fig. 27a,b) were incorrect due to faulty GPS transmissions. The few bad points in these plots were removed and filled in by interpolation. No further problems in the coordinates of this drifter were encountered.

In deployment #1 (Fig. 27a) three microstars were released under the same atmospheric forcing described above for the ispheres. Driven by wind-induced currents, the drifters initially moved northwestward but slightly to the east of the isphere tracks (Figs. 26a), and the strong rightward leeway was possibly due to additional Stokes-Coriolis force from waves. Upon nearing the shore, however, the microstars turned westward and followed the northern shoreline closely until they turned to the southwest early on the 25th. The deployment covered nearly 13*km* over a 24.5*hr* period and the average speed was ~14.7*cm* s^{-1} (~0.3*kts*). The drifters also exhibited very little dispersion and remained close together, similar to previous deployments in June and September.

The following day the same three microstars were deployed ~1*km* west of the release point of group #1 (Fig. 27b). At this time, the southeast winds were still strong, but they began shifting in direction before steadily blowing from the northeast at an average speed of ~4*m* s^{-1} over the next two days (Fig. 21e). The microstars initially followed a track similar to the drifters released in deployment #3, but the initial speeds (~18*cm* s^{-1}) were slightly higher by comparison. The drifters then turned westward and traveled along the north shore again, albeit a bit farther to the south. However, after midnight the winds shifted to the consistent northeasterly directions and the drifters exhibited highly varied responses. For example, m004 and m005 made small cyclonic turns back to the north before either proceeding slowly westward (m005) or making a second anticylonic turn to the south (m004) (Fig. 27b). In contrast, m006 moved progressively westward, making a wide turn to the southwest and then moving westward along the southern side of the fjord.

The motions of m006 in the outer fjord were partly a response to the northeast winds being moderated by the tides. For example, m006 accelerated during the last flood tide on the 26th to a maximum speed of 15*cm* s^{-1}. The winds were in opposition to the tide, which explains the southward turning. However, they were too weak to generate such a strong southward flow, and the current at 1*m* would have been at most 5*cm* s^{-1}. So, what induced the remaining flow is uncertain. One possibility is that surface transport during the period of southeasterly winds may have caused an increase in sea surface elevation along the northern shore, thus resulting in a barotropic flow to the west; such a flow was indicated by all the subsurface drifters (see also Fig. 28a and e). The northeast winds possibly dispersed and weakened the current but it still possibly had enough momentum to produce an additional 10*cm* s^{-1} of flow to that of the wind.

On the 26th, three microstars (group #5) were deployed in the east-central fjord (Fig. 27c). These drifters were released under the same wind conditions that occurred at the end of deployment #3, and initially they followed westward trajectories similar to m006 the day before. However, after more than 40*hrs* they began making wide cyclonic orbits on the 28th. Two of the drifters turned eastward on the last flood tide on the 29th, at which time they accelerated to maximum speeds of 15*cm* s^{-1} prior to making anticyclonic turns to the southern shore (Fig. 27c). It is uncertain, but the latter accelerations and southward turnings were possibly responses to the weak westerly winds, moderated respectively by the flood and ebb tides.

Fig. 27d shows the continuation of microstars 004 and 005 from deployment #3, and a redeployment of m006 after it was retrieved in the outer fjord on the 27th (Fig. 27b). The winds were weakening, but still came from the northeast up through the 28th, after which, the prolonged period of calm to light westerly winds occurred (Fig. 21e). These drifters remained in the central to outer fjord basin until the end of the experiment, but at about 0500*hrs* on the 30th m004 moved away from the group and proceeded southward. From the initial trajectories it appeared that all of the drifters were driven westward due to the northeast winds, albeit at variable speeds of 7, 12 and 15*cm* s^{-1} for m005, m004 and m006 respectively (Fig. 27d). A maximum speed of 17*cm* s^{-1} was attained by m006 during the second flood tide on the 28th. The winds were weakening at this time, however, and the southwest trajectory is very similar to m006's track the previous day. During the subsequent period of calm to very weak westerly winds, all the drifters began making wide cyclonic orbits similar to deployment #5. These patterns showed little correlation with tidal phases and since there was no other obvious forcing it appears that they were simply affected by large-scale turbulence in the outer fjord, as observed during the other surveys when flows were very weak.

4.12.3 SVP Drifters (10 and 40m)

The release of the 10*m* SVP drifters initially coincided with the deployment of ispheres and microstars in group #1 (Fig. 28a). The trajectories of these drifters on the 24th to the 25th was nearly identical to the tracks of the 1*m* microstars, the main difference being that the SVPs traveled slower and exhibited greater dispersion along the northern side of the fjord. The average speeds of these drifters ranged from 7 to 10.7*cm* s^{-1} (0.14 to 0.21*kts*), but s005 attained a maximum speed of 17*cm* s^{-1}(0.33*kt*s) on the same day and in a similar location as microstars 004, 005 and 006 (Fig. 27a). As aforementioned, this indicated that a westward barotropic flow occurred in the upper water column, as suggested by the ADCP data for depths below 7*m*. The deployments occurred completely during a period of southeast winds (Fig. 21e) and the currents at 10*m* for a 7*m* s^{-1} wind would have been 4*cm* s^{-1}. The remainder of the velocity was possibly due to tides, although the effects were subtle. At the end of the drift period, however, much of the acceleration of s005 occurred during the first ebb tide on the 26th (Fig. 28a).

The trajectories for the SVP's on the 25th to the 29th (Fig. 28b) occurred mostly during the extended period of moderate northeast winds. Initially, the drifters were released as the winds were shifting from southeast to northeast, and the drifters moved slowly around to the west of the release points at speeds of only 5 to 6*cm* s^{-1}. This motion is nearly impossible to disentangle, as it occurred over nearly 6 tide cycles and under the steady northeast winds (Fig. 27b). Following the second flood tide on the 28th, however, the drifters began moving steadily westward on the ebb tide. The winds were weakening at that time, but the drifter speeds were much faster than the empirically derived wind driven currents, which for winds speeds of 4 to 5*m* s^{-1} would have been only 1 to 2*cm* s^{-1} at 10*m* depth. The speed of the currents at 10*m* along the northern shore was nearly 9*cm* s^{-1}, and this must have been due to both the ebb tide and barotropic flow since the winds had dropped to a maximum speed of only 2.5*m* s^{-1} (Fig. 28b). The drifters then moved westward along the north shore at an average speed of 10*cm* s^{-1} and they appeared to accelerate on the ebb to a maximum speed of 13*cm* s^{-1} prior to dispersing either towards the shore (s005 and s007) or turning southward (s002).

The drifters of group #5 followed a similar trajectory as those described for deployment #3. The main difference was that at the end of the drift period there was no southerly turning, and all the drifters dispersed along the northern shore (Fig. 28c). All six of the SVP's were recovered and redeployed on the 29th in the northwest region of the central basin (Fig. 28d). These drifters all exhibited cyclonic turning or nearly one full orbit before they were retrieved on the 30th. This drift period occurred over two tide cycles and the start of the weak westerly winds (Fig. 28d). The drifter speeds ranged from 6 to 8.5*cm* s^{-1}.

The trajectories of the 40*m* SVP drifters are shown in Fig. 28e,f. The barotropic nature of the currents was shown by the drift pattern of #001, deployed on the 24th at nearly the same location as the 10*m* SVPs. This drifter exhibited a pattern very similar to both the microstars (Fig. 27a) and the 10*m* SVPs (Fig. 28a) and covered over 12*km* in three days, giving it an average speed of 7*cm* s^{-1}. The Ekman depths (D_E) for winds ranging 8 to 10*m* s^{-1} during initial drift period are 36 to 46*m* and for gusts of 13*m* s^{-1} the D_E is closer to 60*m*. Given the persistence of the easterly winds over time a general westward drift could have easily developed at this depth. The ADCP data (Fig. 24) certainly suggest this was indeed the case.

The 40*m* SVP retrieved on the 27th was redeployed along with #002 on the same day in a similar location as the previous deployment. The deployments of these two drifters covered ~ 6 tide cycles and remained very close together during the entire 3 day period. They moved at an average speed of ~6.5*cm* s^{-1}, and as the winds subsided the tracks turned southward in direction. The effects of the tides on the drift pattern were very subtle until near the very end of the deployment on the 30th, when the last three tide phases appear to steer the drifters in a zig-zag pattern, inward on the flood and outward on the ebb (Fig. 28f).

4.13 Dynamic Topography and Geostrophic Velocities

4.13.1 June 2016

Fig. 29 shows the dynamic topography (1/100*db*) in June for four sets of CTD casts: (A to C) collected during the initial 36*hr* and (F) collected at the end of the five-day oceanographic survey (see Fig. 4). The first set (Fig. 29a) shows a background flow to the south in the inner basin and to the southwest in the outer fjord. This assumes that the velocities were in geostrophic equilibrium so that the flows from high to low geopotential (Φ) (i.e. dynamic hts.) were in balance with Coriolis, and thus follow the contours of dynamic heights. The latter assumption is probably not totally valid, and although the flows were affected by Coriolis, as indicated by Rossby numbers < 1 (discussed above), it is doubtful they achieved full geostrophic balance as implied by eqn. 6. This was also evident by the marked changes in topography for the subsequent CTD sets. For example, set B (Fig. 29b) shows that the field reversed in direction to the north, and the highest dynamic heights then occurred in the inner basin. Set C (Fig. 29c) shows a pattern similar to set A, whereas the last set (F) exhibited an entirely different pattern, in which flows moved westward from the inner basin and then turned southward towards Jackson Pt. (Fig. 29d).

The vertical structure of the geostrophic flows for CTD sets A and F (Fig. 29a,d) is shown in Figs. 30 to 32. In almost all cases the highest magnitudes occurred in the upper 5 to 10*m* in association with strong nearsurface density stratification caused by the initial increase in seasonal runoff (Figs. 6 and 7). For example, the along-fjord transects (Fig. 30) show that during set-A strong southward cross-channel flow (-0.4 to -1.6*m* s^{-1}) occurred in the nearsurface water of the outer fjord, close to Mineral Creek and Gold Creek. As aforementioned, large fronts of freshwater were observed in this region during the initial portion of the 36*hr* survey. A similar flow structure occurred at mid-fjord (Fig. 30b), but along the southern side (Fig. 30c) the nearsurface cross-channel flows alternate between southward flow at PV17-13 to northward flow at PV10-7 and then resume a southward direction at PV7-4.

The cross-fjord transects for set A (Fig. 31) show that westward along-channel geostrophic flows (0.4 to > 1.6*m* s^{-1}) occurred in the nearsurface water of the outer fjord (Fig. 31a), and when taken together with the orthogonal cross-channel components indicates that currents ranging from 0.5 to ~2*m* s^{-1} flowed to the southwest, just as implied by the dynamic topography (Fig. 29a). The inner fjord, by contrast, exhibited currents with much lower magnitudes (0.2 to 0.6*m* s^{-1}) and the directions also varied depending on the transect. It should be noted here that the geostrophic currents are relative flows only and some of the magnitudes are much higher than expected based on drifter speeds and the ADCP data. The lowest

velocities occurred at mid-fjord, however, (Fig. 31c), and this is where the ADCP data periodically showed a breakpoint between flows in the inner and outer basins.

During CTD set F, (Fig. 30d-f) the along-fjord transects show that moderate cross-channel geostrophic flows ranging from 0.1 to 0.4$m\ s^{-1}$ occurred again in the nearsurface water, but between PV14 and 11 the flow structure changed dramatically, and currents ranging from 0.1 to 0.8$m\ s^{-1}$occurred at deeper depths from ~60m to 30m (Fig. 30d). The latter structure implies that freshwater was mixed vertically at PV14, and indeed the individual T/S profiles (Appendix A) show both thermostads and halostads (small, vertically mixed regions) occurred at PV14, possibly giving rise to the deeper geostrophic velocities. It is very likely these properties arose due to a combination of wind induced mixing over time at the head of the fjord and possibly downwelling or interleaving due to advection. However, similar physical properties were not seen in any of the earlier data sets.

The cross-fjord transects during set F (Fig. 32) show that the along-channel geostrophic flows varied both in magnitude and direction across the fjord, but, as with the cross-channel components, the flows in the northwestern region at transect 1 varied from 0.2 to 0.4$m\ s^{-1}$ to the east at PV1-2 but at transect 3 the eastward flows occurred across all stations and were strongest in the south at PV6-7, where flows ranged from 0.2 to 0.45$m\ s^{-1}$. When considered together with the cross-channel velocities the geostrophic flows in the northeastern fjord were eastward at PV2-6 and to the northeast at PV1-5. In the inner basin, where surface freshwater content was highest, the geostrophic flows in the northeastern fjord at PV14-11 were northwestward at 0.8 to 1.6$m\ s^{-1}$ but in the southern region the flows were relatively weak (~0.2$m\ s^{-1}$) and to the west.

All of the flow vectors indicated from the combined along-channel and cross-channel components agree with the general flows implied by the dynamic topography. In addition, the magnitudes of the geostrophic flows beneath the nearsurface water (1-5m) are similar in value to the vectors shown by the ADCP data in the upper 50m, which ranged from 0.1 to 0.2$m\ s^{-1}$. Although some of the geostrophic velocities in the nearsurface layer were much higher than the current speeds tracked by the drifters, they nevertheless imply that estuarine gradients were important drivers of the surface flows. Also, the agreement of the subsurface ADCP currents with the geostrophic velocities indicates the subsurface flows were also significantly driven by the subsurface mass field.

4.13.2 September 2016

As in June, the dynamic topography in September (Fig. 33) varied widely among data sets, indicating that the spatial density structure was constantly in flux during the oceanographic survey from various factors such as cooling, freshening, mixing and advection. The magnitude of the dynamic heights were also much higher relative to June due to a deepening of the pycnoclines from vertical mixing over the summer to early fall. The contours also alternated between a longitudinal and lateral structure, indicating that the geostrophic velocities switched from cross-channel flow early in the survey for sets A and B (Fig. 33a,b) to along channel flow in set E (Fig. 33c).

The flow directions in sets A and B were predominantly to the north, whereas the flows in set E were widespread and to the west. Also, in set B there was evidence of a possible cyclonic eddy at PV16. In contrast, data set H showed highly varied flows between the inner and outer basins. The contours of dynamic heights bear a structure in the inner basin resembling CTD set F collected in June (Fig. 29d), but the flow directions were reversed and in September there was also a high pressure center at PV16 that indicated the possible presence an anticyclonic eddy. As in June, the flow in the outer basin was northward, but instead of turning sharply to the east it flowed outward to the northwest (Fig. 29d).

The localized cyclonic and anticyclonic eddies exhibited in sets B and F occurred in exactly the same location, and showed up in the contours despite block-averaging the data and using a tension factor > 0. This led me to believe that these eddies were real and possibly attributed to northwestward flow of the Lowe River plume.

Figs. 34 and 35 show the vertical structure of the geostrophic velocities for the along-fjord and cross-fjord transects respectively from data sets A and H. The cross-channel velocities for CTD set A (Figs. 34a-d) indicated that the northerly flows inferred by the dynamic heights occurred over the entire upper water column, but the magnitudes of the velocities decreased with depth. The strongest flows (0.8 to 1$m\ s^{-1}$) were observed in the northeast where the maximum dynamic heights also occurred, and the flow strength diminished in magnitude to the southwest. The along-channel velocities in the outer to mid fjord (Fig. 35a,b) were eastward and together with the cross-channel components the resultant flows in this region were to the northeast at speeds ranging from 0.45 to 0.9$m\ s^{-1}$. The highest resultant velocities, however, occurred in the eastern region where the flows were northward at 0.8 to 1$m\ s^{-1}$.

For CTD set H, the cross-channel geostrophic velocities for the two northernmost transects (Fig. 34e,f) were reduced by nearly an order of magnitude in comparison to data set A. The components along the southern transects were higher by comparison (Fig. 34g,h), but were still only about a third of the value of the cross-channel flows for data set A. The along-channel components (Fig. 35d-f) were also reduced in general, but the one exception occurred for transect 9 (Fig. 35f), where maximum easterly and westerly flows of -1.0 and 1.6$m\ s^{-1}$ occurred respectively to the north and south of the anticyclonic eddy at PV16 (Fig. 29d).

The marked reduction in geostrophic velocities in September actually began with CTD set B, which was collected late on the night of the 21st. The winds at this time (Fig. 13e) began to increase in speed and shift to the northeast, and this change in direction may have allowed freshwater to disperse over the outer fjord. This would have reduced the amplitude of the geopotential gradients relative to set A, when the maximum estuarine conditions were confineded to the inner fjord (Fig. 14). During CTD set E, however, the winds were initially weak and variable on the morning of the 24th, but they began to blow consistently from the west over a period of 7 to 8*hrs* (Fig. 13e). The westerly winds may have forced freshwater to the north leading to the marked cross-channel gradient in dynamic heights (Fig. 29c).

4.13.3 March 2017

As expected, the magnitudes and ranges of dynamic heights in March (Fig. 36) were very low in comparison to previous months, and this was due to marked increases in density in the upper water column caused by surface cooling and salinification over the winter. The physical properties also became relative homogeneous from vertical mixing by both winds (Fig. 21a,e) and thermohaline convection. Because of the strong leeway of the survey vessel due to wind-drift, casts in March did not always reach 100*m*. This occurred despite the use of a cannonball attached to the CTD frame, providing an additional weight of ~11.4 to 13.6*kg* (25 to 30*lb*). As such, the depths of the lower pressure levels were adjusted for the shallowest cast within a given data set. The effects of the latter can be seen in the differences in magnitudes, which ranged from ~ 205 to 253 for sets D and C respectively. However, the relative variation in dynamic height within each data set was not affected by the depth adjustments, and as a check on this, the dynamic topography was calculated at 0/80*db* for sets A/B and C. The results showed that the same patterns occurred, albeit with reduced magnitudes, but with nearly the same values as D (Fig. 36c).

The patterns in dynamic heights were consistent among the three data sets, with the highest magnitudes always observed in the northeastern region of the fjord and the lowest values observed in the western and southwestern regions of the outer basin (Fig. 36). The flows associated with the density (mass) field would be expected to be very low, and this was indeed the case, as shown by the small geostrophic

velocities for both the along-channel and cross-channel transects (Figs. 37 and 38). The maximum velocities of the flows ((0.05-0.125$m\ s^{-1}$) were orders of magnitude lower in comparison to both June and September (0.8-1.5$m\ s^{-1}$), but the flow directions were predominately to the north to northwest, just as implied by the dynamic topography (Fig. 36).

The highest geostrophic velocities occurred for set A/B, which showed an east-west gradient of 4*dyn cm*. The maximum cross-channel flows (0.065$m\ s^{-1}$) were observed in the northwestern region of the outer basin (Fig. 37a) and the strongest along-channel flows (0.125$m\ s^{-1}$) occurred in the northeastern portion of the inner basin (Fig. 38a). These are also the two areas in which the largest horizontal gradients in Φ occurred, and the resultant flows were northwest at 0.07$m\ s^{-1}$ and at 0.13$cm\ s^{-1}$ respectively. The other data sets showed similar flow patterns, but the gradients in Φ ranged from only 1 to < 2*dyn cm* for sets C and D respectively. Thus the maximum geostrophic velocities (0.005 to 0.03$m\ s^{-1}$) were smaller by comparison. However, the resultant flows were still northwestward at ~0.02 to 0.05$m\ s^{-1}$.

4.14 Drifter Speeds and Dispersion Rates

4.14.1 June 2016

Fig. 39 shows the speeds and dispersion characteristics for ispheres, microstars and svp 10*m* drifters released during the first experiment on June 27th. The three groups of drifters moved initially in separate directions following a clockwise pattern over depth (Fig. 11a-c), and the speeds of the surface and 1*m* drifters exhibited marked accelerations after 4 to 5*hrs* (Fig. 39a,b) probably in response to the westerly winds. The initial rotation of the surface currents and flows at 1*m* were >>180° relative to each other suggesting that additional forcing, such as geostrophic (i.e. estuarine) flow, played a role in moving the drifters. However, after 4*hrs* the ispheres moved at ~ 10° relative to the wind and accelerated to speeds of ~ 50$cm\ s^{-1}$. The microstars accelerated to 50$cm\ s^{-1}$ and moved at ~ 45° leeway to the wind, which clearly indicates winds were the dominant forcing. After about 8hrs, however, the two sets of drifters exhibited marked decelerations (Fig. 39a,b) followed by both extreme changes in direction (Fig. 11a,b) and increased speeds (Fig. 39a,b). Moving westward at this time along the southern shore, the microstars accelerated beyond the speeds of the ispheres and reached a maximum speed of ~32 $cm\ s^{-1}$.

The average distance to the center of mass (DCM) (Fig. 39e) indicated that dispersion was continuous over time for the microstars, which reached a maximum DCM of 1.3*km*, but the ispheres remained very close together until after about 10*hrs*, after which they exhibited minor dispersion (~0.25*km*). The microstars began their maximum dispersal at that time as well. However, the positive and negative changes in area (Fig. 39 f,g) suggest that the linear flows at 1*m* along the southern shoreline (Fig. 11b) allowed the microstar DCMs to continue to increase but at the same time caused the ± area fluctuations. A similar pattern in speeds and dispersal occurred for the second set of microstars (group B), just without the rapid increases in DCMs later in the deployment and extreme dispersion rates shown for group A.

The svp10*m* drifters showed an entirely different dispersion pattern in comparison to the surface and 1*m* drifters. While moving in broadening cylonic orbits (Fig. 11c) they exhibited regular periods of acceleration followed by deceleration with an average speed of ~ 10$cm\ s^{-1}$. The DCMs remained very close together up until about 20*hrs*, after which they began to move apart (Fig. 39e). The areas did not begin to expand until about five hours later, however, and they also exhibited periods of ± dispersal (Fig. 39f,g), indicating that changes occurred in their positions from linear to lateral conformations. This was followed by a rapid increase in dispersion in the outer fjord (~38$m^2\ s^{-1}$) to a maximum area of ~0.25km^2.

During the second dispersion experiment (Fig. 11d-f), the ispheres again exhibited the highest average speed (> 40$cm\ s^{-1}$) but the northern isphere (#9460) exhibited consistently higher velocities in comparison

to its southern counterpart (Fig. 40a). The reciprocal change in magnitudes at the end of the plot simply reflects the earlier grounding of the northern drifter (Fig. 11d). After adjusting for the initial distance between the two ispheres, the DCMs (Fig. 39e) showed rapid spreading followed by a decreased distance as the southern drifter closed the gap between them.

The two groups of microstars (A and B) also exhibited periods of acceleration to speeds of 20 to > 35*cm* s^{-1} (Fig. 40b,c), followed by decelerations as they moved eastward into the fjord (Fig. 11e). The speeds of group A were consistently much higher than group B, however, and after ~4*hrs* dispersion of the northern group (A) significantly outpaced the southern drifters, reaching a maximum area of 0.1km^2 (Fig. 40e-f).

The two groups of svp10*m* drifters also exhibited periods of rapid initial acceleration to speeds of ~17 to 18*cm* s^{-1}**,** but showed minimal dispersion up until about 26*hrs* (Fig. 40e-g). After this, the southern group (B) crossed the track of group A (Fig. 11f) and began to disperse at a rate of ~2.5m^2 s^{-1}, and by 30*hrs* the area of the drifters had increased by 0.02km^2 (Fig. 40f,g). The DCMs for group B were also significantly higher in comparison to group A, but the dispersion rates based on the changes in area remained relatively stable between the two groups until near the end of the track at 44*hrs*. At this time, the dispersion of group B began to significantly increase by 5 to 6 m^2 s^{-1} in relation to group A (Fig. 40g).

The final dispersion experiment on June 29th included three separate deployments of microstars (Fig. 11g,h). Some of these deployments had the highest speeds and dispersion rates of all three experiments (Figs. 39 to 41). For example, the initial speeds of the three groups ranged from 50 to ~70*cm* s^{-1}, and group A maintained an average speed of ~50*cm* s^{-1} over a 7*hr* period as the drfiters moved westward along the northern shoreline (Fig. 11g). The latter group also exhibited ± dispersal rates over the first 10*hrs*, followed by a marked increase of ~50m^2 s^{-1} along the western side of the fjord (Fig. 11g).

Group B (deployment 12b in Fig. 11h) initially showed relatively limited changes in DCM and almost zero dispersion rates (Fig. 41d-f). At 5*hr* the DCM increased significantly to over 500*m* but by 7*hr* the drifters had come back together, and no changes in area occurred thus the dispersion rates remained nearly constant and close to zero (Fig. 41e,f). The latter conditions suggested that the drifters alternated between dispersing into a long line and back to triangular configurations, but at about 18*hr* they began to disperse markedly (Fig. 41e,f). At this time the DCM values steadily increased, but despite this, both the changes in area and dispersal rates oscillated widely between ± values (Fig. 41e,f). After 30*hr*, however, the dispersal increased steadily to maximum area exceeding 3km^2.

4.14.2 September 2016

In September, almost all the deployments were done in pairs and dispersion was measured solely by distance from the center of mass (DCM). Examples of drifter speeds and dispersion for various deployments are shown in Figs. 42 to 49.

As in June, the patterns of acceleration in the surface and 1*m* drifters in September were due to marked changes in wind speeds, but early in the survey the continuous northeast winds (Fig. 13) caused drifters to maintain high speeds throughout most of the deployments. This occurred for ispheres and microstars during deployments #1 and #2 (Fig. 42), when drifters moved westward at speeds ranging from 30 to 58*cm* s^{-1}. In contrast, the SVP10*m* drifters showed more variable drift patterns in response to the same winds. Group A, for example, moved relatively slowly but exhibited cyclical bursts of speed as they moved eastward into the inner basin. However, large variations in speed also occurred for this group when s005 dispersed westward in advance of s006 (Fig. 20a). In contrast, group B exhibited three major periods of acceleration with average peak speeds of ~30, 43 and 28*cm* s^{-1} respectively The first two periods occurred at 18*hrs* and 29*hrs* respectively and were associated with large cyclonic orbits as the drifters moved eastward (Fig. 20a). However, once the group reached the southeastern side of the fjord

they exhibited nearly identical flow reversals, and moved westward at low speeds (7 to 15*cm* s^{-1}) until near the end of the deployment when s002 accelerated to ~20*cm* s^{-1} (Fig. 42f).

The dispersion of the ispheres and microstars in group A followed a similar pattern, and DCM values initially increased along with drifter speeds (Fig. 42g). At ~10*hrs*, however, the dispersion steadily decreased indicating that the drifters within each group converged despite the faster velocities (Fig. 42a,c). The ispheres in group B showed patterns in speeds and dispersal similar to group A (Fig. 42b,h), but the maximum speeds were nearly 20*cm* s^{-1} lower by comparison. The microstars in group B accelerated to steady speeds of ~30*cm* s^{-1} for about 6*hrs*, followed by a moderate deceleration to 18*cm* s^{-1} but then ended with a burst of speed reaching 45*cm* s^{-1} (Fig. 42d). The initial dispersion remained slow, albeit steady, but the distance between the two drifters never exceeded 0.5*km*. The dispersion of the SVP drifters in group A was also slow and steady, and after 35*hrs* the DCM reached only ~0.75*km* (Fig. 42g). At 40*hrs*, however, s005 accelerated to 35*cm* s^{-1}, causing an increase in average speed of ~10*cm* s^{-1} (Fig. 42f). The other drifter (s006) remained in the inner basin where it moved very slowly until ~43*hrs*. By this time, however, the rapid westward dispersion of s005 caused the DCM to increase to over 5*km*.

Drifter speeds and dispersion for deployments #3 and #4 (Fig. 43) showed the ispheres in group B to continually accelerate, particularly after they entered Valdez Arm and subsequently escaped into PWS proper (Fig. 18b). Driven by the strong northeast winds and accelerating through the 'Narrows', these two ispheres reached a maximum average speed of ~118*cm* s^{-1} (> 2*kts*). The dispersion remained minimal, however, and at 11*hrs* they had reached a maximum DCM of only ~0.4*km*. Afterwards they converged and came to within 50*m* of each other as they accelerated through the 'Narrows' (Figs. 43d and 18b). The microstars in groups A and B, by contrast, accelerated to maximum average speeds of 55 to 60*cm* s^{-1} (Fig. 43b,c) as they steadily moved westward under the combined influence of wind and (possibly) estuarine outflow. However, once the drifters reached the outer fjord they began to disperse rapidly, particularly group A, which moved both north and south, reaching a maximum DCM of ~1.5*km* (Fig. 43d). Group B, by contrast, moved entirely southwestward and became grounded along the shore (Fig. 19b), where the two drifters reached a maximum DCM of ~0.75*km* (Fig. 43d).

During the majority of the subsequent deployments from the 23rd to the 28th, the winds were much lighter and variable but the predominant direction was from the west (Fig. 13). At this time the ispheres exhibited highly varied tracks (Fig. 18c-f), partly due to the fact they were driven directly by the winds. The speeds and dispersion of the drifters varied substantially over this period, however. For example, on the 24th (Fig. 44) the average speed and dispersion remained mostly under 30*cm* s^{-1} and 300*m* respectively. The following day as the two sets of drifters moved rapidly westward (Fig. 18d), however, the average speeds increased to > 80*cm* s^{-1} and the dispersion for the two groups ranged from 100*m* to 500*m* (Fig. 45). The extreme value of 4.8*km* for group A was due to grounding in the Narrows.

The general drift direction for the microstars during the above periods was westward (Fig. 19c-e). For example, during deployments #5 to #7 the drifters released on the 23rd (group A) moved steadily westward at an average speed of 38*cm* s^{-1} (Fig. 44a) but exhibited only minor dispersion that ended with a DCM of < 250*m* (Fig. 44g). On the following day, groups B and C (deployments #6 and #7) also moved initially westward. However, midway in the drift group B reversed direction and maintained speeds of ~10*cm* s^{-1}. Group C, by contrast, continually moved outward along the northern shoreline (Fig. 19d) and accelerated to a maximum speed of 30*cm* s^{-1} (Fig. 44b). The dispersion of both groups was negligible, however (Fig. 44g,h). On the 25th (Fig. 45) the two groups again moved steadily westward (Fig. 19e), but whereas group A accelerated to the southwest over 15*hrs* to a maximum average speed of ~28*cm* s^{-1}, group B started to the northwest at speeds of 15 to 17*cm* s^{-1} but then stalled along the northern shore and the end velocities were low at ≤ 5*cm* s^{-1} (Fig. 45d). The patterns in the dispersion rates for the two groups were very similar and both reached a maximum DCM of < 0.7*km* (Fig. 45g,h).

The two groups of SVPs launched and 24th and 25th exhibited much different speeds and dispersion rates (Figs. 44 and 45). Group B, for example, exhibited a wide variation in speeds between s004 (< 10 to 40*cm* s^{-1}) and s008 (≤ 10*cm* s^{-1}), and although the drifters initially remained close together, starting at 10*hrs* they began to rapidly disperse and reached a maximum DCM of ~1.4*km* (Fig. 44g). In contrast, group C moved at average speeds of ≤ 10 *cm* s^{-1} and attained a maximum DCM of only ~25*m*. On the 25th, however, a much different pattern emerged and the SVPs exhibited oscillations in speed very similar to dispersion experiment #2 on June 29th (Fig. 40d). The main difference was that the periods of highest speeds (12 -15*cm* s^{-1}) occurred at the end of the deployments in September instead of at the beginning as in June. The dispersion for the two groups in the fall was similar, and the northern group (A) reached a peak DCM of ~0.7km prior to redeploying s008 close to its counterpart (Fig. 20d) and group B, deployed farther to the west, showed slightly less dispersion, with a maximum DCM of ~0.4*km* (Fig. 45h).

During the next six deployments (Figs. 46 to 48), both the speeds and dispersion rates among drifters again varied significantly. The drifter types alternated in terms of maximum dispersion, but the microstars tended to have relatively high rates as they continued to move generally westward from nearly all points of deployment (Fig. 19f-g). The one exception occurred for deployment #14, when m003 and m007 remained very close together (Fig. 48d). The ispheres exhibited a very large dispersal only on deployment #10b, when they attained a maximum DCM > 3.2*km*. The speeds of the latter also exhibited large oscillations, as did the other drifter types (Figs. 46 to 48), but lacking the direct forcing of strong winds, the ispheres only occasionally outpaced the speeds of the microstars, and only when there were short bursts of winds from the west (Fig. 13). Deployment #16 differed somewhat, however, and the two ispheres accelerated continually over ~15*hrs* with minimal oscillations in speed (Fig. 49a). They also showed a very consistent dispersal and quickly reached a maximum DCM of ~0.5*km* (Fig. 49e).

The SVPs during deployments #11, #12 and #16 also exhibited numerous oscillations in speeds, but the maxima rarely exceeded 12*cm* s^{-1} (Figs. 47 and 48). On the latter deployment (#16), these drifters exhibited a much larger dispersal reaching DCM values of 0.85 to 0.93*km* (Fig. 48d). In contrast, the ispheres and microstars showed DCM values of only 50*m* to 100*m* respectively.

Near the end of the survey, the winds shifted to the northeast and accelerated to speeds of 4 to 5*m* s^{-1}, with gusts reaching ~12*m* s^{-1} (24*kts*). At this time the two groups of microstars exhibited much different drift patterns (Fig. 19i). They both initially moved eastward at the end of a flood tide along with a westerly wind, but once the wind shifted to the east out of the Lowe River Valley, all the drifters were forced northward. The western group (B) was advected at over 20*cm* s^{-1} towards the City Dock, where they grounded with negligible dispersion (Fig. 49e). In contrast, group C, deployed within the inner basin, was closer to the wind plume and the drfiters accelerated rapidly to speeds > 30*cm* s^{-1}. However, when the wind speeds slackened slightly the drifters showed oscillations in speeds between ~10 to 25*cm* s^{-1}. Afterwards, they accelerated again to widely varying speeds ranging from 12 to 45*cm* s^{-1} (Fig. 49c). The two drifters also exhibited moderate dispersion at the end, reaching a maximum DCM of 370*m*. The SVPs during deployment #18, by contrast, showed minimal response to the increased wind speeds. The drifters rarely exceeded 10*cm* s^{-1} and exhibited very limited dispersion (Fig. 49e).

4.14.3 March 2017

The speeds and dispersion of drifters in March are shown in Figs. 50 to 55. During the first five days of the survey the winds were very strong and alternated in direction from the southeast to the northeast (Fig. 21e). Due to the harsh conditions, drifters were not deployed until the 24th.

At the time of deployments #1 and #2, the immediate effects of the southeasterly winds could be seen in the trajectories of the ispheres, which were forced rapidly northwestward at maximum speeds ranging from 40 to 45*cm* s^{-1} (Fig. 50a,d). The first group (A) quickly grounded (i.e. where speeds = 0), and taking

into account the initial separation during the deployment they exhibited a flat dispersion, with a peak DCM (~0.2*km*) that mostly represents the initial distances apart (Fig. 24a). This resulted in negligible changes in area between the drifters, and thus the dispersion rates were also nearly flat (Fig. 50f,g). Group B also accelerated rapidly to an average speed of 40$cm\ s^{-1}$, with very little dispersion (Fig. 50e-g).

The microstars and SVPs launched on the 24th accelerated to maximum average speeds of 25 and 12$cm\ s^{-1}$ respectively, but there was marked variation in the individual drifter speeds, particularly for the SVPs (Fig. 50b,c). The two groups showed limited dispersion, however, but exhibited both positive and negative rates indicating that the drifters diverged and converged respectively, but after about 15*hrs* the SVPs began to gradually move apart (Figs. 28a and 50e-g). In contrast, the microstars converged during the last portion of their deployment, with dispersion rates falling to nearly zero (Figs. 27a and 50e-g). It should be noted here that the dispersion for the microstars was calculated for the interpolated GPS points shown in Fig. 27a.

During the third deployment on the 25th (Fig. 51) the pair of ispheres again accelerated rapidly to average speeds of 30 to 40$cm\ s^{-1}$. The very short drift period also showed negligible dispersion among the buoys (Fig. 51d), which headed exactly to the same region on the northern side between Mineral and Gold Creeks (Fig. 26b). The three microstars, by contrast, exhibited relatively low velocities with very little initial dispersion. The velocities reached an initial maximum of 8 to 18$cm\ s^{-1}$ at the beginning of the deployment before the winds began the prolonged shift to the northeast, but with diminished speeds (Fig. 21e). A second period of higher speeds (> 15$cm\ s^{-1}$) occurred for m006 after about 25*hrs*, however, when this drifter dispersed into the outer basin (Fig. 27b). The relative motion of the latter is what led to the high dispersion shown in Fig. 51d,e, but the rates exhibited a large variance over time (Fig. 51f).

The SVPs in deployment #3 also exhibited very low speeds ranging from < 5 to ~10$cm\ s^{-1}$ over the first 50*hrs* of the deployment, but afterwards they began to accelerate to sustained speeds of 10 to 12$cm\ s^{-1}$. After about 85*hrs*, however, they began to disperse even though the speeds fell to values < 5$cm\ s^{-1}$ (Fig. 51c-f). The winds also ceased during this time and the dispersal was primarily due to buoy s002 moving southwards, whereas the other two became grounded along the outer northern shoreline (Fig. 28b).

On the 26th the northeast winds forced the ispheres directly to the southwest shore (Fig. 26c), but at nearly half the speeds (Fig. 52a) of the first two deployments. The dispersion rates were also essentially zero (Figs. 52f). The microstars and SVP tracks (not shown) exhibited very little motion, as indicated by their minimal speeds of ≤ 8$cm\ s^{-1}$ and ≤ 5$cm\ s^{-1}$ respectively (Fig. 52b,c). Interestingly, despite the low speeds they still showed limited dispersion, and the maximum DCM and area values were 630*m* and 530*m*, and 0.12 and 0.02km^2 respectively (Fig. 52d-e). At the end of the deployment, however, their speeds increased significantly (Fig. 52b,c) and they converged, as indicated by the negative dispersion rates (Fig. 52f).

Due to both northeast winds and an ebbing tide, the ispheres during deployment #5 (Fig. 53) initially moved westward again, but at mid-drift they abruptly turned southward (Fig. 26c). At the time of the turning (6 to 7*hrs*) there was a lull in the winds and the drifter speeds diminished slightly (Fig. 53a). At about 9*hrs*, however, the winds resumed and the ispheres moved WSW directly into Anderson Bay (Fig. 26c). During the entire drift period there was minimal dispersion among the ispheres, except during the lull in the wind speeds. Afterwards, the drifters showed limited convergence (Fig. 53d-f). The microstars and SVPs, by contrast, exhibited a much different response to the northeast winds (Figs. 27d and 28c), and during the initial portions of the deployments the average speeds were relatively low (Fig. 53b,c) and showed small oscillations of 5 to 7$cm\ s^{-1}$. At about 35*hrs*, however, the speeds of both groups increased to 18 and 13$cm\ s^{-1}$ respectively.

The microstars initially moved to the WNW (i.e. to the right of the wind as expected), but as the winds slackened the drifters began making large cyclonic orbits, unlike anything observed in the prior months.

The SVPs also moved to the right of the wind to the NW as expected (only if a classic Ekman spiral had occurred due to the sustained northeast winds). The microstars continued to oscillate in speed during the cyclonic orbits, but the average speed of the SVPs dropped to near zero as they dispersed along the northern shoreline (Fig. 28c). The dispersion patterns of the SVPs and microstars also exhibited oscillations in DCM values until at about 55*hrs* and 68*hrs* respectively. At these times, the dispersion of both drifter groups increased dramatically (Fig. 53d-f), but the DCM and area values of the microstars are nearly 10 and 200 times larger in comparison to the SVPs (1500 vs. 650*m* and 2.4 vs. 0.14km^2). The dispersion rates for the microstars also exhibited periods of divergence and convergence during the cyclonic orbits followed by marked dispersion during anticylonic turning to the south (Fig. 27d).

The speeds and dispersion rates for ispheres during deployments #6 and #7 are shown in Figs. 54 and 55. The final two tracks of these drifters (Fig. 26d) differed significantly as the northeast winds began to diminish, followed by a period of quiescence (Fig. 21e). For example, the tracks on March 27th showed a pattern very similar to deployments #4 and #5, with average speeds of ~30$cm\ s^{-1}$ to the southwest, and with almost no dispersion (Fig. 54d-f). Once these drifters grounded on the southern shoreline, however, the velocities fell to zero for ~ 3*hrs*. Two of the drifters refloated then began to disperse westward along the shore and eventually moved into Anderson Bay (Fig. 26d). It is uncertain what the third drifter (i6350) did at this time, since it quit transmitting and was lost. In contrast, the ispheres in deployment #7 initially exhibited an eastward track at average speeds of 12 to 20$cm\ s^{-1}$that decreased rapidly to an average of ~5$cm\ s^{-1}$ (Fig. 55a). The speeds significantly increased again to values ranging from ~20 to 55$cm\ s^{-1}$ during two large anticyclonic orbits followed by movement to the southeast (Fig. 26d). The dispersion during the drift was minimal, however, with a maximum DCM of less than 100*m* (Fig. 55d).

The microstars in deployment #6 represent a continuation of deployment #3 for drifters m004 and m005 and a redeployment of m006 (Fig. 27c). The speeds initially exhibited oscillations between 0 to 10 and 20 $cm\ s^{-1}$ then assumed an average of ~7$cm\ s^{-1}$ (Fig. 54b). The dispersion starts out relatively high, with a DCM of 1.05*km* and an area ~ 0.9km^2; this was due to the initially large distance between the drifters when m006 was redeployed. However the drifters all gradually converge over time until about 20*hrs*, after which they exhibited aperiodic oscillations between divergence and convergence (Fig. 54d-f).

The pair of 40*m* SVPs released on the 27th exhibited a cyclonic track over a three-day period, and gradually turned northwest, west and finally to the south (Fig. 28f). The range in average speeds (Fig. 54c) was relatively low (0 to ~10$cm\ s^{-1}$), and the total average speed was only about 5 $cm\ s^{-1}$. The dispersion between the two drifters was also minimal, with a maximum DCM of only ~100*m*.

The last deployment of 10*m* SVPs exhibited wide cyclonic turns or nearly closed orbits (Fig. 28d). The speeds of both drifter groups were relatively low, and the total averages ranged from ~5 to 8 $cm\ s^{-1}$ (Fig. 55b,c), but group B was the faster of the two since it followed the outer circumference of the eddy. The dispersion of group A was minimal and the maximum DCM reached ~200*m*, but the changes in area were nearly flat so that the rate of dispersion was close to zero (Fig. 55d-f). In contrast, group B exhibited marked dispersion with a maximum DCM of ~ 650*m* (Fig. 55d). However, cyclical changes in dispersion area and rates (Fig. 55e,f) indicated that aperiodic oscillations occurred in divergence and convergence.

4.15 Principal Axes of Variance and Times of Retention or Flushing

The net directions of water motion were determined from calculations of principal axes of variation of drifter velocities. The method applies two empirical orthongonal functions (EOFs) to the velocity components with the means removed (*U'* and *V'*) to obtain major and minor axes (i.e. directions) along which the maximum and minimum variance in velocities occurs (Emery and Thomson, 2004). The major axes are given by rotation angles relative to the east-west (*u*) direction, with positive rotations being

counterclockwise and negative rotations clockwise. The minor axes are oriented orthogonally to the latter, and the axes lengths are proportional to the respective variances. Estimates of flushing or retention times were also derived based on the average speeds and along-channel components of the flow (*u* velocities) used to respectively calculate the total drift distances and times required for material to either reach the mouth or remain within the fjord. Retention due to grounding was also determined either directly from observations or inferred by the general directions of drifters as they approached the shoreline.

Tables 2 to 4 list the major and minor axes of the velocity variance along with the rotation angles of the major axes. The arithmetic average speeds represent the entire drift distances (up to the initial times of grounding), whereas the *u* velocities are averages of the along-channel components of flow. Negative (westerly) velocities represent flushing whereas positive (easterly) velocities represent retention. The ranges represent combinations shown by the phases (*p*). For example, on June 22nd, i0460a drifted a total of 14*hr* before grounding near the Lowe River (Fig. 10a), but had it continued on course it would have reached the eastern shoreline in 9*hr* based on the average *u* velocity (0.125$m\ s^{-1}$). Also, in cases where either the flushing or retention rates exceeded 500*hr*, the drifters were considered retained indefinitely. This is shown as *inf* in the Tables.

4.15.1 June 2016

In June, the major principal axes for the ispheres and microstars were generally oriented to the WNW to ESE, as indicated by their respective average rotation angles of -7.0^{o} and -10.7^{o} (Table 2b). The individual axes (Table 2a) exhibited a general (-) rotation to the NW in the inner half of the fjord and a (+) rotation to the SW in the outer half (Figs. 56 and 57). The large angle standard deviations (Table 2b) were mainly due to positive (negative) rotations for i5480b (m001b). Both drifters exited Port Valdez on the 22nd and 26th respectively (Fig. 10b,f), and a marked amount of variance in *V'* for m001b is shown by the rotation of the major axis to the south at an angle of -59^{o} (Fig. 56B). The ispheres and microstars also had relatively large major and minor axes (Figs. 56 and 57), and their respective average variances (Table 2a) were respectively 10 to 17 times and 4 to 8 times the variances of the SVPs (Table 2b). The average rotations for the 10*m* and 40*m* principal axes were slightly positive (3.6^{o}) and negative (-7 ^{o}) respectively, and the drifter motions were generally slow and exhibited relatively small velocity variances (Table 2a,b). This was also shown for the 10*m* SVPs by their very small major and minor axes (Fig. 56C and 57A,B).

The fastest flushing rates occurred for i5480 on June 22nd (Fig. 56A), which had two phases to its drift (Fig. 10b). The first included a flushing past the mouth in 7*hr* followed by movement past the 'Narrows' into Valdez Arm over an additional 11*hr*. The second phase, however, included the time to return past the mouth (9*hr*) followed by another 25*hr* to ground off Mineral Creek (Table 2a). The fastest flushing for the microstars occurred in deployment 12a (Fig. 57C) when they exited the fjord in about half a day (Table 2a). The microstars in deployment #6 (Fig. 57A) also exhibited flushing and traveled an average distance of 10.6*km* over 17*hr* but based on the average along-channel (*u*) velocity (Table 2a) they would need another 5*hrs* on average to reach the mouth. The range, however, shows that the lead drifter was already at the mouth when the slowest drifter was still 13.6*hr* to the east (Table 2a). This means that material transported by all the 1*m* flows in deployment #6 would take 17 to 31*hr* to completely flush from the fjord.

The most rapid eastward (inward) motions were shown by the ispheres in deployment #10/11 (Fig. 57B) and microstars in deployment # 13 (Fig. 57C and Table 2a). All other times for the individual ispheres indicate they were retained within the fjord (i.e. shown by times to reach the inner basin and eastern shore or the times of grounding respectively). The individual microstars exhibited both flushing and retention, but three major anomalies occurred respectively for deployments #3 (m007b), #5 (m003) and #12b (m008), in which highly erratic reversals in direction resulted in very slow individual average *u* velocities of -0.005, -0.0003 and 0.0003$m\ s^{-1}$. This created extremely long flushing and residence times > 21 days.

Thus the times in Table 2a for these drifters were considered to be indefinite. However, it should be noted that the flushing/retention times were calculated assuming that conditions remained stable, which is entirely unrealistic. Were the drifters to remain in the fjord past the recovery dates, they would very likely be subjected to conditions that would have likely caused them to ground somewhere inside the fjord.

As aforementioned, the only case of flushing for the ispheres was the 7*hr* period when i5480 exited past the mouth, but due to frequent grounding the average isphere retention time was only 35*hr* +/- 24*hr* (Table 2b). The microstars had an average flushing time of 33*hr* +/- 32*hr*, which was significantly faster than the SVPs, but the average retention (69*hr* +/- 99*hr*) was nearly double in value in comparison to the ispheres. The 10*m* SVPs were nearly evenly split between flushing (45%) and retention (55%), but the average retention time and SD value (171*hr* +/- 111*hr*) were relatively high in comparison to the average flushing time (70*hr* +/- 36*hr*). Also, the single case of retention for the 40*m* SVP was very high at 260*hr*.

4.15.2 September

In September the conditions generally favored flushing (Table 3a) and the principal axes of the drifter velocities (Fig. 58) were more closely aligned on average with the along-channel (*u*) direction, as shown by the mean rotation angles for the respective surface to 40*m* depths of 0.2^o, -3.7^o, -1.1^o and -0.8^o (Table 3b). However, with exception of the 10*m* and 40*m* SVPs the angles had much higher standard deviations (SD) in comparison to June (Table 2b), and this indicated that the surface and 1*m* flows had relatively large variations in cross-channel (*v*) flows. For the ispheres this was also shown by a very high ratio of the SD to the mean of 141:1, and the small rotation angle (0.2^o) was due to a nearly equal distribution of large, positive versus negative angles, in which the major axes were oriented respectively either to the NW to SE or the NE to SW (Fig. 58). In general, the average variances for the major and minor axes were much smaller in comparison to June (Tables 3b and 2b), and this was due to cases in which the flows exhibited more consistent speeds with most of the variance being aligned along the major (rotated) axis (Fig. 58). The cross-channel flows were still important and resulted in some very large rotation angles (Table 3a), particularly for the ispheres in deployments #8 and #10b (Figs. 58C,D) and for the microstars in deployment #1 and #17 (Figs. 56A,G). The average retention times in September were shorter than in June, and the flushing rate at 10*m* was twice as long (Table 3b). Also, 60% of the isphere deployments had strong cross-channel velocities that caused groundings before the drifters could exit the fjord. In contrast, only 29% of the microstar deployments resulted in groundings and none of the 10*m* SVPs did so.

One noteworthy case occurred for deployment #8 in which isphere group A had a large negative *u* velocity ($-0.31 m\ s^{-1}$) that inferred flushing, but the rotation of the major axis was extreme (82^o) meaning that the cross-channel range of *V'* was higher than the along-channel range of *U'* (Fig. 58C). The ispheres in deployment #9 had similar results, but the rotation of the major axis was only 40% of the former (Table 3a). The analysis for both deployments was limited to flows just passing the mouth to avoid including southward velocities through the 'Narrows'. So these were unusual results for flushing, which typically showed the major axes in the same general direction as the flows (e.g. in this case the -*u* direction).

The velocity variances were significantly larger in comparison to June and the average variances for the major and minor axes were again highest for the ispheres and lowest for the SVPs (Table 3b). In contrast to June, however, the along-channel (*u*) velocities were predominately negative and 2 to 12 times larger in value, indicating that flushing was faster and more frequent. The exception was for the 10*m* and 40*m* SVPs, which exhibited relatively small total average *u* velocities (-0.007 and $-0.015 m\ s^{-1}$). For the 10*m* drifters this was due to the fact that the along-channel velocities (Table 3a) showed only 20% more negative values (i.e. flushing) as opposed to positive values (i.e. retention), thus reducing the average. It should be noted, however, that 30% of the classifications for the 10*m* SVPs were questionable since either the trajectories at the end of the drift were inconsistent with the sign of the *u* velocities or that the flushing or retention times were excessive due to negligible velocity magnitudes (Table 3a).

The average retention times in September for the surface and 1*m* buoys were nearly two and 1.25 times higher in comparison to the respective average flushing times (Table 3b), but in comparison to June (Table 2b) the retention times were respectively longer by 18*hr* and shorter by 37*hr* on average. Due to the relatively long deployment periods for the SVPs, their average retention times were also high, just as in June (6 vs. 7 days), whereas two of the 40*m* SVPs grounded in about 6 days, thus reducing the average retention time in September by nearly half in comparison to June. There were also three cases in which retentions exceeded 500*hr* and were therefore classified as indefinite (Table 3a). Although the ispheres again exhibited faster average speeds than the microstars (19.5 vs. 14.3$cm\ s^{-1}$), the two groups had similar average *u* velocities (-0.112 vs. -0.106$m\ s^{-1}$) and thus they also had nearly equal average flushing times (Table 3b). The percentage of the deployments in September showing flushing for the ispheres and microstars was also very similar at 71% and 78% respectively, as compared to 13% and 29% in June. In contrast, the 10*m* SVPs showed only a moderate increase in flushing in September at 60% of the cases in comparison to 45% in June. The 40*m* SVPs remained within the fjord during their entire deployments, but on the 20th they moved westward prior to either flushing or grounding and the total average time of flushing was lengthy at 231*hr* or 9.6 days (Table 3b).

4.15.3 March 2017

In March the major principal axes for the isphere and 10*m* SVP velocities (Fig. 59) had average alignments to within 3^{o} to 6.3^{o} of the along-channel (*U'*) direction (Table 4b). The SD values were both very high, however, (~41^{o}) due to some excessive positive and negative rotation angles for certain deployments (Table4a). In contrast, the microstars had a moderately negative average rotation due to the large negative angle for m006 (-89^{o}) in deployment #3 (Table 4a). Under influence of strong southeast winds (Fig. 21e) the rotation angles in deployments #1 to #3 were mainly negative and aligned towards the northwest (Fig. 59A) or west (Fig. 59B). Two exceptions occurred, however, where the flows for the ispheres in deployment #2 and microstars in deployment #3 exhibited extreme positive and negative angles respectively (70^{o} and -89^{o}). Like the group-A ispheres on September 25th, the former deployments represent unusual cases in which the major axes were not aligned with the general flow directions. Instead, they were aligned along the *V'* axis since variance of the latter was greater than that of the *U'* velocities (Figs. 59A,B). In the case of m006 this was due to a marked cross-channel exchange in the outer basin, but for the ispheres the orthogonal exchange to the NNE was negligible due to the very small velocity variance (Table 4a). In fact, the variances of the major and minor axes for all deployments were about an order of magnitude lower in general in comparison to September (Tables 3a and 4a).

During deployment #5 (Fig. 59C), all rotation angles were positive and indicated a general southwest trend to the motion. For the ispheres (Fig. 26c) this reflected the steady effects of the northeast winds, but over the course of 3.8 days the cyclonic orbits of the microstars in deployment #5 also exhibited minor southwest trends in their motions (Figs. 59C and 27c). A similar flow pattern occurred over a three-day period for microstars in the continuation of deployment #3 and for m006 released on the 27th (Figs. 27d and 59D). The variances were slightly greater for the latter in comparison to deployment #5, however, and the major axis is aligned almost due west (0.2^{o}). In contrast, the rotation angle of the ispheres in deployment #6 increased to 27^{o} showing that the surface flows were oriented to the southwest (Figs. 26c and 59D). The 40*m* SVPs in deployment #6 exhibited a much different trend by comparison over a three-day drift, and showed a large negative rotation (-67^{o}) to the SSE (Table 4a). Finally, during deployments #7 and #8 under a period of calm followed by very light west winds, the ispheres exhibited the largest major axis variance for the entire experiment (Table 4a) with a small rotation angle (-8^{o}) that indicated a general trend in flow to the southeast (Fig. 59E). The 10*m* SVPs in #8, by contrast, exhibited both positive and negative angles (Table 4a). Group B had much larger variances in comparison to group A and nearly equivalent major and minor axes (Fig 58E), but whereas group A was primarily aligned to the southeast, the axes of group B were aligned to the ENE and NNW respectively due to the cyclonic orbits.

The along-channel *u* velocities were relatively high in March (Table 4a) and thus produced rapid flushing times. For the ispheres these times ranged from 10 to 31*hr*, but in almost all cases grounding occurred within the fjord resulting in indefinite retention. A maximum retention time of 70*hr* also occurred at the end of the experiment when the only positive *u* velocity occurred indicating inward transport (Table 4a). In contrast, both the microstars and SVPs showed large ranges in flushing times (without grounding) of 28 to 325*hr* and 45 to 483*hr* respectively, but these cases only comprised 27% of the total deployments. Still, the average flushing and retention times were much higher in comparison to the ispheres (Table 4b). Also, there were three periods for the microstars and two periods for the SVPs in which either grounding occurred in conjunction with flushing or the results were inconclusive regarding whether flushing or retention actually occurred.

4.16 Average Speeds and Along-Channel (*u*) Velocities, and Time Series of Flushing vs. Retention

The monthly and within month averages of speeds and u velocities were computed from Tables 2 to 4 for all drifter types and the results are listed in Appendix D. Only 44% of the differences between months were statistically significant at the 5% level[7], and only one significant difference occurred at the 10% level for the means of the microstars between June and September. For example the average speeds of the ispheres in June differed from September by 5.5c*m* s^{-1} and from March by only 0.2 c*m* s^{-1}, but neither of these differences was significant due to the high standard deviations (SD). The differences in monthly mean speeds for the microstars, however, were all significant ($p < 0.05$ and 0.1), and differences in mean speeds for the 10*m* SVPs were significant for March versus both June and September (Appendix D). The differences in mean speeds among drifter types within months, by contrast, were all significantly different at either the 5% or 10% level; the one exception was for the microstars and SVPs in March (Appendix D).

The mean *u* velocities of the ispheres in September and March were all significantly different in comparison to June ($p < 0.05$), and the negative average velocities for the former two months generally indicated flushing conditions, whereas positive *u* velocities in June inferred retention. Differences in mean *u* velocities for the microstars between September and both June and March were all significant ($p < 0.05$), whereas the SVPs showed only one significant difference ($p < 0.05$) between September and March. In contrast, none of the mean *u* velocities in June differed significantly among drifter types, but the other two months exhibited significant differences at the 5% level for the SVPs and all other drifters in September, and at the 10% level between the ispheres and all other drifters in March (Appendix D).

4.16.1 June 2016

Figure 60a to c shows the depth profiles of average drifter speeds and along-channel (*u*) velocities, and the average velocity components from the ADCP data in June. The drifter profiles were separated into two segments (Fig. 60a) that show data collected during the oceanographic survey (segment #1) and the second half of the experiment (segment #2) respectively. Also, note that whereas all the points at 100*m* (Fig. 60a,b) were from the ADCP data (Fig. 60c), at 40*m* the points in the first segment were from the ADCP data and the points in the second segment were from the actual drifter data.

In all cases, the average speeds of the ispheres and microstars were significantly faster than the speeds of the SVPs ($p < 0.05$), and the profiles were very similar, showing roughly exponential decreases in magnitude over depth as expected. The average speeds at 1*m* and 10*m* were slightly higher in segment #2 but the only significant difference was for the SVPs ($p < 0.1$). A slight decrease in average surface speed

[7] Results of t-tests (Appendix D) for H_0: no difference between means (i.e. $\overline{Y_1} - \overline{Y_2} = 0$) at an $\alpha = 0.05$ and 0.1.

for segment #2 was also significant ($p < 0.5$), but this was an indirect result of the rapid, westward (flushing) motion of i5480 in segment #1 (Fig. 10b). Based on the along-channel flows, the retention at 1*m* was slightly greater in comparison to the surface during segment #1, but just the opposite occurred during segment #2 where the mean *u* velocities at the surface were significantly greater ($p < 0.05$) in comparison to 1*m* (19.4 vs. 2.8$cm\ s^{-1}$) and all other depths (Fig. 60a).

At 10*m* the average along-channel flows for the first segment were very low (0.25 $cm\ s^{-1}$) and the positive value agreed somewhat with the ADCP data (Fig. 60c). During the second segment the average flow reversed into minor flushing (-0.7 $cm\ s^{-1}$), but the change in velocity was not statistically significant. The complete profiles for June (Fig. 60b) showed very minor flushing at 10*m* and reflect the higher retention at the surface in segment two. In contrast, the average retention at 1.0*m* was consistent over the entire experiment (~2 to 3$cm\ s^{-1}$). The positive average *u* velocity at 40*m* indicated retention, which differed from the ADCP profile (Fig. 60c) but is possibly explained by the fact that the 40*m* SVP was launched late in the survey and it remained confined to the inner basin.

The barotropic tidal currents at the mouth are shown in Fig. 60d. These were calculated by dividing hourly changes in tidal volume (ΔV) by the widest area of the mouth (A) (Dyer, 1997):

$$U = \Delta V(m^3 hr^{-1})/A(m^2)/3600sec\ hr^{-1}.$$

Since the tides at Port Valdez are essentially a standing wave, the currents are synchronous and the maximum flows occur during the middle of each phase and the minimum flows occur at the top and bottom of the flood and ebb phases respectively. The flood currents are positive in value and the ebb currents are negative. The net (integrated) barotropic tidal exchange generated by the imbalance in the tidal prisms in Fig. 60d was calculated as 1.03$cm\ s^{-1}$, which would have slightly enhanced water retention within the fjord.

Combining the surface and 1*m* drifter profiles with the ADCP data showed that during the first half of the experiment the average along-channel flows had three baroclinic modes, alternating between inflow in the upper 20*m*, outflow between 20*m* and 30*m* and inflow over the deep water column. The fact that no evidence of entrainment of subsurface water into the dispersing surface estuarine layer was ever observed and that all the average flows were within the range of the barotropic tidal currents, indicated that the deeper baroclinic inflows and outflows were well balanced, and the water exchange in June therefore possibly occurred as a background flow of the same order of magnitude as the net tidal exchange.

The patterns of retention versus flushing (r/f) within the upper water column over time in June are shown in quasi time series in Fig. 61, and the statistics for these data are listed in Table 5. The r/f percentages were based on average *u* velocity directions and drift durations, and showed that retention was highest in general for the ispheres (93%) and progressively diminished for the microstars (81%) and the 10*m* SVPs (66%). Also, all the layers exhibited relatively high standard deviations (Table 5) that reflected a marked variability in trajectories (Figs. 10 and 11). Much of the retention within the surface and 1*m* layers was a direct result of diurnal, westerly winds. However, the single case of flushing for i5840 was also followed by retention (Fig. 61A). The magnitudes of the respective ± *u* velocities in the outer fjord for i5840 were nearly the same (±60$cm\ s^{-1}$), but since the i5840 became trapped in the Mineral Creek delta region during its inward trajectory the retention period was nearly double the flushing period (34*hr* vs. 18*hr*) (Fig. 61A).

General retention of the surface water was also suggested by the relatively large total average *u* velocity (5.1$cm\ s^{-1}$), but when the velocities were weighted by drift durations the total average flow decreased to a mere 0.25$cm\ s^{-1}$. The average total velocities weighted according to the respective total retention and flushing times were also markedly reduced and nearly balanced (2.1 vs. -1.4$cm\ s^{-1}$), as were ± velocities weighted according to the relative total drift time (Table 5). All these results infer that the exchange of

surface water in June within Port Valdez was negligible, and any contaminants in the surface water would remain within the fjord indefinitely until being flushed by increased estuarine flows and down-fjord winds, both of which occurred in September.

For the 1*m* layer the total average *u* velocity was 2.3$cm\ s^{-1}$, and based on drift durations flushing occurred 19% of the time (Fig. 61B). The weighted average for the first half of the experiment, however, was slightly negative at -0.4$cm\ s^{-1}$, and the total weighted average was even lower at -0.11$cm\ s^{-1}$. Both values were extremely small in comparison to the total average shown in Figs. 60b and 61B. Nevertheless, these values indicate that flushing would be indefinite, ranging from 52 to 189 days, and thus retention would occur by default.

The time series for the SVPs (Fig. 61C) showed a very small average outflow at 10*m* (-0.3$cm\ s^{-1}$), and the r/f percentages were 66% and 34% respectively. Since the long (79*hr*) flushing period for svp004 ended in grounding near the mouth (Fig. 10g), retention could also be considered for this deployment. This would change the r/f percentages for the SVPs to 87% and 13% respectively. At 40*m* the small, positive average *u* velocity indicated a minor net inflow of 0.9$cm\ s^{-1}$, with 100% retention of the deep, subsurface water within the inner basin.

4.16.2 September 2016

In September, the aforementioned conditions promoting flushing were indicated by the profiles of average drifter speeds and *u* velocities, both of which had similar vertical structures for segments #1 and #2 (Fig. 62a), and hence for the entire survey (Fig. 62b). The speeds in segment #1 were higher in comparison to segment #2 at all depths, and the differences were significant at the 10% level for the surface and the 5% level for the deeper layers (Appendix D). The high speeds in segment #1 also translated into larger, negative *u* velocities at the surface and 1*m* (Fig. 62a), but the only significant difference was for the microstars ($p < 0.05$). One interesting comparison to June, however, was that in September flushing at 1*m* in segment #1 was stronger in comparison to the surface (-16.5 vs. -13.4$cm\ s^{-1}$).

The combined drifter and ADCP data in September indicated that the average baroclinic currents possibly had four modes. However, with exception of the deepest water they were 180^{o} out of phase relative to the currents in June, which was similar to the strongest prevailing winds during the two experiments (Figs. 5e and 13). The average *v* velocities in the ADCP currents in the upper 80*m* also showed a general northerly cross-channel flow (albeit with high variability), which probably intensified closer to the surface. The latter was also inferred by the marked variation in cross-channel flows shown by the principal axis angles for both ispheres and microstars (Fig. 58).

The net tidal exchange was calculated at 1.32$cm\ s^{-1}$, which indicated that tides slightly favored retention, as in June. The amount was negligible, however, in comparison to the average *u* velocities in the surface and 1*m* layers but not for the subsurface water, which had low average *u* velocities of -0.5 and -1.5 $cm\ s^{-1}$ respectively at 10*m* and 40*m*. The variances in the surface and 1*m* flows were also low in comparison to the means (Table 6) and this is a reflection of periodic, direct, outward trajectories (Figs. 18 and 19).

About 73% of all the *u* velocities in Table 3a indicated flushing conditions, but 31% ended in grounding either inside or just outside the fjord. For example, out of twenty-nine cases of flushing, 23% were accompanied by grounding, all of which occurred inside the fjord except for i5600; the latter grounded on the southern side of the 'Narrows' (Fig. 18d). In contrast, 45% of the retention cases were due to grounding (Fig. 63 and Table 3a). Nine percent of all deployments in September were inconclusive regarding as to whether retention or flushing would occur. These cases were all for the 10*m* SVPs and consisted of small to moderate, negative *u* velocities (-0.03 to -2.4$cm\ s^{-1}$) that resulted in indefinite to excessive flushing times (e.g. *inf.* for deployment #8 and 182*hr* for deployment #18).

The time series in Fig. 63 indicates that retention of the surface water was relatively high in comparison to 1*m*. This was mostly due to ispheres that exhibited flushing but grounded inside the fjord (Fig. 63A). In contrast, the majority of the microstar deployments showed flushing without grounding (Fig. 63B). In two cases it was uncertain if the 1*m* flows would have actually exited the fjord, however, and in one case (m003a), grounding occurred on the southeastern shore (Fig. 19f). Drifter m003a obviously showed retention by default and m004 was considered to be flushing, so if the drifters in deployment #5 had indeed exited the fjord then the percentage of flushing would have increased slightly to 87%. Nevertheless, very few of the deployments exhibited positive *u* velocities so it is safe to say that a large majority of any contaminants at 1*m* in depth would have been flushed from Port Valdez in early fall.

At 10*m* (Fig. 63C) the flows exhibited slightly more retention in comparison to flushing (55% vs. 45%). The drift durations were lengthy (avg. = 45.5*hr*) and the average *u* velocities were relatively small (-3.3 to 4.7$cm\ s^{-1}$). This resulted in the extensive average retention/flushing times in Table 3b. The latter were not based solely on drift durations, however, and instead were calculated using distances from the release points to either the mouth (-*u* velocities) or the eastern shoreline (+*u* velocities). In the cases of s005 and the SVPs in deployment #8, for example, the along-channel flows were negligible, thus causing extreme retention/flushing times (> 500*hr*) and hence were indefinite. For the microstars, only deployment #6 had indefinite retention and none of the isphere deployments exceeded the above arbitrary limit. In fact, the maximum flushing/retention times for ispheres was 56 and 125*hr* or 2.3 and 5.2 days respectively.

The flows at 40*m* also had very long drift durations and small, negative average along-channel flows that indicated flushing (Fig 63C). However, two of the drogues became caught on the bottom along the northern side of the fjord, showing that the deep subsurface flow had indeed reached the sidewall of the northern basin. Due to the small *u* velocities, total flushing times (Table 3b) were relatively high, ranging from 214 to 245*hrs* or 8 to 9 days. The 40*m* drogues moved in mesoscale cyclonic and anticyclonic eddies (Fig. 20f), similar to the 10*m* drifters between the 21st and 23rd (Fig. 18a). However, unlike the latter drifters this pattern continued over the majority of the 40*m* SVP drift periods, and the westerly outflows did not begin until midday on the 29th when the wind speeds increased from the northeast (Fig. 13).

4.16.3 March 2017

The average speeds of the ispheres in March (Fig. 64) were more than three times greater than the speeds of the microstars and SVPs and the *u* velocities were 5 and 4.7 times higher respectively (Table 4b). This was consistent with the additional leeway caused by both the wind and Stokes-Coriolis forces on the surface currents discussed above, and the combined forcing caused all ispheres in deployments #1 to #3 to move rapidly to the northwest (Fig. 26a,b). With the exception of the ispheres in deployment #7, all *u* velocities in March were negative (Table 4a) resulting in 94% cases of flushing. However, in 44% of the deployments retention also occurred from grounding, and 100% of the ispheres with negative *u* velocities never exited the fjord. In contrast, only 20% of the microstars that exhibited flushing possibly would have grounded within the fjord (Fig. 27c) and 40% of the SVP s grounded in the outer fjord (Fig. 28b,c). So although conditions in late winter were conducive to flushing, any contaminants contained in the upper 10*m* of the water column could easily end up in the intertidal zone, and at least 85% of the material at the surface would likely contaminate the shoreline.

In general, the means for drifter speeds and *u* velocities during the first segment in March (Fig. 64a) were significantly greater than the means for the second segment ($p < 0.05$); the exception was for the mean speeds of the two 40*m* SVPs (Appendix D). The vertical structure of the flows also indicated that shear across the upper 1*m* was extreme in the first segment, and given the relatively uniform density field (Figs. 22 to 24) vertical mixing was also very intense during the period of high winds. The average ADCP current profiles (Fig. 64c,d) showed a bimodal structure that was similar in magnitudes and directions to

currents measured in March 1972 at the 'Narrows' by IMS-UAF (Muench and Niebert, 1973). The tidal currents (Fig. 64e) showed that the barotropic flows increased steadily in amplitude over the first segment from neap tides to nearly equal semi-diurnal spring tides, but the integrated net tidal velocity was nearly balanced (-0.012*cm* s^{-1}), and thus tidal flushing was negligible in comparison to that of the winds.

The patterns of flushing versus retention relative to drift durations at all four depths are shown in Fig. 65. A rapid flushing of ispheres for segment #1 (Fig. 65A) was indicated by large, negative *u* velocities, and this resulted in a markedly negative average *u* velocity (-18.9*cm* s^{-1}). Retention of surface water was not evident until deployment #7 on the 27th (Fig. 26d). The first four isphere deployments were very brief (4 to 5*hr*), however, and therefore the r/f percentages (Fig. 65A) slightly favored retention (55%) versus flushing (45%). If all the isphere deployments that resulted in grounding were considered to be retentions by default, then retention of the surface deployments would have been 100%. The microstars also showed initial flushing (Fig. 65B) but the magnitudes were very small by comparison, and by deployment #3 some of the tracks began to indicate retention. However, the greater magnitude of the negative average *u* velocity relative to the positive velocity (-7 vs. 4.2*cm* s^{-1}) along with the much longer drift times for flushing resulted in r/f percentages of 28% and 72% respectively.

For the SVPs the 10*m* drifters exhibited 100% negative *u* velocities (Fig. 64C) and the total average was -3.4*cm* s^{-1}. However, the very small magnitude for deployment 8b (-0.3*cm* s^{-1}) along with inward cyclonic turning (Fig. 28d) indicated possible retention. This yielded r/f percentages of 10% and 90% respectively, thus indicating that the subsurface along-channel currents highly favored flushing. However, five of the six SVPs in deployments #3 and #5 grounded along the northern shoreline (Figs. 28b,c). If all of these groundings were considered to be retentions then the r/f percentages would flip to 73% and 27% respectively. At 40*m* all deployments exhibited flushing over long periods ranging from 70 to 72*hr*, but during the first segment (deployment #1) when the winds were at maximum strength (Fig. 21e) the *u* velocities were slightly greater in comparison to segment #2 (Fig. 64C). Under reduced wind stress during segment #2, however, cross-channel flows in the outer basin forced the drifters to the southwest over a wide cyclonic arc (Fig. 28f), thus it was questionable as to whether deployment #6 actually led to flushing or retention.

5.0 DISCUSSION

5.1 Estuarine Circulation in Relation to Small PWS Fjords and Port Valdez; adapted from Gay (2014)

In most large fjords worldwide, upper layer circulation and water exchange are defined by the volume of freshwater discharge from significant point sources, such as large rivers, and a corresponding estuarine circulation (e.g. Pickard, 1967, 1971; Saelan, 1967; Farmer and Freeland, 1983). This usually takes on the form of an outwardly flowing fresh layer ($S \leq 5$), 1 to 5m in thickness, which becomes increasingly brackish down-fjord due to entrainment of salty subsurface marine water and increases in flow volume due to the additional mass. The stratification sequence is one of progressive changes along the estuary as opposed to one of local controls from tides and river flow (Hansen and Rattray, 1966). Following Knudsen's relations (Dyer, 1997) the salt flux (due to mixing and transport within the out-flowing layer) is typically balanced by a subsurface inflow of marine source water at the mouth. In large fjords, such as Port Valdez, minimal flow should occur in the deep layer below sill depth (160*m*). In addition to estuarine flow, however, density fluctuations due to winds and along-shore currents outside the mouths of certain fjords can cause baroclinic gradients that have marked effects on the circulation and exchange of surface water (Svendsen and Thompson, 1978) and intermediate water (Aure *et al.*, 1996; Klinck *et al.*, 1981).

Likewise, internal waves produced by semi-diurnal tidal flows over sills influence water exchange (Valasenko *et al.*, 2002; Gillibrand and Amundrud, 2007).

Small fjords in PWS are all positive estuaries since they receive more freshwater input than amounts lost by evaporation. However, they also tend to have highly localized watersheds (Gay and Vaughan, 2001), and freshwater input typically occurs from high order streams scattered along the basin periphery. This line-source causes freshwater to disperse over a surface layer, but the volume relative to the cross-sectional area yields negligible freshwater velocities: $u_f = R/A = O(0.0025 m\ s^{-1})$, where R is the freshwater inflow relative to cross-sectional area, A, at the mouth or a constriction. This also causes very low densimetric (freshwater) Froude numbers (Hansen and Rattray, 1966) $Fr_f = u_f / \sqrt{g' h} = O(10^{-4})$, where $g' = \Delta\rho/\rho g$ is reduced gravity due to density stratification and h is the depth of the stratified layer. The tidal prisms have a large range (Δh = 3 to 5m), and thus the small freshwater velocities and Froude numbers indicate they are not conducive to estuarine circulation. The controls on stratification and mixing appear to be strongly viscous as opposed to the hydraulic effects of sills or constrictions (Hetland, 2010).

Based on a combined freshwater discharge rate of 155 to 310$m^3\ s^{-1}$ in June and July from major sources such as the Lowe, Robe and Valdez Glacier Stream (Sharma and Burbank, 1973), Port Valdez would have a u_f ranging respectively from 6.5×10^{-4} to $13 \times 10^{-4}\ m\ s^{-1}$. Using the density profiles in late June 2016, the Fr_f values would be about 4.7 to 9.4×10^{-4}, and thus the same order of magnitude as other fjords in PWS. Port Valdez also conforms to Hansen and Rattray's classification of a fjord according to their stratification-circulation diagram (Dyer, 1997), which plots a stratification parameter $\delta S/\langle S \rangle$ against a circulation parameter equal to the ratio of the surface currents to the freshwater velocity (u_s/u_f). Given a $\delta S/\langle S \rangle$ value in June 2016 of ~ 1.0, a flow ratio > 200 and the Fr_f value above, Port Valdez falls in the class 3b estuary for fjords.

All of the above parameters indicate that most small fjords in PWS should have relatively brackish surface conditions, as confirmed by observations (Gay and Vaughan, 2001). Therefore the circulation is predominately driven by winds, tides and baroclinic gradients, moderated by basin morphometery, internal waves and in certain cases by both offshore and along-fjord winds (Gay, 2013a). Offshore baroclinic gradients markedly affect circulation when small PWS fjords are located downstream from fjords containing tidewater glaciers (Gay and Vaughn, 2001; Gay, 2013b). In such cases, cold, brackish surface and subsurface glacial water creates low-density fields at the mouths that reverses the nearsurface circulation and enhances advection of glacial water into the fjord. These properties appear as upper layer intrusions that interleave within the outer (main) basins, shown by large to small-scale temperature minima and maxima along with atypically high freshwater contents (Gay, 2013b).

Port Valdez differs from many of the small fjords in PWS, in that it is wide enough to have appreciable horizontal features of circulation that are affected by Coriolis, but unlikely in geostrophic balance for any lengthy period. It also has enough freshwater discharge in the fall to develop a marked estuarine flow, particularly along the northeastern shoreline, as shown by both drifter trajectories and geostrophic calculations (Figs. 33 to 35). The fjord also experiences periodic deep water exchange (Collonel, 1981) and in many regards, it behaves physically like a microcosm of PWS proper. So Port Valdez is a large, wide fjord that also has properties of small inland oceanic basin, similar to PWS.

5.2 Wind and Wave Effects on Fjord Circulation

During all three monthly surveys, the winds in Port Valdez played a dominant factor in forcing flows mainly in the surface and nearsurface layers in the summer and fall, and deeper in the water column in the late winter. For example, in June the density stratification from initial freshwater input was concentrated above depths ranging from of 5 to 10m (Figs. 6 and 7). The pycnocline depths were more variable at the

start of the survey and surface mixing from westerly (up-fjord) winds gusting to 8*m s*$^{-1}$ (Fig. 13a,e) likely caused the varied mixing, evident in the mean T/S profiles on the 22nd (Fig. 6a). By the 26th, however, wind speeds decreased to < 2*m s*$^{-1}$ and buoyancy of the brackish surface water allowed additional runoff to restore an even, shallow pycnocline over the fjord (Fig. 6b).

Studies of surface circulation in certain fjords of Norway and Canada, have shown that high amounts of stratification and mixing by waves can limit wind effects to the nearsurface layer (Stacey, 1999; Svendsen and Thompson, 1978). For example, in modeling wind circulation in Knight Inlet, Stacey (1999) parameterized the seawater surface roughness length (z_0) by converting the relationship of z_0 with friction velocity (u_*)[8] and gravitational acceleration (g) established for the air-sea interface ($z_0 = au_*^2/g$) to one according to wind speed:

$$z_0 = 0.2W^2/g. \quad (12)$$

Also, the latter is on the same order as the significant wave height (H_s) estimated by an empirical equation given by LeBlond and Mysak (1988, p.485) that equates H_s with wind speed:

$$H_s \sim 0.3\ W^2/g. \quad (13)$$

According to Pond and Pickard (1983, p. 234) under a wind speed of 5*m s*$^{-1}$ with a duration of 2*hrs* and a fetch of 20*km*, the H_s would be 0.4*m*. This is less than the value of 0.8*m* estimated by eq. 13 but close to a z_0 value of 0.5*m* given by eq. 12. On June 22nd and 23rd the hourly diurnal winds (Fig. 13e) were close to 5*m s*$^{-1}$ and the duration was ~12*hrs* each day, thus although the fetch is about 10 to 11*km* the sea state was likely to have been fully developed. Also, wind gusts frequently reached 8*m s*$^{-1}$ (Fig. 13a) and according to eqns. 12 and 13 the values of z_0 and H_s would be 1.3*m* and 1.9*m* respectively. Although the latter value for H_s is probably overstated, and the true value is probably closer to 1.5*m* (Pond and Pickard, 1983, p.233), the range of kinetic energy transfer by breaking waves (z_0 = 0.5 to 1.3*m*) clearly shows that much of the wind energy in June was concentrated at the 1*m* depth of the microstars.

If the concentration of wind energy was indeed closer to the surface as predicted by many studies, than the effective Ekman depth (D_E) may have only barely reached the level of the 10*m* SVPs. If that were true, then it would explain the lack of response to the winds generally shown by these deeper drogued drifters. The currents at the surface and at 1*m* based on a D_E of 10*m* according to eqns. 2 and 3 given a 5*m s*$^{-1}$ wind would be 15.5 and 9.5*cm s*$^{-1}$ respectively, but the flow at 10*m* would be negligible (0.7*cm s*$^{-1}$).

The motions of surface ispheres have been found to be affected by a combination of direct wind drag, Stokes Drift due to waves and wind-driven surface currents (Rohrs et al. 2012). The first factor accounts for ~1/3 of a drift leeway, ranging from 3% to 5% of the wind speed, while and transfer of wind-wave energy and the so-called Stokes-Coriolis force accounts for the remainder (Röhrs and Christensen, 2015). Röhrs and Christensen (2015) found that the drift trajectories of ispheres were also coherent with winds at both cyclonic and anticyclonic subinertial frequencies[9], whereas the 1*m* CODE drifters (similar to microstars) were found to be mainly coherent with tidal and near-inertial oscillations[10].

In September, the nearsurface pycnocline deepened to ~10*m*, but there was also a thick partly mixed layer beneath the latter to a depth of about 40*m* (Figs. 14 and 15). The wind effects probably deepened slightly

---

[8] Friction velocity is given by the square root of wind stress divided by water density: $(\tau_a/\rho_w)^{-1/2}$, where $\tau = W^2 C_D \rho_a$ and C_D and ρ_a are the drag coefficient and density for air respectively.

[9] The frequencies referred to here are based counterclockwise and clockwise components of rotary-cross spectral analyses of drifter trajectories on the open ocean.

[10] Tidal and near-inertial periods refer to the semi-diurnal tide (~12hrs) and the period of fully developed inertial currents due solely to Coriolis (i.e. $d\mathbf{V}/dt = f \cdot \mathbf{V}$).

along with the pycnocline depth, but the motions in the region of the partial mixing were probably driven mostly by tides and strong baroclinic flows suggested by the geostrophic velocities (Figs. 33 to 35). The ADCP data at these depths (Figs. 16 and 17) also support this conclusion.

In late winter, however, the density structure is nearly uniform (Figs. 22 and 23) and the depth of the wind effects was probably closer to the maximum determined by Ekman dynamics for a water column in full balance with wind stress. For example, the surface currents early in the month when wind speeds reached $20 m\ s^{-1}$ (Fig. 23a) reached values as high as $27 cm\ s^{-1}$ (~0.5*kts*) and the D_E may have penetrated as deep as 90*m*. During the experiment, however, the wind speeds diminished to values ranging from 5 to $10 m\ s^{-1}$ with gusts to nearly $14 m\ s^{-1}$ (Fig. 23a,e). The Ekman surface currents for such winds would range from 14 to $18 cm\ s^{-1}$ and at 1, 10 and 40*m* the average currents would be ~ 15, 9 and $2 cm\ s^{-1}$ respectively.

Polton *et al.* (2005) described the effects of the aforementioned Stokes-Coriolis forcing (δ_s) on wind-induced current profiles, and the interaction of the two forces creates what is known as the Ekman-Stokes layer. Although the depth of influence for δ_s is $<< D_E$, it does affect the entire profile by rotating the flows farther to the right of wind than classical Ekman solutions. These effects are beyond the scope of this report, but they will be considered in the following discussion of winds and other forcing mechanisms in relation to drifter speeds, patterns in trajectory and dispersion rates.

5.3 Factors Affecting Horizontal Circulation

5.3.1 Winds, Coriolis and Tides

In each of the drifter experiments, the primary forcing mechanism for the surface and 1*m* flows was wind. Precise wind directions in the outer fjord were uncertain, but data at the NOAA weather station provided a robust record that was very useful in gauging wind effects on the surface and 1*m* drifters. In addition, Port Valdez is long and wide enough for Coriolis force to cause significant rightward deflection (i.e. leeway) of the wind forced currents.

For example, depending on the length scale used, Rossby numbers[11] (R_0) for flows (U) of 10 to $20 cm\ s^{-1}$ range from 0.05 to 0.09 for the entire 18*km* fjord and 0.4 to 0.8 for 2*km* (the approximate de-correlation length scale). Over the course of 1*hr* (3600*s*) the same currents would travel a distance (Ut) of 360*m* to 720*m* and the horizontal accelerations from Coriolis ($C_H = fU$) would be (1.275 and 2.55) x $10^{-5} m\ s^{-2}$ respectively. The rightward leeway ($1/2\ C_H\ t^2$) is 83*m* and 165*m*, with a deflection angle of 12.95° given by $\tan^{-1}(0.23)$. Thus, even for short spatial scales Coriolis was relatively important in affecting the flow directions during each experiment, and the surface and 1*m* drifter velocities induced by winds mainly reflect this clockwise rotation. Also, through Stokes-Coriolis force and drift (Röhrs and Christensen, 2015), wave action may also play a role in turning these flows. But when combined with additional forces such as wind drag (for ispheres), tides and estuarine (geostrophic) flow the ispheres reached maximum speeds exceeding $60 cm\ s^{-1}$ (~1.2*kts*) and the microstars frequently reached speeds of $40 cm\ s^{-1}$ (~0.8*kts*).

In contrast to the nearsurface currents, tides and baroclinic-geostrophic flows were considered to be the dominant forcing mechanisms for the subsurface flows at 10*m* and 40*m*. However, there are other wind related factors to be considered including a sloping sea-surface from wind driven transport and subsurface flows induced by continuity[12]. The former creates barotropic currents throughout the water column

[11] Rossby no. $R_0 = U/\Omega L$, where U is the velocity scale, Ω refers to the Coriolis parameter (f) at 61° latitude = 1.275 x 10^{-4} $rad\ s^{-1}$ and L is the length scale (m).

[12] Continuity of volume ($\partial u/\partial x + \partial v/\partial y + \partial w/\partial z = 0$) based on conservation of mass (Gill, 1982).

described by the shallow water equations[13], and the steady-state solution to these equations is pure geostrophic flow (Gill, 1982). Like the tides, the uniform pressure gradient force over depth interacts with other forces, such as horizontal variation in density, to create the net baroclinic currents. Continuity requires that any volume flux in the system in addition to tides (including meteorological effects such as barometric pressure) must be balanced by a negative flux provided by vertical flows, such as upwelling or downwelling near material surface boundaries along with subsurface inflow or outflow.

Good examples of possible wind-driven subsurface reversals are shown by the ADCP data in June on the 21st during ebb tide 1 (Fig. 8B) and on the 23rd during flood2-ebb2 (Fig. 8C,D) and ebb2-flood3 (Fig. 8E). In each case, there were different conditions causing the subsurface forcing. In case #1, for example, the strongest outflows are within the upper 7 to 40*m* in various points in the inner fjord, but at mid-fjord the flows are uniformly to the west. This is also a time when surface transport by winds possibly set up a reversed flow that was in phase with the tide but out of phase with the wind. The deep layer, by contrast, was in phase with the wind creating a system similar to wind driven subtidal flow described for Puget Sound by Matsuura and Cannon (1997). During the transition from flood 2 to ebb2 (case #2), the pattern changed significantly and a marked inflow occurred between 7 and 40*m* that appears to be balanced by outflow at 5 to 10$cm\ s^{-1}$ over the entire deep water column. During the transition from ebb2 to flood 3 (case #3) the pattern returned to a moderate subsurface outflow (10 to 15$cm\ s^{-1}$) centered at 40*m* but with cells that penetrated to over 80*m* in depth.

5.3.2 Estuarine Conditions and Baroclinic-Geostrophic Flow

In the early summer and fall, gravitational circulation set up by the low density of the freshwater input was also an important factor. In this way Port Valdez is similar to many other fjord systems, except that steady-state seaward flow driven by vertical entrainment[14] of salty subsurface water (Dyer, 1997) was not evident in the system. Typically, the latter is accompanied by a compensatory subsurface inflow of oceanic water that balances the salinity flux and thus forms a true estuarine circulation (Farmer & Freeland, 1982). Instead, in Port Valdez the salinity appears to be balanced by horizontal variations in estuarine dispersal (typically along the northern side) and saltier inflows (mainly in the south). In June and occasionally in September the above pattern was set up by strong westerly winds, but in September this was subject to marked disruption by easterly winds.

In June, freshwater was concentrated mainly at the surface (Figs. 6 and 7) and thus the baroclinic-geostrophic[15] flows forced by horizontal density variation were also focused within this layer (Figs. 30 to 32). A noteworthy exception occurred, however, the northeastern region of the fjord late in the oceanographic survey (Figs. 30d and 32e). What produced these anomalies is uncertain, but the deep, brackish vertical salinity gradient within this region may have been a result of downwelling due to the diurnal transport of surface water into the inner fjord by westerly winds. As such, this may be responsible for creating the strong subsurface geostrophic flows calculated for the northeast side of the fjord.

In any case, the diurnal fluctuations in wind speeds and directions in June and their effects on the density field appeared to be a proximate cause of the horizontal flow variation and possibly also a separation of flows between the inner and outer basins. The latter was hinted at by certain ADCP transects and the

---

[13] The shallow water momentum equations replace density and horizontal pressure ($1/\rho\partial p\partial \mathbf{x}$) with gravitational acceleration and perturbation pressure defined as variation in sea surface elevation ($g\partial\eta'\partial \mathbf{x}$) (Benoit and Cushman, 2008; Gill, 1982).

[14] Entrainment is a one-way turbulent process that transports salt into a fresh surface layer by breaking of internal waves created at the density interface (i.e. pycnocline) by the down-fjord gravitational motion of freshwater input by a river (see Dyer, 1997).

[15] The vertical density gradients (i.e. the pycnoclines) are continuous, therefore the estuarine flows are essentially a surface extension of baroclinic flows, and since the geostrophic method was used to calculate their magnitude they are referred to as such.

dynamic topography for CTD set F (Fig. 29d), which showed the geostrophic flows in the inner basin turning cyclonically to the southwest, whereas the flows in the northeast at the top of transects 7 and 9 flowed outward to the northwest. In contrast, the flows in the outer basin (transects 1 and 3) exhibited varied directions starting to the north, then to the east, and finally northward.

In September, the surface salinities were similar to June but vertical mixing by strong easterly winds, such as on 9th and 10th (Fig. 13), probably created the deep, broadly dispersed estuarine layer observed over the central to inner basins (Figs. 14 and 15). Although true estuarine circulation was not evident in the density profiles, the outflow of a brackish nearsurface layer certainly increased in depth over the inner fjord.

For example, on September 21st the surface and 1*m* drifters responded significantly to the estuarine gradient combined with forcing by strong northeast winds, and both sets of drifters moved outward at maximum speeds ranging from ~ 55 to 65$cm\ s^{-1}$ respectively (Figs. 42a). On the 22nd the same conditions indeed caused i0600 and i2460 to escape Port Valdez, and while traveling southward through Valdez Arm on the 23rd (Fig. 18b) they attained maximum speeds of ~ 120$cm\ s^{-1}$ (Fig. 43a). At this time the strong westward velocities of both types of drifters could only be explained by additional forcing from estuarine (geostrophic) outflows. In contrast, periods of westerly winds likely constrained the estuarine outflows to the northern side by piling freshwater inside the fjord, similar to effects of off shore winds (blowing up-fjord) in the Jösen fjord in Norway (Svendson and Thompson, 1978).

Such conditions in Port Valdez were inferred by the northwesterly isphere trajectories on September 24th and again on the 25th (Fig. 18c,d). The estuarine conditions on the 24th and 25th were significantly affected by the Lowe River plume, which was observed moving diagonally to the northwest due to Coriolis. At this point it undoubtedly joined the discharge of Mineral and Gold Creeks, and thus created a persistent estuarine (geostrophic) outflow along the northern side of the fjord. However, when the westerly winds relaxed on the 25th, the ispheres then followed broad, meandering outflows along the northern side of the fjord as they once again exited Port Valdez (Fig. 18d).

The two sets of microstars launched on September 24th exhibited markedly different responses to the variable westerly winds and geostrophic outflow. For example, the microstars launched in the inner basin on the 24th (group #7) initially moved northward, followed by a down-fjord motion overnight along the northern shoreline (Fig. 19d) forced by the estuarine conditions described above. In contrast, group #6 initially moved WSW but then changed direction after 7.5*hr* and moved inward to the ESE. The winds during the outflow were light (~ 1.8$m\ s^{-1}$) and from the west and the currents at 1*m* would have been only ~1.5$cm\ s^{-1}$. The microstars moved outward at a steady speed of 5$cm\ s^{-1}$ that appeared to be forced by estuarine (geostrophic) outflows (~2$cm\ s^{-1}$) (Fig. 33c) and ebb tide currents (< 1$cm\ s^{-1}$) (Fig. 62d). Thus, it was unlikely that any wind energy penetrated to 1*m* and this produced the additional shear in this layer shown in the average *u* velocities (Fig. 62a). At night the winds became very light and variable (Fig. 13) but increased slightly from the west in the morning. The drifters appeared to move inward with the flood tide and then back again on the ebb, but over the final 3*hr* they accelerated to the north (Fig. 44b). How all of the above factors affected these highly varied tracks of this group is uncertain.

5.3.3 Large and Small Scale Turbulence

A circulation pattern that occurred at intermediate depths in June was cyclonic turning at mid-fjord (Figs. 8A, D, E and 9a,b). This pattern was even more obvious in September, when a closed core cyclonic circulation at 7 to 23*m* was seen early in the survey on the 21st (Fig. 16A). Note also, that the bulk of the outflows balancing the ebb tide volume changes at this time were centered at 40*m* with speeds of 10 to 20 $cm\ s^{-1}$. Above the outflows, the cyclonic circulations appear to be induced by local vorticity caused by horizontal shear between outflow on the northern side and inflow on the southern side. The cyclonic cell occurred near the end of a period of westerly winds, which gave way to steady winds from the northeast

(Fig. 13). Although the cyclonic turning was evident to some degree during the wind shift (Fig. 16B), it was progressively disrupted by the easterly winds, and early on the 22nd it appeared only at depths of 15 to 30*m* (Fig. 16C). By 09:00 on the 22nd it nearly vanished and by the 23rd (Fig. 16D) it had entirely dispersed. It did not appear again until the 25th (Fig. 17C) with the reoccurrence of light westerly winds.

Small-scale turbulence (eddy viscosity) that affected drifter dispersion was typically very minor O(5-10m^2 s^{-1}). Exceptions occurred at the end of the drift periods when dispersion infrequently increased significantly O(100-500m^2 s^{-1}). In other cases, the drifters dispersed into long, linear configurations similar to descriptions of flow patterns during ebb tides made from dye studies in the early 1970's by UAF-IMS (Nebert et al., 1973). In such cases, the distances to the center of mass were large but the eddy viscosities were small due to minimal changes in area. Of course whenever only two drifters were released together, the only measure of dispersion was the midpoint of the linear distance between them. These effects of dispersion are discussed at length below in section 5.5.

The strong vertical shear exhibited by the average flows in the upper water column (Figs. 60, 62 and 64) showed that dispersion in Port Valdez primarily occurred within separate depth layers, which points to the importance of both winds and the highly baroclinic structure of the flow field. The response of the surface and 1*m* layer to the winds in June caused marked nearsurface flow shear that was quite obvious in the disparate directions and minor dispersion shown by the ispheres and microstars in the first dispersion experiment (Fig. 11a.b). In contrast, the subsurface baroclinic field was set-up in part by continuous pycnoclines that created an infinite number of baroclinic modes (Gill 1982) to depths of 15 to 40*m* (depending on season). The horizontal gradients in water density, therefore, cause geostrophic flows over most of the upper stratified layer, which is quite common in PWS (Niebauer, et al., 1994; Vaughan et al., 2001; Halverson et al., 2013a,b) and in many of the small fjords (Gay and Vaughan, 2001; Gay 2013). This gives Port Valdez properties of a small marginal (land-locked) sea, similar to PWS, but with much more fjord-like characteristics.

One of the primary differences in the two systems, however, is that unlike PWS which at times exhibits large, closed geostrophic circulations, Port Valdez has small, closed eddies caused by large-scale turbulence due to horizontal shear from local vorticity caused by variations in the flows. Although planetary vorticity (Coriolis) has been shown to affect the flows, it never created steady-state conditions. Another difference between the two systems is that western PWS is influenced significantly by cold, subsurface brackish water emanating from within tidewater glacial fjords that creates deep baroclinic flows in the upper 100*m* (Gay, 2013). In contrast, the strongest geostrophic flows within the Port occurred in the nearsurface water in early summer due to salinity gradients arising from freshwater runoff. These gradients were deeper in the fall due to vertical mixing over time, but in both seasons the resulting estuarine outflows were highly moderated by either up or down-fjord winds.

5.4 Lagrangian Flow Patterns

5.4.1 Early Summer

From the foregoing discussion it is obvious that the motion of the drifters, particularly at the surface and 1*m* depth, were affected by a complex set of factors, and to fully understand how these conditions forced the Lagrangian flows observed during this study will probably require modeling the circulation. In open oceanic conditions, for example, Röhrs and Christensen (2015) found that the drift speeds of both ispheres and 1*m* CODE drifters (similar to microstars) were correlated with wind speeds at the 99% significance level, but the correlation coefficients were very low, signifying that winds alone could not predict the drifter motions.

In the present study, similar conclusions were drawn regarding wind effects. A good example occurred on June 22nd when westerly winds with sustained speeds of 5*m s*$^{-1}$ would have caused surface and 1*m* currents of 7 and 6*cm s*$^{-1}$ respectively. However, at that time i0460 and m007 attained maximum speeds of ~ 70 and 60*cm s*$^{-1}$ (Figs. 10a,e), thus a marked amount of additional forcing is required to explain the observed flows. The published leeway for ispheres is 3% to 5% of the wind speed (Rohrs and Christensen, 2015), which gives a maximum leeway on June 22nd of 25*cm s*$^{-1}$. This brings the total speed for i0460 to 32*cm s*$^{-1}$; which is still less than half of the observed value. The velocity differential for the microstar is even worse at ~ 54*cm s*$^{-1}$. Clearly, something else was driving the high drifter speeds.

The Stokes-Coriolis force may play a partial role in creating greater leeway to the right of the wind but it does not explain such large discrepancies in the currents. The shallow density stratification in June may have concentrated the wind energy within the upper 10*m* (Stacey, 1999), in which case the surface currents would have peaked at 15 to 16*cm s*$^{-1}$. This still leaves ~ 30*cm s*$^{-1}$ of current unaccounted for. The maximum barotropic tidal currents for the 3.7+*m* flood tide on the 22nd were estimated at 1.7*cm s*$^{-1}$ (Fig. 60d). Therefore, the only significant forcing mechanism remaining is the estuarine (geostophic) velocities due to varied freshwater input around the basin.

The absolute geostrophic velocities were uncertain since true levels of no motion could not be determined, but nevertheless the density field was clearly an important driver of the nearsurface flows in early summer. For example, density driven flows shown by the dynamic topography and cross-channel geostrophic velocities for CTD set A (Figs. 29a and 31c,d) indicated that a nearsurface flow close to the launch area was indeed moving inward at speeds of 40 to 60*cm s*$^{-1}$. Also, at the end of the trajectories the flow reversed in direction (Fig. 31e), thus possibly forcing the anticyclonic turning observed in both layers. For CTD set B, the dynamic topography (Fig. 29b) showed that as the winds relaxed during the night the geopotential gradient diminished in strength, but the gradient was down-fjord and the flows (if in geostrophic balance) were moving northwards. Such currents could have caused a northern component of motion for the surface and 1*m* drifters, i5480 and m001, thus constraining them close to shore as they were moved outward during the night by along-shore currents (Figs. 10b,e). Similar nocturnal outflows were shown by the microstars deployed in the evening of the final drifter experiment on June 29th (Fig. 11g,h).

Another example of density driven flows in June occurred on the afternoon of the 23rd, when the geopotential gradient showed an inward flow pattern similar to the previous day (Fig. 29c). At this time, a combination of westerly winds, a flood tide and geostrophic inflows caused i9469 and m007 to move rapidly to the southeast at speeds reaching 60 to 65*cm s*$^{-1}$. Following this, however, both drifters reversed direction and moved outward to the west-northwest (Fig. 10c,e). Although hydrography data were not collected at that latter time, in the late afternoon of June 24th the dynamic heights (not shown) indicated that geostrophic currents were indeed flowing in a similar direction as the drifters the previous day. It is quite possible a similar geostrophic flow field was set up by the winds on the 23rd.

Effects of geostrophic flows also occurred at 10*m* (Fig. 10g,h) where forcing was mostly by subsurface baroclinic currents, shown in the ADCP data (Figs. 8 and 9). The 10*m* SVP drifters launched early in the survey exhibited wide, cyclonic (counterclockwise) turns in the central and outer basin (Fig. 10g), but they also showed a tendency to move either inward or outward, depending on where and at what time they were released. Although there was scant evidence of direct wind effects at 10*m*, near the end of the survey the westerly winds persisted for more than a day. At this time, the eastward motions of both the 10*m* and 40*m* SVPs were probably not directly caused by currents in the Ekman-Stokes layer, but instead, may have been an indirect response to reversed nearsurface flows during the extended period of winds. Flow reversals at 1*m* were observed in the first dispersion experiment conducted on June 27th (Fig. 11a,b) and were probably the cause of the large shear in average *u* velocities at 0 and 1*m* in the second segment (Fig. 60a). Other examples of subsurface flow reversals were described above in section 5.3.1.

5.4.2 Early Fall

In section 5.3.2, a number of examples of the effects of wind-induced currents on the surface and 1*m* Lagrangian drifter tracks were described for early in the September survey. At this time the strong westward velocities of both types of drifters could only be explained by additional forcing from estuarine (geostrophic) outflows. During the remainder of the experiment, however, the tracks of the ispheres (Fig. 18e-g) differed widely in response to variable combinations of winds (Fig. 13) and nearsurface currents shown by the dynamic topography and geostrophic velocities (Figs. 33 to 35).

For example, the ispheres launched on the 26th and 27th (Fig. 18e,f) were all initially influenced by moderate westerly winds that eventually weakened and either varied from the north (group #10a,b) or blew steadily from the northeast (groups #11 to #13). The outer two groups (#10a and #11) were launched in similar locations and moved with minimal dispersion (Figs. 46 and 47) but in different directions. The other groups did the same, except for the inner drifters on the 26th (#10b), which dispersed widely to the north (i5600) and WNW (i6350) (Fig. 46). The variance in the trajectories may be partly explained by the above winds, but the effects of wind induced currents on ispheres were confounded to some degree by the additional leeway caused by direct forcing from wind drag and wave action.

The dynamic topography (Fig. 33) may also explain some of the variance in the isphere tracks. For example, the diagonal (NW) track of i6350 possibly followed the motion of the Lowe River plume, which was indicated by the dynamic heights on the 22nd (Fig. 33b). Also, the sudden inflection and rapid westward motion of group #10a was probably caused by the estuarine flow that this plume and other freshwater sources created along the northern shoreline; the latter was indicated by marked geostrophic outflows to the west throughout the fjord on the 24th (Fig. 33c). In contrast, the anticyclonic turning and orbits of the ispheres on the 26th were possibly related to inertial oscillations during tide changes when the winds were weak. A caveat to this, however, is that small to mesoscale turbulence from horizontal current shear could also be responsible for the turning, and this may only be sorted out by modeling.

In contrast to the highly varied isphere tracks, the microstars exhibited consistent down-fjord motions from the 25th to the 30th (Fig. 19e-i), albeit with marked variation in cross-channel velocities among groups (Fig. 58). For example, on the 25th the drifters moved down-fjord under light and variable winds (Fig. 19e) but the dynamic topography (Fig. 33d) indicated that geostrophic currents possibly caused the northwest motion of the outer group and the southwest motion of the inner group. On the 26th, however, the whole system possibly fluctuated due to moderate westerly winds (Fig. 13). This was inferred by the initial outward motions of both groups at the end of the ebb tide, followed by marked inflections to the south and southeast (Fig. 19f) as the tide changed and west winds increased in speed. After moving southeastward, however, the inner group turned sharply back to the west possibly due to the action of an anticyclonic eddy at PV16 observed the previous day (Fig. 33d). What is not clear is why the velocities of m004 accelerated to the west (Fig. 46d). The northerly winds were too weak and the dynamic heights indicated that the flows should have circulated back into the inner basin.

The westward motion of the outer group (#10a), by contrast, is indicated by the dynamic topography on the 25th and this forcing along with the ebb tide may have caused the latter group's acceleration along the southern shore until they eventually diverged in the outer basin (Fig. 46e). What caused the marked dispersion of group #10a is uncertain, but it may be related to acceleration of winds northwestward out of the 'Narrows' at Potato Point (not shown), which possibly resulted in cross-channel winds interacting with geostrophic outflows.

Similar Lagrangian flow patterns under nearly identical tidal and wind conditions (Fig. 13) occurred again for the microstars on the 27th (Fig. 19g). The one exception was m008, which lost its drogue after making the cyclonic southward turn. Acting as a quasi-isphere it moved diagonally to the northwest similar to the

ispheres for group #13 (Fig. 18f). On the following day the shift from westerly to northeasterly winds occurred again and all drifters initially moved either southward or to the southeast (Fig. 19h). However, the inner two microstars (m004 and m006) exhibited anticyclonic inflections possibly due to the combined action of inertial flow along with the changes in winds and tides. Indeed, the sharp turning of m004 and m006 coincided respectively with the ebb and flood tides (Fig. 19h).

The strong easterly winds on the 29th, by contrast, forced all drifters initially to the northwest, but group #18 then moved rapidly down-fjord, whereas group #17 quickly traveled northward and grounded next to the City Dock (Fig. 19i-k). It is possible that the strong easterly winds forced the Lowe River plume farther down-fjord prior to its turning to the northwest, but that is purely speculative at this point. It was definitely apparent, however, that when the winds blew steadily from the northeast a pattern of outflow in the nearsurface layer occurred, similar to currents during start of the experiment (Fig. 19a,b).

The deeper subsurface flows at 10*m* and 40*m* in September (Fig. 20) were much slower and variable in comparison to the nearsurface currents. Due to the strong stratification it was doubtful that the wind energy significantly affected these layers directly. However, the surface wind-driven transport could certainly have caused deeper baroclinic reversals due to continuity, as described for Puget Sound by Matsuura and Cannon (1997). The subsurface flows exhibited cyclonic orbits in the outer basin (Fig. 20a) that were also observed in the ADCP data at 7 to 23*m* (Fig. 16A), whereas the deeper flows at 40*m* were unidirectional and conformed with flows required to balance the changes in tidal volume.

Cyclonic turning and flow shear were described above in section 5.3.2 and frequently were observed in the ADCP data for the outer basin (Figs. 16 and 17). The geostrophic currents also showed periods of strong cross-channel flows leading to the conclusion that the large cyclonic flow patterns in the fall were driven by a combination of subsurface geostrophic currents moderated by mesoscale turbulence. For example, the action of Coriolis is typically viewed as inertial affects that cause anticyclonic turning, whereas it is more likely that the cyclonic turning was induced by flow shear between the northern and southern sides of the fjord, and hence local vorticity. Coriolis may act to broaden cyclonic orbits, but there was no evidence from the hydrography these were part of a closed steady-state geostrophic flow, such as occurs in central PWS (Niebauer et al. 1994; Vaughan et al., 2001; Halverson et al., 2013b).

5.4.3 Late Winter

The Lagrangian flow patterns in late winter differed significantly from the patterns in the early summer and fall, and during the first two thirds of the March survey the forcing of flows at all depths (Figs. 26 to 28) was dominated by strong katabatic winds from either the southeast or northeast (Fig. 21e). For example, the first drifter deployments on the 24th occurred in the morning when wind speeds had dropped to ~ 6 to 6.5$m\ s^{-1}$. All the ispheres moved rapidly northwestward at maximum average speeds of 40 to 45$cm\ s^{-1}$ and with almost no dispersion (Figs. 26a and 50). In considering the Ekman dynamics, the above drifters would have been forced by a surface current of 8.1 to 8.8$cm\ s^{-1}$ and given a maximum leeway of 5% of the wind speed the total speeds would range between 38 and 41$cm\ s^{-1}$. Thus the additional 2 to 4 $cm\ s^{-1}$ may have been due to the Stokes Drift-Coriolis force caused by wave action. On the following day, the ispheres again accelerated steadily to a maximum speed of ~ 40$cm\ s^{-1}$ with little dispersion (Figs. 26b and 51). The average wind speeds were slightly higher in the morning of the 25th (~ 7$m\ s^{-1}$). Given an Ekman surface current of ~15.5 $cm\ s^{-1}$and a leeway of 3.5% the total current comes to exactly to the above observed value of 40$cm\ s^{-1}$.

The microstars and 10*m* SVP drifters also moved initially to the northwest during the period of strong winds, but instead of grounding they moved in westerly tracks along the northern shoreline (Figs. 27a and 28a,e). The average speeds of the both sets of drifters (Fig. 50b,c) were also nearly double the magnitudes predicted by Ekman dynamics for winds ranging from 6 to 10$m\ s^{-1}$. The 40*m* SVPs reached a maximum

speed of ~8*cm* s^{-1}, which also far exceeded calculated values of 1 to 3*cm* s^{-1} based on winds ranging from 10 to 14*m* s^{-1}. Since the water column was well mixed (Fig. 22 to 24) the geostrophic velocities were essentially nil (Figs. 36b and 37b) and the barotropic tidal currents were also very limited in magnitude (Fig. 64e). That leaves only the possibilities of the Ekman-Stokes (wave) dynamics for the microstars and also the presence of a shelf-break or along-shore current set up by northerly transport by east winds that gusted to over 14*m* s^{-1} on the 21st and 22nd (Fig. 21a).

On the 26th the wind speeds diminished to ~5 *m* s^{-1}, with gusts up to 7 *m* s^{-1} (Fig. 21a,e). The directions shifted to the northeast for a period of two days, however, and although the southwest surface flows exhibited marked effects of the winds with little dispersion (Fig. 26c and 53), the flows at the other depths began to show some divergence and variable tracks (Figs. 27b, 28b and 53). At this time, the microstars exhibited repeated cyclonic orbits; a pattern that lasted until the end of the experiment (Fig. 27c,d). In contrast, the 10*m* SVPs continued to follow westerly tracks along the northern shoreline during the northeast winds and exhibited dispersion only at the end of each drift (Fig. 28b,c). During the period of slack winds starting on the 29th, however, the SVPs began moving in cyclonic circulations (Fig. 28d), with dispersion rates that oscillated from positive (divergence) and negative (convergence) (Fig. 55f). Along with the earlier patterns of cyclonic motions of the microstars, such vagaries in the flows were indicators of large-scale turbulence in the system.

5.5 Drifter Dispersion Rates

The dispersion of drifters provided an estimate of turbulent dissipation, which is quantified by eddy viscosities used in the equations of motion (Gill, 1982; Benoit and Chapman, 2008). The dispersal of drifter groups over time provided estimates of horizontal viscosities (m^2s^{-1}), but the spread of drifter pairs provided only an index of dispersion expressed as the distance between the center of mass (DCM).

The microstars exhibited some of the highest dispersion rates and hence viscosities due to a lower tendency to ground. In contrast, the ispheres typically had much shorter drift periods and frequently grounded due to wave action, but the dispersion and viscosities also varied depending on the prevailing wind conditions. In early summer and fall, the dispersion rates (Figs. 39 to 49) also increased whenever ispheres or microstars approached the shore. This was expected due to the effects of material surface boundaries forcing flows to become along-shore currents (Gill, 1982), but for the ispheres this typically required much lower amounts of wind forcing and waves. Examples of this occurred on June 27th and the 30th (Fig. 11a,b,g and h) and again on September 21st and the 24th (Figs. 18c and 19a).

Drifters at all depths exhibited positive and negative dispersion rates indicating flow divergence and convergence respectively, but whereas the rates for the ispheres and microstars varied significantly in the early stages of their trajectories, the 10*m* SVPs typically exhibited relatively gradual, limited dispersion until the middle to late portions of their deployments. Good examples of this occurred on June 27th and 29th (Figs. 39 and 40), which showed that the dispersion of the SVPs was very limited while they followed cyclonic circulations (Figs. 11c,f), then after 20*hr* during the first experiment they began to separate (Fig. 39e). The two groups on the 29th appear to move at coherent[16] velocities (Fig. 40d), but dispersion of Group B increased as they moved northward of Group A. In both cases, however, the speeds and dispersion rates oscillated over time (Figs. 39 and 40), indicating that turbulence (i.e. viscosities) also varied over space and time.

[16] Coherency (γ^2) is defined as the ratio of the cross-spectra squared to the product of the individual spectra for the velocities, and it indicates a general correlation at all the frequencies over time. Two series are considered highly coherent if $\gamma^2(f) \sim 1$ and in phase, $\phi(f) = 0$ (Emery and Thomson, 2004).

Another interesting difference between the above two deployments is how the SVPs on the 27th continued to orbit cyclonically, whereas the two groups on the 29th moved abruptly to the east after initially making northward cyclonic turns. All three deployments were subjected to westerly winds, but on the 29th the winds increased in strength and continued through July 1st (Fig. 5e). At that time the 10*m* layer appeared to be in phase with the winds, whereas on the 27th the flows were out of phase, thus providing a good example of the varied response of the subsurface water motion to wind-forcing in the upper 1*m*.

Under certain conditions the microstars in June exhibited marked variation in DCM and hence viscosity. For example, the two groups released in deployments #6 and #7 on the 27th (Fig. 11b) moved in opposite directions, but group A showed much higher dispersion in comparison to B (1.3 vs. 0.6*km*). Both groups also exhibited positive and negative dispersion rates thus showing marked variation in eddy viscosity, but near the end of the drift period the viscosity of group A increased dramatically from -20 to 88$m^2\ s^{-1}$. In contrast, deployments #12a and b on 29th (Fig. 11g,h) exhibited extreme variation in DCM and viscosity (Fig. 41). Both groups initially moved to the east, exhibiting minimal dispersion under the moderate westerly winds (Fig. 5e), but after making cyclonic turns in the north-central basin the two groups diverged overnight. Group A moved at high average speeds (40 to 60$cm\ s^{-1}$) but with limited dispersion until reaching the western shoreline where the dispersion (and hence viscosity) increased mainly due to grounding of m006. In contrast, group B showed extreme differences in relative motion that appeared to be tied to the respective locations of the two drifters and hence differing responses to diurnal wind stress on July 1st (Fig. 5a). For example, on July 1st the winds diminished overnight to speeds < 1$m\ s^{-1}$ (Fig. 5a) and the drifters reversed course probably due to the action of geostrophic currents and also from barotropic flows caused by sloping of the sea surface described in section 5.3.1. The large oscillations in dispersion rates after 20*hr*, however, (Fig. 41e,f) were entirely due to the relative motions of m007 and m008 that resulted in a peak DCM of 2.7*km* and extreme variation in the viscosity of ±300$m^2\ s^{-1}$ (Fig. 41f). An interesting pattern in the trajectory of m008 was its reversed motion back to the NW overnight on July 1st (Fig. 11h). This was very similar to earlier motions of m007 on the 21st and i0460 on the 26th.

In the fall, the dispersion of all drifters was based solely on changes in DCMs (Figs. 42 to 49), which were highly varied depending on their release locations and state of the winds. The highest initial rates, however, again occurred for both the ispheres and microstars. For example, deployments on September 21 and 22 occurred during strong northeast winds (Figs. 18a,b) and on the 21st the ispheres exhibited some of their highest dispersion, with DCMs exceeding 1.2*km* (Fig. 42). On the 22nd, however, despite having much higher average speeds (≥ 80 vs. 40-60$cm\ s^{-1}$) dispersion of the ispheres remained negligible until they reached the Narrows, but even then the DCM reached only 0.4*km* (Fig. 43). In contrast, the deployments #6 to #9 all occurred under light and variable westerly to northeasterly winds (Figs. 18c,d). The dispersion over this period was relatively minor and even the very high value of 4.8*km* for group A on the 26th (Fig. 45g) was due solely to grounding of i5600 on the western shore after passing through the Narrows.

During the remainder of the fall experiment the dispersions of the ispheres remained limited, with exception of group B on the 26th (Fig. 18e). At this time, under light to moderate (but variable) winds i5600 and i6350 diverged significantly overnight to a DCM of nearly 3.2*km*. The initial southward turning of both drifters was apparently a response to a shift in westerly winds to the northeast, but it was uncertain as to what caused the pair to drift apart so radically (Fig. 18e). The anticyclonic turning in the southeastern fjord shown by i6350 had been observed in past deployments of microstars, and the northwest trajectory of this drifter was possibly due to entrainment into the Lowe River plume, as described above in section 5.2.2. Perhaps the reversed motion of i5600 into the northeastern fjord can also be explained by northward spreading of the Lowe River and Valdez Glacier Stream plumes (Fig. 1).

The microstars also exhibited highly varied dispersion in the fall, at rates that occasionally exceeded the ispheres over the same set of environmental conditions. For example, during deployments #1 and #2 on

the 21st both groups exhibited a general outward motion under the combined influence of northeast winds and geostrophic currents, but whereas group A dispersed to a distance of ~2*km*, which exceeded the ispheres by ~0.7*km*, group B dispersed to only about one tenth in former value, i.e. 0.2*km* (Fig. 42g,h). The dispersion of the microstars at the end of #3 and #4 (Fig. 43d) also exceeded dispersion of the ispheres by 0.3 to 1.2*km* respectively. In contrast, during the period of light winds from September 23rd to the 27th, group A released on the 23rd (deployment #5) accelerated to a relatively high average speed of 40*cm* s^{-1}, but the maximum dispersion was only ~ 0.35*km*. Also, the other two groups released on the 24th barely dispersed at all (Fig. 44g,h). The average speed of group A (#5) was much greater in range (i.e. variance), and this gave them a higher dispersal in comparison to groups B (#6) and C (#7) (Fig. 44a,b).

The dispersion for the microstars for deployments #8 and #9 on the 25th occurred under very light winds (Figs. 19e) but varied geostrophic flows, which showed flow divergence at mid-fjord (Fig. 33d). Group A, which had a slightly wider range in speeds and hence greater dispersal in comparison to group B, moved outward against the diverging currents, whereas group B appeared to follow the geostrophy and moved to the NW. Deployment #10 on the 26th, however, occurred under moderate westerly winds that became light and variable (Fig. 19f). The two microstar groups again exhibited similar flow patterns and dispersed rapidly after ~15*hr* to distances of ~1.9 to 2.5*km*, (Fig. 46). However, whereas dispersion of group A was due to a marked separation of flows at the mouth (i.e. divergence) to the north and south, dispersion for group B was mostly due to grounding of m003 (Fig. 19f).

From the foregoing discussion it is obvious that the variance of the group velocities correlates well with dispersion rates but no so for velocity magnitudes, and this was thought at first to be seen in differences in speeds and dispersal rates for microstars in deployments #11 and #12 on the 27th (Fig. 47). The winds at that time were light and variable, coming from the west initially then shifting to the northeast (Fig. 19g). The drifters all seemed to respond to the wind shift by suddenly moving southward, but this direction was not in accordance with Ekman dynamics, which should have caused motions rotated to the west. The marked inflection of m008 was indeed in that direction and this created an extreme dispersion for group A of ~2*km*. However, recovery of m008 showed that it lost its drogue, converting it into a quasi-isphere described above. The northerly track of m008 was similar to the track of ispheres in #13 but not in #12 (Fig. 18f), and this provided yet another good example of a much higher variance in the surface flows due to the interaction of winds, waves and tides in comparison to currents below the surface centered at 1*m*.

The final microstar deployments #17 and #18 on the 29th (Fig. 19i) also showed extreme differences in speeds and dispersion rates for the two groups (Fig. 49e). This occurred when winds from the southeast significantly increased in speed (Fig. 19i), and although both groups initially responded by moving northward, group B quickly grounded and thus limited their total dispersion. In contrast, group C accelerated quickly under the strong southeast winds and moved rapidly outward under the combined forcing of the northeast winds and geostrophic flows (Fig. 19i). These conditions eventually resulted in an extreme maximum dispersion of > 3.5*km* within the outer fjord (Fig. 49e).

The 10*m* SVPs also exhibited highly varied amounts of dispersion in the fall (Figs 42 to 49) and, similar to June, the rates were typically limited until the middle to later portions of their deployments. Maximum magnitudes for the fall experiment (1.7 to >5*km*) occurred during deployments #1 and #2 on the 21st under conditions of steady northeast winds and cross-channel geostrophic currents (Figs. 13 and 33a,b). The interaction of these two factors may have been responsible for the cyclonic circulations initially seen in both the drifter tracks (Fig. 20a) and ADCP data on the 22nd, which confirmed these same flow patterns occurred in both the inner and central basins (Fig. 16D). The marked dispersion of the northern group on the 23rd occurred when geostrophic currents were aligned with the along-channel direction, as shown for the 24th in Fig. 33c, and the ADCP data again confirmed that a strong outflow indeed occurred on the northern side of the fjord at that time (Fig. 17A). The southern group also responded to these changes and

turned westward but with considerably less dispersal. The latter pattern was also confirmed by the ADCP data that showed slow but consistent outflow in the afternoon on the 23rd (Fig. 17A).

The dispersion of SVPs during deployments #6 and #7 on the 24th differed significantly, with the northern group B exhibiting a wide flow separation and a DCM of ~1.3*km*. In contrast, group C barely diverged at all (Fig.44). The ADCP data on the 24th (Fig. 17B) showed that flows on the southern side of the inner to mid basin were relatively uniform, but a horizontal gradient formed to the north causing cross-channel shear. These variations in flow help explain the lack of eddy viscosity in the southern drifters, whereas turbulent dissipation due to vorticity from the current shear forced a wide divergence of the northern drifters. The remainder of the SVP deployments showed relatively limited dispersion (Figs. 45, and 47 to 49), but the one exception occurred for deployment #16, in which dispersion reached nearly 1*km*. In contrast, deployment #18 was performed at the same time to the southeast in the inner basin (Fig. 20e). These two groups showed some similarity in their patterns of flow and dispersion as in groups #6 and #7 above, and this was likely due to the same flow shear and hence turbulence to the north.
During the March survey, forcing of the drifters was primarily due to the both direct and indirect effects of winds and barotropic tidal currents, as shown by the ADCP data (Fig. 25). There was an indication of slight amounts of freshwater input causing minor geostrophic flows within the northeastern region of the fjord (Fig. 36a, 37 and 38), but by the time the drifters were released, the winds had mixed the water column to the point where physical properties were very homogeneous (Figs. 23 and 24) and spatial variation in dynamic heights were negligible (Fig. 36b).

The initial deployments on the 24th were under strong southeast winds (Fig. 21e) and the ispheres showed almost no dispersion (Fig. 50e-g). However, it should be noted that the flat DCM of ~ 250*m* for group A after 6*hr* was due to their rapid, simultaneous grounding (Fig. 26a). Group B was headed to a similar fate but were recovered before they reached shore. Very limited dispersion rates of 0 to <10$m^2\ s^{-1}$ occurred for the ispheres throughout the remainder of the deployments from the 25th to the 30th (Figs. 26b-d and 51 to 55), and even as winds relaxed on the 28th and the trajectories began anticyclonic orbits possibly due to the combination of tides and inertial currents (Fig. 26d), the DCMs peaked at < 100*m*. The only exception occurred on the 27th when the ispheres were forced southward by northeast winds (Figs. 54e-f and 26d). When they reached shore, however, they dispersed to a DCM ~0.6*km* with a peak viscosity of 20$m^2\ s^{-1}$.

The microstars and 10*m* SVPs both showed higher variance in speeds relative to the ispheres and thus greater dispersion rates in general (Figs. 50 to 55), but during the deployment #1 the highest rates were shown by the 10*m* SVPs, which accelerated in speed and dispersion over the latter two-thirds of their drift period (Fig. 50). The highest dispersion of microstars, however, occurred in deployment #3 due to the westward motion of m004, which resulted in a peak DCM of over 4*km* and viscosities >150$m^2\ s^{-1}$. The dispersion at 40*m* was unknown for deployment #1 since only one drifter was released (Fig. 28e), but under the period of light winds (starting on the 27th) the two 40*m* SVPs dispersed to only 100*m* (Fig. 54d).

Both the microstars and 10*m* SVPs continued to exhibit varied dispersion rates during the remainder of the study, but the highest dispersion rates, however, occurred when moderate 5 to 6$m\ s^{-1}$ northeast winds gradually gave way to a period of quiescence (Fig. 21e). For example, after having initially moved westward in deployments #5 and #6 the microstars began showing the effects of large-scale turbulence (Fig. 27c,d). At this time they exhibited marked dispersion and DCMs peaked at ~1.7*km* but viscosities oscillated at a maximum rate of ± 200$m^2\ s^{-1}$ (53d-f). In contrast, the 10*m* SVP drifters exhibited much more limited dispersion by comparison, and in deployment #3 this occurred at the end of the drift period along the outer, northern shoreline and mainly due to the southerly motion of s002 (Figs. 28b and 51). When wind speeds began to drop during deployment #5, the SVPs dispersed again over the same area and reached a maximum DCM of ~0.7*km* and with minimal viscosities (Figs. 28c and 53d-f).

5.6 Circulation Patterns Affecting Flushing and Retention

In a past study of water exchange for Port Valdez, Collonel (1981) concluded that flushing of the Port occurred in a matter of several days, but a unique residence time was inappropriate due to the randomness of weather systems passing through PWS that appeared to be more effective in promoting deep water exchange. He does, however, state a composite residence time estimated at a few weeks.

Although measuring the net exchange of water between Port Valdez and PWS was not a goal of this study, the conditions causing either flushing or retention were inferred by the drifter trajectories and the magnitudes of the along-channel (*u*) velocities. The latter differed significantly for the upper 1*m* layer versus the subsurface water (Appendix D) depending on the patterns of winds and baroclinic flows, driven respectively by the seasonal changes in meteorology and hydrography. In June, for example, the times of flushing or retention at 10*m* were consistent with Collonel's estimates, with averages of 2.5 to 6.5 days respectively (Table 2b). Certain deployments also suggested retentions up to 15 days or longer.

A caveat to interpreting these estimates, however, is that they are somewhat arbitrary since they presume that the conditions causing drifter motions remain stable. The time series in section xxx were constructed to place retention and flushing in a perspective based on *u* velocities and drift durations.

5.6.1 Early Summer

In June, the along-channel flows were strongest for the ispheres (Table 2a) and the positive average (net) *u* velocity (5.1$cm\ s^{-1}$) indicated that the surface water was mostly being retained (Fig. 61A). Also, due to the added effects of wind and wave action 88% of the isphere deployments ended with grounding. The water at 1*m* also exhibited a general retention (Fig. 61B) but with only two cases of grounding. Also, when the trajectory of m001a was split into respective r/f values the total net *u* velocity increased to 2.3$cm\ s^{-1}$. Although the principal axes of the surface and 1*m* drifters in June showed an average water motion aligned along a WNW to ESE axis (Table 2b), the large standard deviations (SD) of the rotation angles indicated that cross-channel (*v*) velocities had marked effects on the flows (Figs. 56 and 57). This was also quite evident by the large oscillations within the fjord exhibited by many of the ispheres and certain microstars (Figs. 10a,c,e,f). The motions of the 10*m* and 40*m* SVPs were much more subdued by comparison, and whereas the former drifters generally exhibited large, mesoscale cyclonic circulations (Fig. 10g,h), the 40*m* SVPs just oscillated back and forth at low rates of only 2 to 10$cm\ s^{-1}$ (Fig. 10i). Over time the net *u* velocity at 10*m* was small and negative (-0.3 $cm\ s^{-1}$), but the bulk of the subsurface motion showed retention (Fig. 61C). The small, eastward flow at 40*m* (0.9 $cm\ s^{-1}$) also suggested that the deep subsurface water was being retained within the inner basin (Fig. 10i).

The dispersion experiments conducted on June 27th (Fig. 11a-c) showed extreme shear within the upper 1*m*, as ispheres and microstars moved in nearly opposite directions (~130^{o}). A similar velocity shear was also shown by the profile of the average *u* velocities for the second segment of the experiment (Fig. 60a). In contrast, the flows at 10*m* during the first dispersion experiment were decoupled from the upper layers and moved in progressively wider cyclonic orbits (Fig. 11c). A number of studies of wind-induced circulation in fjords (Svendsen and Thompson, 1978; Klink et al., 1981; Stacey et al., 1995 and Stacey, 1999) have shown that when the density stratification is strong the direct effects of winds are limited to the upper few meters. In addition, model results of Svendsen and Thompson (1978) and Klink et al. (1981) have indicated that when the fresh surface layer is quite thin ($\leq$ 1*m*), as it was for Port Valdez in June (Fig. 6), the layers become distinct and the pressure gradient in the upper layer sets up a strong velocity shear across the layer directly beneath. The above studies also showed that whereas the currents at 5 and 10*m* were out of phase with the wind, the water below 20*m* was in phase.

All of the above descriptions were generally consistent with the observations of drifter motions in June within Port Valdez. However, during the second dispersion experiment on June 30th the circulation mode at 10*m* changed rapidly from open cyclonic turning to linear, easterly flow not long after diurnal, westerly winds had increased to speeds of 5 to 6*m* s^{-1}. During the previous afternoon sea breezes, the SVPs showed significant initial accelerations to speeds of 17 to 37*cm* s^{-1} (Fig. 40d) followed by periodic bursts in speed that peaked at 8 to 12*cm* s^{-1}. All of this indicated that the wind driven currents were reaching 10*m* in depth, but based on the Ekman dynamics (eqns. 1 to 3) these currents could have ranged from only 1.7 to 2.6*cm* s^{-1}. So, obviously, some additional forcing was required to produce both of the above circulation modes. Since ADCP data were not available to examine the vertical changes in flow structure, the causes of such unusual trajectories remain uncertain, and a circulation model may therefore be required to fully unravel the true effects of wind and other factors forcing the baroclinic subsurface flows in June.

As mentioned above, the flushing and retention times calculated for each deployment assumed that conditions remained stable over time, and to predict how these properties might extend beyond retrieval times required considering the positions of drifters during recovery and either the prevailing wind and oceanographic conditions occurring at that time or how drifters of the same type responded during prior releases for similar locations and conditions. For example, the microstars in deployment #12b exhibited flushing at -1.3*cm* s^{-1} (Fig. 61B) but it was apparent that due to the strong westerly winds on July 1st (Fig. 5e) both drifters would have most likely been retained within the fjord. This conclusion was predicated on the drift patterns exhibited by m001 and 7 on the 23rd (Fig. 10e,f), which also occurred during strong westerly winds. Such winds would have impeded surface estuarine currents and created marked fronts of freshwater similar to those observed along the Mineral Creek delta early in the June survey (see section xxx). In contrast, the strong net negative *u* velocities (-22.6*cm* s^{-1}) observed overnight for microstars in deployment #12a indicated that they could have eventually flushed out of the fjord. This rapid outflow would possibly have been a product of the combined effects of current reversals due to piling of water in the inner fjord by wind transport followed by the release of estuarine outflow similar to the observations for the Jøsenfjord in Norway (Svendsen and Thompson, 1978) described above. A lingering question is how much water would have actually been exchanged and how much would have simply moved back into the Port, as in two such cases of flushing for ispheres and microstars (Fig. 10b and 10e).

A similar pattern of flushing occurred along the southern side of the fjord overnight on the 27th for microstars in deployment #6. In this case, however, the net *u* velocities were less than half the values of the northern drifters (Table 2a). Freshwater discharge is minor on the southern side of the fjord (Sharma and Burbank, 1973) but any discharge would tend to disperse northward and eastward due to Coriolis. The slower outflows on the southern side were thus possibly a barotropic response caused by both the restoration of a level sea-surface following a change in wind stress and an ebbing tide, and at 1*m* these flows may have been impeded (slightly?) by an eastward estuarine pressure gradient. However, another possible cause of reversed currents close to the sides of the fjord is frictional stress at the solid boundaries. In Puget Sound, for example, Matsuura and Cannon (1997) found that following maximum acceleration of flows during wind events, such frictional effects caused deceleration and reversal of currents even though the wind direction had not changed.

5.6.2 Early Fall

In September flushing at the surface increased by 31% relative to June but conditions still generally favored retention (Fig. 63A). In contrast, flushing at 1*m* significantly increased by 60% and at 10*m* the subsurface water exhibited only a modest increase in flushing of 11% (Fig. 63C). Although the average principal axes for all depths were closely aligned with the along-channel direction, the rotation angles for the surface and 1*m* flows had very high SD values (Table 3b). The variances for the major and minor axes were smaller in comparison to June (Table 3a) and indicated that the cross-channel (*V'*) flows had less influence on the currents. As a result, the variance of the flows was more aligned along the major axes

(Figs. 57 and 58). For the ispheres the cross-channel flows were still important, however, and grounding occurred in all cases of retention. Although large rotation angles occurred for some of the isphere and microstar deployments (Table 3a and Figs. 56A,G), the net *u* velocities were 2 to 13 times greater than in June (Tables 2b and 3b), causing faster drift times on average in the upper 1*m* (Figs. 61 and 63).

The proximate causes of the increased flushing for the surface and 1*m* flows were changes in wind stress. For example, in deployments #1 and #2 westerly winds (Fig. 13) appeared to initially impede the outward motion of both sets of drifters, but after the winds reversed all the drifters accelerated to average speeds ranging from 40 to 60$cm\ s^{-1}$ (Fig. 42). This was likely also due concurrent restoration of the sea-surface elevation and a release of estuarine surface flow, and as a result, both sets of drifters had relatively large negative average *u* velocities ranging from -10 to -18$cm\ s^{-1}$ (Fig. 63A). The ispheres turned gradually to the southwest after nearing Shoup Bay, whereas the microstars either continued westward and grounded or turned southwest into the 'Narrows' (Fig.19a). On the following day, all the ispheres and microstars flushed completely from the fjord (Figs. 18b and 19b). The principal axes (Fig. 66) showed that the flow variances for all six drifters were closely aligned with the along-channel direction in contrast to the previous day (Fig. 58A) when large, positive rotations indicated greater effects of cross-channel (*v*) velocities. The winds each day were strong and from the northeast (Fig. 13) and blowing down-fjord, so it was uncertain as to what caused the varied trajectories. However, an examination of the wind data collected near the mouth at Potato Point revealed a possible explanation.
On the night of the 22nd the winds remained strong (8 to 10$m\ s^{-1}$) and were from the north (16 ^{o} to 18^{o} true), whereas on the night of the 23rd the winds were weaker (<1 to 5$m\ s^{-1}$) and variable in direction. This indicated that crosswinds at the mouth were possibly responsible for the southward isphere trajectories, but the 1*m* flows showed less of a response due to the limited fetch and duration of the wind. On the following day the reduction in wind stress was the most likely cause for all the drifters to adhere more closely to the along-channel direction. A similar pattern to September 22nd occurred for the ispheres in deployments #14 and #16, in which the principal axes (Fig. 58F,G) are directed towards the northwest where i5600 and i9180 grounded just to the east of Shoup Bay (Fig. 18g).

The remainder of the isphere deployments showed mixed responses to a decrease in wind speeds and variable directions (Fig. 13e), with 67% of the tracks showing flushing and 33% showing retention (Table 3a). Thus, it seemed that the varied combinations of direct effects of winds on leeway along with Stokes-Coriolis force and cross-channel surface currents caused 100% grounding of the ispheres exhibiting retention and 40% for the ispheres exhibiting flushing along with grounding in the fjord (Fig. 63A). Had all of the latter drifters escaped, the r/f percentages would be reversed, i.e. 32% and 68% respectively.

Of the remaining microstar deployments, 67% resulted in flushing with only three cases of grounding inside the fjord in (Table 3a). Also, the majority of the retentions (83%) were the result of grounding on the far western shoreline after the drifters had flushed past Shoup Bay (Figs. 19b,e-f). All these results suggest that circulation at 1*m* was also driven by combinations of wind stress and estuarine surface currents. At times, the currents were dominated by opposing winds, but if the winds were in the same direction (hence synergistic), the water at 1*m* moved outward at relatively high speeds. When winds were light and variable, however, the estuarine surface flow dominated and caused gradual flushing.

In contrast to the surface and 1*m* drifters, the 10 and 40*m* SVPs appeared to mainly respond to tidal and geostrophic flows and indirectly to wind stress. For example, with no density stratification the currents at 10*m* under a 4$m\ s^{-1}$ wind would be < 1.0$cm\ s^{-1}$. However, stratification from freshwater in September was still predominately above 5*m* in the water column (Fig. 14), thus the flows ≥ 10*m* were likely decoupled from direct effects of winds, but not from baroclinic responses to wind driven surface transport. For example, during deployments #1 and #2 the net flows at the surface and 1*m* (Figs. 18a and 19a) were westward and in phase with the wind (Fig. 13e), whereas the currents at 10*m* (Fig. 20a) appeared to be decoupled between the middle and inner basin. The flows in both basins initially moved eastward (Fig.

20a), but the SVPs at mid-fjord reversed to the west and then began making cyclonic orbits while moving steadily inward, and thus showed retention (Fig. 63C). In contrast, the SVPs in the inner basin quickly began making closed cyclonic circulations, but eventually they exhibited flushing by moving westward within the northern half of the basin where they dispersing widely within the outer fjord (Figs. 20a and 42). At 40*m* the westward motions of SVP 002 (Fig. 20f) were initially in phase with the northeasterly winds (Fig. 13e), then over the next few days when SVPs 001 and 003 were released, the motions of all the drifters showed highly varied cyclonic and anticyclonic patterns under a lengthy period of low wind stress. At the end of the experiment, however, the strong northeasterly winds resumed (Fig. 13) and all three drifters exhibited westward motions that were in phase with the wind.

The middle and inner regions of the fjord basin also showed varied responses to baroclinic currents driven by the density field (Fig. 33a,b). For example, when the winds were from the west the geostrophic flows showed a northward cross-channel exchange within the inner basin that eventually changed to an along-channel (westward) direction after the winds switched to the northeast (Fig. 13e). Due to continuity, the cross-channel exchange may have initiated a balancing inflow of saltier oceanic water in the south, which would have forced the aforementioned eastward estuarine gradient closer to the southern side of the fjord. Eventually, this would have set up the changes in dynamic topography (Fig. 33b) that caused the outward motion, but only if the flows were indeed in geostrophic equilibrium.
The remainder of the 10*m* SVP deployments showed varied responses to fluctuations in wind stress and the effects of geostrophic currents within the inner basin versus the outer fjord. Although a nearly equal number of the remaining cases showed flushing versus retention, four were questionable (#9, #11, #12 and #18) and in one case (#8) the average *u* velocity was so negligible that the retention exceeded 1000*hr*. Deployment #12 also showed retention (Table 3a) and exhibited an anticyclonic circulation mode similar to #8 and #18 within the inner basin. However, flushing of the subsurface layer was only definite when both wind and geostrophic currents caused outflows within the northern half of the basin (Fig. 20a) or under light and variable winds geostrophic currents caused outflows in the middle to outer basin (Fig. 20c,d). Even under these conditions, however, the time of flushing exceeded 3.5 days (Table 3).

5.6.3 Late Winter

The conditions in March generally favored flushing, as indicated by the predominance of large, negative along-channel (*u*) velocities (Table 4 and Fig 65). For example, the *u* velocities in March were 5 to 11 times higher on average in comparison to June (Table 2b) and 2 to 5 times higher for the surface and subsurface currents in September (Table 3b). The average flow at 1*m*, by contrast, was significantly lower in March ($p < 0.05$) (Appendix D), and this was related to rapid decelerations of the microstars due to the reduction in wind stress in the middle of the experiment.

The large velocity shear between the surface and 1*m* during segment one (Fig. 64a) was unusual, however, in that the vertical transfer of wind momentum should have been unimpeded given the negligible density stratification (Figs. 22 to 24). For example, the shear in the *u* velocities was significant ($p < 0.05$) with an average variation between the surface and 1*m* equal to ~ -23$cm\ s^{-1}$. During the first segment, the wind speeds ranged from 8 to 12$m\ s^{-1}$ (Fig. 21a,e), and this would have generated surface currents ranging from 10.6 to 16.3 $cm\ s^{-1}$. However, the ispheres had average speeds of 37.4 to 39$cm\ s^{-1}$ (more than double the above speeds) and maximum speeds that reached 40 to 45$cm\ s^{-1}$ (Fig. 50a,d). The average speed of the microstars (14.4$cm\ s^{-1}$) was smaller by comparison but was within the range of the wind driven currents for 1*m* (e.g. 9.7 to 15.4$cm\ s^{-1}$). The maximum speeds, however, exceeded 25$cm\ s^{-1}$.

The lack of density stratification in March resulted in very limited magnitudes for both dynamic heights (Fig. 36) and geostrophic flows (Figs. 37 and 38), and thus the additional energy causing the high velocities of the ispheres probably came from direct wind forcing and Stokes-Coriolis forcing by waves (Röhrs and Christensen, 2015). The additional bursts of speed at 1*m* may also have been caused by the

latter force, but wind energy affecting both this layer and the surface may have also been greater than the amounts predicted by the Ekman euqation solutions alone. This also was evident in both 10*m* and 40*m* SVP drifters early in the March experiment. At this time all drifter tracks indicated that the effects of winds penetrated the entire upper 40*m* of the water column. For example, steady 10*m* s^{-1} winds yielded an estimated Ekman depth of 46*m*, and the wind-generated currents at 10*m* and 40*m* would have been only 6.8 and 0.9*cm* s^{-1}. However, the average speeds of the SVPs were ~9 and 5*cm* s^{-1} respectively, indicating that actual amounts of wind momentum were much greater than the predicted amounts at both depths. Also, earlier in the month the winds reached 20*m* s^{-1} (Fig. 21), which would have produced a $D_E > 90m$. This left no doubts that the motions of even the deep 40*m* SVPs (Fig. 40e) were under marked influence of the katabatic, easterly winds early in the experiment.

The velocities of the ispheres exhibited rapid responses to changes in wind directions between the first and second segments of the March experiment. For example, During the initial deployments (#1 to #3) easterly winds drove all ispheres rapidly to the northwest to ground on the shoreline, whereas in deployments #4 to #6 the moderate northeast winds drove them more slowly to the southwest shore where they dispersed to the west (Fig. 26a to d). Eventually, a period of calm ensued followed by light westerly winds (Fig. 20e). At this time, the ispheres began their slow average eastward motion (5.6*cm* s^{-1}) back into the fjord (Fig. 20d) and thus showed the only case of retention based on *u* velocities (Fig. 65A). The flushing rates for the above periods (Table 4a) also directly reflected the changes in winds, and ranged on average from 10 to 20*hr* under the influence of strong easterly winds and 31 to 70*hr* as northeast winds gave way to calm conditions.

The water at 1*m* also initially exhibited flushing under the action of the easterly winds (Fig. 27a). What was interesting, however, were the rapid changes in circulation modes that occurred once the winds shifted to the northeast and diminished to a consistent speed of ~ 4*m* s^{-1} (Fig. 21e). In deployment #3, for example, the response to the change in winds was highly varied, and m006 exhibited flushing while m004 and 5 showed slight retention (Fig. 65B). In deployments #5 and #6 the winds relaxed allowing mesoscale turbulence to move the microstars in a series of lengthy cyclonic orbits of in the outer fjord (Fig. 27c,d). In both deployments the average *u* velocities were very small, and even though they were negative the flushing periods were long, and ranged from 3.6 to 4 days for deployment #5 and 8 to 20+ days for deployment #6, thus causing classifications as both flushing and retention (Table 4a). Indeed, the flushing rates for the 1*m* layer ranged on average from 28 to 45*hr* under the strong easterly winds and from 197 to 325*hr* during the transitional period from northeast winds to calm conditions.

The flows at 10*m* and 40*m* exhibited significant lag times in response to the changes in wind stress. For example, the 10*m* SVPs during deployments #3 and #5 (Fig. 28b,c) exhibited a much different response to the northeast winds and decelerations in this layer significantly lagged that of the 1*m* layer. By the morning of the 29th, however, turbulence began to also affect the 10*m* SVPs, as shown in deployment #8 by the large, cyclonic turning in the outer basin (Fig. 28d). The negative average *u* velocities indicated that flushing was occurring in this layer, but due to the very small velocity in deployment #8b (Fig. 65C) the water was actually retained by default, whereas the drifters in deployment #8a exhibited very slow flushing. The lag time for slowing of the 40*m* SVPs (Fig. 28f) significantly exceeded that of the 10*m* drifters, as shown by a very slow, cyclonic arc in their trajectories from the 27th through the 29th. The deep subsurface layer did not start to decelerate until the 30th when the drifters started to meander southwards. The average *u* velocity was negative, albeit very small, and thus it was questionable whether this layer would have continued flushing or have been retained (Fig. 65C).

5.7 Changes in Circulation Modes due to Winds

All of the circulation patterns described above showed that winds in Port Valdez played a major role in causing rapid changes in circulation modes, sometimes on the order of hours. Disruption of a mesoscale cyclonic eddy in central PWS by winds was described by Halverson et al. (2013b), in which the circulation shifted between three modes: anticyclonic, open cyclonic and closed cyclonic, all of which depended on the strength and direction of the wind stress. The transition between the two cyclonic modes, for example, occurred in as little as one day and was related to the magnitude of northerly wind driven currents impeding southerly geostrophic recirculation on the western side of central sound. When southeast wind stress was weak the closed core circulation developed and vice versa for the open mode.

In Port Valdez, the winds in June alternated between strong westerly (up-fjord) winds in the afternoons and evenings followed by weak and variable winds at night that frequently blew from the northeast and hence down-fjord (Fig. 5e). Although the circulation in the upper meter initially exhibited mesoscale oscillations due to the diurnal shifts in wind, the subsurface flows at 10*m* and 40*m* were much less affected, showing mostly large to medium cyclonic eddies at 10*m* and very small oscillations at 40*m* with gradual eastward motion. On June 27th, however, the winds slackened somewhat and the circulation at the surface and 1*m* showed marked amounts of shear, with the ispheres moving eastward and the microstars moving initially to the south followed by westward motion along the shore (Fig. 11a,b). During next deployment the west winds began to increase again and moved the microstars eastward into the inner basin. On the following day (29th) the west winds continued to gain strength and both the ispheres and microstars were driven towards the southeast, where the ispheres quickly grounded on shore.

In September, the winds again rapidly disrupted the circulation at the surface and 1*m* but exhibited a lag time in affecting the subsurface flows. For example, prior to the fall experiment from September 20th to the 21st the winds exhibited a pattern similar to summer with daily (diurnal), moderate westerly winds, shifting to nightly, light and variable down-fjord winds (Fig. 13). The initial circulation at 10*m* showed the drifters following closed cyclonic and anticyclonic eddies similar to June, but early on the 23rd these patterns were disrupted by a marked increase in wind stress from the northeast and drifters in both deployments began to move down-fjord in the direction of the winds. The closed cyclonic eddy patterns at 10*m* were never observed again over the remainder of the fall experiment. The three 40*m* SVPs, by contrast, exhibited eddy circulations that persisted throughout the period of weak, variable winds, until September 29th when strong northeast winds (Fig. 13) possibly along with geostrophic outflow moved these drifters westward along the northern shoreline (Fig. 20f).

A similar, but reversed, scenario occurred in March, when relaxation of wind stress allowed mesoscale turbulence to reestablish cyclonic eddies at mid-fjord for both the 1*m* and 10*m* flows. In all cases, however, once the katabatic winds commenced again, any material in the upper 40*m* within the outer fjord would likely flush from the system. So although conditions in late winter were conducive to flushing, any contaminants contained in the upper 10*m* could easily also end up in the intertidal zone, and much of the material moved by surface currents would likely contaminate the shoreline.

5.8 Locations at Risk from Contaminants

The Lagrangian flow patterns shown by the drifter trajectories indicated where currents either moved water onshore or closely followed the shoreline and hence locations that may be at risk of contamination from spilled oil due to the circulation. Although these patterns did not occur continuously, some of them were repeated frequently enough to warrant discussion of what are the most probable natural collection sites in Port Valdez. The 10*m* and 40*m* SVPs did not ground frequently but if dispersants were applied to

spilled oil, allowing it to mix vertically in the water column, the motions of these drifters could also indicate where oil might contaminate the intertidal to deeper subtidal benthic zones.

Fig. 67a shows a hypothetical schematic of oil dispersing northeastward from the Valdez Marine Terminal (VMT) based on the prevailing westerly winds in June 2016 (see insets of wind vectors and histogram of directions in wind rose). The colored lines in the figure indicate locations where drifters either grounded or came close to shore. Thus depending on which release points (Fig. 2d) the 'dispersed' oil reached, these would be the potential areas at risk of contamination. This would also depend on the mixing depth, which in turn is moderated by the seasonal meteorological and oceanographic conditions.

For example, if oil were spilled in early summer then most of the wind induced mixing would be contained at depths well above the pycnocline, which ranged from 5 to 15*m* (Fig. 6). The limitations on vertical mixing due to the presence of very fresh surface water in early summer were discussed above. However, high amounts of retention in June also caused numerous cases of grounding for the surface drifters (88%) and a few cases at 1*m* (31%). The drifters also came very close to shore on occasion, and as a result there were thirteen locations in June that were deemed as probable natural collection sites for oil spread within the upper 1*m*. These included various points shown as red and blue lines along the northern shoreline extending from east of Shoup Bay to Gold Creek and Mineral Creek Deltas and along the peninsula one nautical mile to the east; the eastern shoreline from the Valdez Glacier Stream northwards to the 'Duck Flats' region; the southeast region from the Lowe River to Solomon Gulch; the southwest shoreline east of Anderson Bay and at Entrance Island; and the entire western shoreline south of Shoup Bay. Only 20% of the 10*m* SVP deployments resulted in grounding, and these occurred in two intertidal/subtidal sites shown in green at Entrance Isl. and the shoreline west of Gold Creek (Fig. 67a).

In the fall, the prevailing wind directions were still westerly (Fig. 67b) but the speeds were low in magnitude in comparison to the two periods of northeast (down-fjord) winds (Fig. 13). This might cause oil to initially disperse laterally along the southern side of the fjord, as shown in Fig. 67b, and based on the high amount of density stratification the mixing depths may also be limited to the upper water column as in June. However, the surface salinities tended to be more brackish by comparison and the pycnoclines were deeper, and this might allow strong down-fjord winds to mix 'dispersed' oil deeper than 15*m*, possibly down to the depths of the thermostads and quasi halostads (Fig. 14).

The conditions in September favored flushing, but 64% of the surface deployments and 44% of the 1*m* deployments resulted in grounding or currents coming close to about sixteen 'sensitive sites', many of which were similar to June. These included the southwest shorelines at Valdez Narrows, Entrance Island and points east of Anderson Bay; the western shoreline south of Shoup Bay; the northwest shoreline between Shoup Bay and Gold Creek delta; the northeast shoreline both west and east of the harbor entrance and potentially into the 'Duck Flats' and nearby islands; the eastern shoreline north of the Valdez Glacier Stream; and southeast shoreline near Solomon Gulch (Fig. 67b). Although there were no groundings of the 10*m* SVPs in the fall, some came very close to northern shoreline east of Mineral Creek and the southeast shoreline near Solomon Gulch possibly putting the intertidal/subtidal areas there at risk. The 40*m* SVPs remained well offshore until late in the survey, at which time they appeared to respond to a second period strong northeast winds and grounded west of Gold Creek (Fig. 67b).

In late winter, strong easterly winds would cause an initial northwestward motion of oil shown in Fig. 67c. The vertical mixing of the 'dispersed' oil could be quite deep given the lack of buoyancy in the upper water column due to the homogeneous water density (Figs. 22 and 23). An alternate scenario is also shown in which oil initially disperses to the east under the influence of weak westerly winds (the light grey area extending towards the Lowe River). However, once the strong katabatic winds recommenced (Fig. 21), this oil would also move rapidly to the northwest. Such conditions caused 100% of the surface drifters to ground while flushing (Table 4a and Fig. 65A) and although all the 1*m* and 10*m* drifters also

exhibited flushing, only 20% of the former and 40% of the latter grounded along the southern and northern shorelines respectively (Fig. 65B and C).

In March, the prevailing down-fjord winds were from the southeast and northeast (Fig. 67c), and this would cause both sides of the fjord to be at risk from oil contamination due to marked cross-channel flows. However, the responses to the wind forcing varied between the surface and subsurface layers. For example, during the easterly wind events both Coriolis and Stokes-Coriolis forces along with direct wind forcing caused the surface drifters to reach the northern shore in a matter of hours. In contrast, the subsurface drifters at all depths turned westward after reaching the northern side and moved outward along the shore (Figs. 26 to 28). Potential 'sensitive sites' were thus distributed along the entire northern shoreline extending from one nautical mile east of Mineral Creek all the way to Shoup Bay (Fig. 67c). During the northeast wind event, however, the surface drifters moved southwestward as expected (Fig. 26c,d), whereas the 1*m* microstars began a series of cyclonic circulations that kept them in the main fjord until near the end of their drift periods when the winds ceased (Fig. 27c,d). Thus the shoreline at various points between the Security Zone and Anderson Bay were at risk from surface oil, but when weak westerly winds commenced the 1*m* drifters also turned southwards, and had they not been retrieved, they too potentially would have reached the southern side (Fig. 67c).

The 10*m* and 40*m* SVPs exhibited a completely different response to the extended period of northeast winds in comparison to the surface and 1*m* drifters. For example, both sets of subsurface drifters continued to move outward along the northern shoreline as if driven by an inertial current (Fig. 28b,c and e). The 10*m* drifters grounded twice just east of Shoup Bay (Fig. 67c), but ultimately the subsurface outflow subsided and these drifters began a series of tight cyclonic (counter-clockwise) orbits maintaining their position in the middle of the outer fjord basin (Fig. 28d). In contrast, the two 40*m* SVPs made wide cyclonic turns to the southwest (Fig. 28f), and although none of these drifters grounded they did come close to the northern shoreline during both deployments (Fig. 28e,f). Thus all the subtidal locations at risk, including some of the deeper 40*m* regions along the side of the fjord, were mainly confined to the northern shoreline between Shoup Bay and Gold Creek (Fig. 67c).

From the foregoing discussion it can be seen that although the meteorological and oceanographic conditions differed between the summer and fall, the locations at risk of contamination by oil dispersed in the upper 1*m* are very similar in both seasons. There were other 'sensitive' sites as well during these seasons, but the common collection areas were unexpected due to the marked differences in wind patterns and density stratification from freshwater content. Late winter represented a completely separate scenario, however, in which failure to contain any spilled oil could result in a rapid and widespread contamination of the outer fjord, particularly over the northern shoreline. The frequent shifting of strong winds from east to northeast also means that the southwestern region could also be very much as risk as well.

5.9 Dispersant Effectiveness with regards to Temperature and Salinity

Past studies reviewed by Fingas (2004) show that the effectiveness of surfactants in dispersing oil depends on the type of dispersant, salinity, temperature and the specific type of oil. Surfactants (the primary ingredient in dispersants) create either water-in-oil emulsions or oil-in-water emulsions depending on the hydrophilic-lipophilic balance (HLB) (Becher, 1977). Dispersants with HLB values of 1 to 8 promote the formation of water-in-oil emulsions, whereas those with values ranging from 12 and 20 promote the formation of oil-in-water emulsions. The typical dispersant is formed from two non-ionic components and one ionic component, yielding an HLB of ~10. This gives the dispersant a molecular force with equal amounts of hydrophilic and lipophilic tendencies.

The hydrophilic portion of a surfactant is strongly affected by the ionic strength of seawater based on

salinity (Becher, 1977). The higher the salinity, the greater the ionic strength promoting stability to the surfactant-stabilized droplet. In this regard, surfactants applied in low salinity environments have long been known to be much less effective in dispersing oil (Martinelli and Lynch, 1980; Belk et al., 1989; Fingas et al., 1991; 1995b; MacKay, 1995).

The effectiveness of dispersants on Alaska North Slope (ANS) oil has also been shown in laboratory tests conducted by Moles et al. (2001, 2002) to be related to both temperature and salinity. The lower the values of both variables, the less effective is the dispersant. However, this varied depending on the type of dispersant tested; these included Corexit 9527 and Corexit 9500. The latter relationship was also stronger for fresh versus weathered or emulsified oil. The general conclusions by the above authors was that under the range of temperatures and salinity (T/S) of most Alaskan estuaries dispersants would be largely ineffective, and that the maximum effectiveness would be ~10%.

Prior to changes in Alaskan dispersant policy circa 2016, there had been three distinct dispersant zones designated in Prince William Sound based on T/S data collected by Gay and Vaughan (2001) and Vaughn et al. (2001), and modeling work performed by Bang and Mooers (2003). Each zone had differing levels of permissions required for the use of dispersants. Zone 1, for example, required no government permissions, whereas zone 2 required consultation with both the EPA and the State of Alaska. Zone 3 allowed no dispersants application due to the inherent low salinity of the nearshore zones. Port Valdez, however, was unique in that it had seasonal designations to account for seasonal salinity changes. Following these 2016 changes to policy, the use of dispersants now requires a case-by-case agency consultation process prior to being used *anywhere* in PWS. The actual data and analyses presented through this project and summary report are good examples of the types of information needed to make these decisions.

The current research on Port Valdez has shown that in early summer and fall the surface waters of the Port are very brackish (i.e. low salinity)and cool. In June 2016, for example, the average cross-channel surface temperatures (T) and salinities (S) ranged from 8.5 to >13^oC and ~5 to 12 respectively (Fig. 6). The temperatures within the seasonal thermocline decreased monotonically to ~6^oC at 42m and below this depth T increased only slightly (~7^oC). In contrast, salinity rose rapidly to value of nearly 28 at the base of the halocline at ~10m depth, and then gradually increased with depth to a value of ~32. In September 2016, the range of average surface T/S values was slightly lower (8.5 to ~10^oC) and higher (~8 to 15) by comparison, but the depth of the seasonal halocline was similar to June ending at ~8m. The start of the seasonal thermocline and point where S $\geq$ 28 were significantly deeper, however, ranging from 40 to 50m (Fig. 14), and the depth of the seasonal thermocline also increased to 60 ± 5m. Beneath this layer the T/S values gradually increased to ~ 6.7^oC and 32.5 respectively.

Given the above physical properties in the summer and fall, it is doubtful that surfactants would be very effective on dispersing oil spilled within the surface layer. Although wave action due to winds could potentially increase the depth of mixing of the oil/water droplets, the strong density stratification would likely prevent it from reaching depths where the optimal salinity of 22 would promote increased surfactant effectiveness described in the literature. Instead, both the wind induced currents and Stokes-Coriolis force along with geostrophic flows would disperse the oil around the fjord, where it would either contaminate the nearshore zones or advect it out of the fjord.

In late winter, the physical properties were relatively cold, salty and homogeneous (Figs. 22 and 23), and the lack of density stratification would allow material to become vertically mixed in the upper water column. The high salinities (>32) would also promote a greater HLB and hence create more stability of the oil/water droplets. However, the effectiveness of the high salinity may be partially offset by the very low temperatures (>5 ^oC). Also, depending on the prevailing wind directions the oil could be dispersed along the shoreline and the deeper oil might impact a larger vertical section of the intertidal zone. In

addition, whenever the winds relaxed entirely (e.g. as in late March 2016) the oil/water mixture would simply be retained within the fjord by eddy motions. The effects of circulation on flushing rates are discussed further in the next section.

6.0 SUMMARY AND CONCLUSIONS

Three separate circulation experiments were conducted in Port Valdez, Alaska during early summer (June) and fall (September) of 2016, and late winter (March) of 2017. During each experiment, oceanographic data on currents and hydrography were collected while simultaneously deploying drifter buoys at the surface (ispheres) and depths of 1*m*, (microstars), 10*m* and 40*m* (SVPs). The data on currents were collected over five day periods using a towed 150*kHz* acoustic Doppler current profiler (ADCP) over a series of transects covering the inner basin to the middle of the fjord. Temperature and salinity (T/S) profiles were collected on every other ADCP run with a SeaBird SB19*plus* CTD (conductivity, temperature and depth) profiler at stations located along the transects. Ancillary data were obtained from a NOAA PORTS weather station located at the City Dock in Valdez.

Data analysis in addition to basic statistics included: 1) dynamic topography and geostrophic flows calculated from the density field; 2) wind induced currents for the upper 40*m* calculated from equations based on Ekman dynamics (Pond and Pickard, 1991); 3) drifter dispersion based on the distances to the center of mass and changes in dispersal area (three drifters minimum); and 4) principal axes of variation of drifter velocities, which gives rotation angles showing principal flow directions based on the variances associated with major and minor orthogonal axes. Estimates of flushing and retention times were also derived using the average along-channel (*u*) velocities and either the drift durations or distances from the mouth (i.e. flushing) or the eastern side of the fjord (i.e. retention).

The results showed that patterns of circulation inferred from both Lagrangian flows and ADCP currents differed significantly between seasons, with circulation modes in the summer and fall highly driven by the density (mass) field created by spatial variation in solar heating and freshwater input from cold, glacial sources. The geostrophic currents were significantly moderated by up-fjord and down-fjord winds, which caused changes in circulation modes on the order of hours from open and closed cyclonic and aticyclonic modes to linear flows oriented primarily in the along channel (*u* velocity) direction.

In late winter the water column had nearly uniform physical properties due to vertical mixing from winds and thermohaline convection, and the flows exhibited linear patterns at the surface driven diagonally northwestward where drifters grounded onshore by wind and wave action. The 1*m* and subsurface flows also moved northwestward, but instead of grounding these flows turned cyclonically westward and then moved out along the northern shoreline. When the wind stress was reduced and changed directions, however, mesoscale turbulence reestablished cylonic and anticyclonic modes of circulation in the 1*m* but similar changes in the 10*m* currents lagged the surface currents by about one day following the start of a period of calm conditions.

In all seasons a westerly (outflow) current was observed along the northern side of the fjord, driven by different seasonal forcing mechanisms. In the summer and fall, for example, the outflows were related to estuarine (i.e. geostrophic) currents that were either enhanced or impeded by down-fjord and up-fjord winds respectively. In contrast, the outflow in late winter was generated by strong easterly winds that transported water to the northern side of the fjord, and thus set up a basin-scale cyclonic circulation extending to at least 40*m* in depth.

In many cases the ADCP data verified the 10*m* and 40*m* subsurface Lagrangian flow patterns. For example, in June the 10*m* currents exhibited cyclonic circulations in the mid to outer fjord and northern

inner basin at average speeds of 6 to 10*cm* s^{-1} and 5 to 7*cm* s^{-1} respectively, and anticyclonic flows at slightly slower speeds (3 to 4*cm* s^{-1}) in the southeastern inner basin. In contrast, the water at 40*m* moved very slowly and exhibited mostly small east-west oscillations at along-channel velocities consistent with the tidal currents (~ 1-2 *cm* s^{-1}), but at times the 40*m* flows accelerating to speeds ~ 10*cm* s^{-1}.

In September the ADCP currents increased in both speed (25 to 35*cm* s^{-1}) and depth (25 to 30*m*) due to partial mixing and deepening of the seasonal thermocline and halocline. In contrast, the currents at the surface and 1*m* were primarily driven by combinations of estuarine (geostrophic) flow and down-fjord winds. The ADCP data also showed persistent counterclockwise (cyclonic) currents at 7 to 15*m* depths that were traced by the 10*m* drifters, but only during the initial deployments from the 21st to the 23rd (Fig. 20a). The geostrophic currents due to the density field in September extended deeper into the subsurface water (upper 20*m*) and ranged from 45 to 100*cm* s^{-1}, again the highest velocities occurred for stations close to large sources of freshwater discharge, such as the Lowe and Valdez Glacier Stream.

The first half of the March survey was conducted under the influence of strong winds ranging from 12 to 15*m* s^{-1} coming from either the southeast (Lowe River Valley) or from the northeast (Valdez Glacier Valley). The surface drifters moved predominately to the northwest at 30 to 45*cm* s^{-1} during the southeast wind events and to the southwest at 20 to 27*cm* s^{-1} during northeast winds. Based on dynamics of the Ekman layer and given that the ispheres were directly driven at ~ 3% of the wind speed, the surface currents during the above wind events probably ranged from 10 to 14*cm* s^{-1} and 6.5 to 8.5*cm* s^{-1} respectively due to winds and tidal currents. The latter were estimated at only 1.0 to 1.5*cm* s^{-1} (Fig. 64e) based on the approximate changes in tidal volume and cross-sectional area near the mouth. The nearly continuous winds also affected the deeper flows as well, and forced drifters at all depths to the northwest. The 1*m* and 10*m* drifters moved at maximum speeds of 20 to 25*cm* s^{-1} and 12 to 15*cm* s^{-1} respectively during the initial portions of the March survey, but they also showed marked variation in speeds. During the second half of the survey, the winds diminished and eventually a one-day period of quiescence occurred. At this time the drifter speeds decreased significantly and drifters moved in highly varied tracks exhibiting open and closed cyclonic and anticyclonic modes similar to the previous two months.

In June the along-channel (*u*) velocities and drift times generally inferred retention for 93% of the surface flows and 75% of the 1*m* currents. In the fall and winter, however, conditions changed to favor flushing, and in September flushing increased to 38% and 85% for the surface and 1*m* flows respectively, and in the late winter the percentages of flushing at the above depths were 45% and 72% respectively. The flows at 10*m* in June showed 66% retention and the net eastward motion of water at 40*m* in the inner basin resulted in 100% retention (Fig. 65C). In the fall retention of water at 10*m* decreased only slightly (55%) and winter the subsurface layers and the deep subsurface water at 40*m* exhibited 100% flushing (Fig. 63C). However, in two of the 40*m* cases grounding occurred in the outer fjord along the northern shore, which would change the percentage of flushing to 39%. Flushing predominately occurred for the flows at 10*m* and 40*m* in the late winter, with percentages of 90% and 100% respectively (Fig. 65C), but in two of the 10*m* SVP deployments the drifters grounded on the northern shore. If the latter were considered to be retentions then the r/f percentages would have increased from 10/90% to 73/27%.

In all seasons the cross-channel (*v*) velocities were also important and resulted in circulation modes varying from wide oscillatory motions to rapid, diagonal down-fjord or up-fjord motions resulting in grounding along the shoreline. In June and September, for example, the *v* velocities were responsible for grounding 100% of the ispheres exhibiting retention (+*u*) and 67% and 40% respectively for surface drifters showing flushing (-*u*) but that also grounded inside the fjord; the latter considered to be retentions by default (Fig. 61). The microstars, by contrast, were driven ashore in only two deployments in June and none of cases of flushing resulted in grounding. In the fall, however, the percentage of groundings for flushing microstars was only 6%. However, four of the 1*m* cases considered to be flushing (Fig. 63) were questionable due to grounding on the western shoreline beyond the mouth.

Port Valdez and PWS share some common oceanographic characteristics. However, they also differ significantly in certain properties that drive circulation. For example, eddy circulations in Port Valdez occur from mesoscale turbulence caused by local vorticity in the flow field, as opposed to closed geostrophically balanced eddies that occur in central PWS. As such, these features in Port Valdez are highly ephemeral and frequently occurred as open cyclonic and anticyclonic turns. Lateral dispersion due to turbulence is also generally limited in both systems but also highly variable depending on prevailing conditions of winds, estuarine (geostrophic) flows and lateral shear in the flow field. Although dispersion in Port Valdez typically increased when flows reached the shore as expected, during periods of low winds the large-scale turbulence in the system created mesoscale eddies that gradually dispersed material, but also caused longer retention in comparison to flushing by currents forced by wind and estuarine driven currents. The maximum flushing should therefore occur for the surface and 1*m* layers, as they exhibited the most rapid down-fjord motions that periodically entered Valdez Arm. In contrast, the deeper flows at 10 and 40*m* were typically much slower and dispersion at these depths occurred later in the deployments.

Conclusions

Early Summer:

1) Oil spilled within the fjord in early summer (June) could be held within the system for long periods depending on the prevailing meteorological and oceanographic conditions. For example, surface oil dispersing into the central fjord basin could either contaminate the southeast shoreline in as little as 9*hr* or flush from the fjord in less than half a day (7*hr*) depending on whether diurnal, westerly winds forced inward retention or if oil became entrained into an outflow along the northern side of the fjord that is enhanced by weak, down-fjord winds at night.

2) A caveat is that due to strong, reversing actions of westerly winds in combination with flood tides at the “Narrows’ oil that flushed from the fjord at night could return the following day and contaminate the northern shoreline in about one day (25*hr*).

3) In other cases, retention of oil could occur for as long as 64 to 66*hr*, and result in contamination of multiple areas due to wide oscillatory motions within the fjord, or oil could move directly into the inner basin and contaminate the eastern to northeastern shorelines.

4) If dispersants were applied allowing the oil to vertically mix then flushing at 1*m* in depth in June could occur in 17 to 27*hr*. However, oil in this layer could also undergo oscillatory motions similar to the surface water and hence remain in the fjord indefinitely until prolonged flushing conditions returned.

5) Oil mixed to depths of 10*m* and 40*m* would very likely remain within the fjord for long periods (5 to 16 days). At 10*m* it would move in large cyclonic motions before possibly contaminating various subtidal zones around the fjord. In certain cases, however, the oil in this layer may also be caught in mesoscale cyclonic eddies in the outer fjord basin and either eventually flush from the system or gradually move eastward towards the inner basin over 4 to 5 days time due to action of diurnal, westerly winds.

6) Oil mixed to 40*m* that reached the inner basin would remain there indefinitely, whereas in the outer basin the average flows may cause it to gradually flush out of the fjord.

Early Fall:

1) In September strong northeast winds could flush surface oil from the central fjord in six to 21*hr*, but even under the influence of weak, variable winds the strong estuarine outflows during this season could assist in flushing oil out in about 10 to 14*hr*.

2) A caveat is that surface oil moving slowly outward (e.g. 18 to 22*hr*) can be affected by strong cross-channel flows, resulting in contamination of the outer fjord shorelines. Also, retention may ensue due to resumption of eastward along-channel velocities forced by periodic shifts to diurnal, westerly winds. Under such conditions shorelines in the eastern (inner) fjord could be affected by oil in 9 to 21*hr*.

3) At 1*m* the frequency of total flushing was the highest of all depths and all seasons (85%), and under the action of strong, northeast winds flushing could occur in as little as 12 to 16*hr*. Also, out of four of the cases exhibiting retention (15%), two were initially showed flushing but drifters either turned back into the fjord in the outer basin or grounded along the southeastern shoreline when exiting the inner basin.

4) The subsurface water at 10*m* and 40*m* exhibited very long residence times in the fall, ranging from 5 to 10 days respectively, but whereas the upper layer at 10*m* exhibited more variability in flushing due to effects of mesoscale turbulence (SD = 41*hr*), the 40*m* flows moved steadily outward at 5$cm\ s^{-1}$ resulting in much lower variation in flushing times (SD = 16*hr*). Under indirect effects of strong, northeast winds, however, flows at 40*m* could also strike the deep benthic regions on the northern side of the fjord.

Late Winter:

1) Flushing in late winter (March) was very strong due to the action of easterly winds, but little effects of density driven flows occurred since the water column physical properties were relatively homogeneous.

2) Marked cross-channel flows from wind and wave action invariably led to grounding of surface drifters, and under the action of strong southeasterly winds from the Lowe River Valley, for example, the northwestern shoreline could be contaminated by surface oil in as little as 10 to 11*hr*.

3) The water at 1 to 40*m* would move in the same general direction as the surface flows, but any oil at these depths would flush outward due to a long-shore current developed by piling of water along the northern shore from wind driven transport.

4) In contrast, when winds shift to the northeast surface oil could contaminate the southwestern shoreline in 20 to 31*hr*, but oil at 1*m* could either flush from the fjord in 45*hr* or be retained for nearly 8 days due to extremely small negative along-channel velocities.

5) Under the conditions of very weak winds or quiescence, however, water at both the surface and 1*m* would exhibit moderate to long residence times ranging from 70*hr* before surface flows reached the inner basin to nearly 14 days prior to flushing for water at 1*m*.

6) Under both sets of easterly winds, the flows at 10*m* would flush outward over the course of 2 to 5 days, but when the winds weaken the flows at this depth would begin moving in cyclonic eddies due to mesoscale turbulence. Flushing times under the above conditions exhibited extreme variations ranging from 3 to 20 days, the latter being essentially indefinite.

7) In contrast, the flows at 40*m* would move steadily outward under all conditions at average speeds similar to September (~ 5 $cm\ s^{-1}$), and would flush from the fjord in 86 to 93*hr*.

8) A final conclusion of the study regards areas in the fjord especially at risk of contamination from oil, particularly if dispersants were applied allowing it to mix vertically in the water column. Although these sites varied somewhat with the season and depth of the flows, there was significant overlap in the upper meter, particularly for the early summer and fall periods. In June, for example, thirteen locations were identified and included various points along the northern shoreline extending from east of Shoup Bay to Gold Creek and Mineral Creek Deltas and along the peninsula one nautical mile to the east; the eastern

shoreline from the Valdez Glacier Stream northwards to the 'Duck Flats' region; the southeast region from the Lowe River to Solomon Gulch; the southwest shoreline east of Anderson Bay and at Entrance Island; and the entire western shoreline south of Shoup Bay (see Fig. 67a).

In the fall, the sites included the southwest shorelines at Valdez Narrows, Entrance Island and points east of Anderson Bay; the western shoreline south of Shoup Bay; the northwest shoreline between Shoup Bay and Gold Creek delta; the northeast shoreline both west and east of the harbor entrance and potentially the 'Duck Flats' and nearby islands; the eastern shoreline north of the Valdez Glacier Stream; and southeast shoreline near Solomon Gulch (see Fig. 67b).

In late winter, potential 'sensitive sites' during high easterly wind events were distributed mainly along the entire northern shoreline extending from one nautical mile east of Mineral Creek all the way to Shoup Bay. During the northeast wind events various points between the Security Zone and Anderson Bay were at risk from surface oil, but during periods of calm or weak westerly winds flows at 1*m* also turned southwards, and potentially could contaminate the southern side of the fjord (see Fig. 67c).

Future Work

One of the most obvious uses of the data collected during the Lagrangian drifter experiments is to apply them to models tracking both water and oil circulation within Port Valdez. At present, the various oil spill trajectory models are based on relatively coarse resolution simulations generated by a Regional Ocean Modeling System (ROMS) for PWS developed by Dr. Yi Chou, who is currently at the University of California in Los Angeles. An attempt to simulate the circulation in Port Valdez by reducing the domain size of the PWS ROMS was done last year by Dr. Chou. The nearsurface circulation patterns were similar to the observations, but the flow vectors were too small in scale and lacked the details of the mesoscale turbulence in the system shown by both the ADCP and drifter data. Using the three seasonal data sets, the PWS ROMS could, therefore, be adjusted and validated to provide more accurate simulations of the ocean state and circulation required by oil spill trajectory models. The goals and objectives of a possible study of this type, sponsored by the PWSRCAC, are described in more detail in Appendix E.

7.0 ACKNOWLEDGMENTS

This project was a multi-year effort that required significant communication and interaction among entities to orchestrate safely and gather data efficiently. Both the PWSSC and PWSRCAC would like to acknowledge the contributions and efforts of the following entities:

- Alyeska Pipeline Service Company, for their strong communications through this project and help monitoring drifter buoys and other related study activity, and communicating this information out to other involved entities. Additionally, Alyeska provided advance schedules of tanker movement so study activities could be coordinated and managed safely.

- The United States Coast Guard, Marine Safety Unit Valdez, for their strong communications on this project, facilitation of the Harbor Safety Committee meetings where the project was discussed, and help broadcasting information of this activity to recreational and commercial mariners via their "Notice to Mariners" radio broadcasts.

- Crowley Marine Services, for their efforts monitoring drifter buoys and safely escorting tankers in and out of Port Valdez while study activities were in progress.

- Southwest Alaska Pilot Association (SWAPA pilots), for their efforts monitoring drifter buoys and safely guiding tankers in and out of Port Valdez while study activities were in progress.

Other commercial users of Port Valdez that took the time to attend pre-deployment meetings where study activities and management of buoys was discussed. These specific entities, in no particular order, included: the State of Alaska Marine Highway Ferry System, Alaska department of Environmental Conservation (ADEC), representatives from the Prince Willaim Sound tanker fleet collectively known as the Response Planning Group, local tour boat operators including specifically Valdez based Stan Stephens and LuLuBelle tours, Valdez Fisheries Development Association, North Star Stevedores and representatives from the Valdez Container Terminal, representatives from the City of Valdez Port and Harbor department, local seafood processors Peter Pan and Silver Bay Seafoods, and Petro Star Refinery.

The author would also like to specifically thank the captain and crew of the M/V Auklet for assisting with the towed ADCP transects and hydrography data, and drifter releases during the first half of the experiments. The oceanographic work involved running continuous transects and collecting periodic CTD profiles over the first thirty-six hours, as well as working early mornings and late evenings over the remaining days of each survey. My gratiude is extended to Kirsti Jurica, who served as my field technician during the oceanographic work, and to Dave Rentel, captain of the M/V Vixen, who provided assistance with drifter deployments and retrievals each day during the second half of the experiments. Both the Vixen and Auklet have been chartered for past scientific work before in the greater PWS region, and RCAC thanks them for continued interest in this work.

Special thanks also goes to the Auklet and the PWSSC vessel, the M/V New Wave, for help retrieving the ispheres that escaped into PWS and grounded on Perry and Green Islands, and to the folks at the PWSRCAC for their help in outreach to the community regarding the study and to Jeremy Robida and others for their editorial comments on the manuscript.

8.0 REFERENCES

Aure, J., Molvaer, J., Stigebrandt, A., 1996. Observations of inshore water exchange forced by a fluctuating offshore density field. *Mar. Pollution Bulletin*, 33 (1-6), 112-119.

Bang, I., Mooers, C.N.K., 2003. The influence of several factors controlling the interactions between Prince William Sound, Alaska, and the Northern Gulf of Alaska. *Journal of Physical Oceanography* 33, 19–36.

Becher, P., 1977. *Emulsions: Theory and Practice*, Robert E. Krieger Publishing Company, Huntington, NY.

Belk, J.L., Elliott D.J. and Flaherty, L.M. 1989. "The Comparative Effectiveness of Dispersants in Fresh and Low Salinity Waters", in *Proceedings of the 1989 International Oil Spill Conference*, American Petroleum Institute, Washington, DC, pp. 333-336.

Carlson, R.F., Wagner, J., Hartman, C.W., Murphy, R.S., 1969. Freshwater studies. In: *Baseline data survey for Valdez pipeline terminal environmental data study:* 7-41. Institute of Marine Science, University of Alaska, Fairbanks, Rept. R69-17

Colonell, J. M. 1981. Deep Water Renewal in a Subarctic Fjord. *Journal of the Waterway, Port, Coastal and Ocean Division,* Proceedings of the Society of Civil Engineers, 107 (No.WW4), 223-231.

Dyer, K. R. 1997. *Estuaries: A Physical Introduction*, 2nd Ed. John Wiley & Sons, London, New York, Sydney, Toronto.

Emory W.J. and Thomson, R.E. 2004. *Data Analysis Methods in Physical Oceanography*. second ed. Elsevier, Amsterdam, 638 pp.

Fingas, M.F., I. Bier, M. Bobra and S. Callaghan, 1991. "Studies on the Physical and Chemical Behaviour of Oil and Dispersant Mixtures", in *Proceedings of the 1991 International Oil Spill Conference*, American Petroleum Institute, Washington, DC, pp. 419-426.

Fingas, M.F., D.A. Kyle and E.J. Tennyson, 1995. "Dispersant Effectiveness: Studies Into the Causes of Effectiveness Variations", in *The Use of Chemicals in Oil Spill Response*, STP 1252, American Society for Testing and Materials, Philadelphia, PA, pp. 92-132.

Fingas, M.F., 2004. Dispersants, Salinity and Prince William Sound. Final Report to the Prince William Sound Regional Citizens' Advisory Council (PWSRCAC), Anchorage, Alaska, 48 pp.

Farmer D.M. AND Freeland H.J. 1983. The Physical Oceanography of Fjords. *Prog. Oceanog.* 12, 147-220.

Gay, S.M. III and Vaughan, S.L. 2001. Seasonal hydrography and tidal currents of bays and fjords in Prince William Sound, Alaska. *Fish. Oceanogr.* 10 (Suppl. 1), 159-193.

Gay, S.M. III. 2013A. Physical Oceanographic Characteristics of Nursery Habitats of Juvenile Pacific Herring. *Exxon Valdez* Oil Spill Restoration Project Final Report (Restoration Project. 10100132-E, retrieve from http://www.evostc.state.ak.us).

Gay, S. M. III. 2013b. Estuarine conditions and water exchange in small fjords of Prince William Sound, Alaska. A dissertation submitted to Texas A&M University. pp. 212.

GillIbrand, P.A. AND Amundrud, T.L., 2007. A numerical study of the tidal circulation and buoyancy effects in a Scottish fjord: Loch Torridon. *J. Geophys. Res.* 112 (C05030), 1-22.

Gill, A. 1982. Atmosphere and Ocean Dynamics. International Geophysical Series Vol. 30. Academic Press. 662 pp.

Halverson M. J., Be´langer C., Gay, S. M., III, 2013a. Seasonal transport variations in the straits connecting Prince William Sound to the Gulf of Alaska. *Cont. Shelf Res.* 63 (Suppl. 15), 63-78.

Halverson M. J., Ohlmann, J.C., Johnson, M.A., Pegau, W.S. 2013b. Disruption of a cyclonic eddy circulation by wind stress in Prine William Sound, Alaska. *Cont. Shelf Res.* 63 (Suppl. 15), 13-25.

Hansen, D.V., Rattray, M. Jr., 1966. New dimensions in estuary classification. *Limnol. Oceanog.* 11, 319-326.

Hetland, R.D. 2010. Estuarine Overmixing. *Journal of Physical Oceanography* 40, 199-211.

Johnson, W.R., Royer, T. C., Luick, J. L., 1989. On the seasonal variability of the Alaska Coastal Current. *J. Geophys. Res* 93, 12423-12438.

Klinck, J. K., O'Brien, J. J. , Svendsen, H., 1981. A simple model of fjord and coastal circulation interaction. *Journal of Physical Oceanography* 11, 1612-1626.

LeBlond, P. H. and Mysak, L. A. 1988. *Wave in the Ocean*. Elsevier, 602 pp.

Mackay, D., 1995. "Effectiveness of Chemical Dispersants Under Breaking Wave Conditions", in *The Use of Chemicals in Oil Spill Response*, STP 1252, American Society for Testing and Materials, Philadelphia, PA, pp. 310-340.

Martinelli, F.N. and B.W.J. Lynch, 1980. "Factors Affecting the Efficiency of Dispersants", LR 363 (OP), Warren Spring Laboratory, Stevenage, 18 p.

Moles, A., Holland, L., Short, J., 2001. "The Effectiveness of Corexit 9527 and 9500 in Dispersing Fresh, Weathered and Emulsion of Alaska North Slope Crude Oil Under Subarctic Conditions", Prince William Sound Regional Citizens' Advisory Council, Anchorage, AK, 24 p.

Moles, A., Holland, L., Short, J. 2002. "Effectiveness in the Laboratory of Corexit 9527 and 9500 in Dispersing Fresh, Weathered and Emulsion of Alaska North Slope Crude Oil Under Subarctic Conditions", *Spill Science and Technology Bulletin*, 7, pp. 241-247.

Muench, R.D., Nebert, D.L., 1973. Physical Oceanography, *Environmental Studies of Port Valdez*, D. W. Hood, W. E. Shiels, and E. J. Kelly, eds., University of Alaska, Fairbanks, Alaska, 103-149.

Muench, R.D., Schmidt, G.M., 1975. Variations in the hydrographic structure of Prince William Sound. *Sea Grant Report R75-1*. Institute of Marine Science Report, R75-1, University of Alaska, Fairbanks, 135 pp.

Muench, R.D., Heggie, D.T., 1978. Deep Water Exchange in Alaskan Subarctic Fjords. In *Estuarine Transport Processes*. (Kjerfve, B., ed.) The Belle W. Baruch Library in Marine Science, 7, 239-267.

Nebert, D.L., Muench, R.D. and Hood D.W. 1973. Dye Dispersion Studies, *Environmental Studies of Port Valdez*, D. W. Hood, W. E. Shiels, and E. J. Kelly, eds., University of Alaska, Fairbanks, Alaska, 151-198.

Niebauer, H.J., Royer, T.C., Weingartner, T.J. 1994. Circulation of Prince William Sound, Alaska. *J. of Geophys. Res.* 99, (C7), 14,113-14,126.

Pickard, G.L. 1967. Some oceanographic characteristics of the larger inlets of Southeast Alaska. *J. Fish. Res. Bd. Canada*, 24, 1475-1505.

Pickard, G.L. 1971. Some physical oceanographic features of inlets in Chili. *J. Fish. Res. Bd. Canada*, 28, 1077-1066.

Polton, J. A., Lewis, D. M., Belcher, S. E. (2005), The role of wave-induced Coriolis-Stokes forcing on the wind-driven mixed layer, *J. Phys. Oceanogr., 35*(4), 444–457, doi:10.1175/JPO2701.1.

Pond S., Pickard G. L. 1983. Introductory Dynamical Oceanography, 2nd Edition. Pergamon Press, 329 pp.

Pritchard, D.W. 1967. What is an estuary: physical viewpoint. In *Estuaries:* 3-5. G. H. Lauff (editor). American Association for the Advancement of Science Publication No. 83: Baltimore MD: Horn-Shafer, 3–5.

Röhrs, J., Christensen, K.H., Hole, L., Broström, R G., Drivdal, M.S., Sundby, M. 2012. Observation-based evaluation of surface wave effects on currents and trajectory forecasts, *Ocean Dyn., 62*, 1519–1533

Röhrs, J., Christensen, K.H. 2015. Drift in the uppermost part of the ocean, *Geophys. Res. Lett., 42*, doi:10.1002/2015GL066733.

Royer, T.C., Hansen, D.V., Pashinki, D.J., 1979. Coastal flow in the northern Gulf of Alaska as observed by dynamic topography and satellite tracked drogued drift buoys. *Journal of Physical Oceanography* 9, 555-563.

Royer, T. C. 1982. Coastal fresh water discharge in the northeast Pacific. *J. of Geophys. Res.* 87, 2017-2021.

Saelan, O.H. 1967. Some features of the hydrography of Norwegian fjords. In: *Estuaries:* 63-70. G.H. Lauff (ed.). American Association for the Advancement of Science Publ. No. 83.

Schmidt, G.M. 1977. The exchange of water between Prince William Sound and the Gulf of Alaska, M.S. Thesis, University of Alaska at Fairbanks, 116 pp.

Sharma, G.D. Burbank, D.C. 1973. Geological Oceanography, *Environmental Studies of Port Valdez*, D. W. Hood, W. E. Shiels, and E. J. Kelly, eds., University of Alaska, Fairbanks, Alaska, 15-100.

Stabeno, P.J., Bond, N.J., Hermann, A.J., Kachel, N., Mordy, C.W., Overland, J.E., 2004. Meteorology and Oceanography of the northern Gulf of Alaska. *Continental Shelf Research* 24, 859–897.

Stacey, M.W., Stephen, P., Nowak, Z.P., 1995. A numerical model of the circulation in Knight inlet, BC, Canada. *Journal of Physical Oceanography*. 25, 1037–1062.

Stacey, M.W. 1999. Simulation of the wind-forced circulation in Knight Inlet: a parameterization of the roughness length. *Journal of Physical Oceanography.* 29, 1363-1367.

Svendsen, H., Thompson, R. 1978. Wind-driven circulation in a fjord. *Journal of Physical Oceanography* 8, 703-712.

Vlasenko, V., Stashchuk, N., Hutter K., 2002. Water exchange in fjords induced by tidally generated internal lee waves. *Dynamics of Atmospheres and Oceans* 35, 63–89.

Vaughan S. L., Mooers, C.N.K., Gay, S.M. III, 2001. Physical variability in Prince William Sound during the SEA Study. *Fish. Oceanog.* 10 (Suppl 1), 58-80.

Wilson, J.G., Overland, J.E., 1986. Meteorology. In *The Gulf of Alaska, Physical Environment and Biological Resources.* (D.W. Hood and S.T. Zimmerman, ed.) Alaska Office, Ocean Assessments Division, National Oceanic and Atmospheric Administration, U.S. Dept. of Commerce, No. MMS 86-0095, pp. 31.

Table 1. Drifters deployed during experiments in June and September 2016 and March 2017

Date	*buoy type*	*depth*	*no. on reserve*	*no. deployed*	*trans. rate (hr)*	*total deployments*
June 2016	i-spheres	surf.	6	5	0.5-1	12
	P.G. Microstars	1m	1	7	0.5	26
	P.G. SVPs	10m	2	6	0.5	16
	P.G. SVPs	40m	2	1	0.5	1
	totals		11	19		55
Sept 2016						
	i-spheres	surf.	2	9	0.5-1	29
	P.G. Microstars	1m	3	5	0.5	37
	P.G. SVPs	10m	1	7	0.5	24
	P.G. SVPs	40m	0	3	0.5	3
	totals		6	24		93
March 2016	i-spheres	surf.	4	8	0.5-1	19
	P.G. Microstars	1m	2	6	0.5	13
	P.G. SVPs	10m	2	6	0.5	18
	P.G. SVPs	40m	0	2	0.5	3
	totals		8	22		53

Table 2a. Principal Axes of Variation of velocities, Average Speeds and *u* Velocities, Distances and Drift/Flush Times in June 2016.

				Principal Axes:			*Speeds, Distances and Times of Drift and Retention or Flushing:*							
Dates	*Depl. No.*	*Drifter*	*Depth (m)*	*Angle*[1]	*Maj. Axis*[2]	*Min. Axis*[2]	*Avg Spd*[3]	*Avg uvel*[4]	*Dist (km)*	*Time (hr)*[5]	*Time (hr)*[6]	*p*	*Range (hr)*	
June 22-23	1	i0460a	0	-6.0	0.0541	0.0042	0.194	0.125	9.8	14.0	9	r/g	9	14
22-23	2	i5480a	0	8.1	0.2671	0.0322	0.523	-0.266	33.7	17.9	7	f/e*	7	18
23-25	2	i5480b	0	26.7	0.1596	0.0364	0.277	0.140	33.9	34.0	25	r/g*	9	34
23-26	3	i9460	0	-11.9	0.0473	0.0035	0.179	-0.013	42.6	66.0	204	f/rg	66	204
24-27	4	i0460b	0	-2.5	0.0581	0.0113	0.211	-0.008	48.6	64.0	288	f/rg	64	288
25-27	5	i6350	0	-14.2	0.0436	0.0025	0.147	0.042	22.2	42.0	50	r/g	42	50
22	1	m007a	1	-3.0	0.0552	0.0011	0.199	0.086	7.5	10.5	13	r/g?	11	13
22-23	2	m001a	1	11.6	0.0416	0.0095	0.153	-0.152	9.7	20.1	20	f	20	---
23	2	m001a	1	5.4	0.0346	0.0041	0.311	0.297	5.0	16.8	17	r	17	---
23-27	3	m007b	1	-12.6	0.0750	0.0037	0.123	-0.005	43.0	97.0	inf	f/r	inf	---
24-26	4	m001b	1	-59.2	0.0060	0.0048	0.129	-0.093	18.6	40.0	27	f	27	---
25-27	5	m003	1	-14.2	0.0278	0.0021	0.135	-0.003	21.9	45.0	inf	f/r	inf	---
22-26	2	svp004	10	1.0	0.0087	0.0010	0.073	-0.025	22.4	85.0	79	f/rg	79	85
23-27	3	svp008	10	-1.8	0.0020	0.0007	0.043	0.016	15.0	98.0	138	r	138	---
24-27	4	svp007	10	10.7	0.0020	0.0020	0.078	0.013	18.8	67.5	202	r	202	---
25-27	5	svp002	10	-11.8	0.0026	0.0006	0.051	0.006	8.2	44.5	380	r	380	---
27-28	6	ispheres	0	-22.5	0.0361	0.0022	0.183	0.116	9.2	14.0	21	r/g	20	22
27-28	6	mstars	1	-9.4	0.0266	0.0026	0.173	-0.100	10.6	17.0	22	f	17	31
27-29	6	SVP10	10	11.6	0.0072	0.0031	0.102	-0.030	16.0	43.5	100	f	86	111
28-29	7	mstars	1	-13.9	0.0358	0.0014	0.157	0.059	13.8	24.5	52	r/g?	47	60
28-29	8	svp004,6	10	27.1	0.0037	0.0006	0.097	-0.089	7.6	22.0	30	f/rg	26	35
28-29	9	svp005	10	-16.5	0.0042	0.0008	0.073	0.021	6.0	23.0	73	r	73	---
29-30	10/11	ispheres	0	-34.0	0.0149	0.0039	0.289	0.272	5.2	5.0	13	r/g	11	15
29	10	mstars	1	-17.1	0.0121	0.0026	0.222	0.214	4.8	6.0	17	r	15	19
29-7/1	10	SVP10	10	17.7	0.0121	0.0011	0.064	0.031	10.4	45.0	118	r	115	120
29	11	mstars	1	-19.1	0.0044	0.0002	0.086	0.073	1.9	6.0	50	r	43	54
29-7/1	11	SVP10	10	-5.3	0.0030	0.0007	0.060	0.031	9.8	45.0	115	r	110	121
29-30	12a	mstars	1	9.9	0.0728	0.0179	0.366	-0.266	18.4	14.0	9	f/g	8	9
29-7/1	12b	m003	1	-4.9	0.0279	0.0042	0.080	0.009	10.9	38.0	268	r/g	268	---
29-7/1	12b	m007&8	1	-11.8	0.0506	0.0069	0.180	-0.013	24.7	38.0	inf	f/r?	89	inf
30	13	mstars	1	-4.7	0.0185	0.0084	0.243	0.217	4.8	5.5	17	r	16	17

1 Rotation angles in +/- degrees from the east-west (*u*) axis.

2 Major and minor axes of variation in the velocities $(m/s)^2$.

3 Arithmetic average speed of all drifters in a release group (m/s).

4 Average along-channel (u) velocity of a release group (m/s).

5 Drift times in *hr* based on the avg. speeds and distances.

* times to flush past the mouth and then return based on an avg speeds of $0.58 m\ s^{-1}$ and $0.40 m\ s^{-1}$

6 Average times in *hr* of either flushing or retention/grounding (Note phase (p): f = flushing, r = retention, e = escape into the 'Narrows' or into PWS and g = grounding).

Table 2b. Averages and Standard Deviations of Rotation Angles, Speeds, *u* Velocities and Flushing/Retention Times in June 2016.

	Averages:					*Drift:*		*Flush*	*Retention*
Drifter	*Rot. Angle*	*Maj Axis*	*Min Axis*	*Avg Spd*	*avg uvel*	*Dist (km)*	*Time(hr)*	*Time(hr)*	*Time(hr)*
isph	-7.0	0.0851	0.0120	0.2503	0.051	25.6	32	7	35
mstars	-10.7	0.0375	0.0050	0.1808	0.009	15.5	28	33	69
SVP10	3.6	0.0051	0.0012	0.0712	-0.003	12.7	53	70	171
SVP40*	-7.0	0.0010	0.0002	0.0297	0.009	15.1	141	---	260
	Standard Deviations:								
isph	18.6	0.0852	0.0141	0.1205	0.158	16.5	23	0	24
mstars	17.3	0.0257	0.0047	0.0785	0.129	11.0	25	32	99
SVP10	14.3	0.0035	0.0008	0.0196	0.039	5.6	26	36	111
SVP40*	---	---	---	---	---	---	---	---	---

* single observation in June

Table 3a. Principal Axes of Variation of velocities, Average Speeds, Distances and Drift/Flush Times in September 2016.

	Depl.		Depth	Principal Axes:			Speeds, Distances and Times of Drift and Retention or Flushing:						
Date	No.	Drifter	(m)	Angle[1]	Maj. Axis[2]	Min. Axis[2]	Avg Spd[3]	Avg uvel[4]	Dist (km)	Time (hr)	Time (hr)[6]	p	Range (hr)	
Sept 21-22	1	isph	0	25.4	0.0613	0.0166	0.284	-0.179	18.4	18	17	f/gr?	17	18
21-22	1	mstars	1	12.8	0.0369	0.0035	0.230	-0.186	14.9	18	16	f/gr?	16	17
21-23 & 25	1	SVP10	10	-1.5	0.0134	0.0014	0.099	-0.033	23.2	65	93	f	84	102
21-22	2	isph	0	20.3	0.0340	0.0143	0.211	-0.099	14.4	19	21	f/gr?	21	21
21-22	2	mstars	1	49.0	0.0167	0.0046	0.207	-0.173	13.4	20	12	f/e	12	12
21-23	2	SVP10	10	14.1	0.0317	0.0096	0.186	0.047	29.4	44	68	r	57	86
22-23(Oct 6)*	4	isph	0	10.8	0.0311	0.0010	0.476	-0.473	12.0	7	6	f/e	6	6
22-23	3	mstars	1	10.6	0.0326	0.0068	0.206	-0.206	15.0	20	16	f/gr	15	17
22-23	4	mstars	1	9.0	0.0326	0.0053	0.216	-0.215	14.0	18	13	f/gr	13	14
22-30	4	SVP40	40	6.9	0.0032	0.0007	0.056	-0.013	37.0	184	245	f	245	---
23	5	mstars	1	-1.1	0.0292	0.0046	0.272	-0.224	8.8	9	14	f/r	13	14
23-25	5	svp005	10	-8.3	0.0050	0.0004	0.061	0.001	10.4	47	inf	r	inf	---
23-30	5	SVP40	40	-2.4	0.0030	0.0005	0.050	-0.013	29.2	161	234	f/gr?	234	---
24-25	6	isph	0	23.5	0.0446	0.0058	0.227	0.016	7.4	9	125	r/g	93	189
24-25	6	mstars	1	12.7	0.0056	0.0025	0.082	0.002	6.7	22	inf	r	503	inf
24-25	6	SVP10	10	-12.8	0.0113	0.0017	0.083	0.009	6.7	23	329	r	124	510
24-25	7	isph	0	2.1	0.0042	0.0021	0.098	0.066	3.9	11	12	r/g	11	12
24-25	7	mstars	1	17.7	0.0101	0.0031	0.139	-0.120	11.3	23	17	f	17	17
24-25	7	SVP10	10	-18.1	0.0019	0.0002	0.061	-0.047	4.6	21	89	f	89	90
24-30	7	SVP40	40	-6.8	0.0024	0.0005	0.045	-0.019	21.3	131	214	f/gr?	214	---
25-26	8	isph	0	82.0	0.0130	0.0029	0.334	-0.311	10.8	9	10	f/eg	10	10
25-26	8	mstars	1	-5.6	0.0033	0.0012	0.161	-0.153	13.6	23	20	f	19	22
25-27 & 28	8	SVP10	10	-3.4	0.0033	0.0002	0.044	-0.0003	11.2	70	inf	f/r	inf	inf
25-26	9	isph	0	33.4	0.0116	0.0053	0.188	-0.154	11.5	17	14	f/e	13	14
25-26	9	mstars	1	-13.6	0.0054	0.0008	0.093	-0.071	8.0	24	29	f	26	33
25-27	9	SVP10	10	-0.3	0.0032	0.0002	0.053	-0.032	8.6	45	66	f	60	73
26-27	10a	isph	0	-1.3	0.0321	0.0164	0.207	-0.047	15.7	21	44	f	42	47
26-27	10a	mstars	1	-32.9	0.0099	0.0037	0.159	-0.130	11.4	21	16	f/gr?	15	18
26-27	10b	i5600	0	-59.8	0.0134	0.0027	0.094	0.013	6.4	19	63	r/g	63	---
26-27	10b	i6350	0	-27.6	0.0288	0.0014	0.162	-0.075	11.1	19	56	f	56	---
26-27	10b	mstars	1	-21.4	0.0146	0.0009	0.106	-0.038	7.7	20	109	f/gr	58	inf
27-28	11	isph	0	-28.3	0.0357	0.0027	0.150	0.057	10.8	20	39	r/g	39	39
27-28	11	mstars	1	-31.7	0.0094	0.0008	0.159	-0.129	11.8	20	22	f	20	23
27-30	11	SVP10	10	6.5	0.0094	0.0004	0.048	-0.024	11.8	68	116	f/r?	110	123

27-28	13	isph	0	-31.0	0.0504	0.0036	0.235	-0.128	15.2	18	28	f/gr	27	30
27-28	12	mstars	1	-17.9	0.0109	0.0073	0.158	-0.116	10.2	18	31	f/gr?	29	33
27-29	12	SVP10	10	1.5	0.0020	0.0002	0.043	0.019	6.9	45	84	r/f?	70	106
28-29	14	isph	0	-16.5	0.0116	0.0032	0.128	-0.059	10.1	22	42	f/g?	41	43
28-29	14	mstars	1	-11.1	0.0025	0.0006	0.111	-0.104	9.2	23	24	f	24	25
28-30	16	SVP10	10	10.4	0.0032	0.0001	0.051	0.010	8.6	47	217	r	140	481
28-29	16	isph	0	-29.7	0.0122	0.0058	0.148	-0.107	11.2	21	25	f/gr	24	27
29-30	17	mstars A	1	-38.1	0.0124	0.0017	0.112	0.040	3.2	8	39	r/g	36	43
29-30	18	mstars B	1	2.4	0.0124	0.0050	0.188	-0.143	15.6	23	29	f	25	34
29-30	18	SVP10	10	-7.5	0.0028	0.0015	0.057	-0.023	4.9	24	182	f/r?	172	194

1 Rotation angles in +/- degrees from the east-west (*u*) axis.

2 Major and minor axes of variation in the velocities $(m/s)^2$.

3 Arithmetic average speed of all drifters in a release group (m/s).

4 Average along-channel (u) velocity of a release group (m/s).

5 Drift times in *hr* based on the avg. speeds and distances.

6 Average times in *hr* of either flushing or retention/grounding (Note phase (p): f = flushing, r = retention, e = escape into the 'Narrows' or into PWS and g = grounding).

* ispheres 2460 & 0600 exited PV on 9/23 at 0:00 and entered PWS at 08:30. Note that both drifters grounded on Perry I. on 9/25 but i0600 continued southward down KIP and then moved northeast up MS and grounded on Green I. on Oct 6, 2016 (see Fig. 18b).

Table 3b. Averages and Standard Deviations of of Rotation Angles, Speeds *u* Velocities and Flushing/Retention Times

Drifter	*Averages:*					*Drift:*		*Flush*	*Retention*
Type	*Rot. Angle*	*Maj Axis*	*Min Axis*	*Avg Spd*	*avg uvel*	*Dist (km)*	*Time(hr)*	*Time(hr)*	*Time(hr)*
isph	0.2	0.0274	0.0060	0.210	-0.106	11.3	16	26	53
mstars	-3.7	0.0153	0.0033	0.163	-0.123	10.9	19.4	26	32
SVP10	-1.7	0.0079	0.0014	0.071	-0.007	11.5	45.4	109	147
SVP40	-0.8	0.0029	0.0006	0.051	-0.015	29.2	158.7	231	146
	Standard Deviations:								
isph	36.0	0.0171	0.0055	0.102	0.146	3.8	5	16	40
mstars	22.6	0.0112	0.0022	0.054	0.076	3.5	4.7	25	10
SVP10	9.7	0.0088	0.0028	0.042	0.028	7.8	17.7	41	56
SVP40	7.0	0.0004	0.0001	0.005	0.004	7.9	26.6	16	21

Table 4a. Principal Axes of Variation of velocities, Average Speeds, Distances and Drift/Flush Times in March 2017

	Depl.		*Depth*	*Principal Axes:*			*Speeds, Distances and Times of Drift and Retention or Flushing:*							
Date	*No.*	*Drifter*	*(m)*	*Angle*[1]	*Maj. Axis*[2]	*Min. Axis*[2]	*Avg Spd*[3]	*Avg uvel*[4]	*Dist (km)*	*Time (hr)*[5]	*Time (hr)*[6]	*p*	*Range (hr)*	
March 24	1	isph	0	-47.4	0.0042	0.0008	0.374	-0.339	5.4	4	11	f/gr	10.3	10.7
24-25	1	mstars	1	-38.0	0.0045	0.0037	0.144	-0.127	13.0	25	28	f	27.9	28.8
24-25	1	SVP10	10	31.0	0.0045	0.0014	0.091	-0.080	7.7	23	45	f	34	72
24-27	1	SVP40-001	40	11.5	0.0009	0.0003	0.048	-0.042	12.5	72	86	f	86	---
24	2	isph	0	70.4	0.0017	0.0003	0.390	-0.340	7.0	5	11	f/gr	10.4	10.8
25	3	isph	0	-17.3	0.0018	0.0004	0.331	-0.319	4.8	4	10	f/gr	10.0	10.2
25-30	3	m004 & 5	1	-17.0	0.0019	0.0007	0.046	-0.017	7.6	46	193	f/r?	159	247
25-27	3	m006	1	-89.1	0.0027	0.0017	0.087	-0.072	14.5	46	45	f	45.0	---
25-29	3	SVP10	10	-1.7	0.0017	0.0009	0.049	-0.029	16.9	95	113	f/gr	106	117
26-27	5	isph	0	12.7	0.0136	0.0047	0.170	-0.153	11.0	18	20	f/gr	19.9	20.2
26-30	5	mstars	1	16.8	0.0049	0.0025	0.075	-0.016	24.6	91	197	f/gr	145.3	313.1
26-29	5	SVP10	10	7.0	0.0049	0.0007	0.053	-0.038	12.9	67	81	f/gr	76.4	83.1
27-28	6	isph	0	27.4	0.0145	0.0014	0.113	-0.096	7.7	19	31	f/gr	27.9	35.2
27-30	6	mstars	1	0.2	0.0059	0.0037	0.086	-0.009	21.4	69	325	f/r	201	562
27-30	6	SVP40	40	-67.3	0.0059	0.0008	0.049	-0.033	12.3	70	93	fr?	93.0	93.8
28-30	7	isph	0	-7.9	0.0255	0.0039	0.139	0.056	21.5	43	70	r	69.5	69.8
29-30	8	SVP10a	10	-42.3	0.0017	0.0007	0.059	-0.020	4.9	23	79	f	73.0	89.8
29-30	8	SVP10b	10	21.2	0.0033	0.0030	0.077	-0.003	6.6	24	483	f/r	172.3	inf

1 Rotation angles in +/- degrees from the east-west (*u*) axis.

2 Major and minor axes of variation in the velocities $(m/s)^2$.

3 Arithmetic average speed of all drifters in a release group (m/s).

4 Average along-channel (u) velocity of a release group (m/s) (Note positive values indicate retention and neg. values flushing).

5 Drift times in *hr* based on the avg. speeds and distances.

6 Times in *hr* of either flushing or retention/grounding (Note phase (p): f = flushing, r = retention and g = grounding).

Table 4b. Averages and Standard Deviations of the Principal Axes,Speeds and Times in March 2017

	Averages:					*Drift:*		*Flush*	*Retention*
Drifter	*Rot. Angle*	*Maj Axis*	*Min Axis*	*Avg Spd*	*avg uvel*	*Dist (km)*	*Time(hr)*	*Time(hr)*	*Time(hr)*
isph	6.3	0.0102	0.0019	0.253	-0.198	9.6	15.5	16	20
mstars	-25.4	0.0040	0.0025	0.088	-0.048	16.2	55.4	158	238
SVP10	3.0	0.0032	0.0013	0.066	-0.034	9.8	46.6	160	215
SVP40	-27.9	0.0034	0.0006	0.049	-0.037	12.4	71.0	91	93

	Standard Deviations:								
isph	40.6	0.0094	0.0019	0.126	0.162	6.2	15.2	9.0	25
mstars	41.0	0.0016	0.0013	0.036	0.051	6.8	25.3	123	75
SVP10	28.3	0.0013	0.0009	0.017	0.033	4.1	19.5	165	232
SVP40	55.7	0.0035	0.0004	0.0004	0.006	0.2	1.4	5.0	---

Table 5. Statistics for along-channel (u) velocities with respect to retention and flushing

		Arithmetic Averages:			Weighted by: +/- (r/f) times			total drift time	
Month	*drifter type*	*tot. avg.*	*(+) avg.*	*(-) avg.*	*tot. avg.*	*(+) avg.*	*(-) avg.*	*(+) avg.*	*(-) avg.*
June 2016	ispheres	5.10	13.90	-9.57	0.25	2.07	-1.39	0.88	-0.80
	microstars	2.33	13.64	-8.99	-0.11	1.07	-0.68	0.28	-0.50
	SVP10m	-0.29	1.97	-4.80	0.02	0.31	-1.22	0.21	-0.38
Sept 2016	ispheres	-9.73	3.44	-16.32	-0.52	0.67	-1.29	0.21	-0.88
	microstars	-10.83	2.1	-12.27	-0.54	0.61	-0.65	0.05	-0.6
	SVP10m	-0.67	1.72	-2.66	-0.06	0.35	-0.39	0.15	-0.23
	SVP40m	-1.51	0	-1.51	-0.49	0	-0.49	0	-0.49
March 2016	ispheres	-18.86	5.60	-22.93	-1.03	5.60	-2.92	2.51	-1.61
	microstars	-2.78	4.23	-6.98	-0.42	1.56	-1.30	0.44	-0.94
	SVP10m	-3.40	0.00	-3.40	-0.66	0.00	-0.66	0.00	-0.66
	SVP40m	-3.75	0.00	-3.75	-1.88	0.00	-1.88	0.00	-1.88
		Standard Deviations:							
June 2016		*tot. std.*	*(+)std.*	*(-) std.*	*Tot. std.*	*(+)std.*	*(-) std.*	*(+)std.*	*(-) std.*
	ispheres	15.79	8.34	14.75	1.08	1.30	1.60	0.55	0.92
	microstars	15.25	10.57	9.67	0.51	0.49	0.58	0.13	0.43
	SVP10m	3.90	1.00	3.56	0.31	0.17	0.29	0.12	0.09
Sept 2016	ispheres	14.43	2.51	13.28	0.60	0.50	0.46	0.16	0.32
	microstars	7.50	2.69	6.38	0.34	0.65	0.31	0.05	0.29
	SVP10m	2.77	1.79	1.55	0.25	0.39	0.26	0.16	0.15
	SVP40m	0.36	0.00	0.36	0.05	0.00	0.05	0.00	0.05
March 2016	ispheres	15.04	0.00	11.49	1.72	0.00	1.46	0.00	0.81
	microstars	6.46	2.02	3.46	0.77	1.02	0.46	0.29	0.33
	SVP10m	2.88	0.00	2.88	0.52	0.00	0.52	0.00	0.52
	SVP40m	0.64	0.00	0.64	0.36	0.00	0.36	0.00	0.36

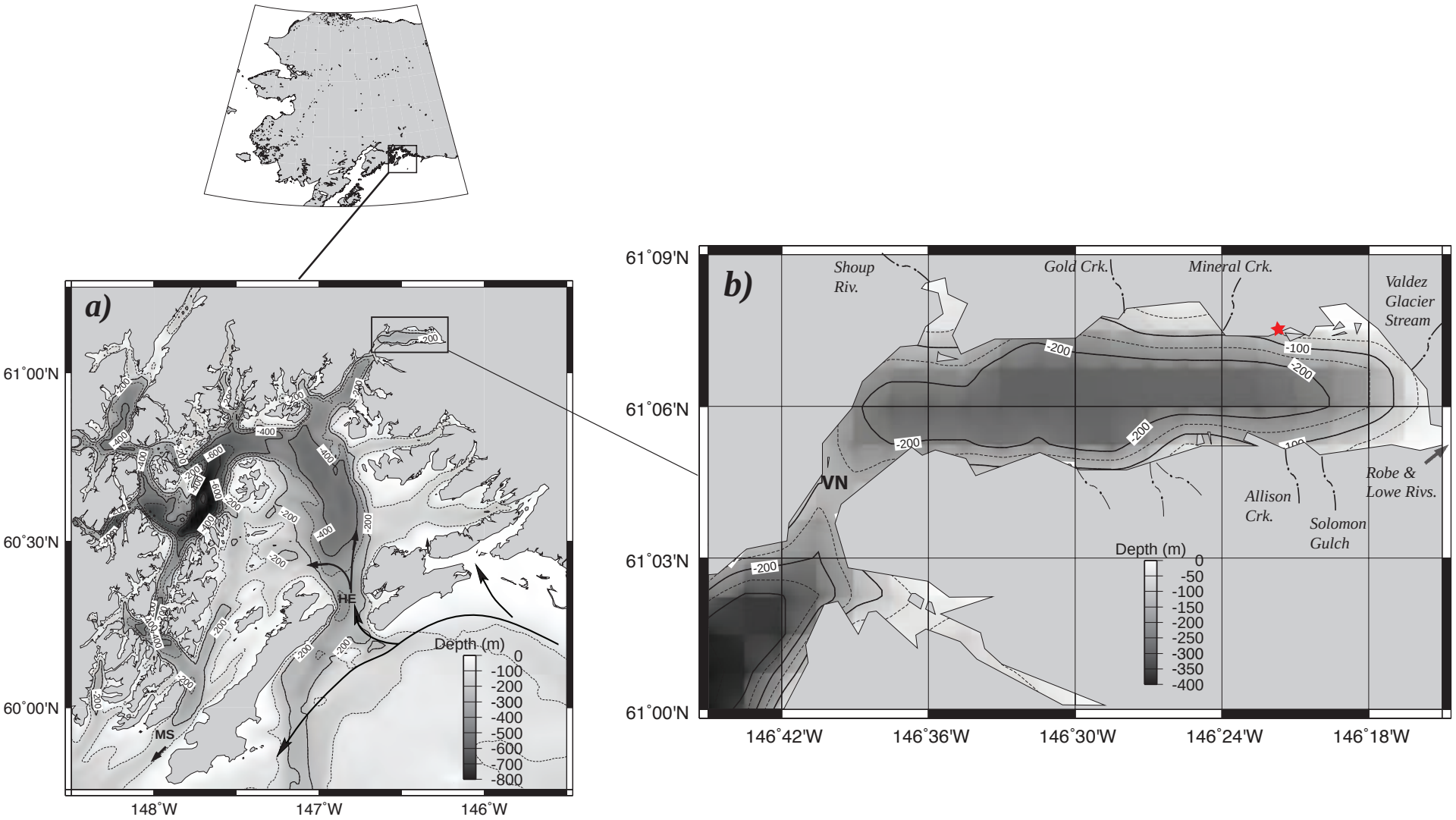

Fig. 1. Location and bathymetry of: a) Prince William Sound (PWS) and b) Port Valdez, Alaska. Lateral constrictions and sills occur in PWS at Hinchinbrook Entrance (HE) and Montague Strait (MS) and in Port Valdez at Valdez Narrows (VN). Sources of freshwater input for Port Valdez are shown as small creeks and rivers, and the approximate position of the NOAA weather station located next to the Alaska Marine Highway Ferry terminal is shown by the red star. The black arrows in panel-a denote the general flow of Copper River water from east to west and locations of inflow and outflow within the sound.

.

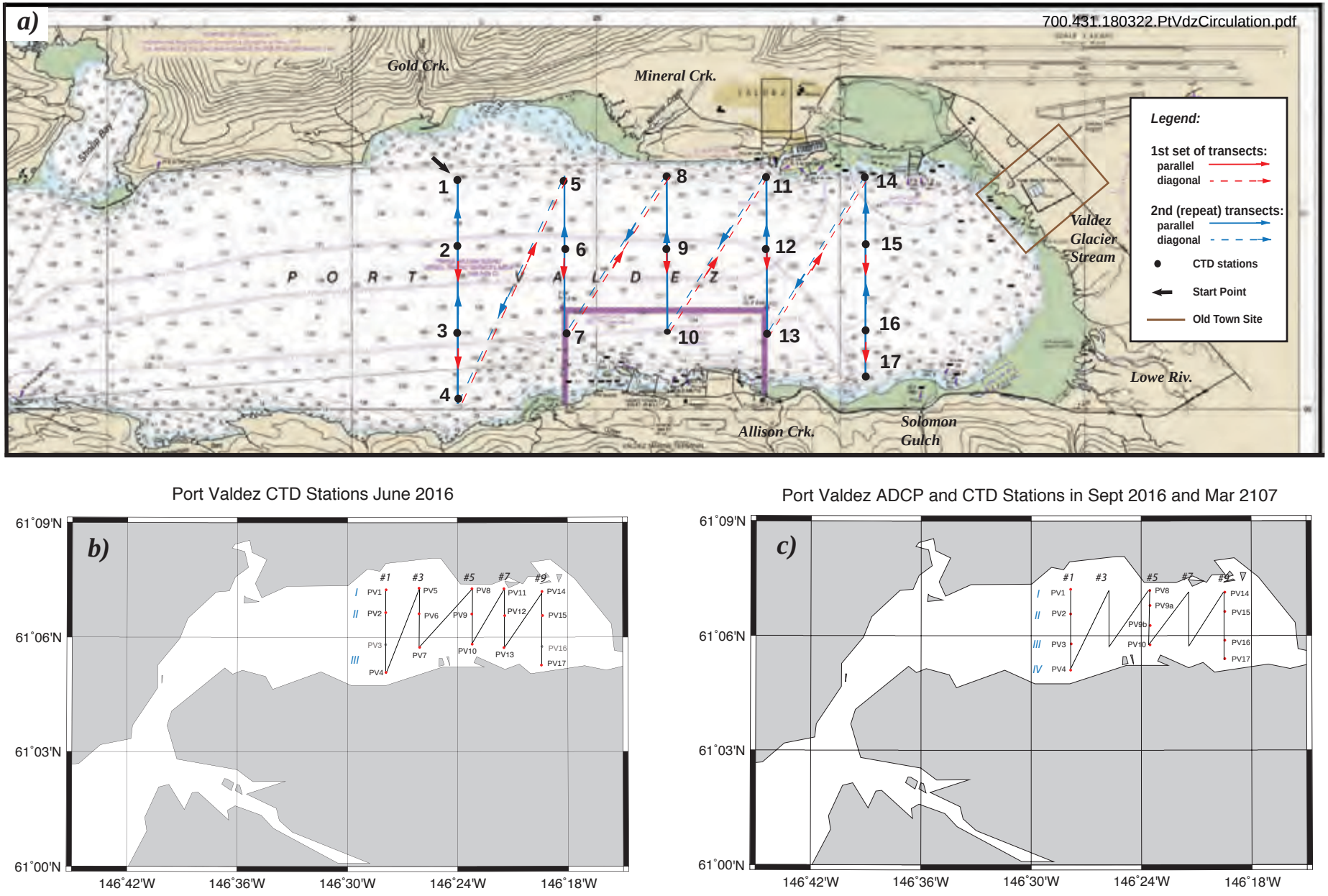

Fig. 2. General schematics of repeated towed ADCP transects and CTD stations occupied during the study. a) Original transects and stations designated for June, 2016, with red arrows denoting the first (inward) transect set and blue the second (outward) set; final transects and CTD stations for b) June 2016, and c) September 2016 and March 2017. Note: oceanographic stations are designated by letters and numbers, whereas cross-channel ADCP/CTD transect numbers are shown across the tops of panels b and c. Along-channel CTD transects are numbered from north to south as blue Roman numerals. Also, the two stations shown in grey in June (PV3 and PV16) were dropped after the initial run in order to save time for later ADCP transects.

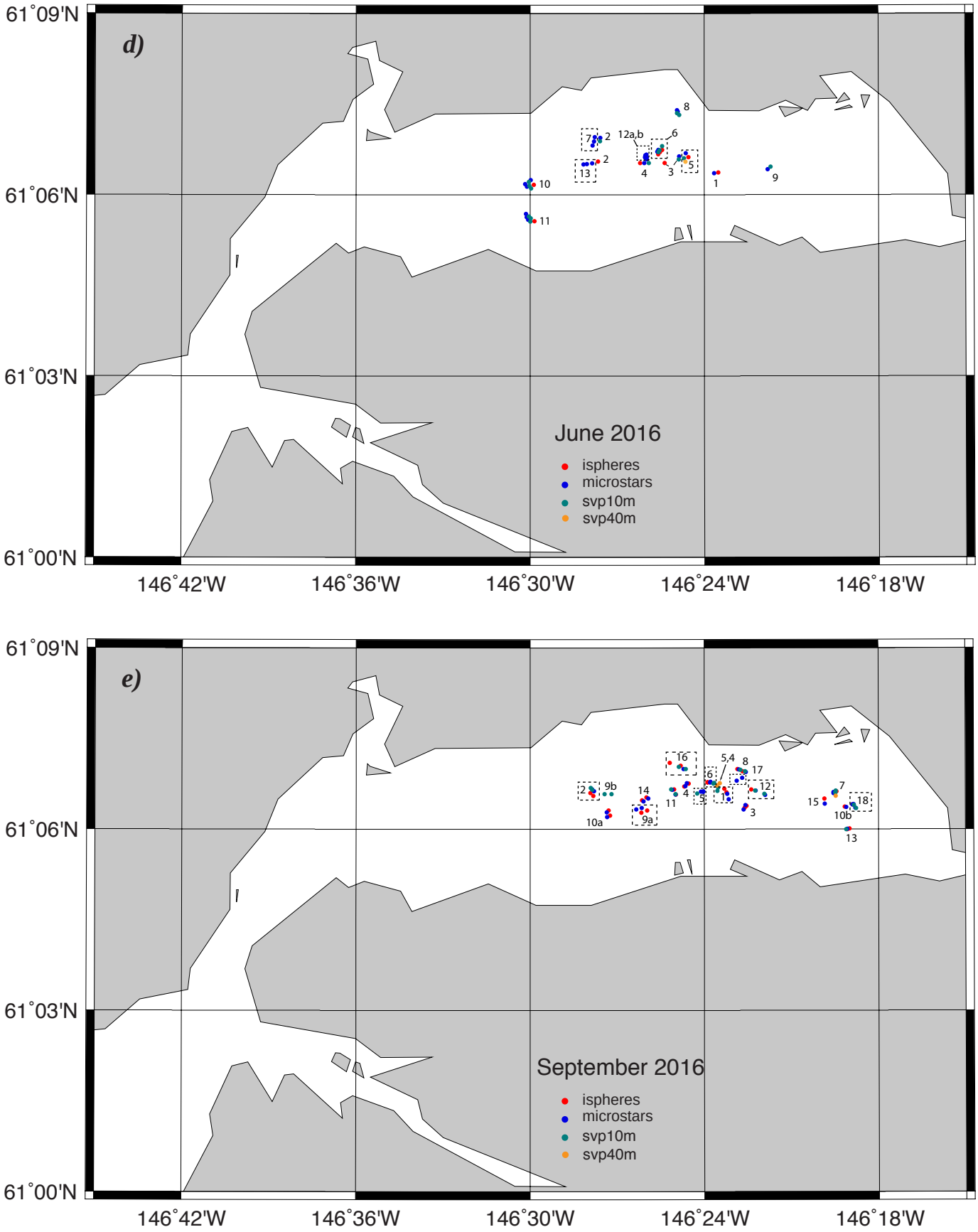

Fig. 2 (cont.). Drifter release points in June (d) and September (e). Note that the numbers shown next to the dots represent deployments listed in Appendix A.

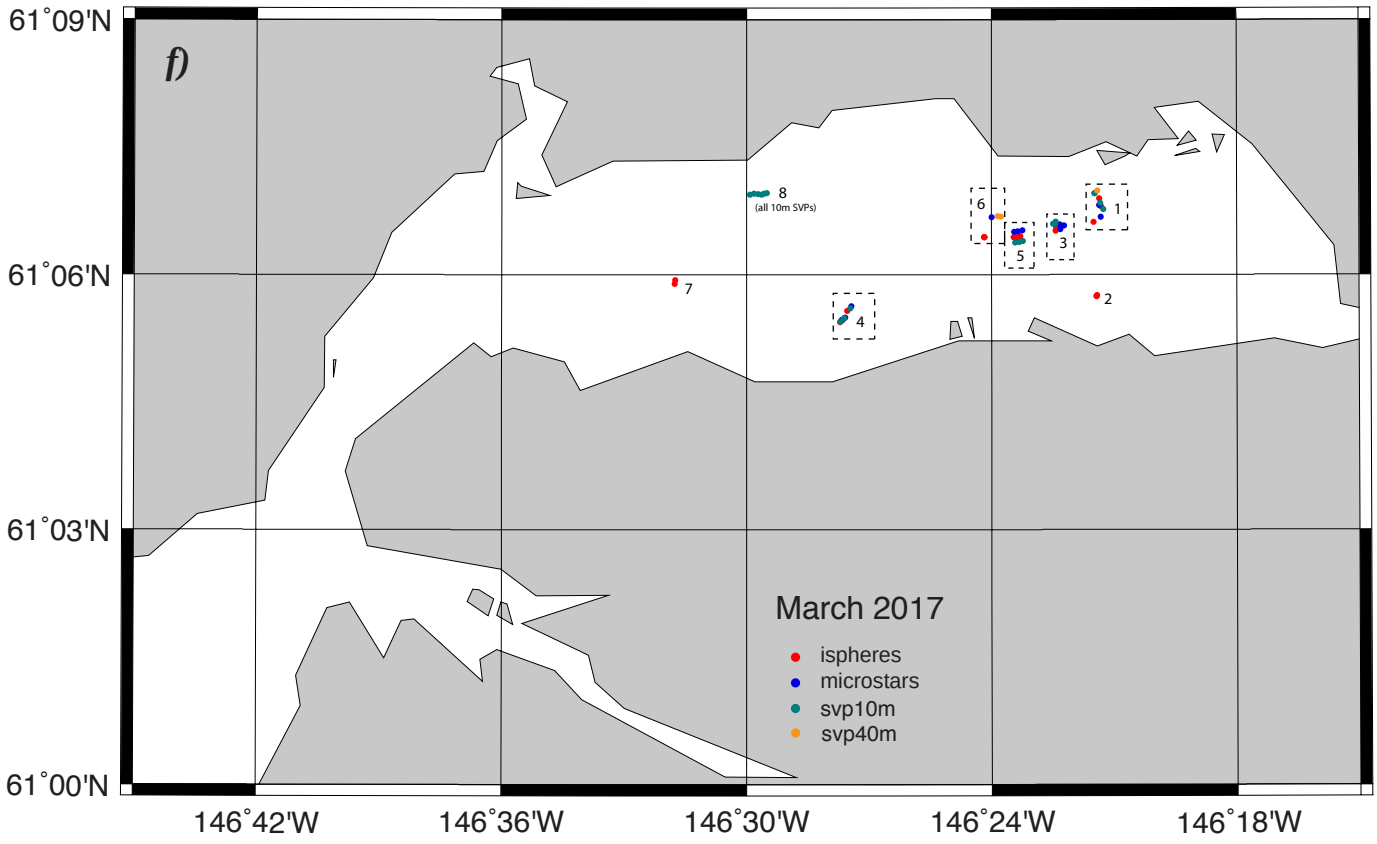

Fig. 2 (cont.). Drifter release points in March 2017 (f). Note that the numbers shown next to the dots represent deployments listed in Appendix A.

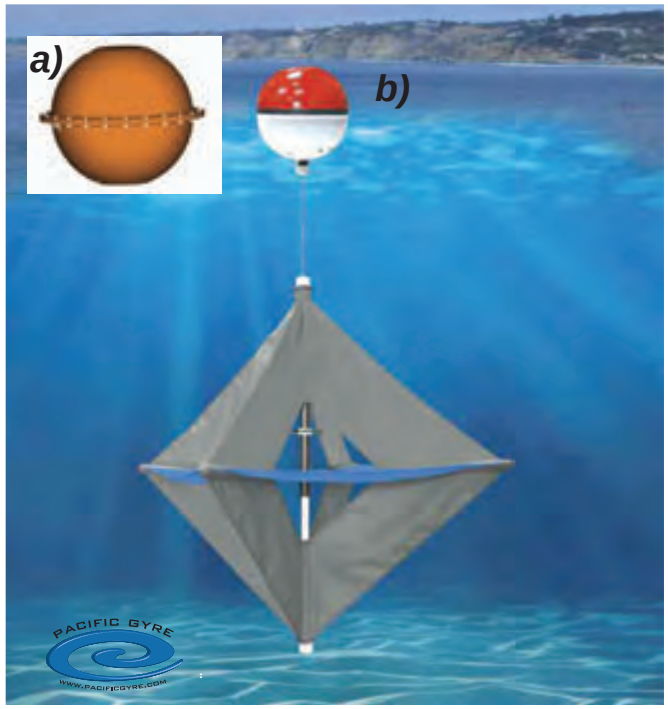

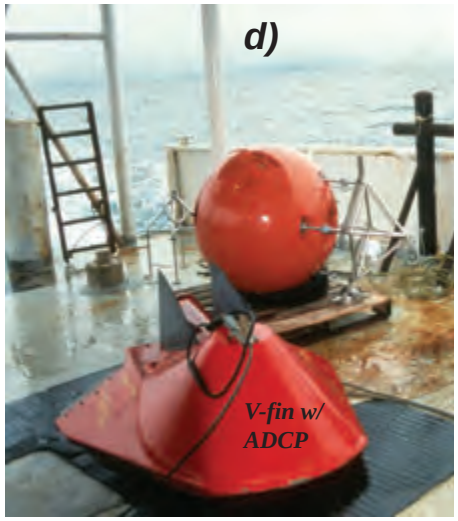

Fig. 3. Examples of oceanographic instruments to be used in the Port Valdez circulation experiment in June 2016. a) Metocean surface oil spill response buoy; b) Pacific Gyre (PG) Microstar with 1m drogue; c) PG Surface Velocity Program (WOCE type) drifter with 10m and 40m holey sock drogues; d) 150 kHz ADCP in Endaco V-fin; and e) SBE 19.03 CTD used to collect the hydrography data.

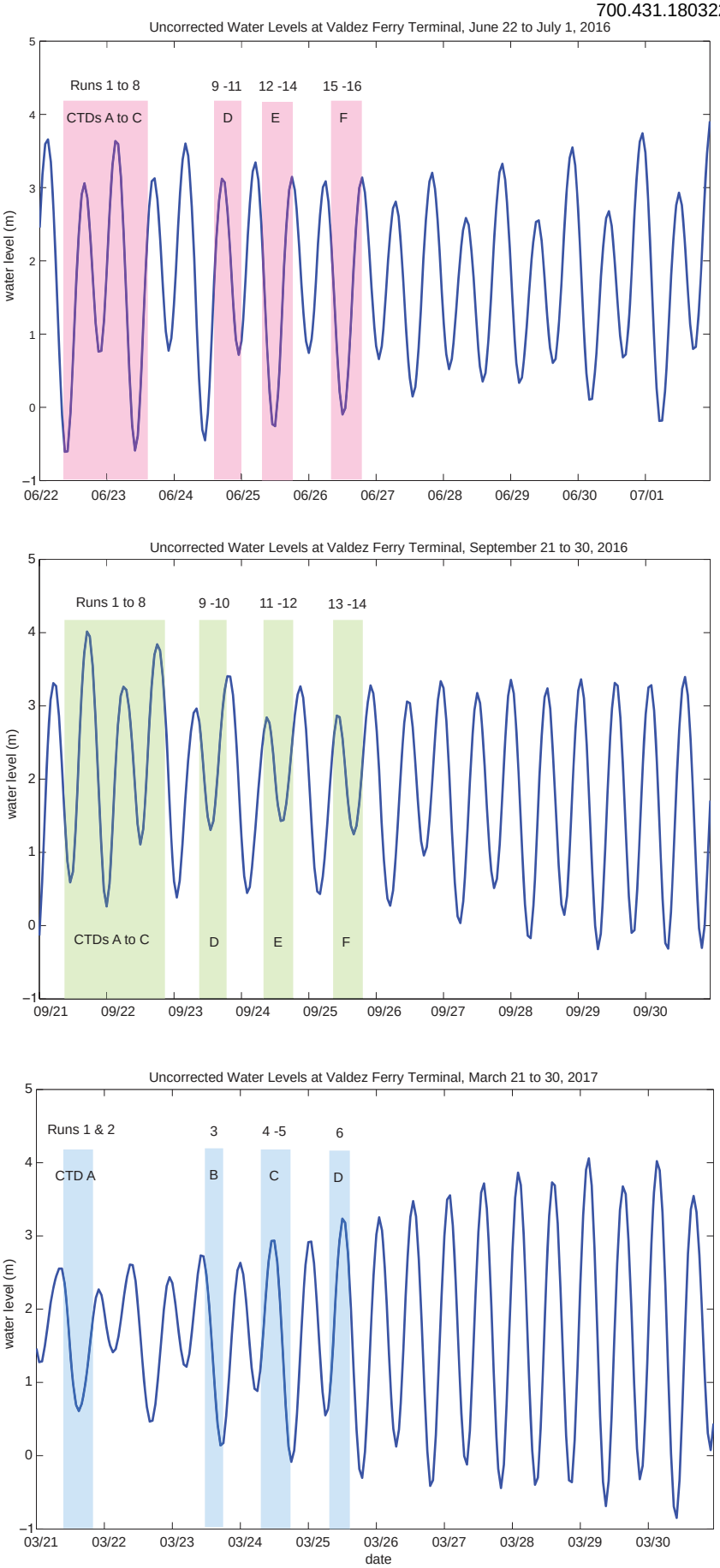

Fig. 4. Semi-diurnal tides occurring during each experiment conducted in a) June 2016, b) September 2016, and c) March 2017. Shaded rectangles denote the periods of tides over which the oceanographic surveys were conducted. Also shown are the number of ADCP transect runs and CTD sets for each period.

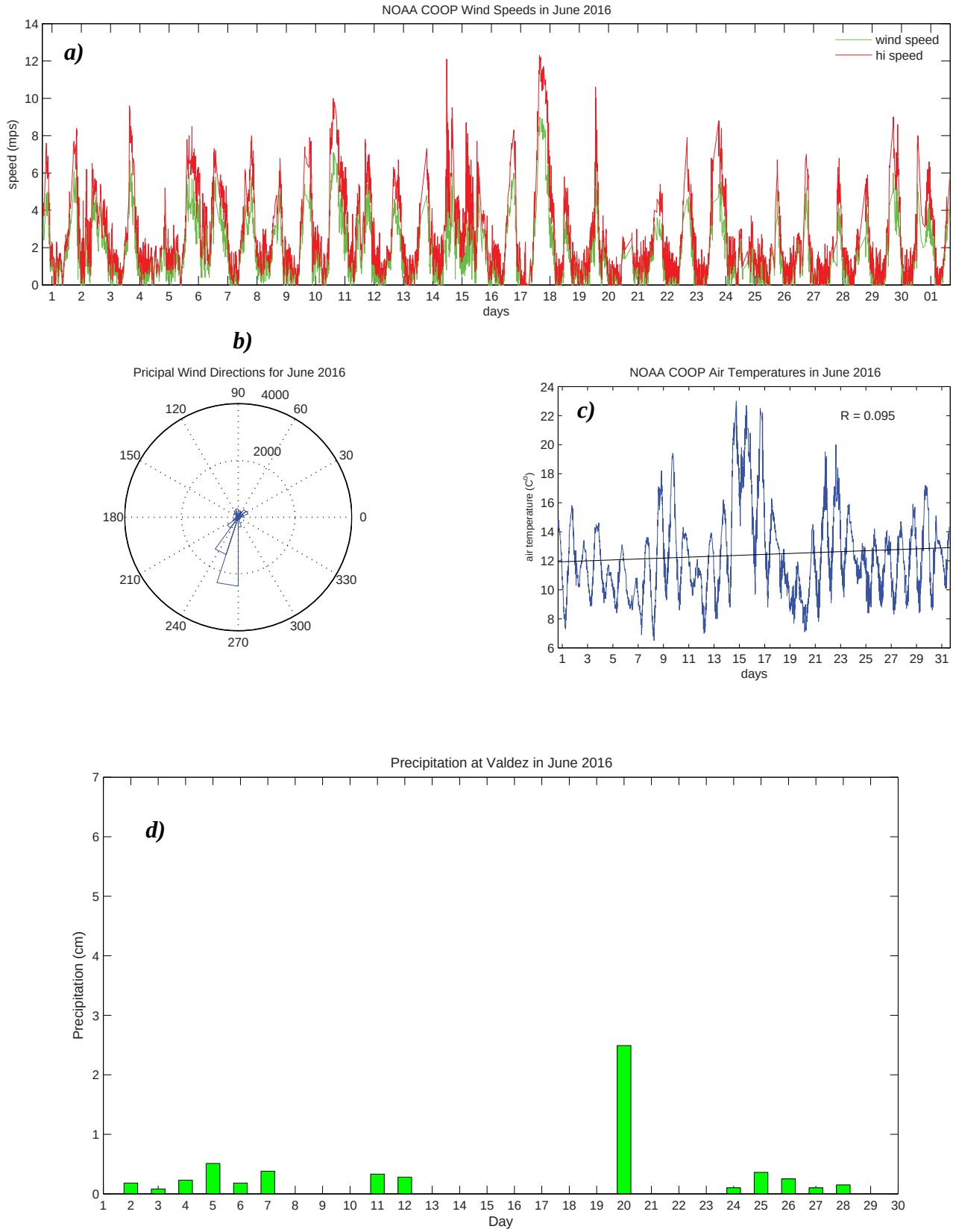

Fig. 5. Meteorological data in June 2016 collected at the Valdez, Alaska NOAA-COOPS station 9454240: a) sustained and high wind speeds measured at 6 min. intervals; b) wind rose showing principal directions (in 20° bins) from which the winds are coming; c) air temperatures at 6 min. intervals; and d) daily precipitation in *cm*.

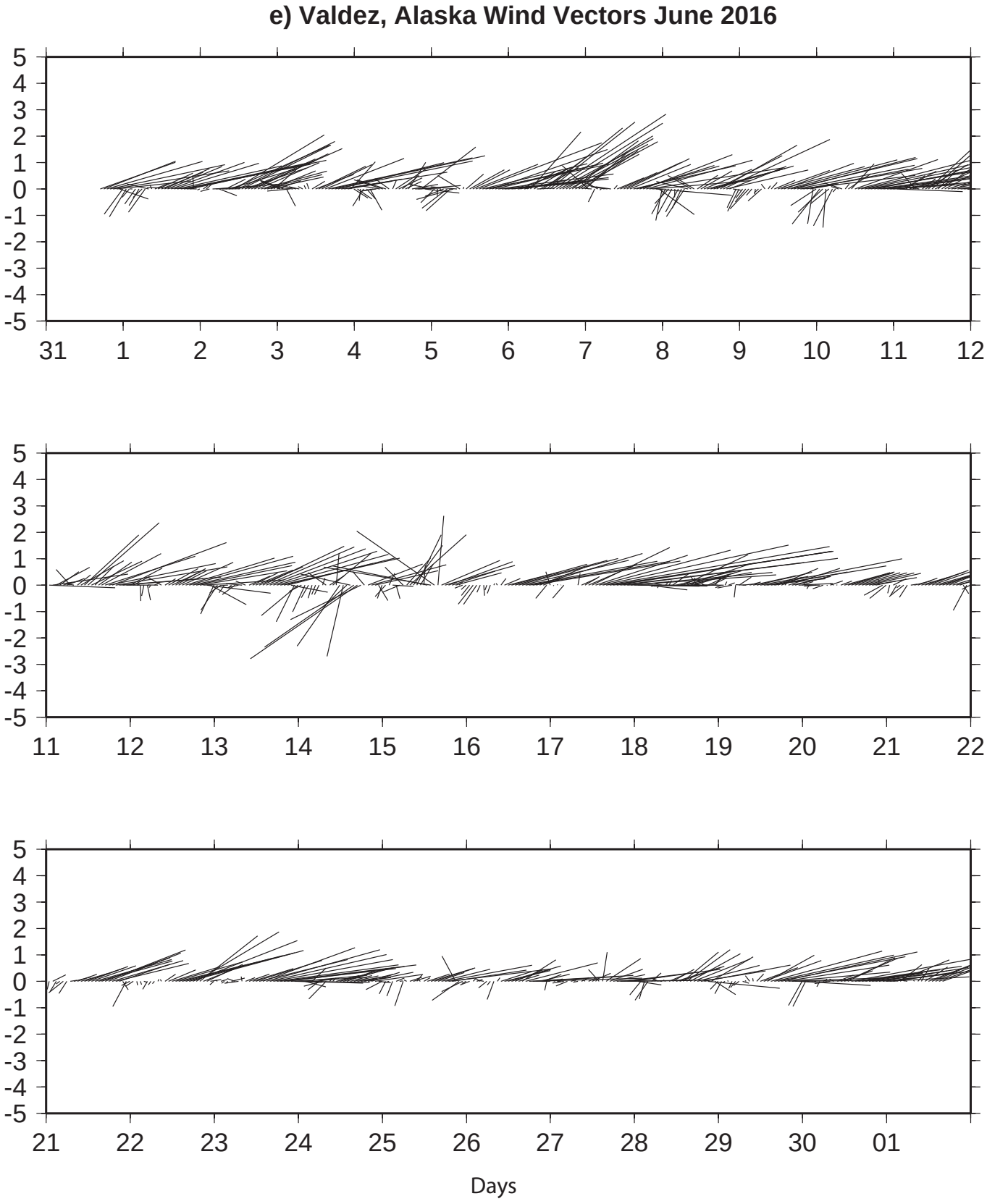

Fig. 5 (cont.). e) Wind vectors for the month of June 2016 measured at the Valdez, Alaska NOAA-COOPS station 9454240. Note that the x-axis is for days starting on May 31 and ending on July 1.

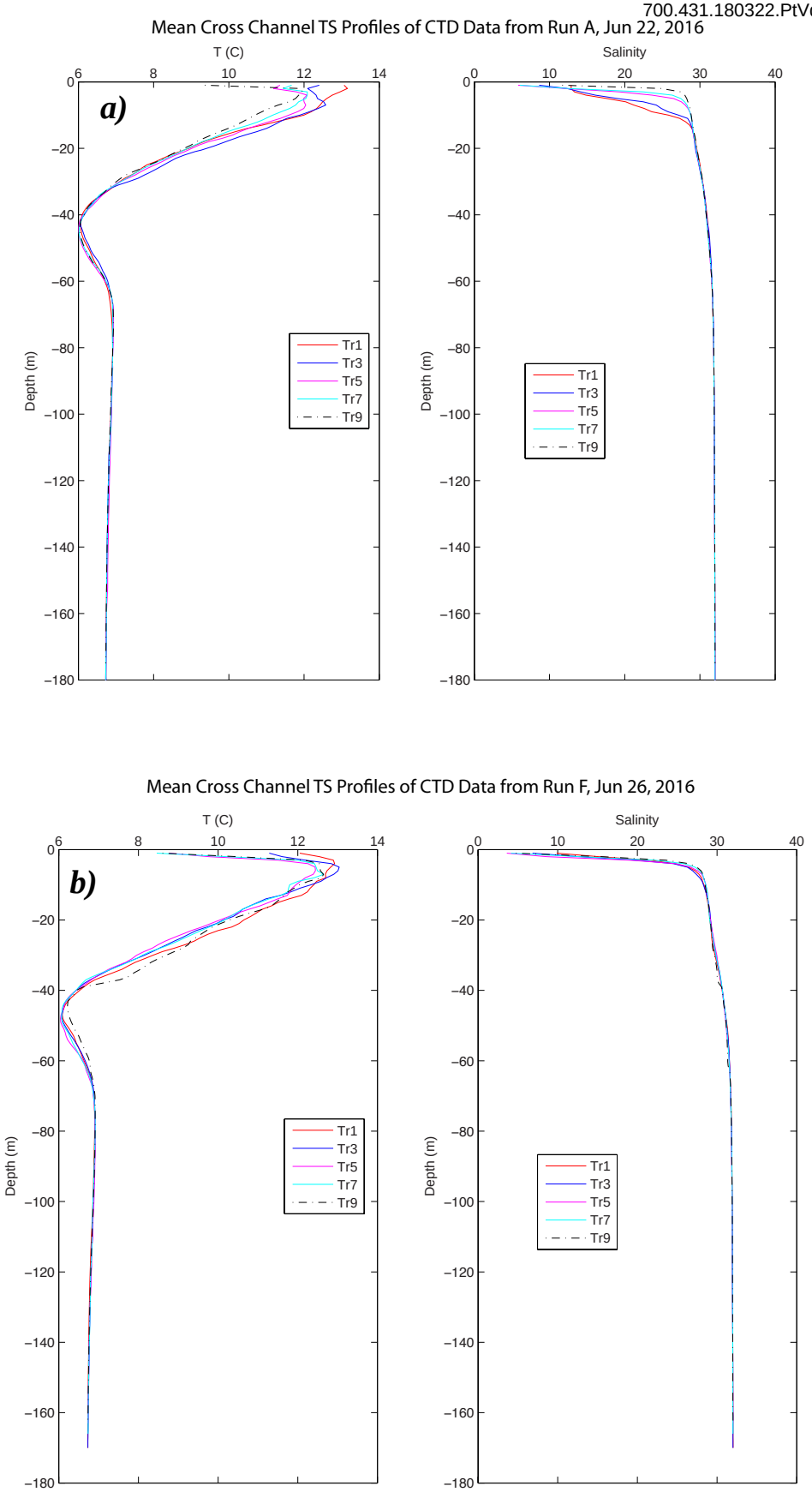

Fig. 6. Mean Cross-channel temperature and salinity profiles for transects 1, 3, 5, 7 and 9: a) Run A on June 22; and b) Run F on June 26.

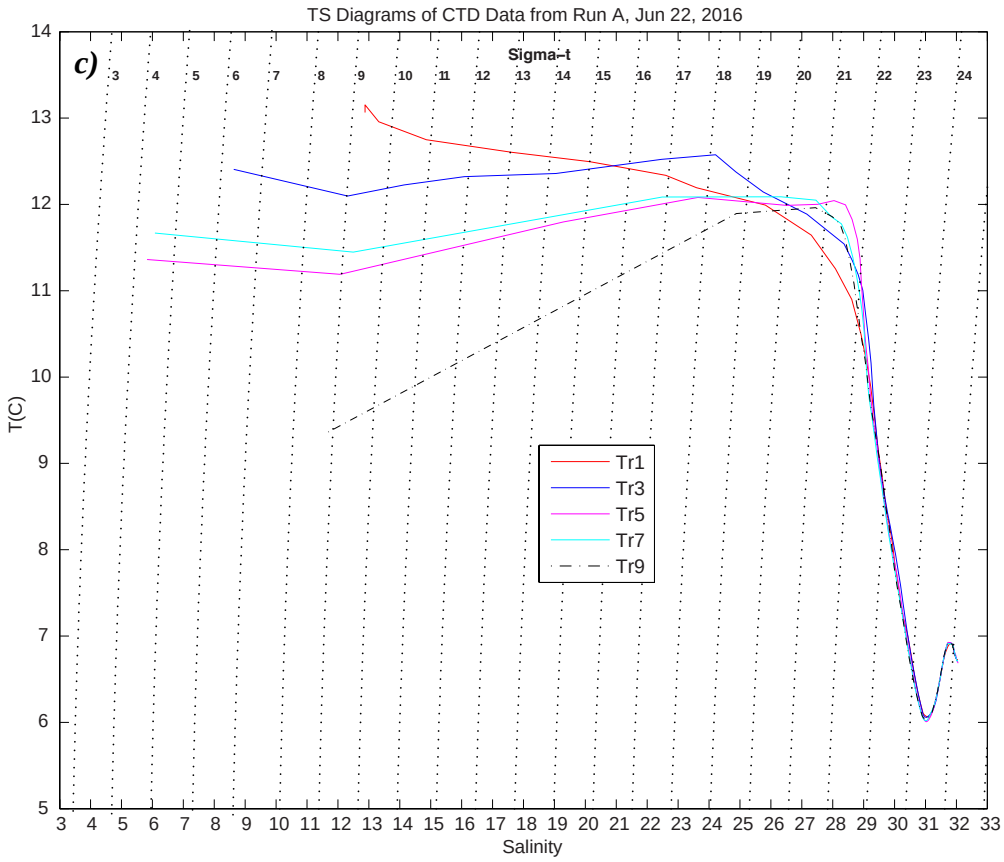

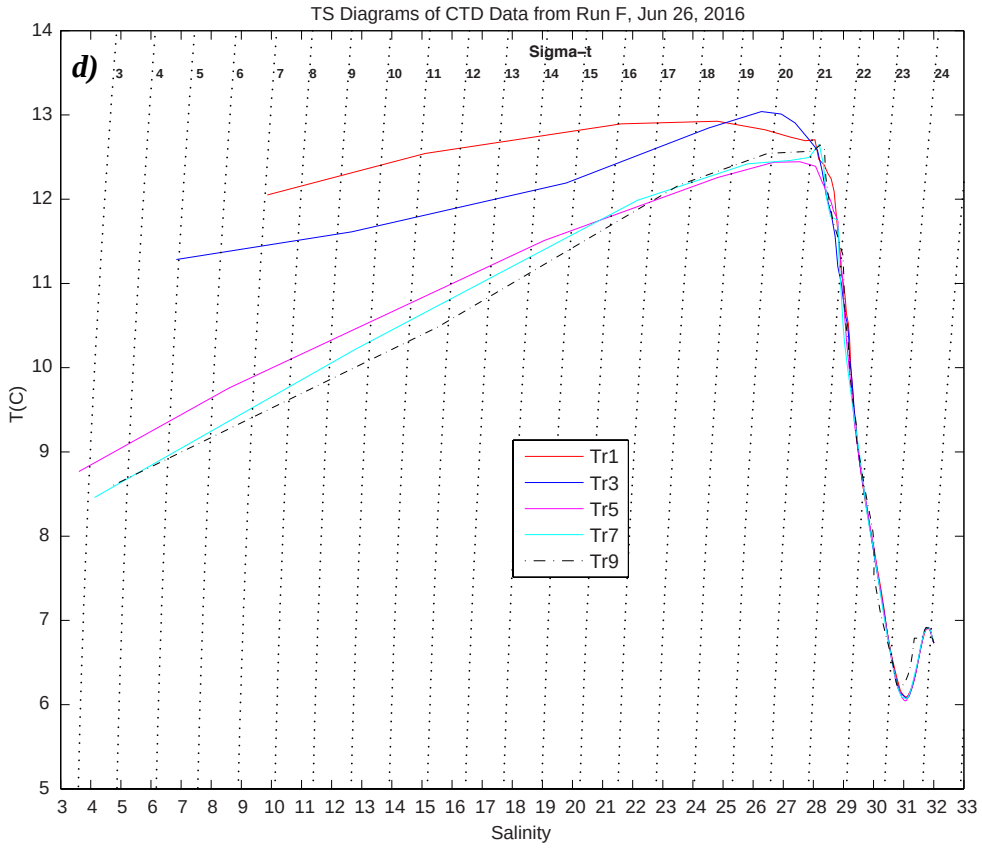

Fig. 6 (cont). Mean cross-channel temperature versus salinity for transects 1, 3, 5, 7 and 9: c) mean profiles on June 21; and d) mean profiles on June 26.

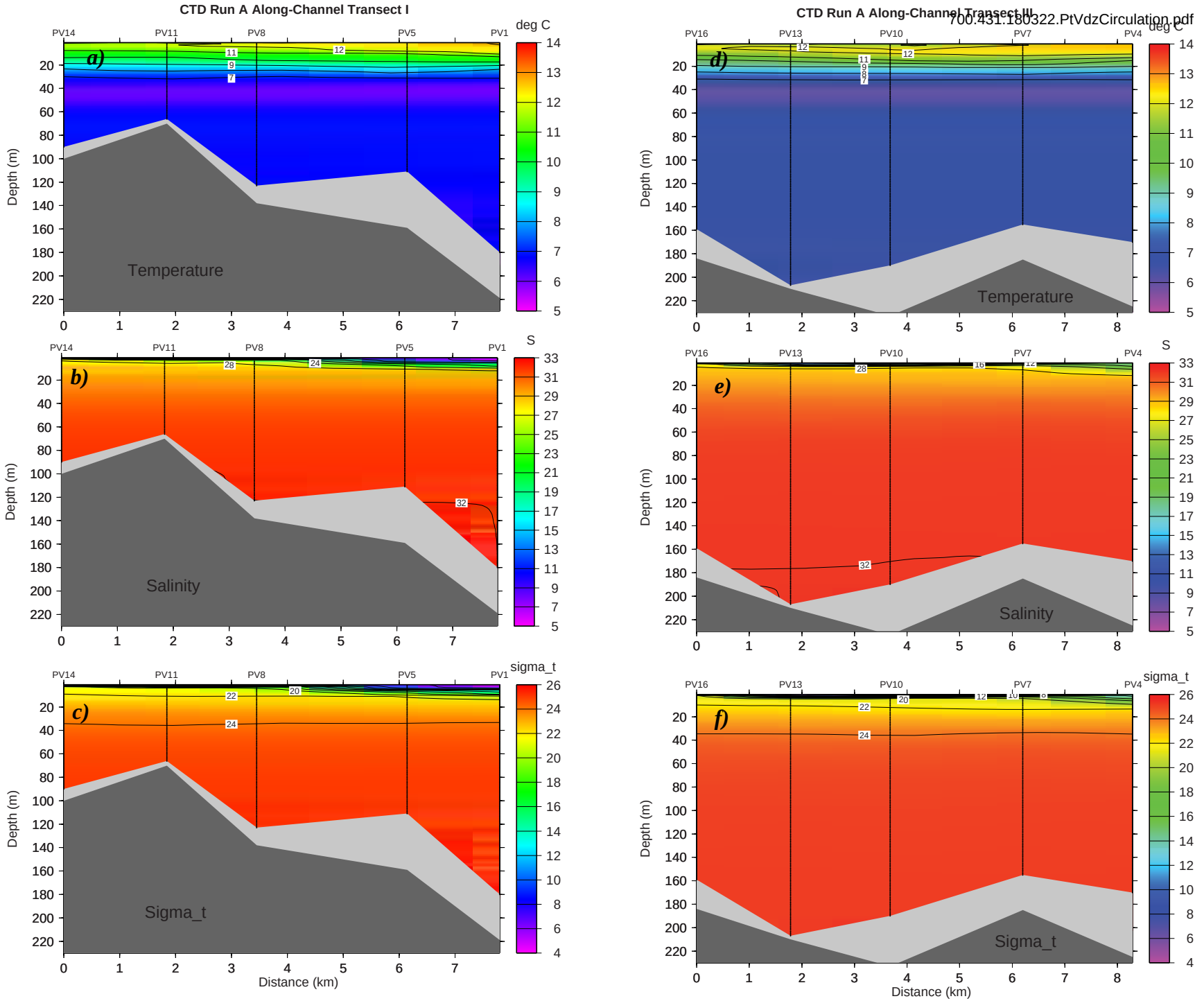

Fig. 7A. Vertical sections of along-channel temperature, salinity and density for CTD transects I and III (Fig. 2b), Run A on June 22, 2016.

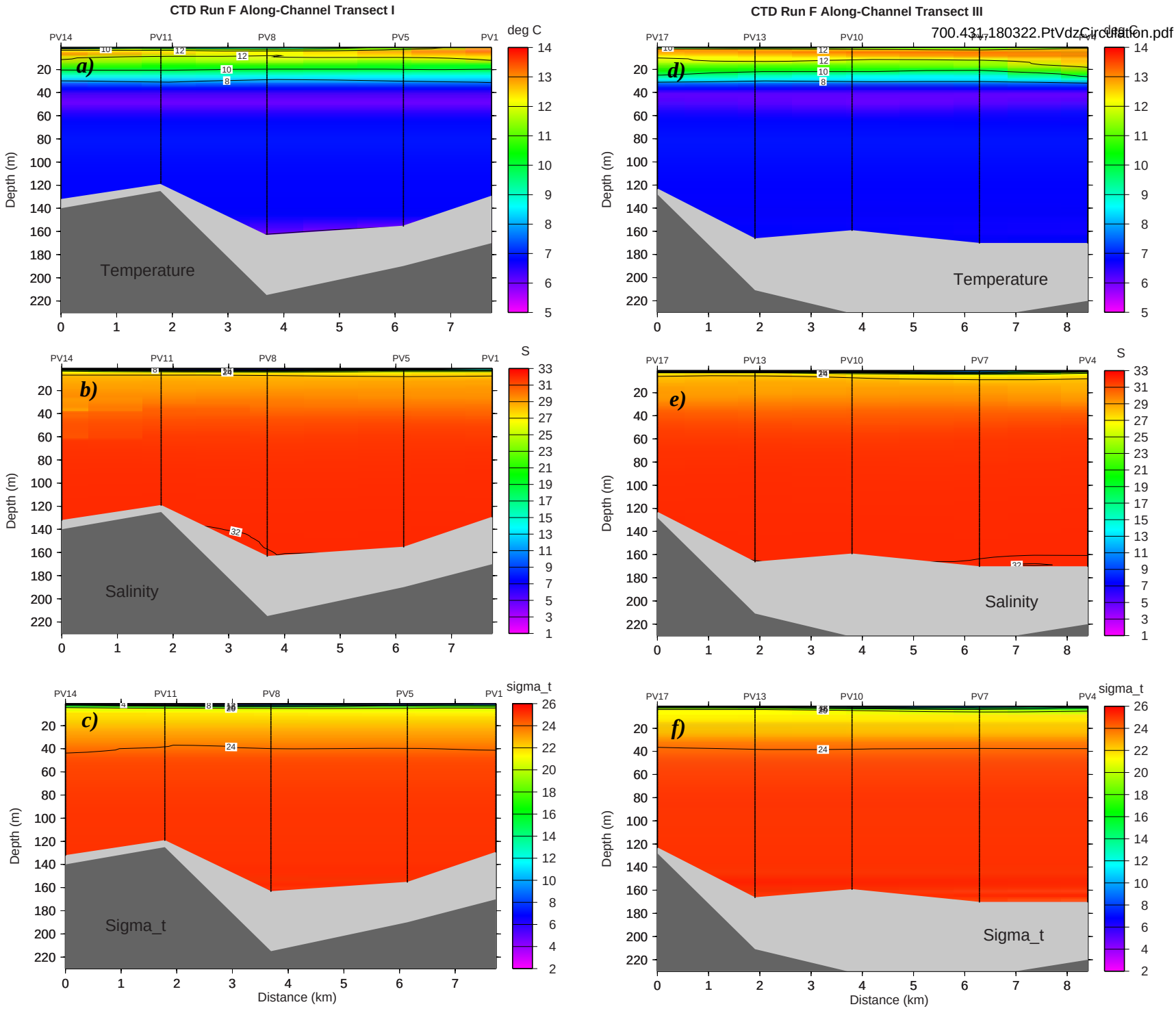

Fig. 7B. Vertical sections of along-channel temperature, salinity and density for CTD transects I and III (Fig. 2b), Run F on June 26, 2016.

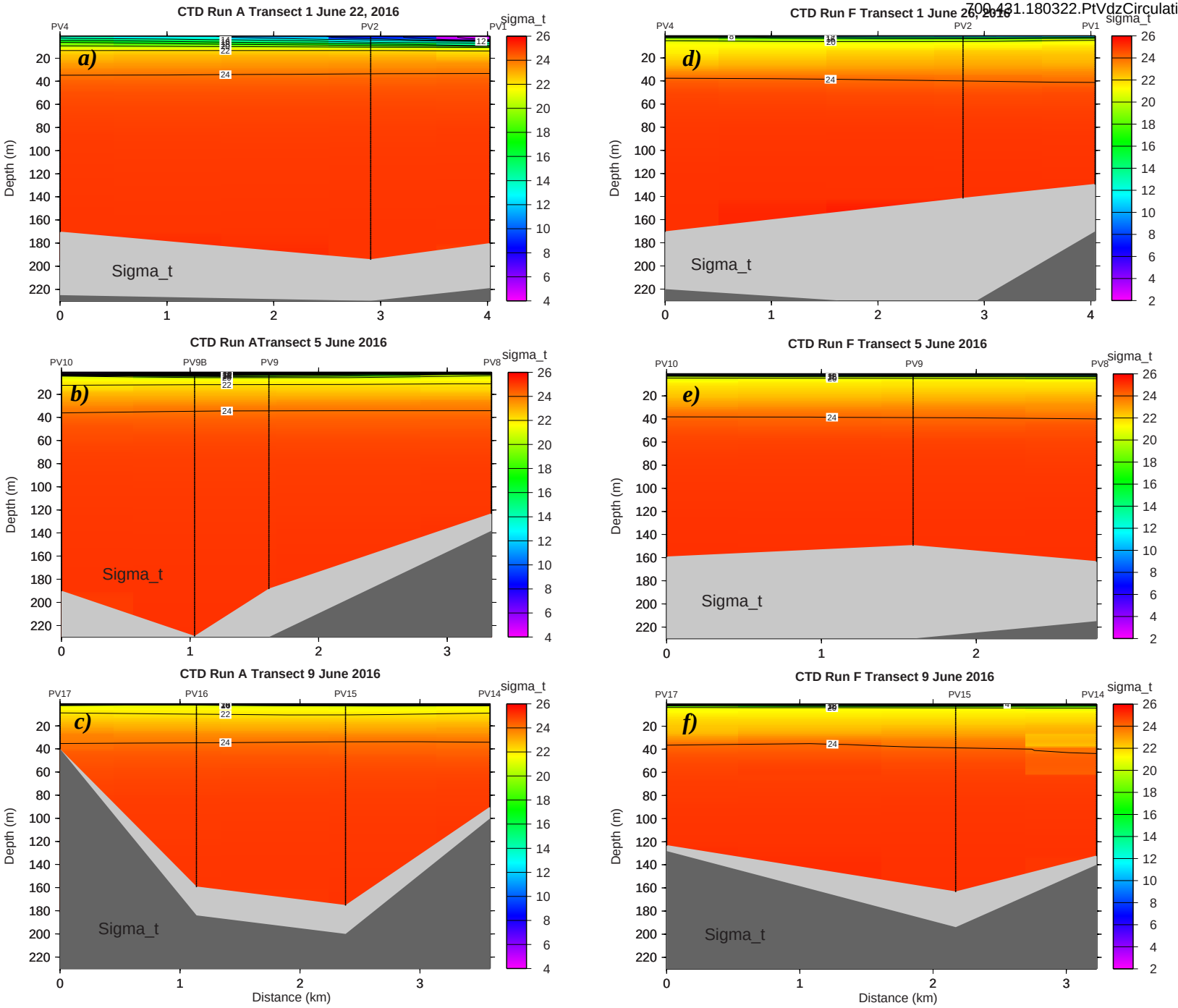

Fig. 7C. Vertical sections of cross-channel density for transects 1, 5 and 9, Runs A and F on June 22 and 26, 2016.

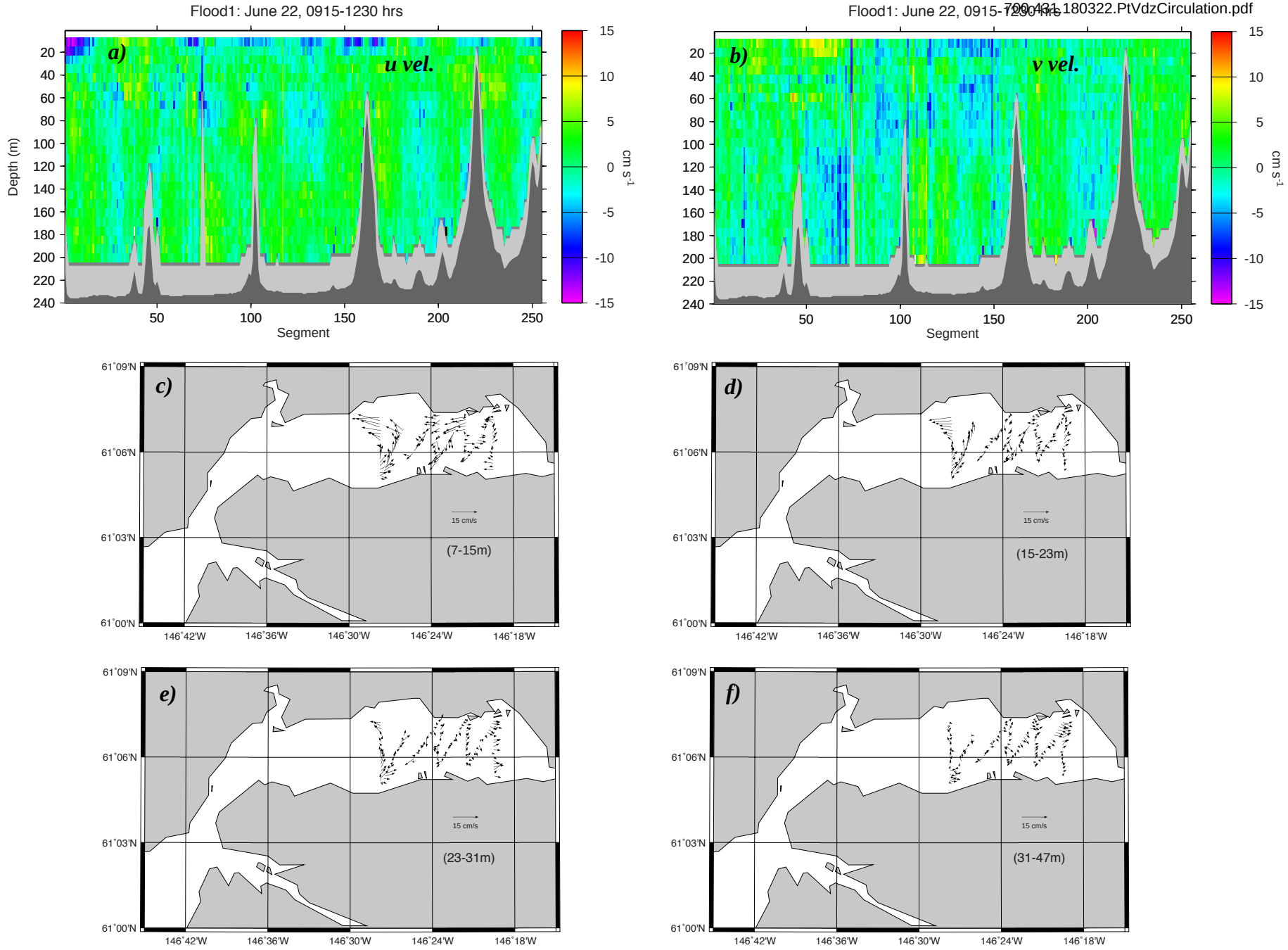

Fig. 8A. ADCP currents measured on June 22, 2016 over the first flood tide during the 36 hr survey: a) *u* velocity components; b) *v* velocity components; c to e) velocity vectors for the first three 8 m depth bins centered at 11, 19 and 27 *m* respectively; and f) velocity vectors averaged over the next two bins from 31 to 47 *m*. Note that transects are from west to east, starting at the northwest corner (tran. #1) and ending at the southeast corner (tran. #9). The vectors are ~ 60 *sec* in length (i.e. averages of every two 30 *sec* segments shown in a and b above.

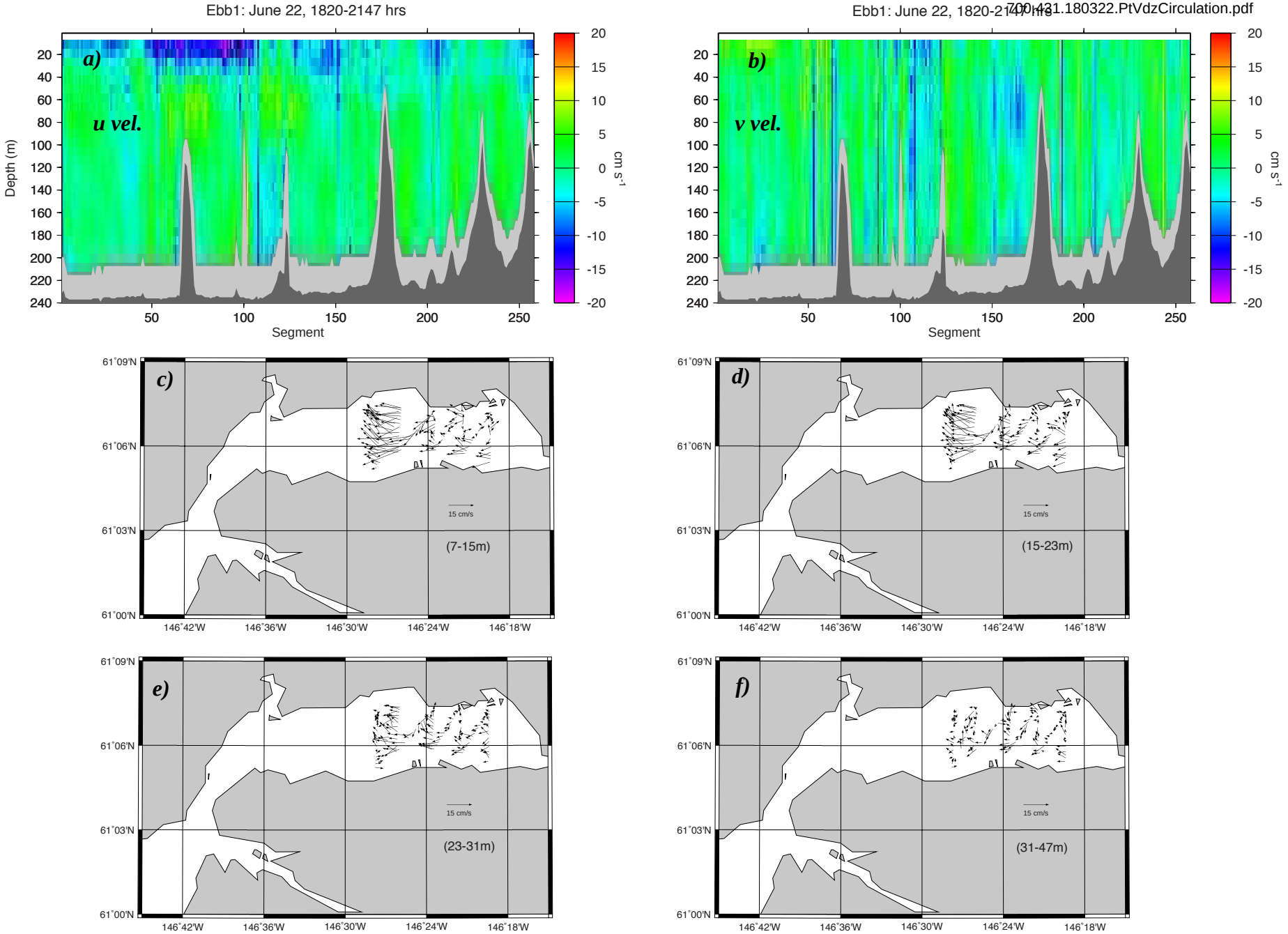

Fig. 8B. ADCP currents measured on June 22, 2016 over the last half of ebb tide 1 and the first 47 min of flood tide 2 during the 36 hr survey: a) *u* velocity components; b) *v* velocity components; c to e) velocity vectors for the first three 8 *m* depth bins centered at 11, 19 and 27 *m* respectively; and f) velocity vectors averaged over the next two bins from 31 to 47 *m*. Note the scale change in the vertical sections (+/- 20 cm s^{-1}) and that transects go from west to east, starting at the northwest corner (tran. #1) and ending at the southeast corner (tran. #9). The vectors are ~ *60 sec* in length (i.e. averages of every two 30 *sec* segments shown in a and b above.

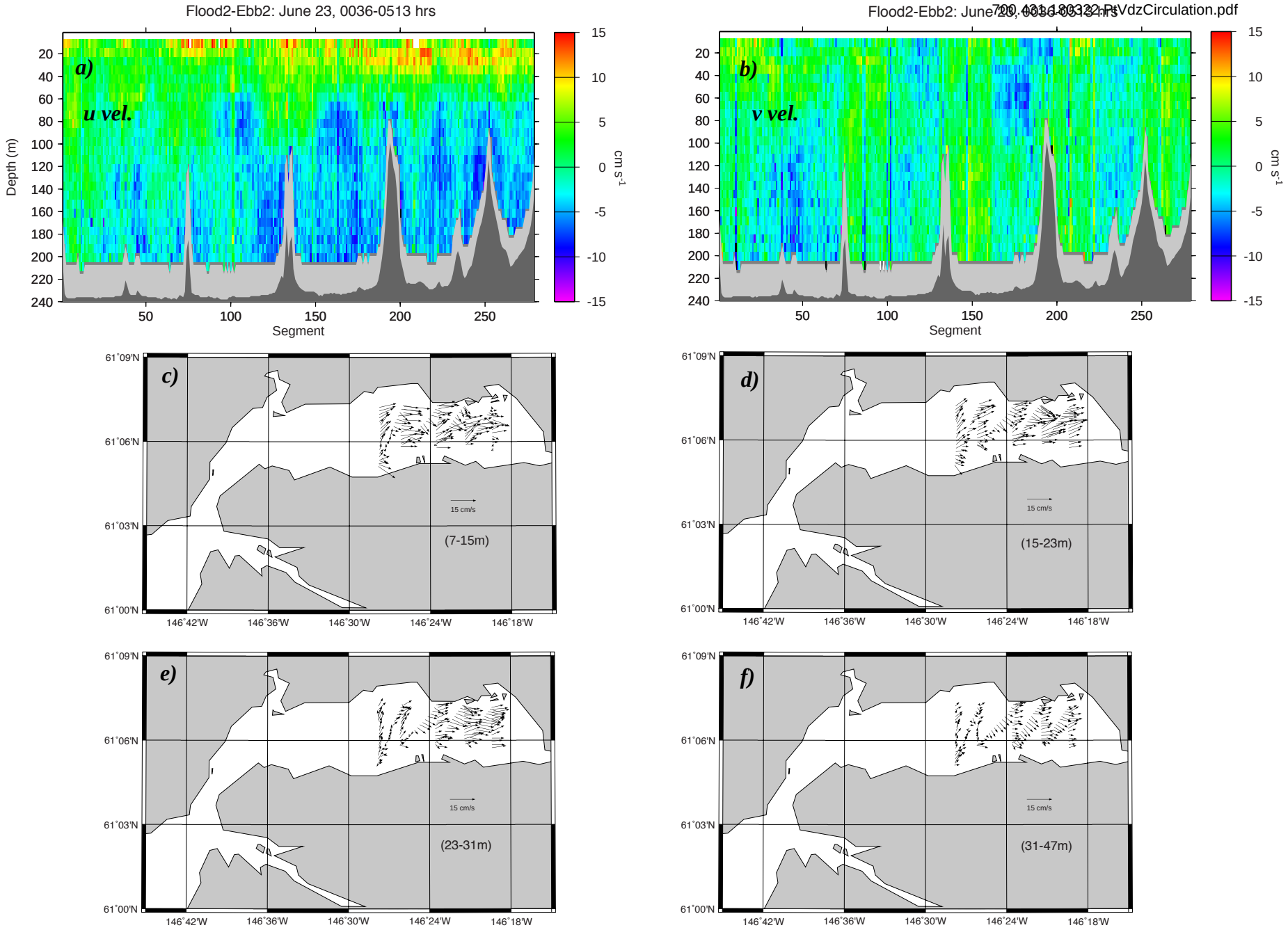

Fig. 8C. ADCP currents measured on June 23, 2016 over the last 2.3 hr of flood tide 2 and the first 2.0 hr of ebb tide 2 during the 36 hr survey: a) *u* velocity components; b) *v* velocity components; c to e) velocity vectors for the first three 8 *m* depth bins centered at 11, 19 and 27 *m* respectively; and f) velocity vectors averaged over the next two bins from 31 to 47 *m*. Note that transects are from west to east, starting at the northwest corner (tran. #1) and ending at the southeast corner (tran. #9). The vectors are ~ 60 *sec* in length (i.e. averages of every two 30 *sec* segments shown in a and b above.

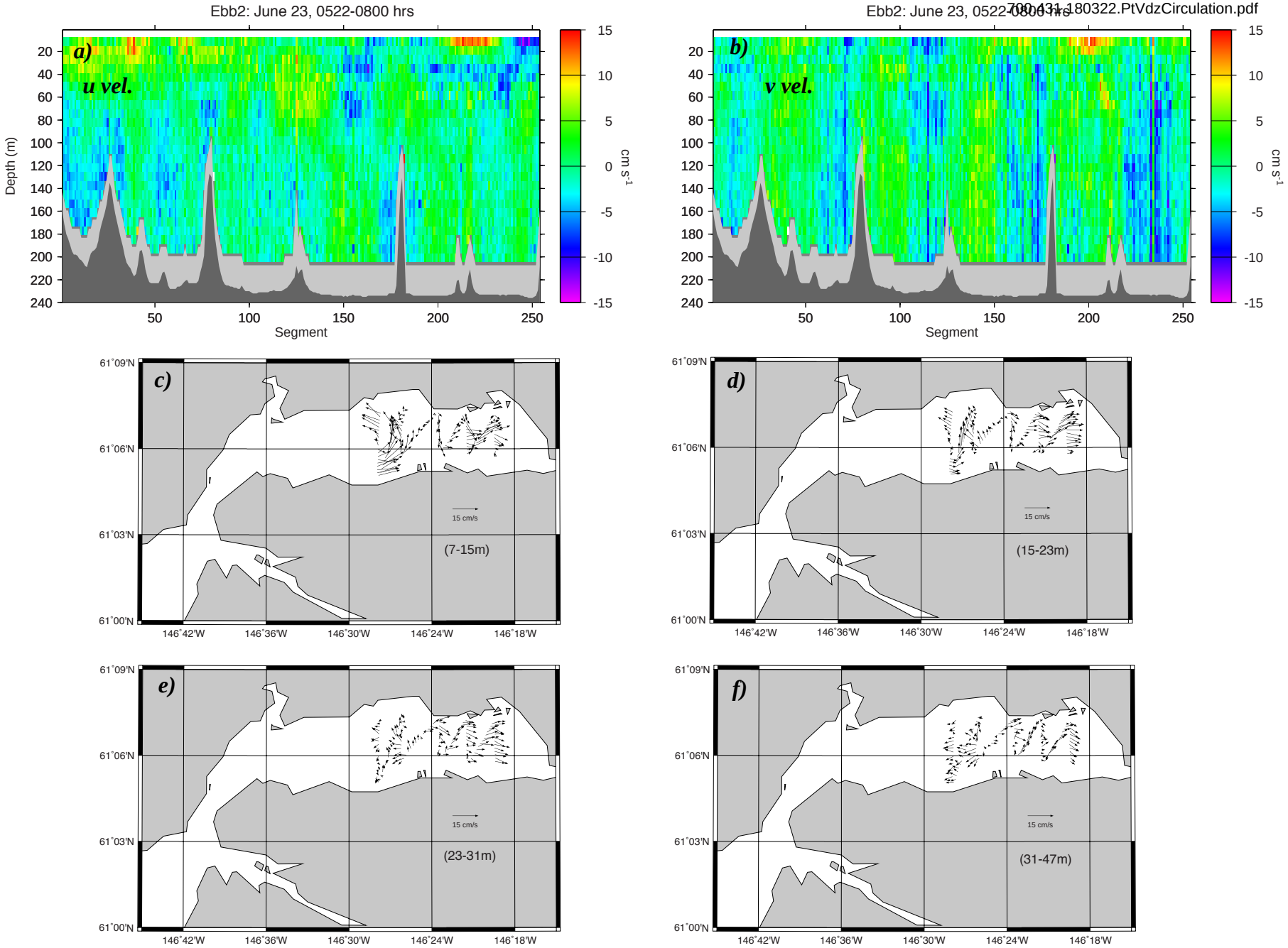

Fig. 8D. ADCP currents measured on June 23, 2016 over the second ebb tide during the 36 hr survey: a) *u* velocity components; b) *v* velocity components; c to e) velocity vectors for the first three 8 *m* depth bins centered at 11, 19 and 27 *m* respectively; and f) velocity vectors averaged over the next two bins from 31 to 47 *m*. Note that transects are from east to west, starting at the southeast corner (tran. #9) and ending at the northwest corner (tran. #1). The vectors are ~ 60 *sec* in length (i.e. averages of every two 30 *sec* segments shown in a and b above.

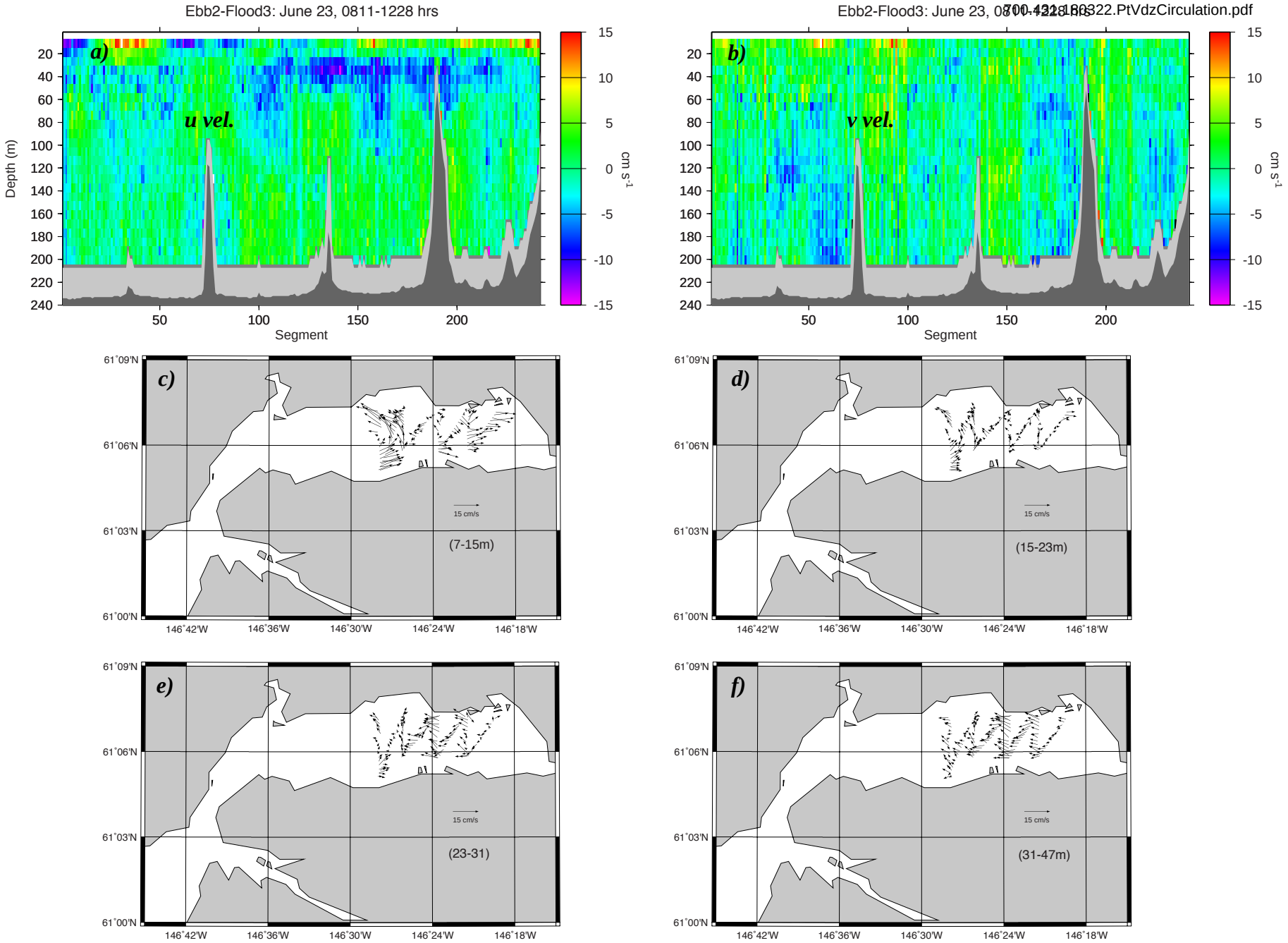

Fig. 8E. ADCP currents measured on June 23, 2016 over the last 2.0 hr of ebb tide 2 and the first 2.5 hr of flood tide 3 during the 36 hr survey: a) *u* velocity components; b) *v* velocity components; c to e) velocity vectors for the first three 8 *m* depth bins centered at 11, 19 and 27 *m* respectively; and f) velocity vectors averaged over the next two bins from 31 to 47 *m*. Note that transects are from west to east, starting at the northwest corner (tran. #1) and ending at the southeast corner (tran. #9). The vectors are ~ 60 *sec* in length (i.e. averages of every two 30 *sec* segments shown in a and b above.

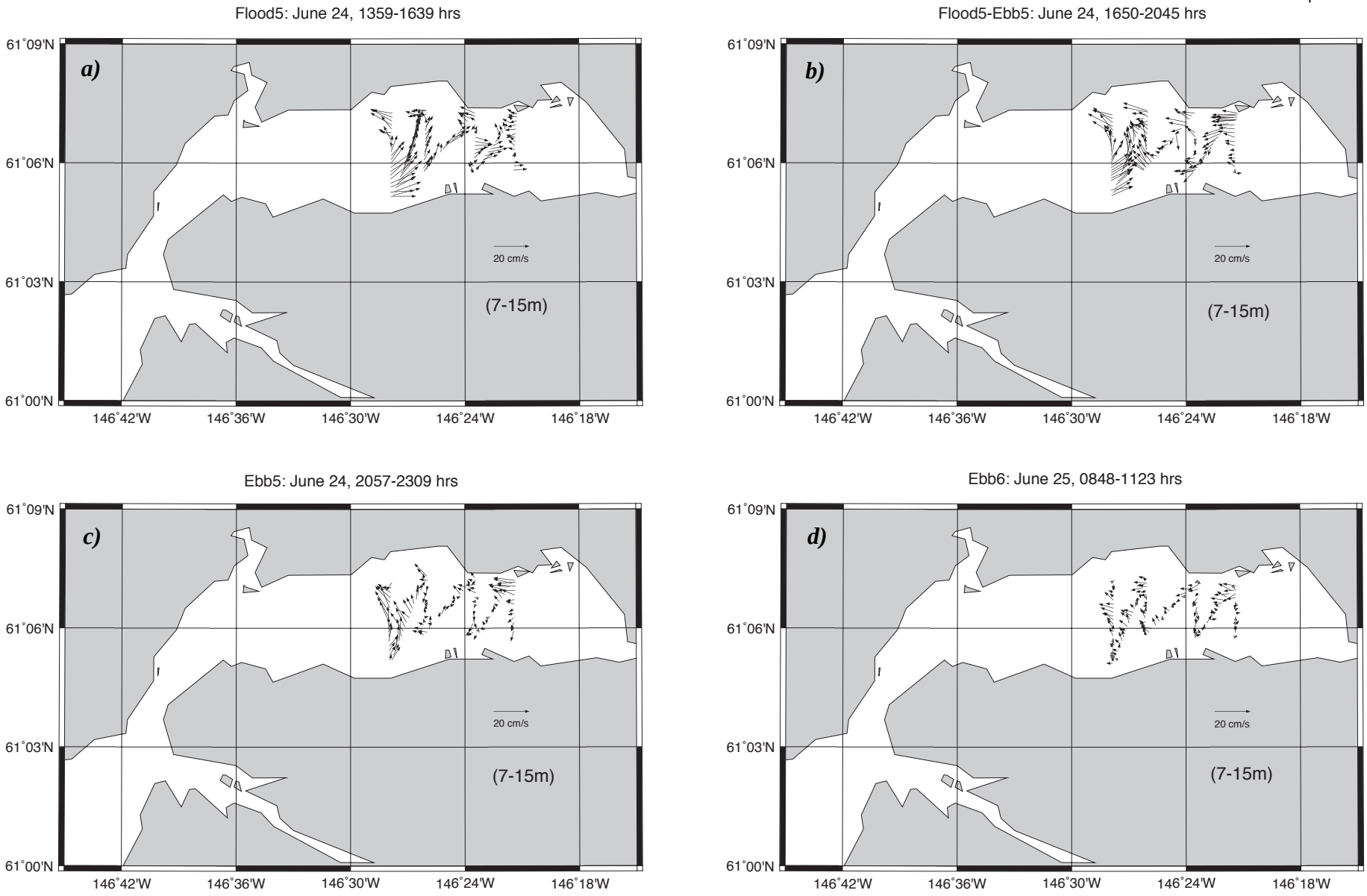

Fig. 9. ADCP current vectors at 7 to 15 *m* measured on June 24 to 25, 2016 following the 36 *hr* survey: a) last half of flood tide 5; b) transition from the last 0.5 *hr* of flood 5 to the first 3.3 *hr* of ebb tide 5; c) last 2.7 *hr* of ebb tide 5; and d) last 2.7 *hr* of ebb tide 6. The vectors are ~ 60 *sec* in length (i.e. averages of every two 30 *sec* segments shown in a and b above.

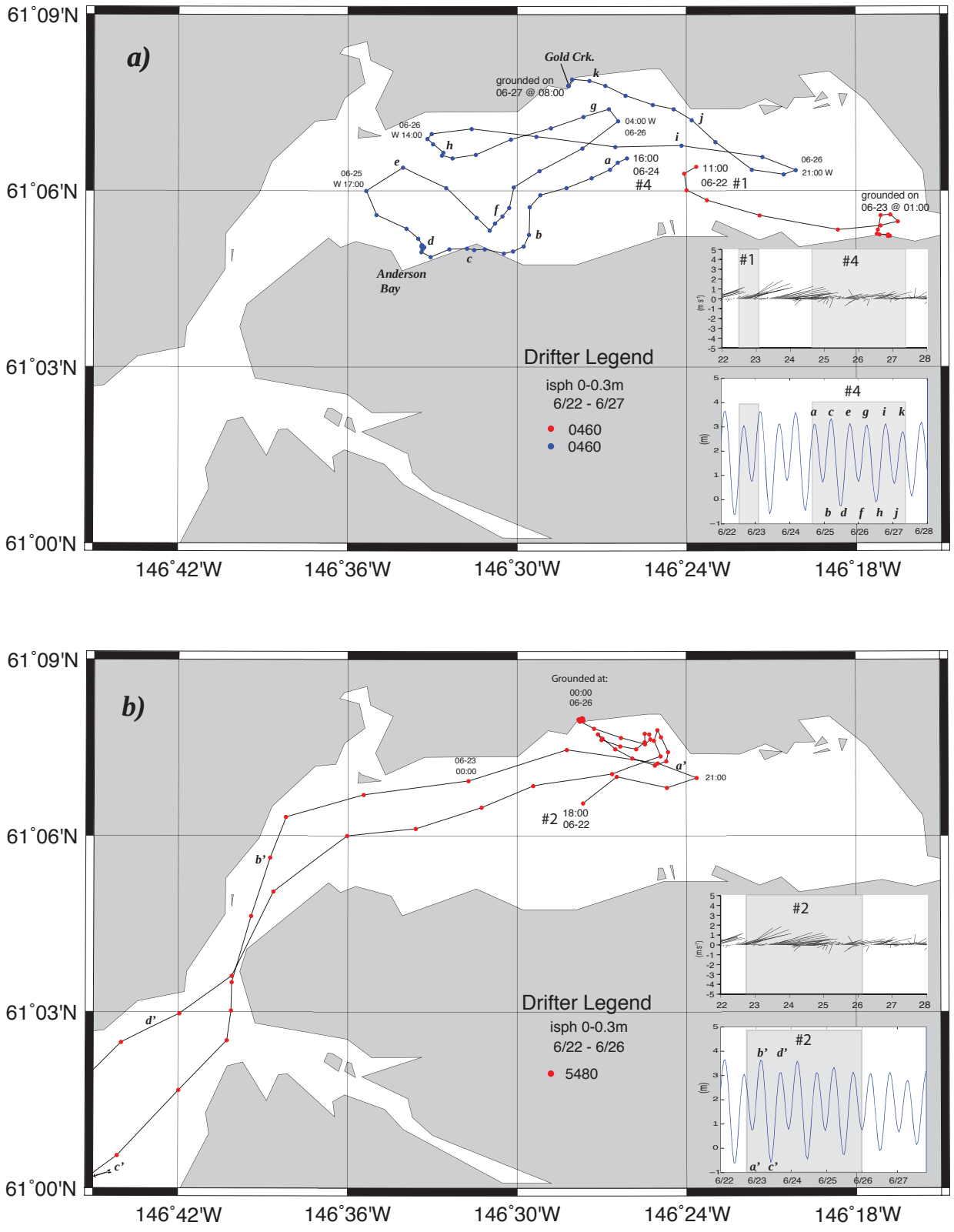

Fig. 10. Trajectories of ispheres showing combined wind and surface flows: a) deployments #1 and #4 for isphere 0460 on June 22nd and 24th. b) deployment 2 of isphere 5480 on June 22. The wind vectors and tides corresponding to the periods of each deployment are shown as shaded regions in the respective plots. Note that positions (dots) are hourly and times are local (ADT). The times of significant wind shifts are shown denoted with a 'W' and tide phases are denoted by small italicized letters in bold.

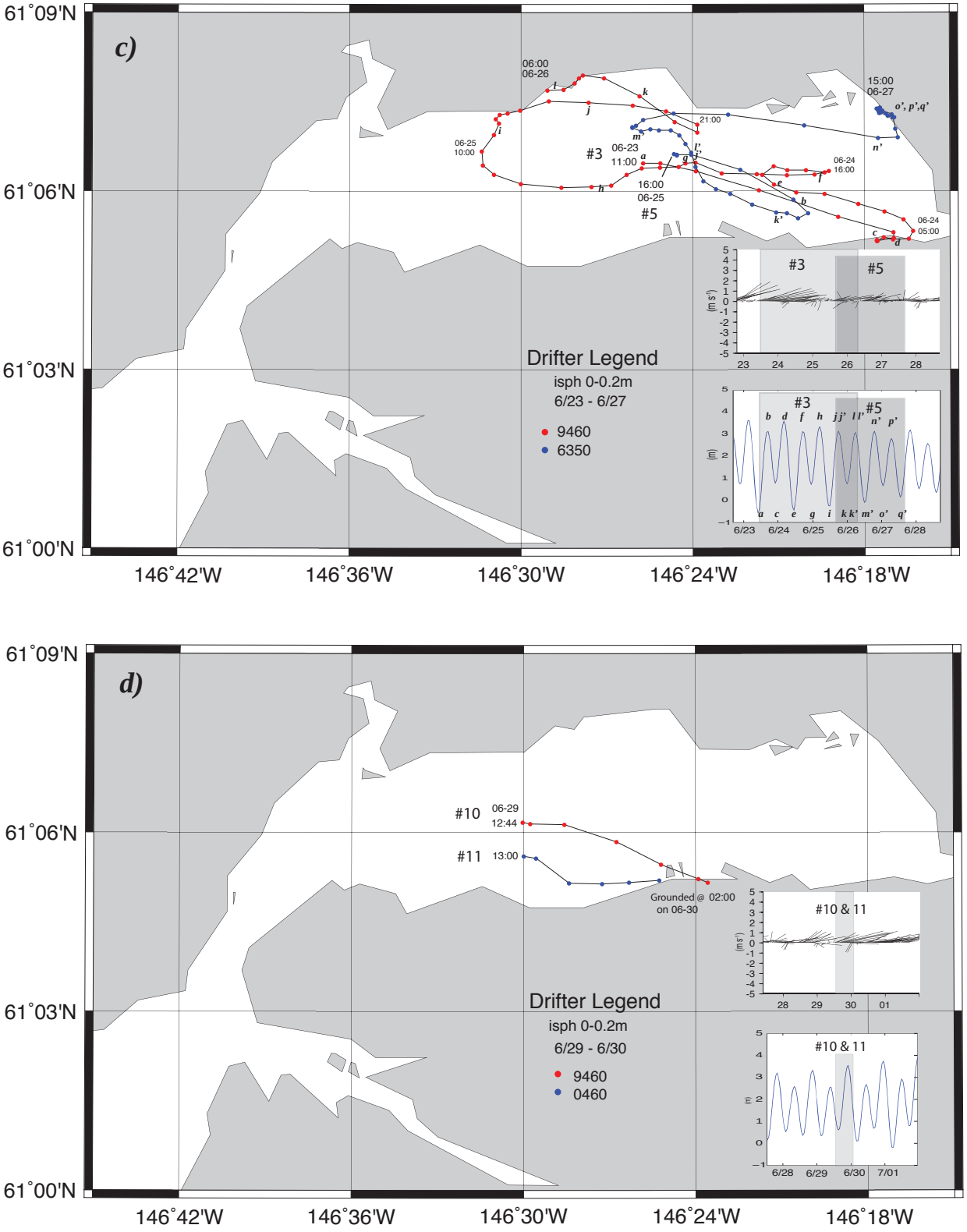

Fig. 10 (cont). c) deployments #3 and #5 for ispheres 9460 and 6350 on the 23rd and 25th respectively; and d) deployments #10 and #11 of i9460 and i0460 on the 29th, which grounded at the Alyeska Oil Terminal on the 30th. The wind vectors and tides corresponding to the periods of each deployment are shown as shaded regions in the respective plots. Note that positions (dots) are hourly and times are local (ADT).

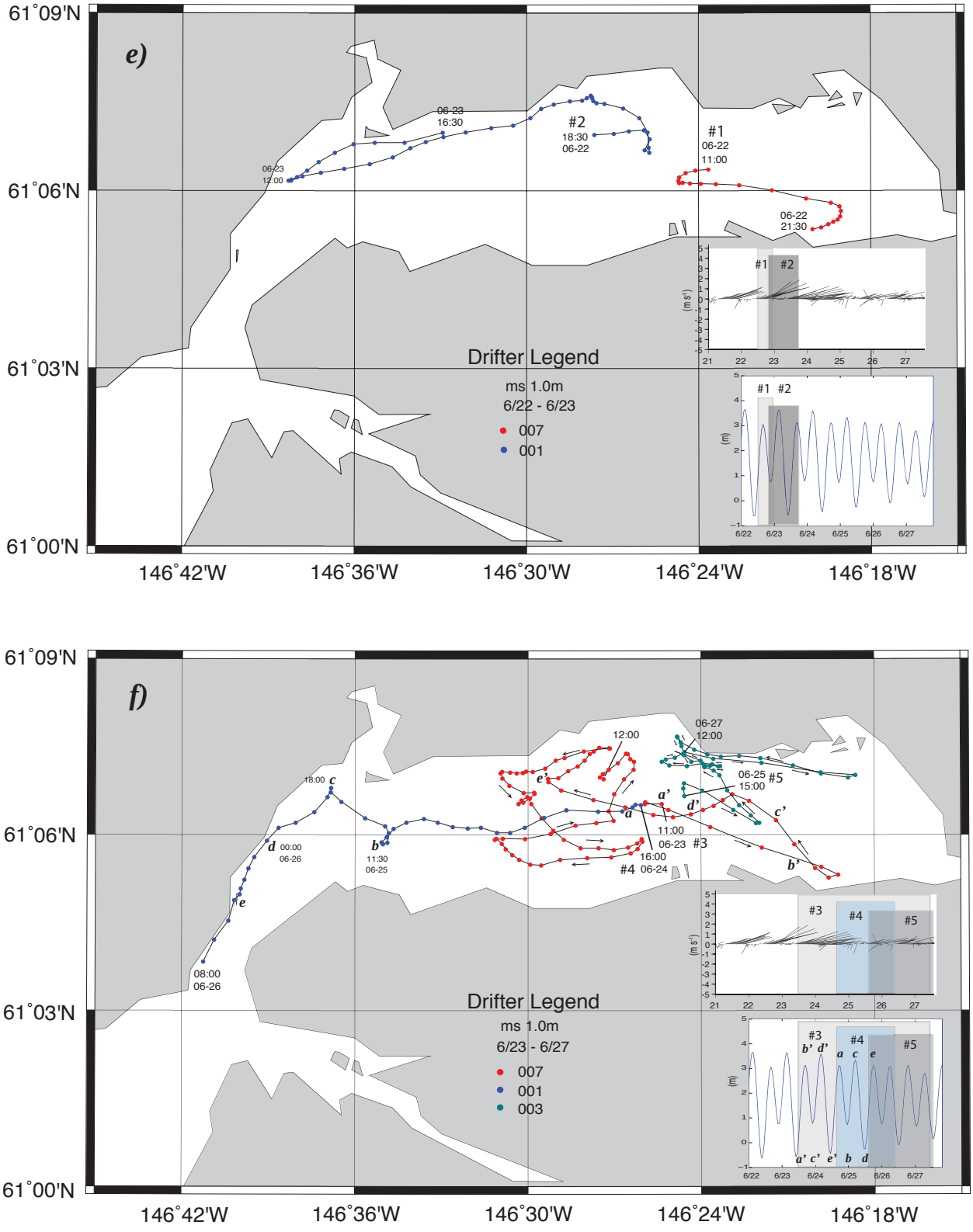

Fig. 10 (cont). Microstar trajectories showing flows at 1*m* depth: e) deployments #1 and #2 on June 22 for m007 and m001; f) deployments #3 to #5 of m007, m001 and m003 on June 23rd, 24th and 25th respectively. The wind vectors and tides corresponding to the periods of each deployment are shown as shaded (colored) regions in the respective plots. Note that positions (dots) are half hourly in panel-e and hourly in panel-f. All times are local (ADT).

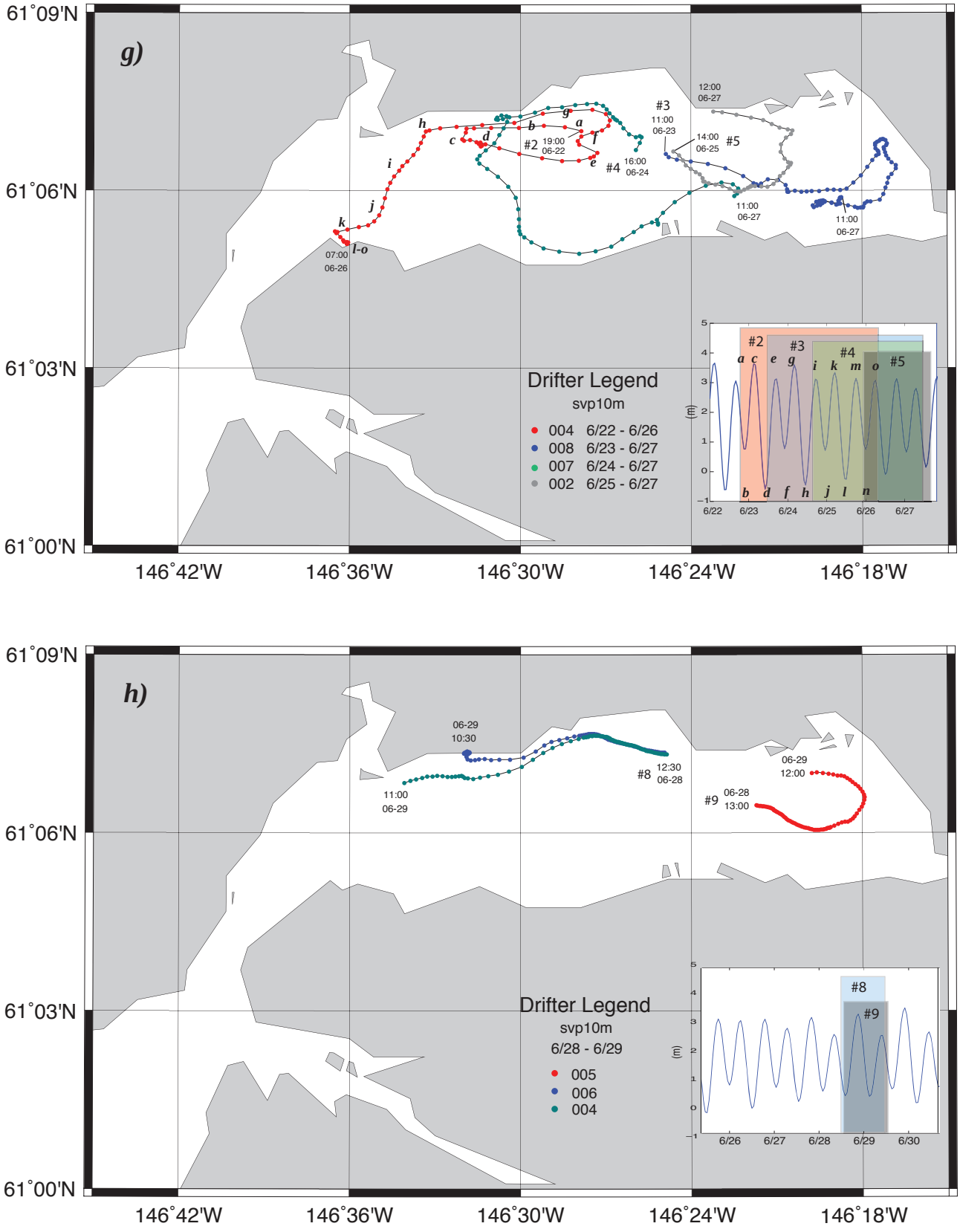

Fig. 10 (cont.). Trajectories of SVP drifters showing flows at 10*m* depths: g) Single deployments #2 to #5 of s004, s008, s007 and s002 respectively from June 22 to 27; and h) deployments #8 and #9 of s005, s006 and s004 respectively on June 28. The wind vectors and tides corresponding to the periods of each deployment are shown as shaded regions in the respective plots. Note that positions (dots) are half hourly and times are local (ADT).

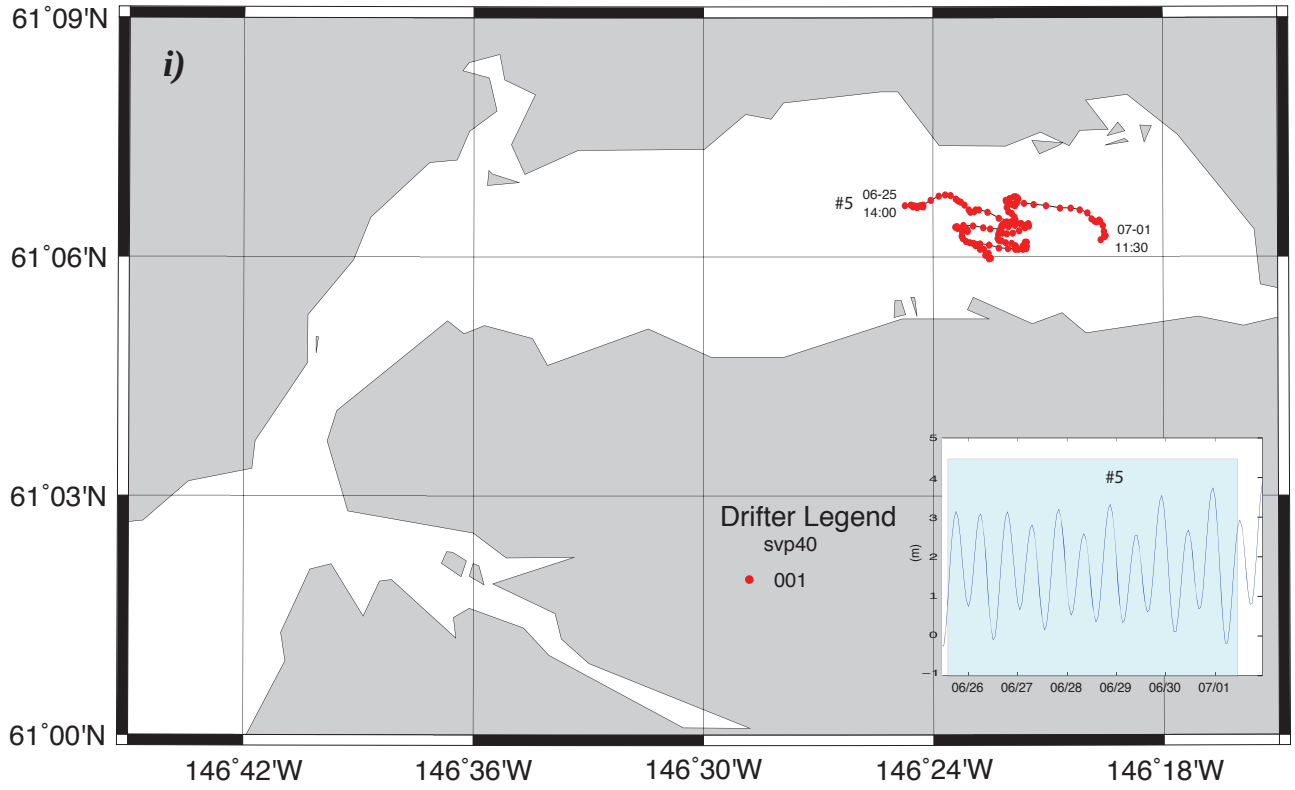

Fig. 10 (cont). i) Trajectory of SVP #001 showing flows at 40*m* depth from June 25 to July 01. The tides corresponding to the deployment period are shown as shaded regions in the lower right-hand plots. Note that positions (dots) are hourly and times are local (ADT).

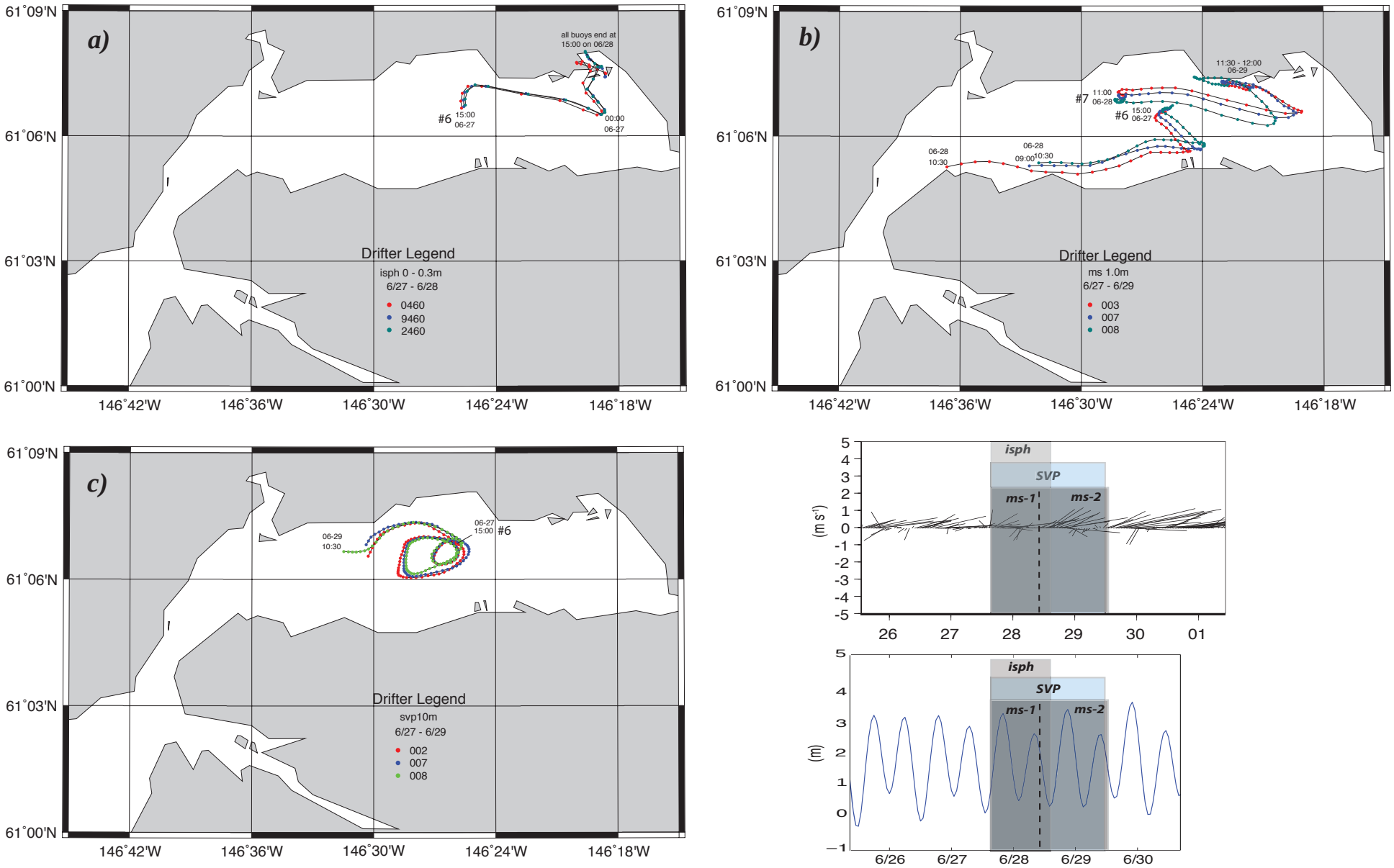

Fig. 11. The first dispersion experiment (deployments #6 and #7) consisting of three sets of drifters released together in the central fjord on June 27 and three microstars redeployed on June 28: a) ispheres 0460, 9460 and 2460 , b) microstars 003, 007 and 008 and c) SVP 10*m* drifters 002, 007 and 008. The winds and tides occurring during the experiment are shown in the two lower right-hand plots. Note that positions are half hourly and times are local (ADT).

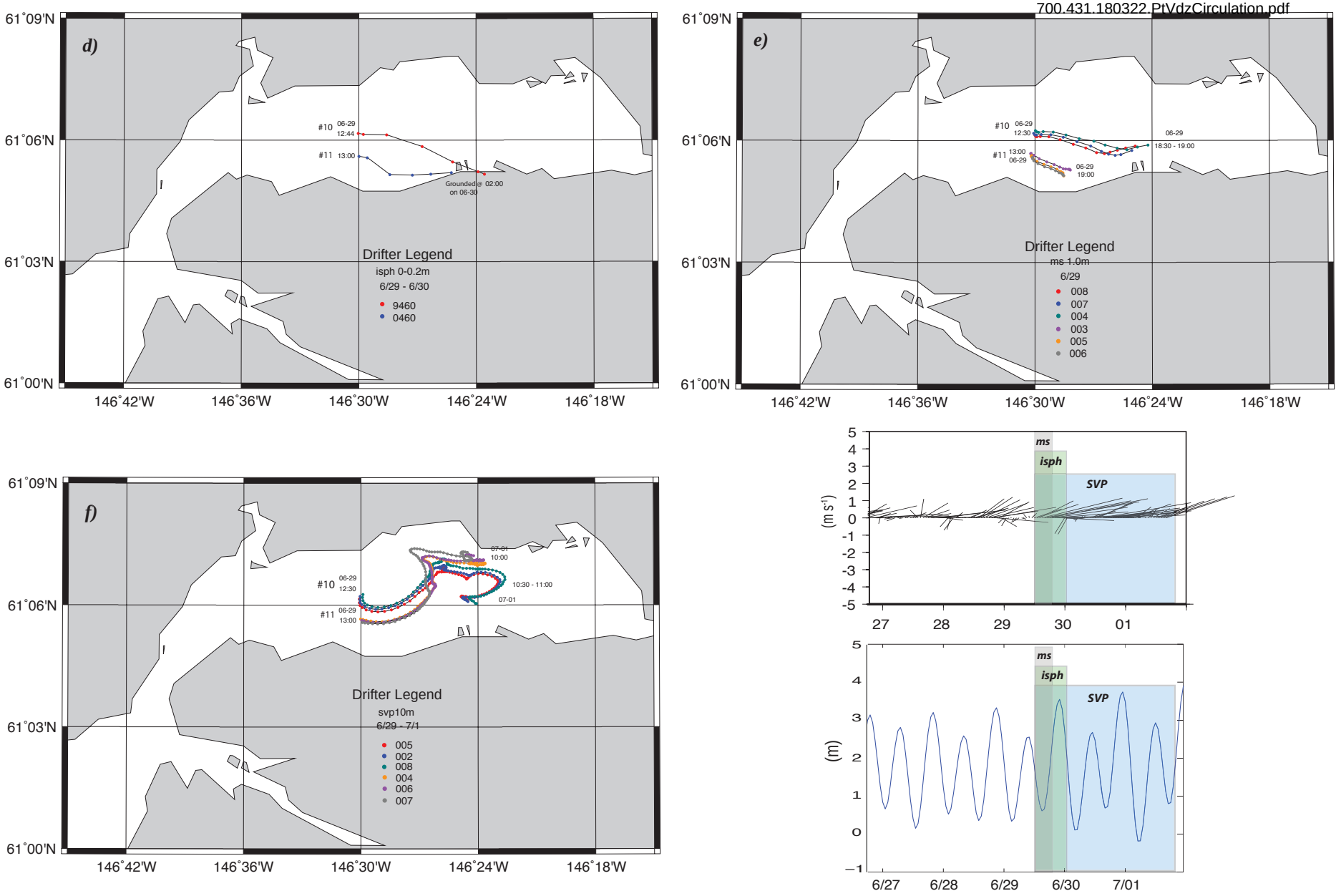

Fig. 11 (cont.). The second dispersion experiment (deployments #10 and #11) consisting of two ispheres and three sets of microstars and 10*m* SVPs released nearly simultaneously in the central fjord on June 29: a) ispheres 9460 and 0460; b) microstars 003 to 008; and c) SVP10*m* drifters 002 and 005 to 008. The winds and tides occurring during the experiment are shown in the two lower right-hand plots. Note that positions are hourly for the ispheres and half hourly all other drifters, and times are local (ADT).

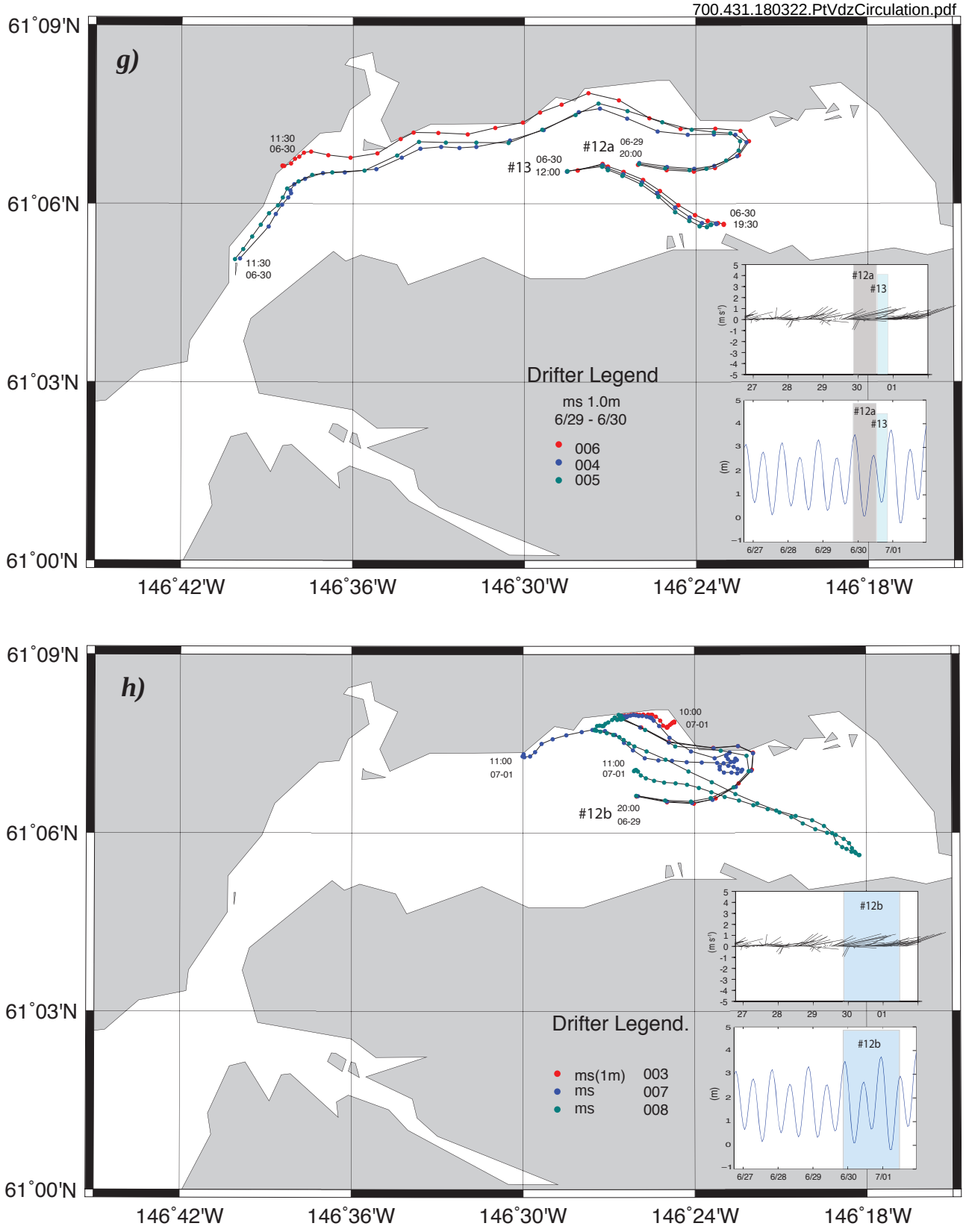

Fig. 11 (cont). Microstar trajectories showing flows at 1*m* depth during the final two dispersion experiments from June 29 to 30, 2016: g) deployments #12a and #13 of microstars 004, 005 and 006 on the 29th and 30th respectively; and h) deployments #12b of microstars 003, 007 and 008 on the 29th. The winds and tides occurring during the experiment are also shown above. Note that positions are half hourly and times are local (ADT).

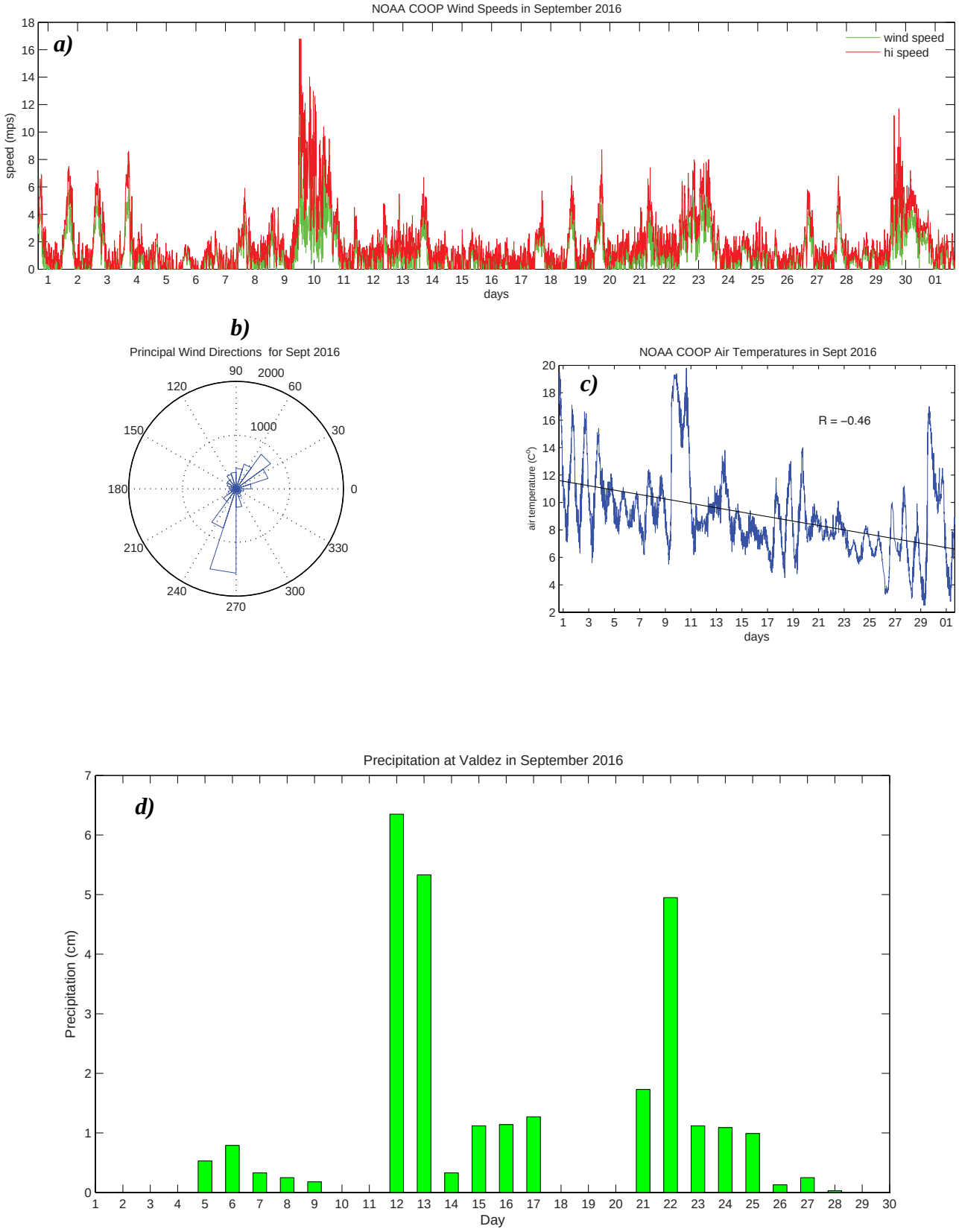

Fig. 12. Meteorological data in September 2016 collected at the Valdez, Alaska NOAA-COOPS station 9454240: a) sustained and high wind speeds measured at 6 min. intervals; b) wind rose showing directions (in 20° bins) from which the winds are coming; c) air temperatures at 6 min. intervals; and d) daily preciptation in *cm*.

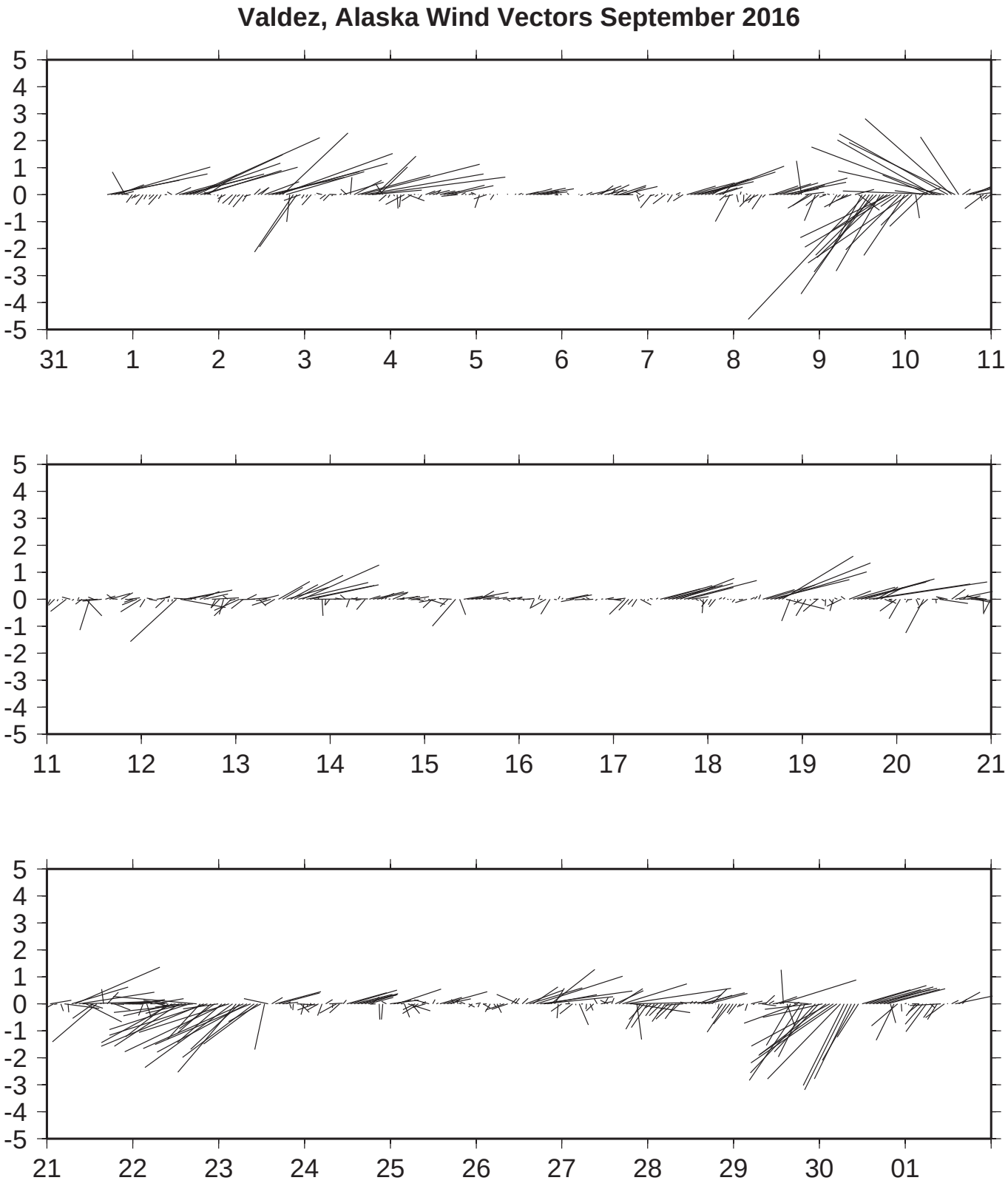

Fig. 13. Wind vectors for the month of September 2016 measured at the Valdez, Alaska NOAA-COOPS station 9454240. Note that the x-axis is for days starting on Aug. 31 and ending on Oct. 1st.

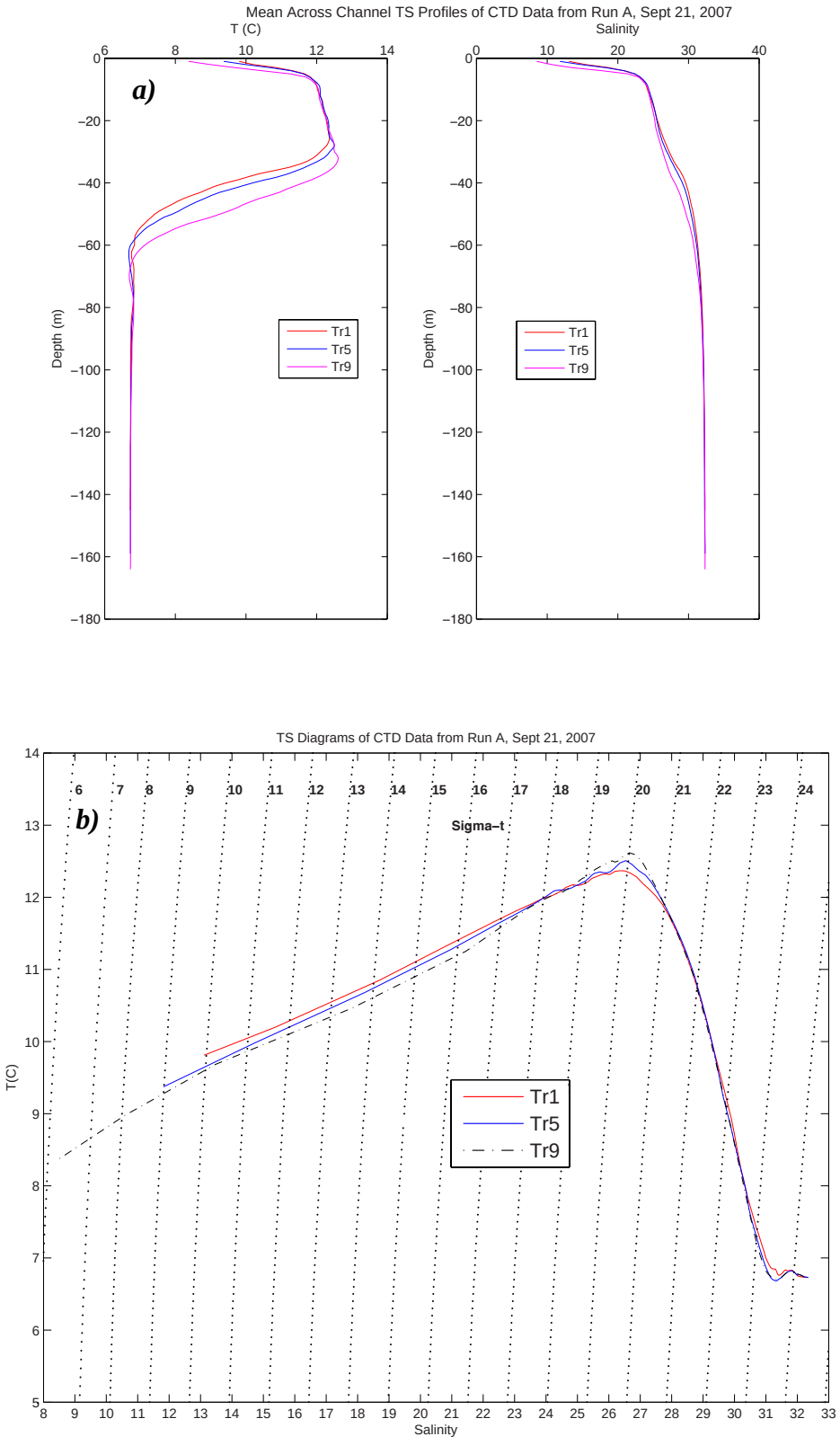

Fig. 14. Mean across-channel temperature and salinity for transects 1, 3, 5, 7 and 9, Run A on September 21, 2016: a) mean T/S profiles; and b) mean T vs. S diagram.

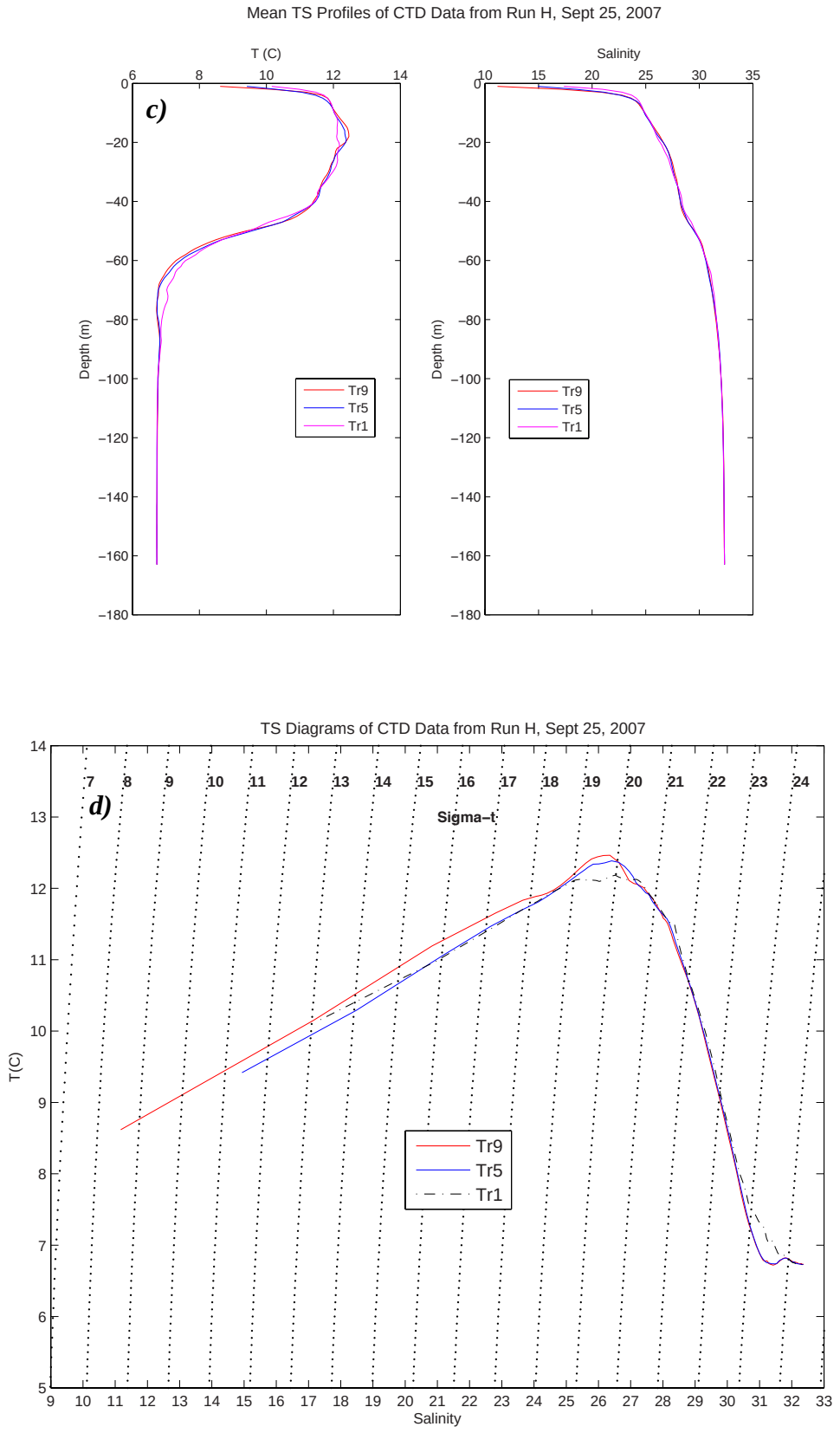

Fig. 14 (cont). Mean across-channel temperature and salinity for transects 1, 3, 5, 7 and 9, Run H on September 25, 2016: c) mean T/S profiles; and d) mean T vs. S diagram.

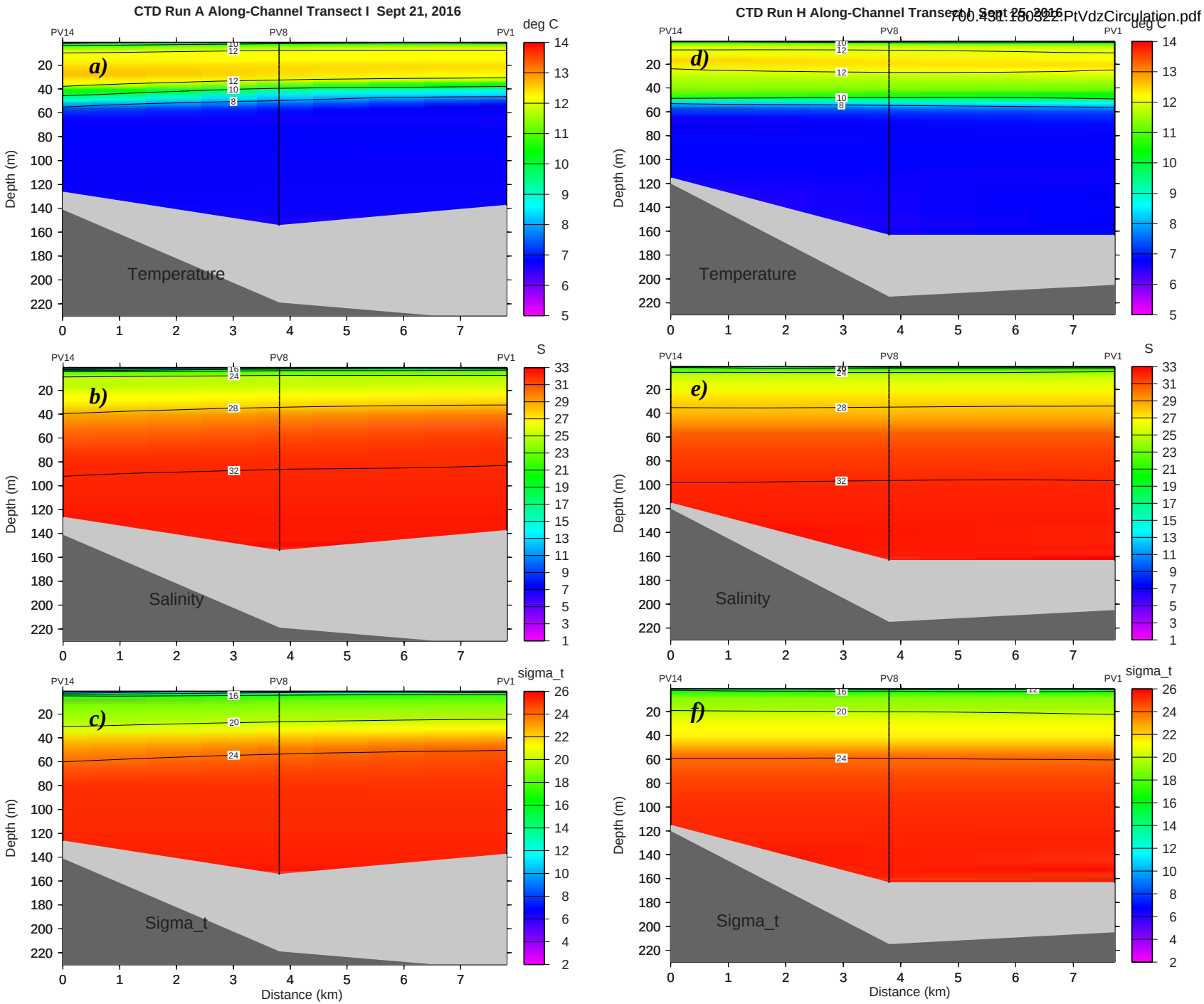

Fig. 15A. Vertical sections of along-channel temperature, salinity and density for transect I, Runs A and H on September 21 and 25, 2016.

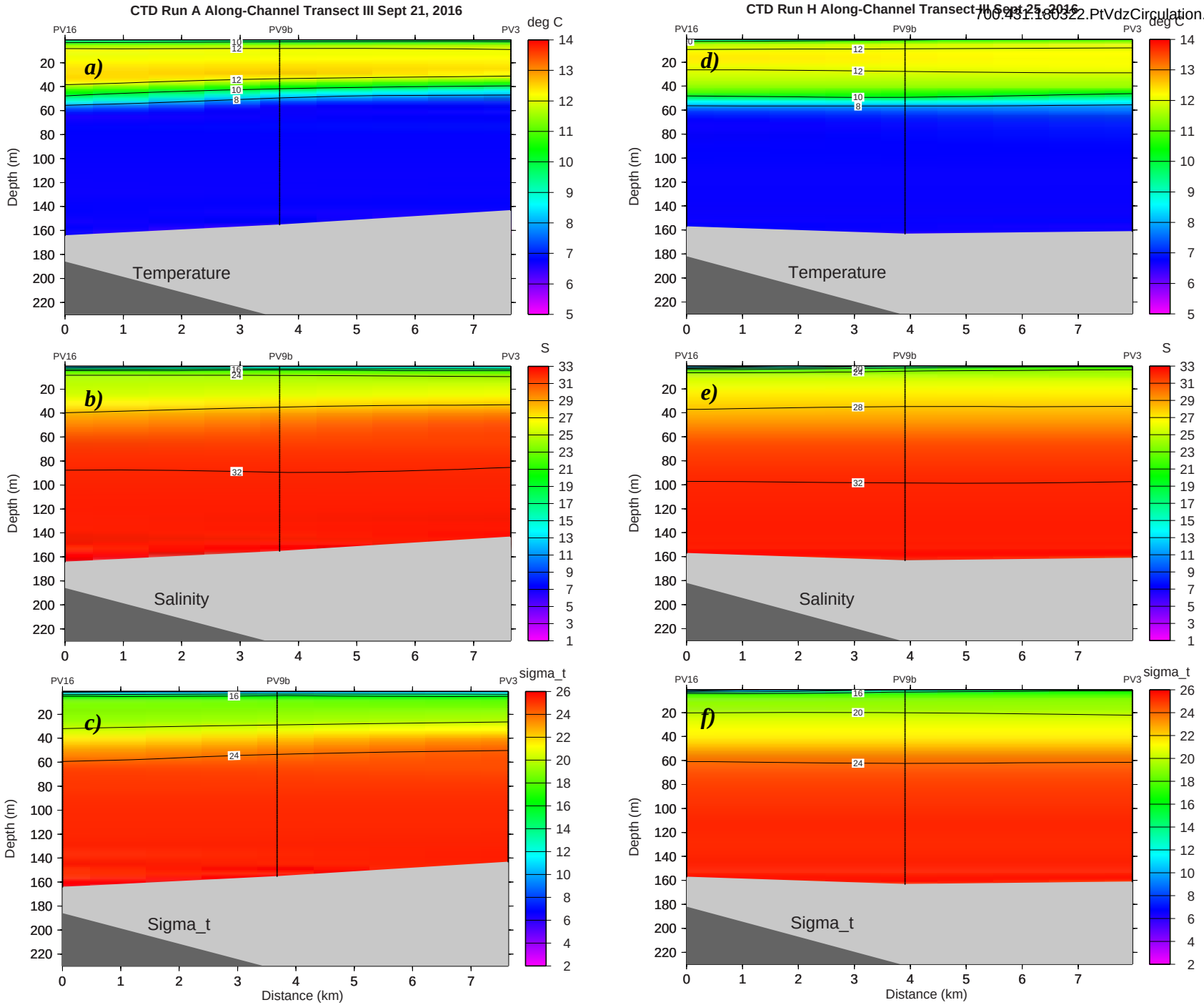

Fig. 15B. Vertical sections of along-channel temperature, salinity and density for transect III, Runs A and H on September 21 and 25, 2016.

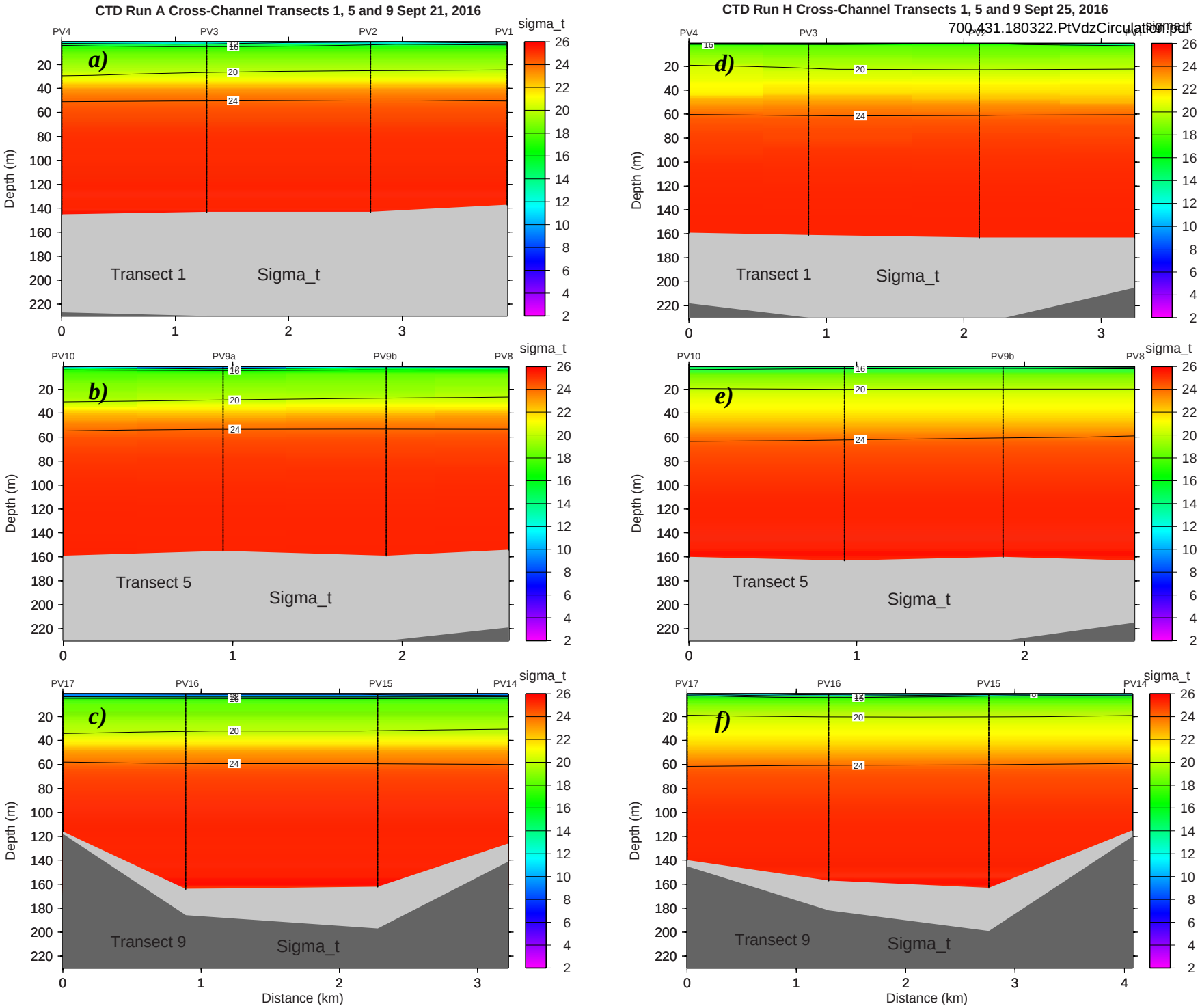

Fig. 15C. Vertical sections of cross-channel density for transects 1, 5 and 9, Runs A and H on September 21 and 25, 2016.

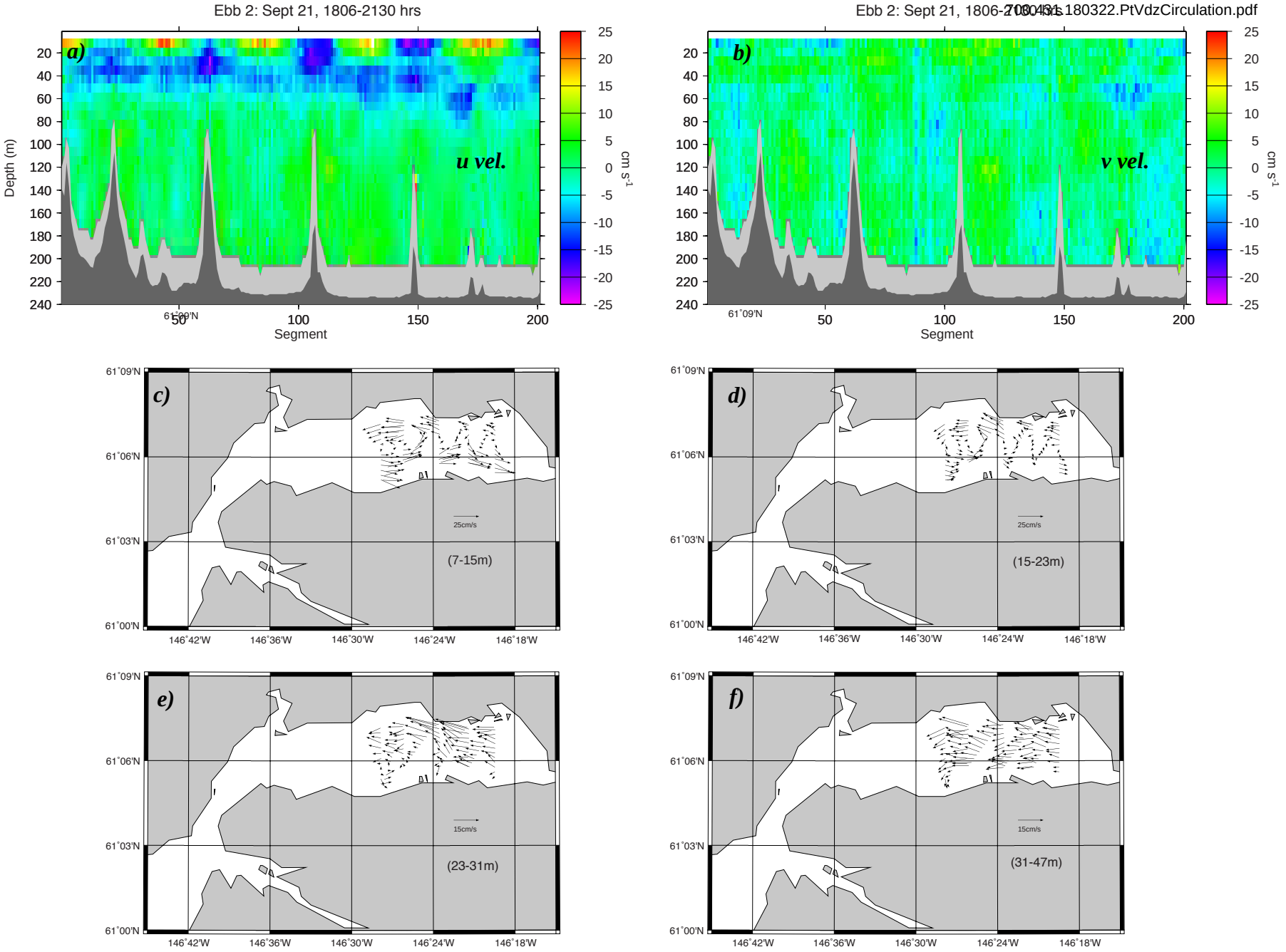

Fig. 16A. ADCP currents measured during the second ebb tide of the 36 *hr* survey on September 21, 2016: a) *u* velocity components; b) *v* velocity components; c to e) velocity vectors for the first three 8 *m* depth bins centered at 11, 19 and 27 m respectively; and f) velocity vectors averaged over the next two bins from 31 to 47 *m*. Note that transects are from east to west, starting at the southeast corner (tran. #9) and ending at the northwest corner (tran. #1). The vectors are ~ 60 *sec* in length (i.e. averages of every two 30 *sec* segments shown in a and b above.

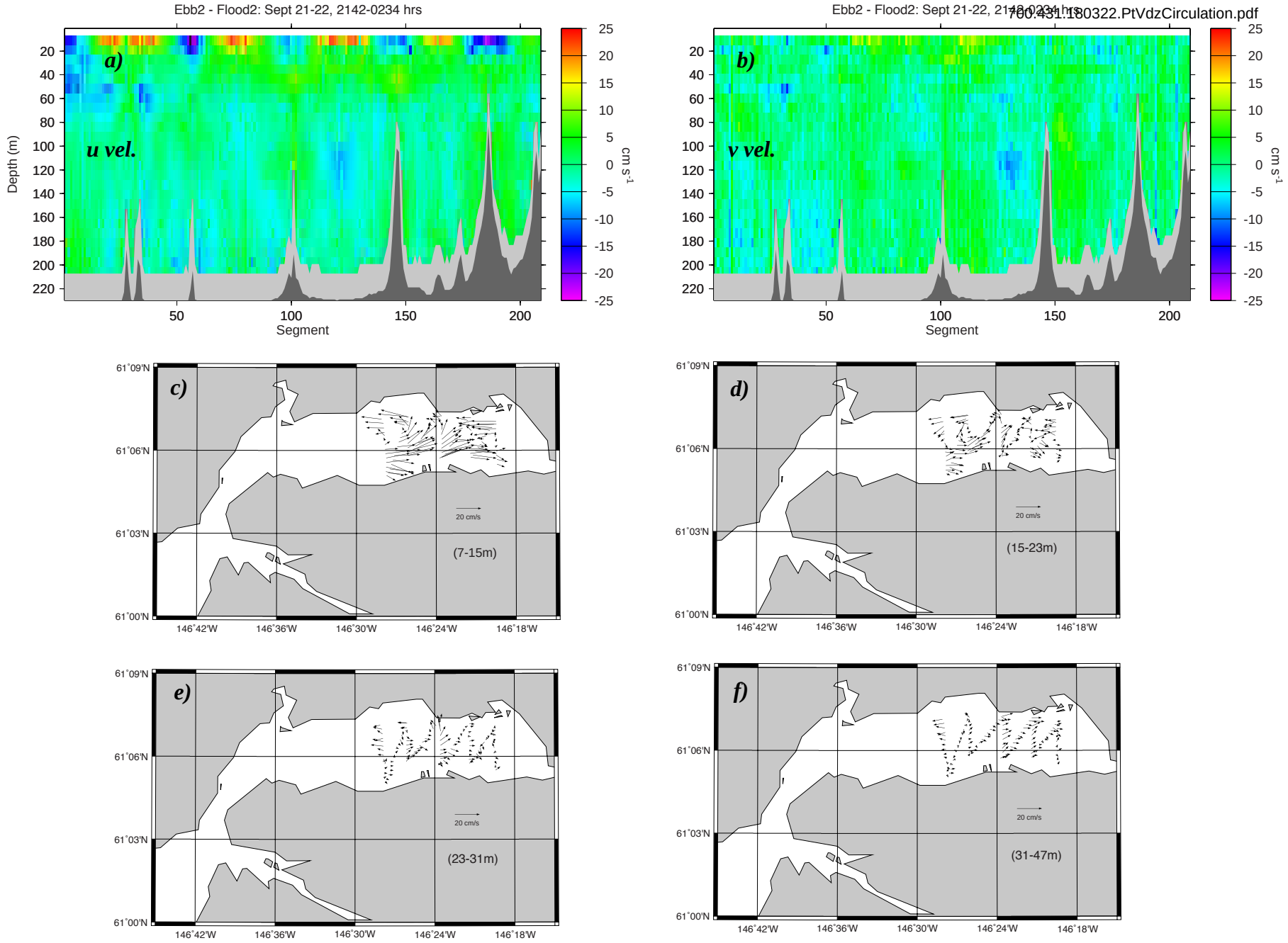

Fig. 16B. ADCP currents measured over the last 2.25 *hr* of ebb tide 2 and the first 2.6 *hr* of flood tide 2 during the 36 *hr* survey from September 21 to 22, 2016: a) *u* velocity components; b) *v* velocity components; c to e) velocity vectors for the first three 8 *m* depth bins centered at 11, 19 and 27 *m* respectively; and f) velocity vectors averaged over the next two bins from 31 to 47 *m*. Note that transects are from east to west, starting at the southeast corner (tran. #9) and ending at the northwest corner (tran. #1). The vectors are ~ 60 *sec* in length (i.e. averages of every two 30 *sec* segments shown in a and b above.

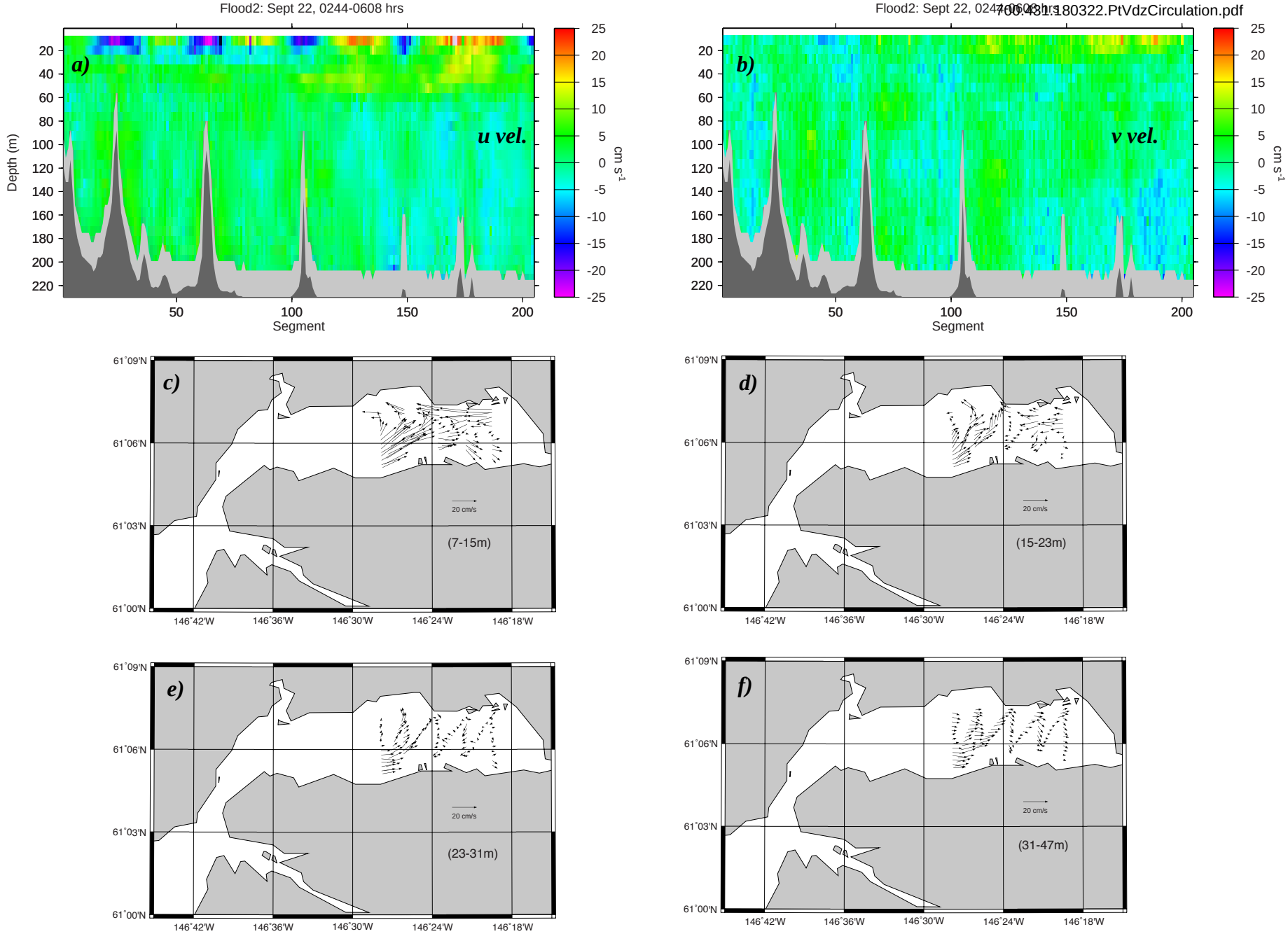

Fig. 16C. ADCP currents measured over the second flood tide during the 36 *hr* survey from September 21 to 22, 2016: a) *u* velocity components; b) *v* velocity components; c to e) velocity vectors for the first three 8 *m* depth bins centered at 11, 19 and 27 *m* respectively; and f) velocity vectors averaged over the next two bins from 31 to 47 *m*. Note that transects are from east to west, starting at the southeast corner (tran. #9) and ending at the northwest corner (tran. #1). The vectors are ~ 60 *sec* in length (i.e. averages of every two 30 *sec* segments shown in a and b above.

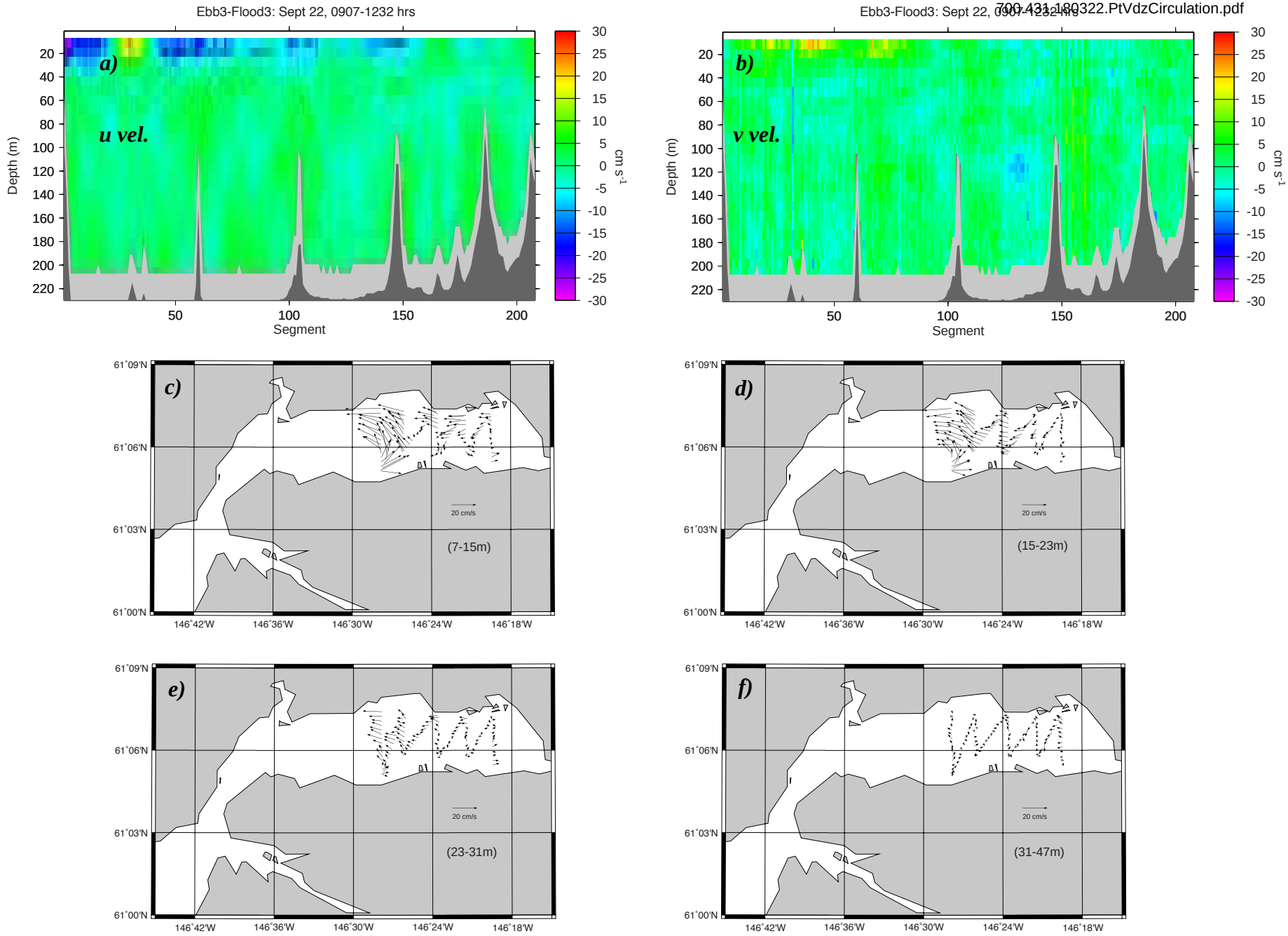

Fig. 16D. ADCP currents measured over the last 2.75 *hr* of ebb tide 3 and the first 0.5 *hr* of flood tide 3 during the 36 *hr* survey from September 21 to 22, 2016: a) *u* velocity components; b) *v* velocity components; c to e) velocity vectors for the first three 8 *m* depth bins centered at 11, 19 and 27 *m* respectively; and f) velocity vectors averaged over the next two bins from 31 to 47 *m*. Note that transects are from east to west, starting at the southeast corner (tran. #9) and ending at the northwest corner (tran. #1). The vectors are ~ 60 *sec* in length (i.e. averages of every two 30 *sec* segments shown in a and b above.

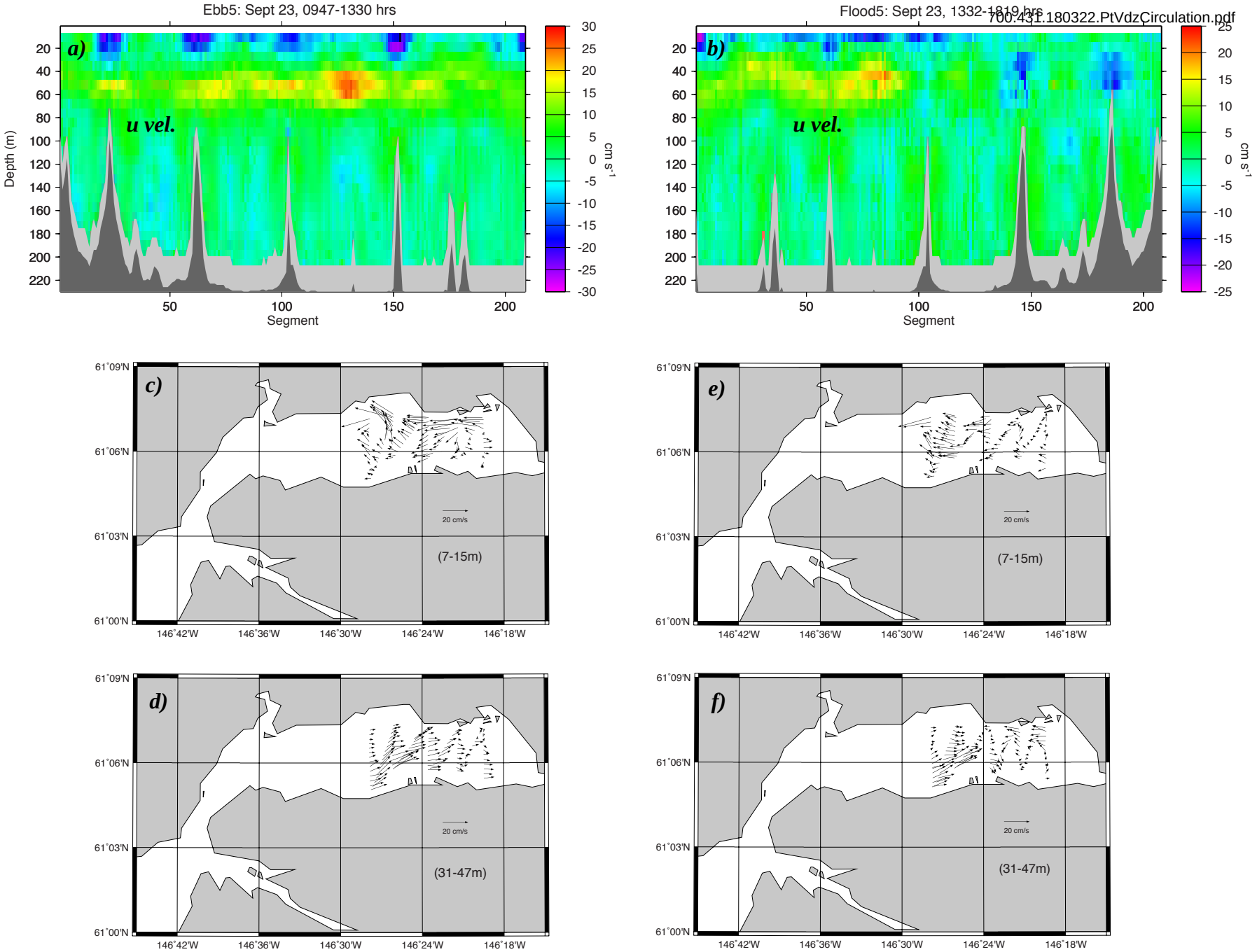

Fig. 17A. ADCP currents measured on September 23, 2016 following the 36 *hr* survey: a) *u* velocities over the last 3.75 *hr* of ebb tide 5 and the first 0.5 *hr* of flood tide 5; b) *u* velocities over the first 4.8 *hr* of flood tide 5; c-d) velocity vectors for ebb 5 for the first 8 *m* depth bin centered at 11*m* and vectors averaged over two bins from 31 to 47 *m*; e-f) velocity vectors for flood 5 for the first 8 *m* depth bin centered at 11 and vectors averaged over two bins from 31 to 47 *m*. Note that transects start from east to west, then return west to east. The vectors are ~ 60 *sec* in length (i.e. averages of every two 30 *sec* segments shown in a and b above).

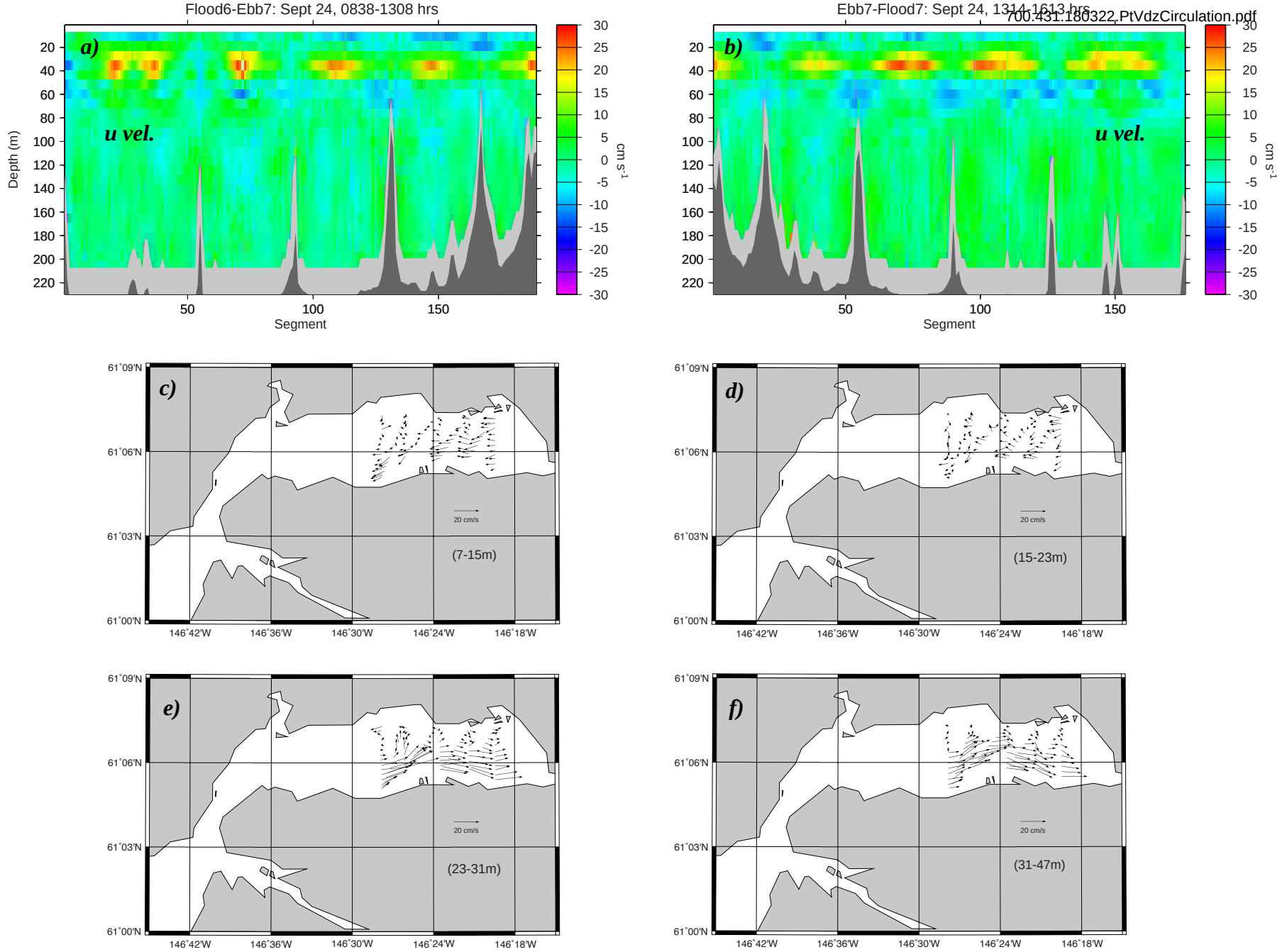

Fig. 17B. ADCP currents measured on September 24, 2016 following the 36 *hr* survey: a) *u* velocities over the last 0.2 *hr* of flood tide 6 and the first 4.5 *hr* of ebb tide 7; b) *u* velocities over the last 0.7 *hr* of ebb tide 7 and the first 1.9 *hr* of flood tide 7; c-d) velocity vectors for flood6-ebb7 for the first 8 *m* depth bin centered at 11 *m* and vectors averaged over two bins from 31 to 47 *m*; e-f) velocity vectors for ebb7-flood7 for the first 8 *m* depth bin centered at 11 *m* and vectors averaged over two bins from 31 to 47 *m*. Note that transects start from west to east, then return east to west. The vectors are ~ 60 *sec* in length (i.e. averages of every two 30 *sec* segments shown in a and b above).

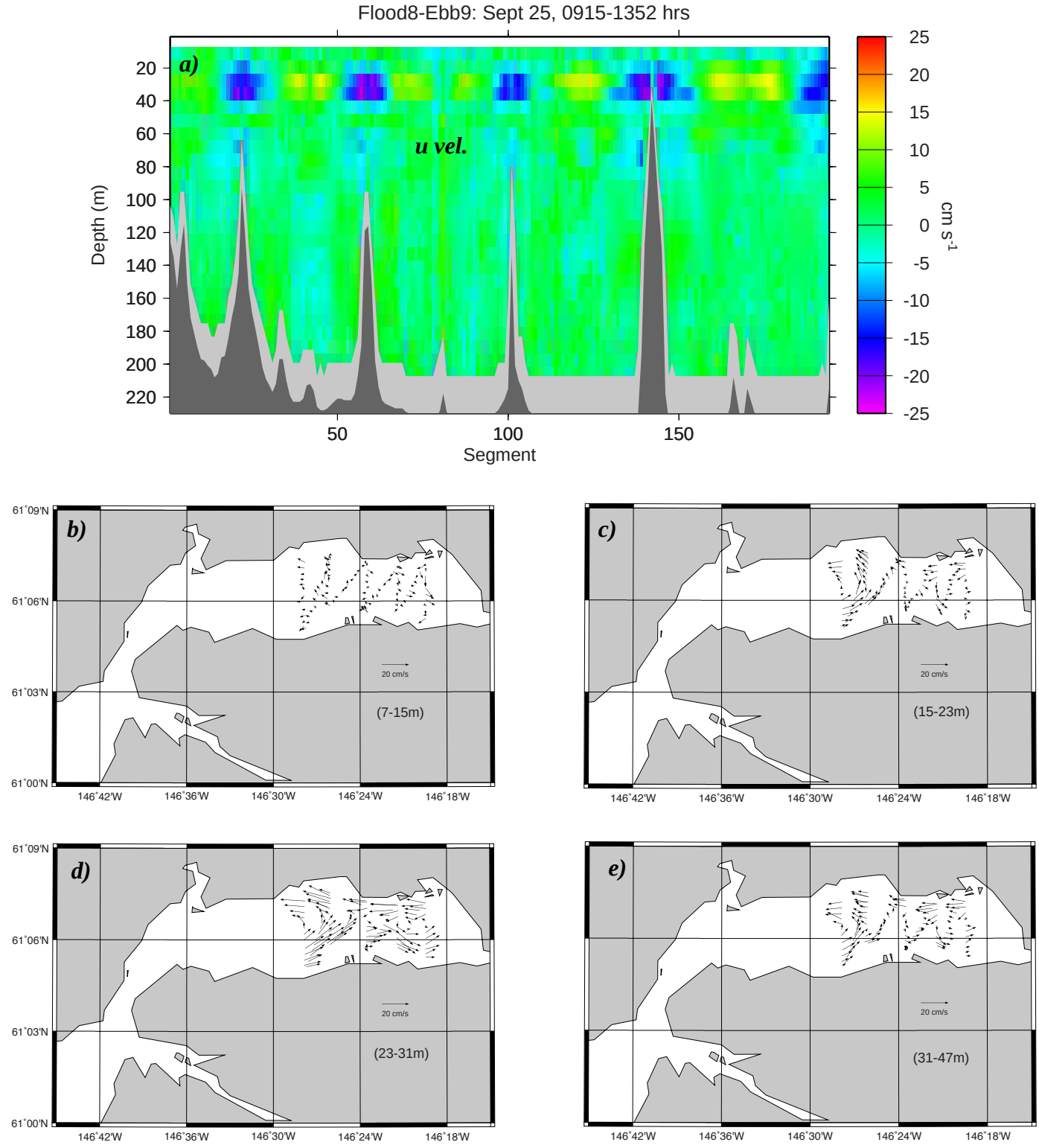

Fig. 17C. ADCP currents measured on September 25, 2016 following the 36 *hr* survey: a) *u* velocities over the last 0.3 *hr* of flood tide 8 and the first 4.25 *hr* of ebb tide 9; b-d) velocity vectors for the first three 8 *m* depth bins centered at 11, 19 and 27 *m* and e) vectors averaged from 31 to 47 *m*, centered at about 40 *m* depth; Note that transects run east to west and the vectors are ~ 60 *sec* in length (i.e. averages of every two 30 *sec* segments shown in panel a above).

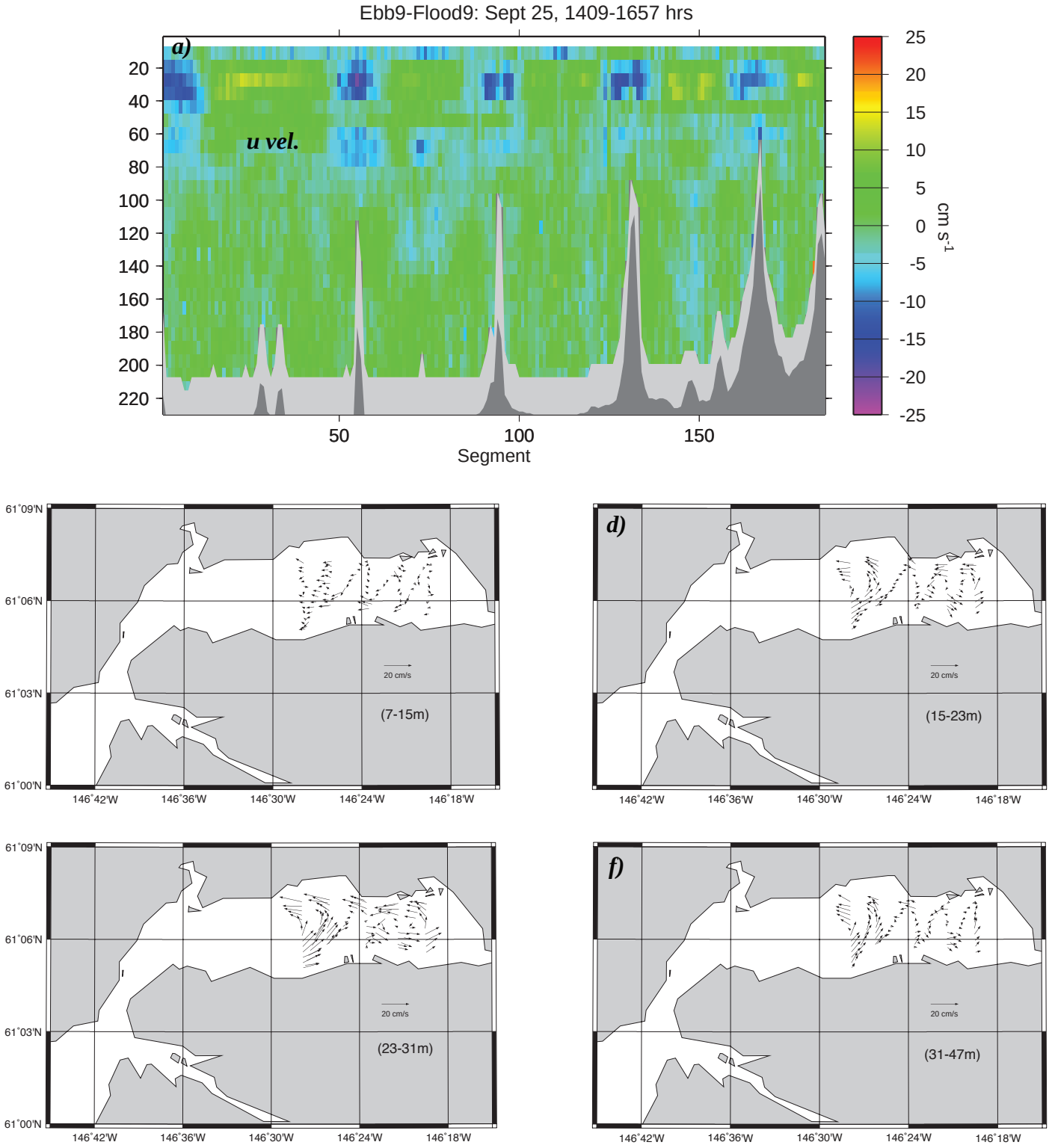

Fig. 17D. ADCP currents measured on September 25, 2016 following the 36 *hr* survey: a) *u* velocities over the last 1.75 *hr* of ebb tide 9 and the first 1.4 *hr* of flood tide 9; b-d) velocity vectors for the first three 8m depth bins centered at 11, 19 and 27 *m* and e) vectors averaged from 31 to 47 *m*, centered at about 40 *m* depth; Note that transects run west to east and the vectors are ~ 60 *sec* in length (i.e. averages of every two 30 *sec* segments shown in panel a above).

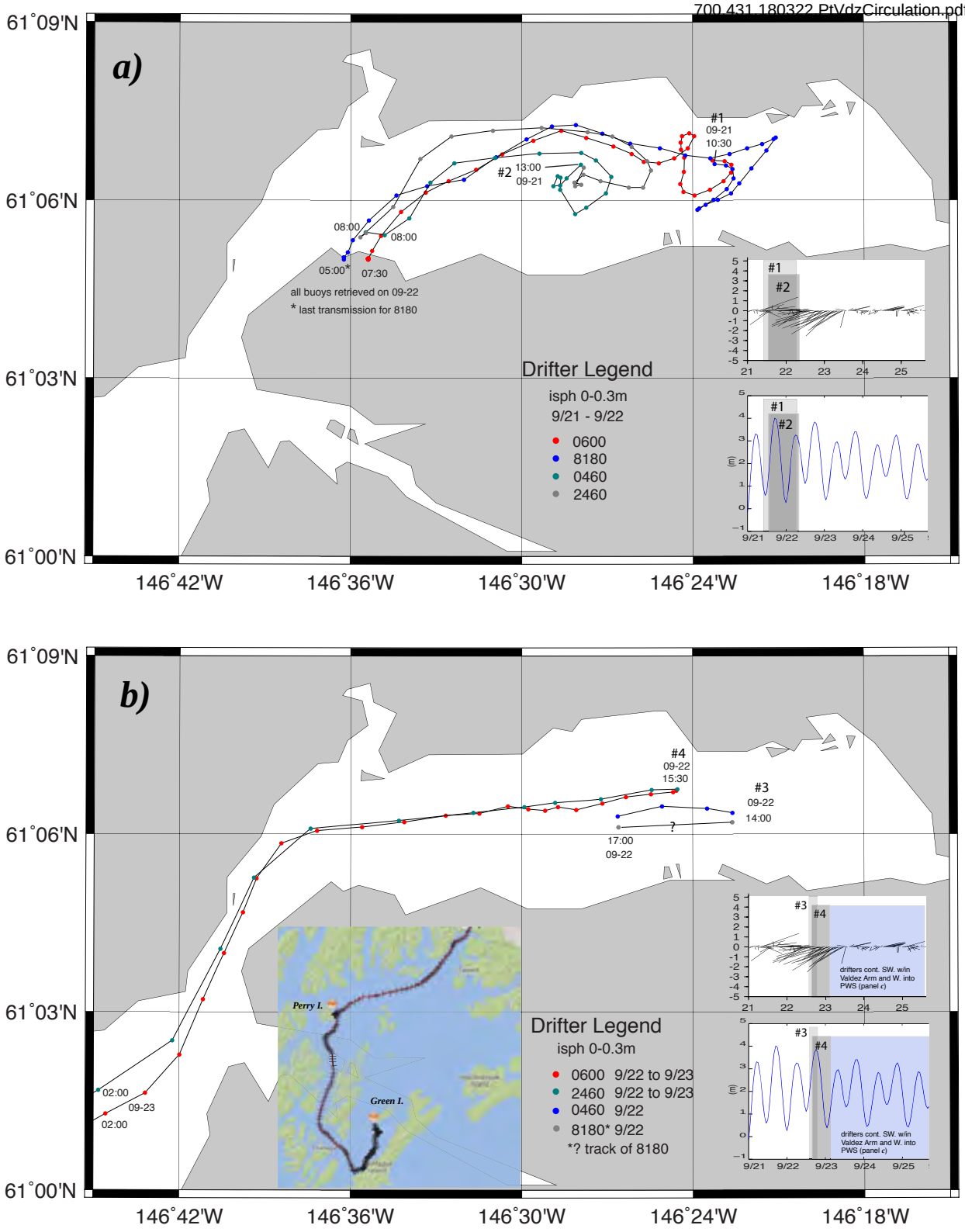

Fig. 18. Trajectories of ispheres showing surface flows on September 21 to 23, 2016: a) group #1 (0600 and 8180) and #2 (0460 and 2460) deployed on Sept 21; b) group #3 (0460 and 8180) and group #4 (0600 and 2460) deployed on Sept 22; inset shows the track of group #4 southwards through Valdez Arm and westward into PWS, where 2460 grounds on Perry I. Drifter 0600 continues southwards, then northwards to ground at Green I. The wind vectors and tides corresponding to the periods of each deployment are shown as shaded regions in the respective plots. The positions (dots) are hourly (except for ispheres 0600 and 8180, which are half hourly) and times are local (ADT).

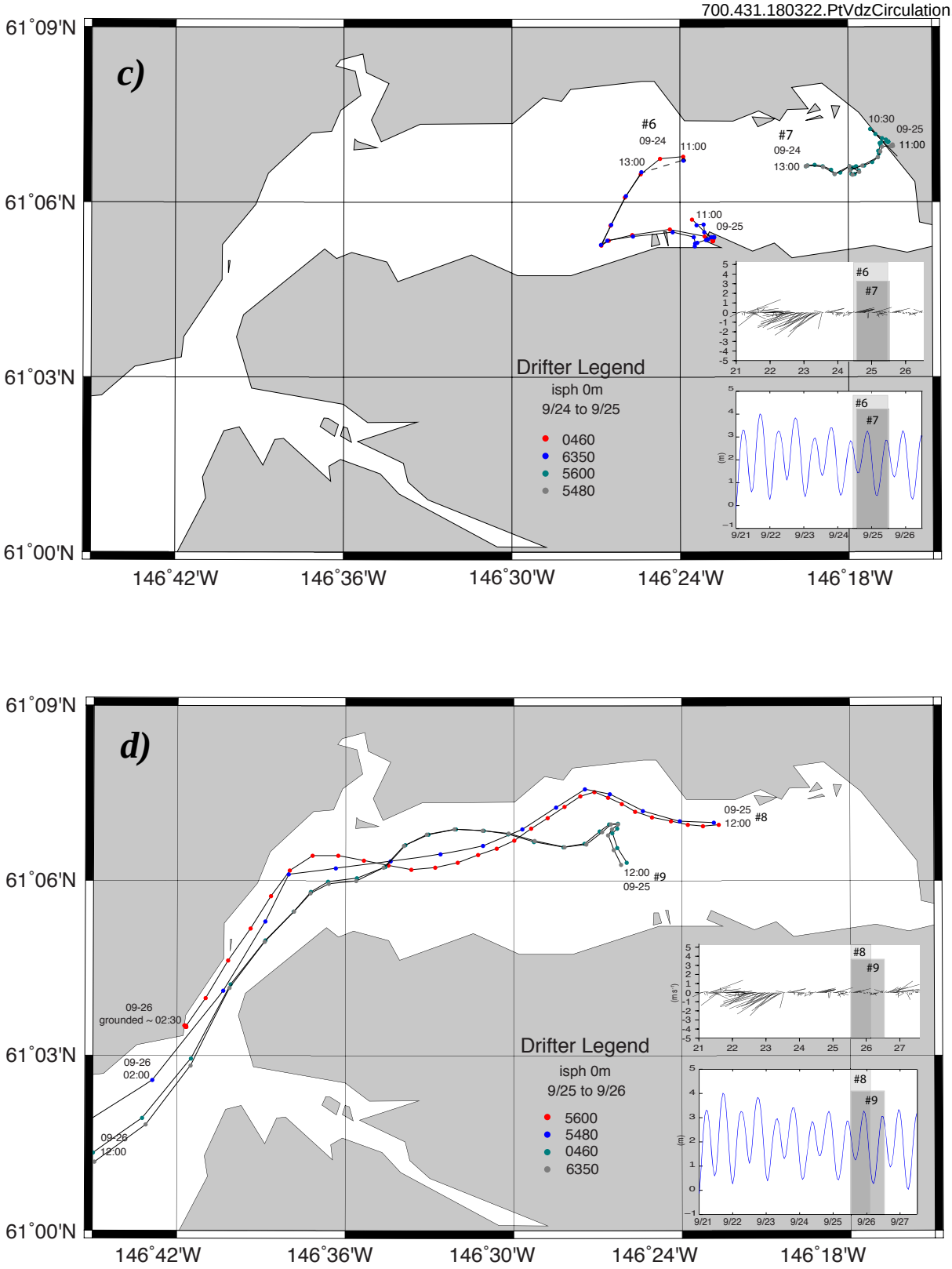

Fig. 18 (cont.). Trajectories of ispheres showing combined wind and surface flows on September 24 to 26, 2016: c) group #6 (0460 and 6350) deployed in the inner fjord and group #7 (5600 and 5480) deployed at mid-fjord on the 25th; d) group #8 (5600 and 5480) released on the 25th east of Mineral Creek and group #9 (0460 and 6350) released in the mid-central basin. Note that the dashed line in #6 indicates where i6350 was not transmitting. The wind vectors and tides corresponding to the periods of each deployment are shown as shaded regions in the respective plots. Note that all positions are hourly, except for i5600, which is half hourly. All times are local (ADT).

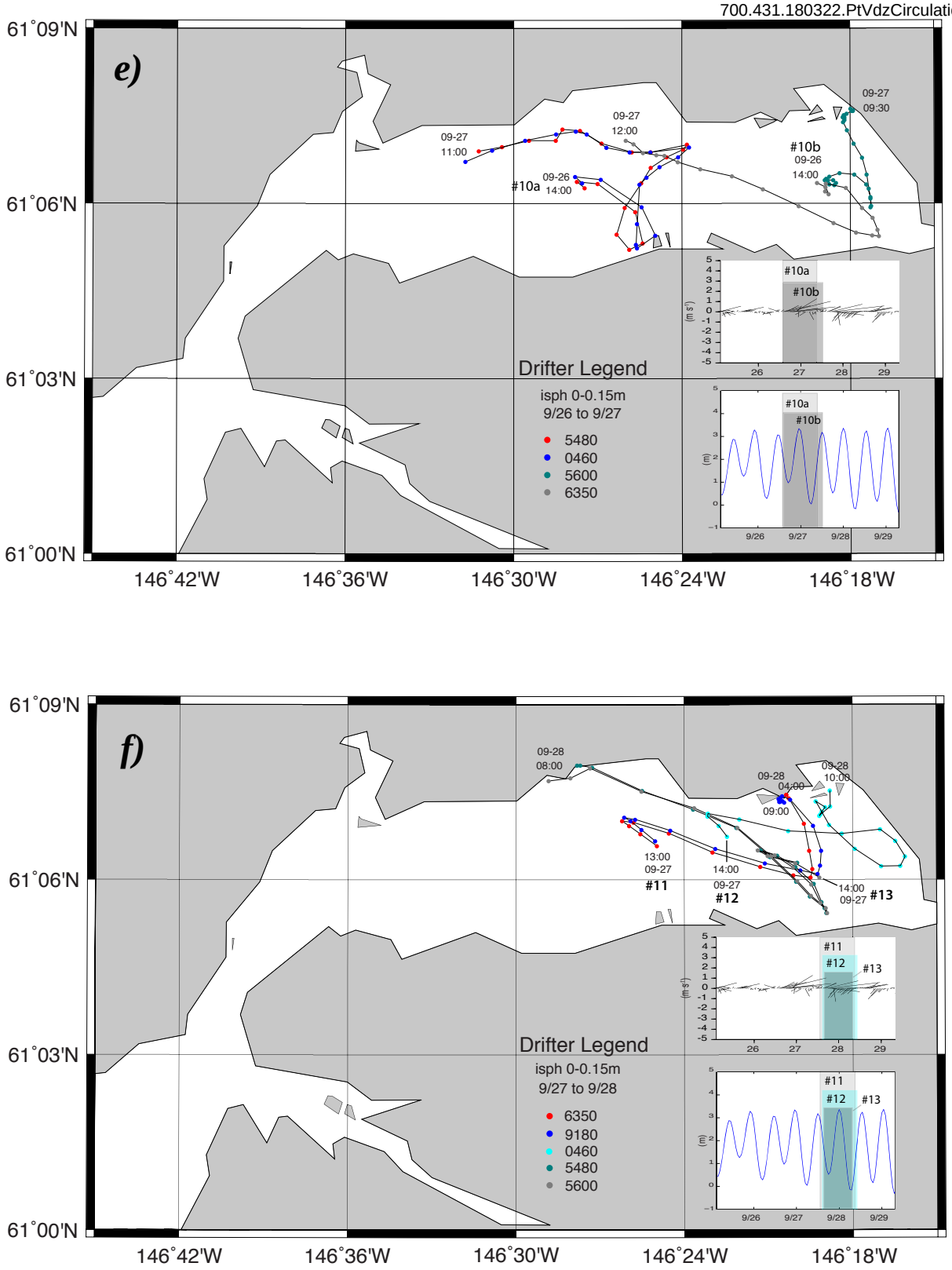

Fig. 18 (cont.). Trajectories of ispheres showing combined wind and surface flows on September 26 to 28, 2016: e) group #10a (5480 and 0460) and #10b (5600 and 6350) deployed in the mid-central and mid-inner basins respectively: f) group #11 (6350 and 9180), #12 (0460) and #13 (5480 and 5600) deployed progressively eastward from mid-fjord. The wind vectors and tides corresponding to the periods of each deployment are shown as shaded regions in the respective plots. Note that all positions are hourly (except for i5600 launched on the 26th) and times are local (ADT).

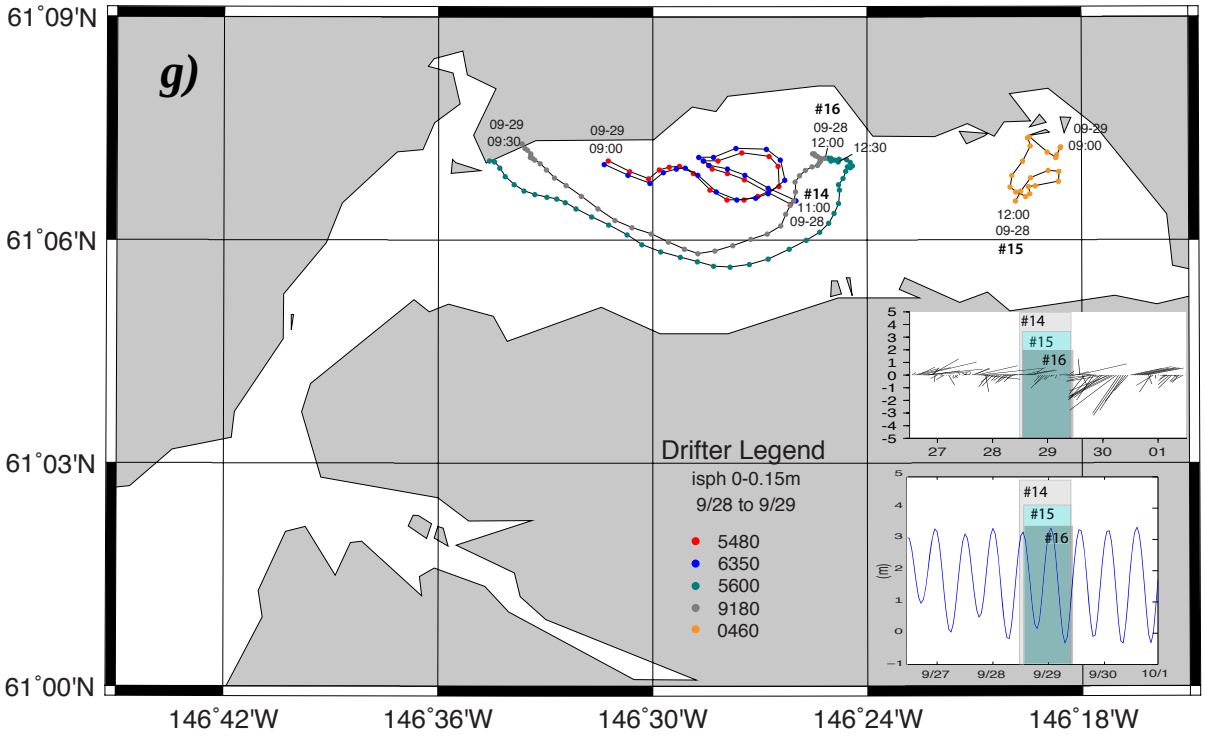

Fig. 18 (cont.). Trajectories of ispheres showing combined wind and surface flows on September 28 to 29, 2016: g) group #14 (5480 and 6350), #15 (5600 and 9180) and #16 (0460) deployed in the mid-central basin, mid-basin south of Mineral Creek and mid-inner basin respectively. The wind vectors and tides corresponding to the periods of each deployment are shown as shaded regions in the respective plots. Note that all positions are hourly and times are local (ADT).

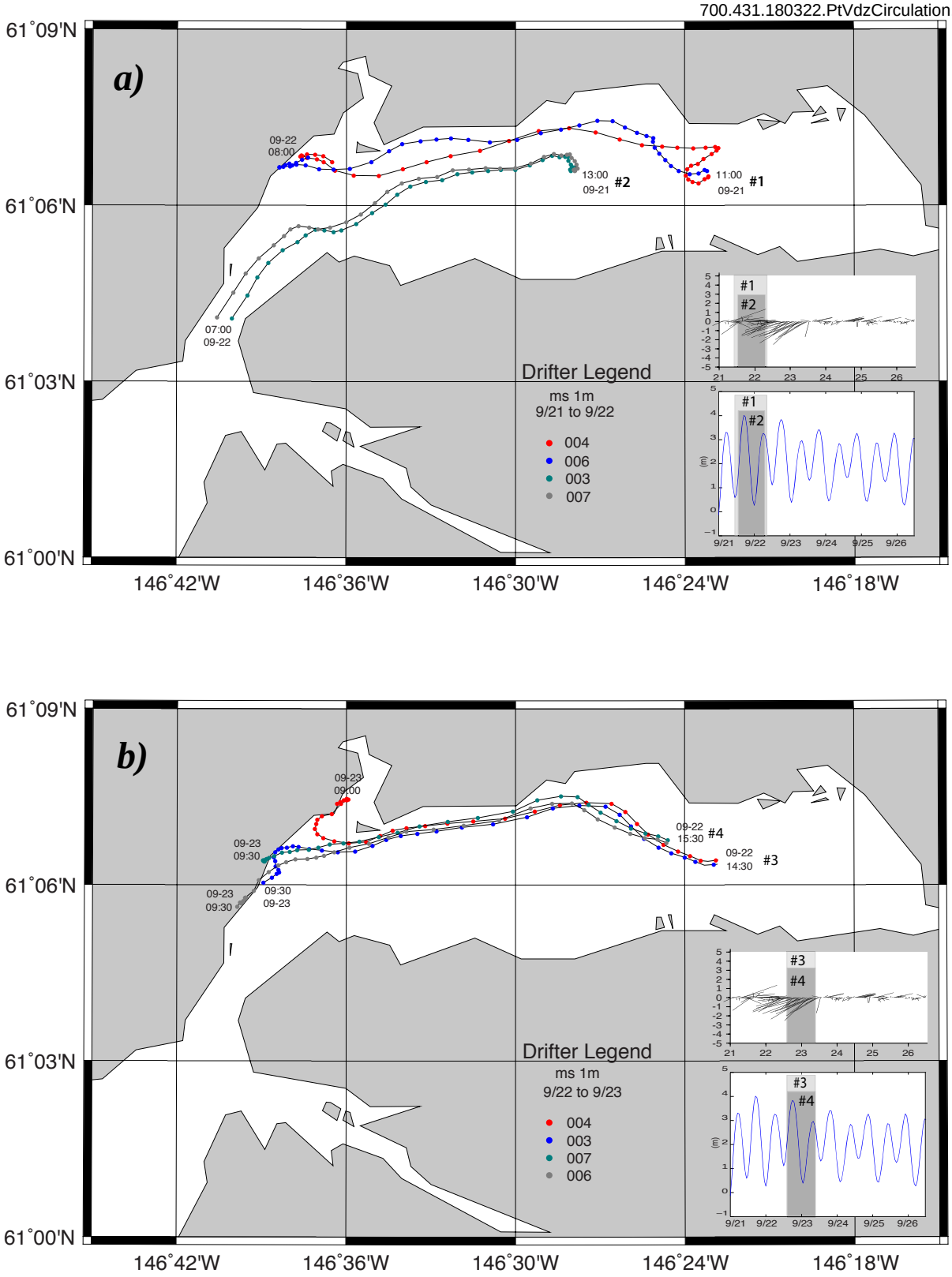

Fig. 19. Trajectories of microstars showing flows at 1*m* depth on September 21 to 23, 2016: a) groups #1 (004 and 006) and #2 (0460 and 2460) deployed on Sept 21; b) groups #3 (004 and 003) and #4 (007 and 006) deployed on Sept 22. The wind vectors and tides corresponding to the periods of each deployment are shown as shaded regions in the respective plots. The positions (dots) are half hourly and times are local (ADT).

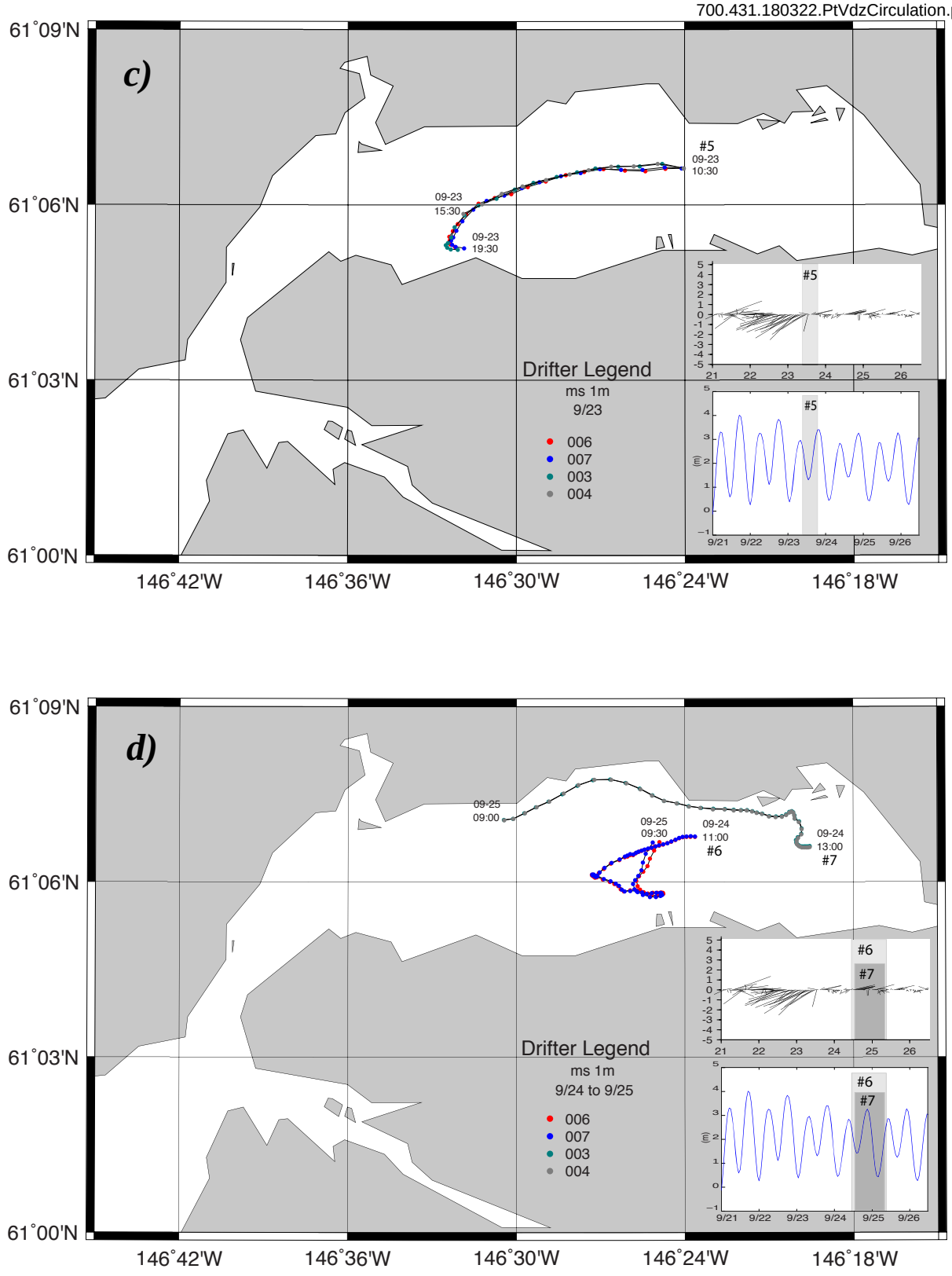

Fig. 19 (cont.). Trajectories of microstars showing flows at 1*m* depth on September 23 to 25, 2016: a) group #5 (003, 4, 6 and 7) deloyed on Sept 23; b) groups #6 (006 and 007) and #7 (003 and 004) deployed on Sept 24. The wind vectors and tides corresponding to the periods of each deployment are shown as shaded regions in the respective plots. The positions (dots) are half hourly) and times are local (ADT).

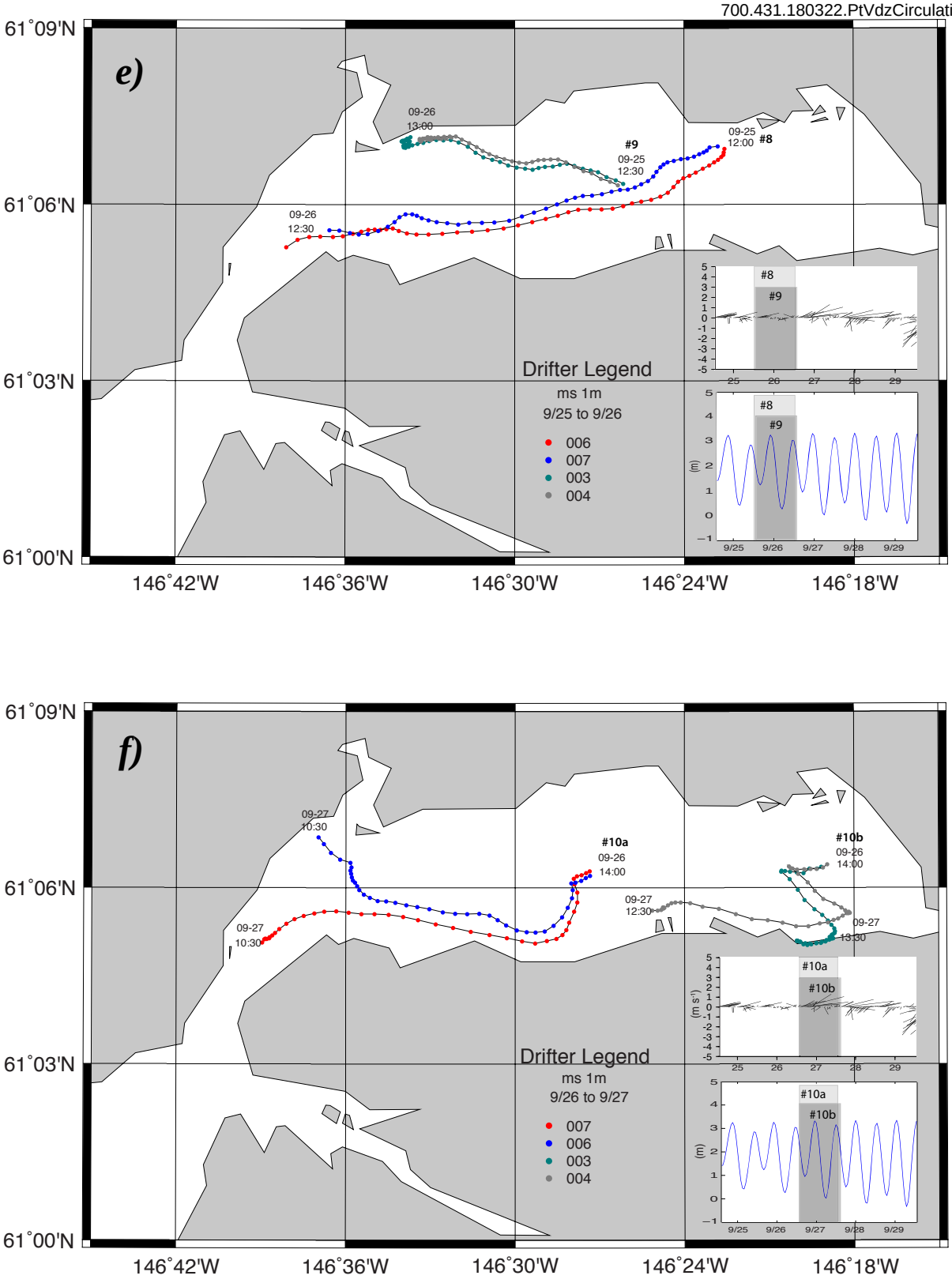

Fig. 19 (cont.). Trajectories of microstars showing flows at 1*m* depth on September 25 to 27, 2016: e) groups #8 (006 and 007) and #9 (003 and 004) deloyed on Sept 25; f) groups #10a (006 and 007) and #10b (003 and 004) deployed on Sept 26. The wind vectors and tides corresponding to the periods of each deployment are shown as shaded regions in the respective plots. The positions (dots) are half hourly and times are local (ADT).

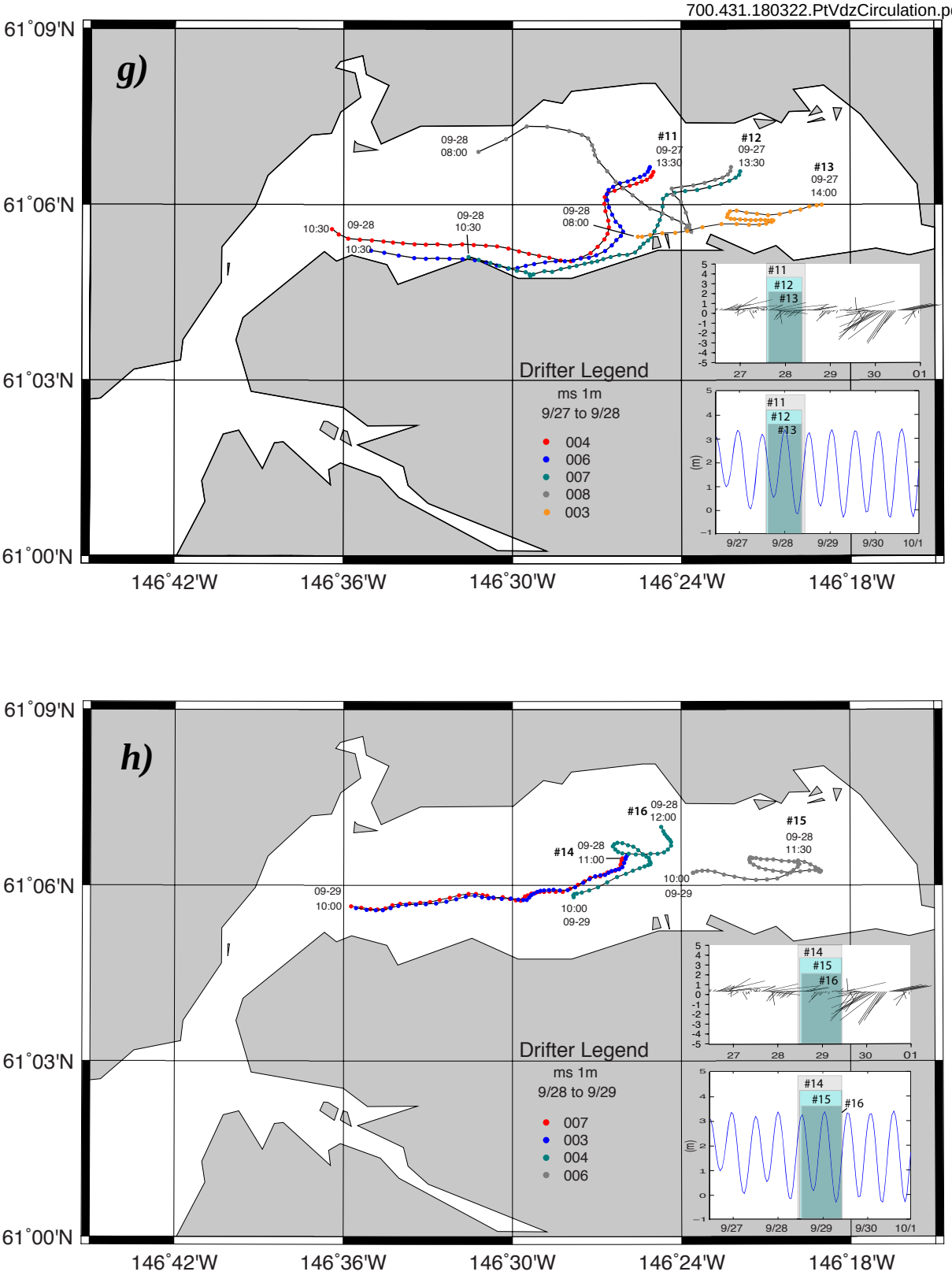

Fig. 19 (cont.). Trajectories of microstars showing flows at 1*m* depth on September 27 to 29, 2016: g) groups #11 (004 and 006), #12 (007 and 008) and #13 (003) deloyed on Sept 27; h) groups #14 (007 and 003), #15 (006) and #16 (004) deployed on Sept 28. The wind vectors and tides corresponding to the periods of each deployment are shown as shaded regions in the respective plots. The positions (dots) are half hourly and times are local (ADT).

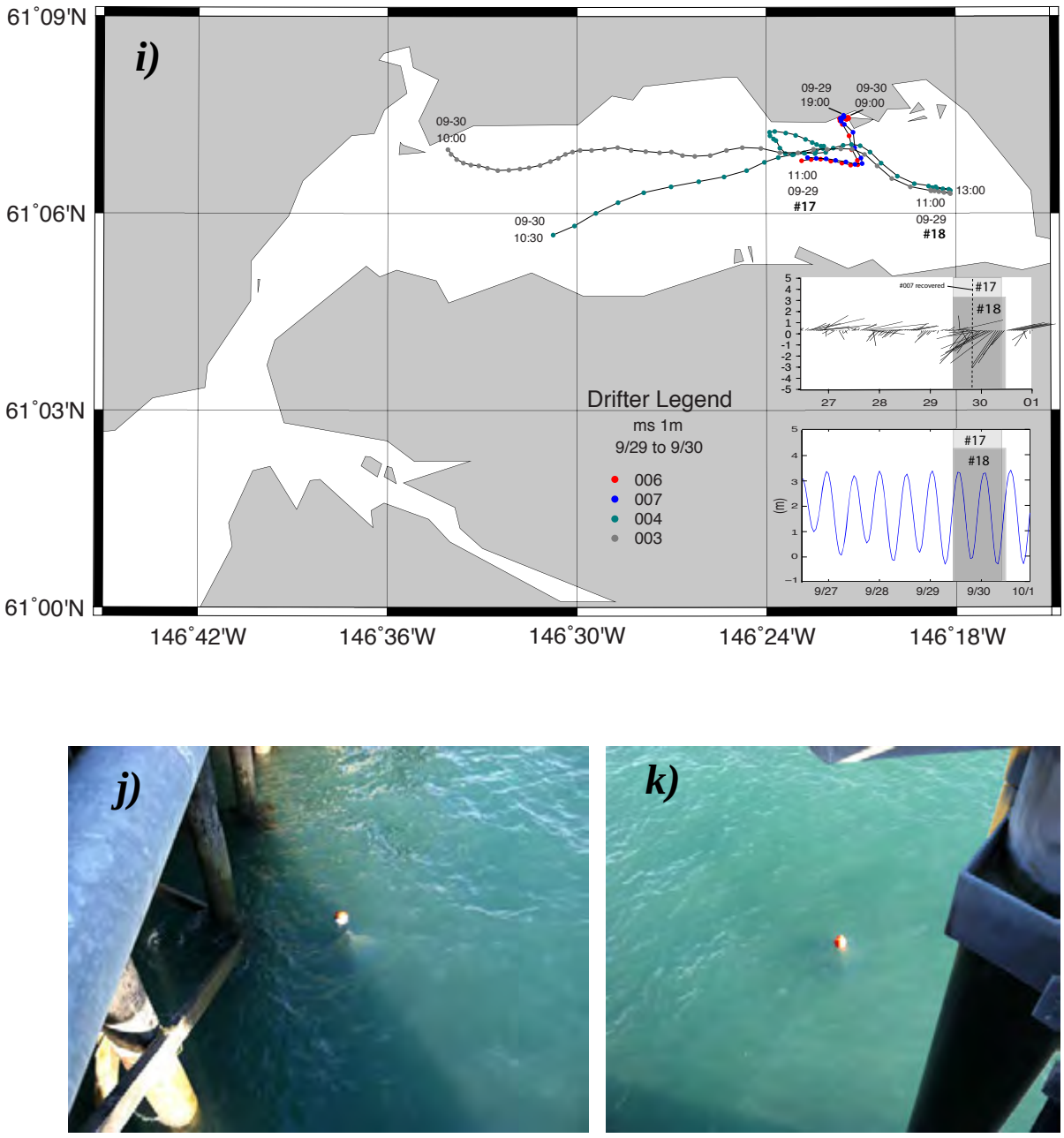

Fig. 19 (cont.). Trajectories of microstars showing flows at 1*m* depth on September 29 to 30, 2016: i) groups #17 (006 and 007) and #18 (003 and 004); j and k) microstars 007 and 006 approachng the City Dock due to east winds from the Lowe River. The wind vectors and tides corresponding to the deployments are shown as shaded regions in the respective plots. The positions (dots) are half hourly and times are local (ADT).

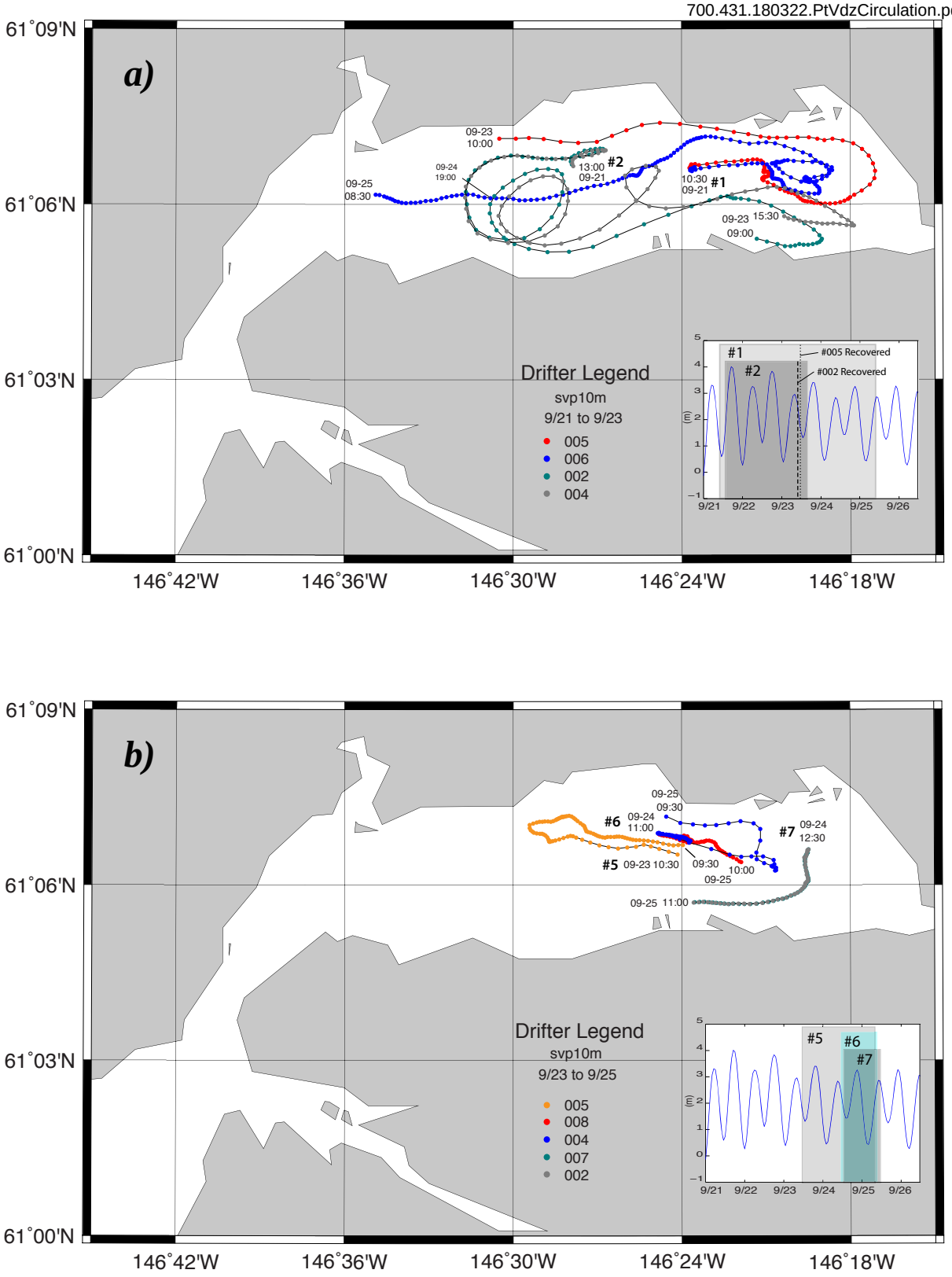

Fig. 20. Trajectories of svp10 drifters showing flows at 10*m* depth on September 21 to 25, 2016: a) groups #1 (005 and 006) and #2 (005 and 004) deloyed on Sept 21; b) groups #3 (008 and 004) and #4 (007 and 002) deployed on Sept 24. The tides corresponding to the periods of each deployment are shown as shaded regions in respective plots (insets). The positions (dots) are half hourly) and times are local (ADT).

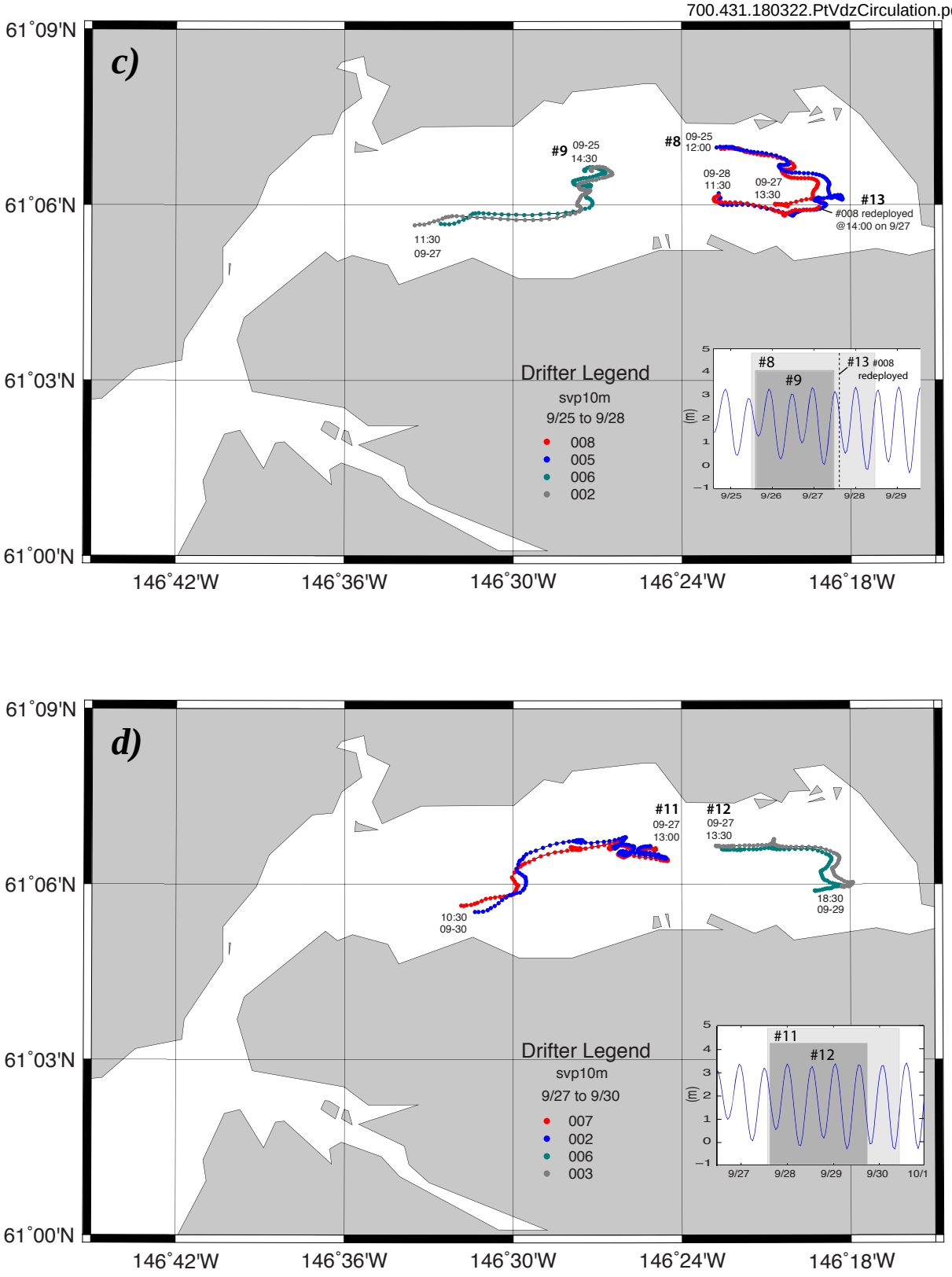

Fig. 20 (cont.). Trajectories of svp10 drifters showing flows at 10*m* depth on September 25 to 30, 2016: c) groups #8 (008 and 005) and #9 (006 and 002) deloyed on Sept 25; and d) groups #11 (007 and 002) and #12 (006 and 003) deployed on Sept 27. The tides corresponding to the periods of each deployment are shown by shaded regions in respective plots (insets). The positions (dots) are half hourly) and times are local (ADT).

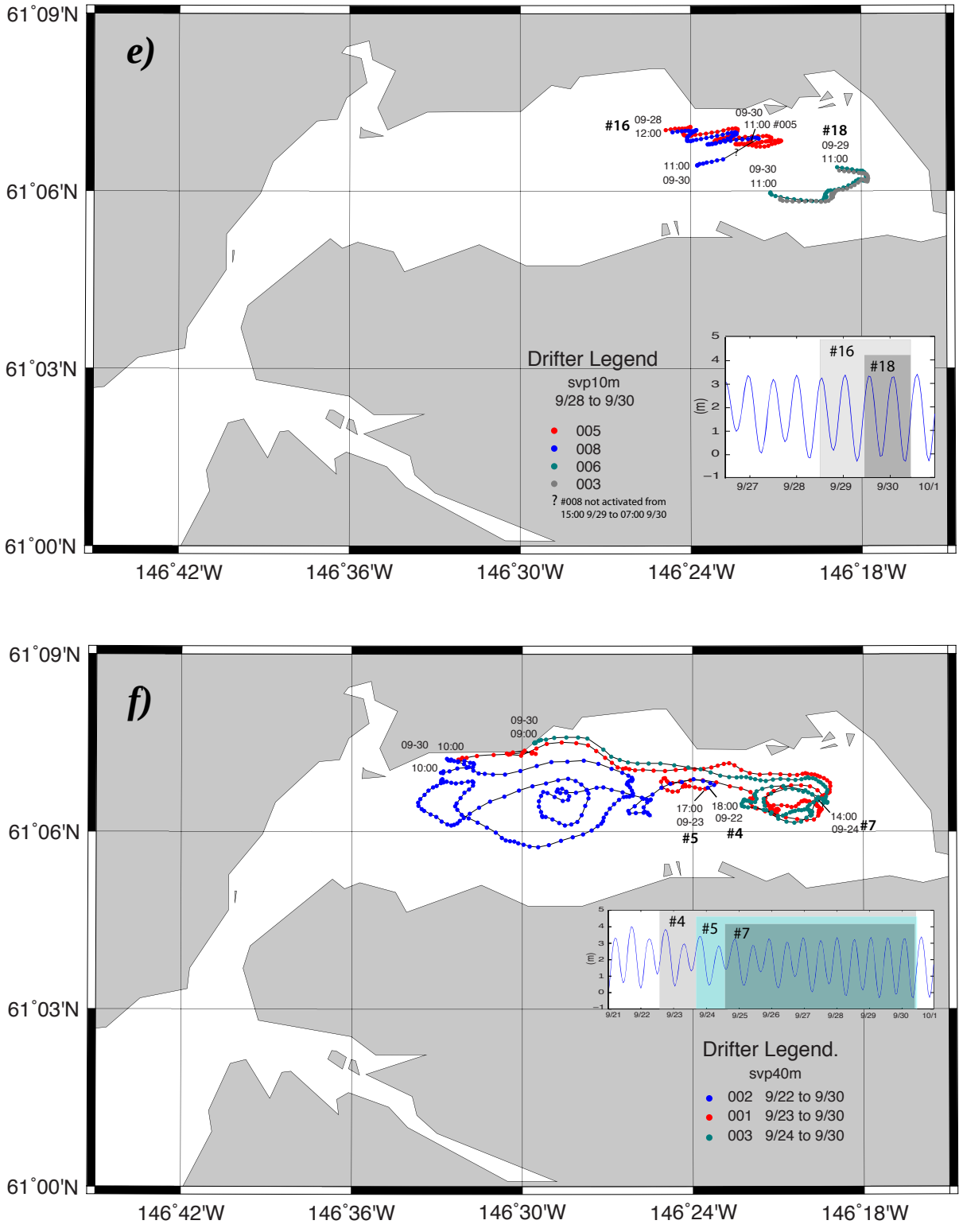

Fig. 20 (cont.). Trajectories of SVP drifters showing flows at 10*m* and 40*m* depths in September 2016: e) Svp10 groups #16 (005 and 008) and #18 (006 and 003) deloyed on the 28th and 29th respectively; f) SVP40 deloyments #2, #5 and #7 (002, 001 and 003) respectively on the 22nd, 23rd and 24th. The tides corresponding to the periods of each deployment are shown by shaded regions in the plot (inset). The positions (dots) are half hourly for panel-e and hourly for panel-f. All times are local (ADT).

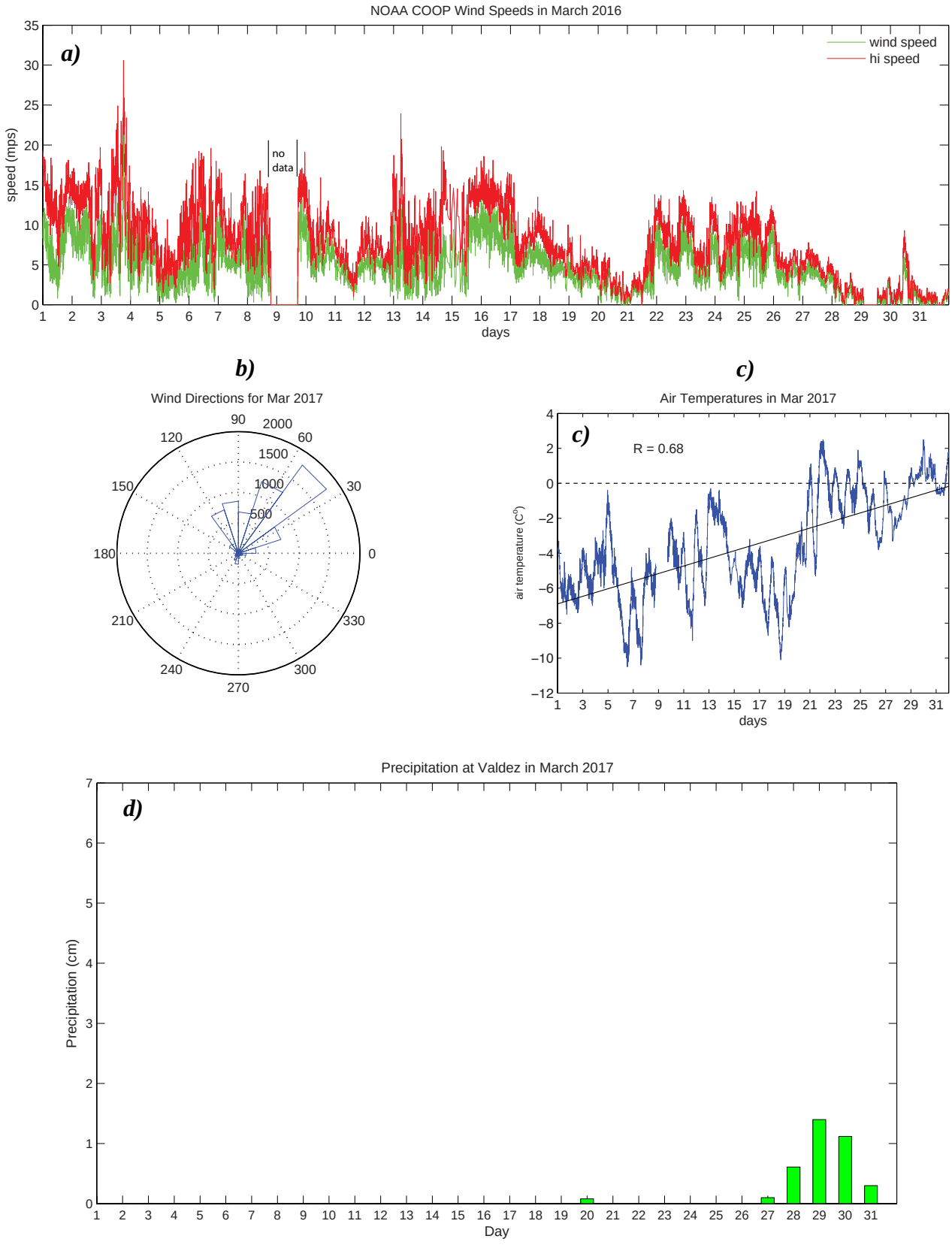

Fig. 21. Meteorological data in March 2017 collected at the Valdez, Alaska NOAA-COOPS station 9454240: a) sustained and high wind speeds measured at 6 *min*. intervals; b) wind rose showing directions from which the winds are coming; c) air temperatures at 6 *min*. intervals; and d) daily preciptation in *cm*.

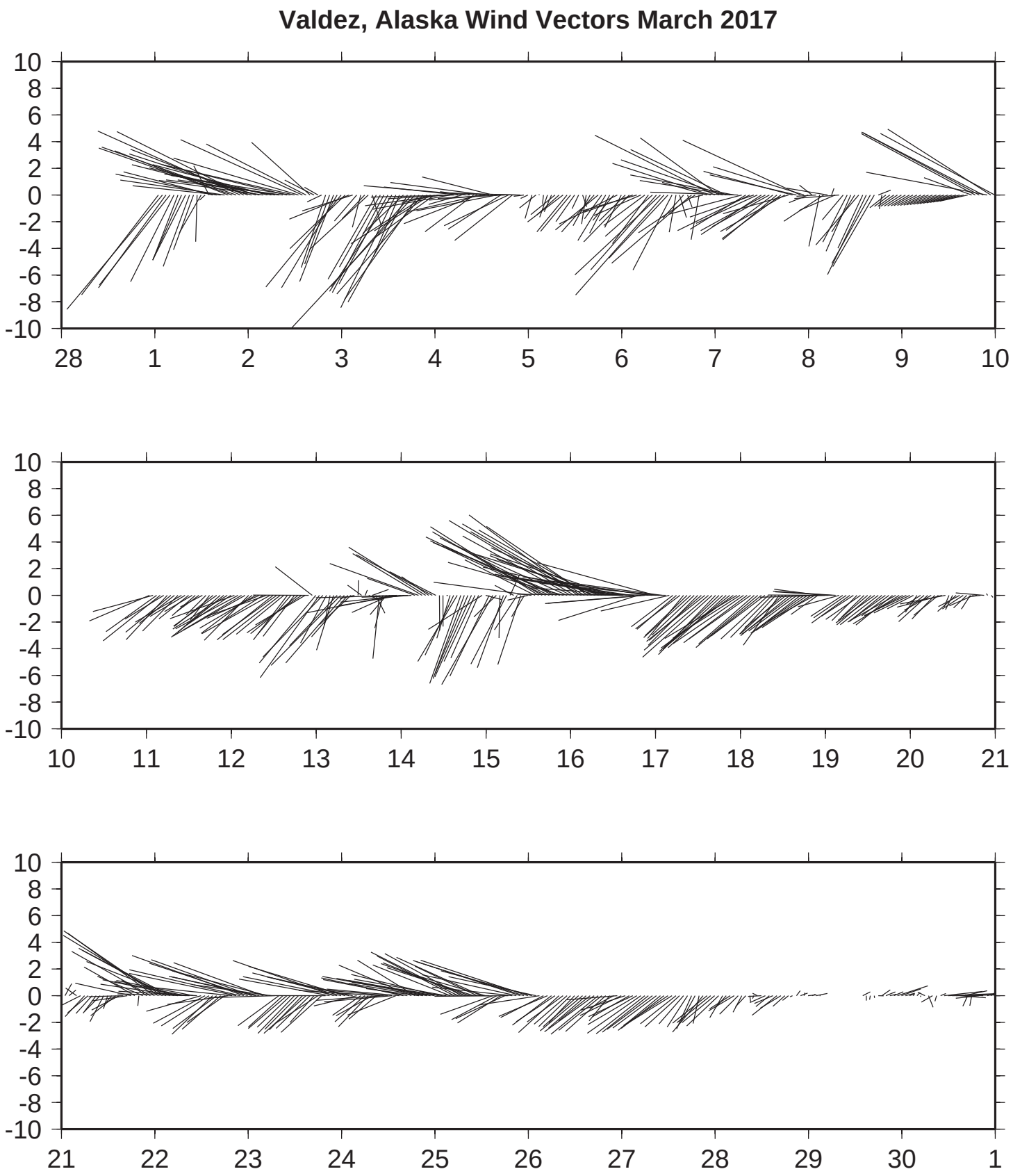

Fig. 21 (cont.). e) hourly wind vectors for the month of March 2017 measured at the Valdez, Alaska NOAA-COOPS station 9454240. Note that the x-axis is for days starting on February 28 and ending on April 1.

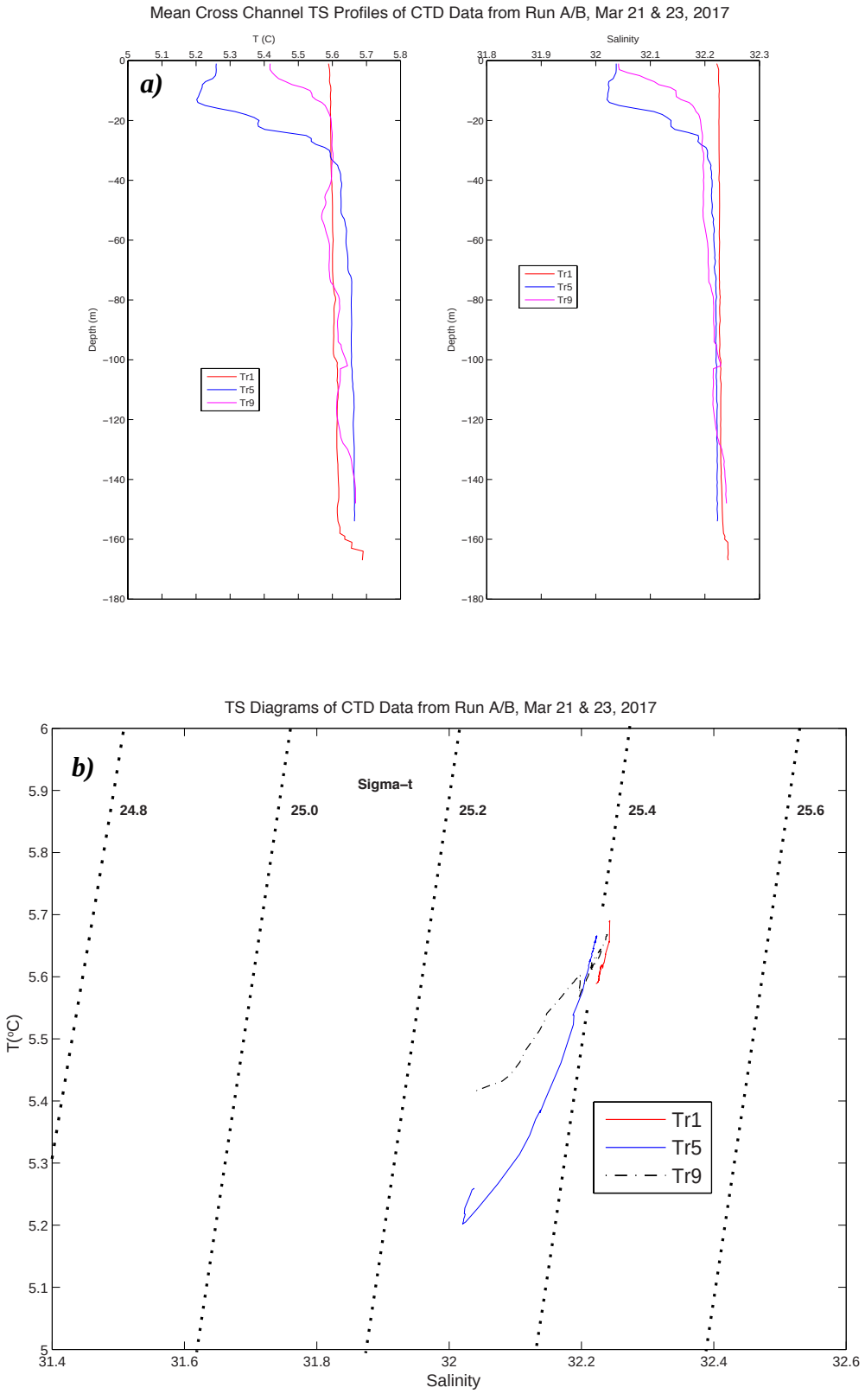

Fig. 22. Mean cross-channel temperature and salinity for transects 1, 5 and 9, Run A/B on March 21 and 23, 2017: a) mean T/S profiles; and b) mean T vs. S diagram.

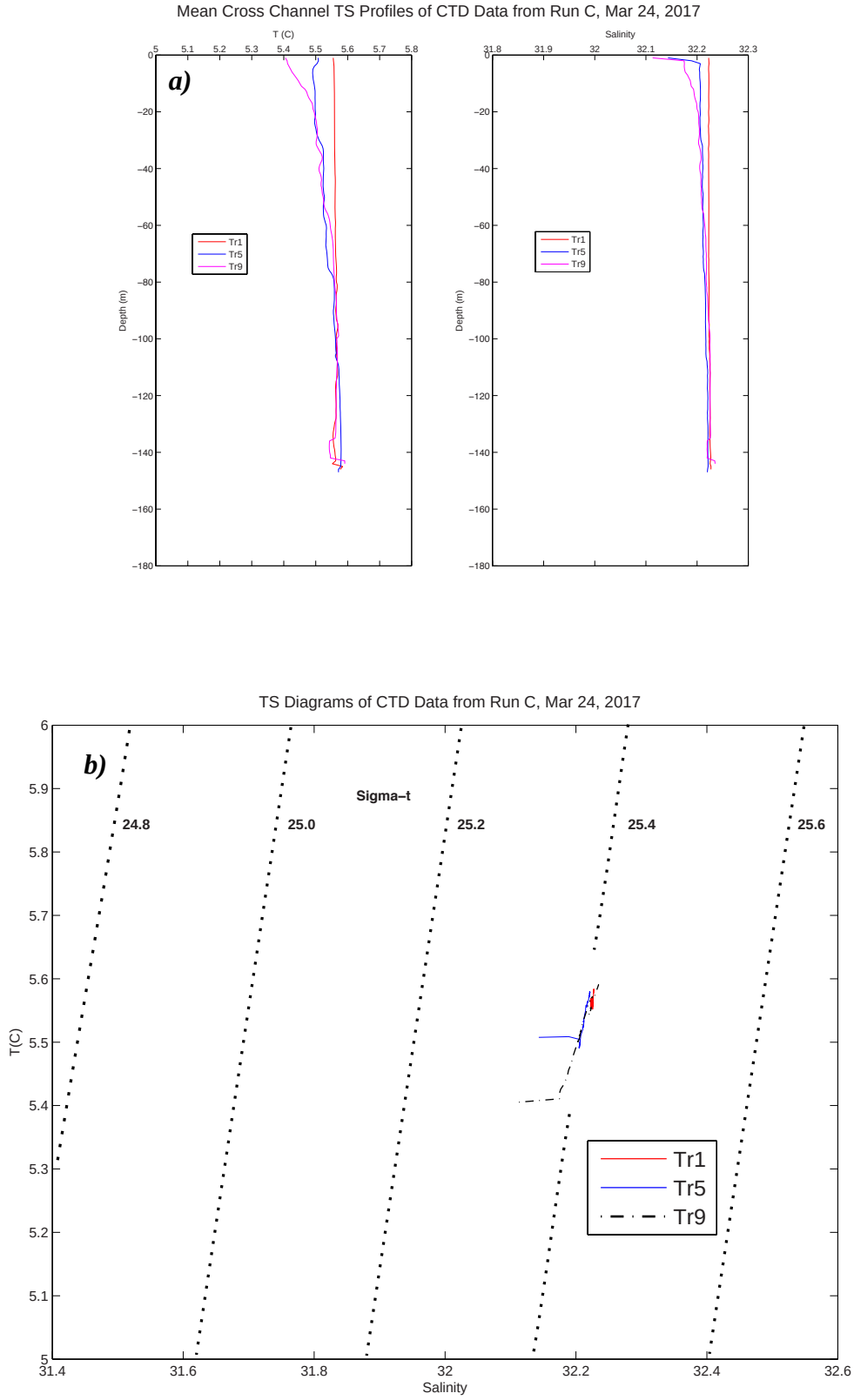

Fig. 23. Mean cross-channel temperature and salinity for transects 1, 3, 5, 7 and 9, Run C on March 24, 2017: a) mean T/S profiles; and b) mean T vs. S diagram.

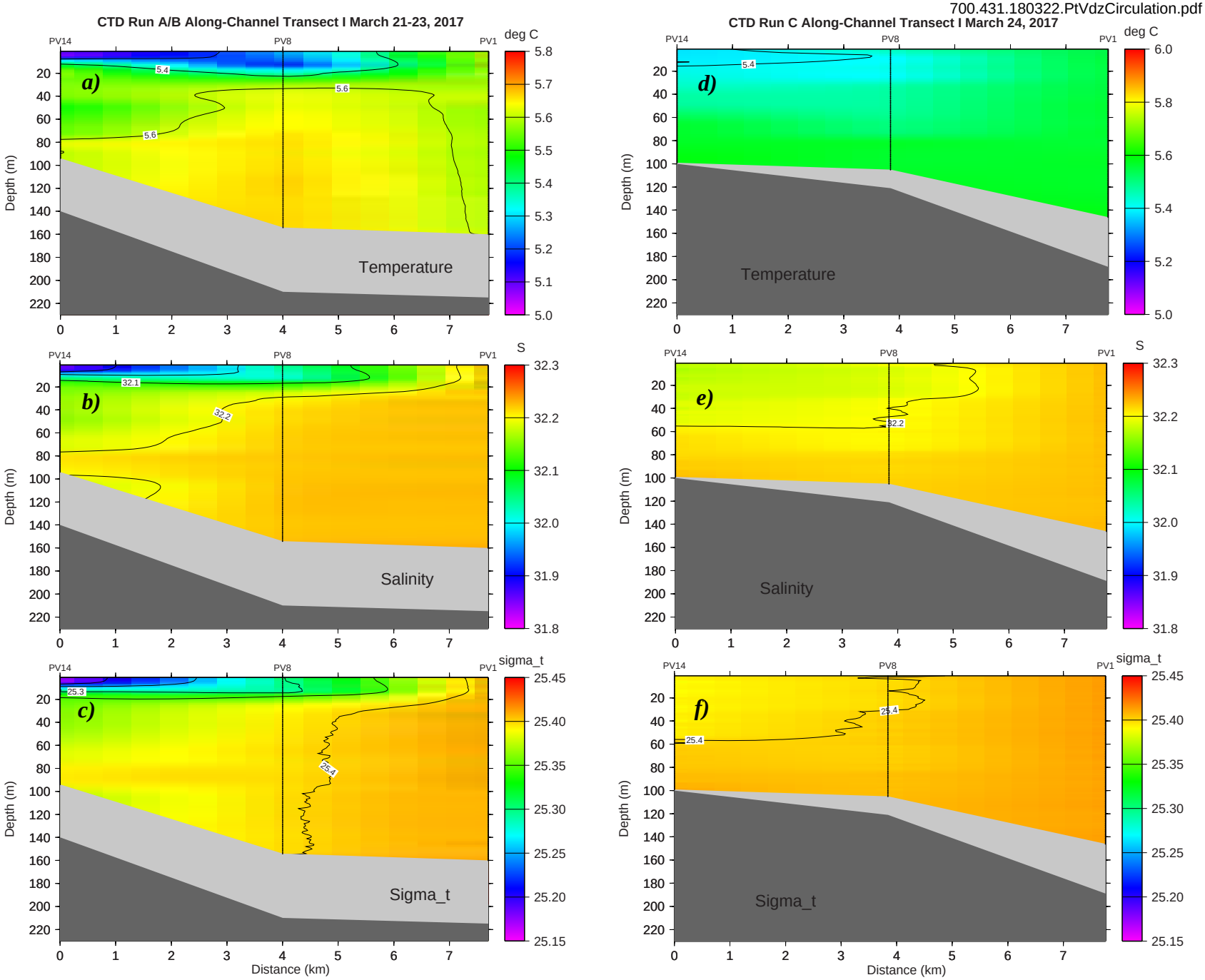

Fig. 24A. Vertical sections of along-channel temperature, salinity and density for transect I on March 21-23 and 24, 2017.

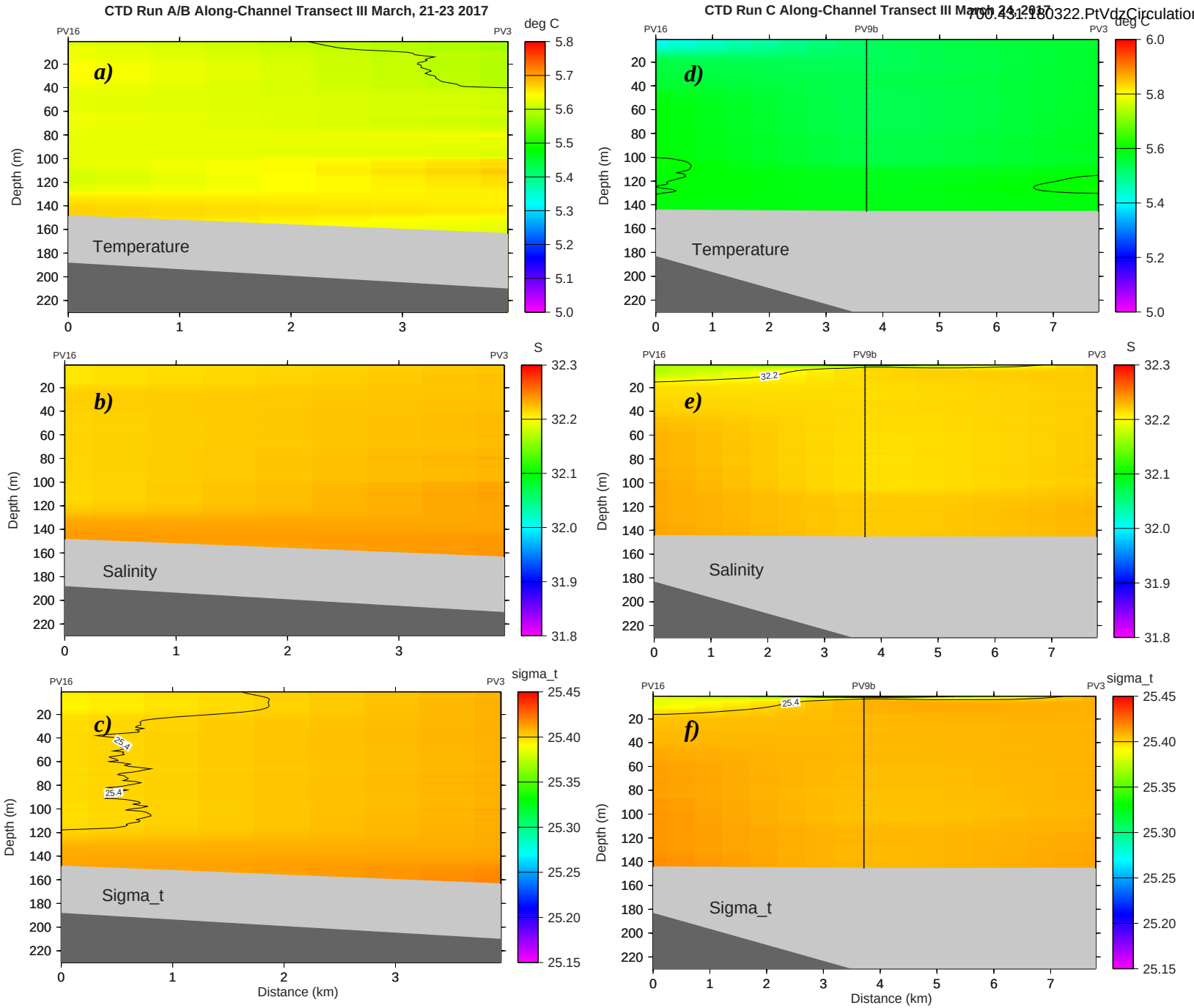

Fig. 24B. Vertical sections of along-channel temperature, salinity and density for transect III on March 21-23 and 24, 2017.

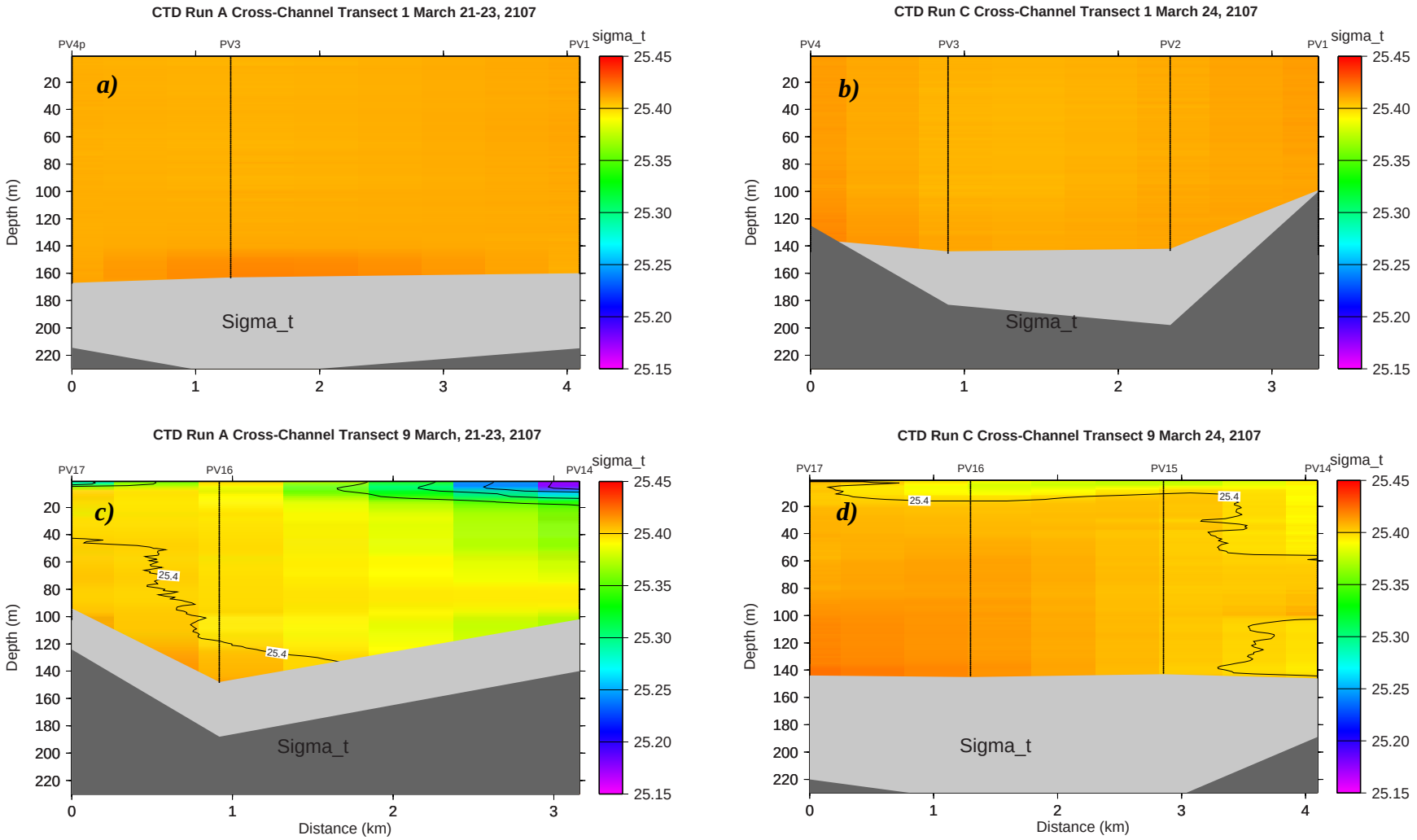

Fig. 24C. Vertical sections of cross-channel density for transects 1 and 9, Runs A/B and C on March 21-23 and 24, 2017.

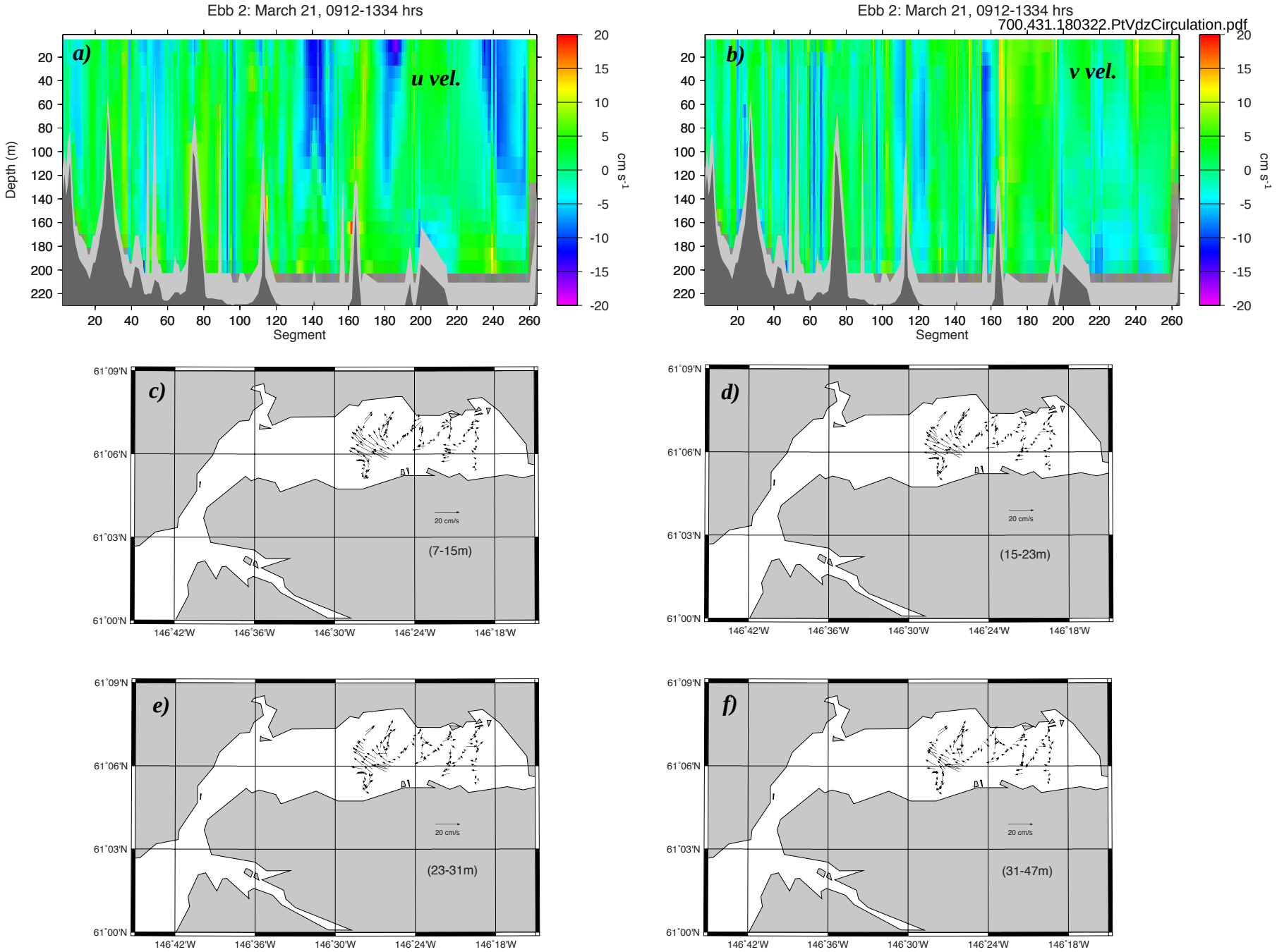

Fig. 25A. ADCP currents measured during the second ebb tide on March 21, 2017 from 09:12 to 13:34 *hrs* : a) *u* velocity components; b) *v* velocity components; c to e) velocity vectors for the first three 8 *m* depth bins centered at 11, 19 and 27 *m* respectively; and f) velocity vectors averaged over the next two bins from 31 to 47 *m*. Note that transects are from west to east, starting at the northwest corner (tran. #1) and ending at the southeast corner (tran. #1). The vectors are ~ 60 *sec* in length (i.e. averages of every two 30 *sec* segments shown in a and b above.

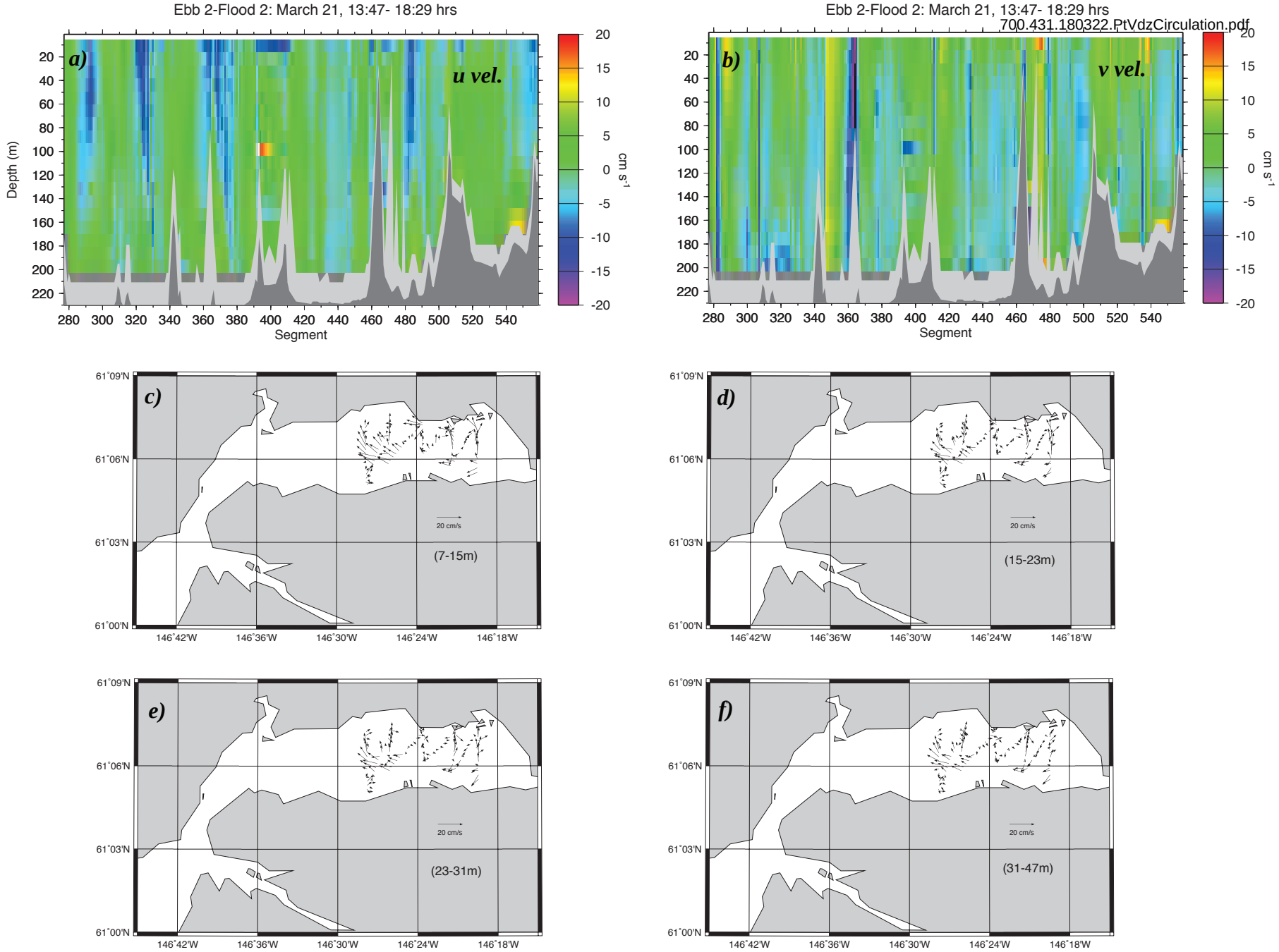

Fig. 25B. ADCP currents measured during the end of ebb tide 2 and first half of flood tide 2 from 13:47 to 18:29 *hrs* on March 21, 2017: a) *u* velocity components; b) *v* velocity components; c to e) velocity vectors for the first three 8 *m* depth bins centered at 11, 19 and 27 *m* respectively; and f) velocity vectors averaged over the next two bins from 31 to 47 *m*. Note that transects are from west to east, starting at the northwest corner (tran. #1) and ending at the southeast corner (tran. #1). The vectors are ~ 60 *sec* in length (i.e. averages of every two 30 *sec* segments shown in a and b above.

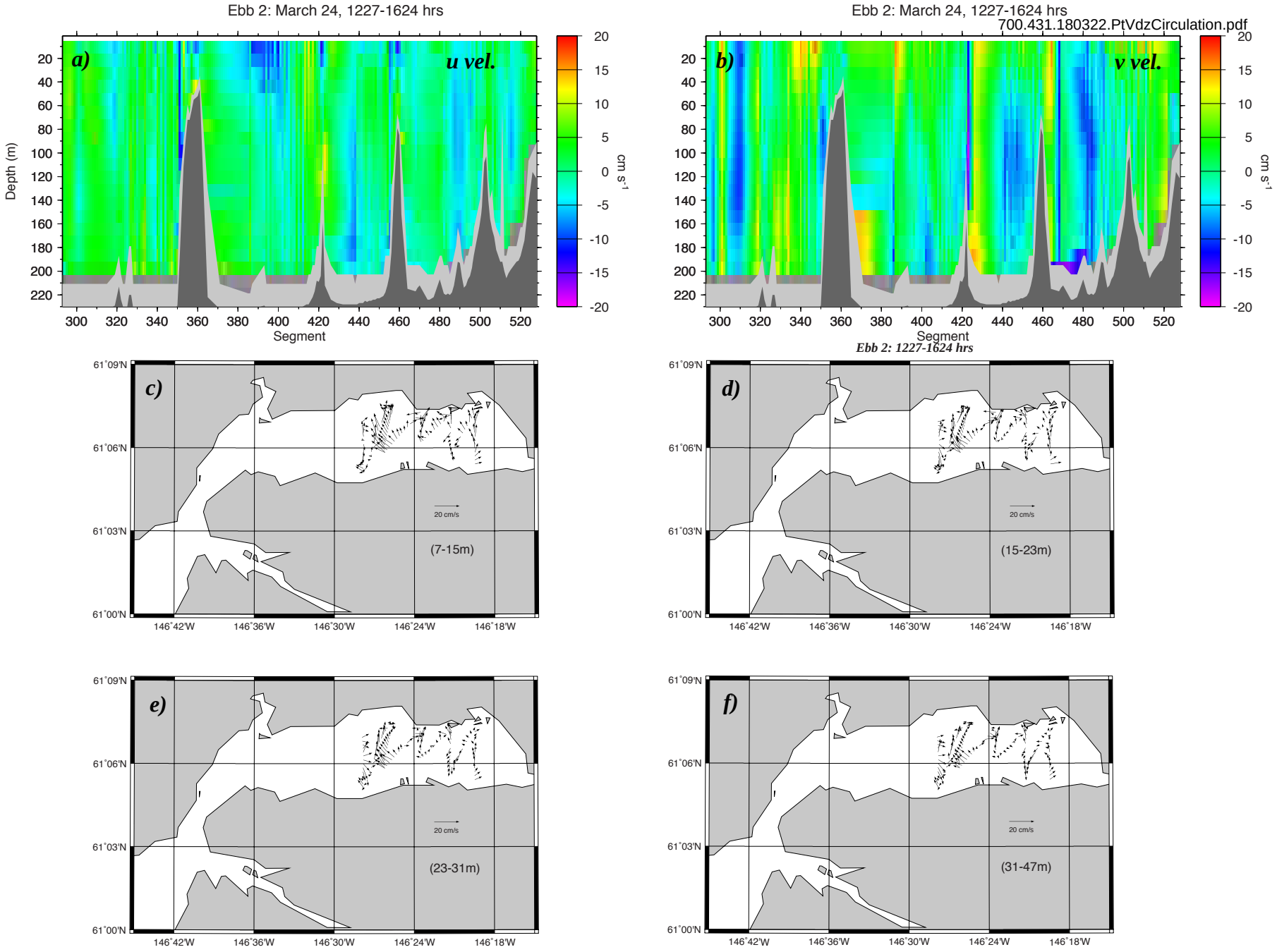

Fig. 25C. ADCP currents measured during the second ebb tide from 12:27 to 16:24 *hrs* on March 24, 2017: a) *u* velocity components; b) *v* velocity components; c to e) velocity vectors for the first three 8 *m* depth bins centered at 11, 19 and 27 *m* respectively; and f) velocity vectors averaged over the next two bins from 31 to 47 *m*. Note that transects are from west to east, starting at the northwest corner (tran. #1) and ending at the southeast corner (tran. #1). The vectors are ~ 60 *sec* in length (i.e. averages of every two 30 *sec* segments shown in a and b above.

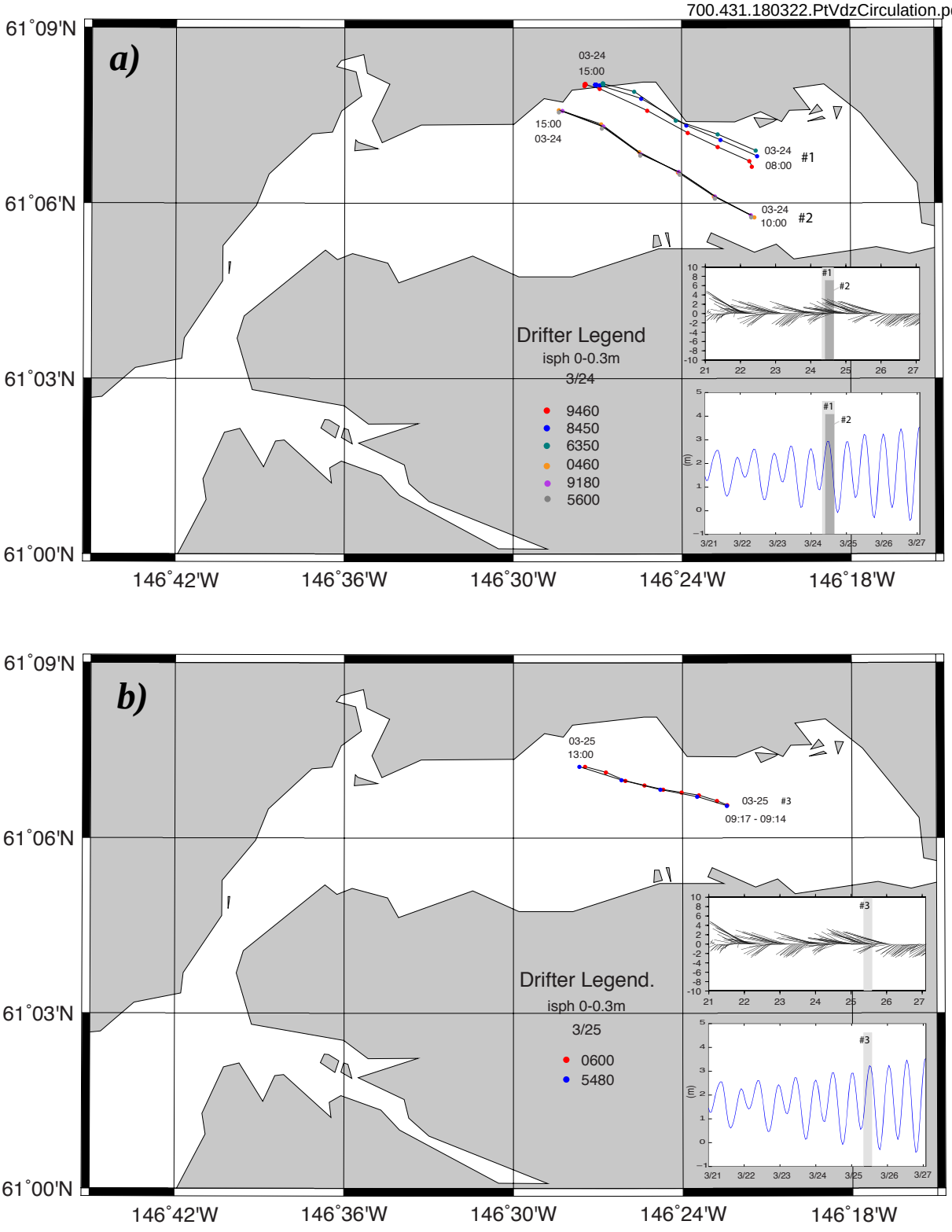

Fig. 26. Trajectories of ispheres showing combined wind and surface flows from March 24 to 25, 2017: a) groups #1 (9460, 8450 and 6350) and #2 (0460, 9180 and 5600) deloyed at 08:00 and 10:00 respectively on Mar 24th; b) group #3 (5480 and 0600) deployed on Mar 25th; The wind vectors and tides corresponding to the periods of each deployment are shown as shaded regions in the respective plots. The positions (dots) are all hourly (except for i0600, which is half hourly) and times are local (ADT).

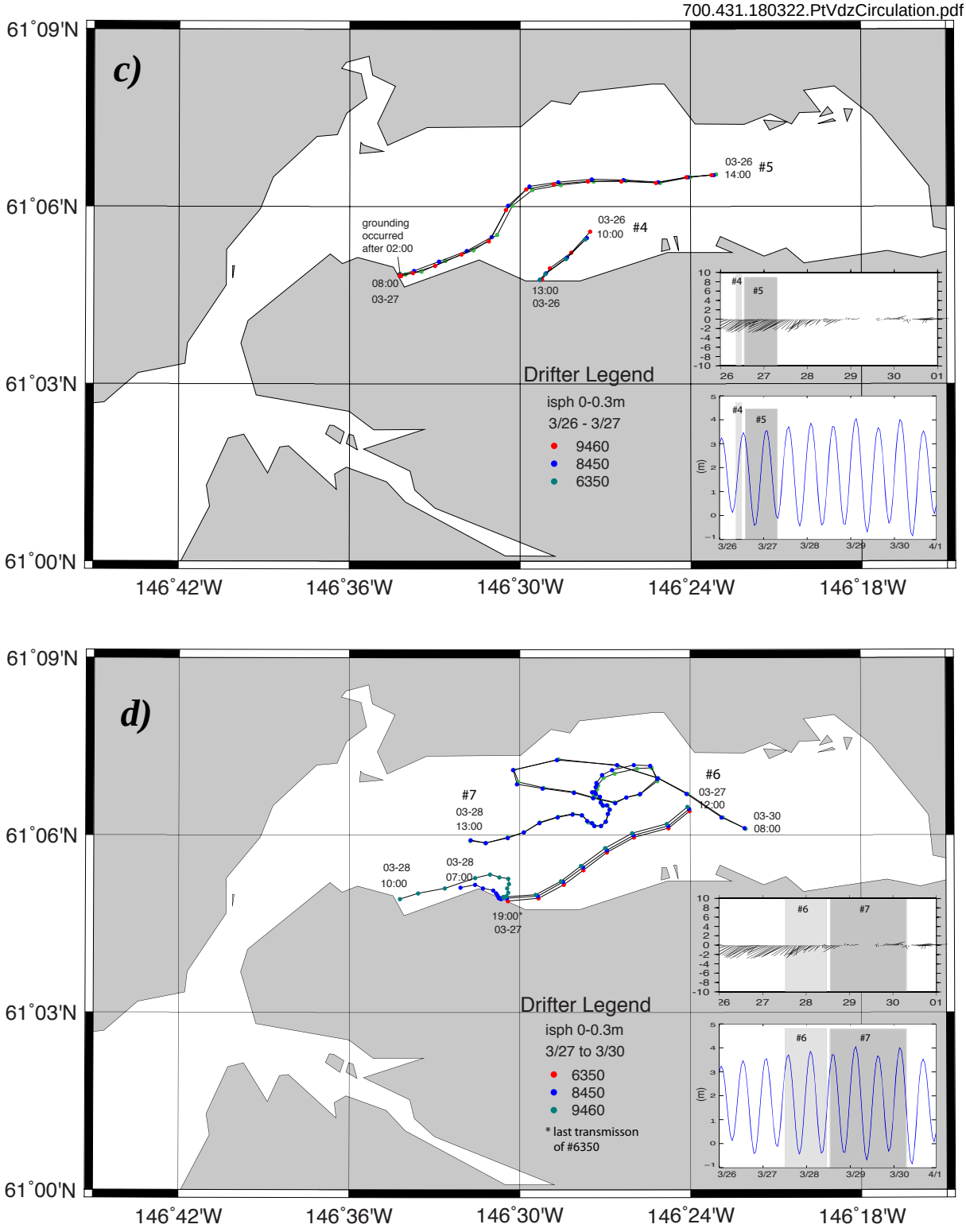

Fig. 26 (cont.). Trajectories of ispheres showing combined wind and surface flows from March 26 to 30, 2017: c) group #6 (9460, 8450 and 6350) deloyed at 12:00 on Mar 26th; and d) group #7 (8450 and 9460) deployed on Mar 28th. The wind vectors and tides corresponding to the periods of each deployment are shown as shaded regions in the respective plots. The positions (dots) are all hourly and times are local (ADT).

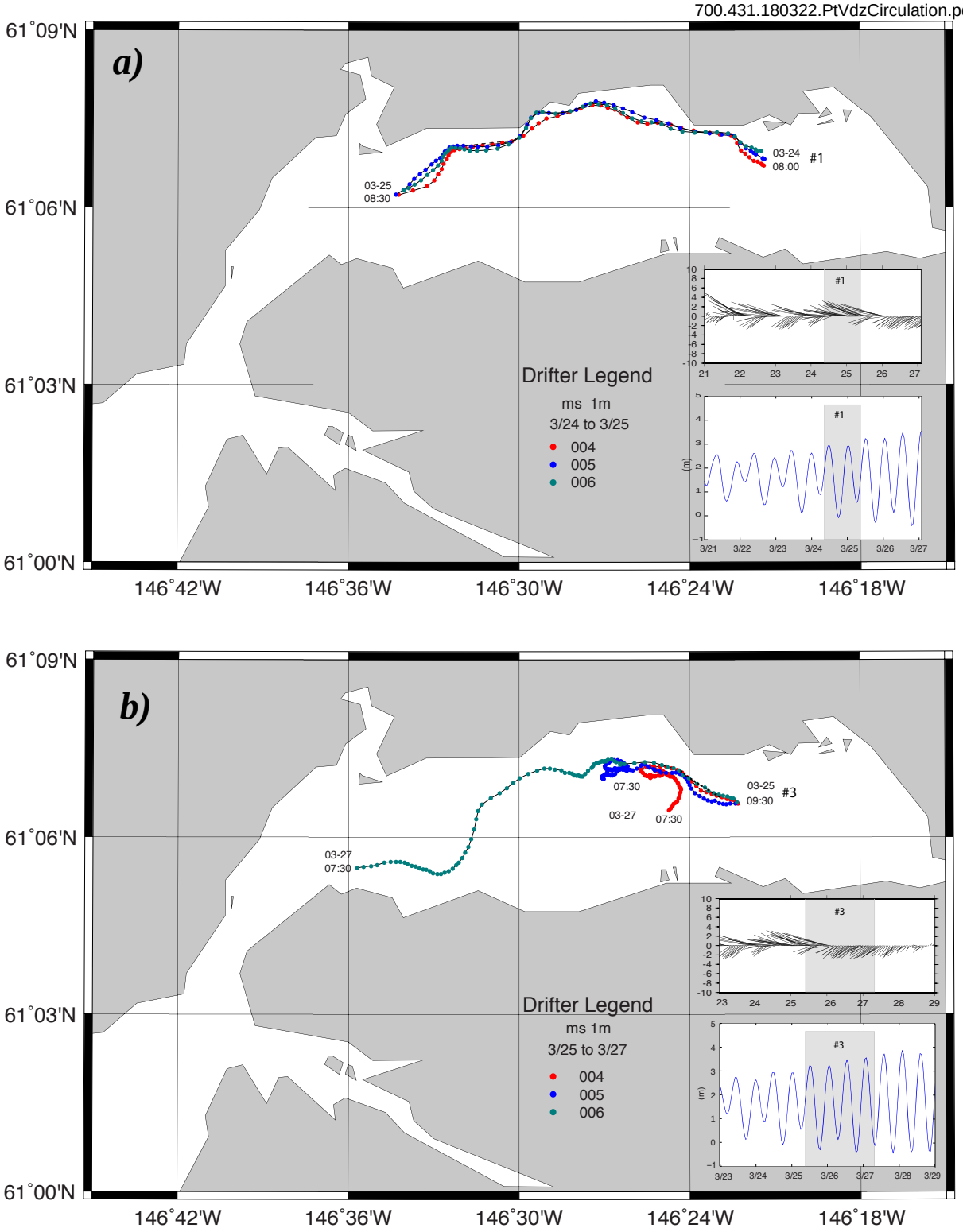

Fig. 27. Trajectories of microstars showing flows at 1m depth on March 24 to 27, 2016: a) group #1 (004, 005 and 006) deloyed on Mar 24th; b) group #2 (same drifter ids) deployed on Mar 25th. The wind vectors and tides corresponding to the periods of each deployment are shown as shaded regions in the respective plots. The positions (dots) are half hourly) and times are local (ADT). Note that unit m004 exhibited periodic problems with GPS positions. The bad points in each plot were removed and interpolated to obtain new coordinates.

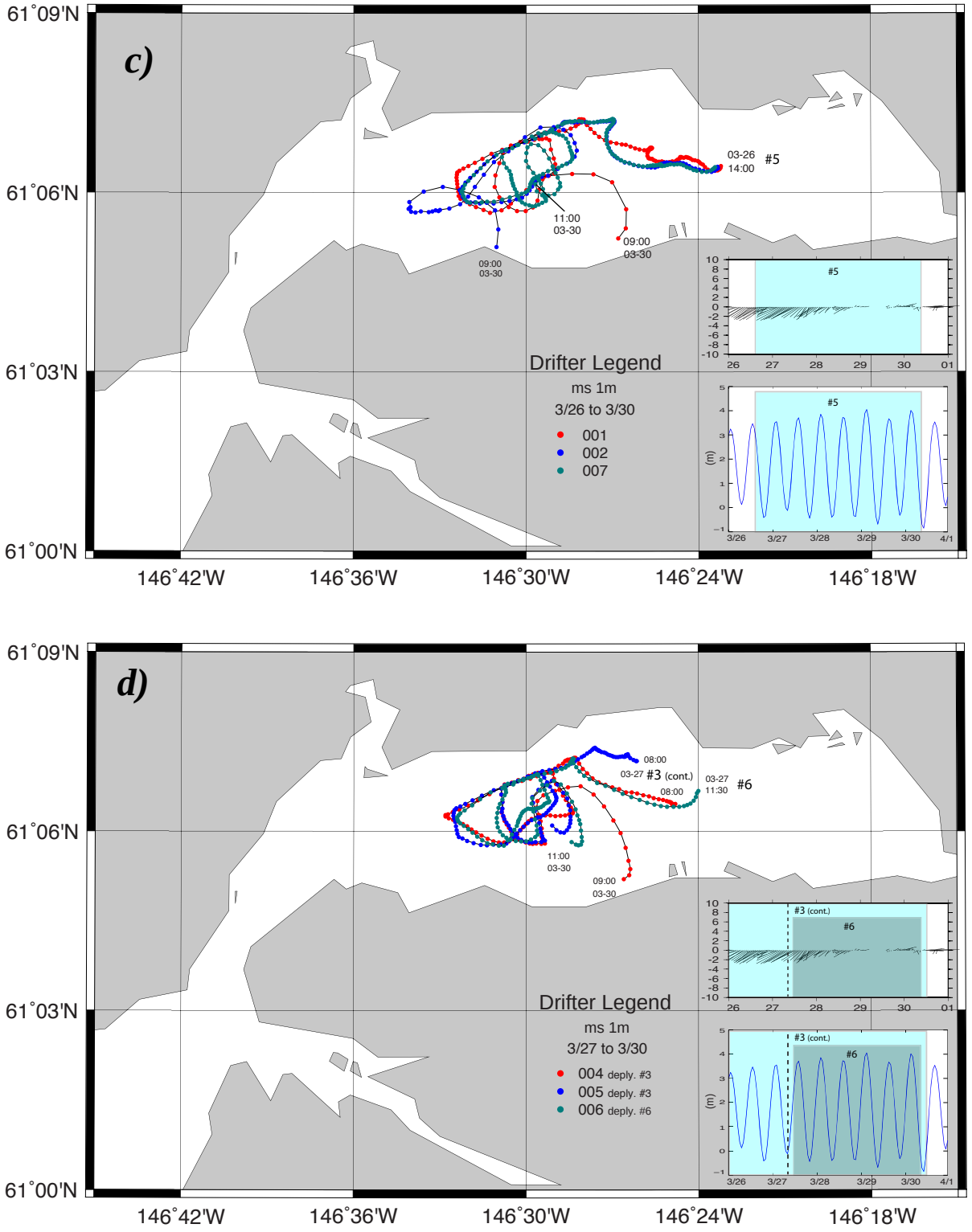

Fig. 27 (cont.). Trajectories of microstars showing flows at 1*m* depth on March 26 to 30, 2017: c) positions at 08:00 of group #2 (004 and 005) originally deloyed on Mar 25th, and redeployment of m006 on mar 27 (#6); d) group #5 (001, 002 and 007) deployed on Mar 26th. The wind vectors and tides corresponding to the periods of each deployment are shown as shaded regions in the respective plots. The positions (dots) are half hourly and times are local (ADT).

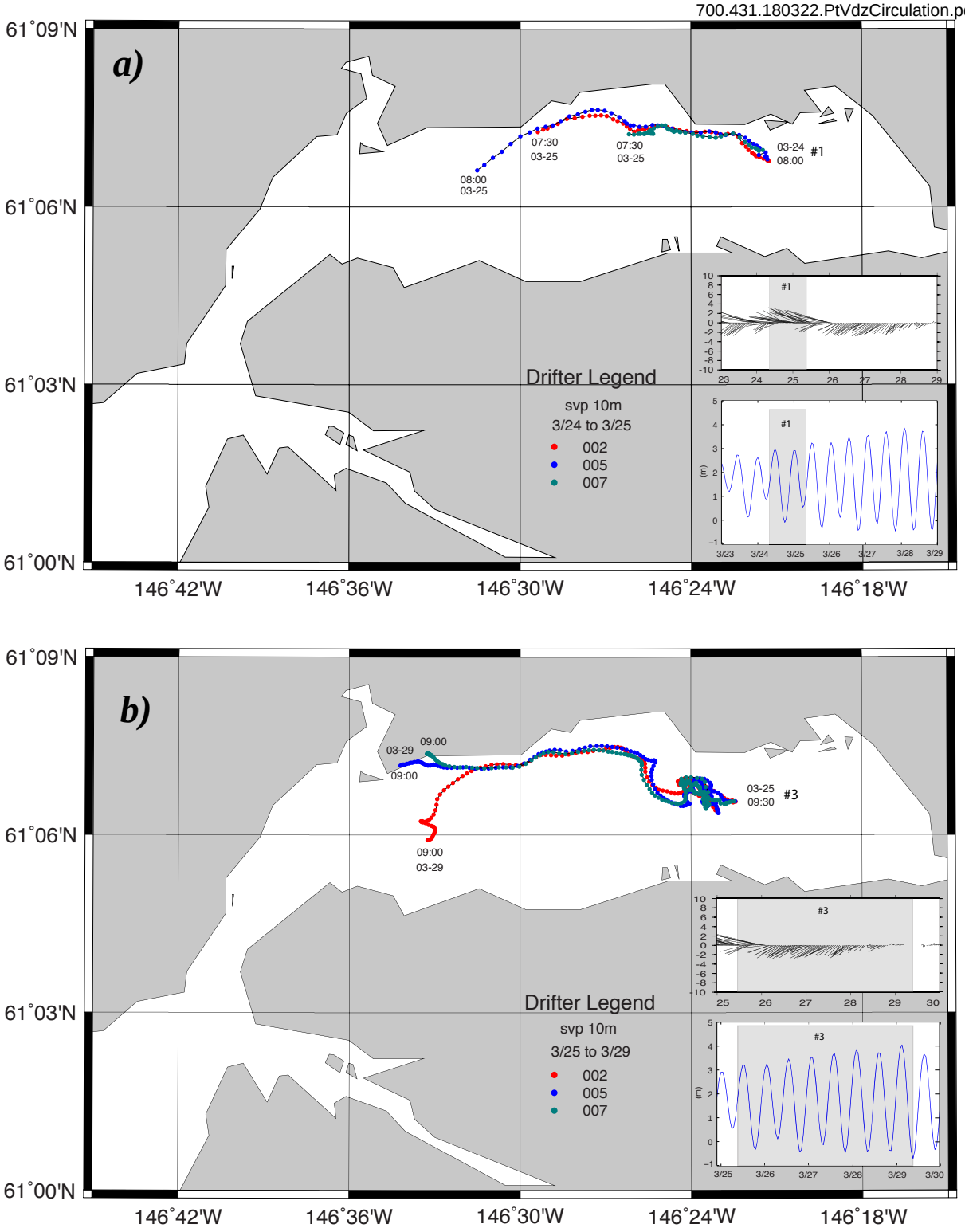

Fig. 28. Trajectories of svp10 drifters showing flows at 10*m* depth on March 24 to 29, 2017: a) group #1 (002, 005 and 007) deloyed on the 24th; and b) group #3 (same drifters) deployed on the 25th. The tides corresponding to the periods of each deployment are shown as shaded regions in respective plots (insets). The positions (dots) are half hourly) and times are local (ADT).

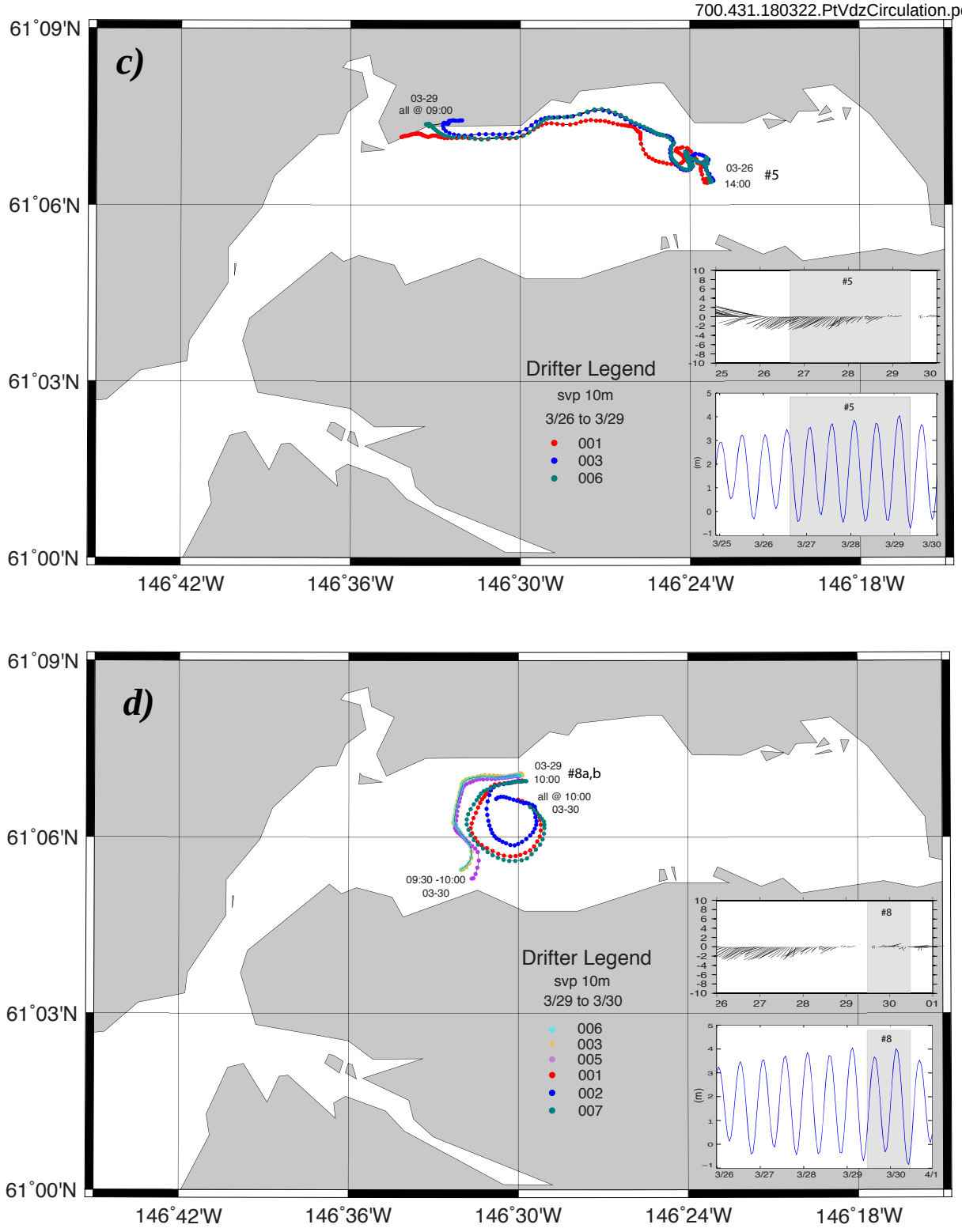

Fig. 28 (cont.). Trajectories of svp10 drifters showing flows at 10*m* depth on March 26 to 30, 2017: c) group #5 (001, 003 and 006) deloyed on the 26th; and d) groups #8a (006, 003 and 005) and #8b (001, 002 and 007) deployed on the 29th. Note that the positions of group #8a are shifted slightly to the NW in order to not obscure the positions of group #8b. The tides corresponding to the periods of each deployment are shown as shaded regions in respective plots (insets). The positions (dots) are half hourly) and times are local (ADT).

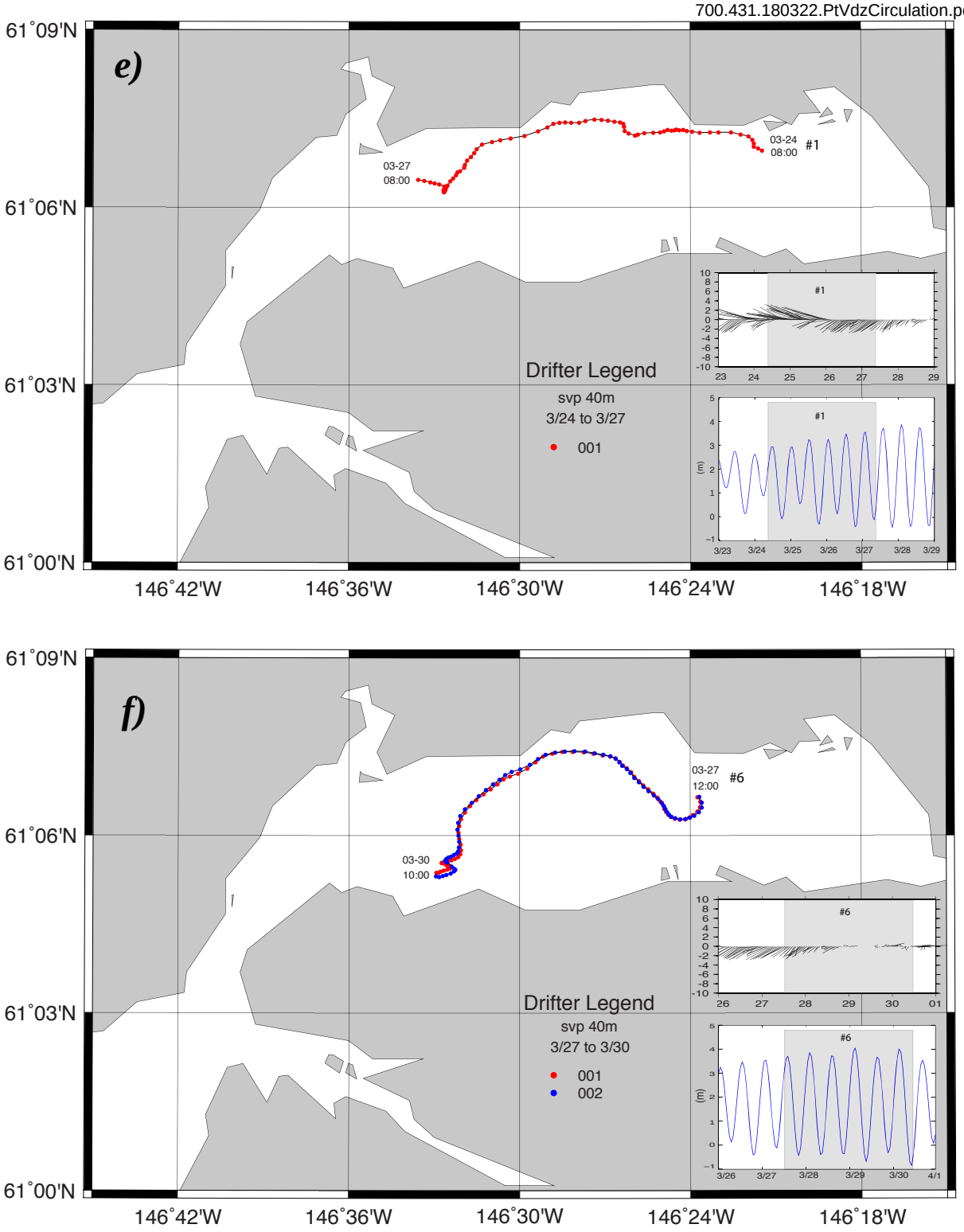

Fig. 28 (cont.). Trajectories of svp40 drifters showing flows at 40*m* depth on March 24 to 30, 2017: e) group #1 (001), deloyed on the 24th; and f) group #6 (001 and 002) deployed on the 27th. The tides corresponding to the periods of each deployment are shown as shaded regions in respective plots (insets). The positions (dots) are hourly and times are local (ADT).

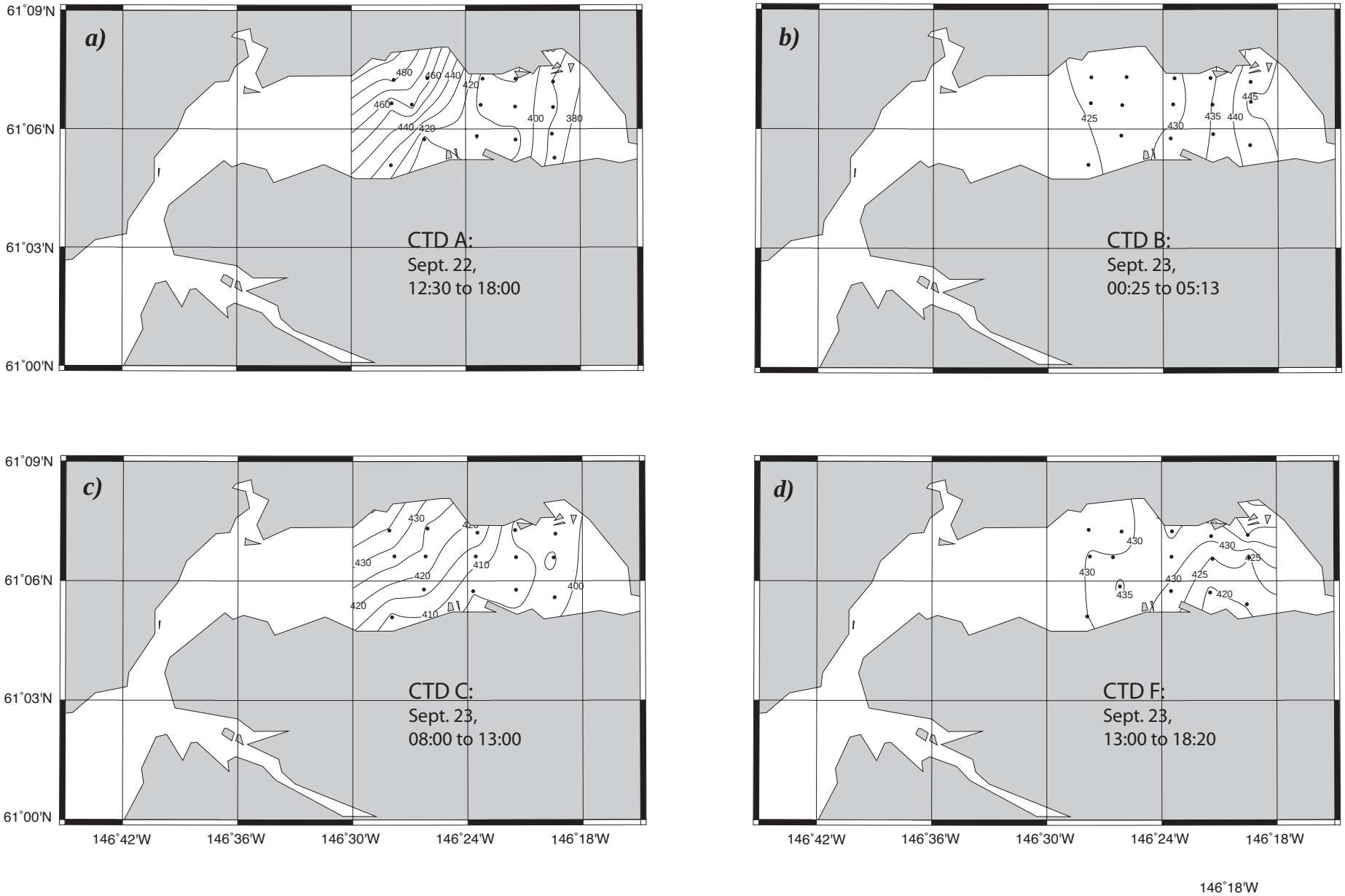

Fig. 29. Examples of dynamic topography (1/100db) in June 2016. a) CTD set A from 12:30 to 18:00 on the 22nd; b) CTC set B from 00:25 to 05:13 on the 23rd; c) CTD set C from 08:00 to 13:00 on the 23rd; and d) CTD set F from 13:00 to 18:20 on the 26th. Note that contour intervals vary from 5 to 20 dynamic cm and that CTD Stations are denoted by black dots.

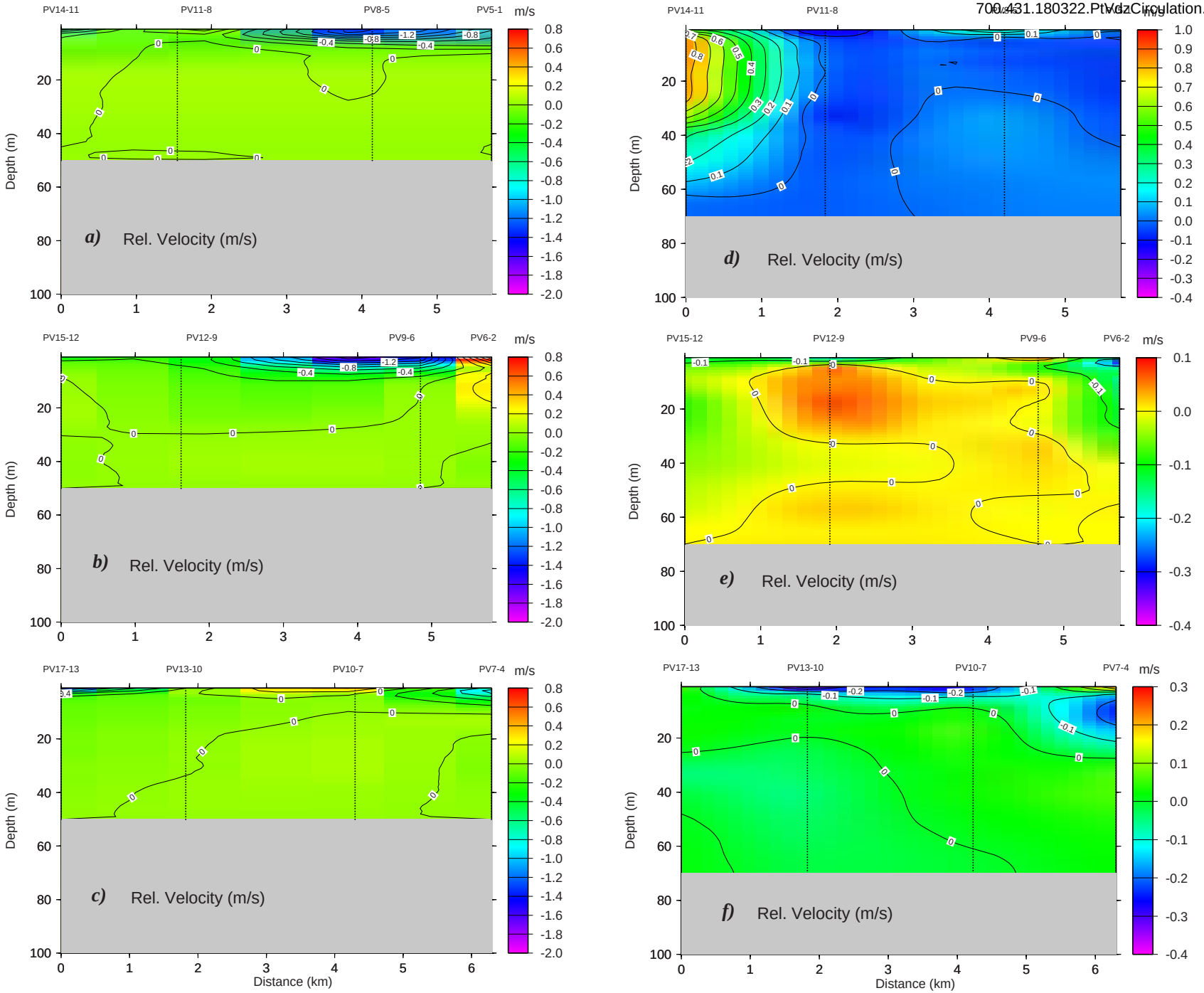

Fig. 30. Geostrophic velocities from along-fjord transects showing the cross-channel flow components based on dynamic topography (1/100db) from CTD sets A on June 22 (a-c) and set F on June 26 (d-f): a) transect I (northern); b) transect II (central); c) transect III (southern); d) transect I (northern); e) transect II (central); f) transect III (southern). Note the differences in scales between the two data sets.

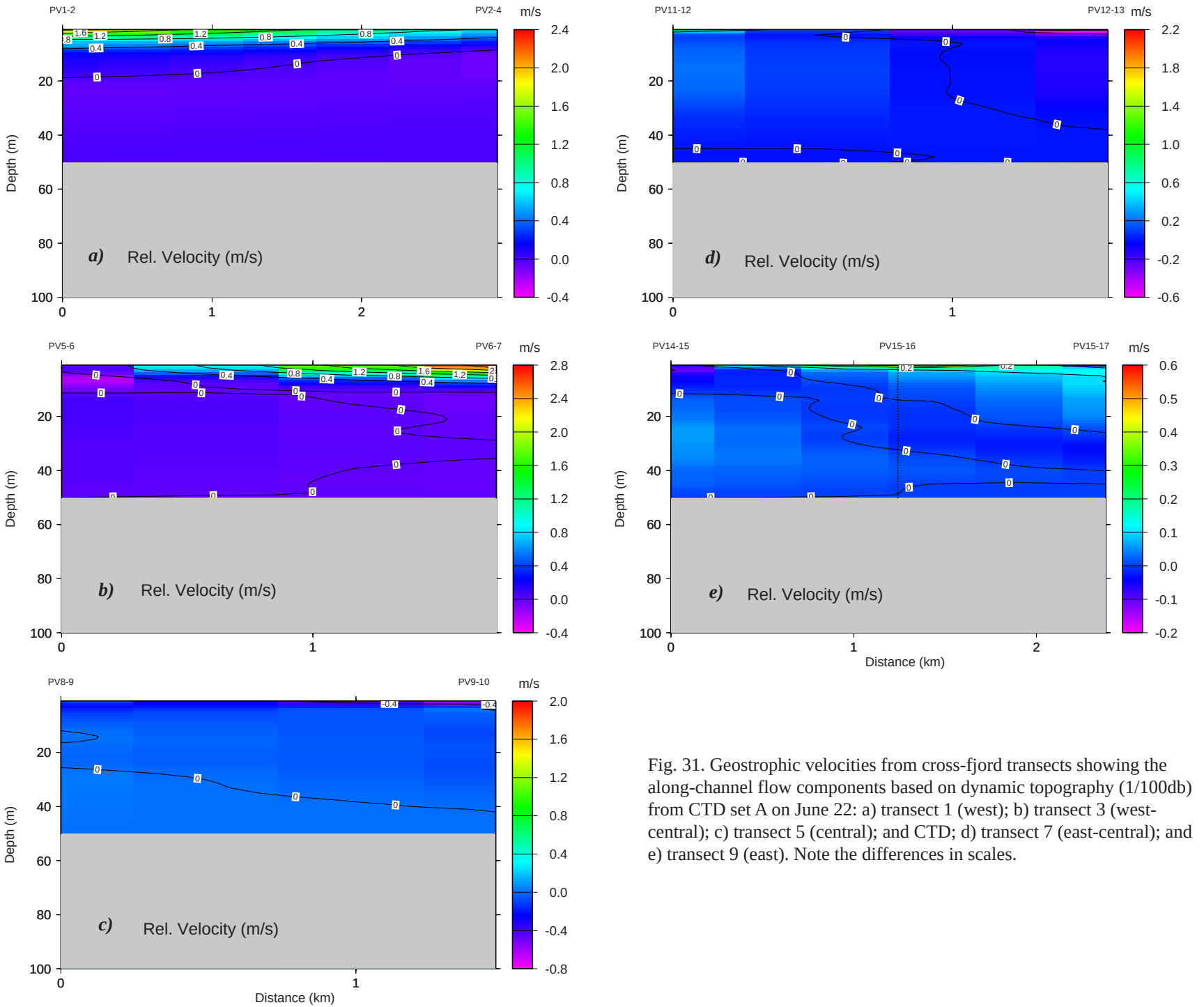

Fig. 31. Geostrophic velocities from cross-fjord transects showing the along-channel flow components based on dynamic topography (1/100db) from CTD set A on June 22: a) transect 1 (west); b) transect 3 (west-central); c) transect 5 (central); and CTD; d) transect 7 (east-central); and e) transect 9 (east). Note the differences in scales.

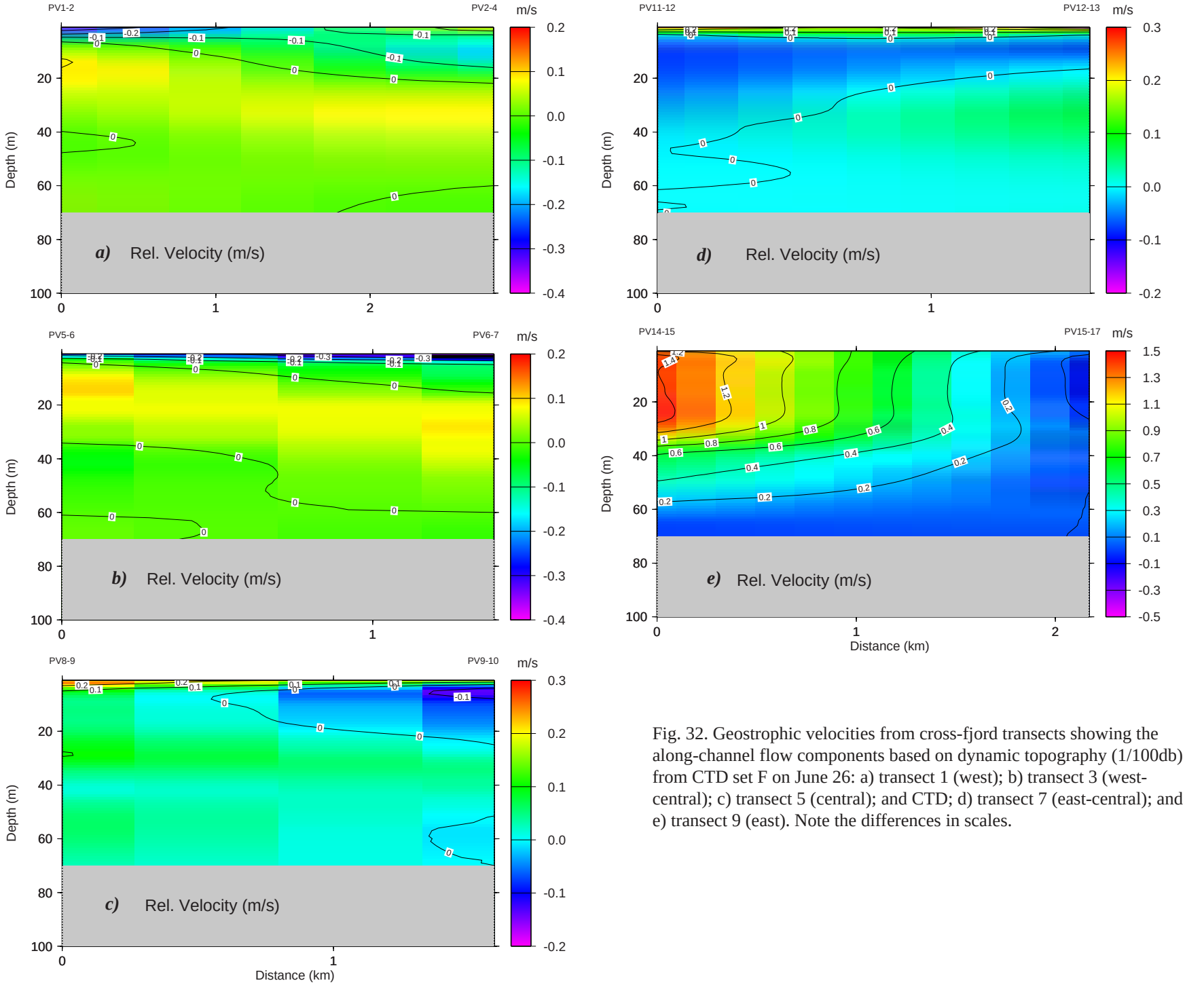

Fig. 32. Geostrophic velocities from cross-fjord transects showing the along-channel flow components based on dynamic topography (1/100db) from CTD set F on June 26: a) transect 1 (west); b) transect 3 (west-central); c) transect 5 (central); and CTD; d) transect 7 (east-central); and e) transect 9 (east). Note the differences in scales.

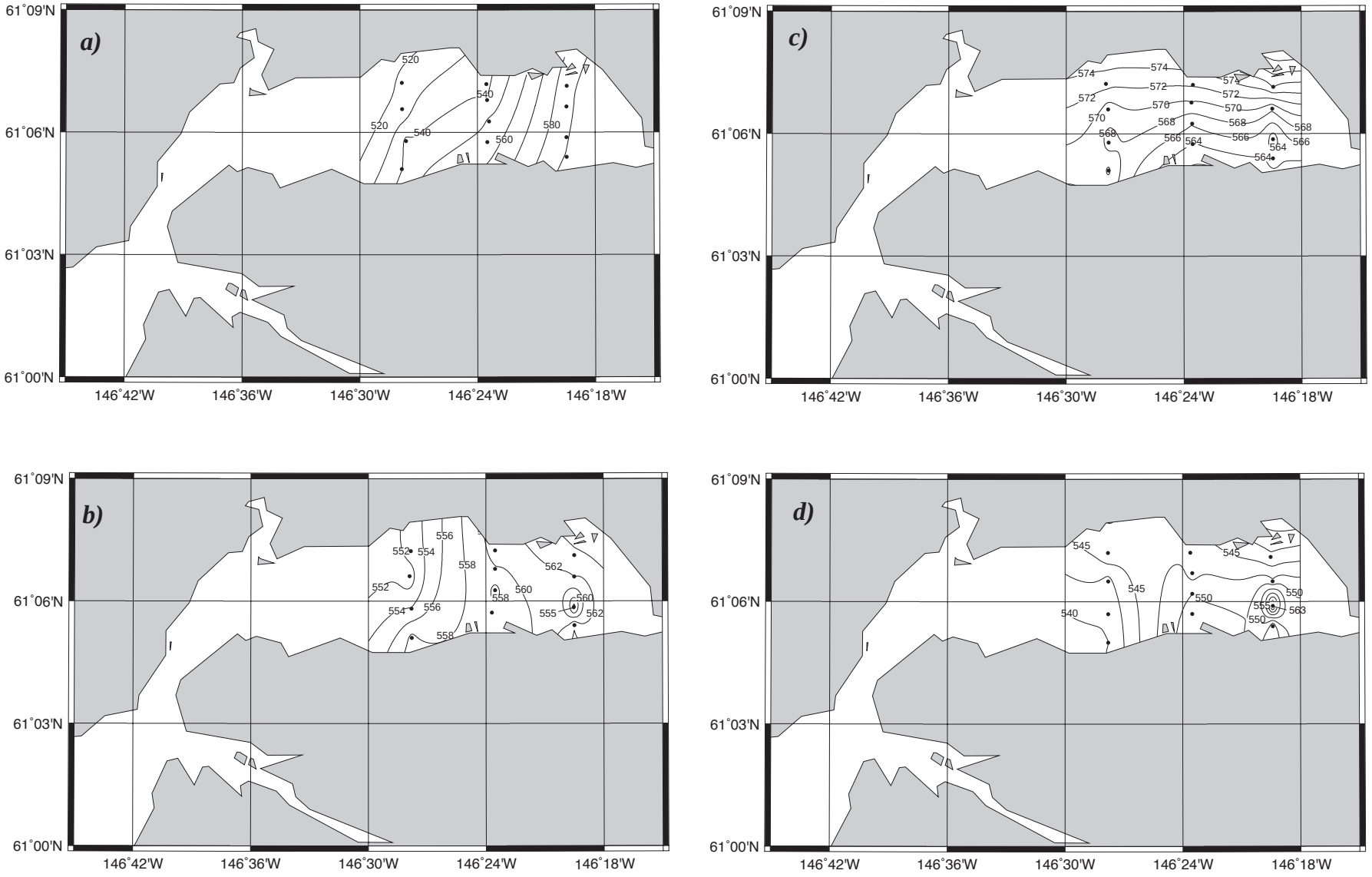

Fig. 33. Examples of dynamic topography (1/100db) in September 2016. a) CTD set A from 13:00 to 18:00 on the 21st; b) CTC set B from 21:34 on the 21st to 02:37 on the 22nd; c) CTD set E from 08:30 to 13:09 on the 24th; and d) CTD set H from 17:18 to 19:54 on the 25th. Note that contour intervals vary from 5 to 20 dynamic cm and that CTD Stations are denoted by black dots.

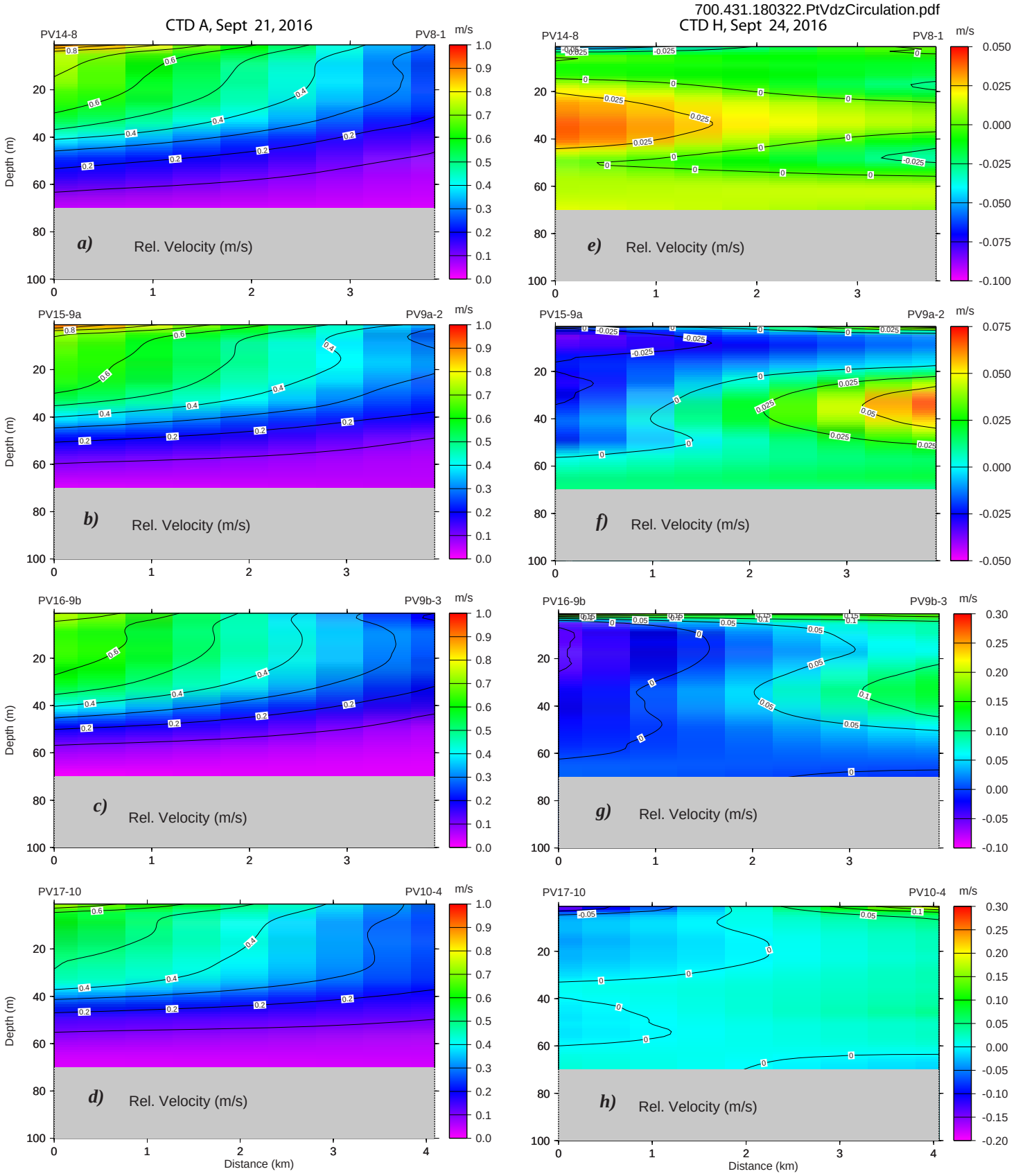

Fig. 34. Geostrophic velocities from along-channel transects showing cross-channel flow components based on dynamic topography (1/100db) in September 2016 from CTD set A on the 21st: a) transect I (northern); b) transect II (north-central); c) transect III (south-central) and d) transect IV (southern); and CTD set H on the 24th: e to h) same transects. Note the differences in scales between the two data sets.

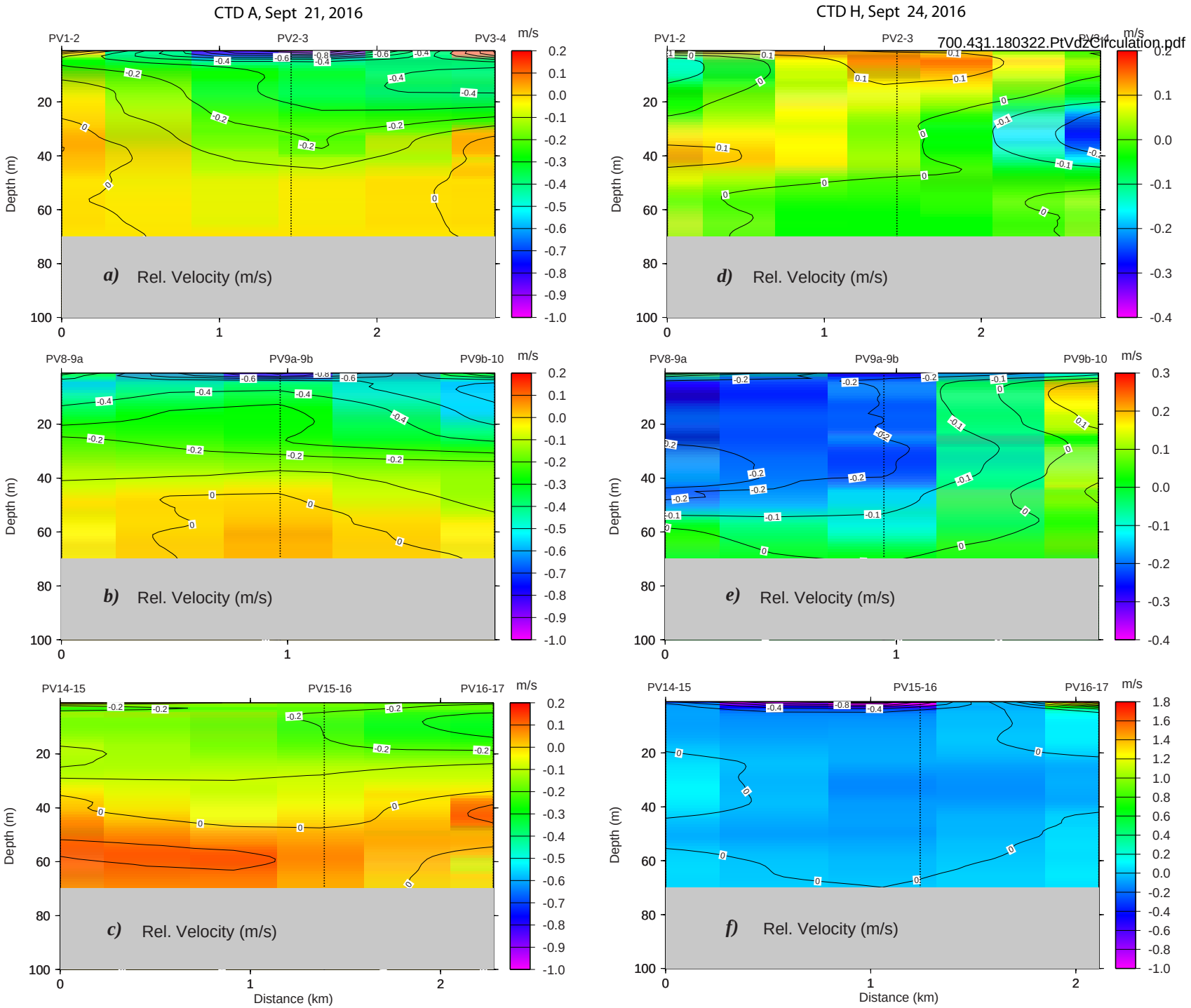

Fig. 35. Geostrophic velocities from cross-fjord transects showing along-channel flow components based on dynamic topography (1/100db) in September 2016 from CTD set A on the 21st: a) transect 1 (west); b) transect 5 (central); c) transect 9 (east); and CTD set H on the 25th; d) transect 1 (west); e) transect 5 (cental); and f) transect 9 (east). Note the marked differences in scales among the data sets.

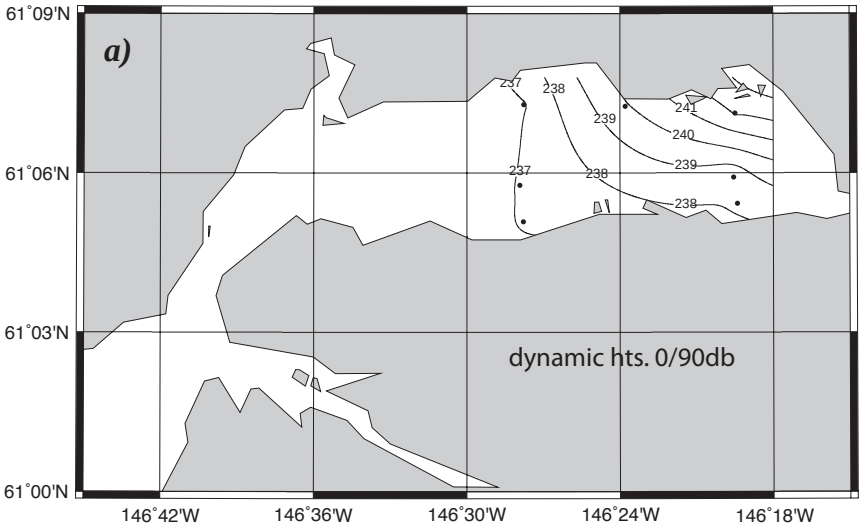

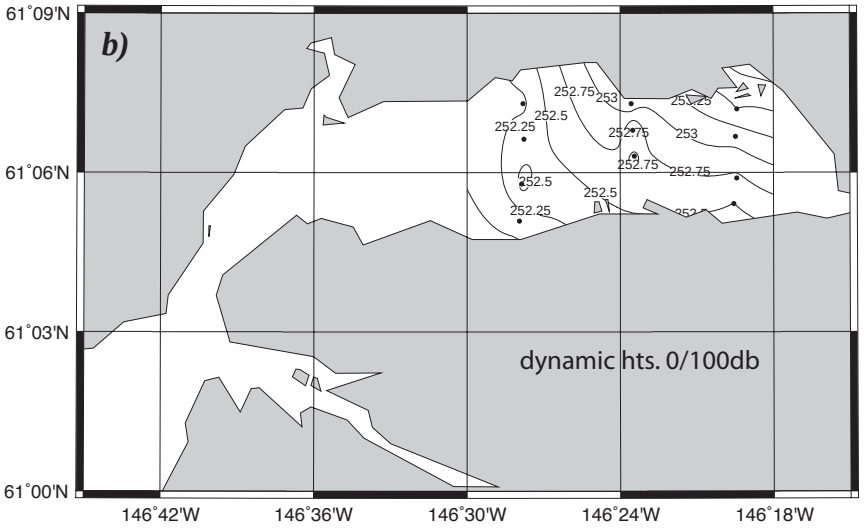

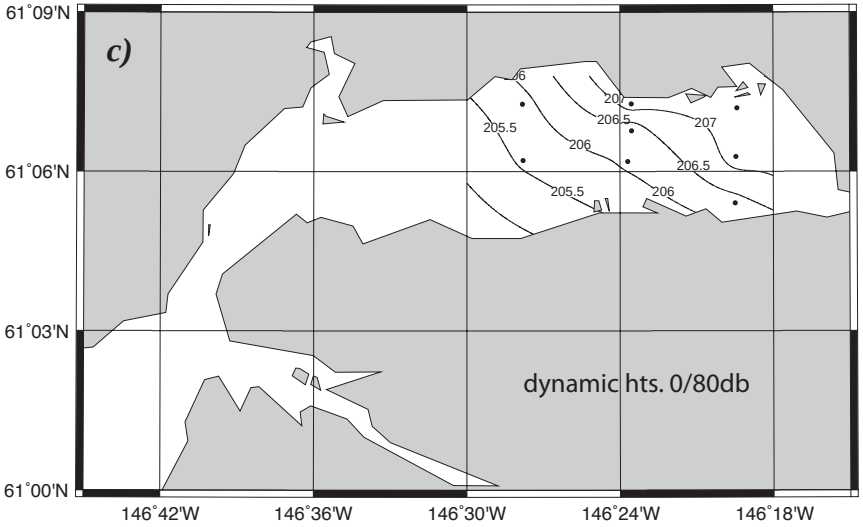

Fig. 36. Examples of dynamic topography in March 2017. a) CTD set A (1/90db) from 12:30 to 13:45 on the 21st and one station (PV1) from set B on the 23rd; b) CTC set C (1/100db) from 08:35 to 13:20 on the 24th; and c) CTD set D (1/80db) from 08:05 to 13:10 on the 25th. Note that contour intervals vary from 0.25 to 1 dynamic cm and that the magnitudes of the dynamic heights differ in part due to the varied levels of no motion. The CTD Stations are denoted by black dots.

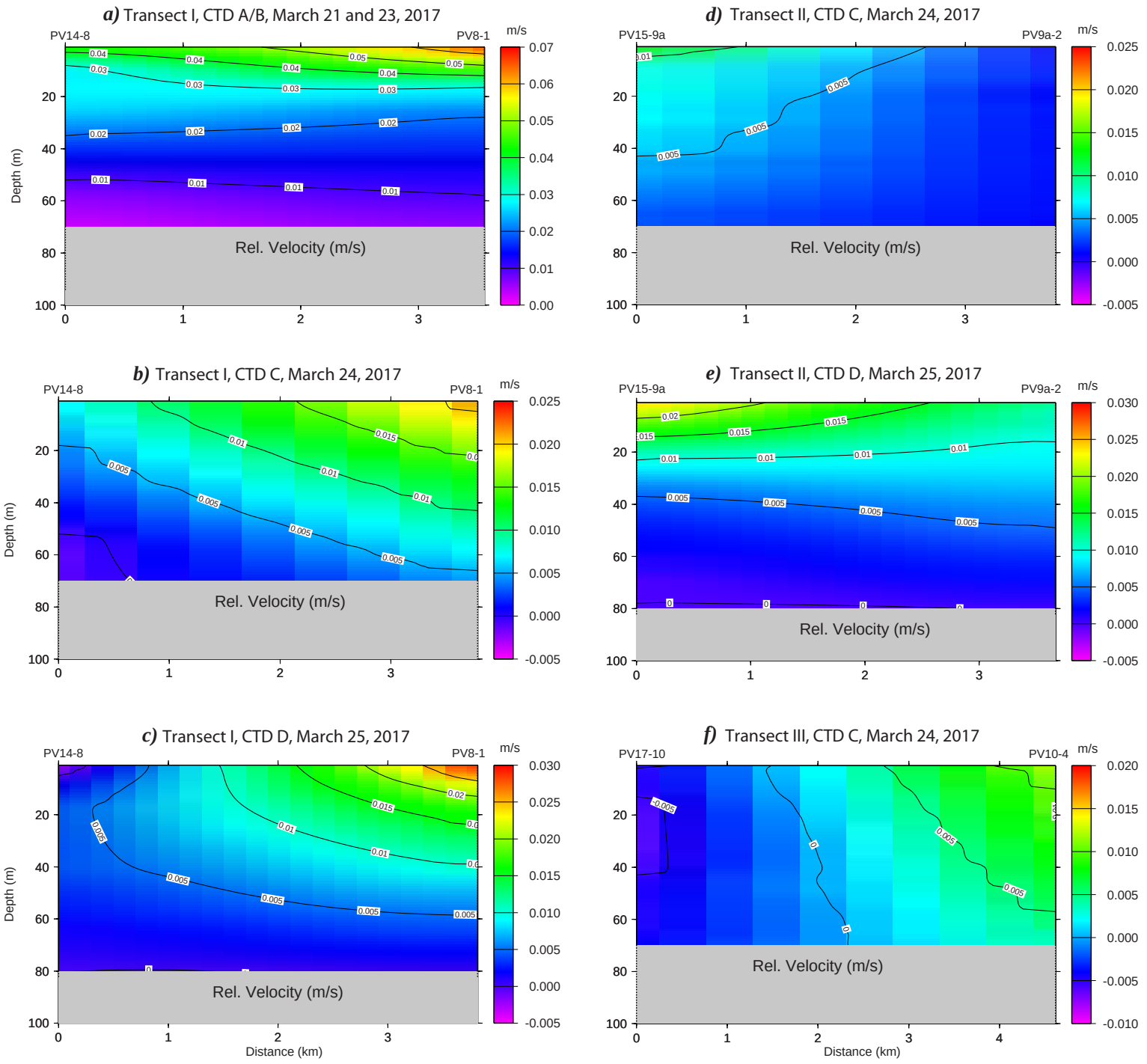

Fig. 37. Geostrophic velocities from along-fjord transects showing cross-channel flow components in March 2017 based on dynamic topography (1/90*db* for CTD set A/B, 1/80*db* for set C and 1/100*db* for set D): a-c) transect I (northern), CTD sets A/B, C and D; d-e) transect II, CTD sets C and D; and f) transect III (southern), CTD set C. Note the differences in scales among the various data sets.

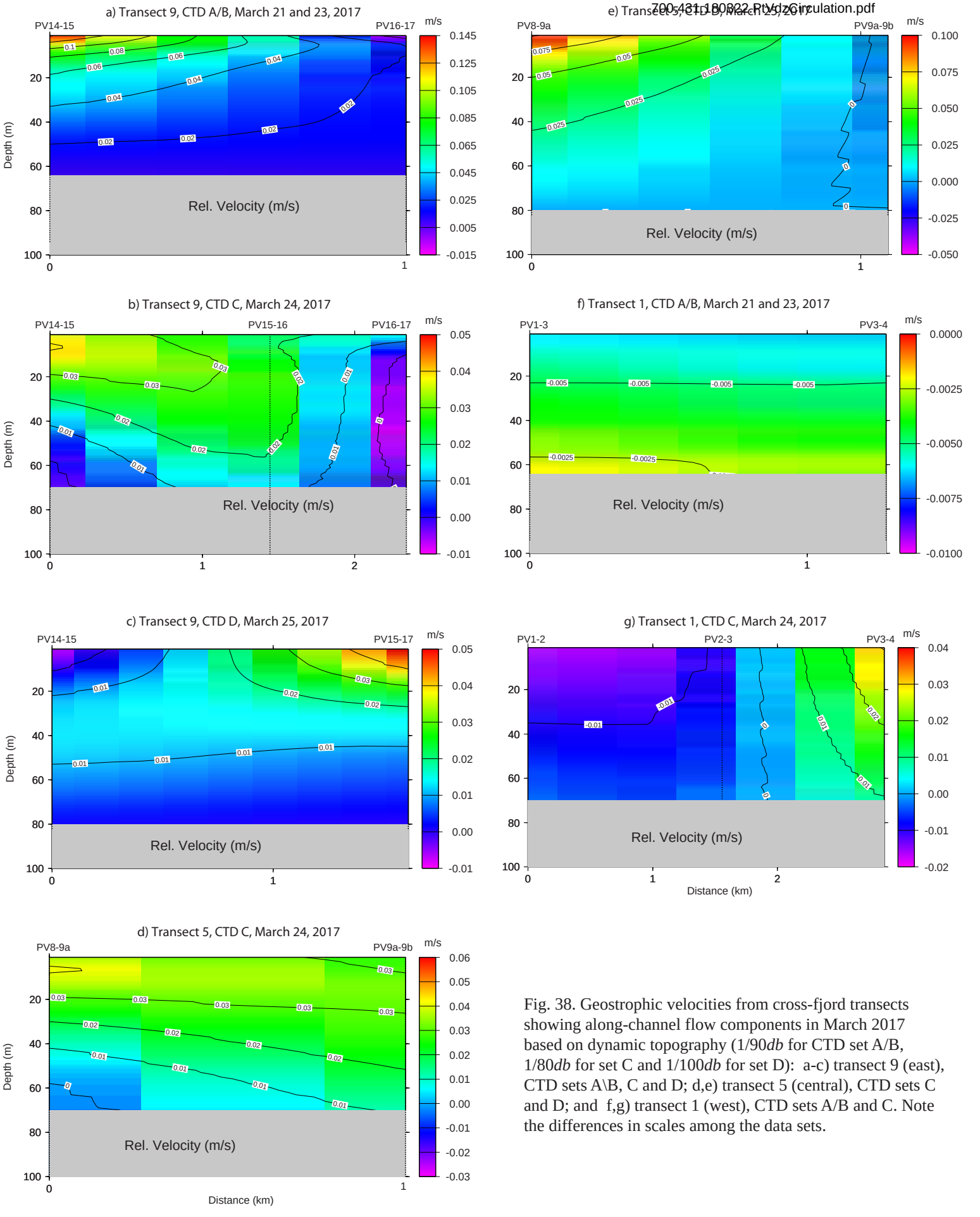

Fig. 38. Geostrophic velocities from cross-fjord transects showing along-channel flow components in March 2017 based on dynamic topography (1/90*db* for CTD set A/B, 1/80*db* for set C and 1/100*db* for set D): a-c) transect 9 (east), CTD sets A\B, C and D; d,e) transect 5 (central), CTD sets C and D; and f,g) transect 1 (west), CTD sets A/B and C. Note the differences in scales among the data sets.

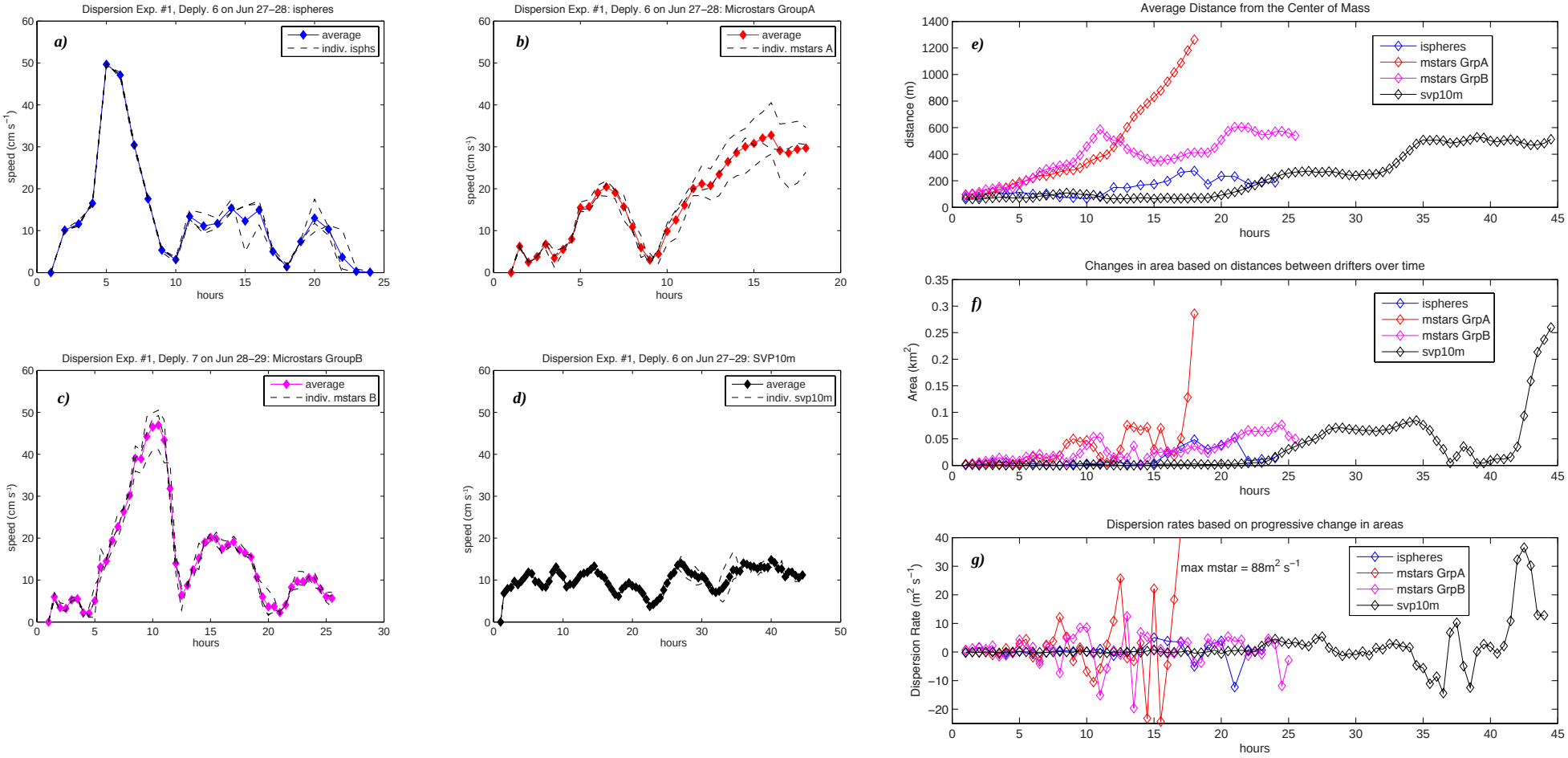

Fig. 39. Drifter speeds and dispersion during the first dispersion experiment conducted from June 27 to 29, 2016. Average and ranges of speeds for a) ispheres group A (dply. #6); b) microstars group A (dply. #6); c) microstars group B (dply. #7); and d) SVP 10*m* group A (dply. #6); e) average distance from the center of mass (*m*); f) changes in triangular area (km^2) based on relative positions over time; and g) dispersion rates over time in $m^2\ s^{-1}$.

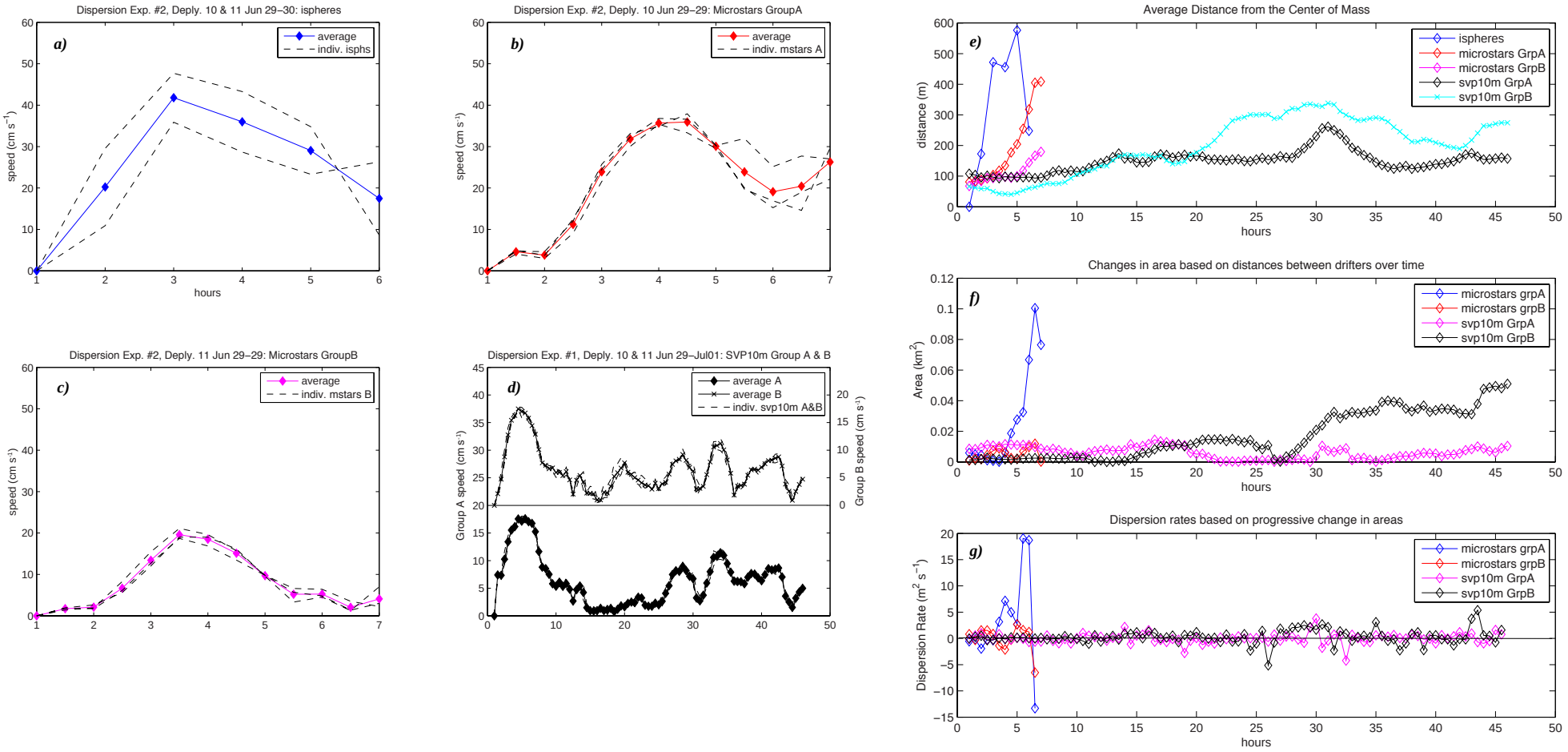

Fig. 40. Drifter speeds and dispersion during the seond dispersion experiment conducted from June 29 to July 1, 2016. Average and ranges of speeds for individual drifters for a) ispheres group A (dply. 10 & 11); b) microstars group A (deply. 10); c) microstars group B (deply. 11); and d) SVP 10*m* group A (deply. 10) and B (deply. 11); e) average distance from the center of mass (*m*); f) changes in triangular area (km^2) based on relative positions over time; and g) dispersion rates over time in $m^2\ s^{-1}$.

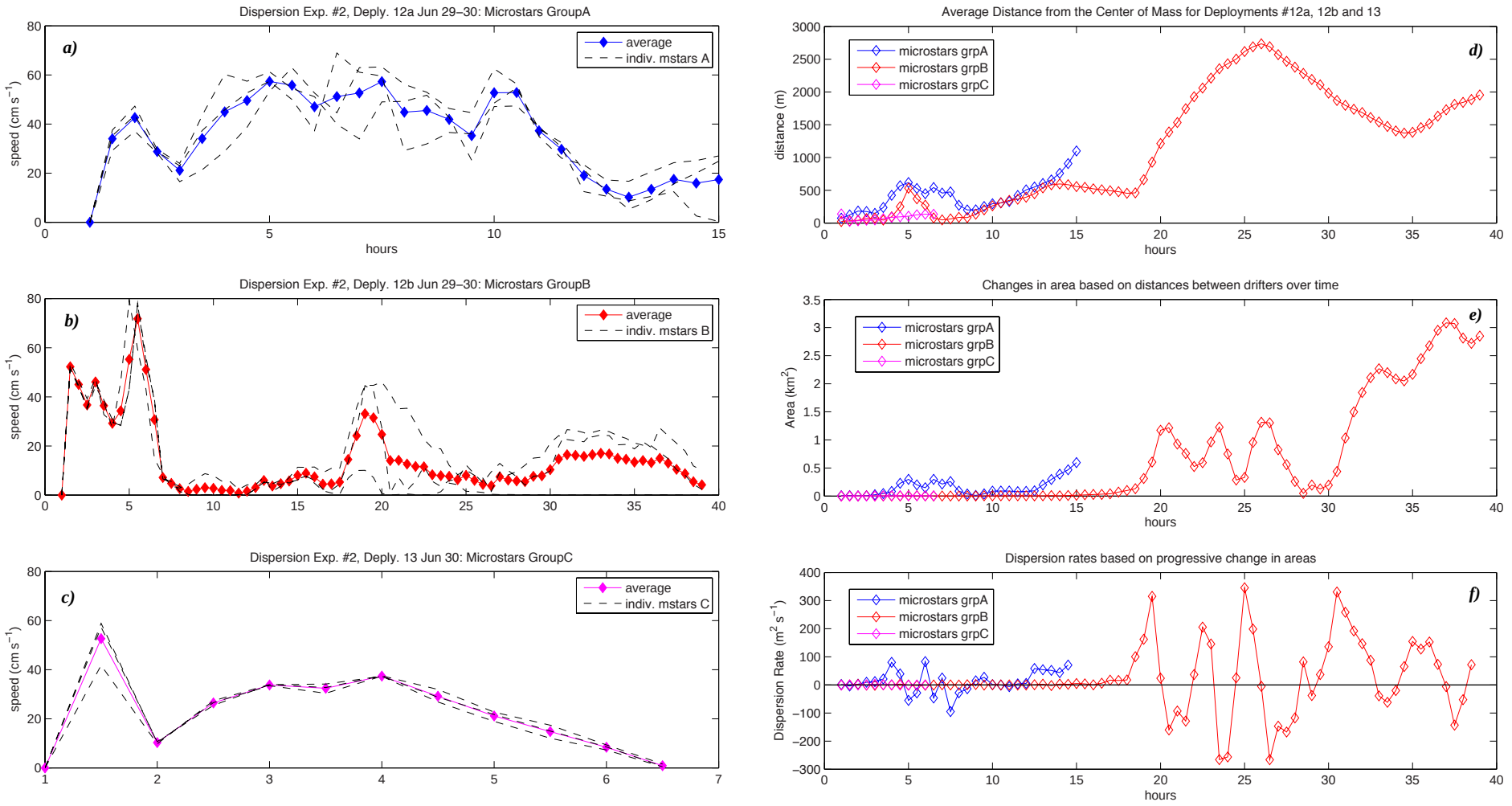

Fig. 41. Drifter speeds and dispersion during the third dispersion experiment conducted from June 29 to 30, 2016. Average and ranges of speeds for individual drifters for a) microstars group A (dply. 12a) released on the 29th; b) microstars group B (dply. 12b) also released on the 29th; and c) microstars group C (dply. 13) released on the 30th; d) average distance from the center of mass (*m*); e) changes in triangular area (km^2) based on relative positions over time; and f) dispersion rates over time in $m^2\ s^{-1}$.

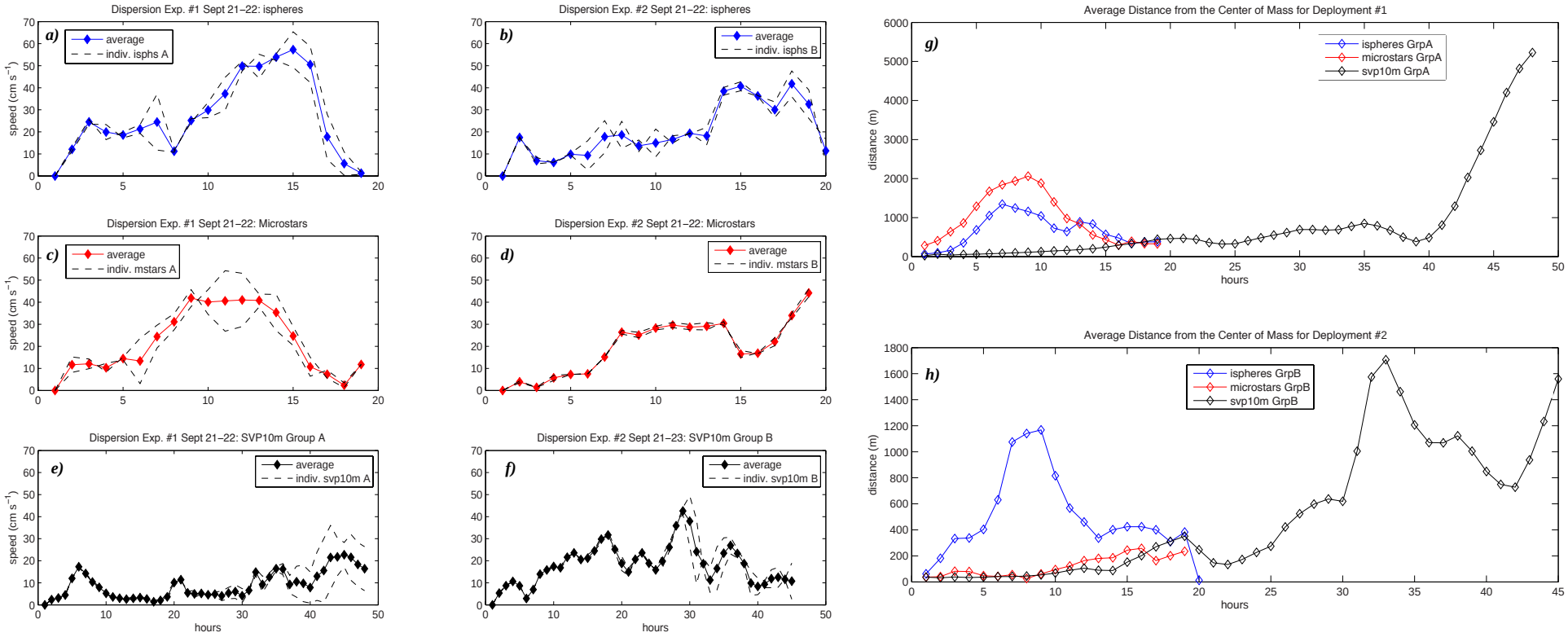

Fig. 42. Drifter speeds and dispersion during the first and seond dispersion experiments conducted from September 21 to 23, 2016: average speeds and ranges of individual drifters for a) ispheres group A; b) ispheres group B; c) microstars group A; d) microstars group B; e) SVP 10m group A; and f) SVP 10m group B; g) average distance from the center of mass for group A ispheres, microstars and svp10m drifters; h) average distance from the center of mass for group B ispheres, microstras and svp10m drifters.

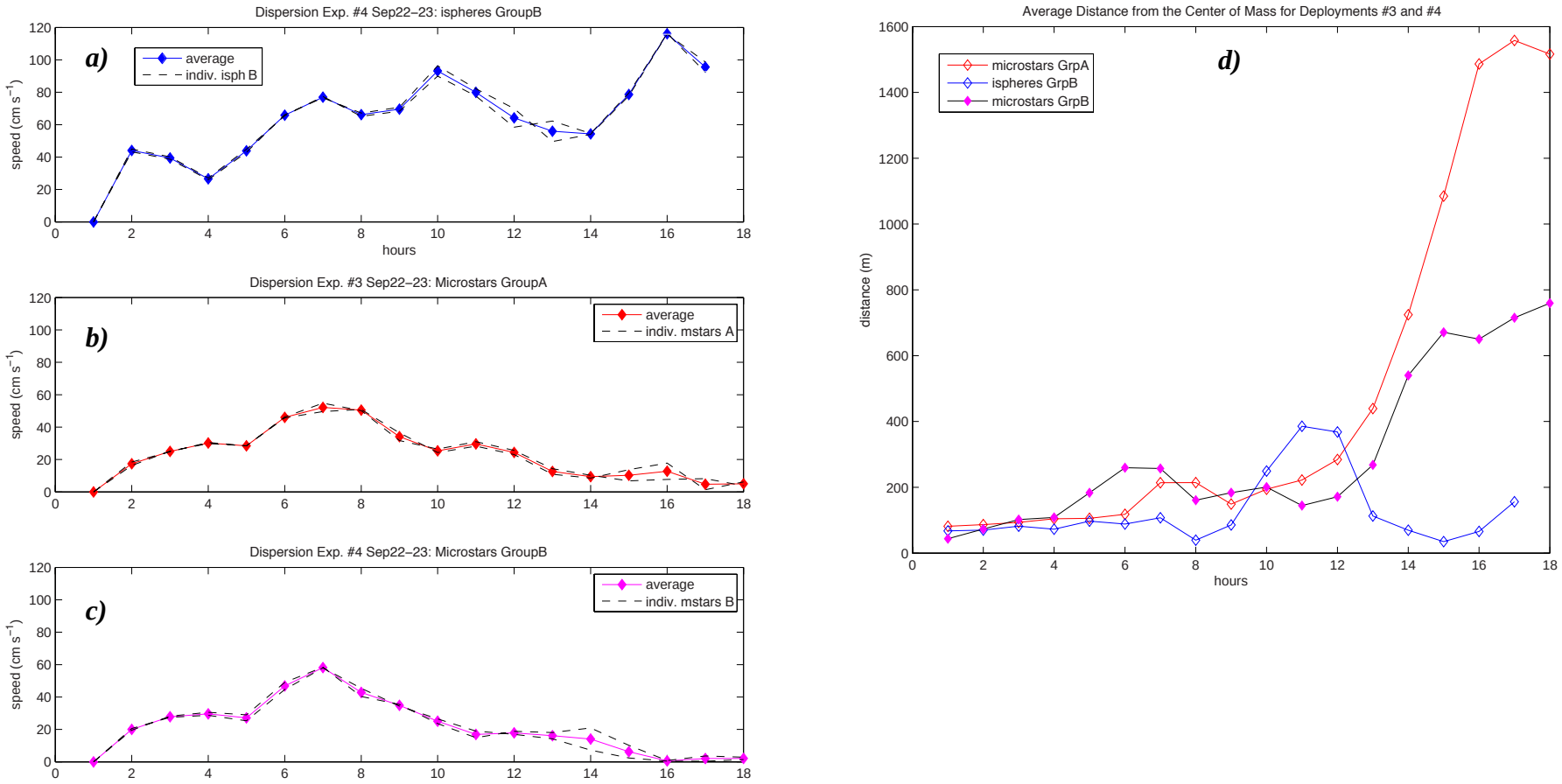

Fig. 43. Drifter speeds and dispersion over time during the third and fourth experiments conducted from September 22 to 23, 2016, showing averages and ranges of individual drifters: a) ispheres group B; b) microstars group A; c) microstars group B; and d) average distances from the center of mass.

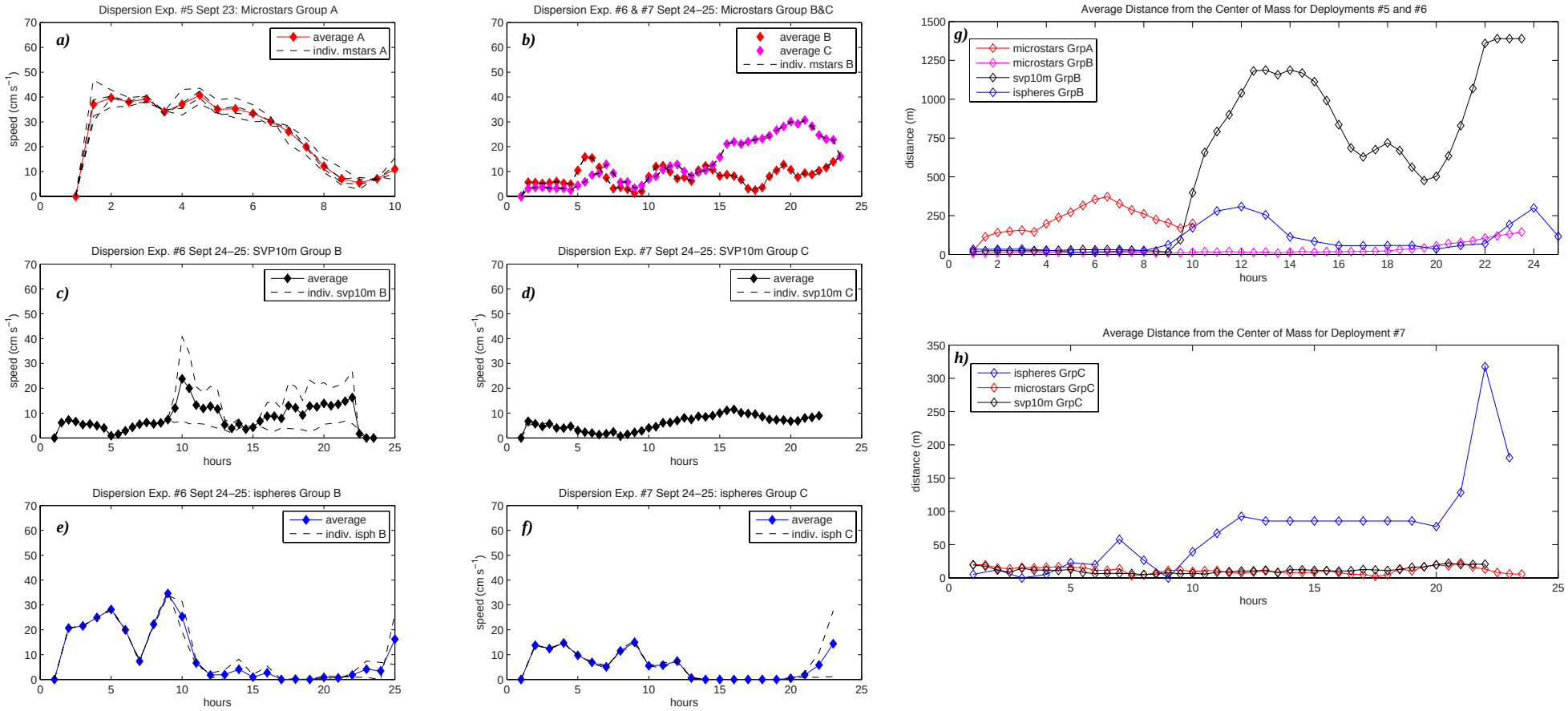

Fig. 44. Drifter speeds and dispersion during the fifth to seventh dispersion experiments conducted from Sept. 23 to 25, 2016: average speeds and ranges of individual drifters for a) microstars group A released on the 23rd; b) microstars group B and C released on the 24th; c,d) SVP 10m group B and C released on the 24th; and e,f) ispheres group B and C released on the 24th; average distance from the center of mass for g) group A and B microstars , group B ispheres, microstars and svp10m drifters; and h) group C ispheres, microstars and svp10m drifters.

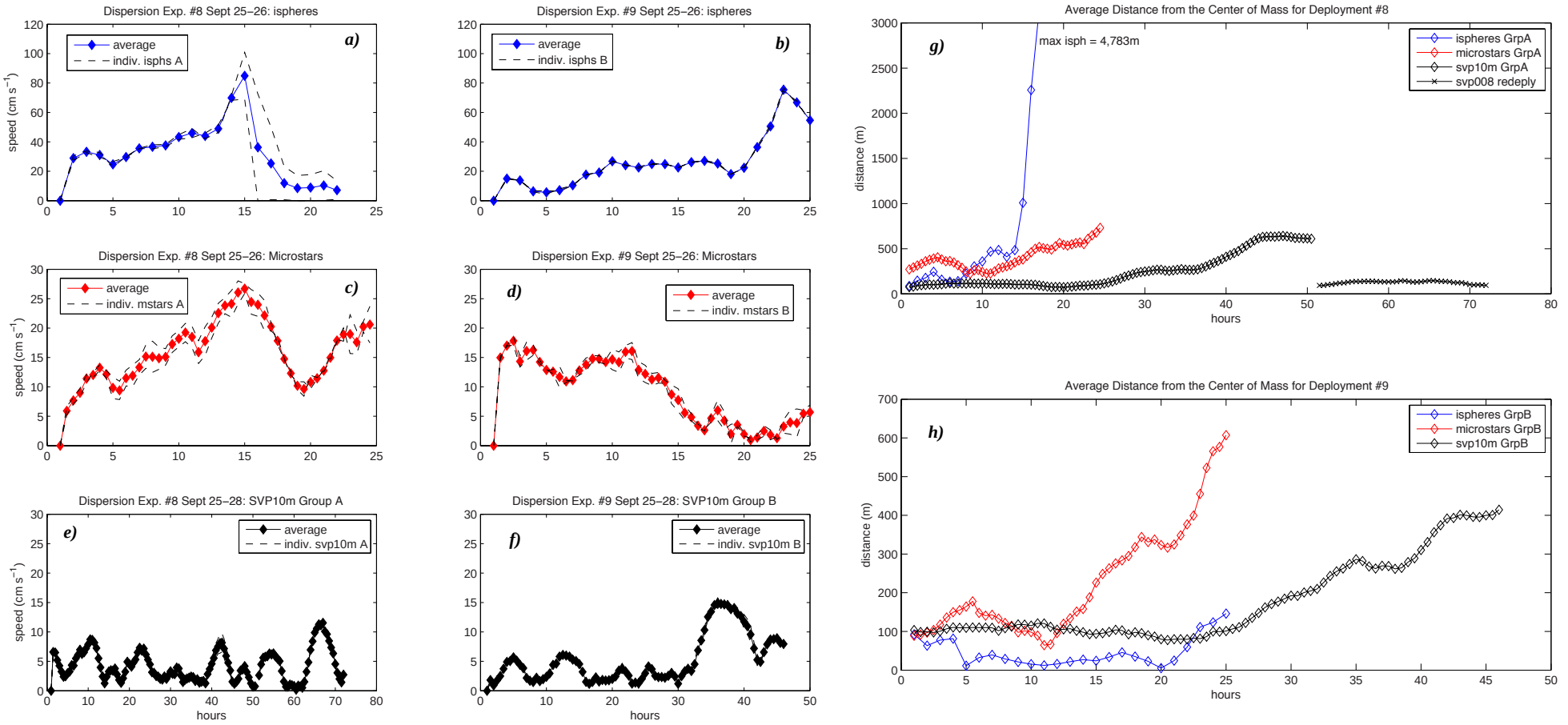

Fig. 45. Drifter speeds and dispersion during the fifth to seventh dispersion experiments conducted from Sept. 23 to 25, 2016: average speeds and ranges of individual drifters for a) microstars group A released on the 23rd; b) microstars group B and C released on the 24th; c,d) SVP 10m group B and C released on the 24th; and e,f) ispheres group B and C released on the 24th; and average distance from the center of mass for g) groups A ispheres, microstars and svp10m drifters; and h) group B ispheres, microstars and svp10m drifters.

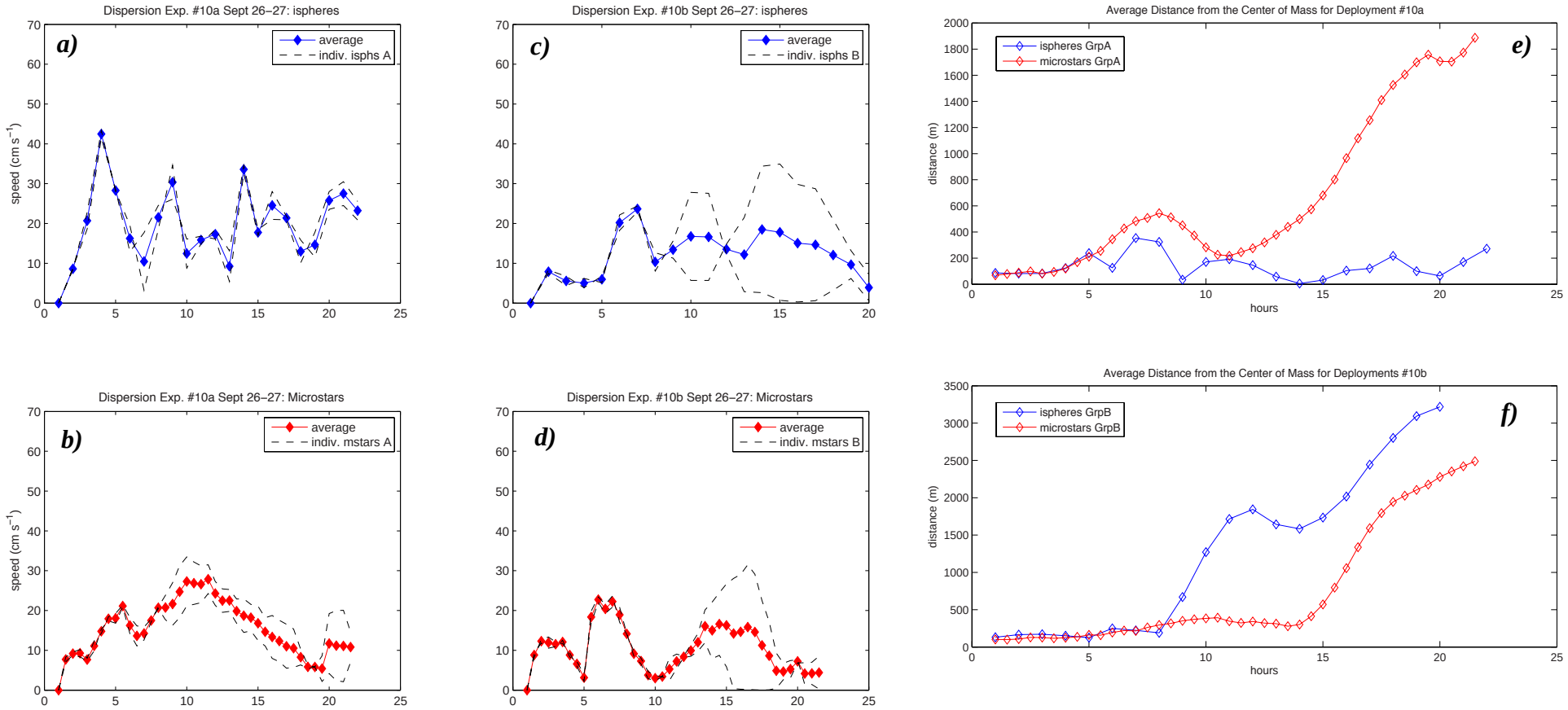

Fig. 46. Drifter speeds and dispersion over time during experiment #10 conducted from September 26 to 27, 2016, showing averages and ranges for individual drifters: a) ispheres group B; b) microstars group A; c) microstars group B; and d) average distances from the center of mass.

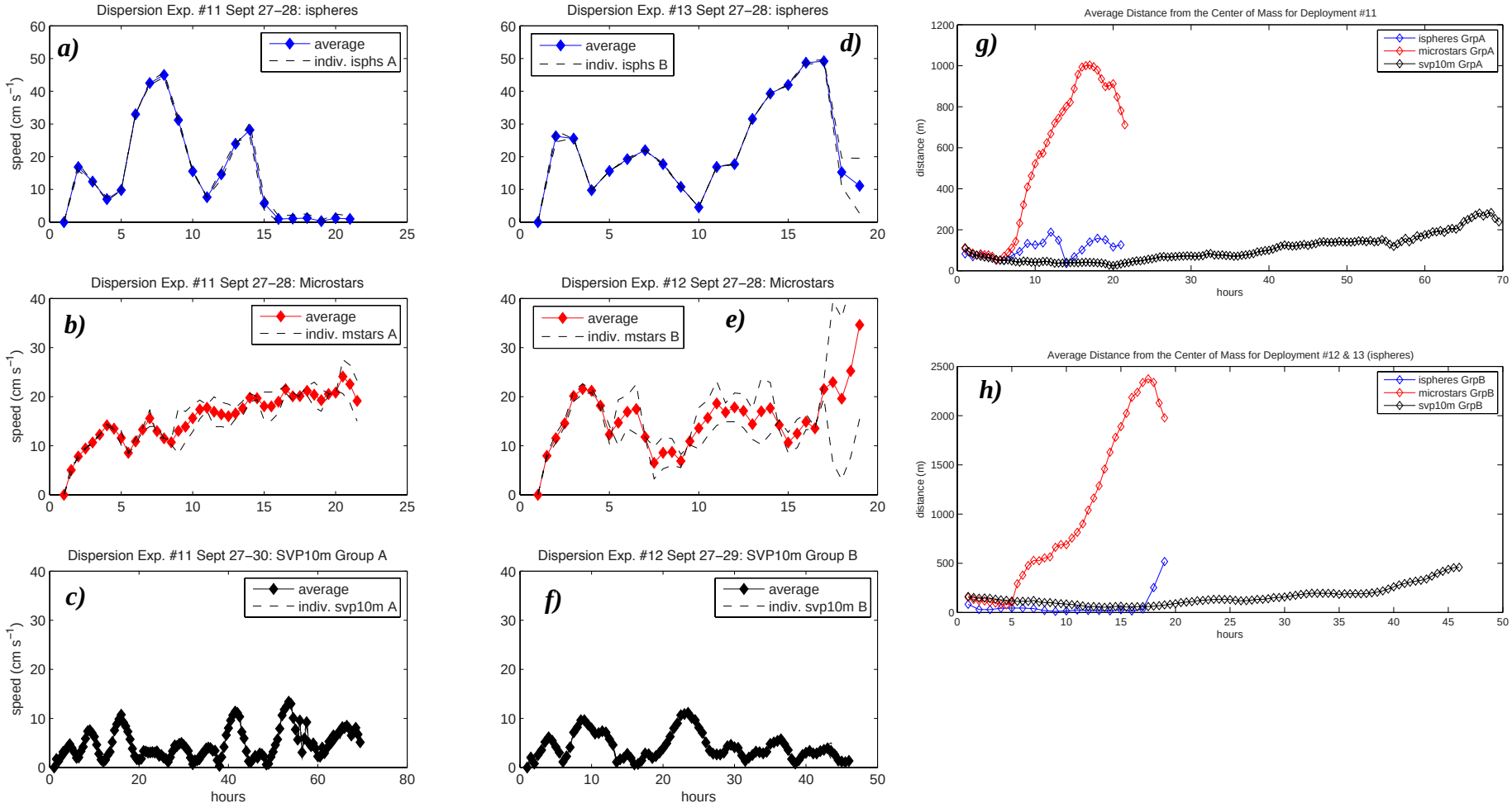

Fig. 47. Drifter speeds and dispersion over time during experiments #11 to #13 conducted from September 27 to 29, 2016, showing averages and ranges for individual drifters: a-c) ispheres, microstars and svp10m drifters for group A; d-f) ispheres, microstars and svp10m drifters for group B; and g,h) average distances from the center of mass for group A and B respectively.

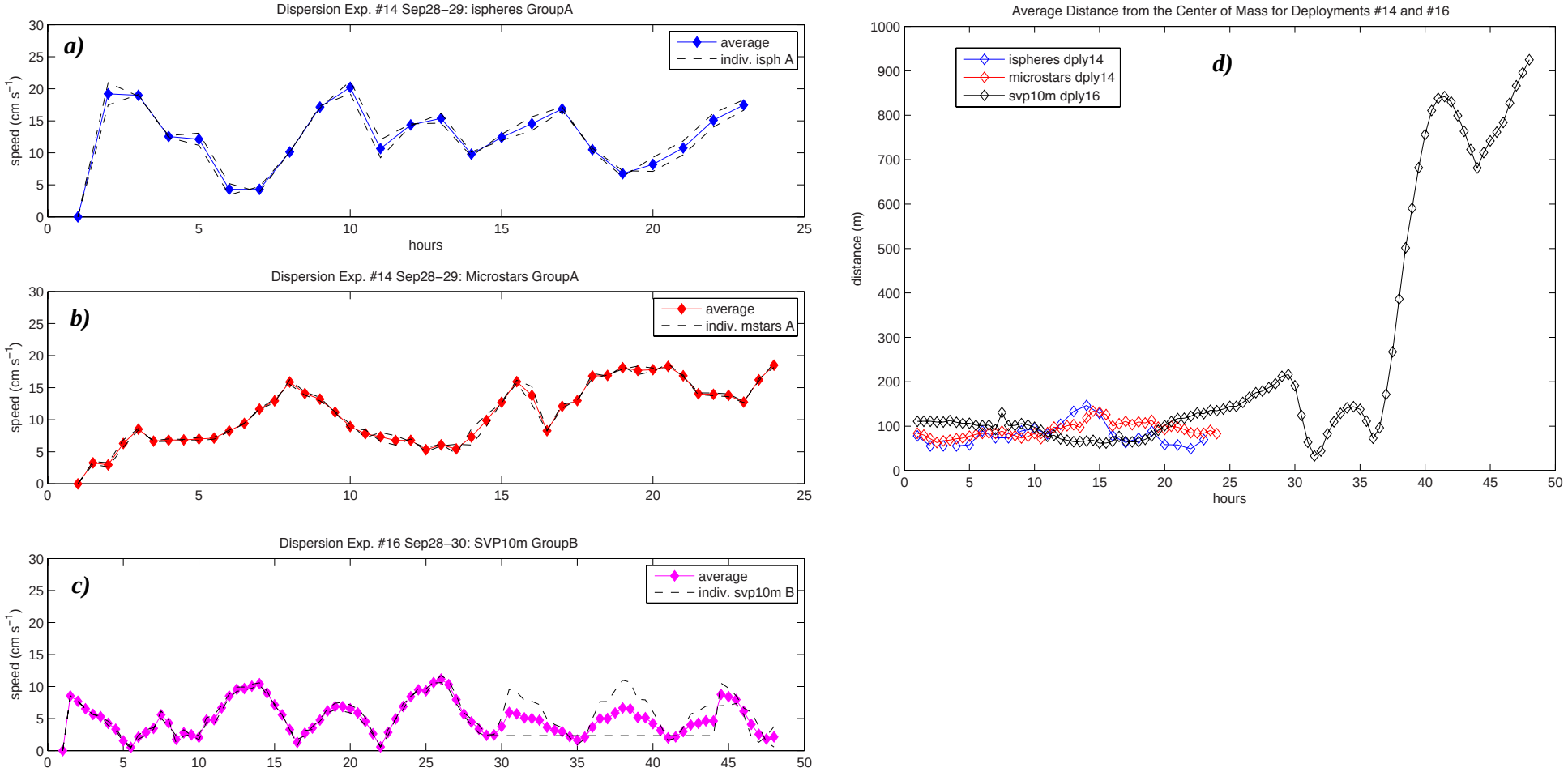

Fig. 48. Drifter speeds and dispersion over time during experiments #14 and #16 conducted from September 27 to 29, 2016, showing averages and ranges for individual drifters: a,b) ispheres and microstars for group A; c) svp10m drifters group B; and d) average distances from the center of mass for groups A and B.

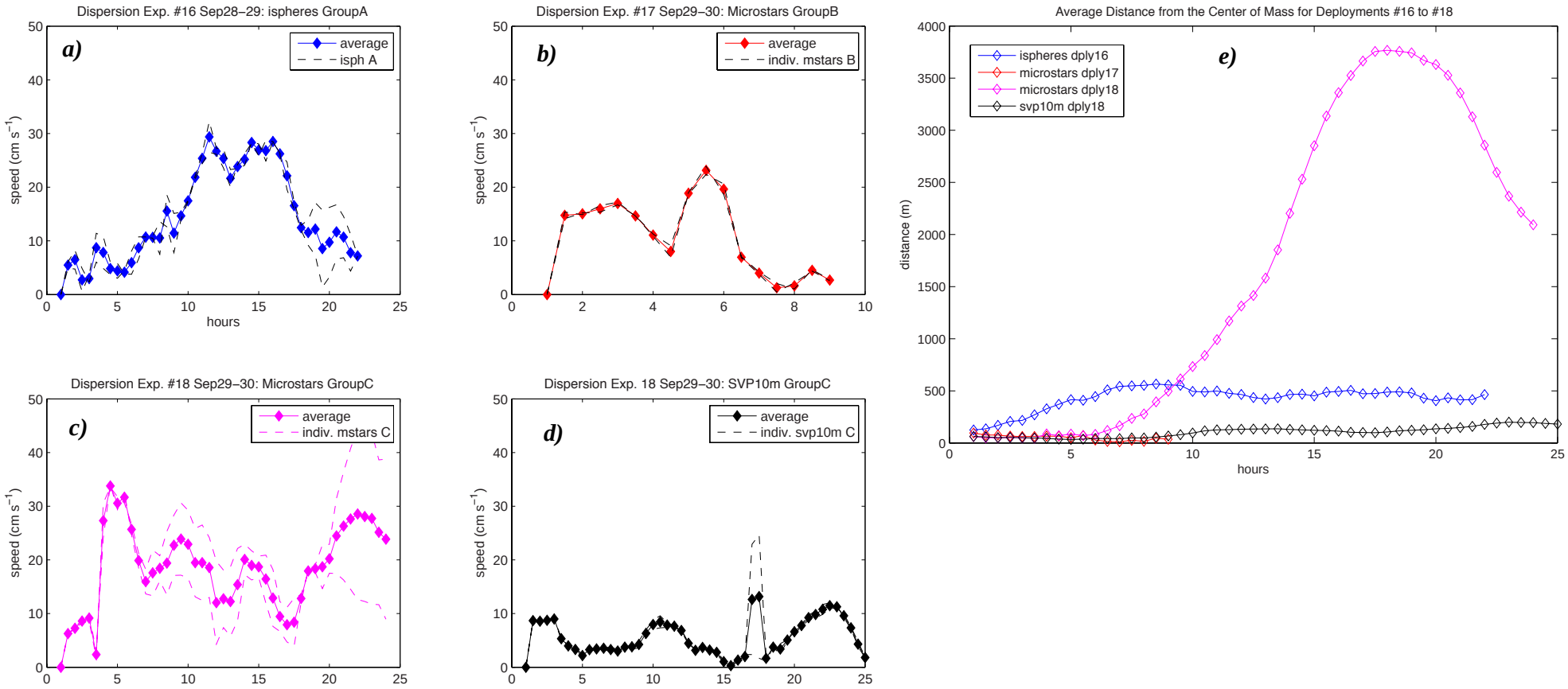

Fig. 49. Drifter speeds and dispersion over time during experiments #16 to #18 conducted from September 28 to 30, 2016, showing averages and ranges for individual drifters: a,b) ispheres group A and microstars group B; c,d) microstars and svp10m drifters group C; and d) average distances from the center of mass for groups A, B and C (deployments #16, 17 and 18 respectively).

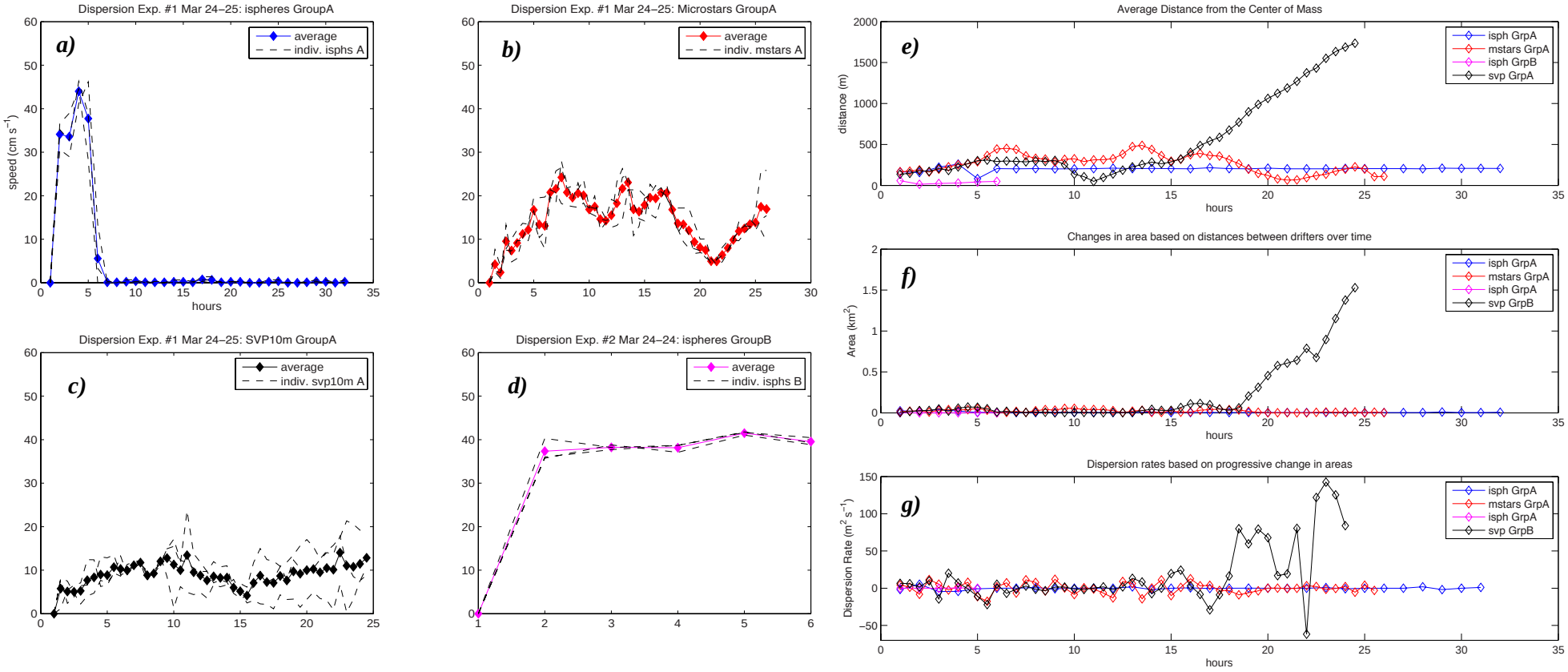

Fig. 50. Drifter speeds and dispersion over time during experiments #1 and #2, conducted from March 24 to 25, 2017, showing averages and ranges for individual drifters: a-c) ispheres, microstars and svp10m drifteers for group A; d) ispheres group B; and e-g) average distances from the center of mass, changes in area and dispersion rates (m s^{-1}) for groups A and B (deployments #1 and #2 respectively). Note that after about 7 hrs, all ispheres of group A were grounded and hence the dispersion is a flat line.

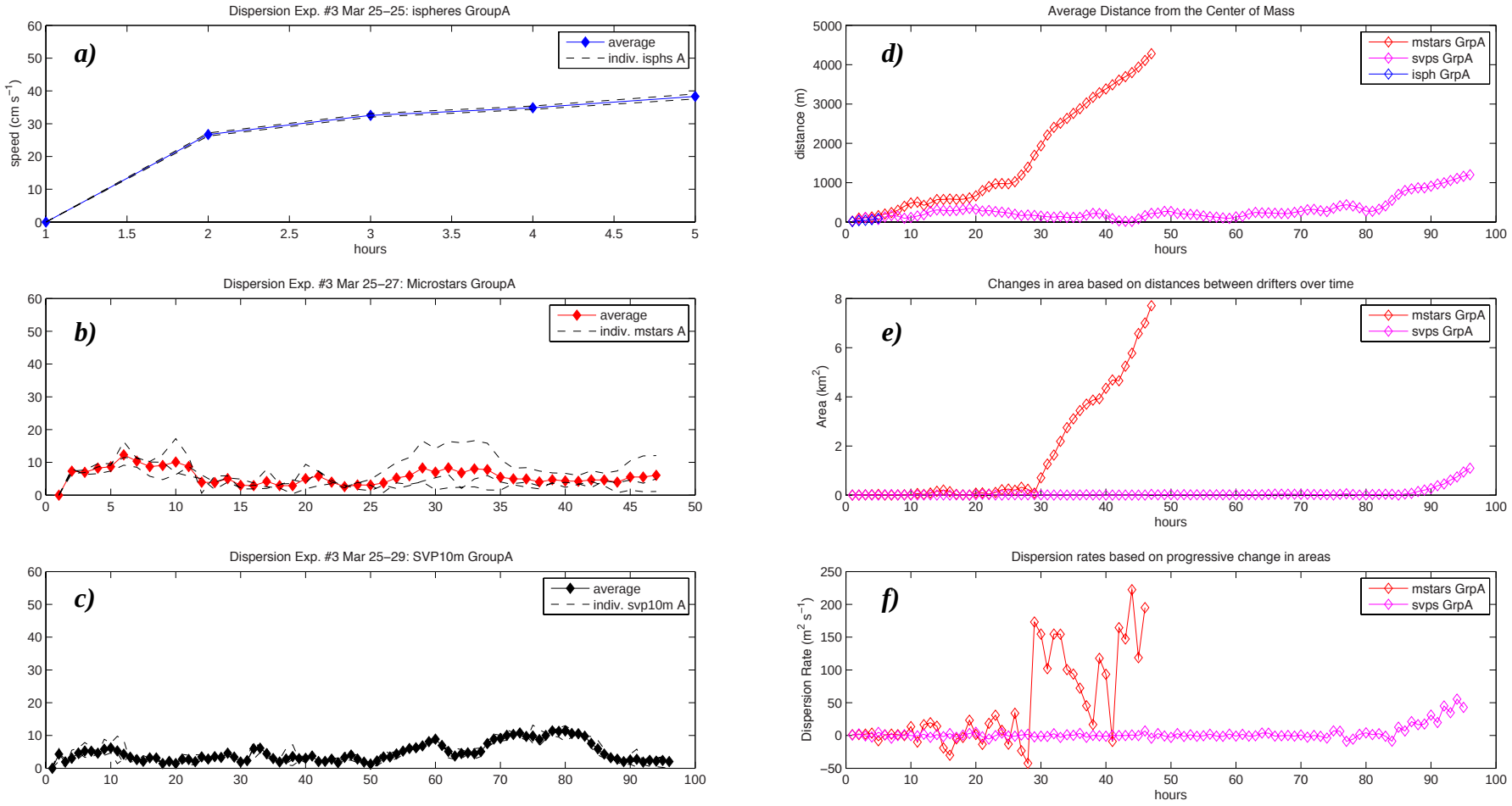

Fig. 51. Drifter speeds and dispersion over time during experiment #3, conducted from March 25 to 29, 2017, showing averages and ranges for individual drifters: a-c) ispheres, microstars and svp10m drifters; d-f) average distances from the center of mass, changes in area (km^2), and dispersion rates ($m^2\ s^{-1}$).

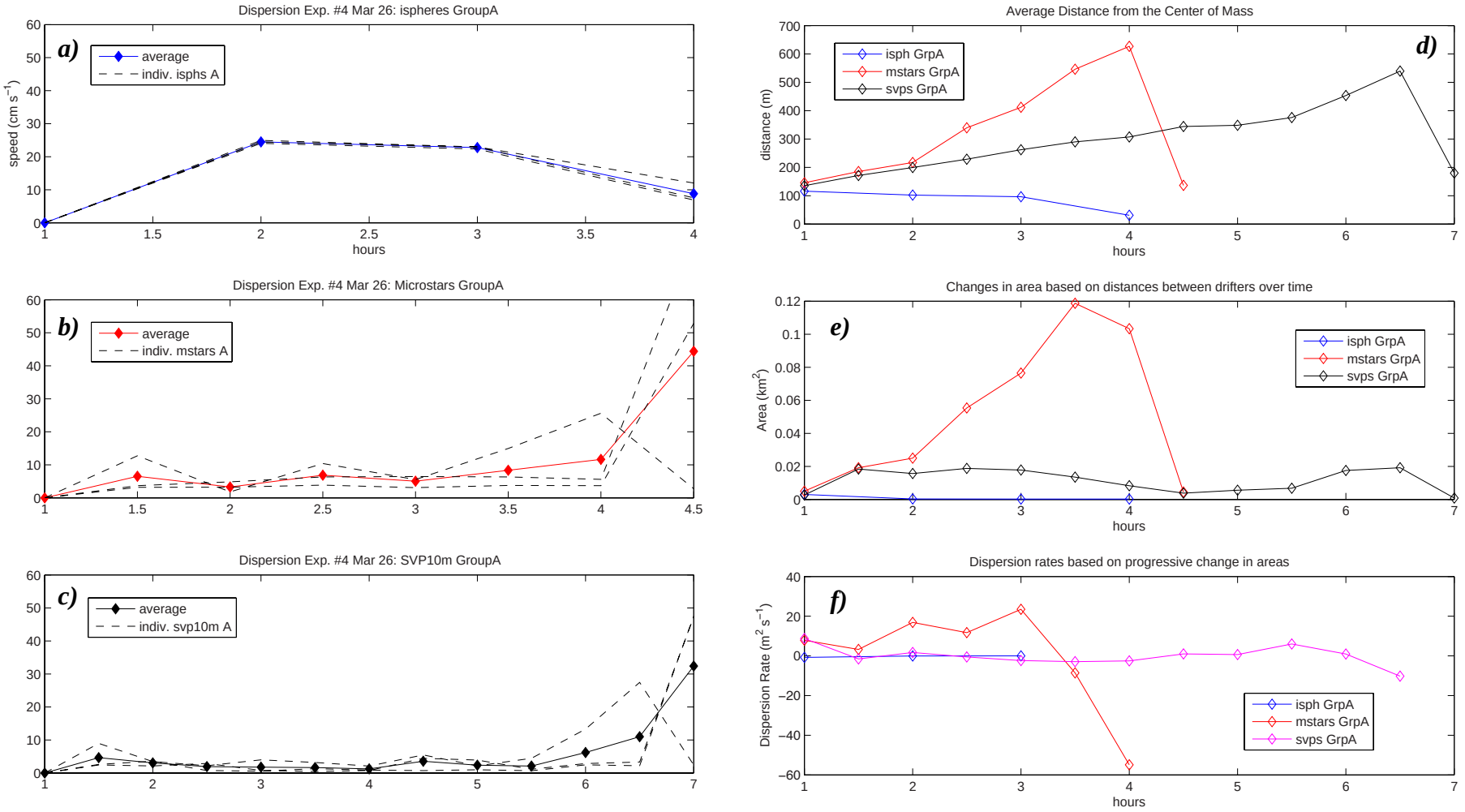

Fig. 52. Drifter speeds and dispersion over time during experiment #4, conducted on March 26, 2017, showing averages and ranges for individual drifters: a-c) ispheres, microstars and svp10m drifters; d-f) average distances from the center of mass, changes in area (km^2), and dispersion rates (m^2 s^{-1}).

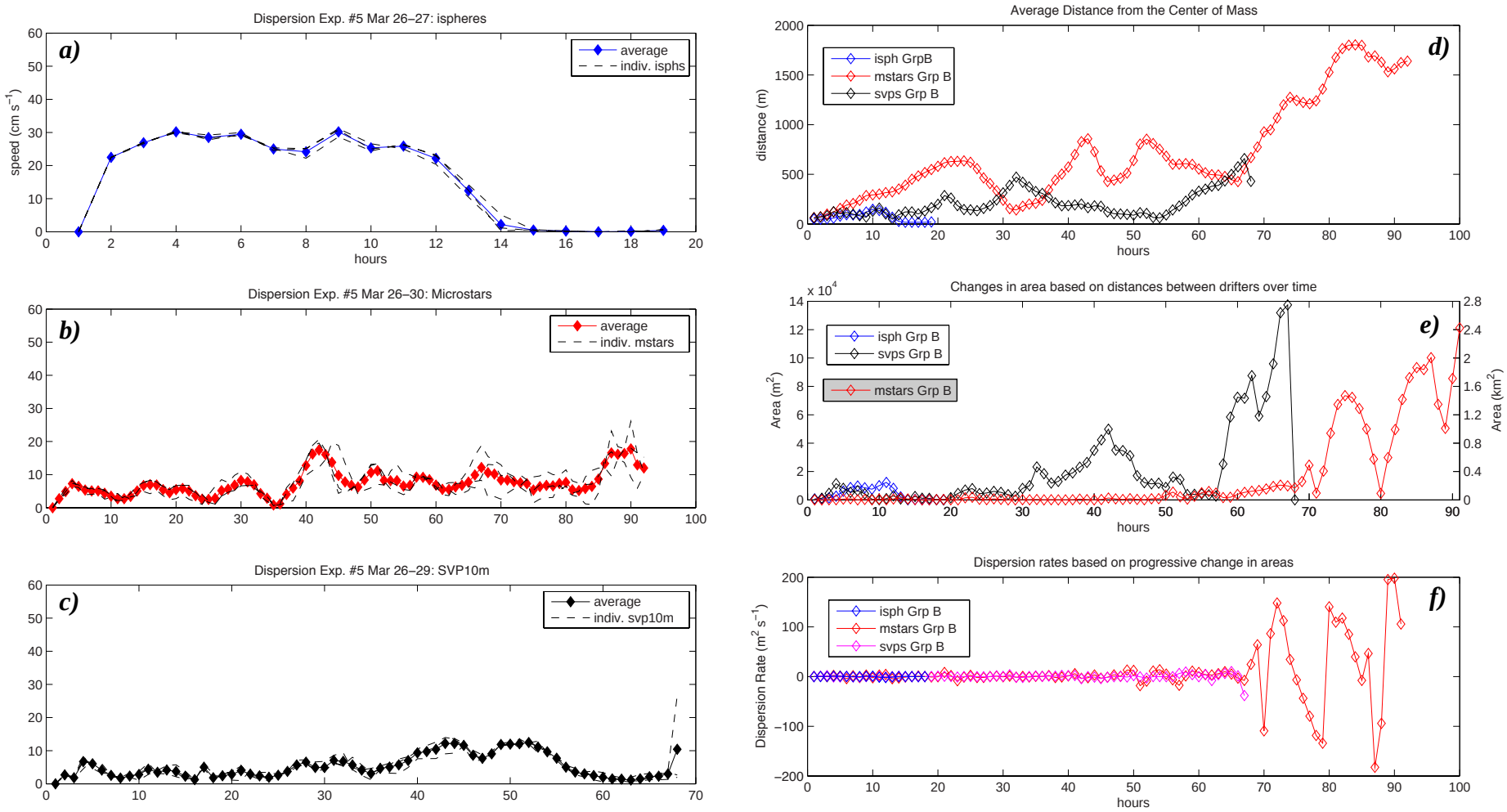

Fig. 53. Drifter speeds and dispersion over time during experiment #5, conducted on March 26 to 29, 2017, showing averages and ranges for individual drifters: a-c) ispheres, microstars and svp10m drifters; d-f) average distances from the center of mass, changes in area (km^2), and dispersion rates (m^2 s^{-1}).

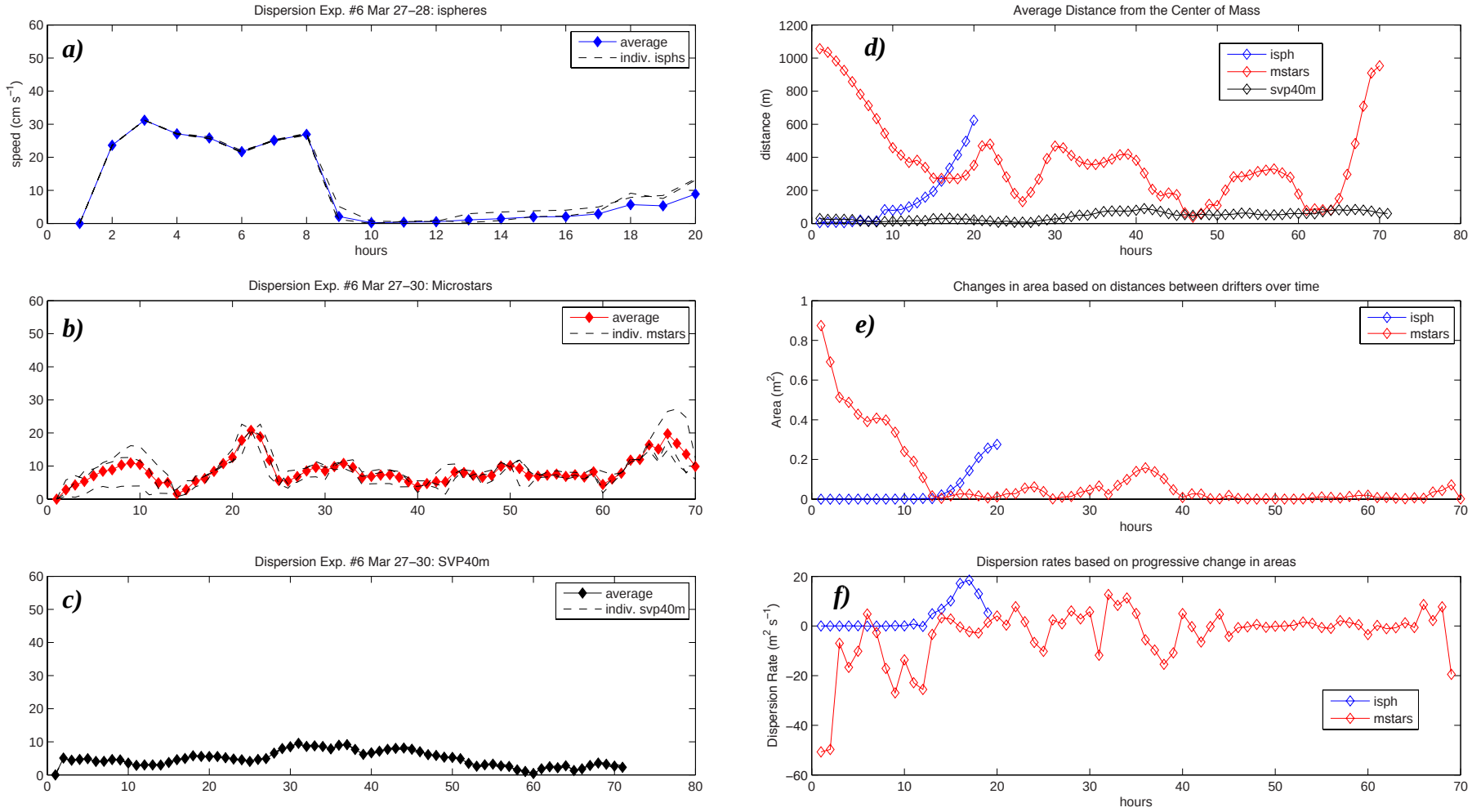

Fig. 54. Drifter speeds and dispersion over time during experiment #6, conducted on March 27 to 30, 2017, showing averages and ranges for individual drifters: a-c) ispheres, microstars and svp10m drifters; d-f) average distances from the center of mass, changes in area (km^2), and dispersion rates (m^2 s^{-1}).

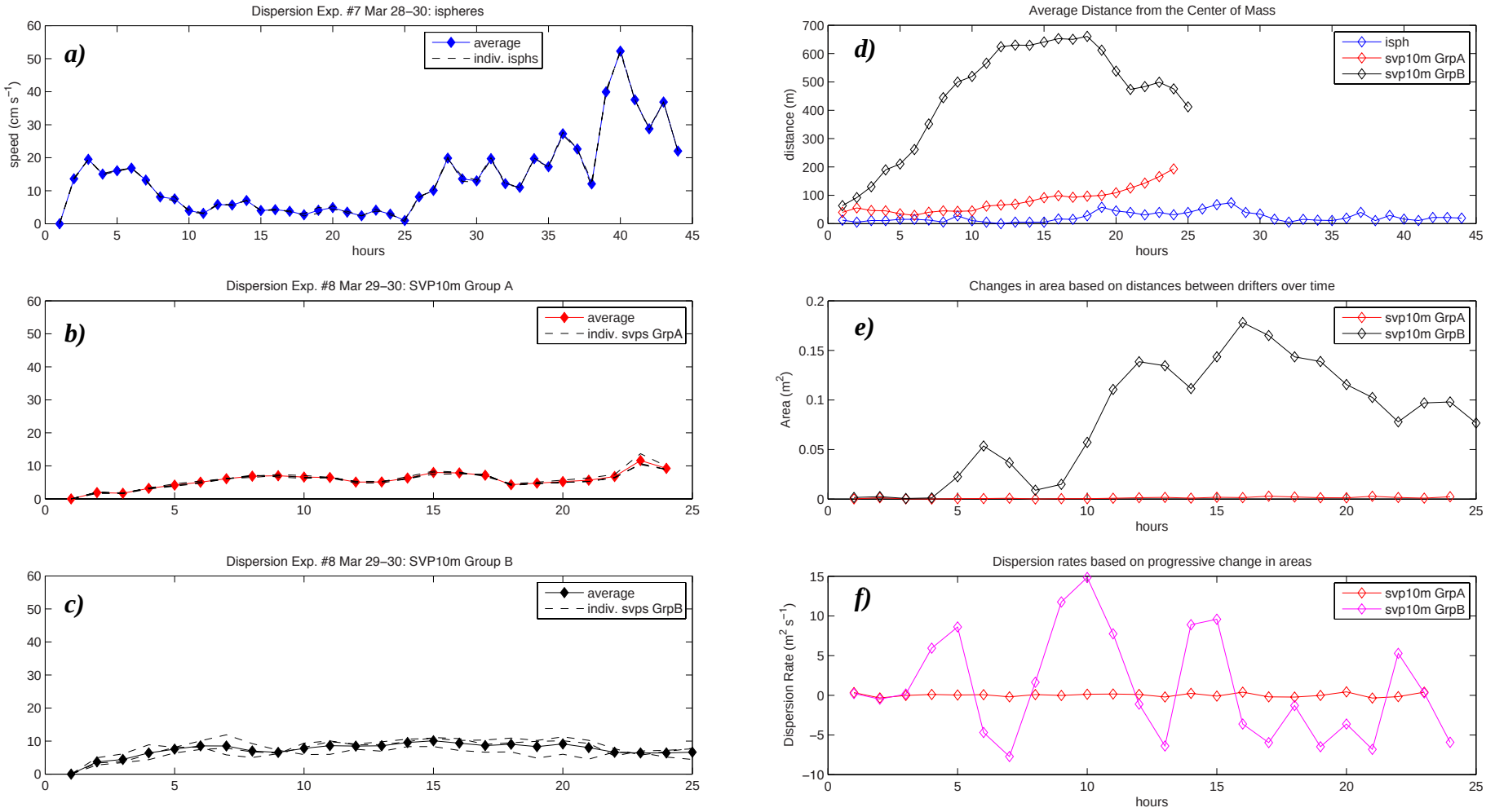

Fig. 55. Drifter speeds and dispersion over time during experiments #7 and #8, conducted on March 28 to 30, 2017, showing averages and ranges for individual drifters: a-c) ispheres, microstars and svp10m drifters; d-f) average distances from the center of mass, changes in area (km^2), and dispersion rates (m^2 s^{-1}).

Scatter plots of *U'* vrs. *V'* and principal axes of variation for ispheres, deployments 1 to 5 on June 22–27, 2016

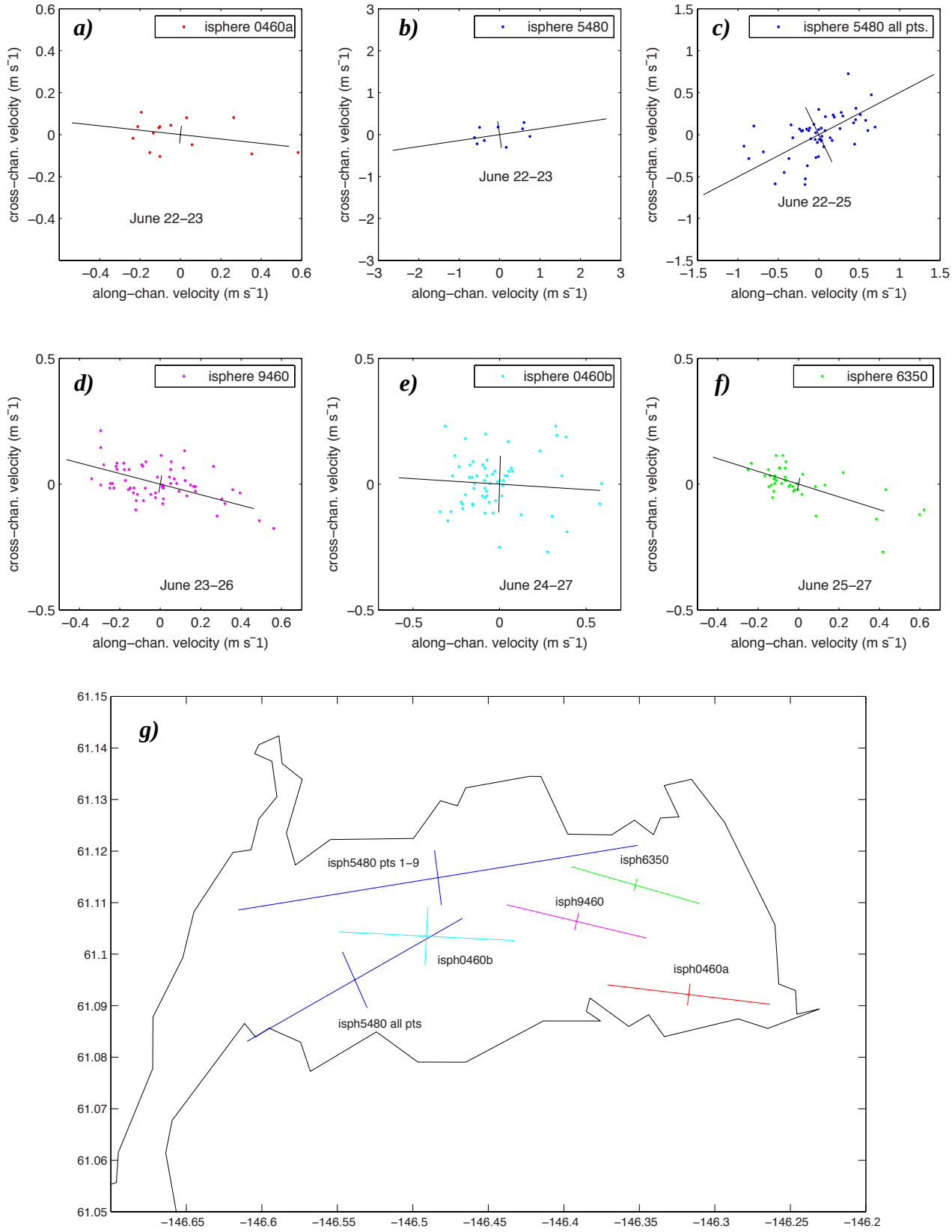

Fig. 56A. Scatter plots of *U'* and *V'* and principal axes of variation for ispheres on June 22 to 27, 2016. Plots of the major and minor principal axes are also shown within Port Valdez. Unless stated otherwise, the scales of the variance are shown at 10 times the actual values given in Table 2.

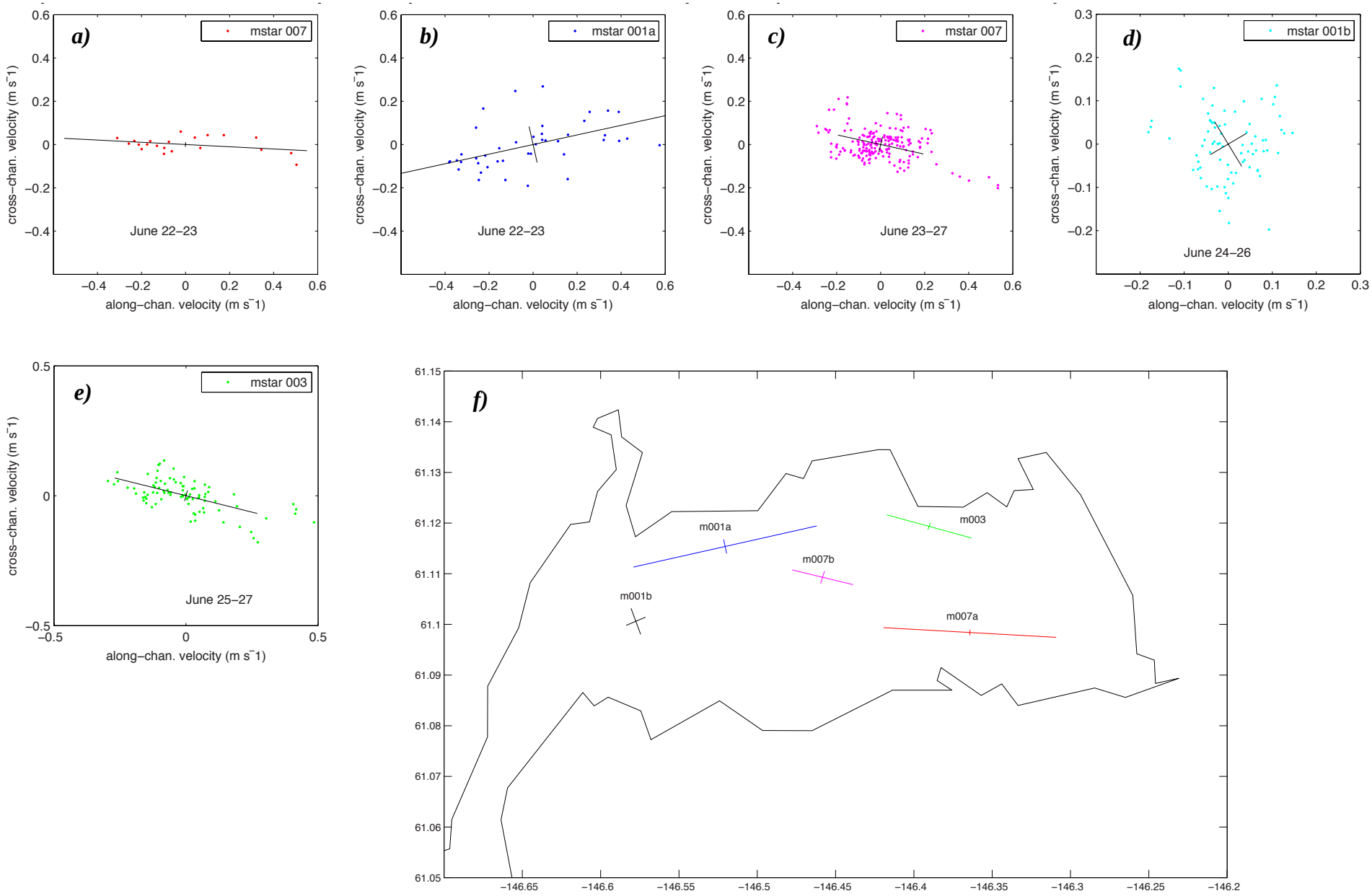

Fig. 56B. Scatter plots of *U'* and *V'* and principal axes of variation for microstars on June 22 to 27, 2016. Plots of the major and minor principal axes are also shown within Port Valdez. Unless stated otherwise, the scales of the variance are shown at 10 times the actual values given in Table 2.

Scatter plots of *U'* vrs. *V'* and principal axes of variation for 10m SVPs, deployments 2 to 5 on June 22– July 1, 2016

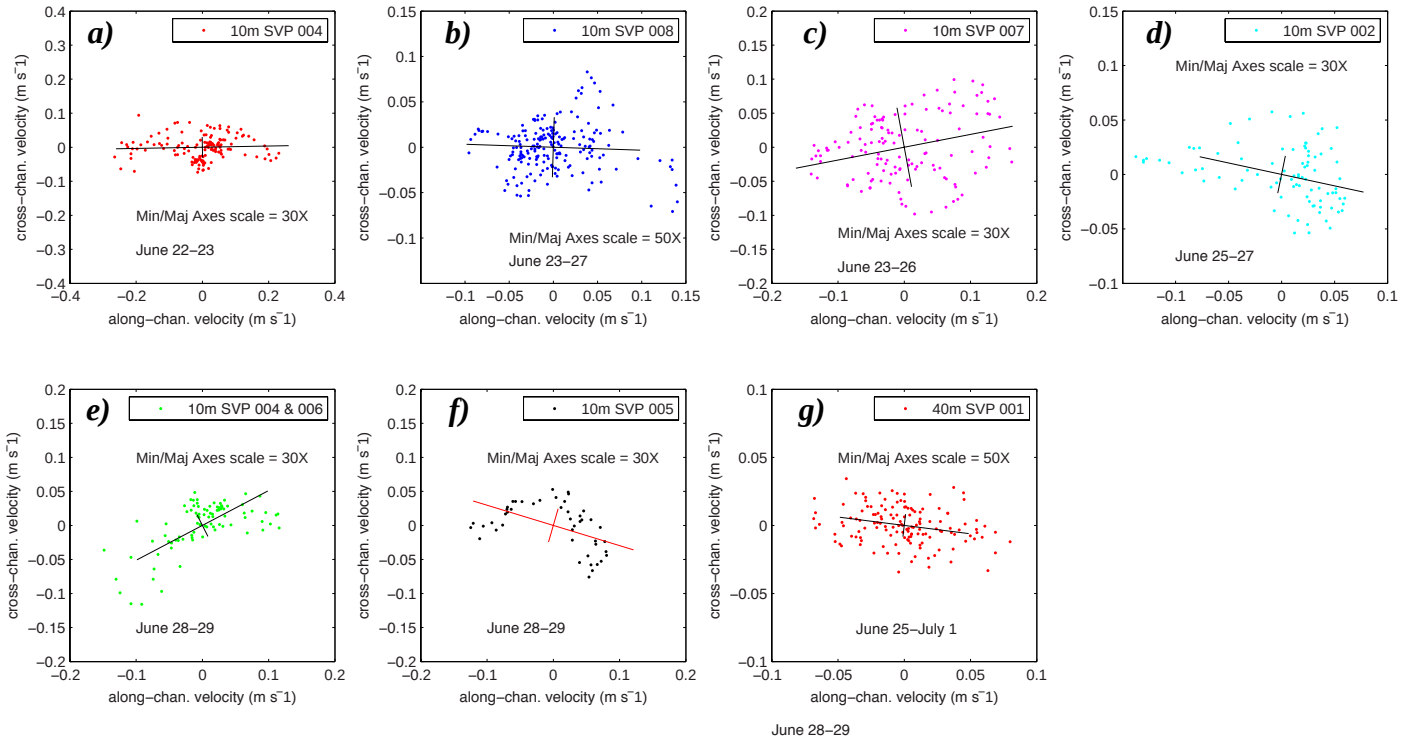

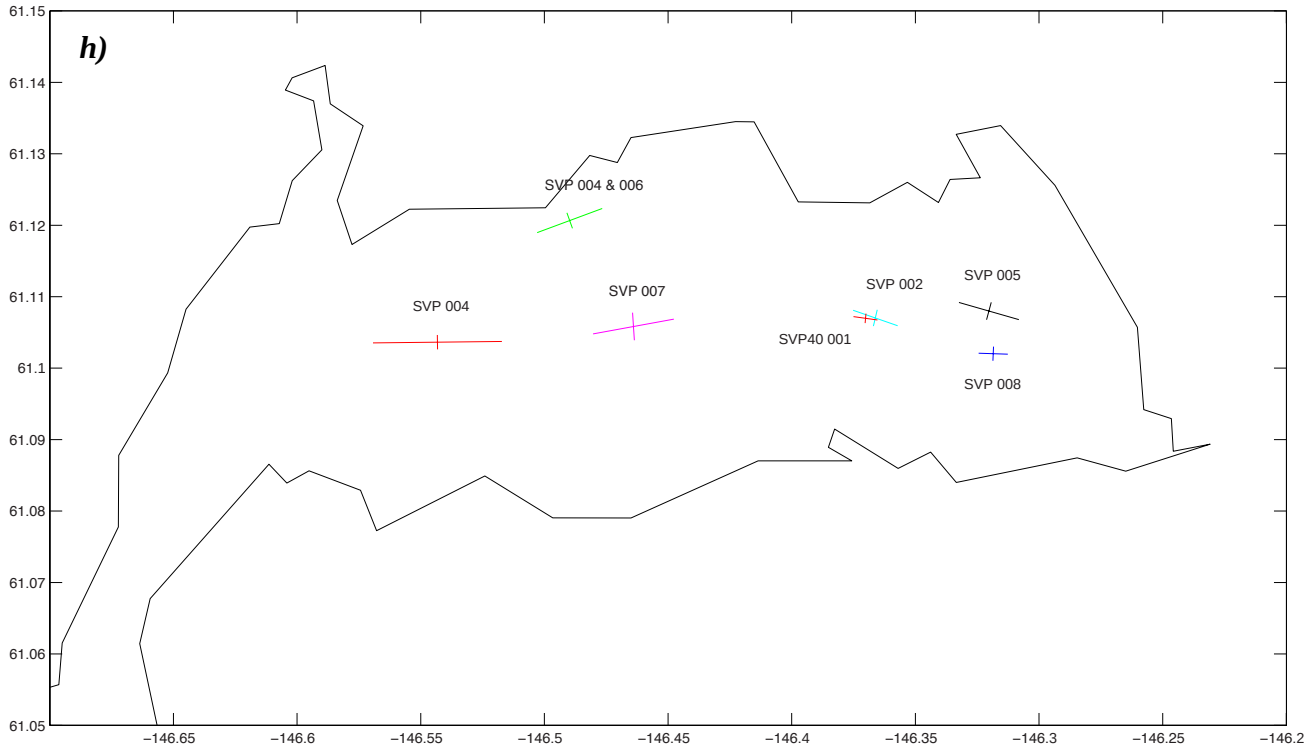

Fig. 56C. Scatter plots of *U'* and *V'* and principal axes of variation for 10m SVPs (a-f) on June 22 to 29 and the 40m SVP (g) on June 25 to July 1, 2016. Plots of the major and minor principal axes are also shown within Port Valdez (h). For purposes of comparison the scales of the variance are shown at 30 to 50 times the actual values given in Table 2.

Scatter plots of *U'* vrs. *V'* and principal axes of variation of velocites for dispersion exp. #1 on June 27, 2016

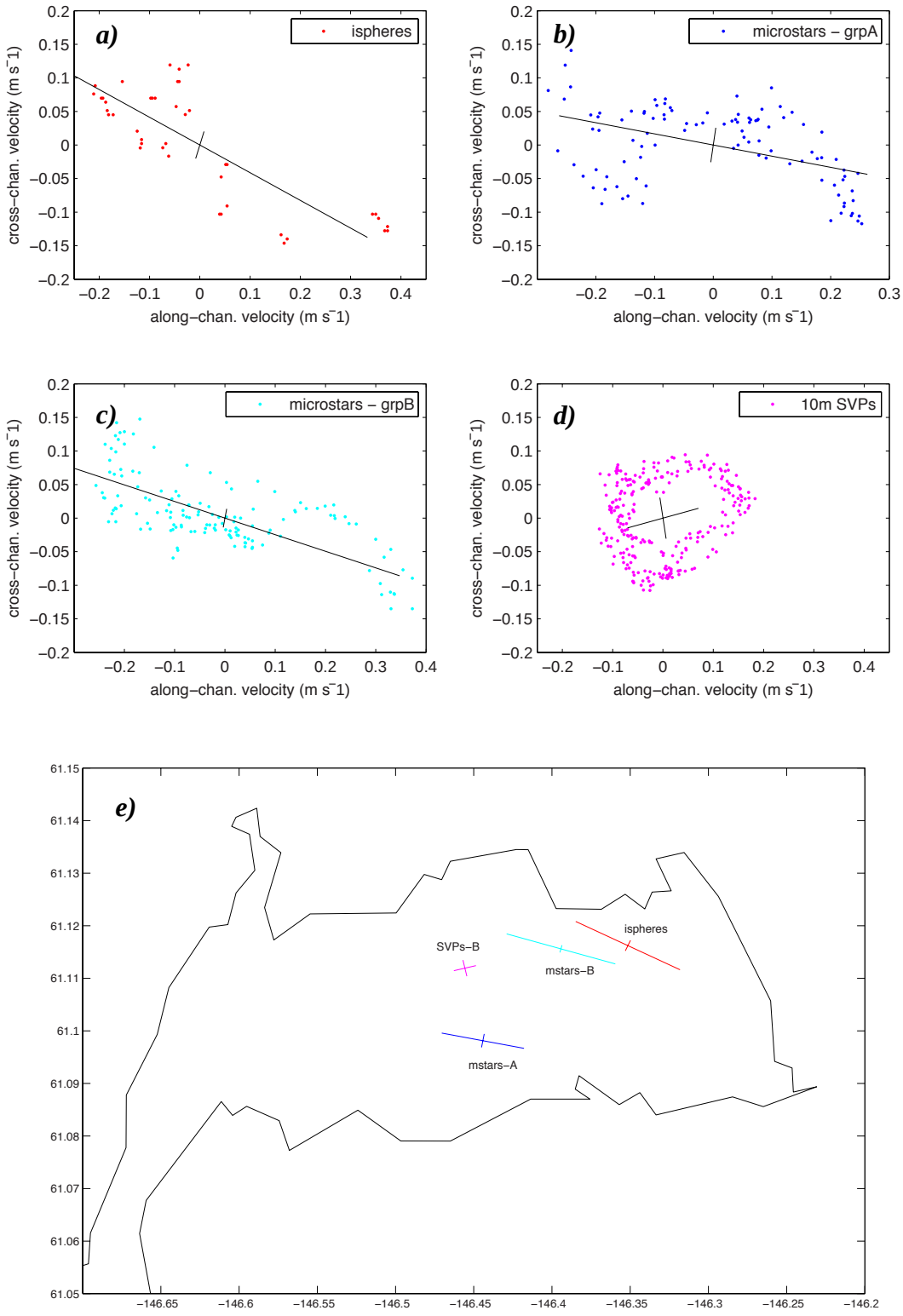

Fig. 57A. Scatter plots of *U'* and *V'* and principal axes of variation for ispheres (a), microstars (b,c) and 10m SVPs (d) for the first dispersion experiment on June 27th, 2016. Plots of the major and minor principal axes are also shown within Port Valdez (e). For purpose of comparison, the scales of the variance are shown at 10 times the actual values given in Table 2.

Scatter plot and principal axes of variation for ispheres, microstars and 10m SVPs for dispersion exp. #2 on June 29, 2016

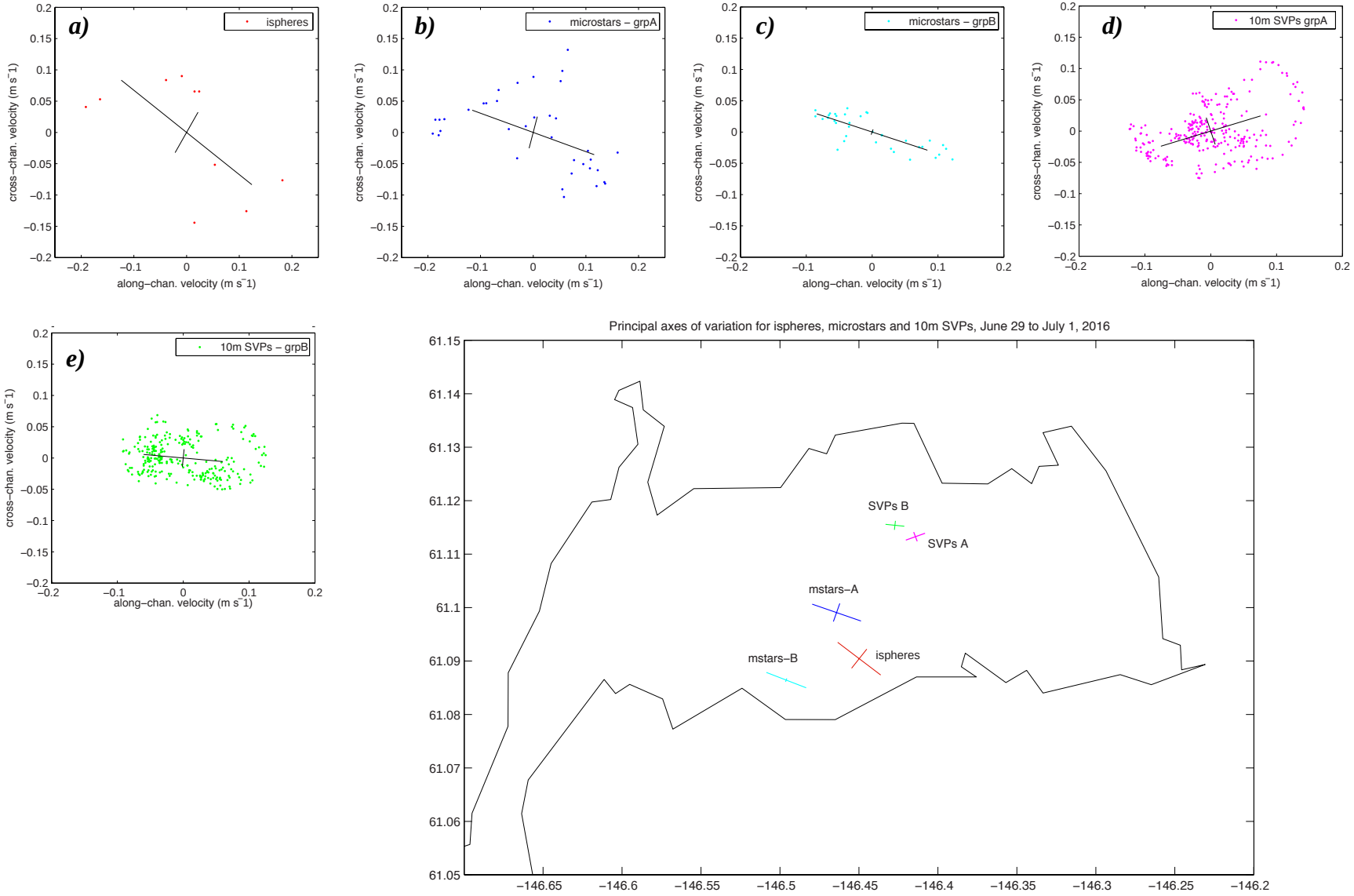

Fig. 57B. Scatter plots of *U'* and *V'* and principal axes of variation for ispheres (a), microstars (b,c) and 10m SVPs (d,e) for the second dispersion experiment on June 29th, 2016. Plots of the major and minor principal axes are also shown within Port Valdez (f). For purpose of comparison, the scales of the variance are shown at 10 times the actual values given in Table 2.

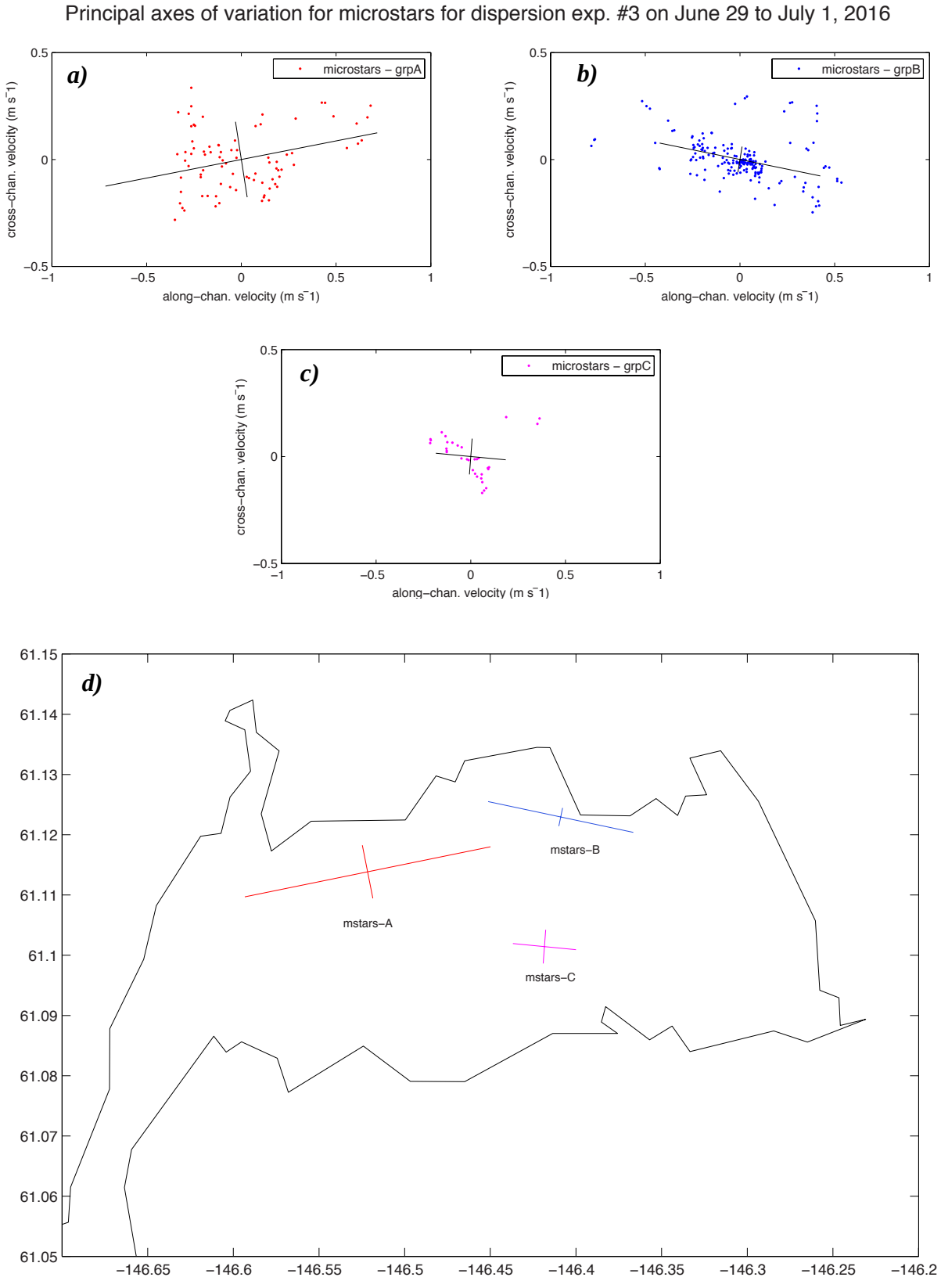

Fig. 57C. Scatter plots of *U'* and *V'* and principal axes of variation for microstars (a-c) during the third dispersion experiment on June 29th, 2016. Plots of the major and minor principal axes are also shown within Port Valdez (d). For purpose of comparison, the scales of the variance are shown at 10 times the actual values given in Table 2.

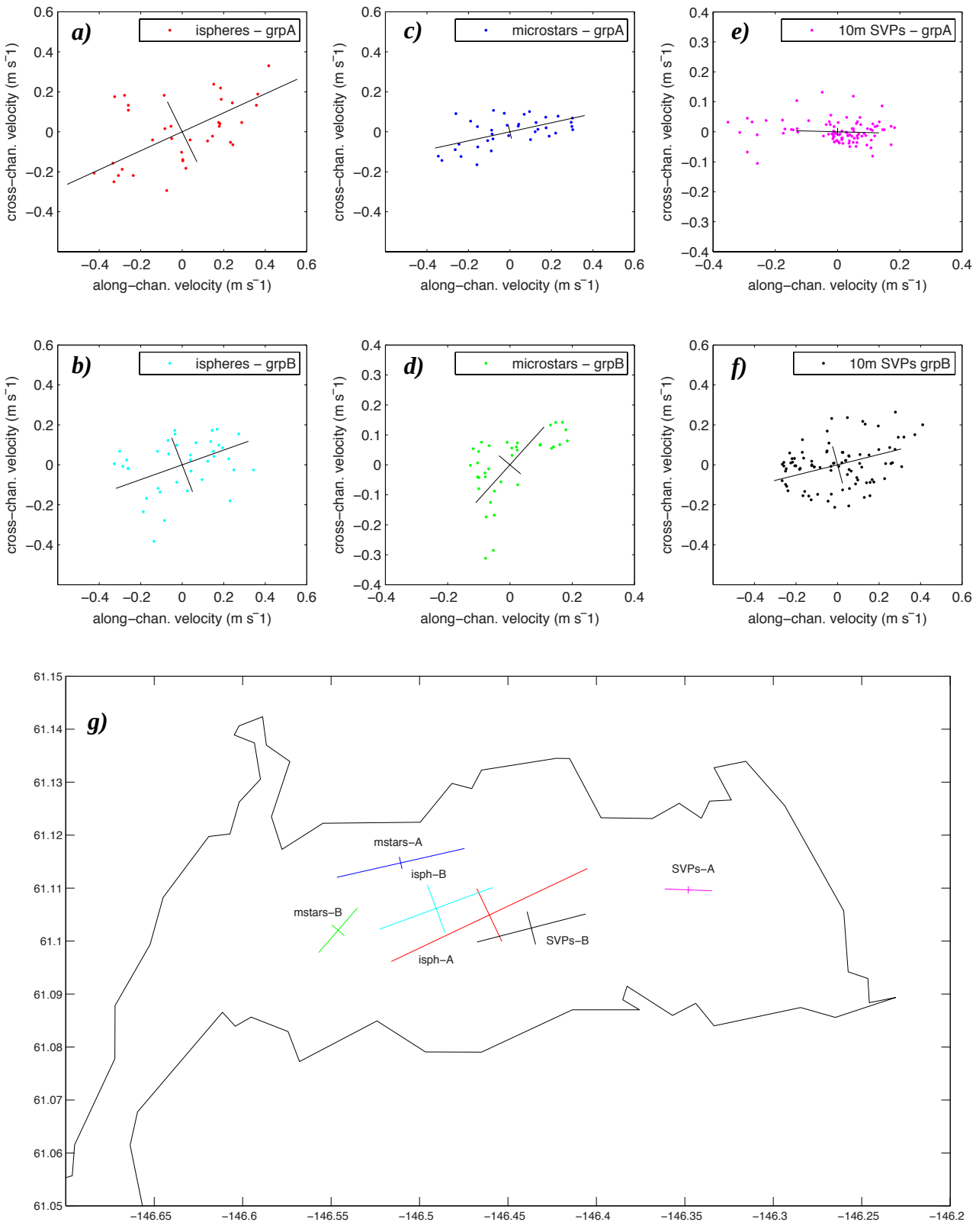

Fig. 58A. Scatter plots of *U'* and *V'* and principal axes of variation for ispheres (a,b), microstars (c,d) and 10m SVPs (e,f) for drifters deployed on September 21, 2016. Plots of the major and minor principal axes are also shown within Port Valdez (g). For purpose of comparison, the scales of the variance are shown at 10 times the actual values given in Table 2.

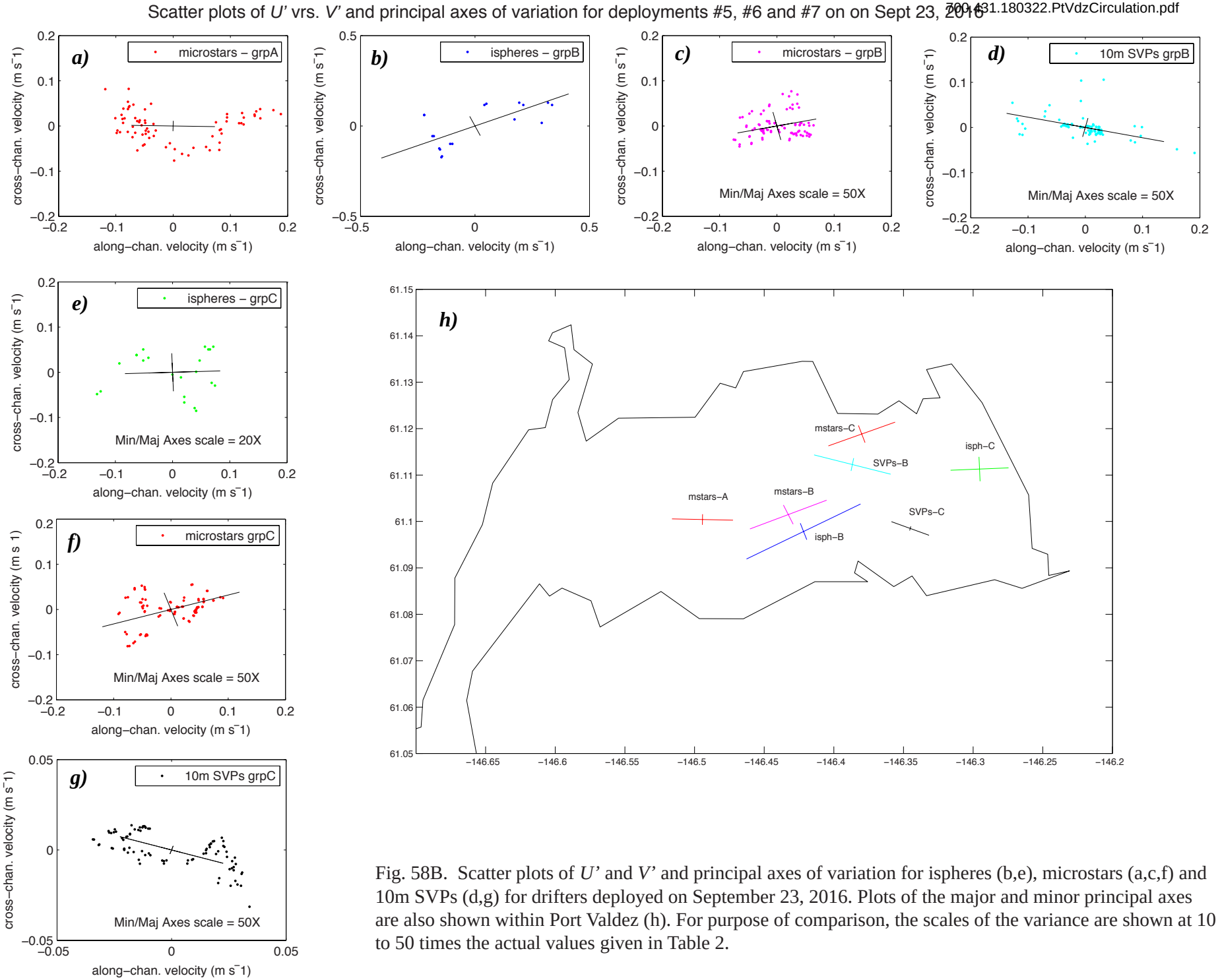

Fig. 58B. Scatter plots of *U'* and *V'* and principal axes of variation for ispheres (b,e), microstars (a,c,f) and 10m SVPs (d,g) for drifters deployed on September 23, 2016. Plots of the major and minor principal axes are also shown within Port Valdez (h). For purpose of comparison, the scales of the variance are shown at 10 to 50 times the actual values given in Table 2.

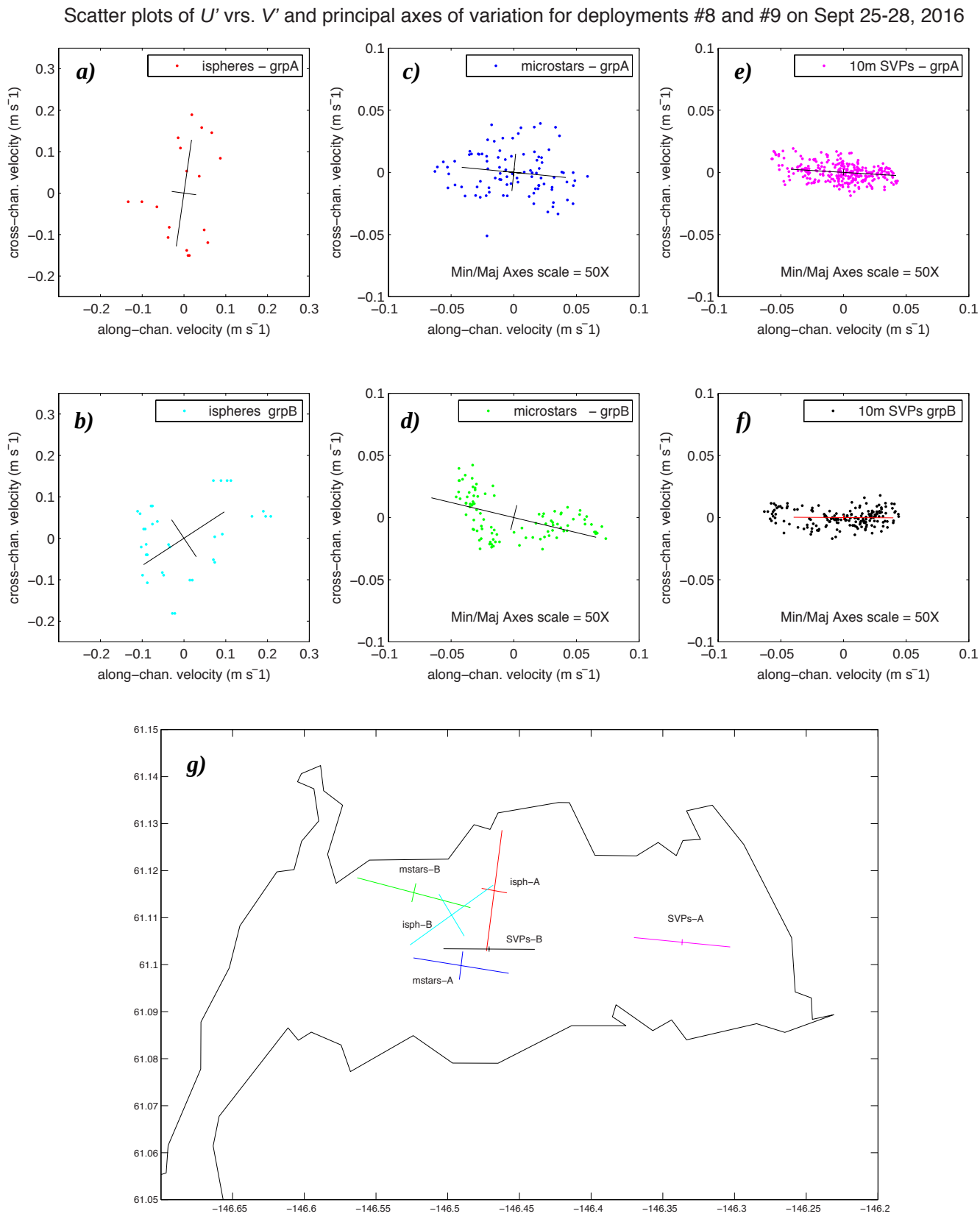

Fig. 58C. Scatter plots of *U'* and *V'* and principal axes of variation for ispheres (a,b), microstars (c,d) and 10m SVPs (e,f) for drifters deployed on September 25, 2016. Plots of the major and minor principal axes are also shown within Port Valdez (g). For purpose of comparison, the scales of the variance are shown at 10 to 50 times the actual values given in Table 2.

Scatter plots of *U'* vrs. *V'* and principal axes of variation for deployments #10a and #10b on Sept 26-27, 2016

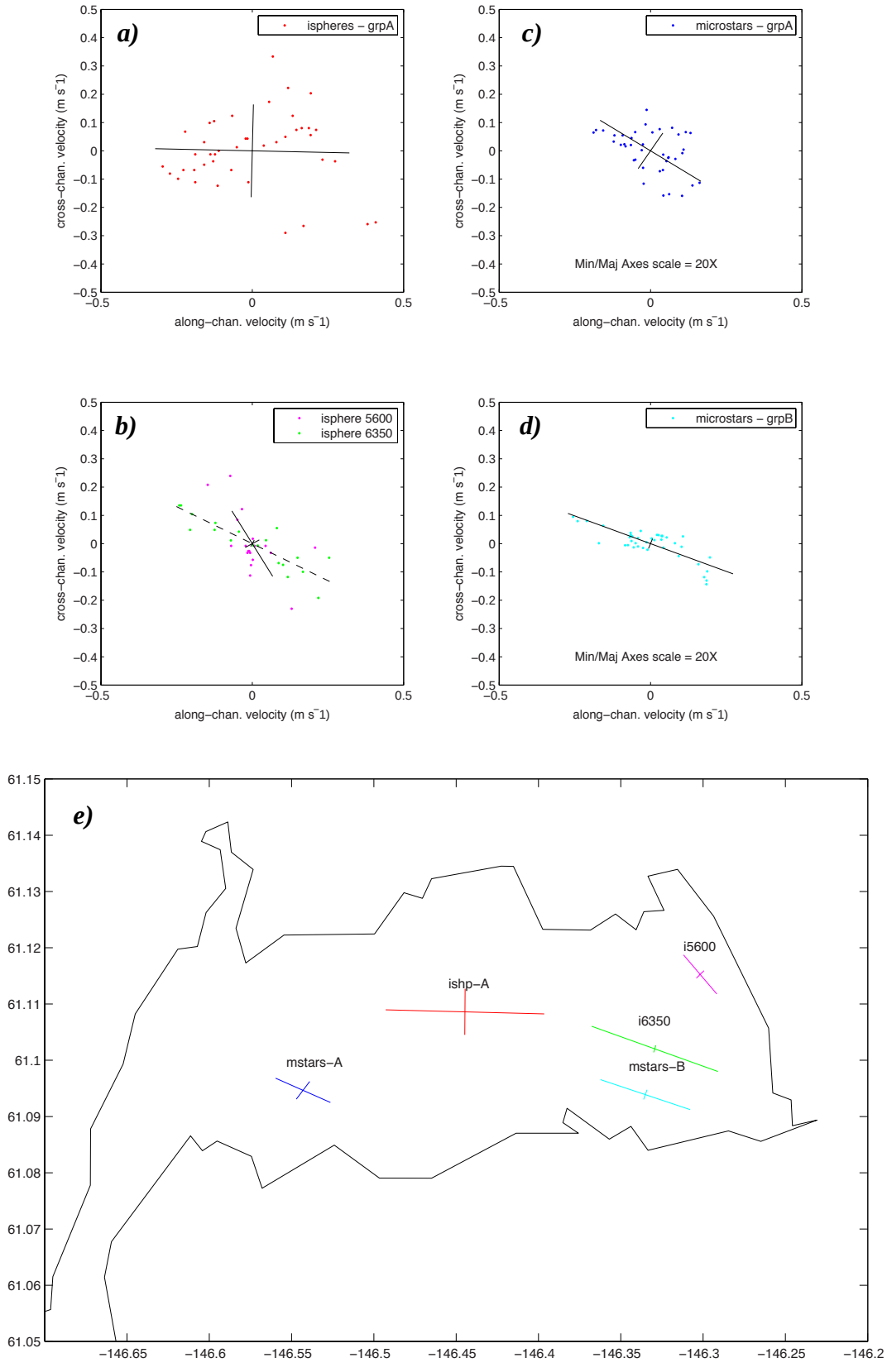

Fig. 58D. Scatter plots of *U'* and *V'* and principal axes of variation for ispheres (a,b) and microstars (c,d) deployed on September 26, 2016. Plots of the major and minor principal axes are also shown within Port Valdez (e). For purpose of comparison, the scales of the variance are shown at 10 to 20 times the actual values given in Table 2.

Scatter plots of *U'* vrs. *V'* and principal axes of variation for deployments #11, #12 and #13 on Sept 27-30, 2016

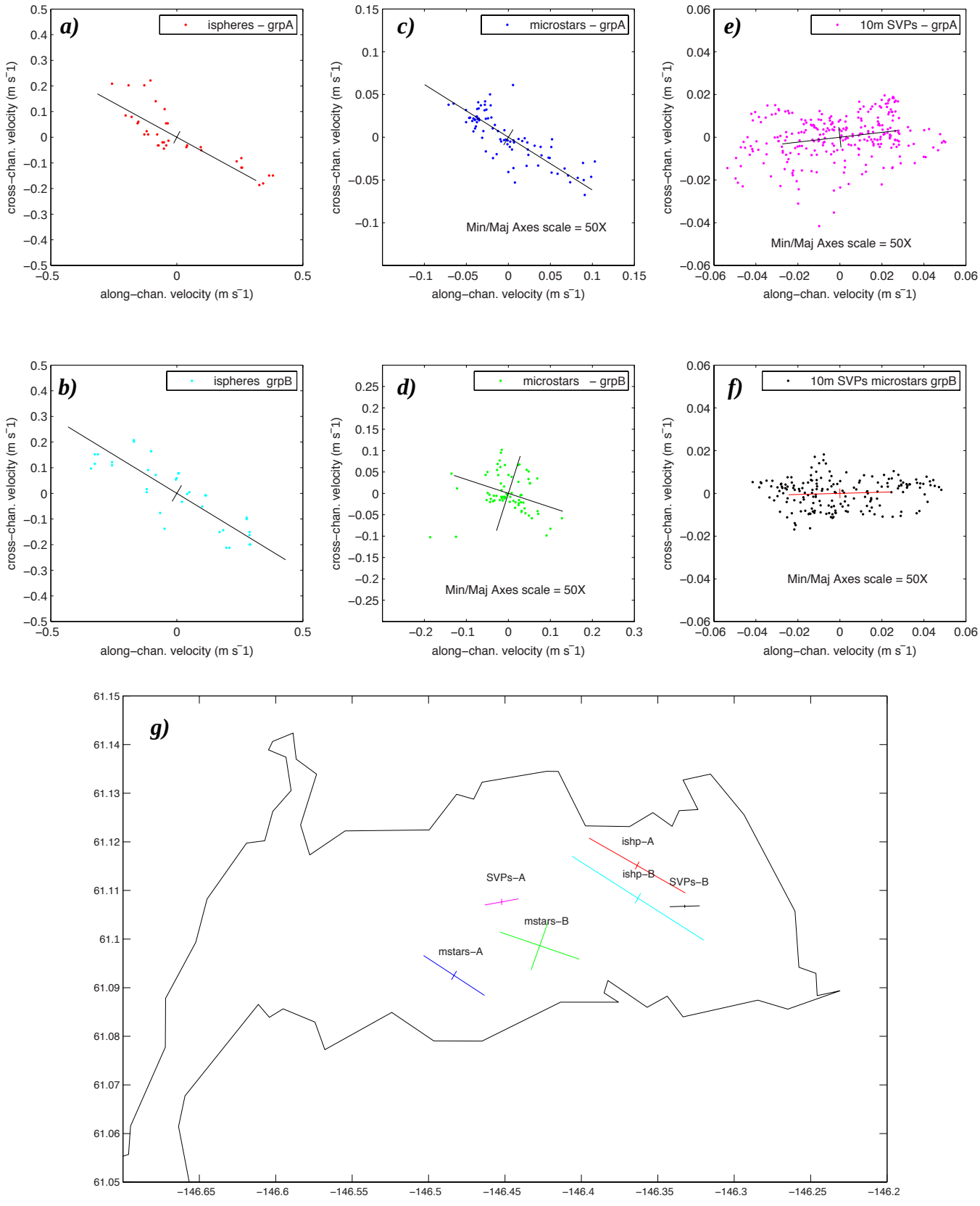

Fig. 58E. Scatter plots of *U'* and *V'* and principal axes of variation for ispheres (a,b), microstars (c,d) and 10m SVPs (e,f) for drifters deployed on September 27, 2016. Plots of the major and minor principal axes are also shown within Port Valdez (g). For purpose of comparison, the scales of the variance are shown at 10 to 50 times the actual values given in Table 2.

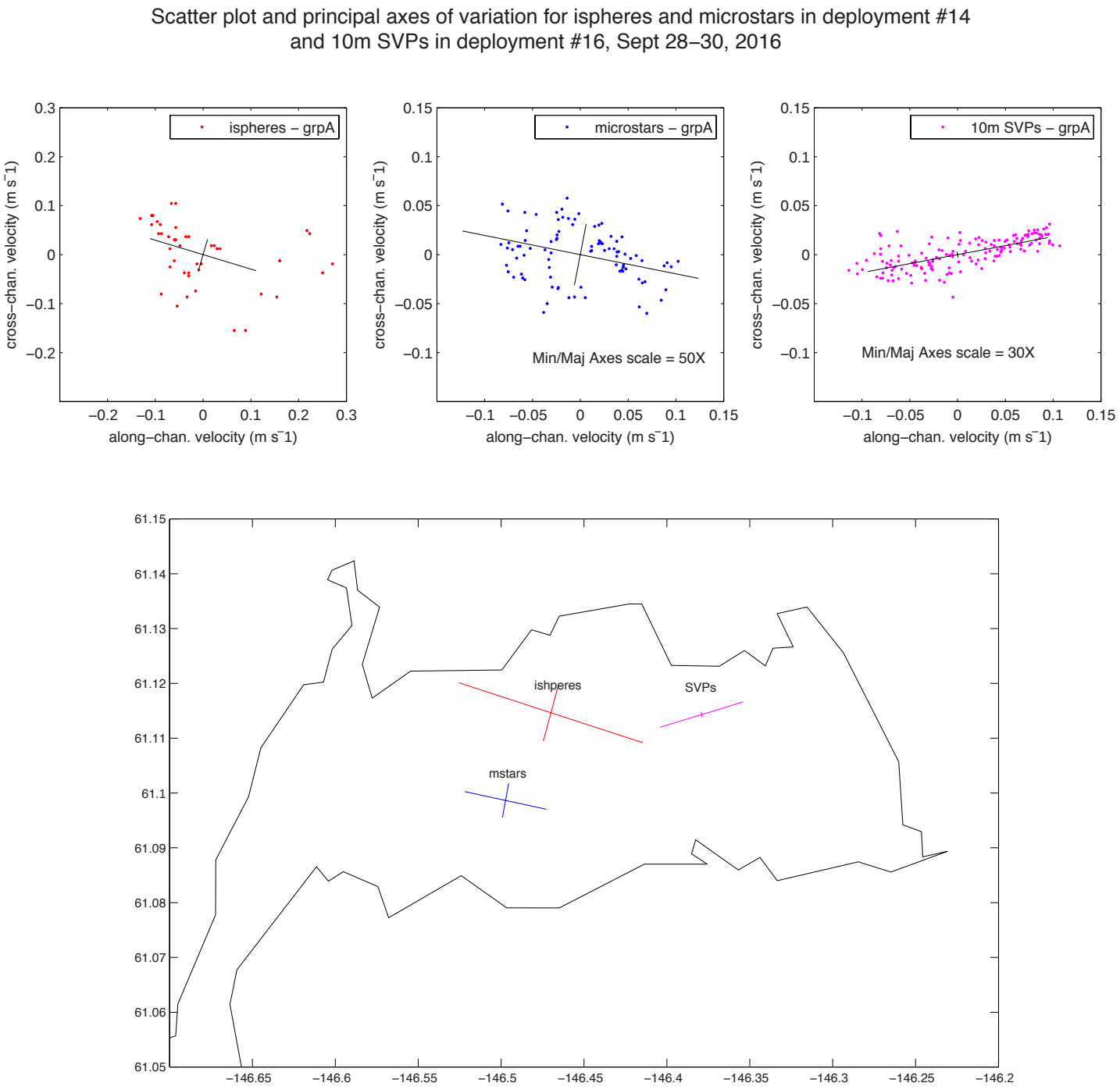

Fig. 58F. Scatter plots of *U'* and *V'* and principal axes of variation for ispheres (a), microstars (b) and 10m SVPs (c) for drifters in deployments #14 and #16 on September 28, 2016. Plots of the major and minor principal axes are also shown within Port Valdez (g). For purpose of comparison, the scales of the variance are shown at 10 to 50 times the actual values given in Table 2.

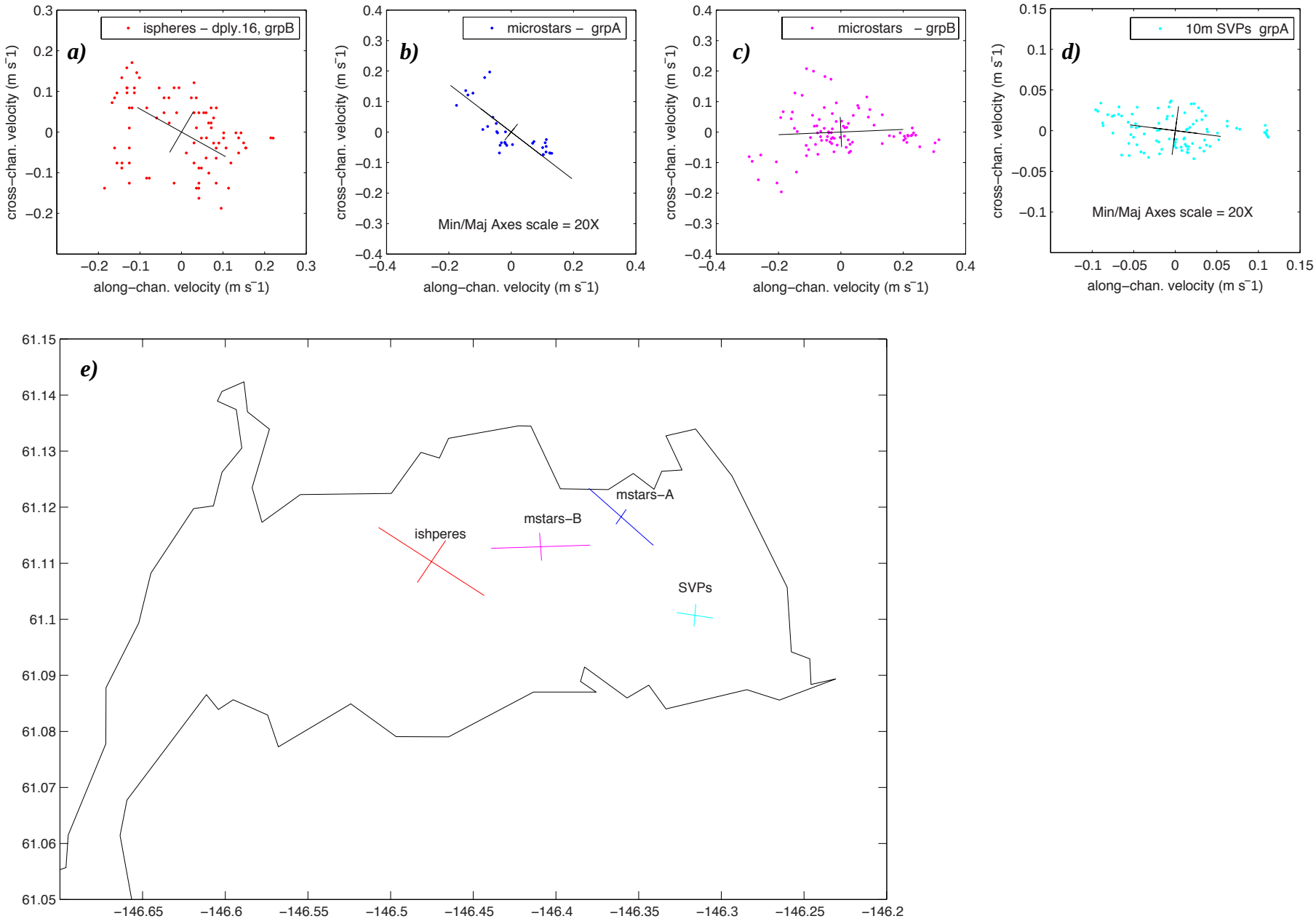

Fig. 58G. Scatter plots of *U*' and *V*' and principal axes of variation for: a) ispheres group B; b) microstars group A; c) microstars group B; and d) 10m SVPs group A for drifters in deployments #16, #17 and #18 on September 28 and 29, 2016. Plots of the major and minor principal axes are also shown within Port Valdez (e). For purpose of comparison, the scales of the variance are shown at 10 to 50 times the actual values given in Table 2.

Scatter plot and Principal axes of variation for 40m SVPs for deployments #4, #5 and #7, Sept 22, 23 and 24 to 30, 2016

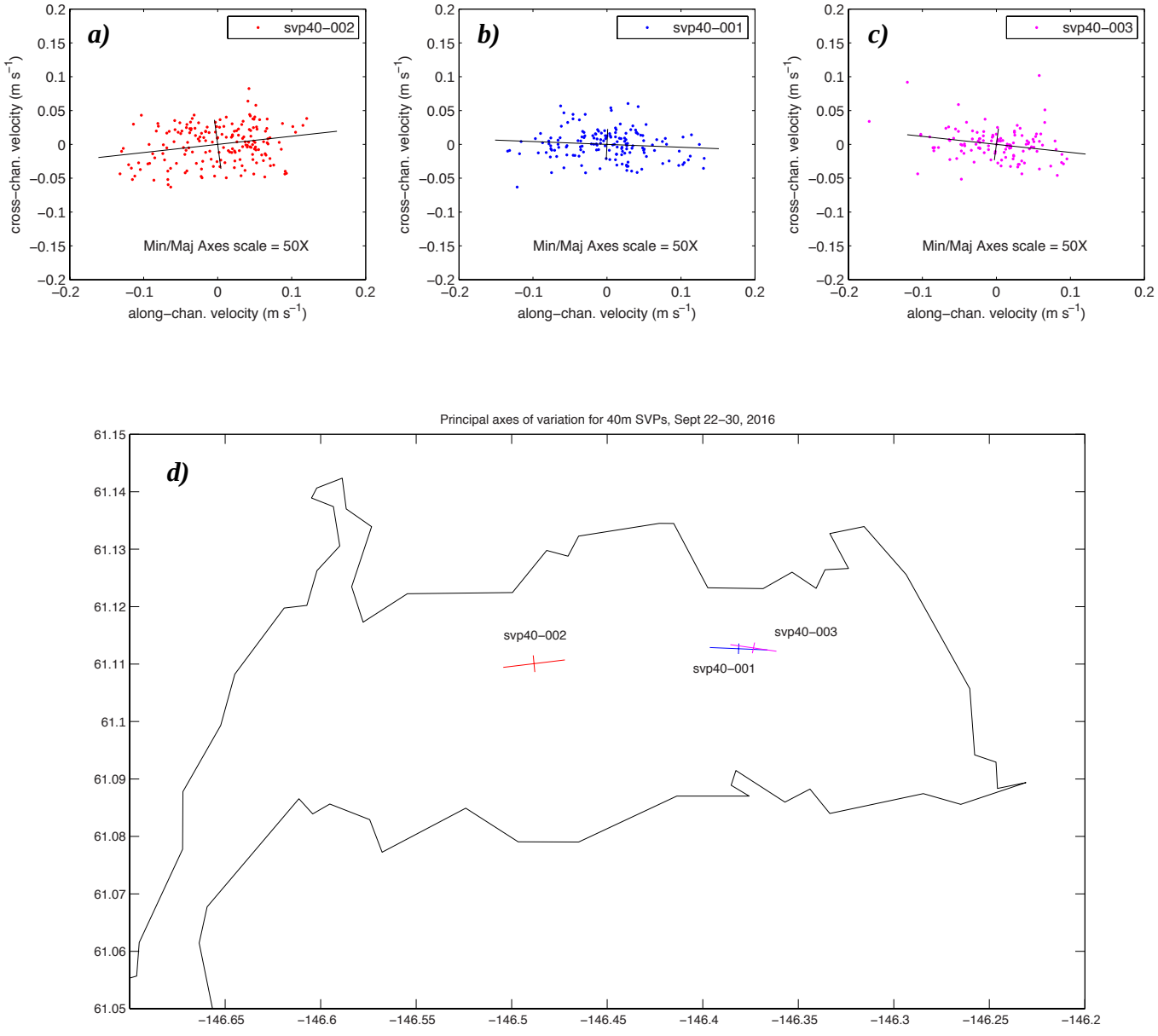

Fig. 58H. Scatter plots of *U'* and *V'* and principal axes of variation for 40m SVPs 002, 001 and 003 launched during deployments 4, 5 and 7 respectively: a) #002 September 22-30; b) #001 September 23-30; and c) #003 September 24-30, 2016. Plots of the major and minor principal axes are also shown within Port Valdez in (d). For purpose of comparison, the scales of the variance are shown at 50 times the actual values given in Table 2.

Scatter plots of *U'* vrs. *V'* and principal axes of variation for ispheres in deployments #1 and #2, and microstars and 10m SVPs in deployment #1 on March 24-25, 2017

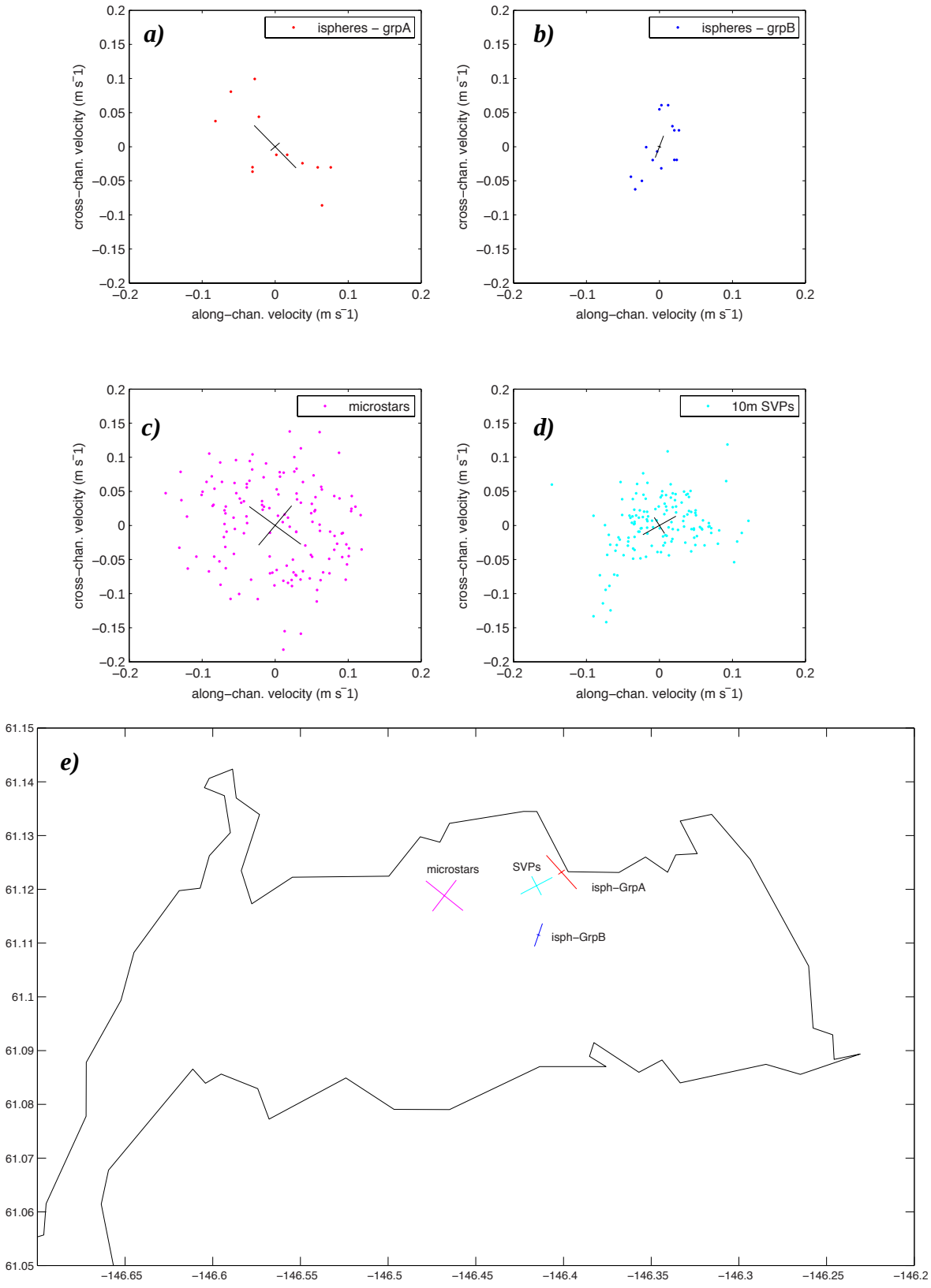

Fig. 59A. Scatter plots of *U'* and *V'* and principal axes of variation for ispheres (a,b), microstars (c) and 10m SVPs (d) for deployments #1 and #2 on March 24, 2017. Plots of the major and minor principal axes are also shown within Port Valdez (e). For purpose of comparison, the scales of the variance are shown at 10 times the actual values given in Table 2.

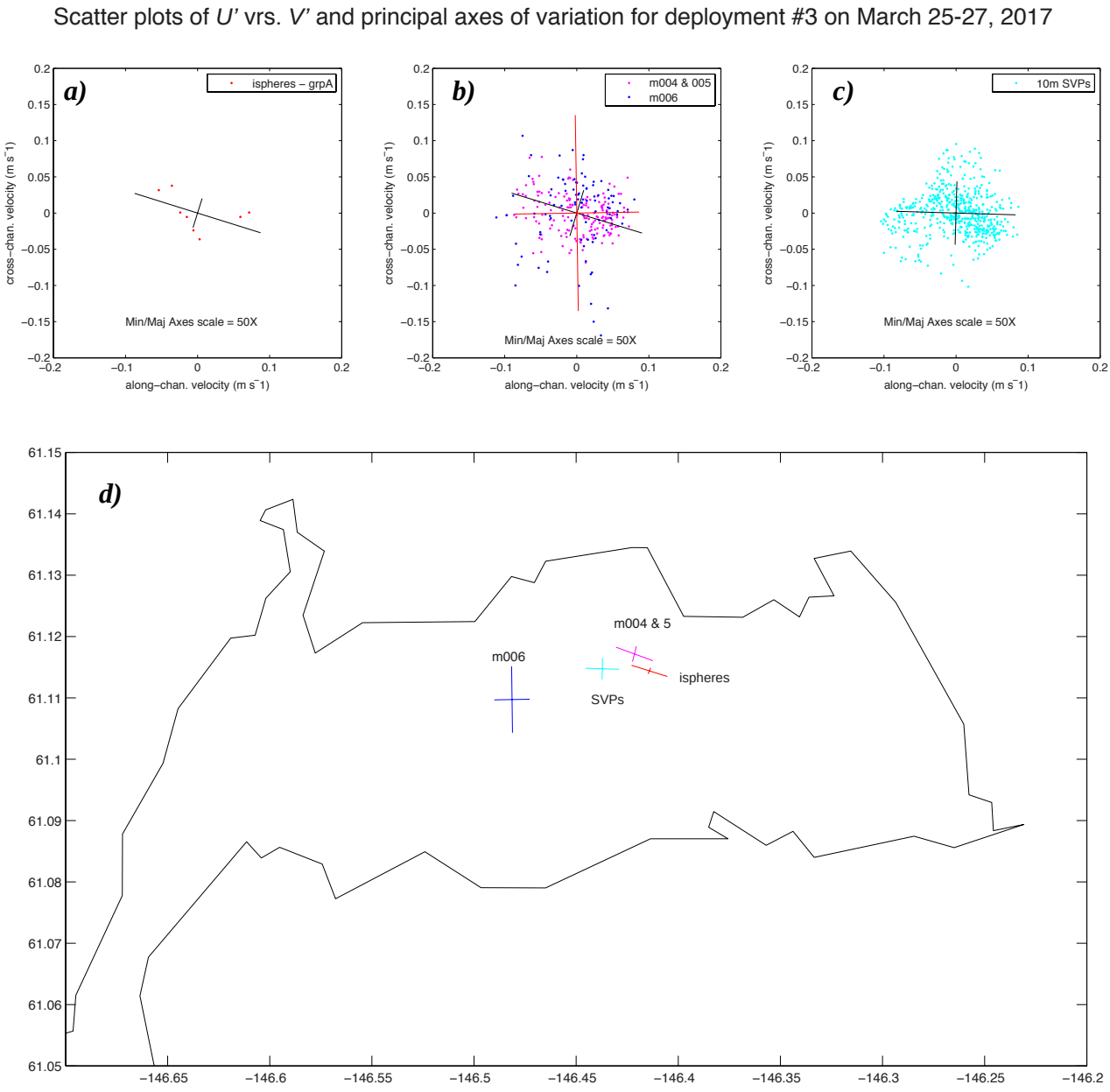

Fig. 59B. Scatter plots of *U'* and *V'* and principal axes of variation for ispheres (a), microstars (b) and 10m SVPs (c) for deployment #3 on March 25, 2017. Plots of the major and minor principal axes are also shown within Port Valdez (d). For purpose of comparison, the scales of the variance are shown at 20 times the actual values given in Table 2.

Scatter plots of *U'* vrs. *V'* and principal axes of variation for deployment #5 on March 26-30, 2017

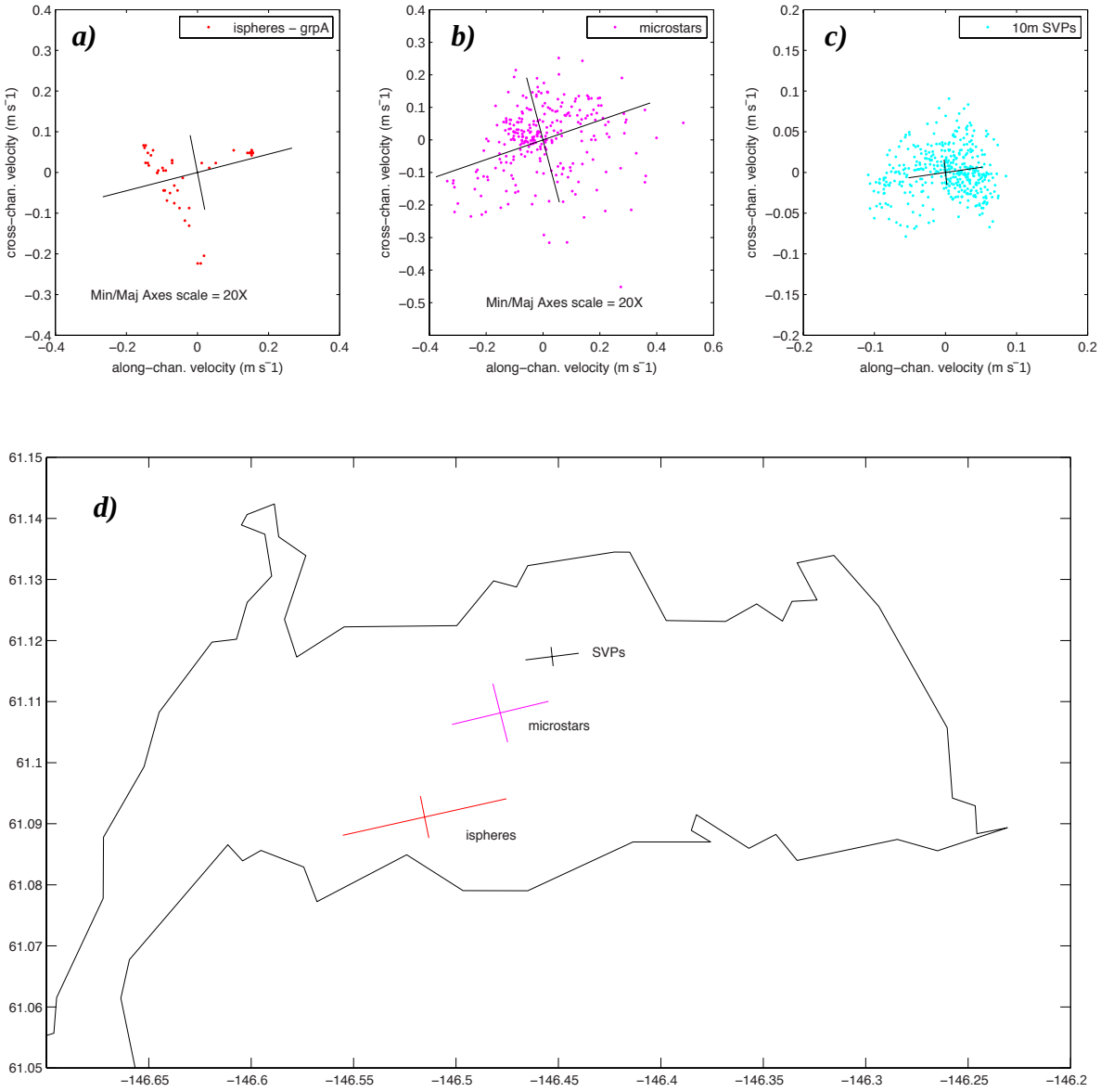

Fig. 59C. Scatter plots of *U'* and *V'* and principal axes of variation for ispheres (a), microstars (b) and 10m SVPs (c) for deployment #5 on March 26, 2017. Plots of the major and minor principal axes are also shown within Port Valdez (d). For purpose of comparison, the scales of the variance are shown at 10 to 20 times the actual values given in Table 2.

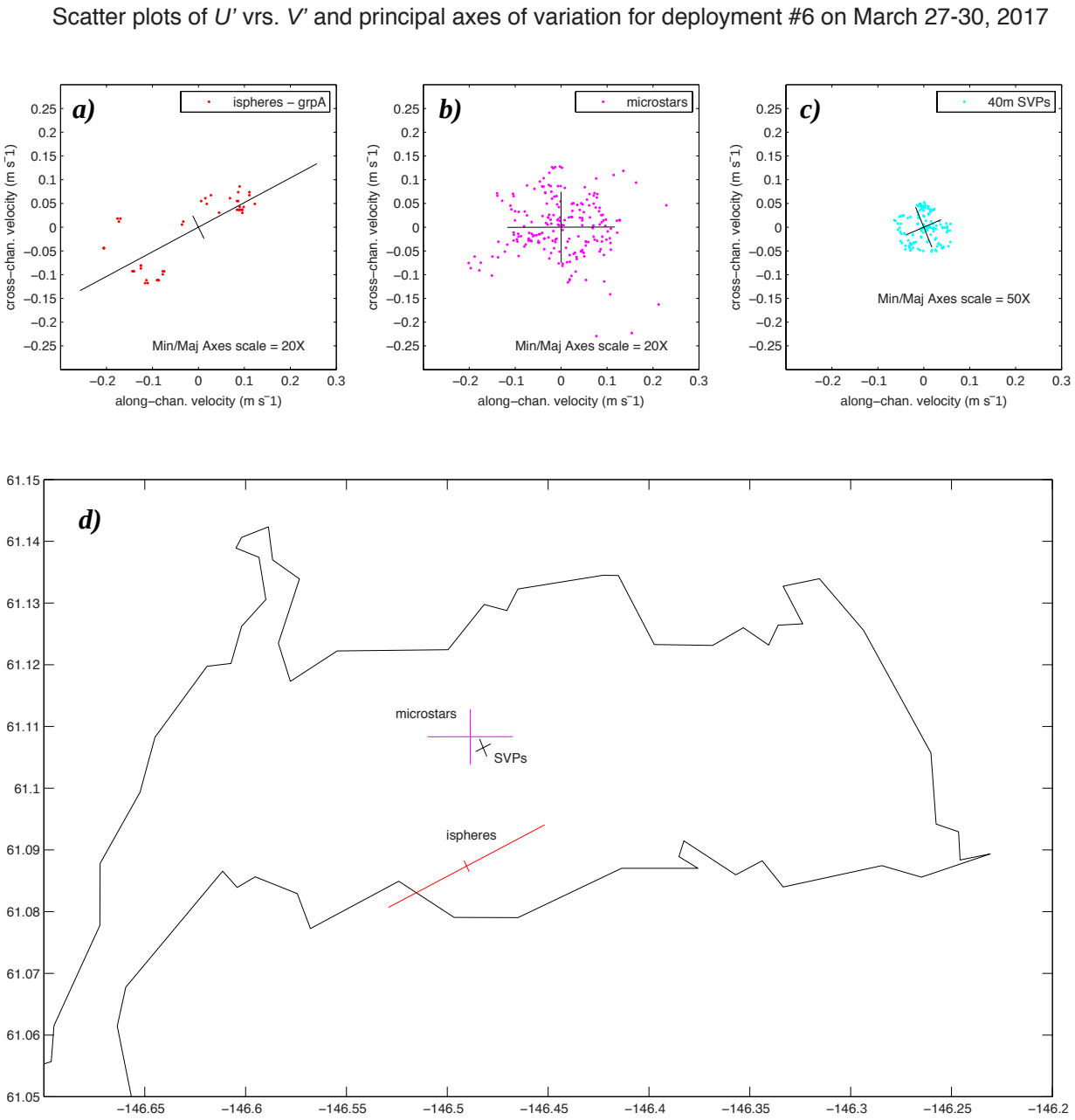

Fig. 59D. Scatter plots of *U'* and *V'* and principal axes of variation for ispheres (a), microstars (b) and 10m SVPs (c) for deployment #6 on March 27, 2017. Plots of the major and minor principal axes are also shown within Port Valdez (d). For purpose of comparison, the scales of the variance are shown at 20 to 50 times the actual values given in Table 2.

Scatter plots of *U'* vrs. *V'* and principal axes of variation for ideployment #7 on March 28-30, 2017

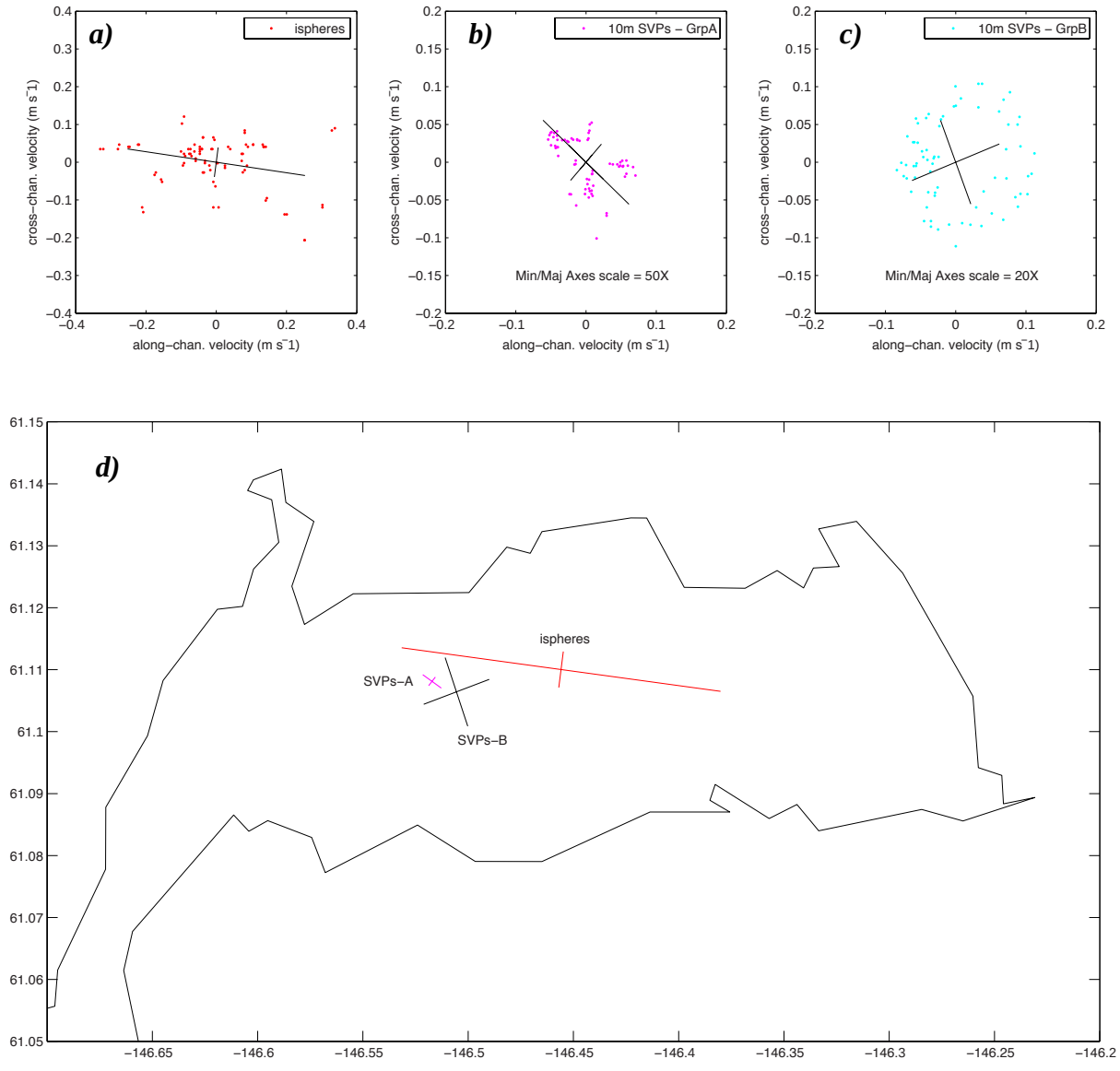

Fig. 59E. Scatter plots of *U'* and *V'* and principal axes of variation for ispheres (a) and 10m SVPs (b,c) for deployment #7 on March 28, 2017. Plots of the major and minor principal axes are also shown within Port Valdez (d). For purpose of comparison, the scales of the variance are shown at 10 to 50 times the actual values given in Table 2.

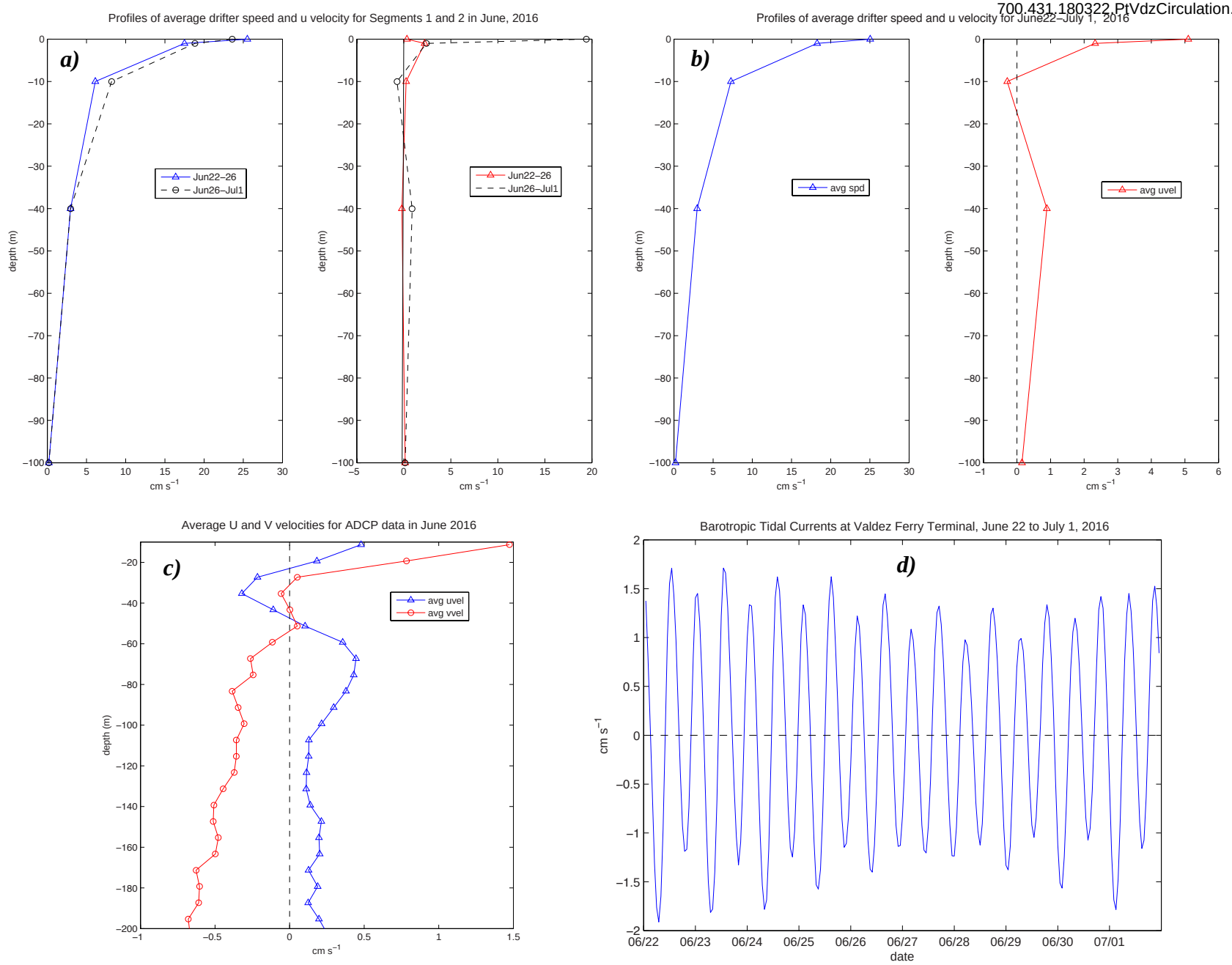

Fig. 60. Profiles of drifter speeds and along-channel (u) velocities, ADCP u and v velocities and barotropic tidal currents in June 2016. a) averages for the first and second segments from June 22 to 26 and 27 to July 1 respectively; b) averages during the entire experiment (June 22 to July 1); c) averages for all adcp data during segment 1 and d) barotropic tidal currents calculated from water level changes measured at the NOAA weather station located at the Alaska Marine Highway terminal in Valdez Alaska.

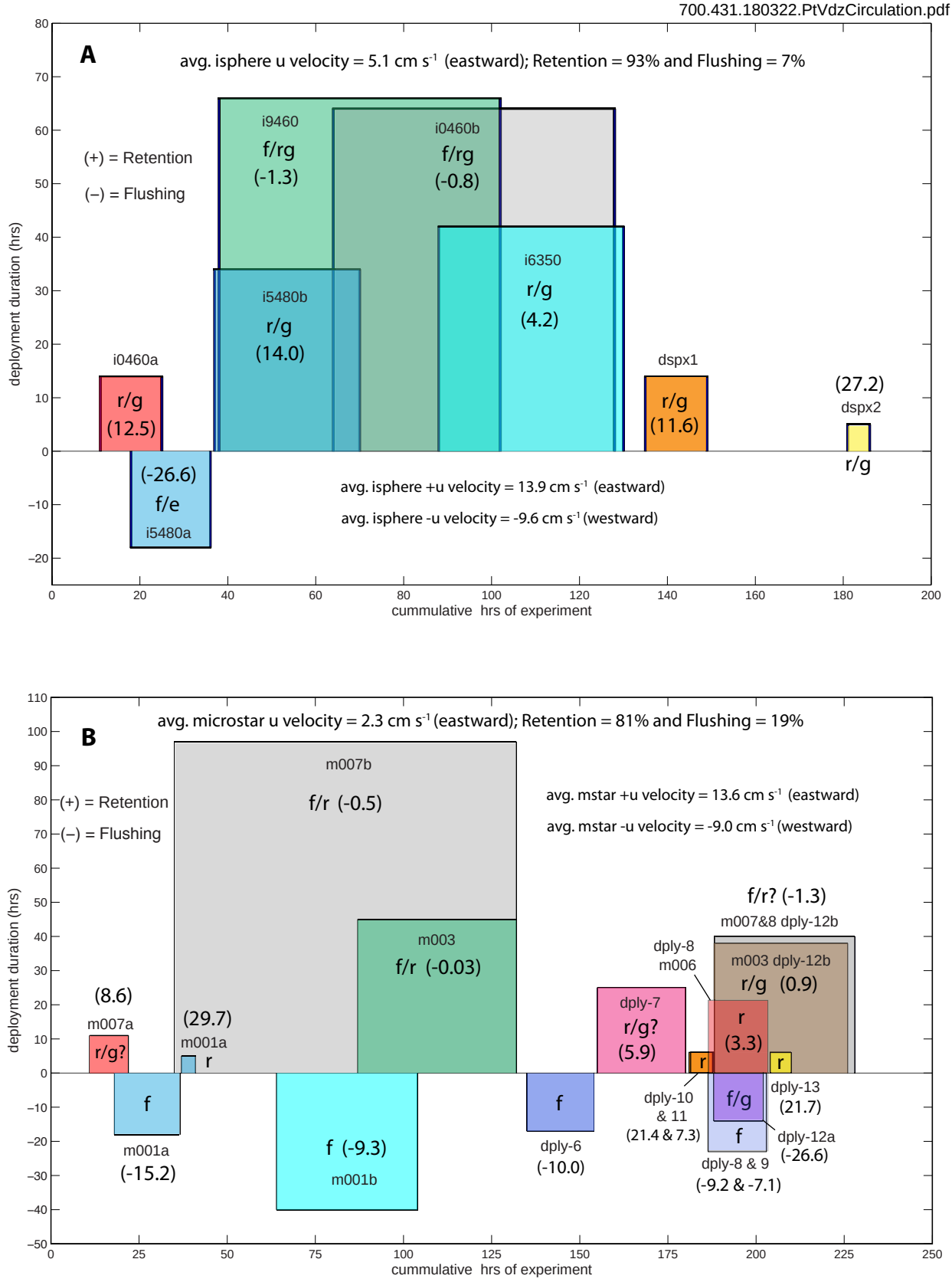

Fig. 61. Duration and cummulative hours of retention versus flushing for A) surface (ispheres) and B) 1m (microstars) deployed in June 2016. Durations of each phase are based on total times of deployments except in cases of grounding. The phases (from Table 2) are shown as lower case letters in each box and defined as follows: r = retention, f = flushing, g = grounding, and ? means the secondary designation was uncertain at the time of retrieval but the likely scenario based on the drift trajectory and patterns shown by other deployments.

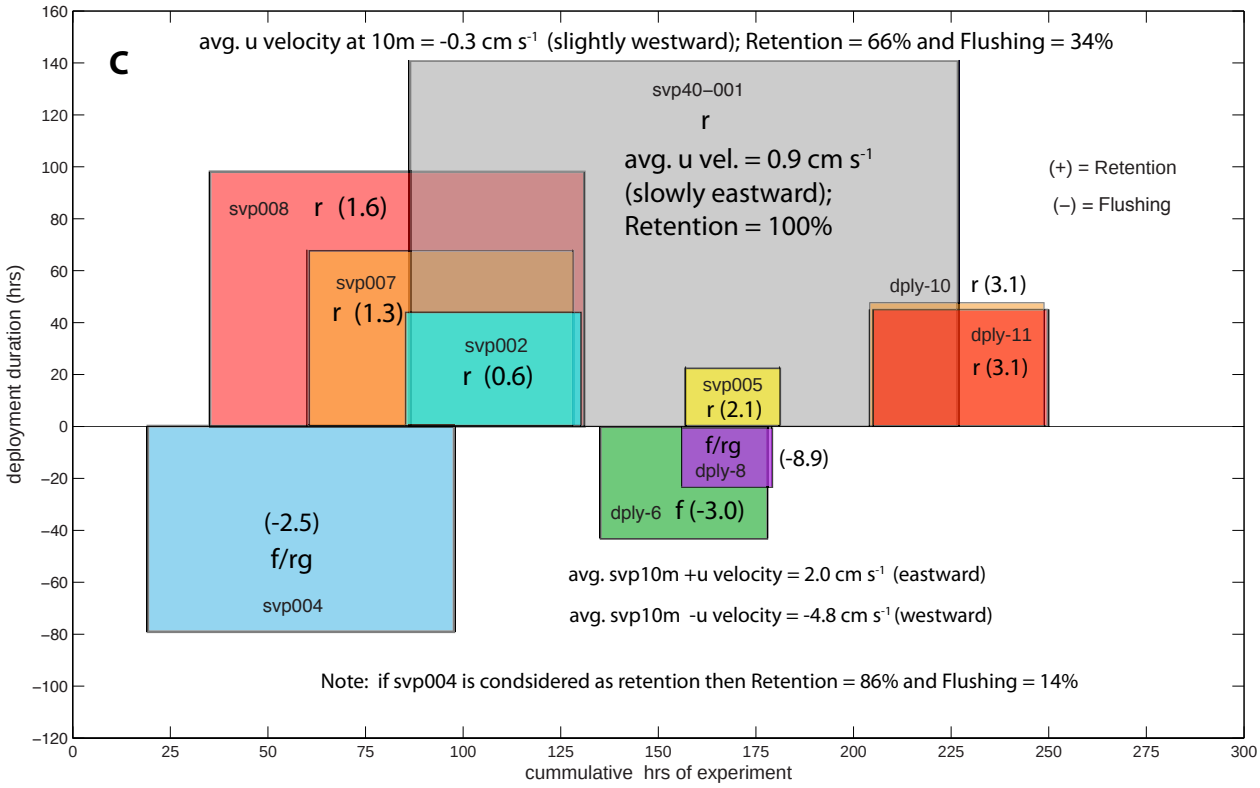

Fig. 61 (cont.). Duration and cummulative hours of retention versus flushing for C) 10m and 40m SVPs deployed in June 2016. Durations of each phase are based on total times of deployments except in cases of grounding. The phases (from Table 2) are shown as lower case letters in each box and defined as follows: r = retention, f = flushing, g = grounding, and ? means the secondary designation was uncertain at the time of retrieval but the likely scenario based on the drift trajectory and patterns shown by other deployments.

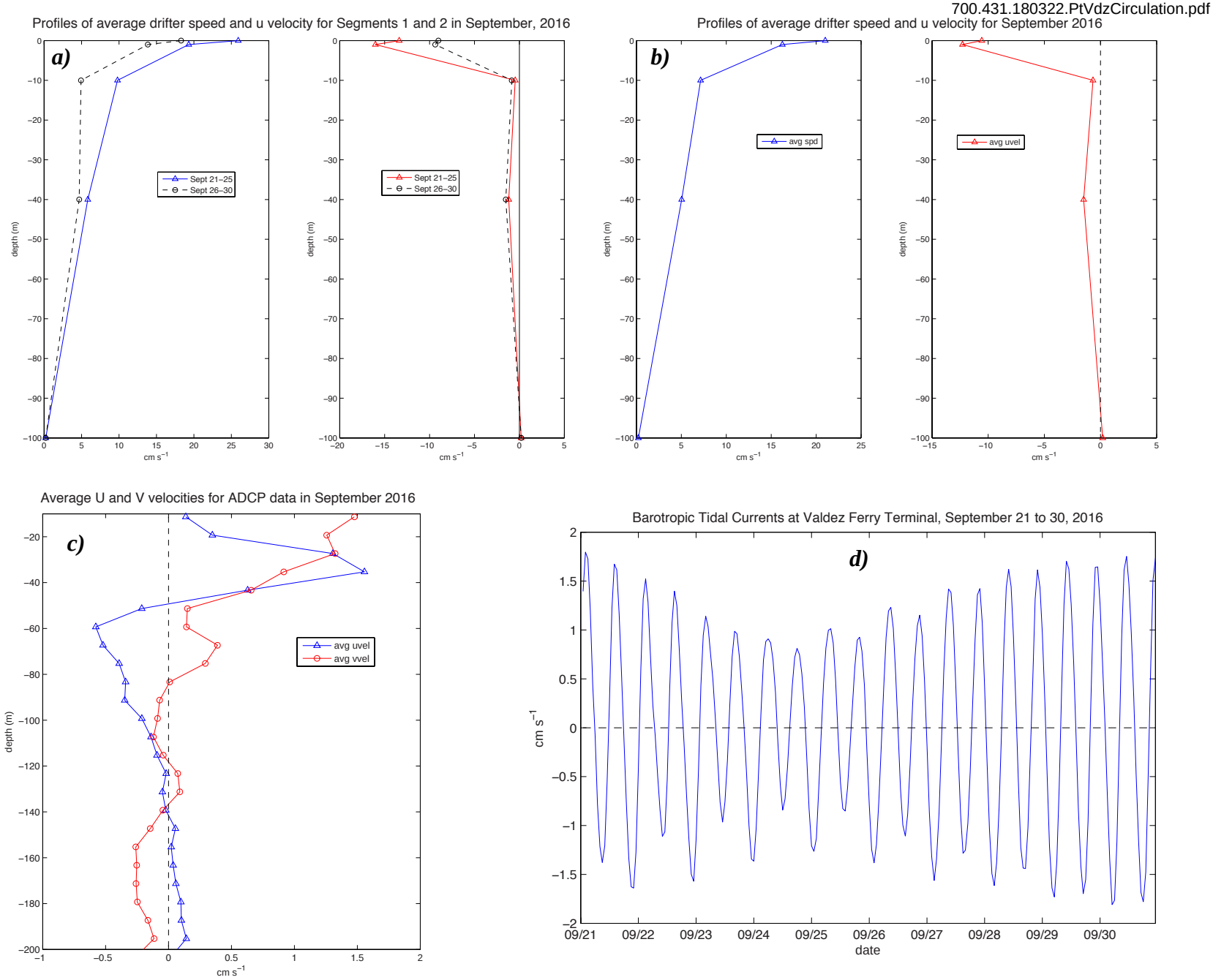

Fig. 62. Profiles of drifter speeds and along-channel (u) velocities and ADCP u and v velocities and barotropic tidal currents in September 2016. a) averages for the first and second segments from September 21 to 25 and 26 to 30 respectively; b) averages during the entire experiment (September 21 to 30); c) averages for all adcp data over segment 1 and d) barotropic tidal currents calculated from water level changes measured at the NOAA weather station located at the Alaska Marine Highway terminal in Valdez Alaska.

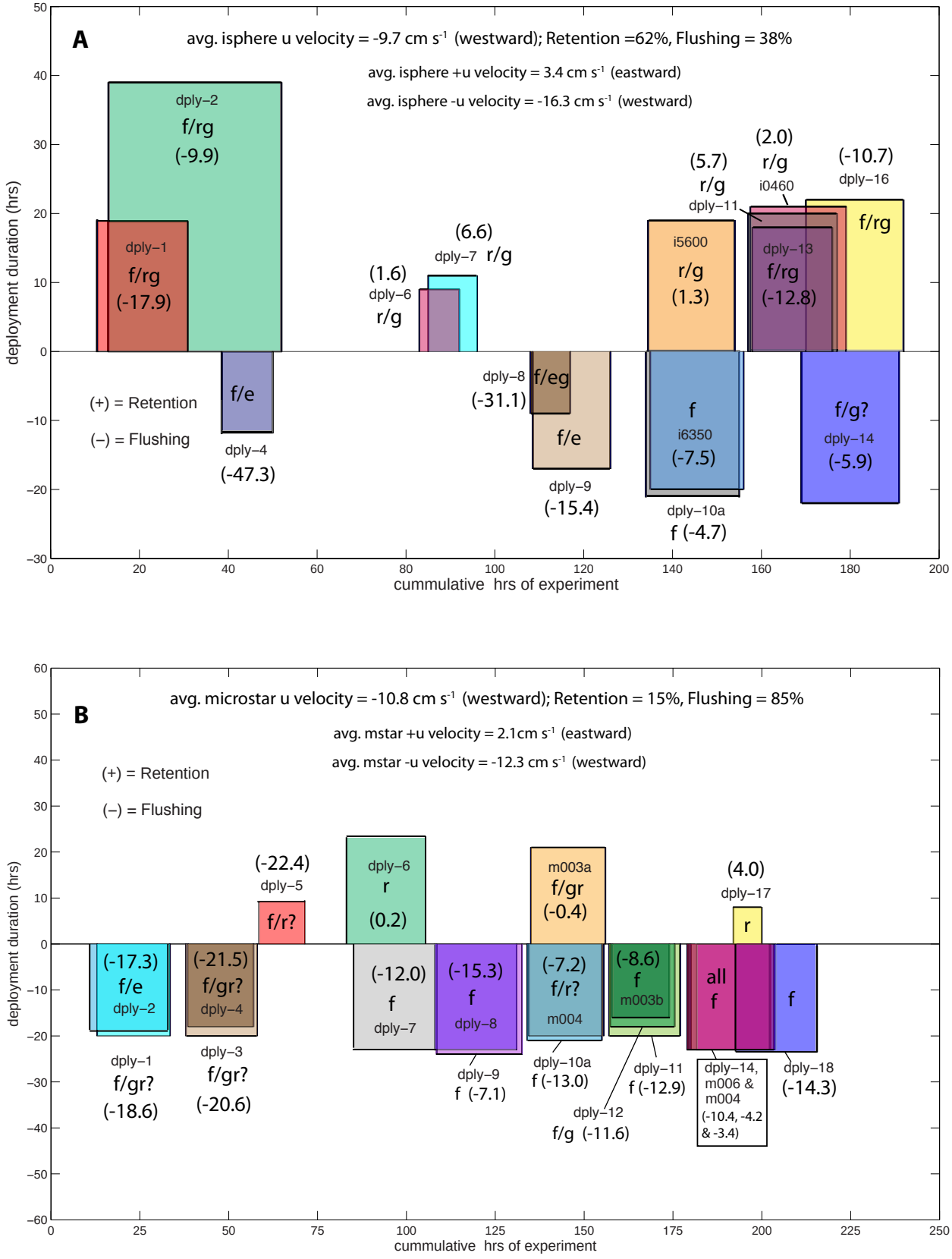

Fig. 63. Duration and cummulative hours of retention versus flushing for A) surface (ispheres) and B) 1m (microstars) deployed in September 2016. Durations of each phase are based on total times of deployments except in cases of grounding. The phases (from Table 2) are shown as lower case letters in each box and defined as follows: r = retention, f = flushing, g = grounding, and ? means the secondary designation was uncertain at the time of retrieval but the likely scenario based on the drift trajectory and patterns shown by other deployments.

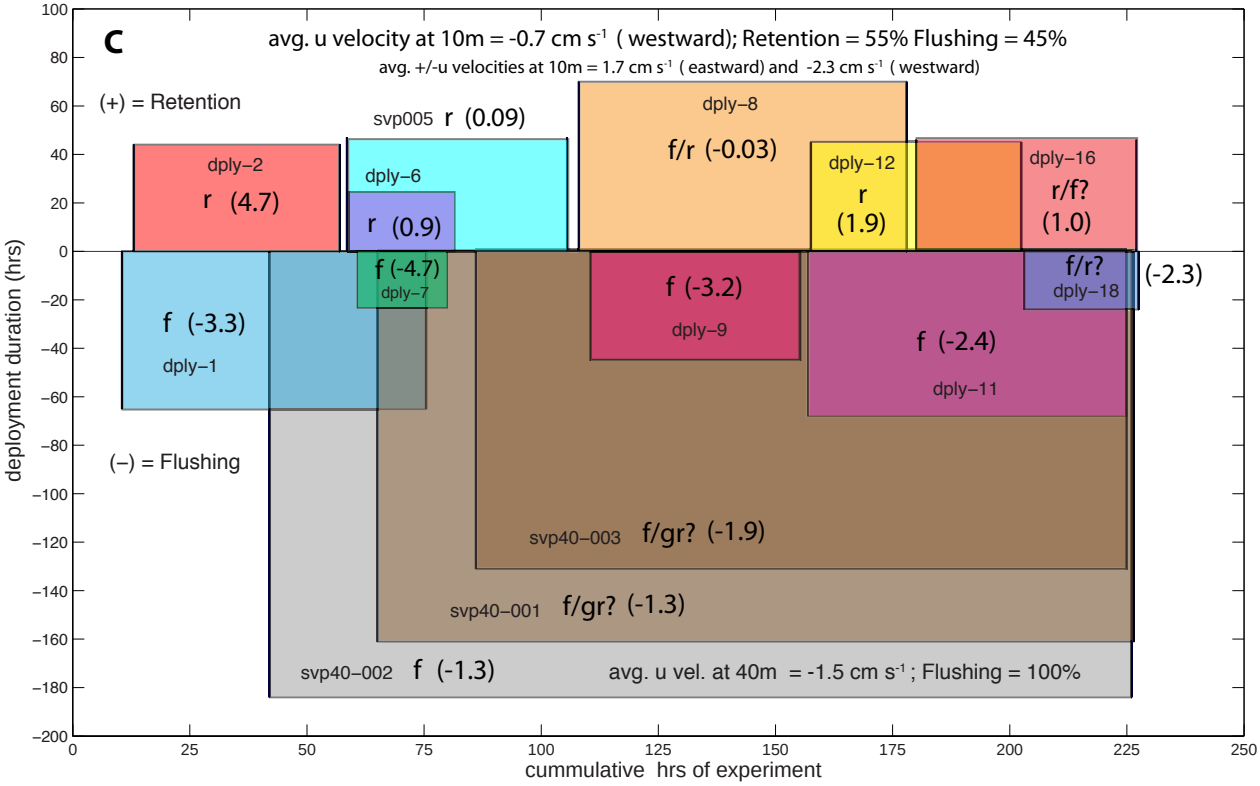

Fig. 63 (cont.). Duration and cummulative hours of retention versus flushing for C) 10m and 40m SVP drifters deployed in September 2016. Durations of each phase are based on total times of deployments except in cases of grounding. The phases (from Table 2) are shown as lower case letters in each box and defined as follows: r = retention, f = flushing, g = grounding, and ? means the secondary designation was uncertain at the time of retrieval but the likely scenario based on the drift trajectory and patterns shown by other deployments.

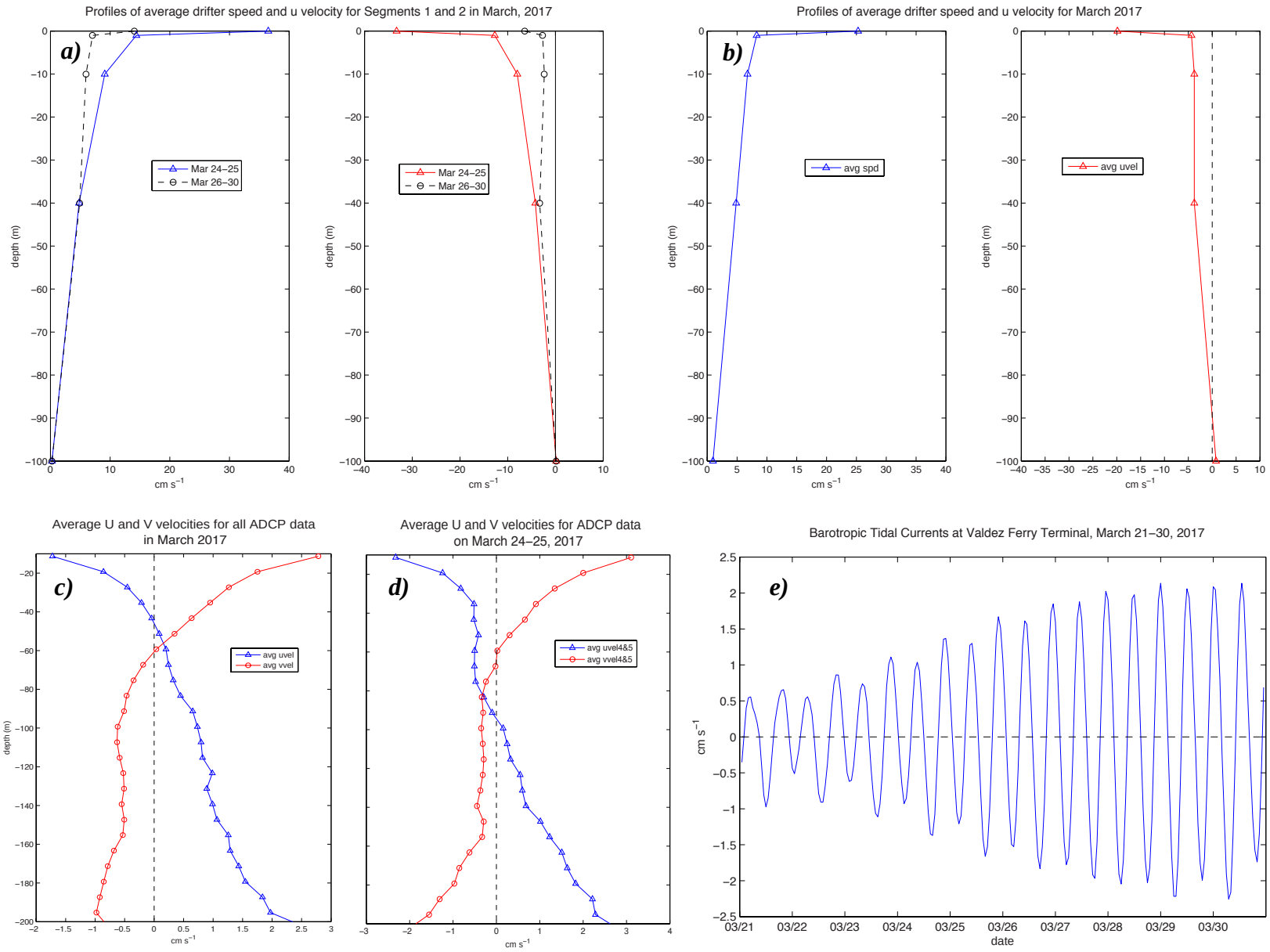

Fig. 64. Profiles of drifter speeds and along-channel (u) velocities and ADCP u and v velocities in March 2017. a) averages for the initial drifter releases in segment 1 (March 24 to 25) and segment 2 (March 26 to 30); b) averages for drifters released over the entire experiment (March 24 to 30); c) averages for all adcp data collected during the oceanographic survey from March 21 to 25; d) averages for adcp data collected on March 24 and 25 and e) barotropic tidal currents calculated from water level changes measured at the NOAA weather station located at the Alaska Marine Highway terminal in Valdez Alaska.

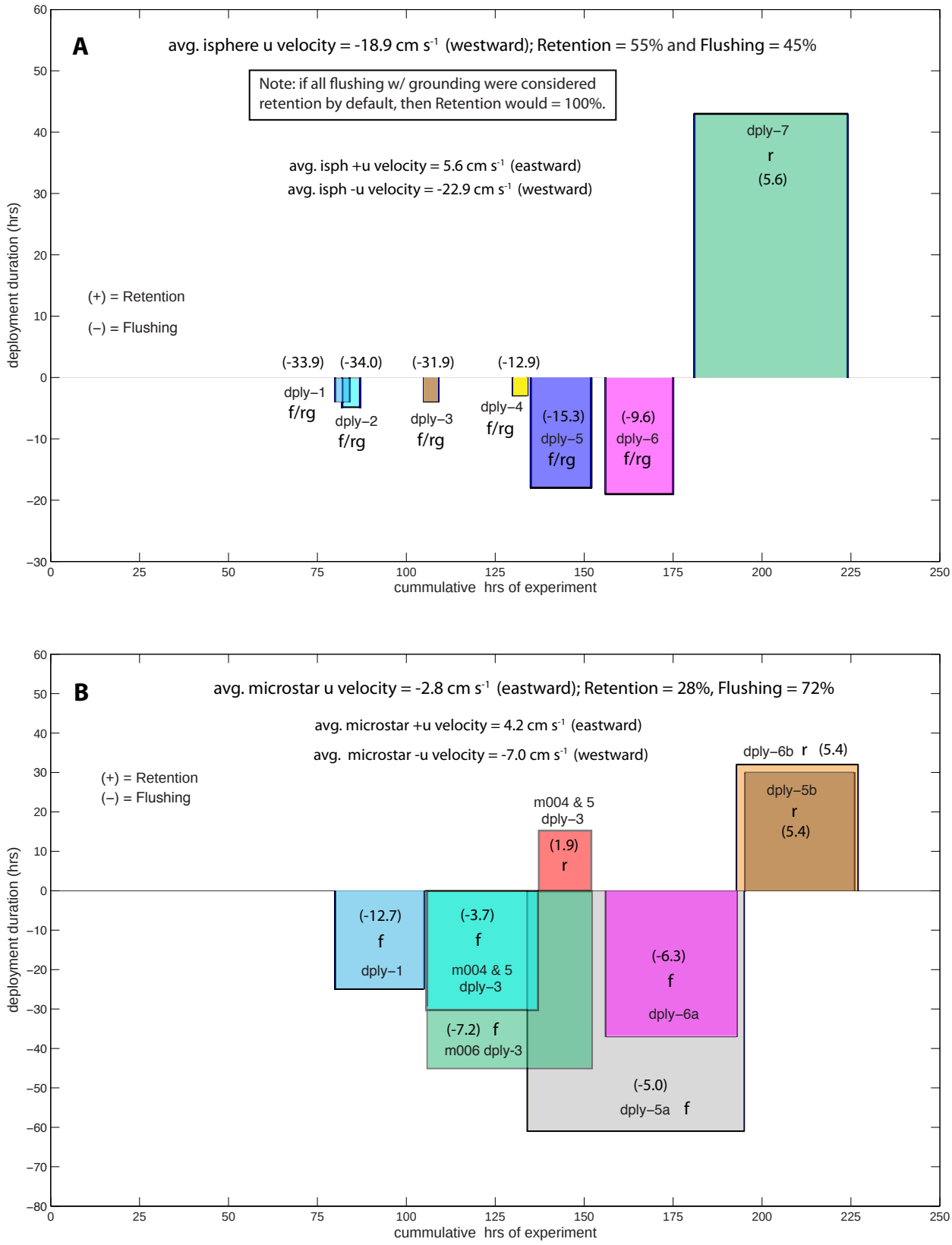

Fig. 65. Duration and cummulative hours of retention versus flushing for A) surface (ispheres) and B) 1m (microstars) deployed in March 2017. Durations of each phase are based on total times of deployments except in cases of grounding. The phases (from Table 3) are shown as lower case letters in each box and defined as follows: r = retention, f = flushing, g = grounding, and ? means the secondary designation was uncertain at the time of retrieval but the likely scenario based on the drift trajectory and patterns shown by other deployments. The microstars in dply. #3 were broken into three segments: flushing by m006 and m004/5, and retention by m004/5.

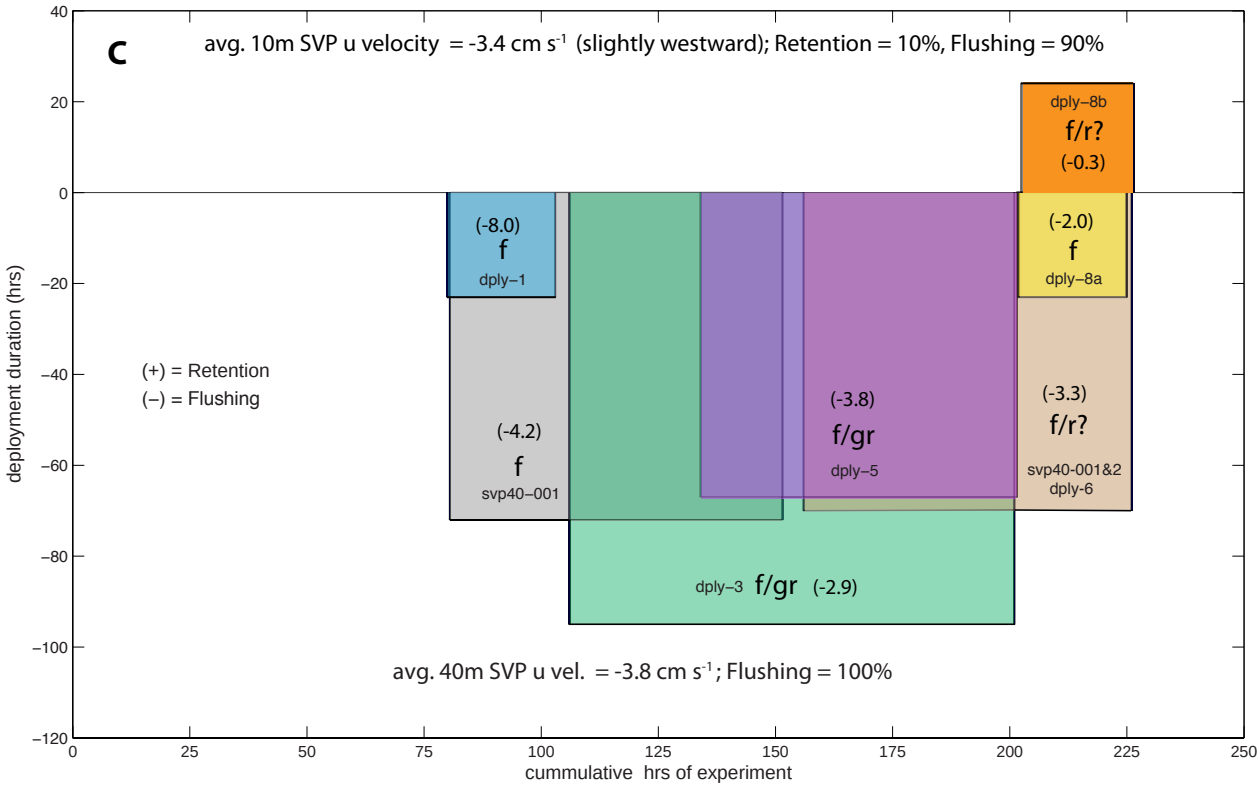

Fig. 65 (cont.). Duration and cummulative hours of retention versus flushing for C) 10m and 40m SVP drifters deployed in March 2017. Durations of each phase are based on total times of deployments except in cases of grounding. The phases (from Table 2) are shown as lower case letters in each box and defined as follows: r = retention, f = flushing, g = grounding, and ? means the secondary designation was uncertain at the time of retrieval but the likely scenario based on the drift trajectory and patterns shown by other deployments.

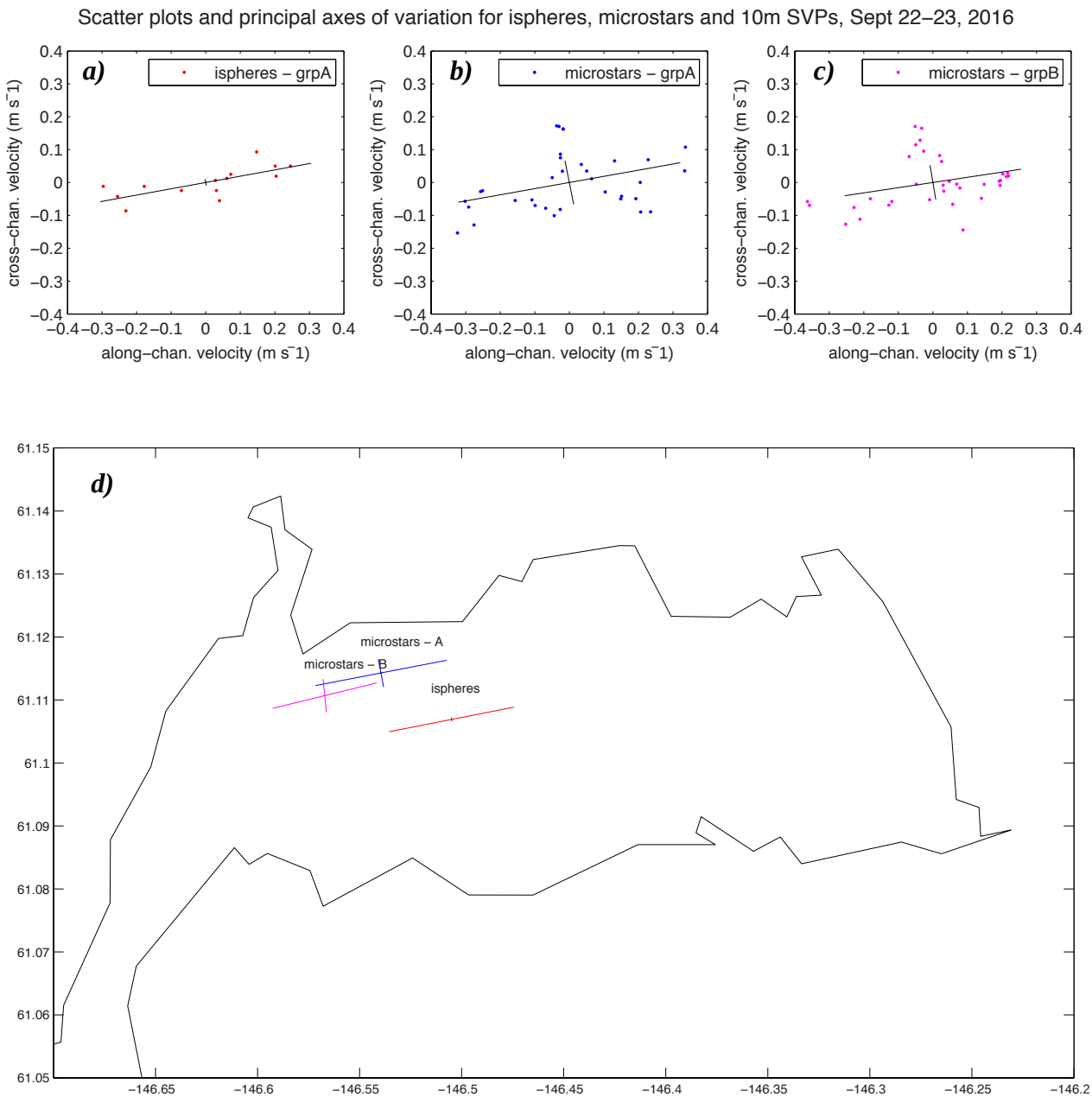

Fig. 66. Scatter plots of *U'* and *V'* and principal axes of variation for: a) ispheres (dply. #4); b) microstars (group-A, dply. #3) and c) microstars (group-B, dply. #4) released on September 22, 2016. d) Major and minor principal axes plotted within Port Valdez. For purpose of comparison, the scales of the variance are shown at 10 to 50 times the actual values given in Table 2.

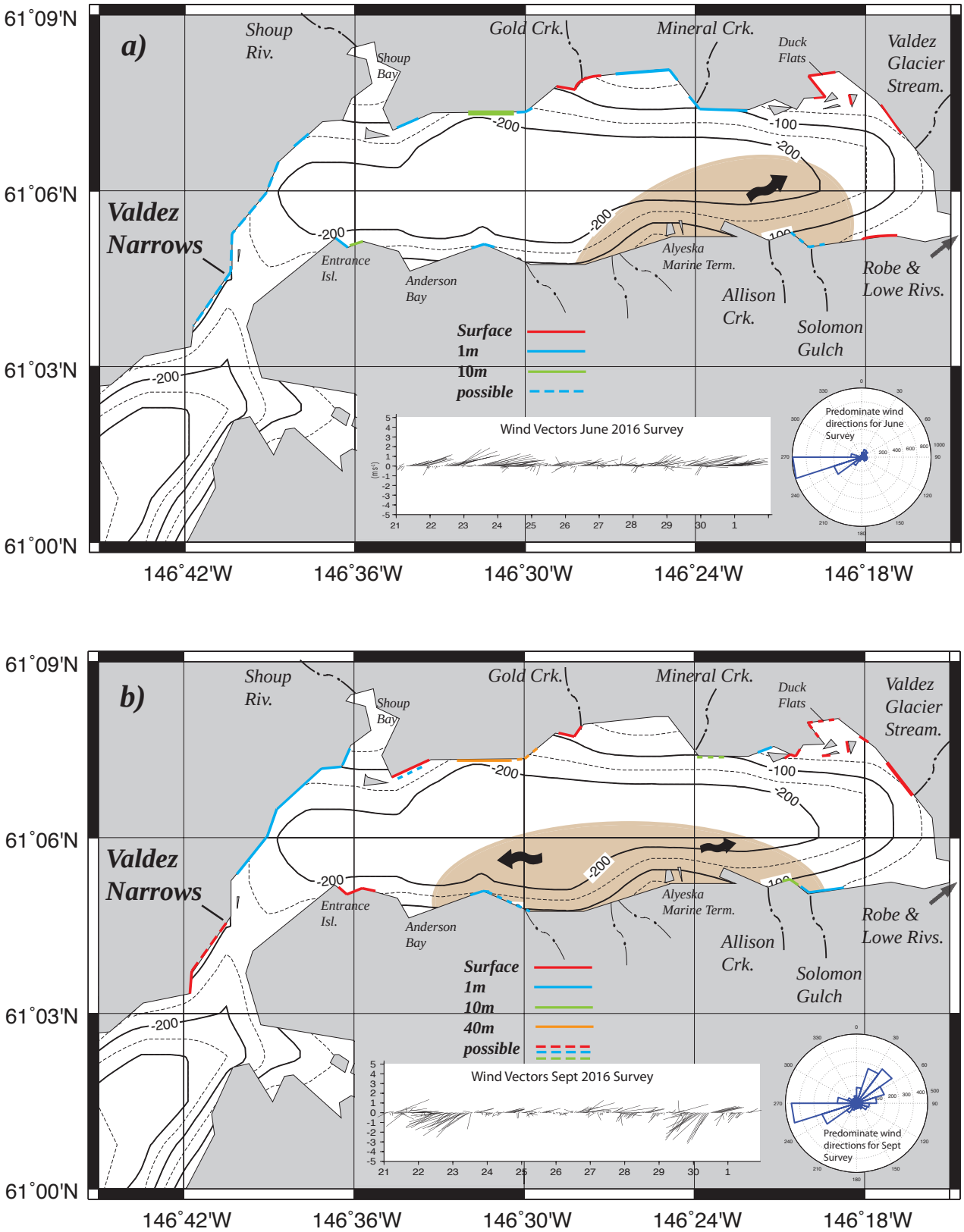

Fig. 67. Locations at a higher risk of contamination from oil advected at various depths shown by drifter trajectories and groundings within Port Valdez in June and September 2016 (a and b) and March 2017 (c). Note that the light brown areas are for schematic purposes only, and indicate where spilled surface oil may initially move given the prevailing winds. Depths are respectively for the surface (red), 1m (blue), 10m (green) and 40m (orange), and dashed lines indicate possible contamination when drifters came close to the shoreline but did not ground. The wind speeds and directions for the survey periods are shown vector plots (left insets). The wind rose plots (right insets) show polar histograms of the predominate wind directions for each survey period.

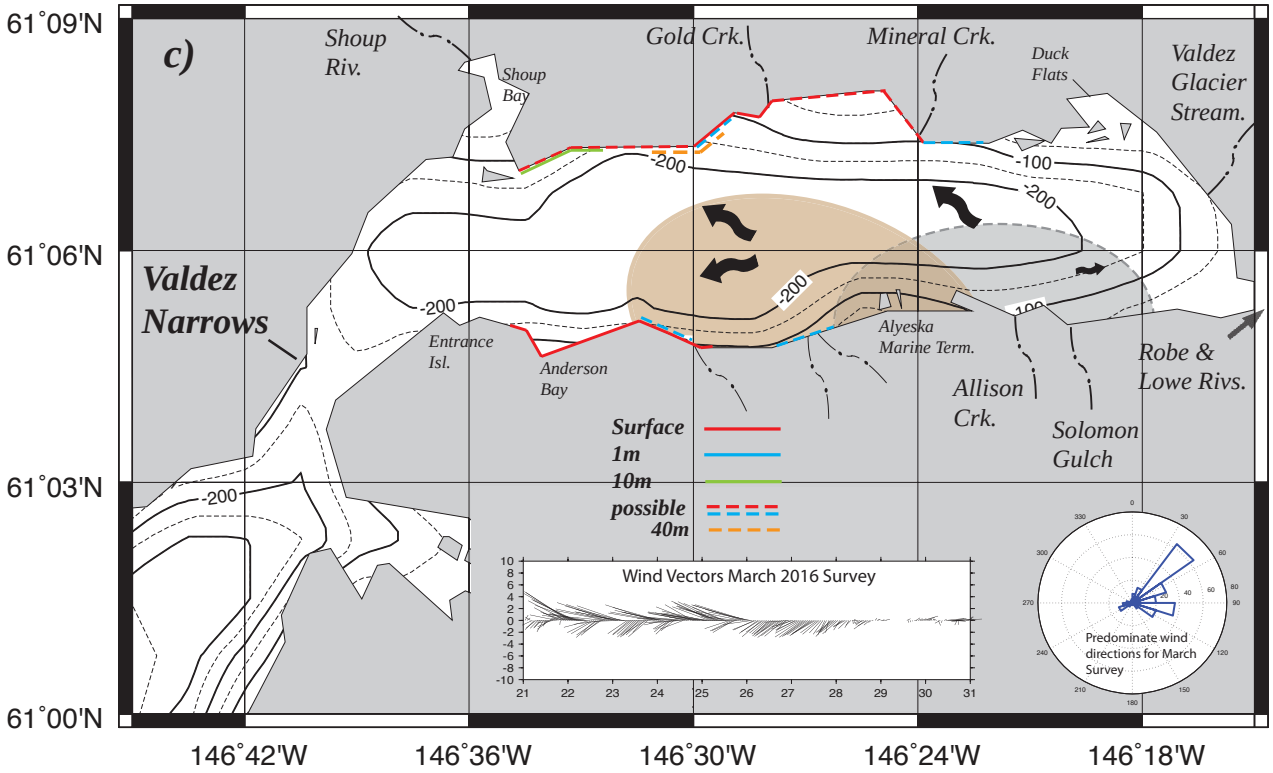

Fig. 67 (cont.). Same legend as previous plots except for the light grey shaded area indicating an alternate oil motion under light westerly winds, as occurred at the end of the March survey, followed by strong easterly winds moving oil towards areas of the northern shore outlined by dashed lines. Note that wind rose is for hourly observations.

Appendix A: Lists of CTD casts, plots of station locations and profiles of temperature and salinity.

JUNE 2016:

Run A

	latitude		*longitude*		*depth*				
Station	*deg.*	*min.*	*deg.*	*min.*	*(m)*	*day*	*month*	*year*	*time*
PV9B	61	6.37	146	23.6	230	22	Jun	2016	10:50:23
PV17	61	5.27	146	19.33	40	22	Jun	2016	12:34:43
PV16	61	5.88	146	19.47	184	22	Jun	2016	12:55:58
PV15	61	6.55	146	19.4	200	22	Jun	2016	13:11:44
PV14	61	7.2	146	19.39	100	22	Jun	2016	13:26:49
PV13	61	5.73	146	21.37	210	22	Jun	2016	13:53:34
PV12	61	6.57	146	21.39	224	22	Jun	2016	14:13:27
PV11	61	7.27	146	21.37	70	22	Jun	2016	14:32:38
PV10	61	5.82	146	23.4	233	22	Jun	2016	14:57:59
PV9	61	6.61	146	23.2	230	22	Jun	2016	15:17:57
PV8	61	7.27	146	23.1	138	22	Jun	2016	15:36:12
PV7	61	5.74	146	26.16	185	22	Jun	2016	16:11:05
PV6	61	6.62	146	26.81	200	22	Jun	2016	16:30:48
PV5	61	7.29	146	26	159	22	Jun	2016	16:53:30
PV1	61	5.08	146	27.92	219	22	Jun	2016	17:25:01
PV2	61	6.65	146	27.88	230	22	Jun	2016	17:52:00
PV4	61	7.25	146	27.77	225	22	Jun	2016	18:09:28

Run B

PV1	61	7.3	146	27.74	170	23	Jun	2016	0:25:09
PV2	61	6.65	146	27.77	236	23	Jun	2016	0:43:49
PV4	61	5.1	146	27.9	220	23	Jun	2016	1:10:29
PV5	61	7.31	146	25.9	159	23	Jun	2016	1:43:21
PV6	61	6.6	146	26.12	237	23	Jun	2016	1:58:40
PV7	61	5.84	146	26.18	236	23	Jun	2016	2:16:29
PV8	61	7.27	146	23.38	144	23	Jun	2016	2:44:27
PV9	61	6.62	146	23.46	232	23	Jun	2016	3:00:07
PV10	61	5.76	146	23.59	234	23	Jun	2016	3:18:06
PV11	61	7.28	146	21.51	110	23	Jun	2016	3:47:14
PV12	61	6.61	146	21.4	225	23	Jun	2016	3:58:38
PV13	61	5.87	146	21.38	200	23	Jun	2016	4:15:58
PV14	61	7.18	146	19.41	100	23	Jun	2016	4:41:35
PV15	61	6.68	146	19.4	198	23	Jun	2016	4:53:18
PV17	61	5.59	146	19.44	100	23	Jun	2016	5:13:51

Run C

	latitude		*longitude*		*depth*				
Station	*deg.*	*min.*	*deg.*	*min.*	*(m)*	*day*	*month*	*year*	*time*
PV1	61	7.27	146	28.08	225	23	Jun	2016	8:01:08
PV2	61	6.62	146	27.82	233	23	Jun	2016	8:19:36
PV4	61	5.09	146	27.95	218	23	Jun	2016	8:44:40
PV5	61	7.32	146	26.08	120	23	Jun	2016	9:18:00
PV6	61	6.62	146	26.19	233	23	Jun	2016	9:33:55
PV7	61	5.79	146	26.28	230	23	Jun	2016	9:52:16
PV8	61	7.21	146	23.47	217	23	Jun	2016	10:32:21
PV9	61	6.62	146	23.57	229	23	Jun	2016	10:47:49
PV10	61	5.74	146	23.71	230	23	Jun	2016	11:04:39
PV11	61	7.28	146	21.51	93	23	Jun	2016	11:32:51
PV12	61	6.6	146	21.46	222	23	Jun	2016	11:46:08
PV13	61	5.78	146	21.46	210	23	Jun	2016	12:02:33
PV14	61	7.19	146	19.4	105	23	Jun	2016	12:30:00
PV15	61	6.59	146	19.49	196	23	Jun	2016	12:41:12
PV17	61	5.42	146	19.45	128	23	Jun	2016	13:02:09

Run D

PV1	61	7.29	146	27.82	218	24	Jun	2016	16:42:20
PV2	61	6.63	146	27.81	236	24	Jun	2016	17:00:12
PV4	61	5.11	146	27.81	222	24	Jun	2016	17:30:24
PV5	61	7.24	146	25.97	232	24	Jun	2016	18:10:56
PV6	61	6.62	146	26.05	238	24	Jun	2016	18:27:23
PV7	61	5.81	146	26.25	235	24	Jun	2016	18:46:15
PV8	61	7.24	146	23.55	217	24	Jun	2016	19:20:28
PV10	61	5.75	146	23.58	230	24	Jun	2016	19:46:37
PV11	61	7.09	146	21.47	140	24	Jun	2016	20:22:27
PV13	61	5.78	146	21.36	211	24	Jun	2016	20:47:02

Run F

PV17	61	5.42	146	19.54	128	26	Jun	2016	13:03:03
PV15	61	6.59	146	19.41	194	26	Jun	2016	13:27:21
PV14	61	7.16	146	19.49	122	26	Jun	2016	13:43:45
PV13	61	5.71	146	21.47	211	26	Jun	2016	14:09:09
PV12	61	6.56	146	21.33	214	26	Jun	2016	14:29:58
PV11	61	7.13	146	21.41	125	26	Jun	2016	14:41:17
PV10	61	5.75	146	23.51	231	26	Jun	2016	15:07:23
PV9	61	6.61	146	23.47	230	26	Jun	2016	15:26:18
PV8	61	7.25	146	23.45	215	26	Jun	2016	15:42:23
PV7	61	5.87	146	26.18	235	26	Jun	2016	16:13:29
PV5	61	7.25	146	26.09	190	26	Jun	2016	16:42:35
PV6	61	6.6	146	26.54	236	26	Jun	2016	17:03:33
PV4	61	5.11	146	27.88	220	26	Jun	2016	17:32:30
PV2	61	6.62	146	27.74	237	26	Jun	2016	17:59:33
PV1	61	7.29	146	27.8	170	26	Jun	2016	18:19:01

SEPTEMBER 2016:

Run A

	latitude		*longitude*		*depth*				
Station	*deg.*	*min.*	*deg.*	*min.*	*(m)*	*day*	*month*	*year*	*time*
PV1	61	7.22	146	27.85	235	21	Sep	2016	13:01:23
PV2	61	6.57	146	27.84	235	21	Sep	2016	13:17:38
PV3	61	5.79	146	27.64	234	21	Sep	2016	13:36:00
PV4	61	5.1	146	27.85	227	21	Sep	2016	13:52:55
PV8	61	7.18	146	23.54	219	21	Sep	2016	15:17:17
PV9a	61	6.79	146	23.5	232	21	Sep	2016	15:31:36
PV9b	61	6.27	146	23.4	233	21	Sep	2016	15:46:19
PV10	61	5.76	146	23.49	234	21	Sep	2016	16:00:47
PV14	61	7.14	146	19.44	141	21	Sep	2016	17:13:40
PV15	61	6.63	146	19.45	197	21	Sep	2016	17:26:42
PV16	61	5.88	146	19.46	186	21	Sep	2016	17:44:14
PV17	61	5.4	146	19.44	118	21	Sep	2016	17:57:16

Run B

PV1	61	7.23	146	27.83	235	21	Sep	2016	21:34:13
PV2	61	6.61	146	27.89	234	21	Sep	2016	21:50:45
PV3	61	5.82	146	27.8	233	21	Sep	2016	22:08:03
PV4	61	5.1	146	27.78	219	21	Sep	2016	22:24:59
PV8	61	7.24	146	23.52	200	22	Sep	2016	23:50:00
PV9a	61	6.79	146	23.53	230	22	Sep	2016	0:01:00
PV9b	61	6.27	146	23.53	230	22	Sep	2016	0:15:00
PV10	61	5.72	146	23.69	231	22	Sep	2016	0:30:09
PV14	61	7.13	146	19.48	140	22	Sep	2016	1:49:36
PV15	61	6.6	146	19.49	196	22	Sep	2016	2:05:16
PV16	61	5.85	146	19.51	180	22	Sep	2016	2:21:43
PV17	61	5.41	146	19.49	130	22	Sep	2016	2:37:14

Run C

PV17	61	5.43	146	19.36	114	22	Sep	2016	12:37:32
PV16	61	5.94	146	19.49	186	22	Sep	2016	12:51:20
PV15	61	6.59	146	19.45	196	22	Sep	2016	13:06:06
PV14	61	7.17	146	19.4	120	22	Sep	2016	13:19:33
PV10	61	5.86	146	23.53	230	22	Sep	2016	14:28:43
PV9b	61	6.22	146	23.56	232	22	Sep	2016	14:40:16
PV9a	61	6.71	146	23.54	231	22	Sep	2016	14:53:45
PV8	61	7.25	146	23.45	201	22	Sep	2016	15:08:50
PV5	61	7.3	146	26.05	145	22	Sep	2016	15:58:54
PV6	61	6.58	146	26.08	236	22	Sep	2016	16:14:24
PV7	61	5.82	146	26.19	236	22	Sep	2016	16:33:41

Run D

	latitude		*longitude*		*depth*				
Station	*deg.*	*min.*	*deg.*	*min.*	*(m)*	*day*	*month*	*year*	*time*
PV1	61	7.24	146	27.91	230	23	Sep	2016	13:34:33
PV2	61	6.6	146	27.93	235	23	Sep	2016	13:49:42
PV3	61	5.82	146	27.73	234	23	Sep	2016	14:08:14
PV4	61	5.13	146	27.69	214	23	Sep	2016	14:26:02
PV8	61	7.19	146	23.42	220	23	Sep	2016	15:49:48
PV9a	61	6.74	146	23.53	230	23	Sep	2016	16:02:04
PV9b	61	6.22	146	23.51	232	23	Sep	2016	16:15:36
PV10	61	5.74	146	23.41	232	23	Sep	2016	16:29:28
PV14	61	7.16	146	19.39	128	23	Sep	2016	17:40:48
PV15	61	6.61	146	19.47	197	23	Sep	2016	17:52:04
PV16	61	5.85	146	19.39	184	23	Sep	2016	18:07:38
PV17	61	5.4	146	19.42	119	23	Sep	2016	18:21:17

Run E

PV1	61	7.23	146	27.97	236	24	Sep	2016	8:29:50
PV2	61	6.6	146	27.85	236	24	Sep	2016	8:48:28
PV3	61	5.79	146	27.83	235	24	Sep	2016	9:04:49
PV4	61	5.1	146	27.83	219	24	Sep	2016	9:18:38
PV8	61	7.2	146	23.52	219	24	Sep	2016	10:31:04
PV9a	61	6.77	146	23.6	231	24	Sep	2016	10:42:58
PV9b	61	6.25	146	23.57	232	24	Sep	2016	10:57:53
PV10	61	5.75	146	23.54	232	24	Sep	2016	11:12:20
PV14	61	7.15	146	19.43	132	24	Sep	2016	12:26:19
PV15	61	6.61	146	19.48	196	24	Sep	2016	12:38:19
PV16	61	5.87	146	19.44	182	24	Sep	2016	12:55:23
PV17	61	5.4	146	19.44	117	24	Sep	2016	13:08:51

Run F

PV1	61	7.25	146	27.79	216	24	Sep	2016	16:15:46
PV2	61	6.61	146	27.84	235	24	Sep	2016	16:28:29
PV3	61	5.8	146	27.8	234	24	Sep	2016	16:43:01
PV4	61	5.09	146	27.78	216	24	Sep	2016	16:56:48
PV8	61	7.21	146	23.41	218	24	Sep	2016	17:35:09
PV9a	61	6.78	146	23.48	231	24	Sep	2016	17:45:57
PV9b	61	6.27	146	23.51	232	24	Sep	2016	17:57:28
PV10	61	5.76	146	23.47	232	24	Sep	2016	18:10:44
PV14	61	7.16	146	19.41	117	24	Sep	2016	18:43:00
PV15	61	6.62	146	19.48	196	24	Sep	2016	18:53:00
PV16	61	5.89	146	19.44	184	24	Sep	2016	19:05:40
PV17	61	5.42	146	19.44	128	24	Sep	2016	19:18:14

Run G

	latitude		*longitude*		*depth*				
Station	*deg.*	*min.*	*deg.*	*min.*	*(m)*	*day*	*month*	*year*	*time*
PV17	61	5.41	146	19.43	122	25	Sep	2016	9:12:48
PV16	61	5.89	146	19.44	184	25	Sep	2016	9:24:44
PV15	61	6.61	146	19.46	196	25	Sep	2016	9:38:45
PV14	61	7.18	146	19.55	117	25	Sep	2016	9:52:07
PV10	61	5.74	146	23.53	233	25	Sep	2016	10:51:57
PV9b	61	6.25	146	23.55	232	25	Sep	2016	11:14:49
PV9a	61	6.79	146	23.47	231	25	Sep	2016	11:28:59
PV8	61	7.24	146	23.69	215	25	Sep	2016	11:42:16
PV4	61	5.08	146	27.83	216	25	Sep	2016	13:09:50
PV3	61	5.81	146	27.8	234	25	Sep	2016	13:24:45
PV2	61	6.58	146	27.86	232	25	Sep	2016	13:38:56
PV1	61	7.29	146	27.8	200	25	Sep	2016	13:55:00
PV1	61	7.29	146	27.8	200	25	Sep	2016	13:55:00

Run H

PV17	61	5.43	146	19.45	145	25	Sep	2016	17:18:18
PV16	61	5.9	146	19.42	182	25	Sep	2016	17:29:02
PV15	61	6.57	146	19.48	199	25	Sep	2016	17:41:10
PV14	61	7.18	146	19.51	120	25	Sep	2016	17:54:17
PV10	61	5.77	146	23.51	232	25	Sep	2016	18:17:14
PV9b	61	6.27	146	23.56	231	25	Sep	2016	18:28:42
PV9a	61	6.78	146	23.51	230	25	Sep	2016	18:40:20
PV8	61	7.2	146	23.6	215	25	Sep	2016	18:50:36
PV4	61	5.09	146	27.82	218	25	Sep	2016	19:17:58
PV3	61	5.79	146	27.83	230	25	Sep	2016	19:30:26
PV2	61	6.58	146	27.87	235	25	Sep	2016	19:42:46
PV1	61	7.29	146	27.82	205	25	Sep	2016	19:53:59

MARCH 2017:

Run A\B

PV4a	61	5.08	146	27.78	211	21	Mar	2017	12:31:08
PV3	61	5.77	146	27.92	235	21	Mar	2017	12:53:08
PV8	61	7.26	146	23.79	210	21	Mar	2017	15:47:52
PV14	61	7.13	146	19.48	140	21	Mar	2017	17:37:51
PV16	61	5.92	146	19.54	188	21	Mar	2017	18:14:16
PV17	61	5.43	146	19.39	124	21	Mar	2017	18:30:08
PV4b	61	5.08	146	27.79	218	23	Mar	2017	12:55:18
PV1	61	7.29	146	27.77	215	23	Mar	2017	13:44:15

Run C

	latitude		*longitude*		*depth*				
Station	*deg.*	*min.*	*deg.*	*min.*	*(m)*	*day*	*month*	*year*	*time*
PV17	61	5.42	146	19.54	125	24	Mar	2017	8:33:01
PV16	61	5.9	146	19.43	183	24	Mar	2017	8:50:07
PV15	61	6.68	146	19.47	198	24	Mar	2017	9:05:51
PV14	61	7.2	146	19.42	100	24	Mar	2017	9:19:18
PV9b	61	6.31	146	23.44	233	24	Mar	2017	10:31:07
PV9a	61	6.8	146	23.51	232	24	Mar	2017	10:43:26
PV8	61	7.3	146	23.57	121	24	Mar	2017	10:56:22
PV4	61	5.09	146	27.94	220	24	Mar	2017	12:27:27
PV3	61	5.79	146	27.85	236	24	Mar	2017	12:43:58
PV2	61	6.63	146	27.77	237	24	Mar	2017	13:01:49
PV1	61	7.3	146	27.8	189	24	Mar	2017	13:17:08

Run D

PV17	61	5.41	146	19.49	128	25	Mar	2017	8:01:09
PV15a	61	6.28	146	19.45	199	25	Mar	2017	8:20:02
PV14	61	7.2	146	19.41	95	25	Mar	2017	8:38:32
PV9b	61	6.19	146	23.69	234	25	Mar	2017	9:59:32
PV9a	61	6.77	146	23.54	232	25	Mar	2017	10:17:46
PV8	61	7.27	146	23.55	217	25	Mar	2017	10:31:22
PV2a	61	6.21	146	27.79	238	25	Mar	2017	12:42:48
PV1	61	7.27	146	27.82	220	25	Mar	2017	13:06:59

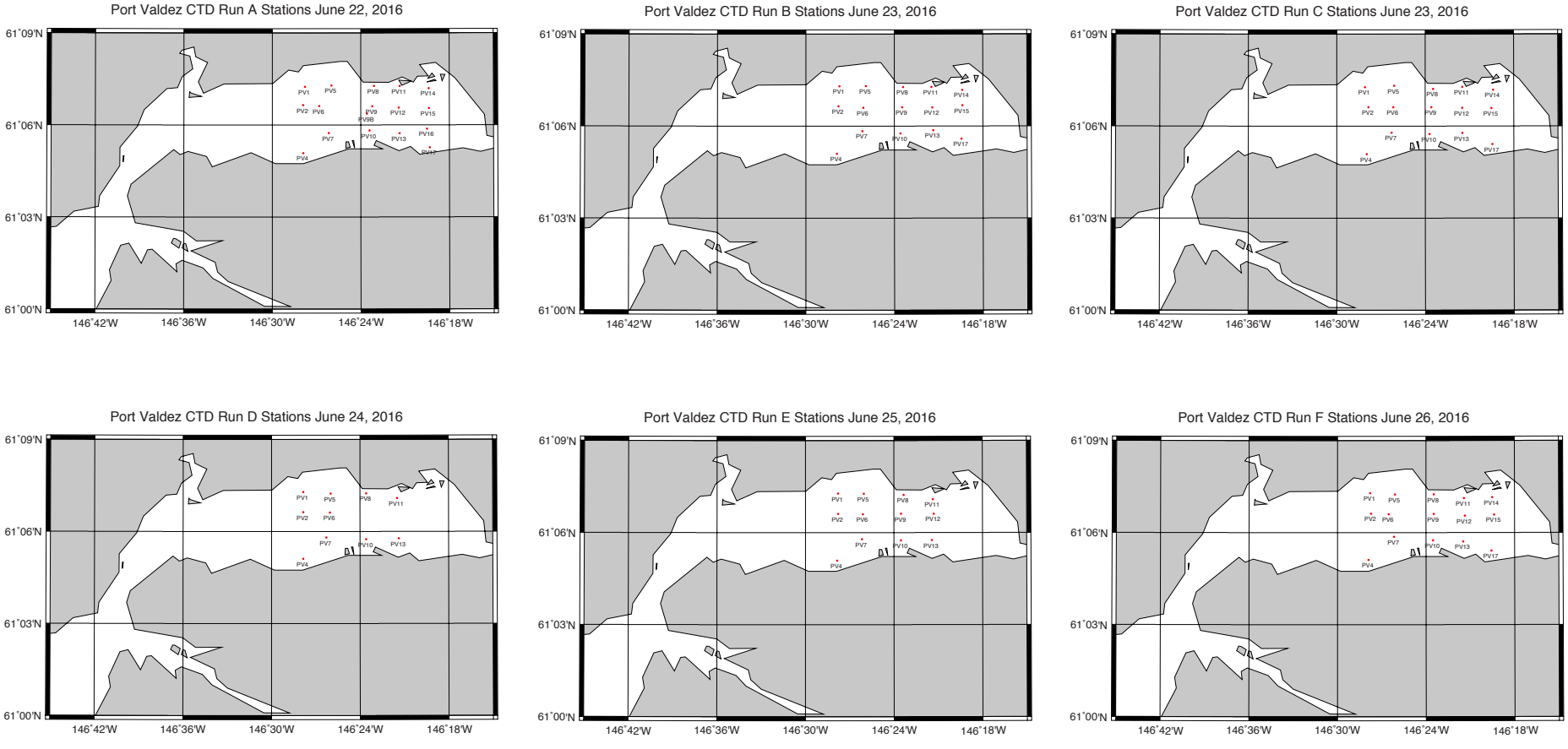

Appendix A (cont.). Locations of oceanographic stations where temperature and salinity were measured in June, 2016.

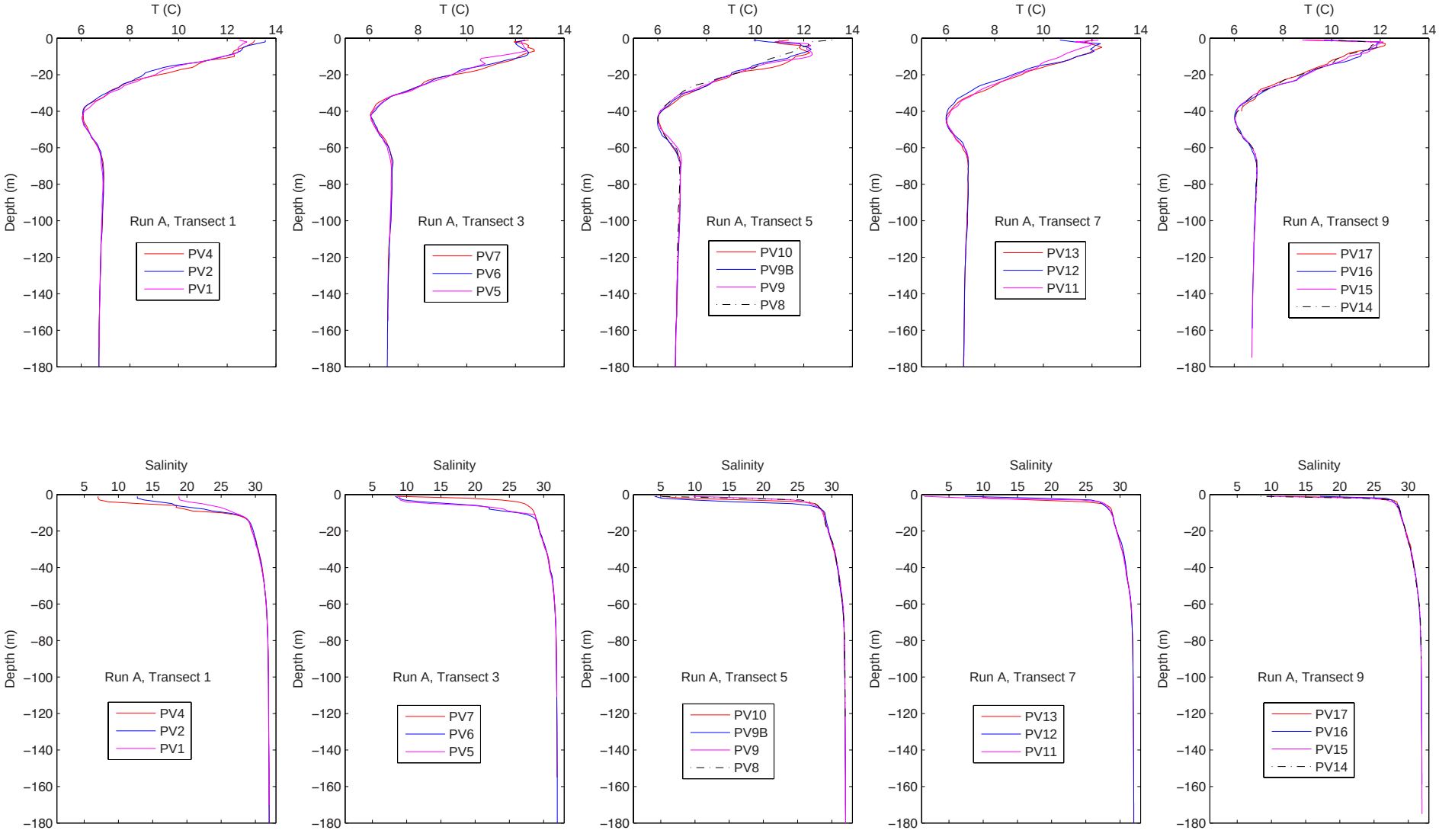

Appendix A (cont.). Temperature and salinity profiles on June 22, 2016 for CTD set A, flood tide 1/ebb tide 1 from 1245 to 1820*hrs*. Transects show cross-channel (north-south) stations, running west to east from the central to the inner fjord basin.

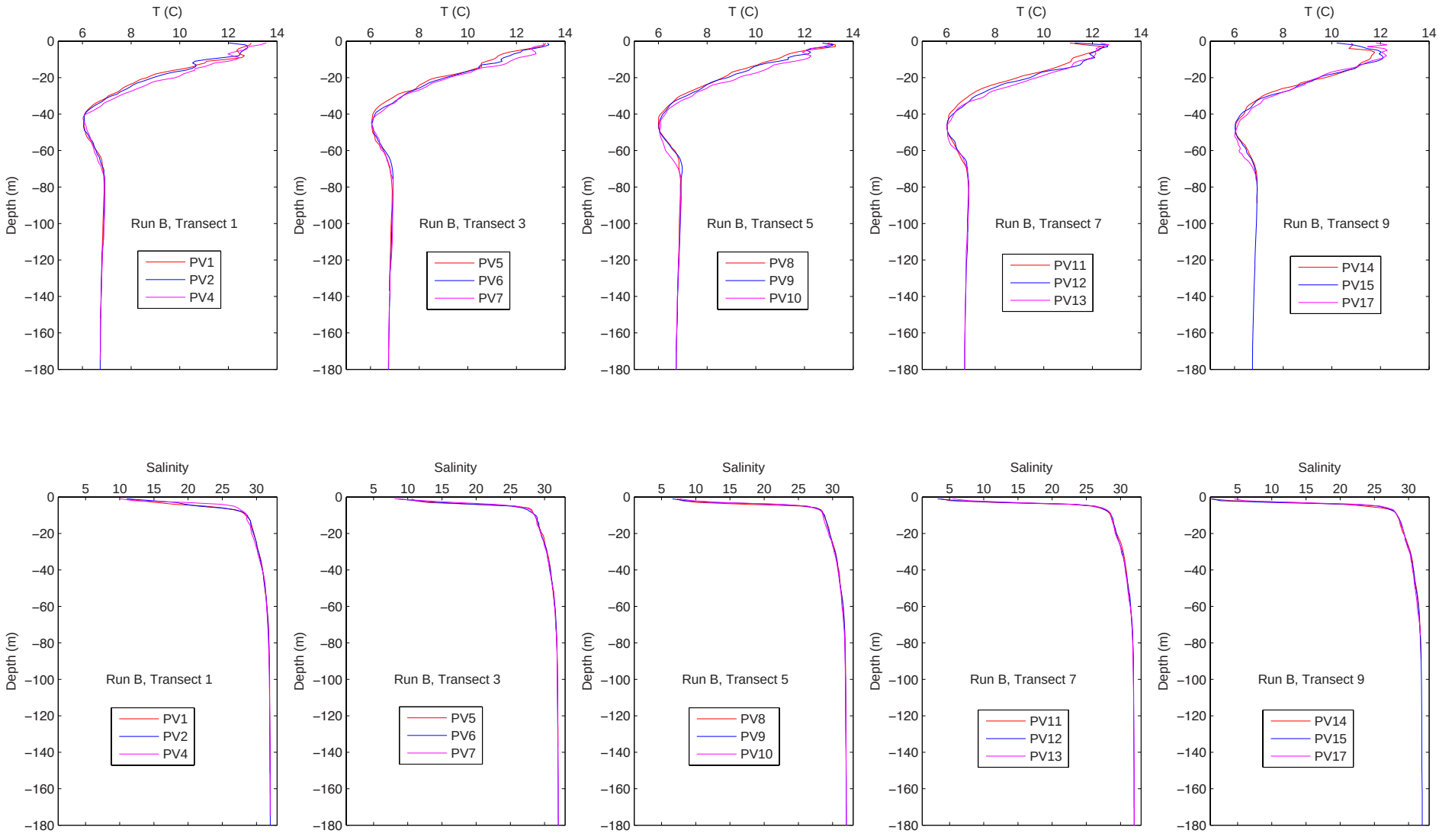

Appendix A (cont.). Temperature and salinity profiles on June 23, 2016 for CTD set B, flood tide 2/ebb tide 2 from 0036 to 0513*hrs*. Transects show cross-channel (north-south) stations, running west to east from the central to the inner fjord basin.

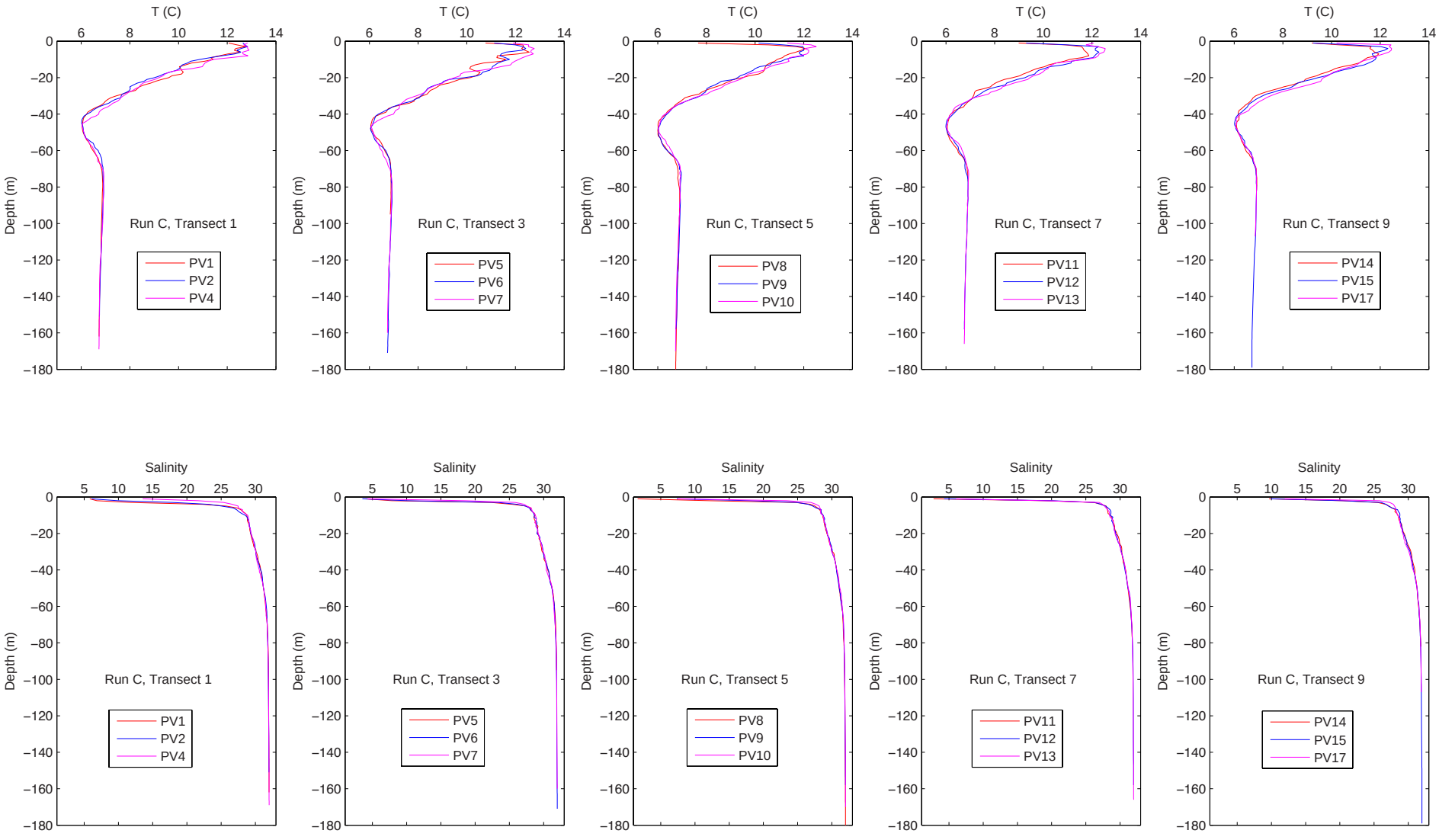

Appendix A (cont.). Temperature and salinity profiles on June 23, 2016 for CTD set C, ebb tide 2/flood tide 3 from 0811 to 1228*hrs*. Transects show cross-channel (north-south) stations, running west to east from the central to the inner fjord basin.

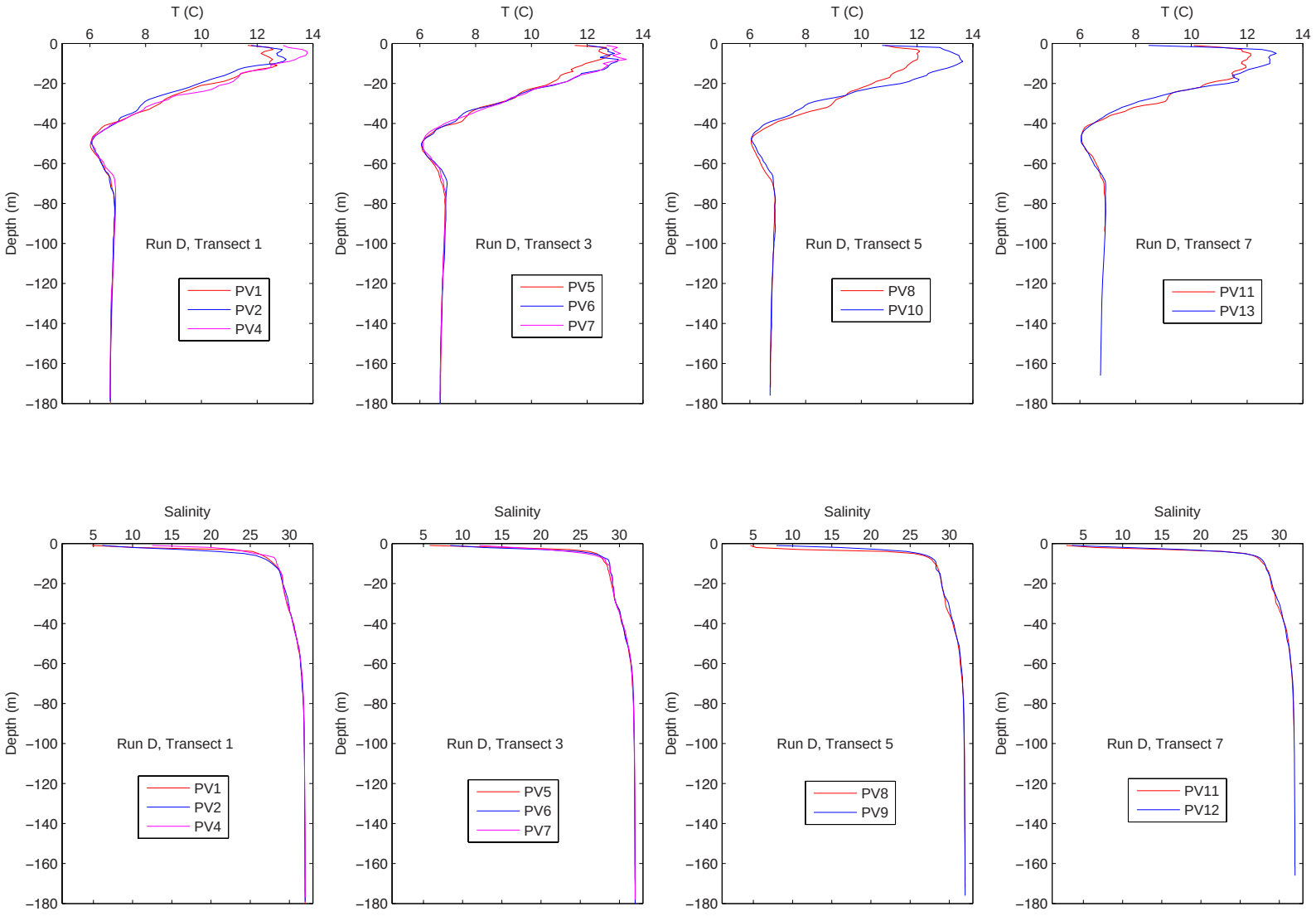

Appendix A (cont.). Temperature and salinity profiles on June 24, 2016 for CTD set D, flood tide 5/ebb tide 5 from 1650 to 2045*hrs*. Transects show cross-channel (north-south) stations, running west to east from the central to the inner fjord basin.

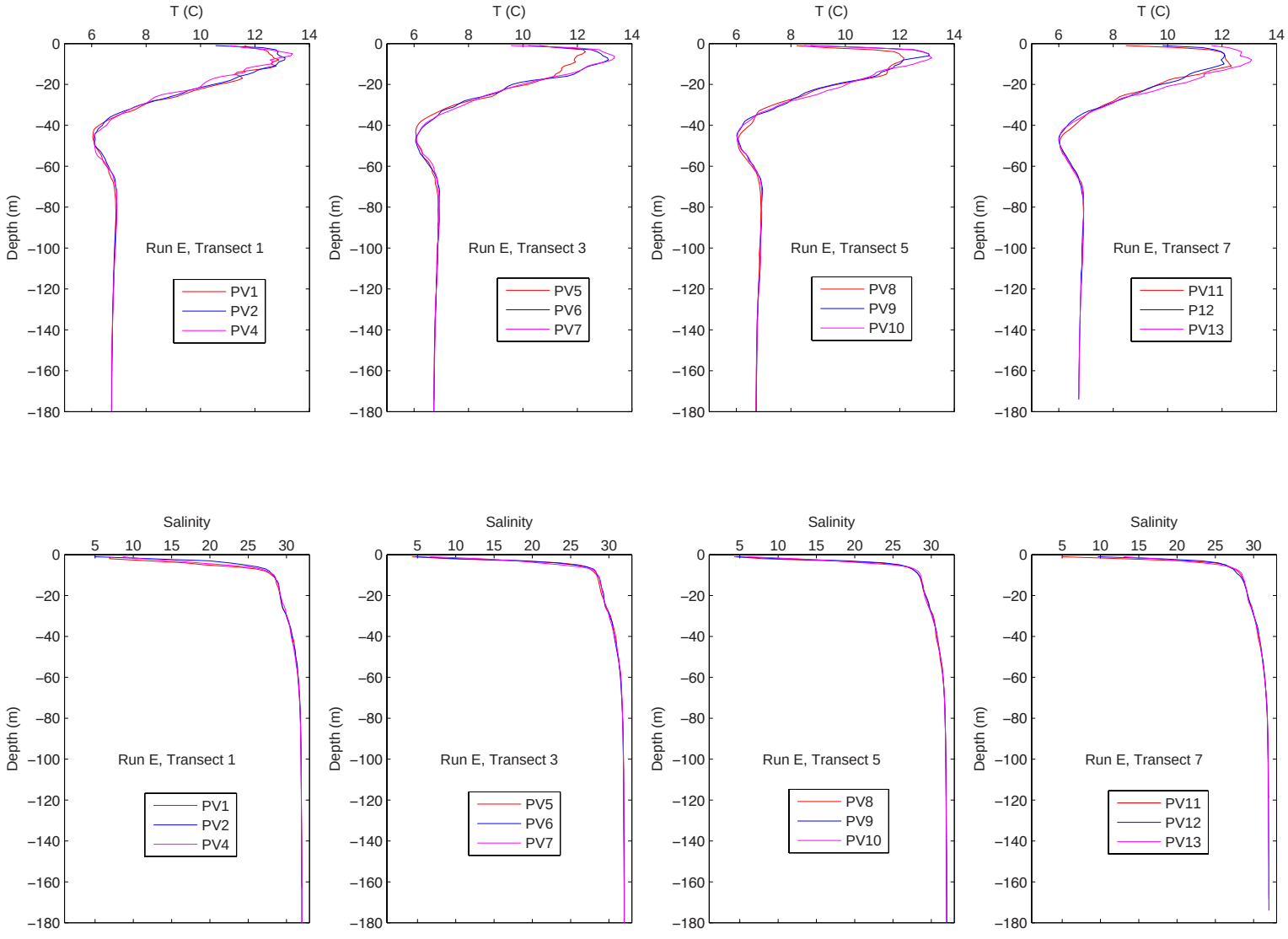

Appendix A (cont.). Temperature and salinity profiles on June 25, 2016 for CTD set E, flood tide 5/ebb tide 5 from 1129 to 1806*hrs*. Transects show cross-channel (north-south) stations, running west to east from the central to the inner fjord basin.

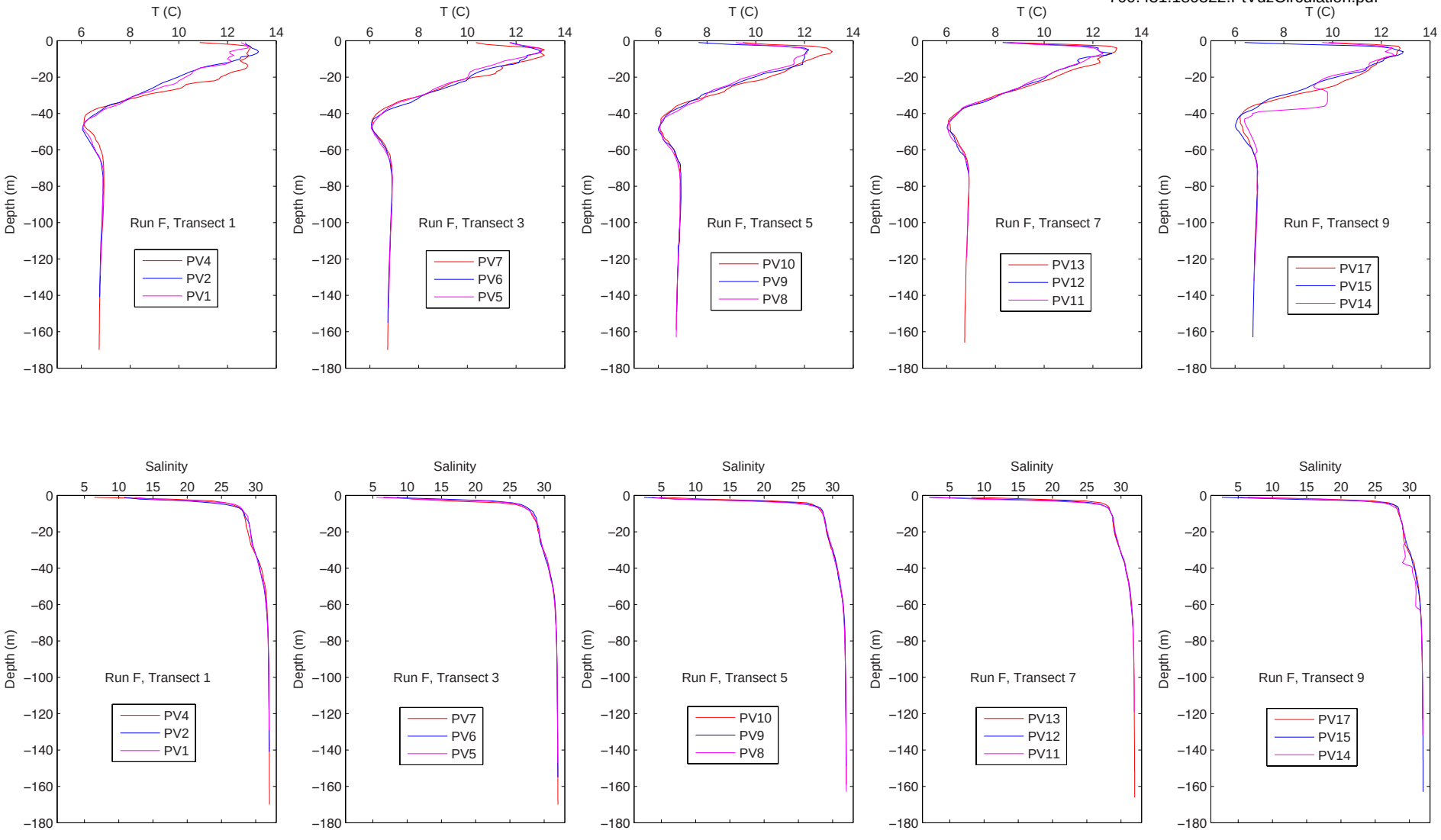

Appendix A (cont.). Temperature and salinity profiles on June 26, 2016 for CTD set F, flood tide 9 from 1214 to 1859*hrs*. Transects show cross-channel (north-south) stations, running west to east from the central to the inner fjord basin.

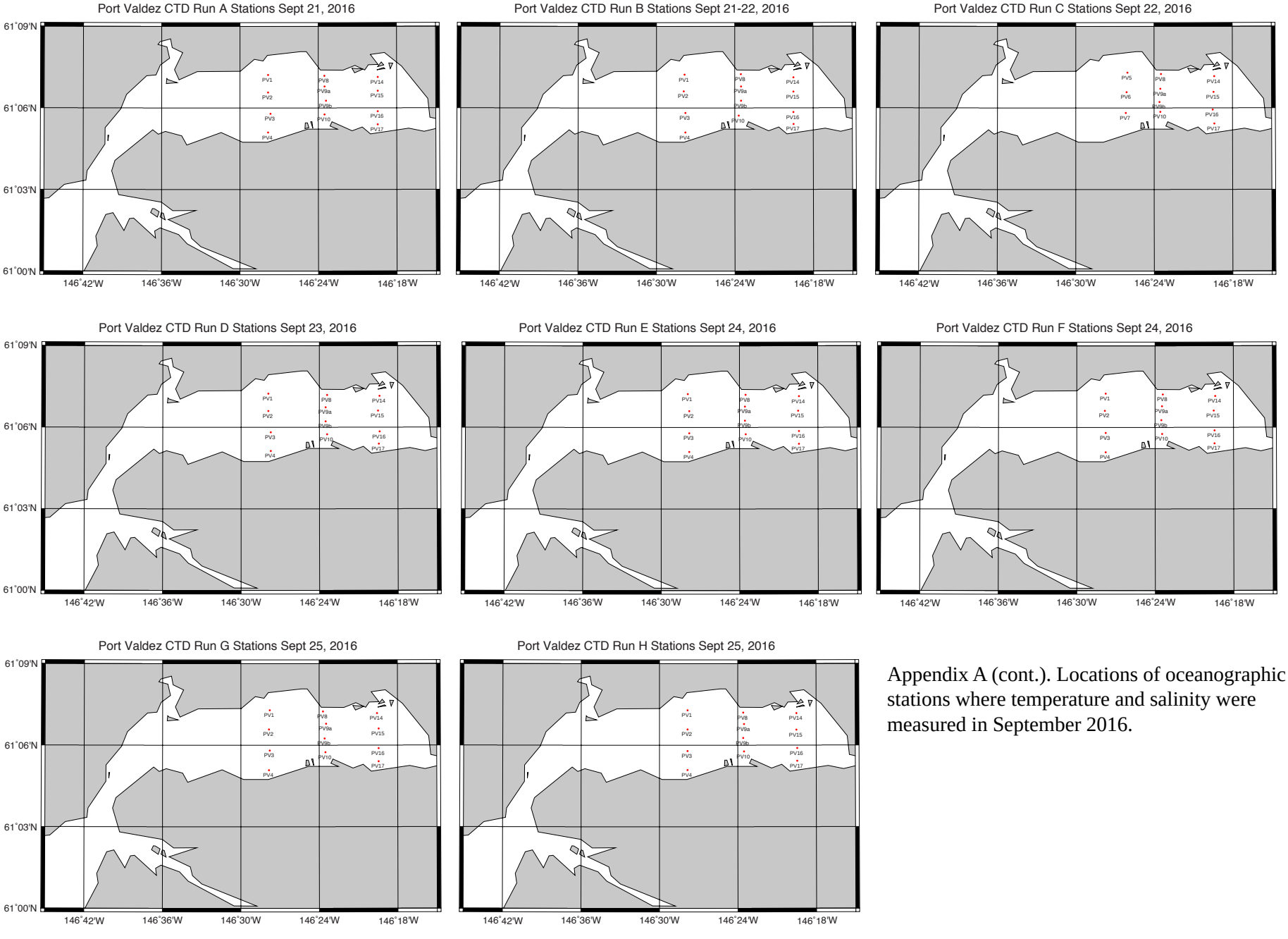

Appendix A (cont.). Locations of oceanographic stations where temperature and salinity were measured in September 2016.

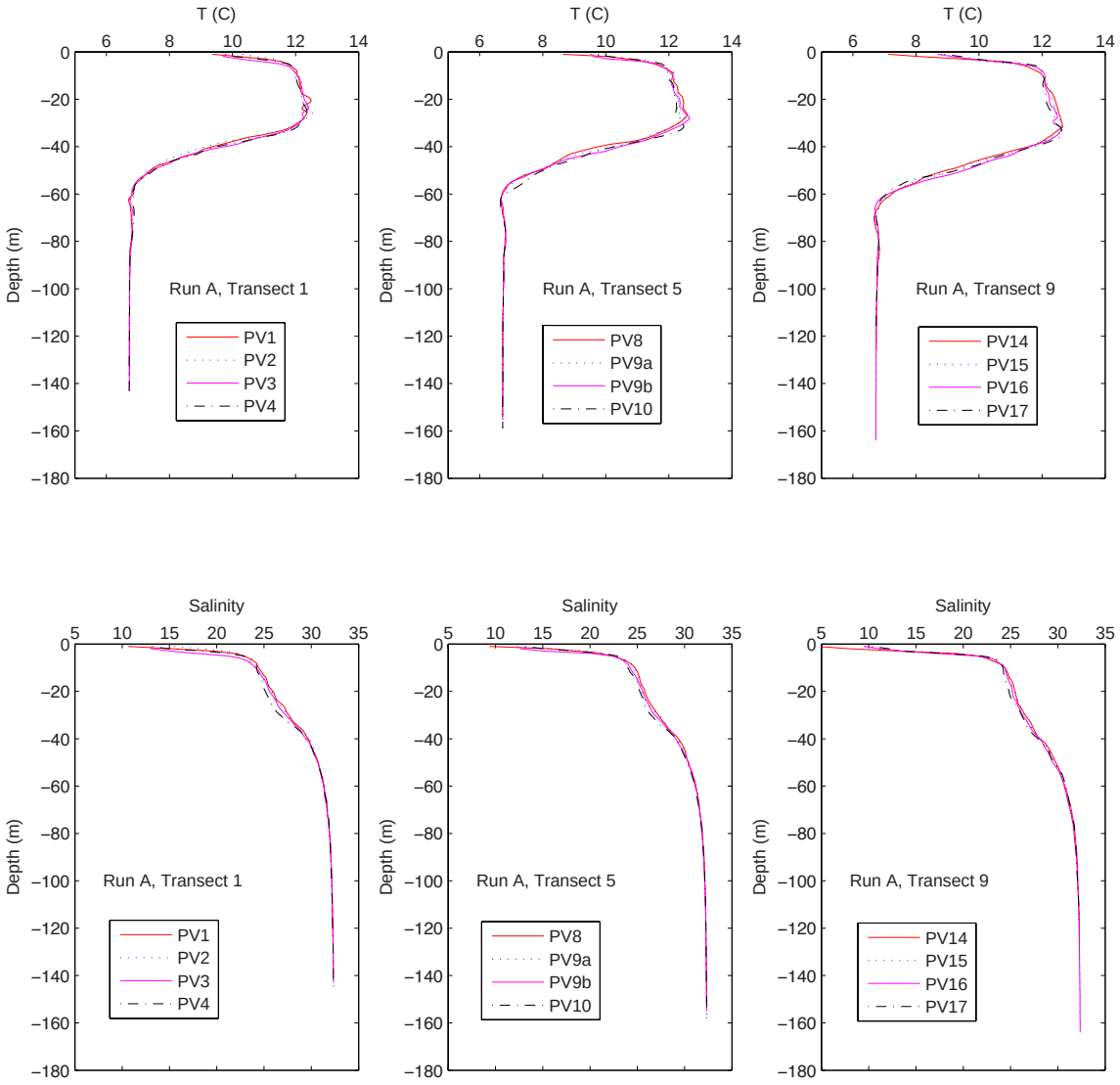

Appendix A (cont.). Temperature and salinity profiles on September 21, 2016 for CTD set A, flood tide 1/ebb tide 2 from 1257 to 1802*hrs*. Transects show cross-channel (north-south) stations, running west to east from the central to the inner fjord basin.

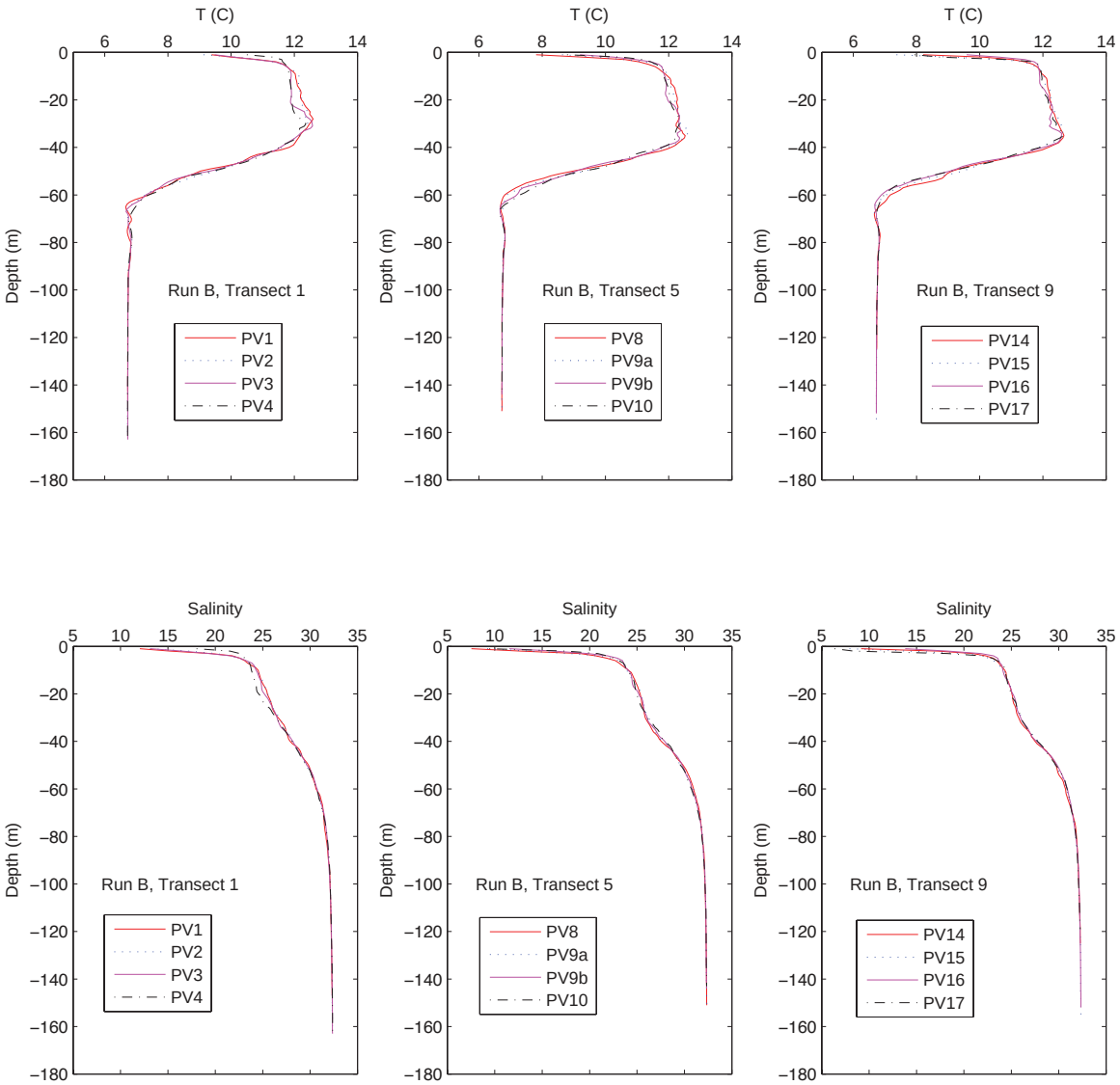

Appendix A (cont.). Temperature and salinity profiles on September 21-22, 2016 for CTD set B, ebb tide 2/flood tide 2 from 2142-0234*hrs*. Transects show cross-channel (north-south) stations, running west to east from the central to the inner fjord basin.

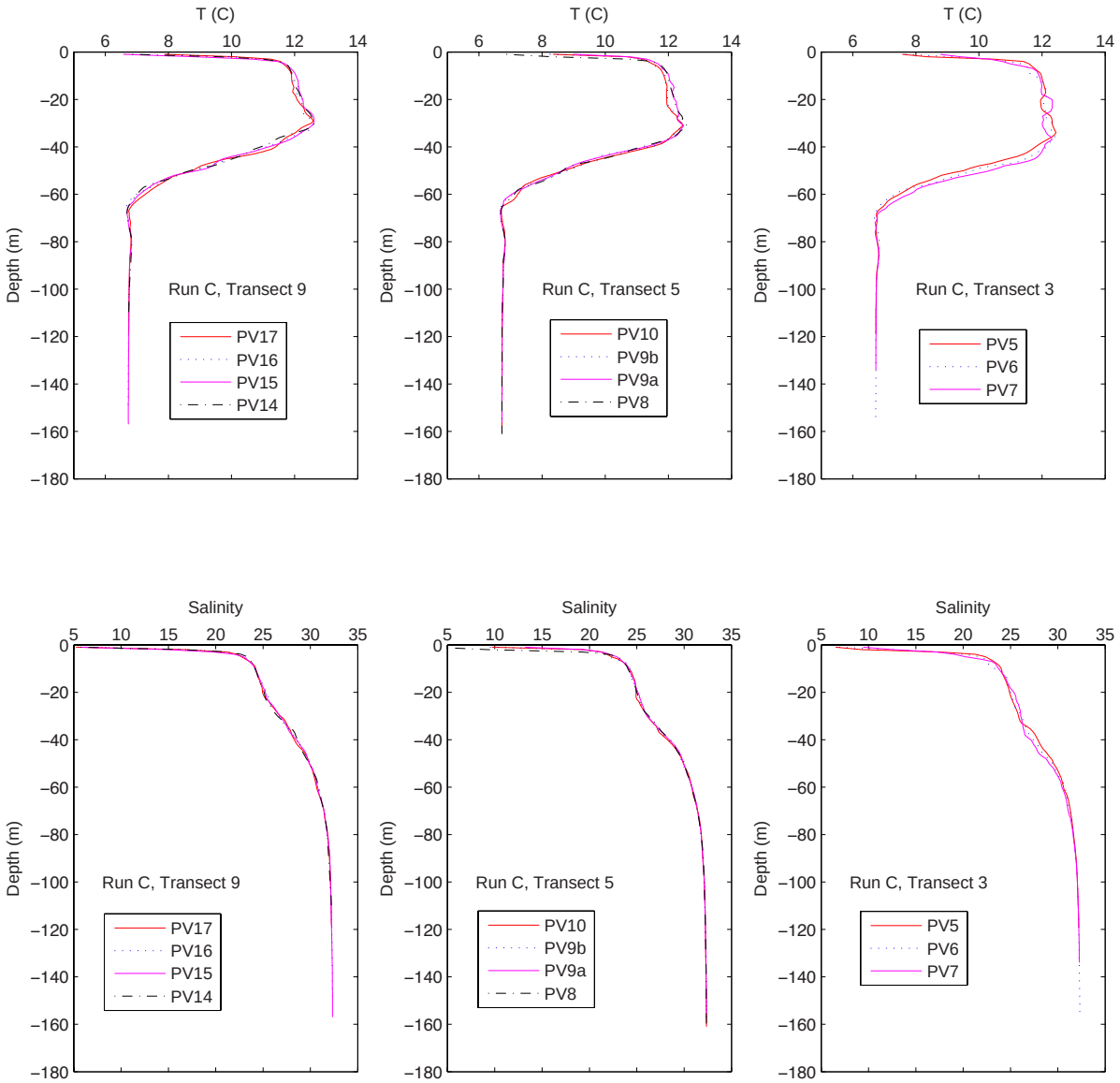

Appendix A (cont.). Temperature and salinity profiles on September 22, 2016 for CTD set C, flood tide 3 from 1244 to 1629*hrs*. Transects for set C show cross-channel (north-south) stations, running east to west from the inner fjord to the central basin, but ending on transect #3 instead of #1. Set D is a partial run lacking transect #1 and runs west to east.

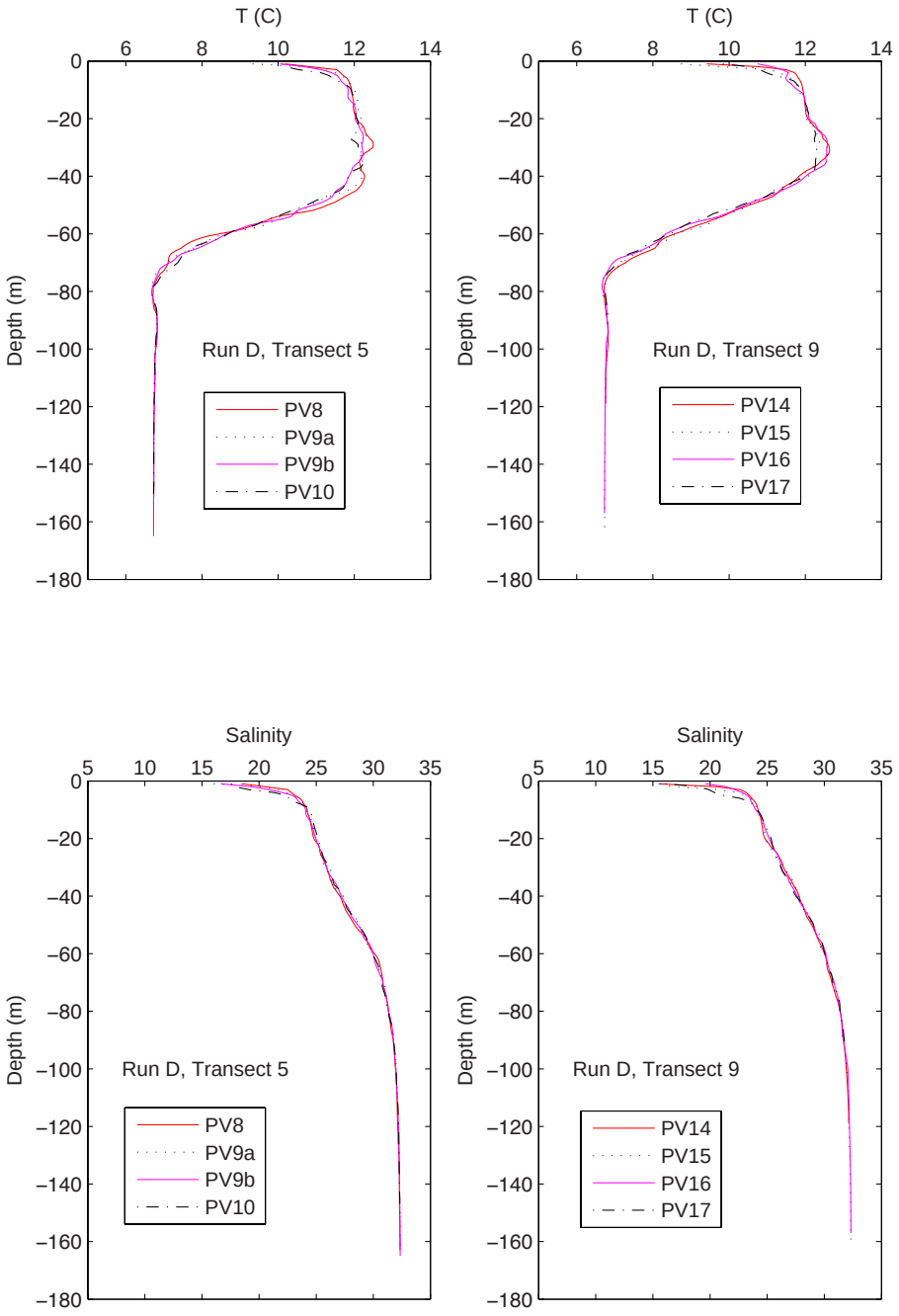

Appendix A (cont.). Temperature and salinity profiles on September 23, 2016 for CTD set D, flood tide 5 from 1332-1819*hrs*. This set is a partial run that lacks transect #1 and runs west to east.

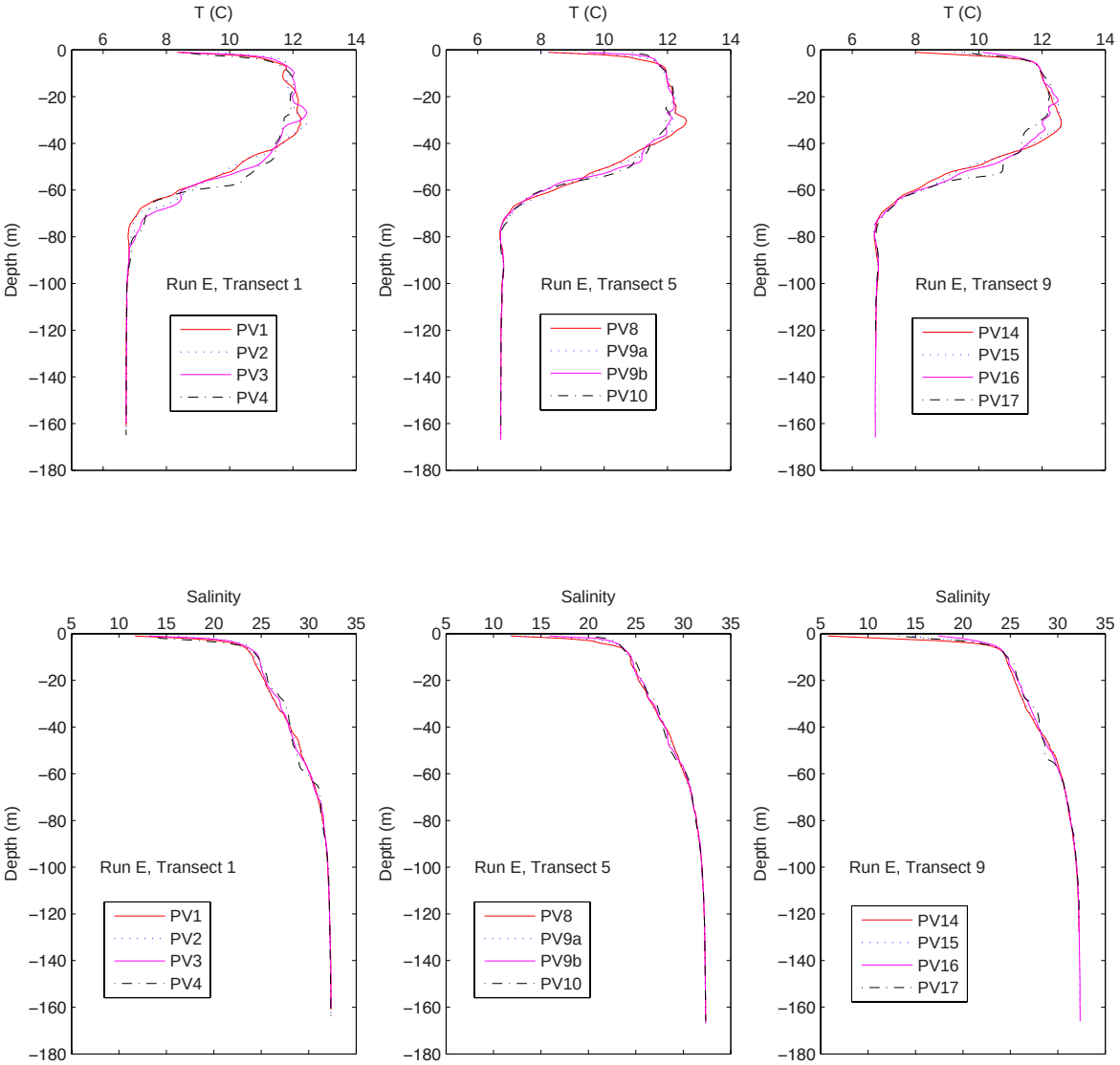

Appendix A (cont.). Temperature and salinity profiles on September 24, 2016 for CTD set E, flood tide 6/ebb tide 7 from 0838 to 1308*hrs*. Transects show cross-channel (north-south) stations, running west to east from the central to the inner fjord basin.

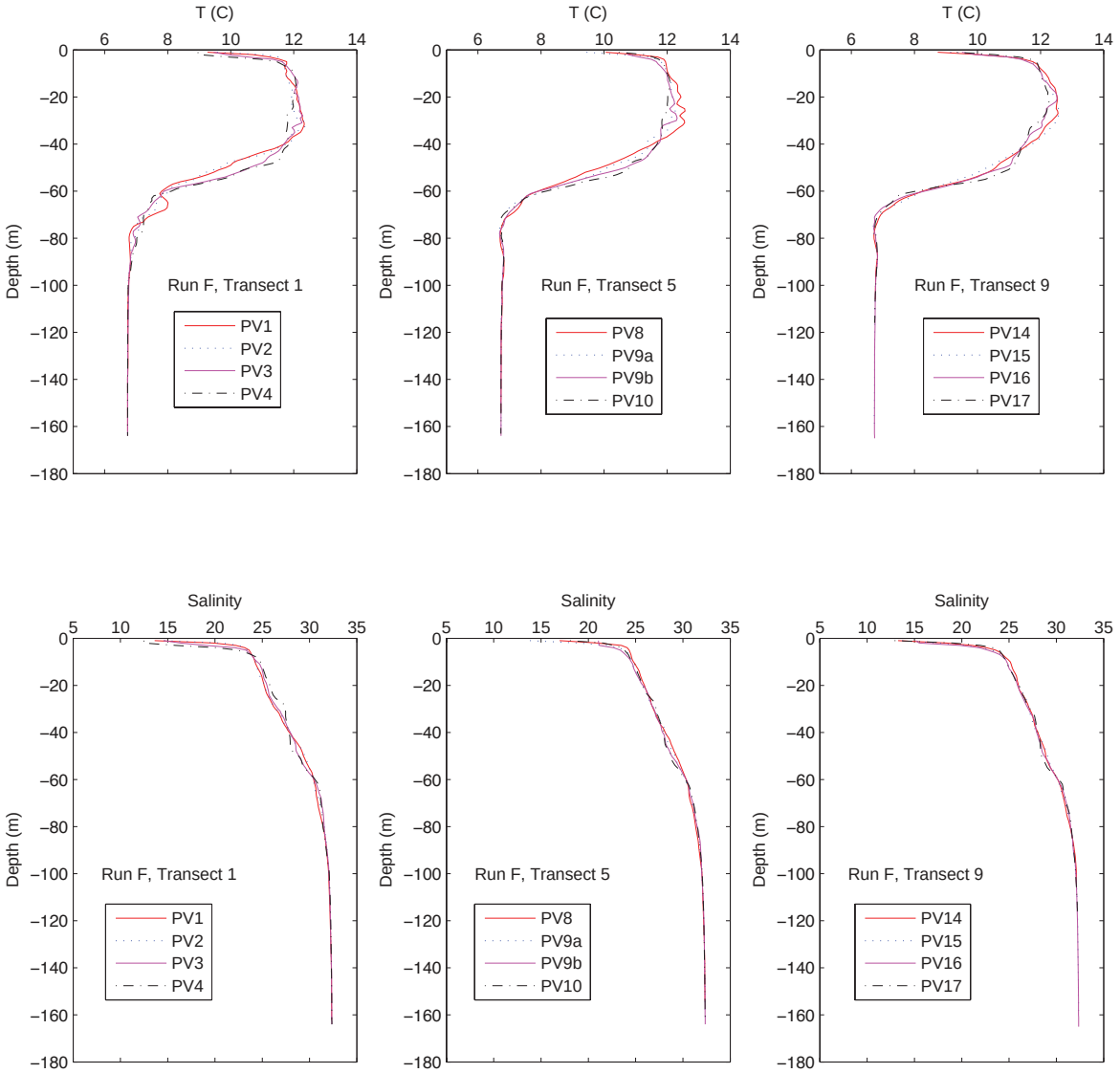

Appendix A (cont.). Temperature and salinity profiles on September 24, 2016 for CTD set F, ebb tide 7/flood tide 7 from 1314-1613*hrs*. Transects show cross-channel (north-south) stations, running west to east from the central to the inner fjord basin.

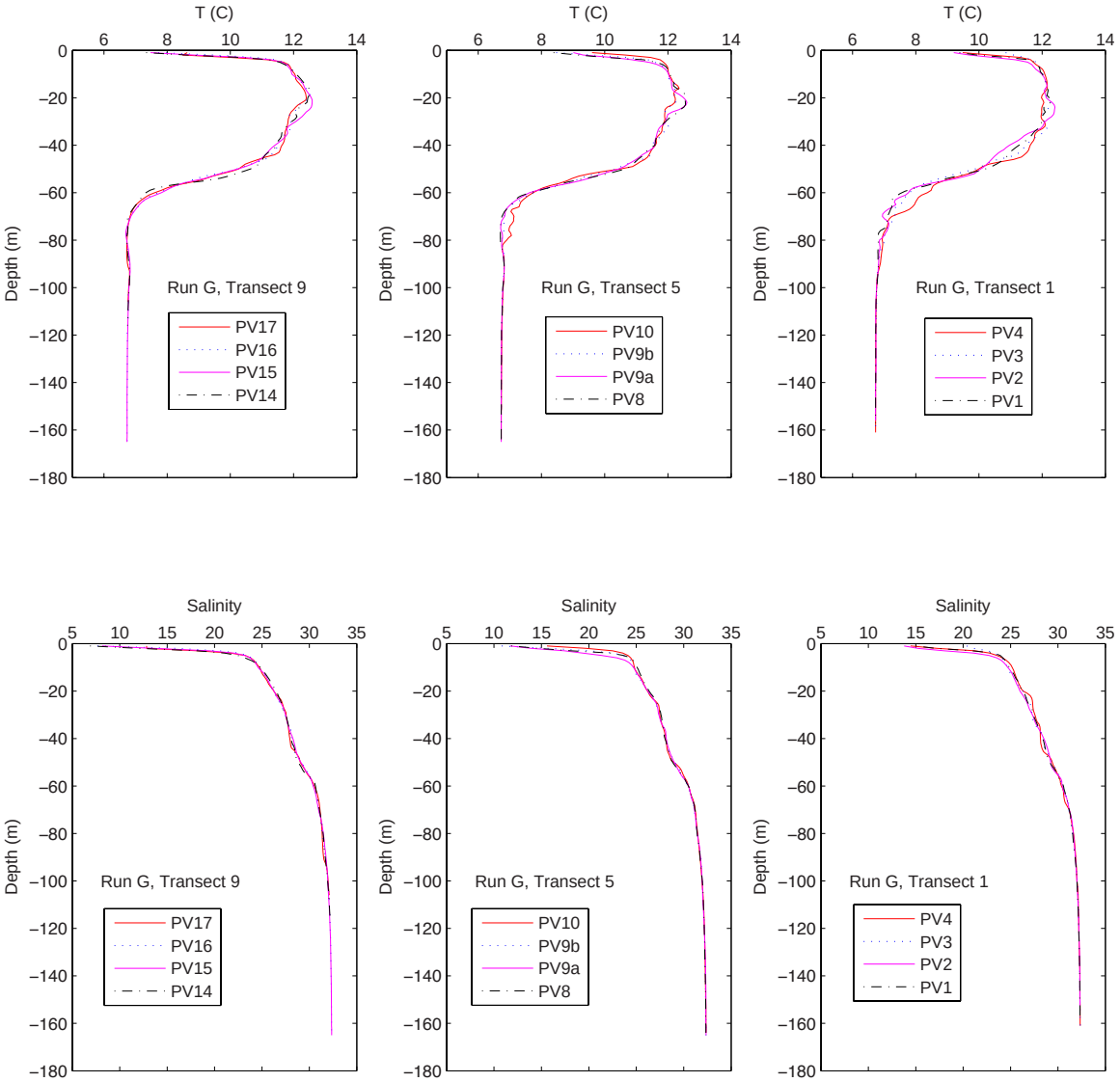

Appendix A (cont.). Temperature and salinity profiles on September 25, 2016 for CTD set G, flood tide 8/ebb tide 9 from 0917 to 1352*hrs.* Transects show cross-channel (north-south) stations, running east to west from the inner fjord to the central basin.

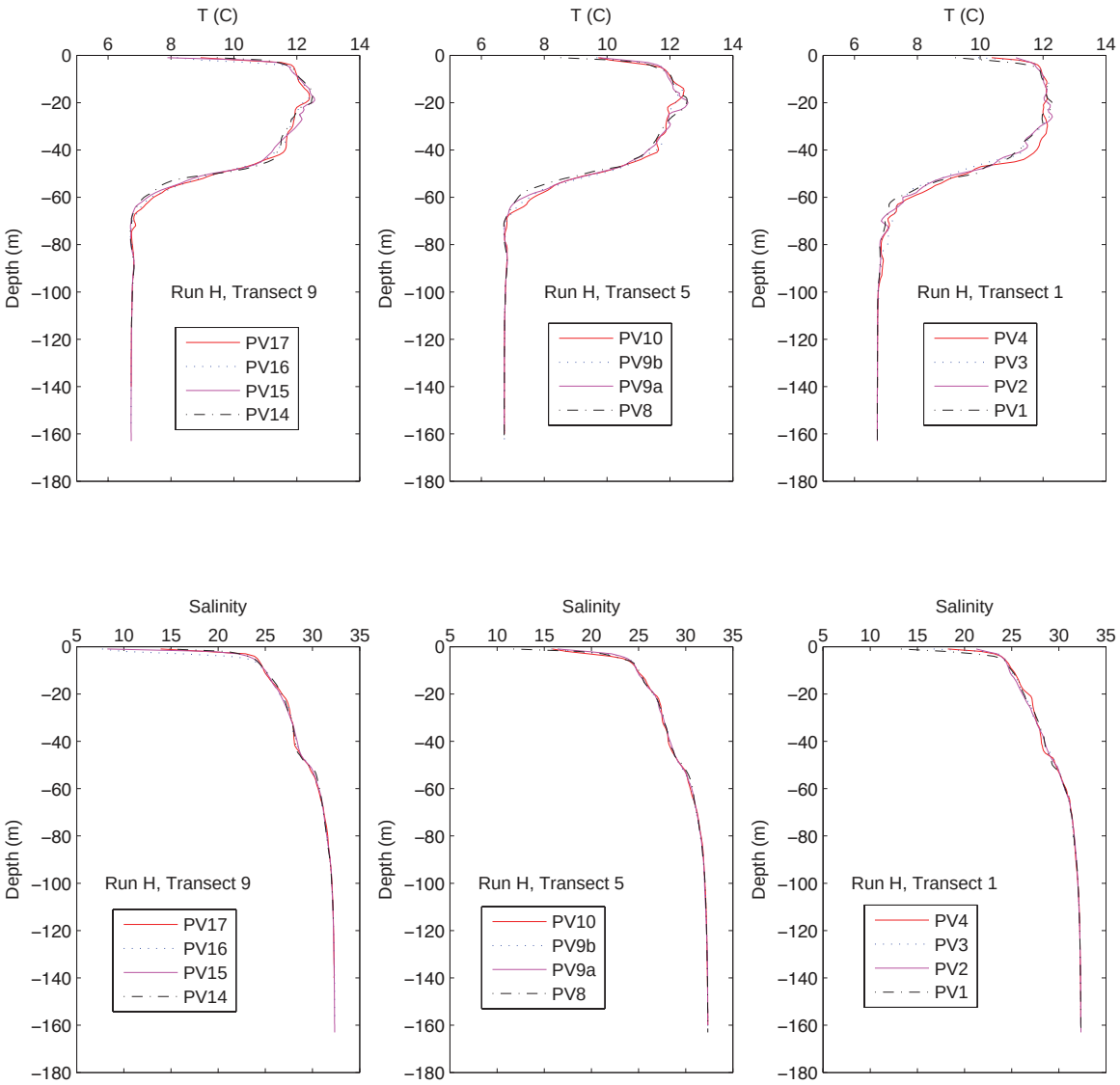

Appendix A (cont.). Temperature and salinity profiles on September 25, 2016 for CTD set H, ebb tide 9/flood tide 9 from 1410-1717*hrs*. Transects show cross-channel (north-south) stations, running east to west from the inner fjord to the central basin.

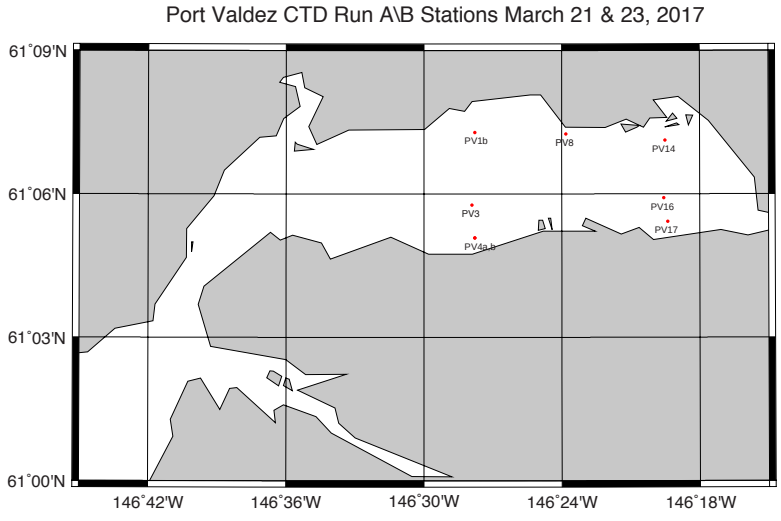

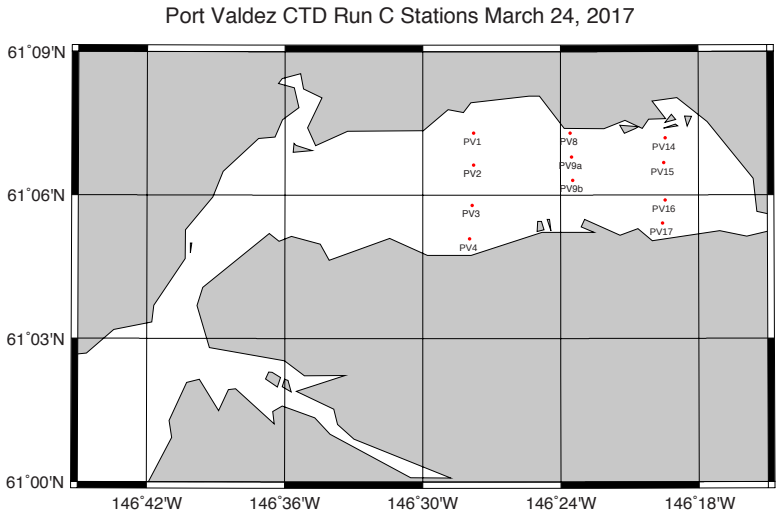

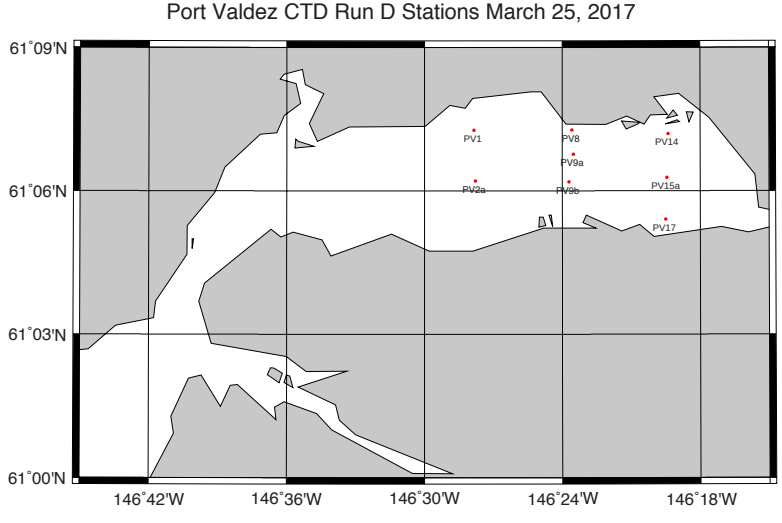

Appendix A (cont.). Locations of oceanographic stations where temperature and salinity were measured in March, 2017.

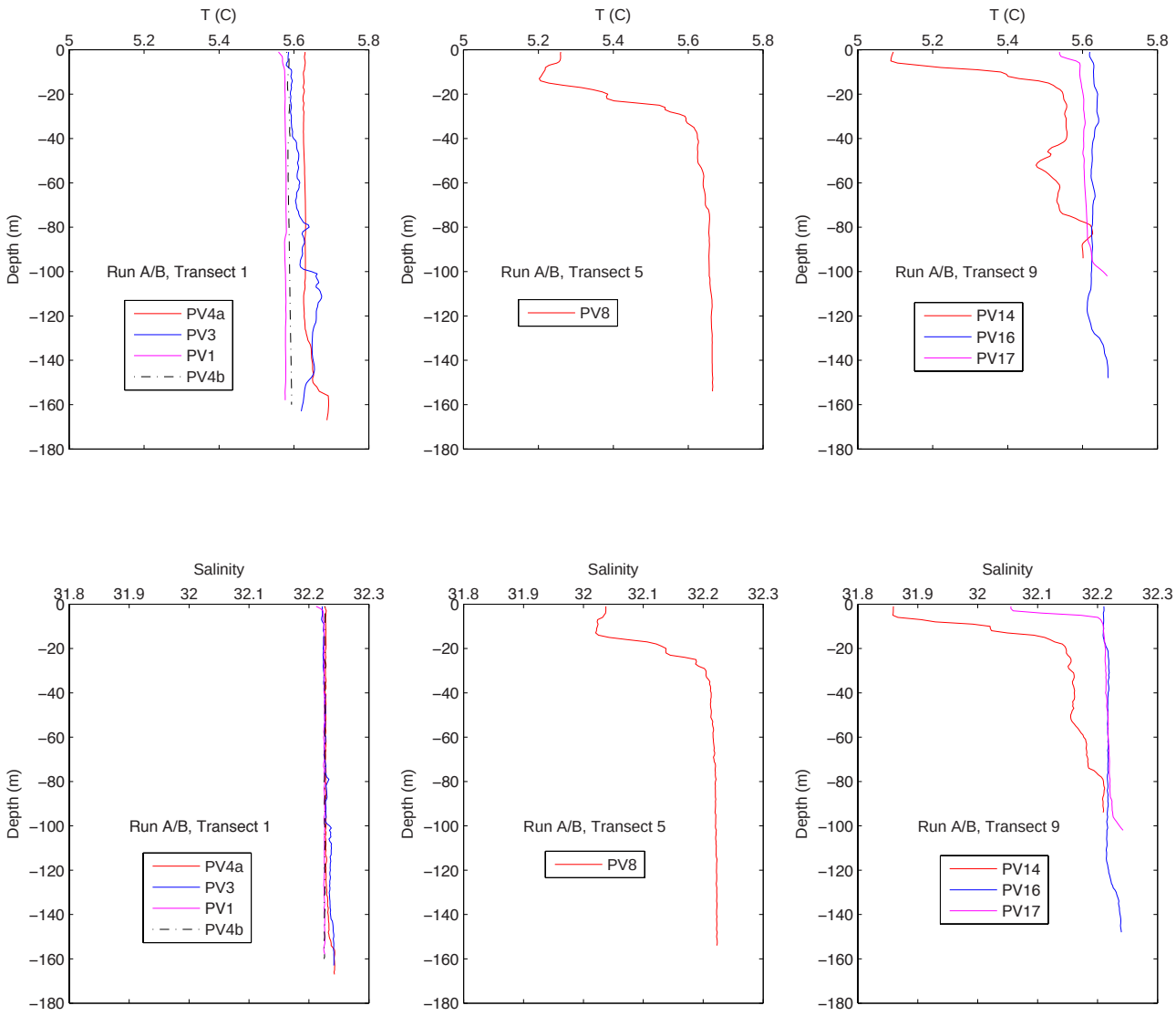

Appendix A (cont.). Temperature and salinity profiles for CTD set A, ebb tide 1/flood tide 1 at 1330 to 1828*hrs* on March 21 and station PV4b, at 1255*hrs* on March 23, 2017. Transects show cross-channel (north-south) stations, running west to east from the central to the inner fjord basin.

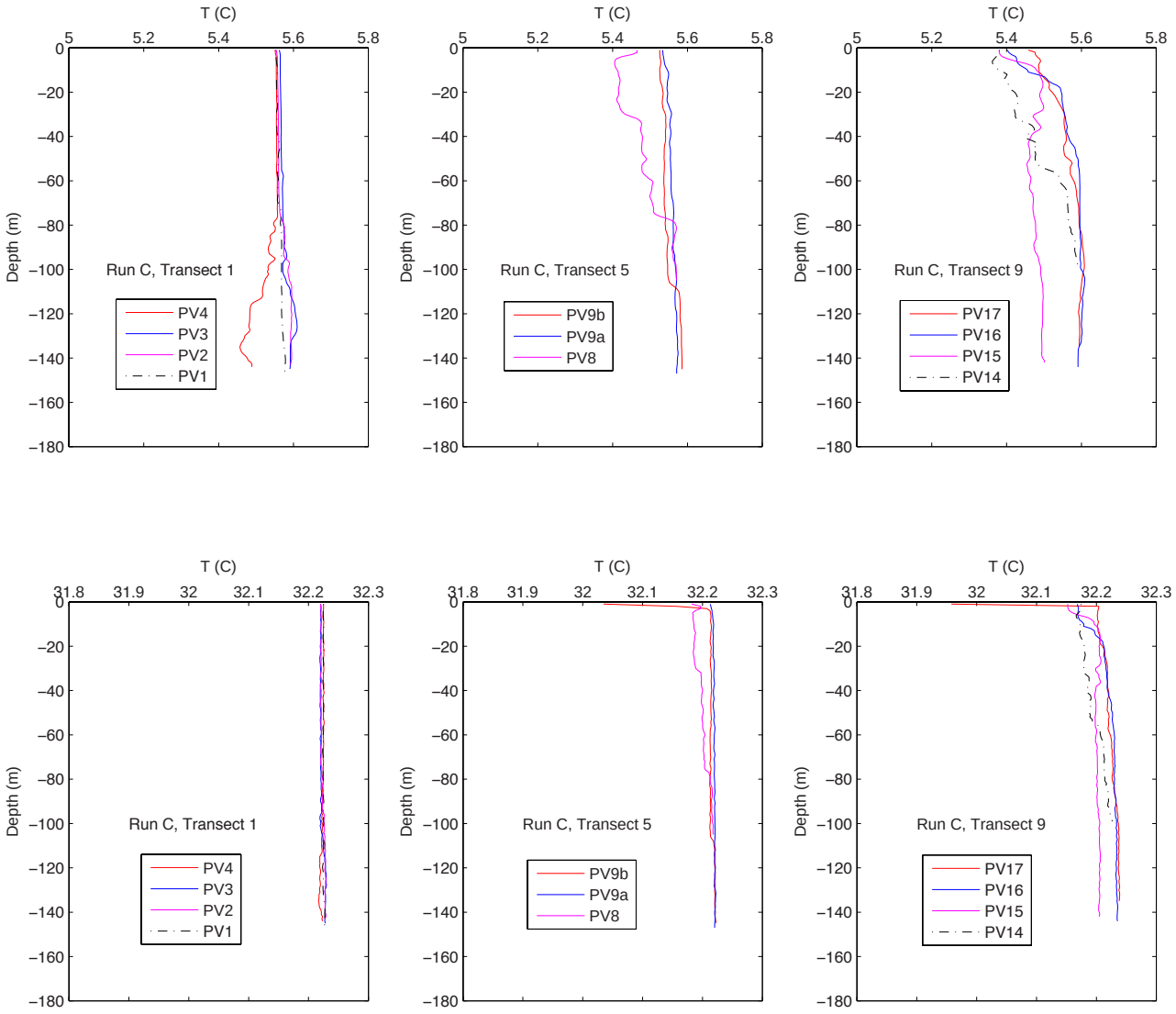

Appendix A (cont.). Temperature and salinity profiles for CTD set C, flood tide 6/ebb tide 7 at 0835 to 1320*hrs* on March 24, 2017. Transects show cross-channel (north-south) stations, running west to east from the central to the inner fjord basin.

Appendix B: Lists of ADCP transect parameters and plots of along-channel (u) velocities and horizontal vectors not shown in the text.

JUNE 2016:

Transect				*starting*						*ending*					
numbers	*yr*	*mn*	*day*	*ens**	*hr*	*min*	*sec*	*longitude*	*latitude*	*ens*	*hr*	*min*	*sec*	*longitude*	*latitude*
01_02	16	6	22	13	9	15	0	-146.4630	61.1209	303	12	28	3	-146.3242	61.0885
04_05	16	6	22	1	12	50	30	-146.3243	61.0919	518	18	7	35	-146.4637	61.1214
06_13	16	6	22	3	18	19	45	-146.4598	61.1205	280	21	47	7	-146.3240	61.0902
14_17	16	6	22	128	21	53	50	-146.3355	61.0915	376	0	22	51	-146.4650	61.1215
18_21	16	6	23	399	0	36	21	-146.4629	61.1209	861	5	12	28	-146.3233	61.0942
22_24	16	6	23	879	5	21	48	-146.3232	61.0962	1140	7	58	28	-146.4645	61.1214
25_26	16	6	23	1161	8	11	11	-146.4680	61.1203	1590	12	27	50	-146.3232	61.1199
27_28	16	6	23	2	13	9	12	-146.3259	61.0913	147	14	34	58	-146.3925	61.1106
29_30	16	6	24	5	13	58	35	-146.3572	61.0966	271	16	38	44	-146.4628	61.1213
31_34	16	6	24	291	16	50	50	-146.4644	61.1207	651	20	45	33	-146.3554	61.0957
35_37	16	6	24	1	20	56	34	-146.3572	61.0988	219	23	8	10	-146.4633	61.1208
38_39	16	6	25	1	8	49	42	-146.3567	61.0960	243	11	21	41	-146.4632	61.1213
40_43	16	6	25	1	11	33	12	-146.4632	61.1213	269	16	2	58	-146.3567	61.0960
44_46	16	6	25	1	16	13	12	-146.3567	61.0960	252	18	52	56	-146.4635	61.1213
47_51	16	6	25	60	18	54	9	-146.4647	61.1226	394	12	58	58	-146.3248	61.0907
52_57	16	6	26	2	13	13	12	-146.3249	61.0922	536	18	31	21	-146.4548	61.1289

SEPTEMBER 2106:

11_11	16	9	22	473	17	57	36	-146.4344	61.1164	617	20	21	36	-146.3236	61.0904
00_01	16	9	21	10	8	33	37	-146.3232	61.0891	272	12	55	48	-146.4634	61.1220
02_02	16	9	21	273	12	56	48	-146.4647	61.1220	579	18	2	48	-146.3240	61.0898
03_04	16	9	21	582	18	5	48	-146.3243	61.0909	786	21	30	12	-146.4640	61.1214
05_05	16	9	21	1	21	42	12	-146.4692	61.1195	209	2	34	12	-146.3239	61.0896
06_06	16	9	22	431	2	44	12	-146.3240	61.0898	635	6	8	12	-146.4638	61.1202
07_08	16	9	22	2	9	4	52	-146.4638	61.1242	209	12	32	36	-146.3239	61.0904
09_09	16	9	22	159	12	43	36	-146.3235	61.0909	384	16	28	36	-146.4368	61.1003
12_12	16	9	23	1	9	46	37	-146.3242	61.0902	209	13	29	37	-146.4633	61.1214
13_13	16	9	23	325	13	31	37	-146.4640	61.1213	612	18	18	37	-146.3237	61.0897
15_15	16	9	24	9	8	38	29	-146.4628	61.1222	278	13	7	29	-146.3237	61.0899
16_16	16	9	24	285	13	14	29	-146.3242	61.0909	464	16	13	29	-146.4634	61.1218
19_19	16	9	25	7	9	16	56	-146.3235	61.0903	282	13	51	56	-146.4630	61.1220
20_20	16	9	25	300	14	9	56	-146.4653	61.1211	487	17	16	56	-146.3240	61.0907

MARCH 2017:

21_22	17	3	21	2	9	11	31	-146.3252	61.0900	264	13	33	31	-146.4614	61.1224
23_23	17	3	21	277	13	46	31	-146.4645	61.1212	559	18	28	31	-146.3240	61.0899
05_05	17	3	24	7	7	43	9	-146.3238	61.0909	273	12	9	10	-146.4642	61.1134
06_06	17	3	24	290	12	26	11	-146.4652	61.1193	528	16	24	11	-146.3241	61.0897
07_07^	17	3	25	11	7	7	17	-146.3259	61.0908	333	12	29	19	-146.4537	61.1268

* The data record number of ensembles of Doppler shifted return echoes averaged temporally every 30sec and vertically into 8m depth bins.

^ This set of transects and some earlier partial runs were too corrupted with noise caused by wave action to be used.

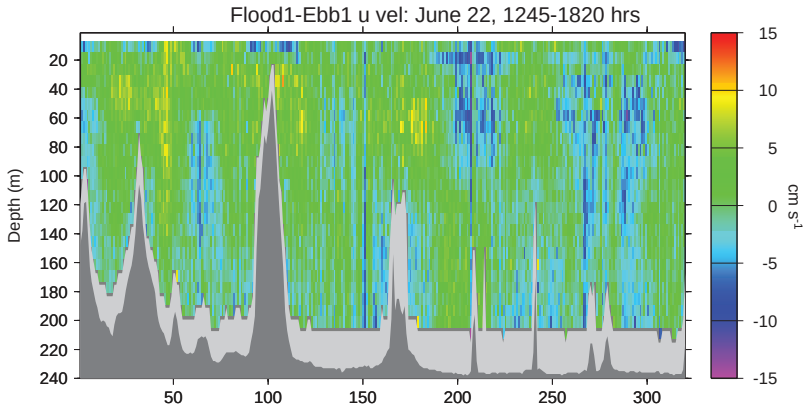

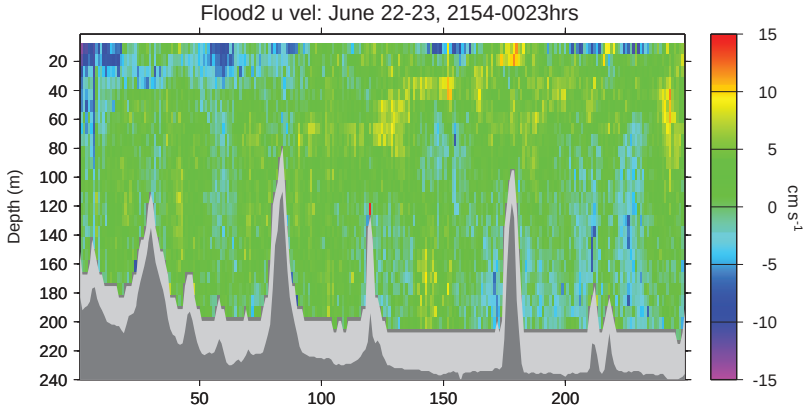

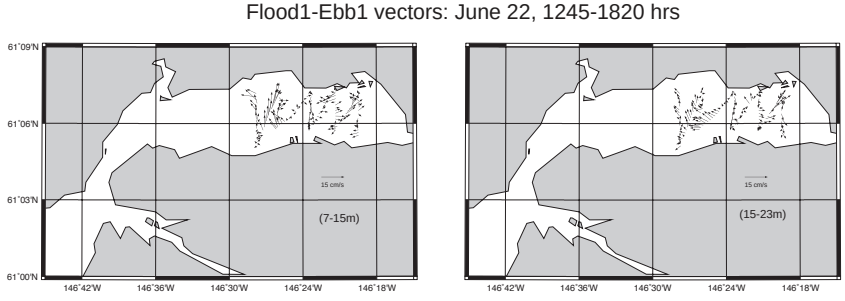

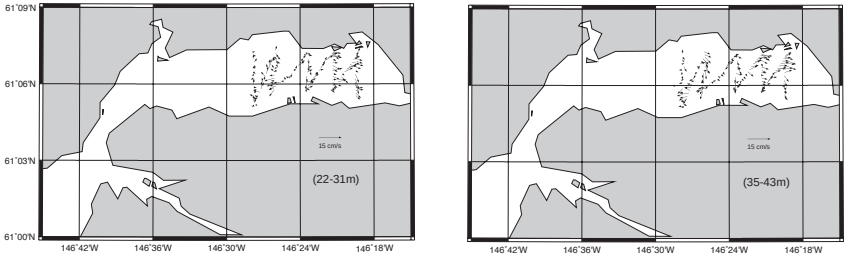

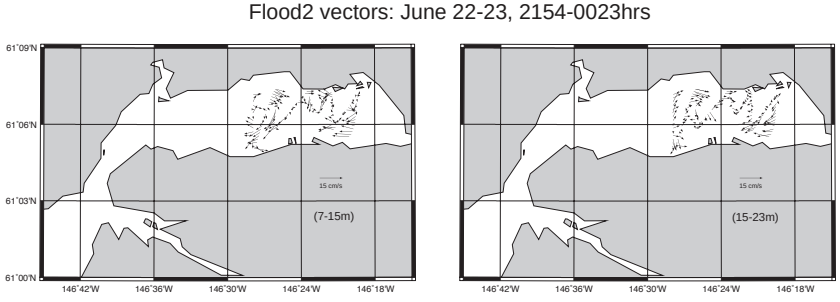

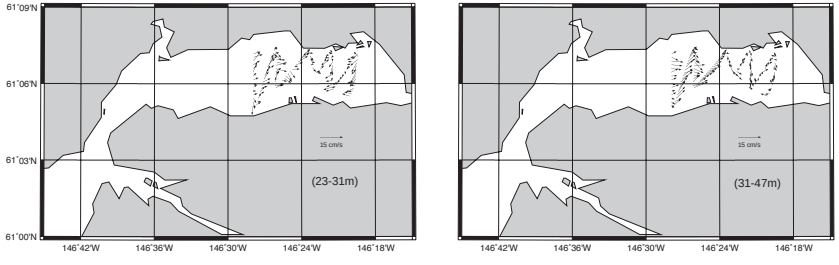

Appendix B (cont.). ADCP along-channel (u) velocities and horizontal vectors in June 2016 for flood1-ebb1 and flood2 on the 22nd and 23rd.

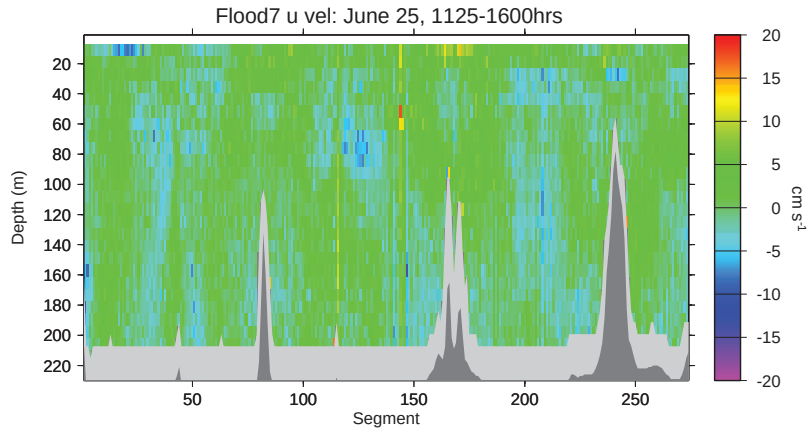

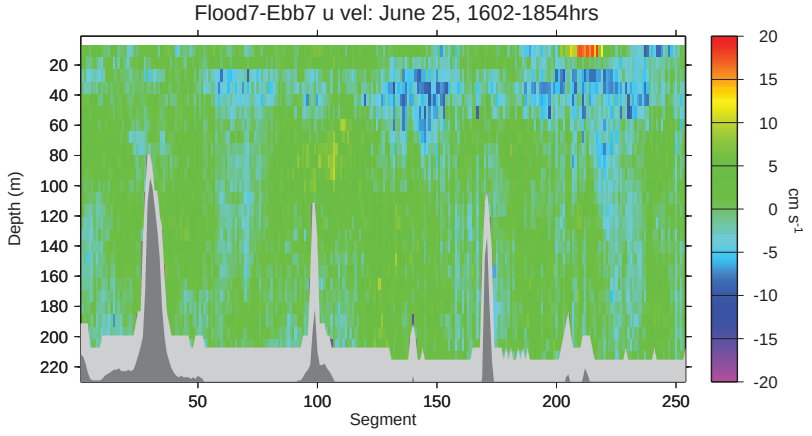

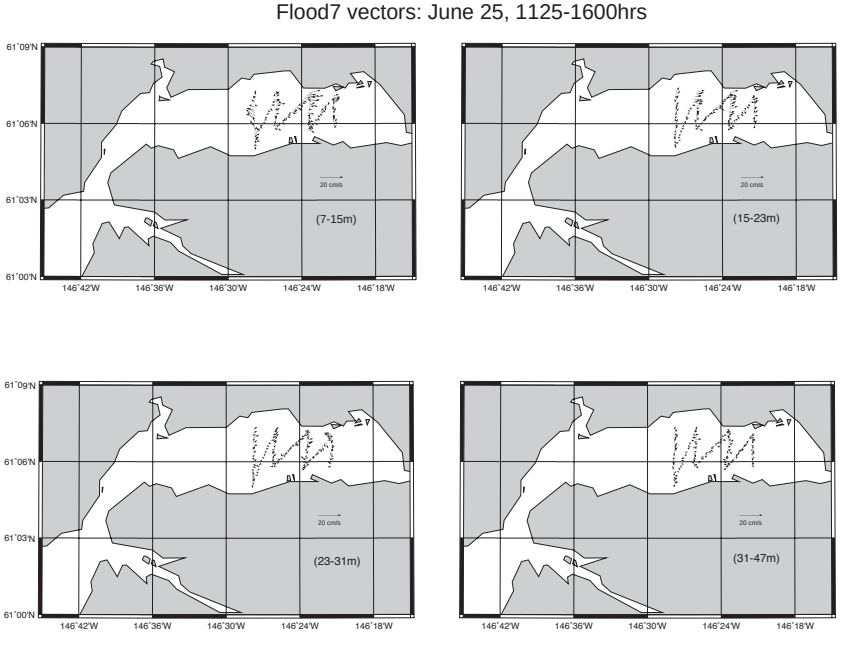

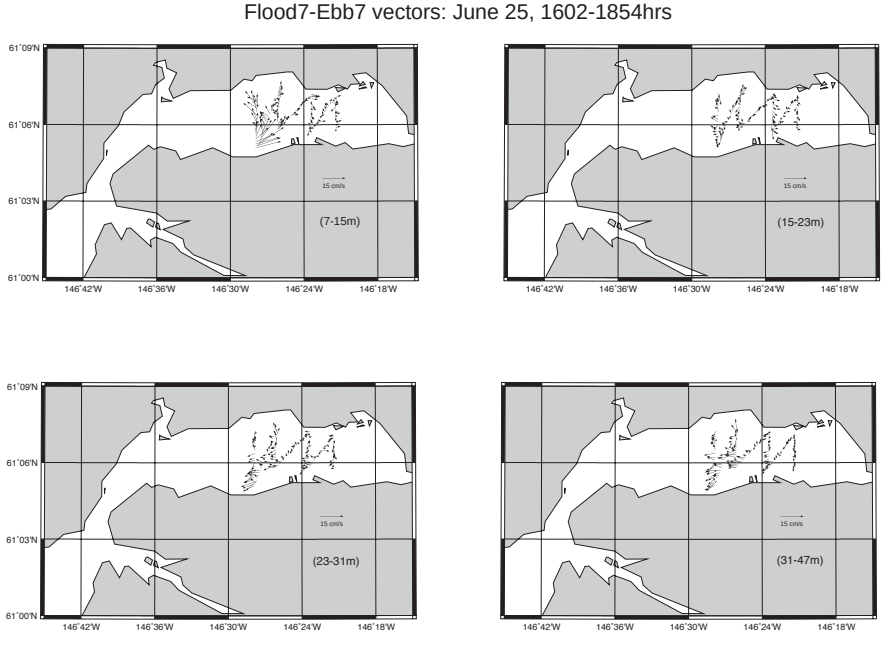

Appendix B (cont.). ADCP along-channel (u) velocities and horizontal vectors in June 2016 for flood7 and flood7-ebb7 on the 25th.

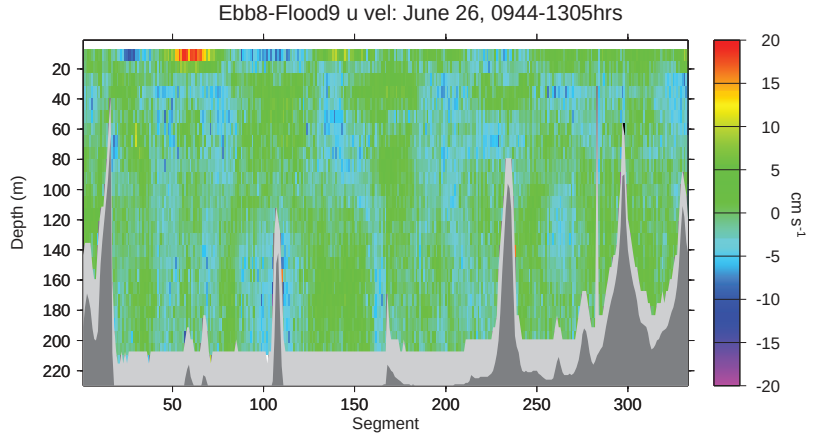

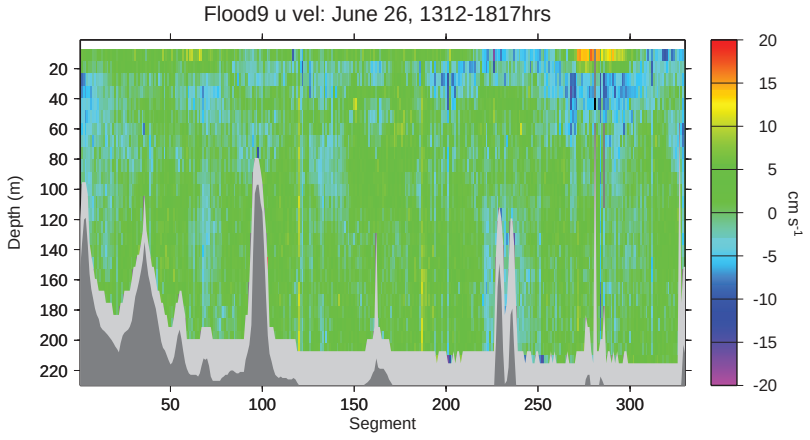

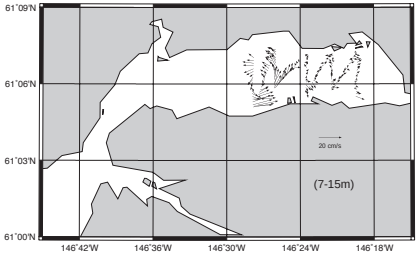

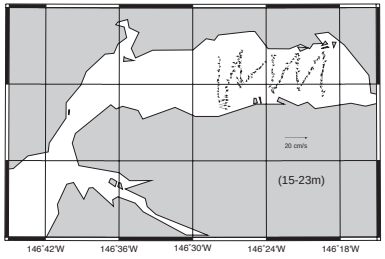

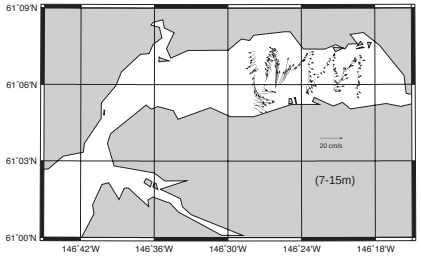

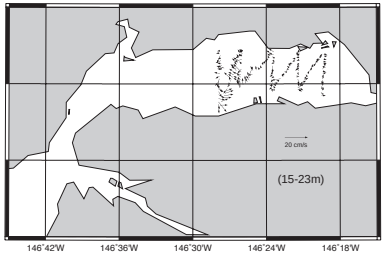

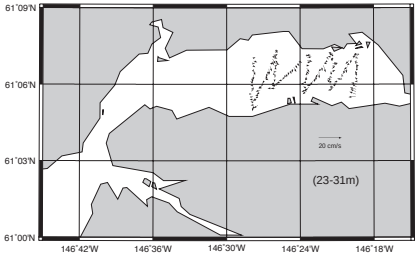

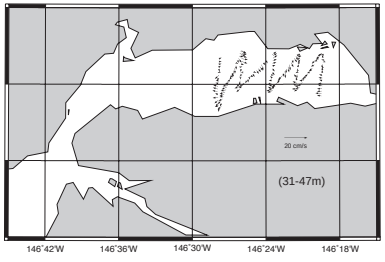

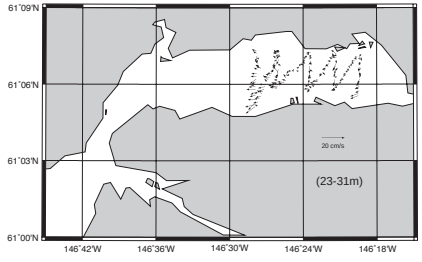

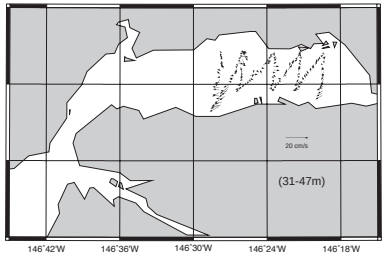

Appendix B (cont.). ADCP along-channel (u) velocities and horizontal vectors in June 2016 for ebb8-flood9 and flood9 on the 26th.

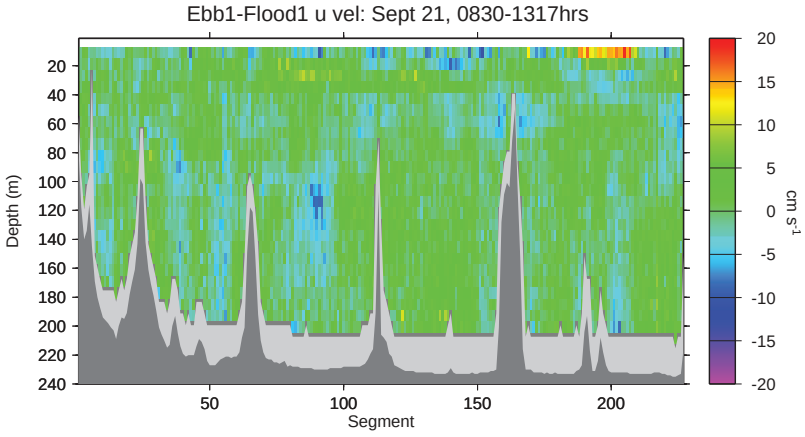

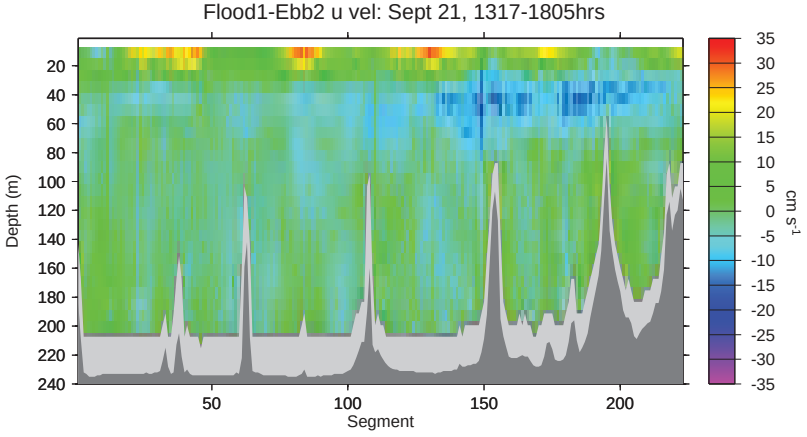

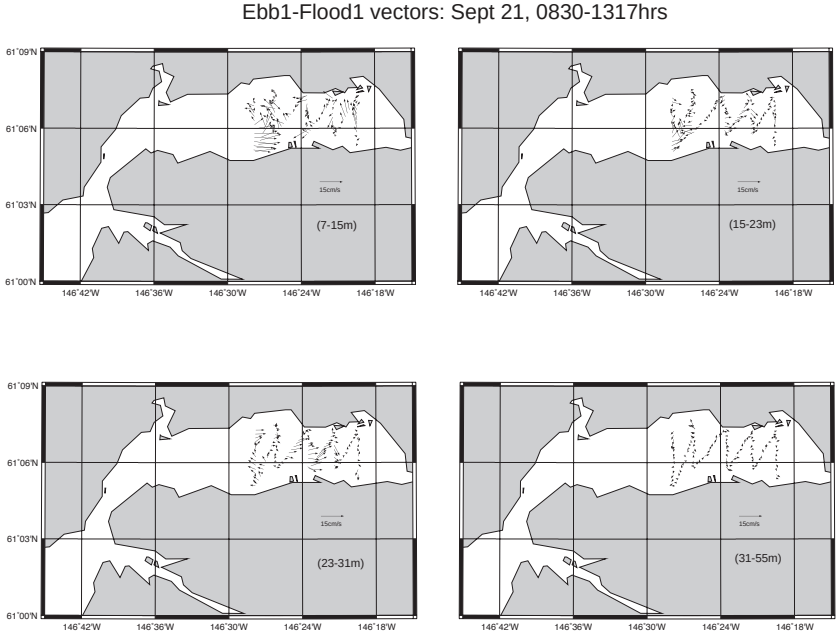

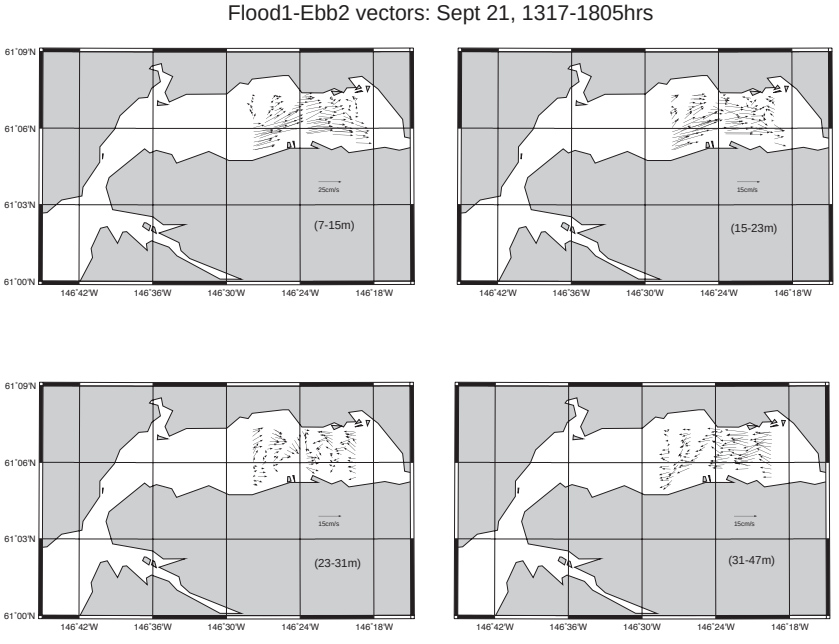

Appendix B (cont.). ADCP along-channel (u) velocities and horizontal vectors in Sepetmber 2016 for ebb1-flood1 and flood1-ebb2 on the 21st.

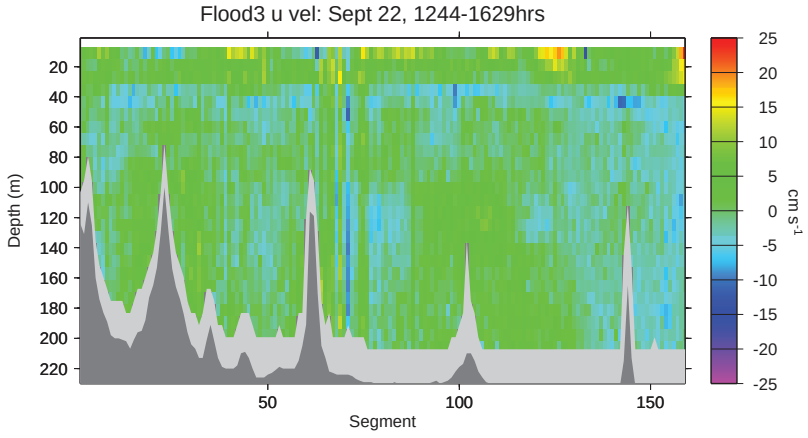

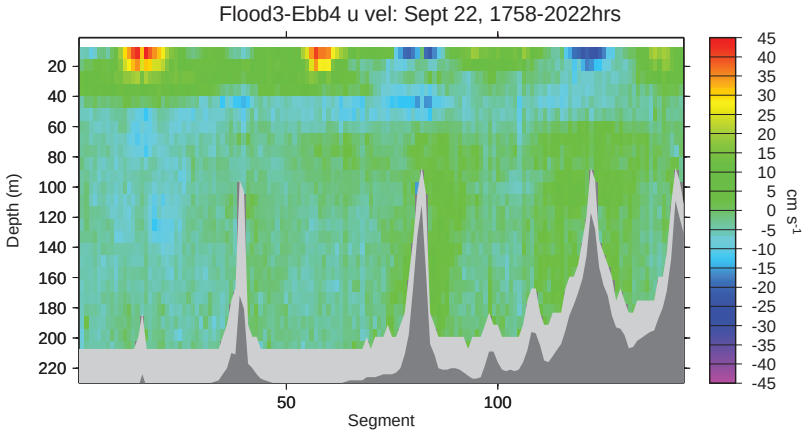

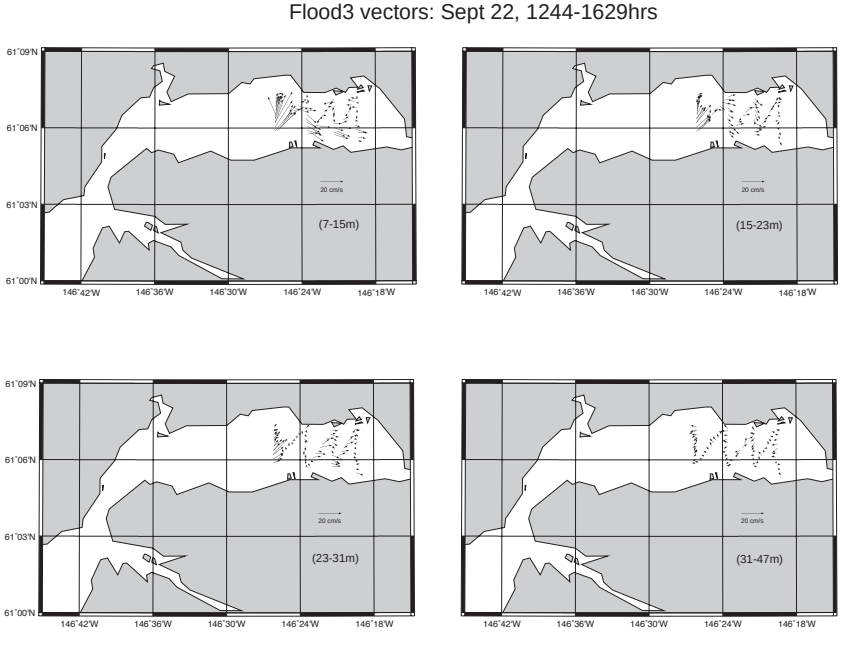

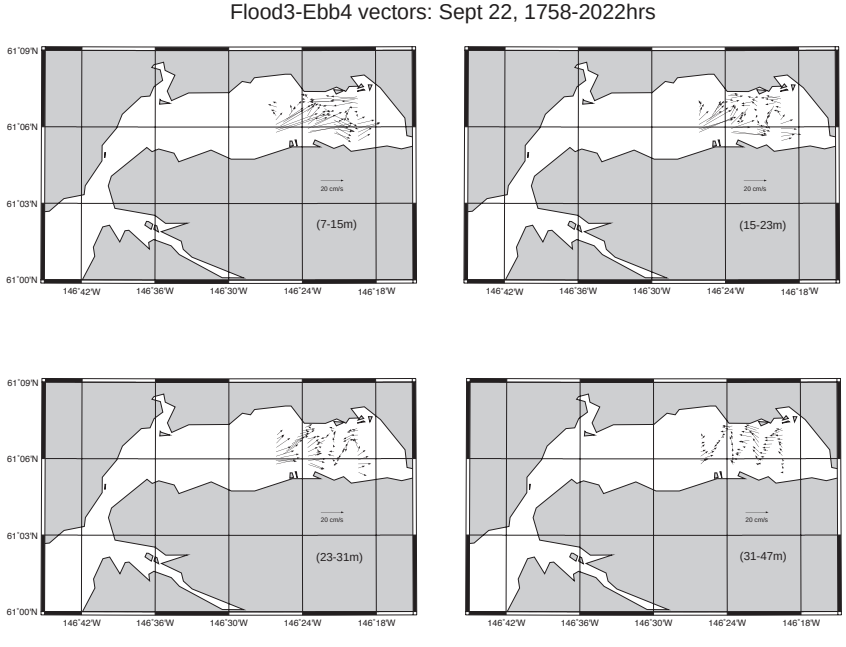

Appendix B (cont.). ADCP along-channel (u) velocities and horizontal vectors in Sepetmber 2016 for flood3 and flood3-ebb4 on the 22nd.

Appendix C: Drifter deployments, including dates, times and start and end coordinates

JUNE 2016:

	Buoy	*Starting:*				*Ending:*			
Deply.	*type & id*	*yr-mn-day*	*time*	*longitude*	*latitude*	*yr-mn-day*	*time*	*longitude*	*latitude*
1	mstar007	6/22/16	19:00:07	-146.3942	61.1060	6/23/16	5:30:06	-146.3337	61.0892
1	isph0460	6/22/16	19:00:00	-146.3936	61.1062	6/23/16	17:00:00	-146.2774	61.0860
2	mstar001	6/23/16	2:30:08	-146.4604	61.1157	6/24/16	0:30:08	-146.5488	61.1164
2	isph5480	6/23/16	2:00:00	-146.4610	61.1092	6/26/16	14:00:00	-146.4616	61.1332
2	svp10004	6/23/16	2:30:08	-146.4615	61.1157	6/26/16	15:30:08	-146.6017	61.0846
3	isph9460	6/23/16	19:00:00	-146.4226	61.1088	6/26/16	14:00:00	-146.4846	61.1282
3	mstar007	6/23/16	18:20:07	-146.4134	61.1102	6/27/16	20:00:07	-146.4567	61.1167
3	svp10008	6/23/16	18:20:08	-146.4136	61.1102	6/27/16	19:30:08	-146.3107	61.0977
4	svp10007	6/24/16	23:30:07	-146.4343	61.1092	6/27/16	19:30:07	-146.3752	61.0975
4	mstar001	6/24/16	23:30:09	-146.4343	61.1092	6/26/16	16:30:09	-146.6882	61.0611
4	isph0460	6/25/16	0:00:00	-146.4350	61.1092	6/27/16	19:00:00	-146.4696	61.1298
5	isph6350	6/25/16	22:00:00	-146.4108	61.1104	6/30/16	21:00:00	-146.2890	61.1242
5	mstar003	6/25/16	22:30:08	-146.4105	61.1115	6/27/16	20:30:37	-146.4146	61.1249
5	svp10002	6/25/16	21:50:05	-146.4115	61.1101	6/27/16	20:30:37	-146.3883	61.1217
5	svp40001	6/25/16	21:50:00	-146.4115	61.1102	7/1/16	19:30:00	-146.3275	61.1035
6	isph0460	6/27/16	23:00:00	-146.4280	61.1112	6/28/16	23:00:00	-146.3102	61.1250
6	mstar003	6/27/16	23:00:07	-146.4305	61.1098	6/28/16	18:30:08	-146.6109	61.0879
6	svp10002	6/27/16	23:00:08	-146.4270	61.1119	6/29/16	19:00:08	-146.5062	61.1076
6	isph9460	6/27/16	23:00:00	-146.4262	61.1118	6/28/16	23:00:00	-146.3104	61.1238
6	mstar007	6/27/16	23:00:36	-146.4261	61.1119	6/28/16	17:00:07	-146.5429	61.0882
6	svp10007	6/27/16	23:00:09	-146.4255	61.1124	6/29/16	18:30:07	-146.5060	61.1138
6	isph2460	6/27/16	23:00:00	-146.4250	61.1124	7/1/16	-----*	-146.3042	61.1336
6	mstar008	6/27/16	23:00:08	-146.4246	61.1124	6/28/16	18:30:07	-146.5350	61.0895
6	svp10008	6/27/16	23:00:37	-146.4241	61.1126	6/29/16	18:30:08	-146.5244	61.1110
7	mstar008	6/28/16	19:00:08	-146.4640	61.1137	6/29/16	20:00:08	-146.3782	61.1193
7	mstar007	6/28/16	19:00:07	-146.4632	61.1148	6/29/16	19:30:07	-146.3568	61.1184
7	mstar003	6/28/16	19:00:08	-146.4628	61.1160	6/29/16	19:30:07	-146.3600	61.1178
8	mstar004	6/28/16	20:10:05	-146.4154	61.1234	6/29/16	19:00:08	-146.5569	61.1210
8	mstar006	6/28/16	20:10:05	-146.4151	61.1229	6/29/16	18:30:07	-146.3647	61.1161
8	svp10004	6/28/16	20:20:05	-146.4143	61.1220	6/29/16	19:00:08	-146.5681	61.1140
8	svp10006	6/28/16	20:20:05	-146.4156	61.1225	6/29/16	18:30:07	-146.5305	61.1222
9	mstar005	6/28/16	21:10:05	-146.3634	61.1071	6/29/16	19:30:37	-146.4700	61.1092
9	svp10005	6/28/16	21:10:05	-146.3619	61.1078	6/29/16	20:00:08	-146.3294	61.1168
10	isph9460	6/29/16	20:44:00	-146.5004	61.1028	6/30/16	2:00:00	-146.3928	61.0860
10	mstar008	6/29/16	20:30:08	-146.5001	61.1024	7/1/16	19:00:08	-146.4341	61.1176
10	mstar007	6/29/16	20:30:07	-146.5011	61.1030	7/1/16	19:00:07	-146.4996	61.1221
10	mstar004	6/29/16	20:30:09	-146.4997	61.1041	6/30/16	2:30:08	-146.4035	61.0982
10	svp10005	6/29/16	20:30:08	-146.5012	61.1025	7/1/16	18:30:08	-146.4089	61.1021
10	svp10002	6/29/16	20:30:08	-146.5006	61.1036	7/1/16	18:30:07	-146.4084	61.1014
10	svp10008	6/29/16	21:00:08	-146.4993	61.1018	7/1/16	19:00:08	-146.4341	61.1176
11	isph0460	6/29/16	20:38:00	-146.4992	61.0928	6/30/16	2:00:00	-146.4210	61.0866
11	mstar003	6/29/16	21:00:37	-146.5023	61.0948	7/1/16	18:00:08	-146.4117	61.1311
11	mstar005	6/29/16	21:00:10	-146.5018	61.0938	6/30/16	3:00:08	-146.4745	61.0856
11	mstar006	6/29/16	21:00:36	-146.5011	61.0932	6/30/16	3:00:08	-146.4745	61.0856
11	svp10004	6/29/16	21:00:08	-146.5006	61.0941	7/1/16	18:00:36	-146.4014	61.1162
11	svp10006	6/29/16	21:00:08	-146.4997	61.0936	7/1/16	18:00:36	-146.4040	61.1201
11	svp10007	6/29/16	21:00:07	-146.4990	61.0927	7/1/16	18:00:08	-146.4093	61.1213

* isph2460 was stuck in the Duck Flats until retreieved on 7/1/2016.

	Buoy	*Starting:*				*Ending:*			
Deply.	*type & id*	*yr-mn-day*	*time*	*longitude*	*latitude*	*yr-mn-day*	*time*	*longitude*	*latitude*
12	mstar006	6/30/16	4:00:07	-146.4337	61.1109	6/30/16	19:30:09	-146.6410	61.1107
12	mstar004	6/30/16	4:00:55	-146.4332	61.1114	6/30/16	19:30:07	-146.6658	61.0847
12	mstar005	6/30/16	4:01:00	-146.4331	61.1112	6/30/16	19:30:07	-146.6688	61.0844
12	mstar003	6/30/16	4:00:08	-146.4336	61.1102	7/1/16	18:00:08	-146.4117	61.1311
12	mstar007	6/30/16	4:00:37	-146.4329	61.1103	7/1/16	19:00:07	-146.4996	61.1221
12	mstar008	6/30/16	4:00:37	-146.4340	61.1104	7/1/16	19:00:08	-146.4341	61.1176
13	mstar004	6/30/16	20:00:37	-146.4634	61.1087	7/1/16	1:30:08	-146.3836	61.0944
13	mstar005	6/30/16	20:00:07	-146.4693	61.1085	7/1/16	1:30:08	-146.3877	61.0947
13	mstar006	6/30/16	20:00:09	-146.4690	61.1085	7/1/16	1:30:07	-146.3905	61.0944

SEPTEMBER 2016:

1	isph0600	9/21/16	18:30:00	-146.3884	61.1112	9/22/16	15:30:00	-146.5894	61.0836
1	isph8180	9/21/16	18:30:00	-146.3872	61.1102	9/22/16	13:00:00	-146.6038	61.0834
1	mstar004	9/21/16	19:00:10	-146.3858	61.1083	9/22/16	16:00:36	-146.6082	61.1123
1	mstar006	9/21/16	19:00:08	-146.3867	61.1098	9/22/16	16:00:10	-146.6225	61.1136
1	svp10005	9/21/16	18:30:07	-146.3919	61.1115	9/23/16	18:00:37	-146.5082	61.1188
1	svp10006	9/21/16	18:30:08	-146.3923	61.1106	9/25/16	16:30:07	-146.5815	61.1028
2	isph0460	9/21/16	21:00:00	-146.4652	61.1100	9/22/16	16:00:00	-146.5910	61.0910
2	isph2460	9/21/16	21:00:00	-146.4636	61.1092	9/22/16	16:00:00	-146.5908	61.0908
2	mstar003	9/21/16	21:00:07	-146.4642	61.1111	9/22/16	15:00:36	-146.6675	61.0679
2	mstar007	9/21/16	21:00:07	-146.4633	61.1106	9/22/16	15:00:36	-146.6762	61.0682
2	svp10002	9/21/16	21:00:08	-146.4651	61.1114	9/23/16	17:00:07	-146.3555	61.0902
2	svp10004	9/21/16	21:00:08	-146.4643	61.1109	9/23/16	23:30:07	-146.3391	61.0966
3	isph8180	9/22/16	22:00:00	-146.3757	61.1065	9/23/16	1:00:00	no transmissions	
3	isph0460	9/22/16	22:17:00	-146.3766	61.1060	9/23/16	1:00:00	-146.4438	61.1050
3	mstar004	9/22/16	22:20:03	-146.3762	61.1067	9/23/16	23:30:08	-146.5313	61.0975
3	mstar003	9/22/16	22:20:05	-146.3774	61.1055	9/22/16	15:00:36	-146.6675	61.0679
4	isph2460	9/22/16	23:30:00	-146.4088	61.1126	9/26/16	23:00:00	-147.8772	60.7132
4	isph0600	9/22/16	23:30:00	-146.4114	61.1118	9/30/16	22:00:00	-147.5024	60.2604
4	mstar007	9/22/16	23:30:05	-146.4100	61.1127	9/23/16	17:33:59	-146.6484	61.1067
4	mstar006	9/22/16	23:30:05	-146.4107	61.1120	9/23/16	23:30:07	-146.5127	61.1020
4	svp40002	9/23/16	2:00:00	-146.3910	61.1124	9/30/16	18:10:00	-146.5578	61.1187
5	mstar006	9/23/16	18:30:37	-146.4005	61.1104	9/24/16	3:30:08	-146.5363	61.0881
5	mstar007	9/23/16	18:30:09	-146.4016	61.1104	9/24/16	3:30:08	-146.5308	61.0877
5	mstar003	9/23/16	18:30:37	-146.4005	61.1104	9/24/16	3:30:08	-146.5347	61.0872
5	mstar004	9/23/16	18:30:36	-146.4005	61.1104	9/23/16	23:30:08	-146.5313	61.0975
5	svp10005	9/23/16	18:30:08	-146.4017	61.1104	9/25/16	17:30:08	-146.3987	61.1131
5	svp40001	9/24/16	1:00:00	-146.3926	61.1121	9/30/16	18:00:00	-146.5351	61.1209
6	isph0460	9/24/16	19:00:00	-146.3980	61.1130	9/25/16	19:00:00	-146.3928	61.0950
6	isph6350	9/24/16	19:00:00	-146.3980	61.1129	9/25/16	19:00:00	-146.3900	61.0934
6	mstar006	9/24/16	19:00:06	-146.3965	61.1130	9/25/16	17:30:07	-146.4149	61.1114
6	mstar007	9/24/16	19:00:06	-146.3964	61.1131	9/25/16	17:30:36	-146.4188	61.1114
6	svp10008	9/24/16	19:00:06	-146.3941	61.1128	9/25/16	18:00:08	-146.3646	61.1066
6	svp10004	9/24/16	19:00:04	-146.3947	61.1126	9/25/16	17:30:07	-146.4090	61.1195
7	isph5600	9/24/16	21:00:00	-146.3240	61.1104	9/25/16	19:30:00	-146.2706	61.1130
7	isph5480	9/24/16	21:00:00	-146.3242	61.1104	9/25/16	19:00:00	-146.2732	61.1160
7	mstar004	9/24/16	20:50:05	-146.3257	61.1099	9/25/16	17:00:13	-146.5072	61.1177
7	mstar003	9/24/16	20:50:05	-146.3257	61.1102	9/25/16	17:00:08	-146.5072	61.1178
7	svp10007	9/24/16	20:40:05	-146.3247	61.1101	9/25/16	19:00:07	-146.3921	61.0951
7	svp10002	9/24/16	20:40:05	-146.3246	61.1101	9/25/16	19:00:07	-146.3929	61.0951
7	svp40003	9/24/16	21:40:00	-146.3243	61.1097	9/30/16	17:40:00	-146.4924	61.1253

	Buoy	*Starting:*				*Ending:*			
Deply.	*type & id*	*yr-mn-day*	*time*	*longitude*	*latitude*	*yr-mn-day*	*time*	*longitude*	*latitude*
8	isph5600	9/25/16	20:00:00	-146.3778	61.1160	9/26/16	18:30:00	-146.6956	61.0586
8	isph5480	9/25/16	20:00:00	-146.3808	61.1166	9/26/16	17:00:00	-146.8248	60.9996
8	mstar006	9/25/16	20:00:37	-146.3761	61.1158	9/26/16	20:30:07	-146.6347	61.0879
8	mstar007	9/25/16	20:00:07	-146.3801	61.1165	9/26/16	20:30:08	-146.6094	61.0927
8	svp10008	9/25/16	20:00:36	-146.3765	61.1160	9/27/16	21:30:07	-146.3370	61.0997
8	svp10005	9/25/16	20:00:08	-146.3792	61.1165	9/28/16	19:30:09	-146.3780	61.1034
9a	isph0460	9/25/16	20:07:00	-146.4328	61.1052	9/26/16	20:00:00	-146.7498	61.0222
9a	isph6350	9/25/16	20:09:00	-146.4360	61.1046	9/26/16	20:00:00	-146.7490	61.0196
9a	mstar003	9/25/16	20:30:08	-146.4358	61.1059	9/26/16	21:00:08	-146.5616	61.1192
9a	mstar004	9/25/16	20:30:36	-146.4390	61.1055	9/26/16	21:00:08	-146.5371	61.1190
9b	svp10006	9/25/16	22:30:07	-146.4571	61.1097	9/27/16	19:30:07	-146.5429	61.0947
9b	svp10002	9/25/16	22:30:08	-146.4533	61.1097	9/26/16	23:50:07	-146.4594	61.1027
10a	isph5480	9/26/16	21:33:00	-146.4540	61.1038	9/27/16	19:00:00	-146.5206	61.1150
10a	isph0460	9/26/16	21:31:00	-146.4548	61.1052	9/27/16	19:00:00	-146.5286	61.1120
10a	mstar006	9/26/16	22:00:04	-146.4558	61.1035	9/27/16	18:30:36	-146.6160	61.1143
10a	mstar007	9/26/16	22:00:08	-146.4558	61.1047	9/27/16	18:30:36	-146.6494	61.0845
10b	isph5600	9/26/16	21:51:00	-146.3148	61.1068	9/27/16	17:30:00	-146.2996	61.1270
10b	isph6350	9/26/16	21:46:00	-146.3192	61.1062	9/27/16	20:00:00	-146.4334	61.1180
10b	mstar003	9/26/16	21:50:05	-146.3184	61.1061	9/27/16	21:30:09	-146.3128	61.0859
10b	mstar004	9/26/16	21:50:05	-146.3147	61.1068	9/27/16	20:30:07	-146.4189	61.0936
11	isph6350	9/27/16	21:00:00	-146.4162	61.1096	9/28/16	12:00:00	-146.3392	61.1242
11	isph9180	9/27/16	21:06:00	-146.4172	61.1110	9/28/16	17:00:00	-146.3404	61.1220
11	mstar004	9/27/16	21:10:03	-146.4163	61.1096	9/28/16	18:30:06	-146.6068	61.0930
11	mstar006	9/27/16	21:10:03	-146.4183	61.1110	9/28/16	18:30:08	-146.5836	61.0869
11	svp10007	9/27/16	21:00:08	-146.4164	61.1098	9/30/16	18:30:07	-146.5306	61.0940
11	svp10002	9/27/16	21:10:05	-146.4190	61.1110	9/30/16	18:30:08	-146.5226	61.0921
12	isph0460	9/27/16	21:20:00	-146.3728	61.1110	9/28/16	18:00:00	-146.3138	61.1256
12	mstar007	9/27/16	21:30:10	-146.3649	61.1095	9/28/16	18:30:37	-146.5260	61.0851
12	mstar008	9/27/16	21:30:05	-146.3704	61.1107	9/28/16	16:00:07	-146.5201	61.1151
12	svp10006	9/27/16	21:20:05	-146.3654	61.1097	9/29/16	18:30:06	-146.3206	61.0981
12	svp10003	9/27/16	21:30:05	-146.3707	61.1107	9/29/16	18:30:07	-146.3037	61.0992
13	isph5480	9/27/16	21:52:00	-146.3166	61.1002	9/28/16	16:00:00	-146.4636	61.1326
13	isph5600	9/27/16	21:56:00	-146.3178	61.1000	9/28/16	16:30:00	-146.4846	61.1282
13	mstar003	9/27/16	22:00:05	-146.3177	61.1001	9/28/16	16:00:07	-146.4267	61.0910
13	svp10008	9/27/16	22:00:05	-146.3184	61.1000	9/28/16	19:30:08	-146.3779	61.1034
14	isph5480	9/28/16	19:00:00	-146.4356	61.1080	9/29/16	17:00:00	-146.5206	61.1178
14	isph6350	9/28/16	19:00:00	-146.4332	61.1088	9/29/16	17:00:00	-146.5226	61.1170
14	mstar007	9/28/16	19:00:36	-146.4347	61.1077	9/29/16	18:00:10	-146.5954	61.0941
14	mstar003	9/28/16	19:00:10	-146.4321	61.1085	9/29/16	18:00:36	-146.5925	61.0936
15	isph0460	9/28/16	20:00:00	-146.3308	61.1084	9/29/16	17:00:00	-146.3096	61.1206
15	mstar006	9/28/16	19:30:08	-146.3306	61.1071	9/29/16	18:00:08	-146.3930	61.1036
15	svp10003	9/28/16	19:30:06	-146.3245	61.1106	9/29/16	18:30:07	-146.3037	61.0992
16	isph5600	9/28/16	20:00:00	-146.4134	61.1176	9/29/16	17:30:00	-146.5762	61.1178
16	isph9180	9/28/16	20:30:00	-146.4198	61.1184	9/29/16	17:30:00	-146.5608	61.1216
16	mstar004	9/28/16	20:00:08	-146.4118	61.1166	9/29/16	18:00:37	-146.4636	61.0967
16	svp10008	9/28/16	20:00:08	-146.4105	61.1166	9/30/16	19:00:08	-146.3959	61.1073
16	svp10005	9/28/16	20:00:08	-146.4144	61.1172	9/30/16	19:00:07	-146.3645	61.1141
17	mstar006	9/29/16	19:00:06	-146.3813	61.1134	9/30/16	17:00:12	-146.3574	61.1242
17	mstar007	9/29/16	19:00:11	-146.3782	61.1142	9/30/16	3:30:07	-146.3524	61.1265
18	mstar004	9/29/16	19:00:07	-146.3141	61.1069	9/30/16	18:30:36	-146.5126	61.0945
18	mstar003	9/29/16	19:00:08	-146.3131	61.1059	9/30/16	18:00:09	-146.5681	61.1162
18	svp10003	9/29/16	19:00:07	-146.3127	61.1058	9/30/16	19:00:07	-146.3473	61.0980
18	svp10006	9/29/16	19:00:08	-146.3140	61.1067	9/30/16	19:00:36	-146.3530	61.0997

MARCH 2017:

	Buoy	*Starting:*				*Ending:*			
Deply.	*type & id*	*yr-mn-day*	*time*	*longitude*	*latitude*	*yr-mn-day*	*time*	*longitude*	*latitude*
1	isph9460	3/24/17	15:44:00	-146.3582	61.1104	3/25/17	23:00:00	-146.4574	61.1338
1	isph8450	3/24/17	15:52:00	-146.3552	61.1134	3/25/17	23:00:00	-146.4510	61.1338
1	isph6350	3/24/17	15:56:00	-146.3560	61.1150	3/25/17	23:00:00	-146.4466	61.1342
1	svp10002	3/24/17	15:50:05	-146.3542	61.1129	3/25/17	15:30:35	-146.4896	61.1211
1	svp10005	3/24/17	16:00:05	-146.3555	61.1141	3/25/17	16:00:35	-146.5252	61.1103
1	svp10007	3/24/17	16:00:05	-146.3578	61.1160	3/25/17	15:30:08	-146.4362	61.1204
1	mstar004	3/24/17	15:50:05	-146.3554	61.1114	3/25/17	16:30:35	-146.5709	61.1038
1	mstar005	3/24/17	16:00:05	-146.3560	61.1137	3/25/17	16:30:07	-146.5721	61.1037
1	mstar006	3/24/17	16:00:05	-146.3578	61.1160	3/25/17	16:30:08	-146.5675	61.1049
1	svp40001	3/24/17	16:00:00	-146.3578	61.1160	3/27/17	16:00:00	-146.5593	61.1078
2	isph9180	3/24/17	17:55:00	-146.3568	61.0960	3/24/17	23:30:00	-146.4860	61.1276
2	isph0460	3/24/17	17:52:00	-146.3570	61.0958	3/24/17	23:00:00	-146.4730	61.1264
2	isph5600	3/24/17	17:55:00	-146.3570	61.0958	3/24/17	23:30:00	-146.4876	61.1276
3	isph5480	3/25/17	17:14:00	-146.3738	61.1092	3/25/17	21:00:00	-146.4610	61.1204
3	isph0600	3/25/17	17:17:00	-146.3736	61.1094	3/25/17	21:00:00	-146.4576	61.1204
3	mstar004	3/25/17	17:30:10	-146.3726	61.1097	3/30/17	17:00:35	-146.4433	61.0868
3	mstar005	3/25/17	17:30:07	-146.3730	61.1095	3/30/17	19:00:08	-146.4848	61.1017
3	mstar006	3/25/17	17:30:08	-146.3721	61.1098	3/27/17	15:30:11	-146.5948	61.0913
3	svp10002	3/25/17	17:31:06	-146.3737	61.1094	3/29/17	17:00:08	-146.5540	61.0985
3	svp10005	3/25/17	17:30:09	-146.3739	61.1095	3/29/17	17:00:08	-146.5700	61.1196
3	svp10007	3/25/17	17:30:07	-146.3747	61.1095	3/29/17	17:00:08	-146.5530	61.1225
4	isph9460	3/26/17	18:00:00	-146.4588	61.0930	3/26/17	21:00:00	-146.4870	61.0794
4	isph8450	3/26/17	18:00:00	-146.4608	61.0912	3/26/17	21:00:00	-146.4882	61.0794
4	isph6350	3/26/17	18:00:00	-146.4618	61.0908	3/26/17	21:00:00	-146.4884	61.0794
4	mstar001	3/26/17	18:00:05	-146.4571	61.0939	3/26/17	21:30:08	-146.4711	61.0989
4	mstar002	3/26/17	18:00:04	-146.4598	61.0917	3/26/17	21:30:35	-146.4697	61.0978
4	mstar007	3/26/17	18:00:05	-146.4612	61.0911	3/26/17	21:30:08	-146.4665	61.0963
4	svp10003	3/26/17	18:00:05	-146.4576	61.0935	3/26/17	21:30:08	-146.4706	61.0994
4	svp10006	3/26/17	18:00:05	-146.4600	61.0916	3/26/17	21:30:08	-146.4666	61.0963
4	svp10001	3/26/17	18:10:05	-146.4615	61.0908	3/26/17	21:30:08	-146.4666	61.0963
5	isph6350	3/26/17	22:00:00	-146.3882	61.1076	3/27/17	16:00:00	-146.5738	61.0796
5	isph8450	3/26/17	22:00:00	-146.3896	61.1074	3/27/17	16:00:00	-146.5736	61.0792
5	isph9460	3/26/17	22:00:00	-146.3908	61.1074	3/27/17	16:00:00	-146.5736	61.0792
5	mstar001	3/26/17	22:01:00	-146.3874	61.1077	3/30/17	17:00:35	-146.4469	61.0876
5	mstar002	3/26/17	22:00:08	-146.3892	61.1075	3/30/17	17:00:35	-146.5175	61.0852
5	mstar007	3/26/17	22:00:36	-146.3908	61.1074	3/30/17	19:00:08	-146.4930	61.1037
5	svp10003	3/26/17	22:00:06	-146.3871	61.1077	3/29/17	17:00:08	-146.5529	61.1225
5	svp10006	3/26/17	22:00:08	-146.3886	61.1075	3/29/17	17:00:22	-146.5538	61.1223
5	svp10001	3/26/17	22:00:09	-146.3904	61.1074	3/29/17	17:00:08	-146.5701	61.1192
6	isph6350	3/27/17	20:00:00	-146.4028	61.1074	3/28/17	3:00:00	-146.5094	61.0820
6	isph8450	3/27/17	20:00:00	-146.4030	61.1074	3/28/17	15:00:00	-146.5372	61.0852
6	isph9460	3/27/17	20:00:00	-146.4028	61.1074	3/28/17	18:00:00	-146.5714	61.0814
6	mstar006	3/27/17	19:30:09	-146.3998	61.1113	3/30/17	19:00:07	-146.4734	61.0970
6	svp40001	3/27/17	19:30:00	-146.3972	61.1115	3/30/17	18:00:00	-146.5487	61.0896
6	svp40002	3/27/17	19:30:00	-146.3961	61.1114	3/30/17	18:00:00	-146.5490	61.0885
7	isph9460	3/28/17	21:00:00	-146.5292	61.0988	3/30/17	16:00:00	-146.3678	61.1022
7	isph8450	3/28/17	21:00:00	-146.5290	61.0990	3/30/17	16:00:00	-146.3684	61.1024
8	svp10001	3/29/17	18:00:08	-146.4968	61.1160	3/30/17	18:00:08	-146.5000	61.1106
8	svp10002	3/29/17	18:00:09	-146.4985	61.1158	3/30/17	18:00:07	-146.5130	61.1108
8	svp10007	3/29/17	18:00:35	-146.4951	61.1159	3/30/17	18:00:08	-146.4930	61.1085
8	svp10003	3/29/17	18:00:08	-146.4917	61.1161	3/30/17	18:00:09	-146.5278	61.0893
8	svp10005	3/29/17	18:00:09	-146.4937	61.1157	3/30/17	17:30:07	-146.5215	61.0869
8	svp10006	3/29/17	18:00:35	-146.4928	61.1159	3/30/17	18:00:36	-146.5277	61.0893

Appendix D. T Tests for means of drifter speeds & u velocities

Speeds (Monthly)

ispheres	*N*	*Avg*	*SD*	S^2	Sp^2*	*yb1 - yb2* ^	*t value*	*t cr. val.*	*req Ho?*
June	8	0.250	0.140	0.0196	0.0138	0.055	1.056	1.725	no
Sept	14	0.195	0.103	0.0107	0.0180	-0.002	-0.032	1.782	no
March	6	0.253	0.126	0.0158	0.0121	0.057	1.067	1.734	no
mstars									
June	13	0.181	0.079	0.0062	0.0041	0.038	1.567	1.314	yes
Sept	16	0.143	0.050	0.0025	0.0052	0.093	2.262	1.753	yes
March	4	0.088	0.036	0.0013	0.0023	0.055	2.057	1.734	yes
SVPs									
June	9	0.073	0.020	0.0004	0.0002	0.028	3.979	1.740	yes
Sept	10	0.045	0.008	0.0001	0.0004	0.007	0.635	1.782	no
March	5	0.066	0.017	0.0003	0.0001	0.021	3.297	1.771	yes

Speeds (w/in Months): ispheres vs. mstars vs. SVPs

June									
isph	8	0.250	0.140	0.0196	0.0111	0.069	1.466	1.328	yes
mstar	13	0.181	0.079	0.0062	0.0094	0.178	3.776	1.746	yes
SVP	9	0.073	0.020	0.0004	0.0039	0.108	4.012	1.721	yes
September									
isph	14	0.195	0.103	0.0107	0.0063	0.052	1.792	1.313	yes
mstar	16	0.143	0.050	0.0025	0.0063	0.150	4.557	1.717	yes
SVP	10	0.045	0.008	0.0001	0.0016	0.098	6.069	1.711	yes
March									
isph	6	0.253	0.126	0.0158	0.0103	0.165	2.512	1.397	yes
mstar	4	0.088	0.036	0.0013	0.0089	0.187	3.269	1.833	yes
SVP	5	0.066	0.017	0.0003	0.0007	0.022	1.222	1.895	no

u velocities (Monthly)

ispheres									
June	8	0.051	0.149	0.0221	0.0216	0.148	2.273	1.725	yes
Sept	14	-0.097	0.146	0.0213	0.0239	0.249	2.988	1.782	yes
March	6	-0.198	0.162	0.0263	0.0227	0.101	1.379	1.734	no
mstars									
June	13	0.023	0.129	0.0167	0.0103	0.135	3.567	1.703	yes
Sept	16	-0.112	0.072	0.0052	0.0139	0.071	1.055	1.753	no
March	4	-0.048	0.051	0.0026	0.0047	0.064	1.665	1.734	yes
SVPs									
June	9	-0.014	0.045	0.0020	0.0013	-0.008	-0.501	1.740	no
Sept	10	-0.006	0.026	0.0007	0.0017	0.020	0.876	1.782	no
March	5	-0.034	0.033	0.0011	0.0008	0.028	1.829	1.771	yes

u velocities (w/in Months): ispheres vs. mstars vs. SVPs

June	*N*	*Avg*	*SD*	S^2	Sp^2*	*yb1 - yb2* ^	*t value*	*t cr. val.*	*req Ho?*
isph	8	0.051	0.149	0.0221	0.0187	0.042	0.679	1.729	no
mstar	13	0.009	0.129	0.0167	0.0114	0.065	1.249	1.746	no
SVP	9	-0.014	0.045	0.0020	0.0108	0.023	0.510	1.721	no
September									
isph	14	-0.106	0.146	0.0213	0.0126	0.007	0.160	1.701	no
mstar	16	-0.112	0.072	0.0052	0.0128	-0.100	-2.134	1.717	yes
SVP	10	-0.006	0.026	0.0007	0.0035	0.107	4.481	1.711	yes
March									
isph	6	-0.198	0.162	0.0263	0.0174	-0.150	-1.763	1.397	yes
mstar	4	-0.048	0.051	0.0026	0.0151	-0.164	-2.209	1.383	yes
SVP	5	-0.034	0.033	0.0011	0.0017	0.014	0.507	1.895	no
June segment 1 vs. 2:									
speeds:									
isph seg 1	6	0.255	0.138	0.0191					
isph seg 2	6	0.157	0.075	0.0057	0.0124	0.098	1.526	1.372	yes
mstar seg1	5	0.169	0.058	0.0034					
mstar seg2	15	0.188	0.092	0.0084	0.0073	0.019	0.440	1.330	no
SVP seg1	4	0.061	0.017	0.0003					
SVP seg2	10	0.094	0.037	0.0013	0.0011	0.033	1.689	1.356	yes
u vels:									
isph seg 1	6	0.003	0.1471	0.0216					
isph seg 2	6	0.194	0.1363	0.0186	0.0201	0.190	2.323	1.812	yes
mstar seg1	5	-0.015	0.06833	0.0047					
mstar seg2	15	0.017	0.15928	0.0254	0.0208	0.032	0.426	1.330	no
SVP seg1	4	0.002	0.01844	0.0003					
SVP seg2	10	-0.006	0.05225	0.0027	0.0021	0.008	0.302	1.356	no
isph seg 2	6	0.194	0.1363	0.0186					
mstar seg2	15	0.017	0.15928	0.0254	0.0236	0.176	2.379	1.725	yes
September segment 1 vs. 2:									
speeds:									
isph seg 1	5	0.259	0.139	0.0192					
isph seg 2	9	0.183	0.071	0.0050	0.0097	0.076	1.386	1.356	yes
mstar seg1	7	0.193	0.063	0.0039					
mstar seg2	9	0.139	0.033	0.0011	0.0023	0.055	2.252	1.761	yes
SVP seg1	5	0.098	0.0517	0.0027					
SVP seg2	6	0.0493	0.0054	0.0000	0.0012	0.049	2.318	1.833	yes
SVP40 seg1	3	0.0583	0.0036	0.00001					
SVP40 seg2	3	0.0468	0.0057	0.00003	0.0000	0.012	2.955	2.132	yes
u vels:									
isph seg 1	5	-0.134	0.213	0.0452					
isph seg 2	9	-0.090	0.106	0.0112	0.0225	0.044	0.522	1.356	no
mstar seg1	7	-0.160	0.080	0.0063					
mstar seg2	9	-0.094	0.062	0.0038	0.0049	0.067	1.885	1.761	yes
SVP seg1	5	-0.005	0.052	0.0027					
SVP seg2	6	-0.008	0.021	0.0004	0.0014	0.004	0.166	1.383	no
SVP40 seg1	3	-0.0119	0.021	0.0004					
SVP40 seg2	3	-0.0152	0.0136	0.0002	0.0003	0.003	0.228	1.533	no

March segment 1 vs. 2:

speeds:	*N*	*Avg*	*SD*	S^2	Sp^2*	*yb1 - yb2* ^	*t value*	*t cr. val.*	*req Ho?*
isph seg 1	3	0.365	0.0305	0.0009					
isph seg 2	3	0.0706	0.0285	0.0008	0.0009	0.294	12.216	2.132	yes
mstar seg1	2	0.1155	0.0403	0.0016					
mstar seg2	4	0.0665	0.0176	0.0003	0.0006	0.049	2.239	2.132	yes
SVP seg1 (1:1)	2	0.091	0.0000	0.0000					
SVP seg2 (2:4)	2	0.060	0.0151	0.0002	0.0001	0.031	2.931	2.290	yes
SVP40 seg1	2	0.0483	0.0031	0.0000					
SVP40 seg2	2	0.0488	0.0004	0.0000	0.0000	0.001	0.227		no
u vels:									
isph seg 1	3	-0.3327	0.0118	0.0001					
isph seg 2	3	-0.0643	0.1080	0.0117	0.0059	0.268	4.279	2.132	yes
mstar seg1	2	-0.100	0.0389	0.0015					
mstar seg2	4	-0.016	0.0047	0.0000	0.0004	0.084	4.881	2.132	yes
SVP seg1 (1:1)	2	-0.08	0.0000	0.0000					
SVP seg2 (2:4)	2	-0.0233	0.0182	0.0003	0.0002	0.057	4.406	2.290	yes

---

* Sp2 = pooled sample variance
^ yb1 - yb2 = difference between means

yes = significant at the 5% alpha level
yes = significant at the 10% alpha level

Appendix E: Detailed description of a possible future RCAC program to model Port Valdez circulation.

Purpose and Description of Program/Project: *Accurate oil spill trajectory modeling efforts within Port Valdez are challenging and less accurate than they could be considering that the models are drawing from coarser central PWS data gathered circa 2009. With the FY16 and FY17 Port Valdez circulation project now complete, a finer resolution, Port Valdez specific data set now exists. This project proposes to construct a high-resolution computer model for Port Valdez and nearby Prince William Sound using the unstructured grid, Finite-Volume, primitive equation Community Ocean Model (FVCOM). This model will be integrated within the Gulf of Alaska model developed by Alaska Ocean Observing System (AOOS) based on the Regional Ocean Modeling System (ROMS). The drifter and other oceanographic data collected during the recent PWSRCAC funded field experiments will be used to validate the developed Port Valdez model. The validated Port Valdez model will be then run in real-time to issue routine forecast of the Port Valdez circulation so that drifting trajectories in case of oil spill can be predicted to support oil spill response and recovery operations.*

How does the program/project support PWSRCAC's mission?
Within OPA 90, PWSRCAC is tasked specifically with studying and monitoring wind and water currents and other environmental factors in the vicinity of the terminal. The Port Valdez circulation project gathered this sort of information, and this proposed project would allow for better visualization of this data and knowledge, and allows us to interact with it via a modeling program. The proposed project essentially represents a logical second phase and gives us a way to access and apply this data as opposed to just reading about it in a report.

How will we know when the project is finished?
The end result of this proposed project is a fully validated computer model that can be used to simulate drifting trajectories in the Port Valdez and nearby Prince William Sound.

How will information and/or results from the program/project be used?
This model will give us real-time forecast of spill trajectories, and the model can also be used to perform hindcast simulations over a multi-year period. Both of these functions will help responders explore various oil spill scenarios and issues, and do so with real data.

List the program/project goals and objectives:

- *Verify that all past Port Valdez circulation data and background materials are in place and have been shared among collaborators.*
- *Construct the Port Valdez model based on this data.*
- *Use buoy trajectories and other circulation features shown by ADCP and hydrography data from past work to verify and fine-tune this model.*
- *Once constructed, the model would be passed on to AOOS for hosting online along with their collection of other modeling and environmental datasets.*
- *Promote and discuss the completed model so the response community is aware this tool exists and are able to use it.*
- *Capture the above process in a summary report.*